POLISH ANATOMICAL SOCIETY

FOLIA
MORPHOLOGICA

Vol. 81   *2022*   *No. 3*

VM
VIA MEDICA

FOLIA
MORPHOLOGICA

EDITORIAL ADVISORY BOARD

VIA MEDICA

R E V I E W   A R T I C L E

Assessment of the incidence of accessory hepatic arteries: a literature review

M. Malicki[1], W. Marcinkowska[1], G.P. Georgiev[2], N. Zielinska[1], Ł. Olewnik[1]

[1]Department of Anatomical Dissection and Donation, Medical University of Lodz, Poland
[2]Department of Orthopaedics and Traumatology, University Hospital Queen Giovanna-ISUL, Medical University of Sofia, Bulgaria

Modern medicine is developing towards application of endovascular techniques such as trans-arterial hepatic chemoembolisation. They displace classic open procedures. However, their correct planning and performance depend on the knowledge pre-operative detection of hepatic arterial anatomical variations. The main abnormality that may generate complications during radiological and surgical procedures is occurrence of an accessory hepatic artery. In the present study we propose our own classification of the variability observed in the vessels based on cases reported in the literature. It analyses more types of variations as compared to previous trials. A great advantage of this study is also a description of different pathological and frequently life-threatening conditions associated with hepatic arteries. This study is of value to medical practitioners, e.g. surgeons. (Folia Morphol 2022; 81, 3: 533–543)

Key words: accessory hepatic artery, liver vascularisation, aneurysm, morphological variations, hepatic artery, new classification, coeliac trunk, superior mesenteric artery, left hepatic artery, right hepatic artery

INTRODUCTION

An uninterrupted blood supply is an essential condition for every organ to maintain life [40]. Anatomical variations of extrahepatic blood vessels are a common occurrence [37]. In the most dominant anatomical pattern the common hepatic artery (CHA) originates from the coeliac trunk (CT) [19]. Past the branch-off point, CHA runs forwards and laterally, reaching the superior surface of the duodenum [45]. Then it divides into the gastroduodenal artery (GDA) and the proper hepatic artery (PHA). GDA feeds into the pylorus and the proximal part of the duodenum [2]. PHA runs between the layers of the lesser omentum, within the hepatoduodenal ligament, then reaching the hepatic hilum [2]. It is located there

posteriorly to the portal vein (PV) [25]. This vessel divides into the left hepatic artery (LHA) and the right hepatic artery (RHA) [19]. They supply the right and left lobes of the liver, respectively [2].

The liver is the largest internal organ in the human body. It receives approximately 25% of total cardiac output at rest. Interestingly, the liver has dual blood supply [2]. Hepatic arteries feed this organ with highly oxygenated blood [35]. Nevertheless, it is only up to 30% of the total blood supply. The remaining 70% is provided by PV [2].

We can define an accessory hepatic artery (aHA) as an additional arterial vessel that supplies the liver. It may fulfil a supportive function only or replace basic arteries supplying the organ [37]. Moreover,

these vessels are divided into left and right depending on which lobe of the liver they reach. The most common variations of such vessels are an accessory right hepatic artery (aRHA) arising from the superior mesenteric artery (SMA) and an accessory left hepatic artery (aLHA) originating from the left gastric artery (LGA) [22].

Hepatic arterial vascularisation may be related to serious disorders. The most serious ones are aneurysm and pseudoaneurysm. It is well-known that a ruptured aneurysm is a life-threatening condition [1]. It has been also reported that an aneurysm developing from an aHA is rather a rare condition [42]. Impairments such as stenosis and thrombosis of hepatic arteries are frequent complications following liver transplantation. When left untreated, they can be dangerous for the patient's life [13, 26, 29]. Interestingly, arterioportal shunts which are a pathologic anastomosis between the hepatic artery and PV may occur [4, 13].

The aim of this study is to systematise the current knowledge on occurrence of aHAs and their variations. We also focus on clinical syndromes related to arterial hepatic vascularisation. Different diagnostic techniques are also presented. The analysed information is crucial for proper performance of surgical procedures such as liver transplantation or pancreaticoduodenectomy. Therefore, the present study is particularly valuable for radiologists and surgeons.

EMBRYOLOGY

Knowledge of embryology is necessary to comprehend the origin of arterial variations in the liver [11]. Based on angiogenesis, hepatic vascular development progresses during embryogenesis in order to form a complex network of hepatic vessels [43]. The embryonic liver in the 5th week of gestation contains three major veins, i.e. the umbilical veins, the vitelline veins and the cardinal veins. The vitelline veins are the major efferent vessels which transport the deoxygenated blood to the inferior vena cava. The left vitelline vein then involutes and blood is directed to the right vitelline vein, which enlarges and forms the hepato-cardiac part of the inferior vena cava [5]. Branches of the vitelline veins also form the hepatic vein. In contrast, the umbilical vein is involved in the development of the afferent hepatic venous system. However, it mostly degenerates. Only a part of the left umbilical vein remains and connects to the right vitelline vein via a ductus venosus. As the umbilical vein collapses, it is replaced by the portal vein as the

Table 1. Hiatt's classification of hepatic arterial anatomic variants

Type	Description
I	CHA from CT (normal pattern)
II	Accessory or replaced LHA from LGA
III	Accessory or replaced RHA from SMA
IV	Co-occurrence of accessory or replaced LHA from LGA and accessory or replaced RHA from SMA
V	CHA from SMA
VI	CHA from the aorta

Abbreviations — see text

main afferent vein [5, 43, 44]. The formation of the hepatic artery occurs later than the development of the veins [43]. The hepatic artery arises from the aorta and passes through the portal vein in the parenchyma and it gradually expands. After birth, there is closure of the umbilical arteries, veins and ductus venosus and they form the medial umbilical ligament, the ligamentum teres and the ligamentum venosum. Postnatal morphology involves blood supply to the liver via the hepatic artery and the portal vein and its outflow through the hepatic veins [5, 43, 44]. It can be hypothesized that arterial variations such as aLHA and aRHA are caused by differences in embryonic development and are remainder of the left and right embryonic hepatic arteries [11].

CLASSIFICATION OF ACCESSORY HEPATIC ARTERIES

The anatomy and various variants of the hepatic arteries have been thoroughly classified and characterised in the literature. In 1966 Michels [31] published the classification system in which he identified ten types of hepatic artery variations [31]. The classification was based on 200 dissections. It contained a division into accessory and replaced hepatic arteries. The types of variants included differences in the supply of specific hepatic arteries. The classification, based on 1000 cases [22], was updated in 1994 by Hiatt et al. [22], who described six types (Table 1) taking into account the presence of accessory or replacement vessels to reduce the division proposed by Michels [31].

Several scientists have also investigated the frequency of the different types. Table 2 presents the investigation trials that analysed the greatest number of cases. Michels's classification is based on dissections [31]. The study conducted by Hiatt et al. [22] involved observations of patients who underwent

Table 2. Summary of variants of accessory hepatic arteries presented in the literature

Type	Hiatt et al. [22] (n = 1000)	Michels et al. [31] (n = 200)	Hanif et al. [20] (n = 1000)	Koops et al. [25] (n = 604)	Abdullah et al. [3] (n = 932)
Normal pattern	75.7%	55%	64.4%	79.1%	68.1%
aLHA from LGA	9.7%	18%	13.5%	3%	8.1%
aRHA from SMA	10.6%	18%	12.1%	11.9%	10.2%
aLHA + aRHA	2.3%	4%	7.3%	1.3%	6.4%
Others	1.7%	5%	2.7%	4.7%	7.2%

Abbreviations — see text
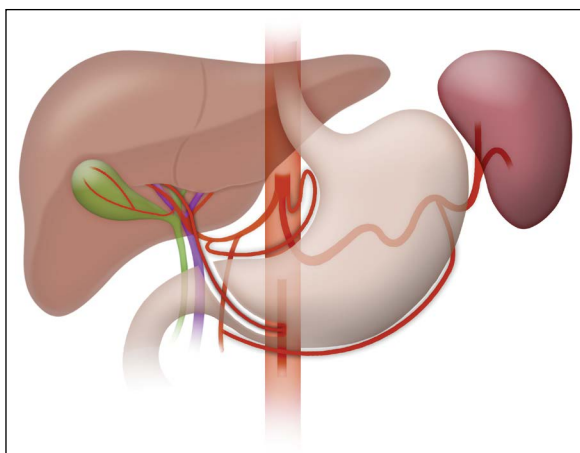
Figure 1. Type III, subtype A — accessory right hepatic artery arising from superior mesenteric artery.
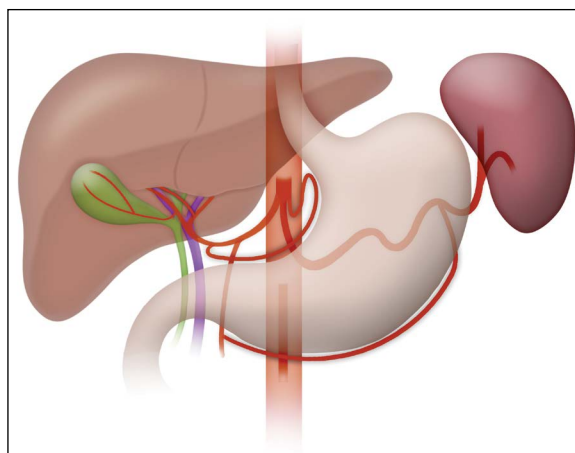
Figure 2. Type II, subtype C — accessory right hepatic artery branching from left hepatic artery.

liver harvesting for orthotopic transplantation [22]. A similar method was applied by Abdullah et al. [3], Hanif et al. [20] and Koops et al. [25] who focused on abdominal angiography in their investigations [20, 25]. Moreover, Hanif et al. [20] examined only the population of Pakistan [20].

Based on the results demonstrated in Table 2, normal anatomy is evidently the most commonly occurring one. Among the variants of aHA, aRHA arising from SMA is observed most frequently. A slightly less commonly occurring one is aLHA branching off from the LGA. The other types are rare.

The occurrence of aRHA branching from SMA (Fig. 1) is widely reported in the literature [12, 14, 28, 32, 48]. This is definitely the most common variant of aRHA categorised as type III in the Hiatt's classification [22]. Li et al. [28] described the case of a 67-year-old female patient who was diagnosed with intrahepatic bile duct cancer [28]. A computed tomography scan revealed aRHA arising from SMA. The accessory vessel passed through the right posterior side of the portal vein, then it was wrapped from the posterior to anterior side to its right branch and it distributed

blood in the right anterior part of the liver, supplying segments V and VIII [28]. The same variation was also reported by Yu et al. [48]. In a 47-year-old female, aRHA originating from SMA was detected during liver transplantation surgery. The vessel supplied the posterior segment of the liver graft [48].

The literature also reports a rare retroportal course of aRHA from LHA [30] (Fig. 2). This variation was identified in the liver of a 52-year-old male. We can observe the arterial vessel located distally to the bifurcation of the portal vein which supplies the right posterior segments VI–VII [30].

Also, aRHA may branch off from GDA (Fig. 3). This case was discovered by Yamashita et al. [47] in a 41-year-old female patient with gallbladder cancer [47]. Three-dimensional angiography revealed that aRHA was running in front of the common bile duct into the anterior segment of the liver. Interestingly, the cholecystic artery branched off it. Thus, aRHA supplied blood both into the liver and the gallbladder [47].

In the literature there are also reports on two capabilities of aRHA branching from the CT [8, 34].
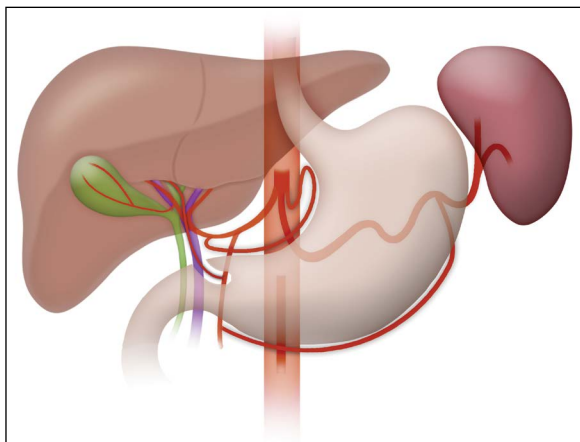
Figure 3. Type II, subtype D — accessory right hepatic artery originating from gastroduodenal artery.
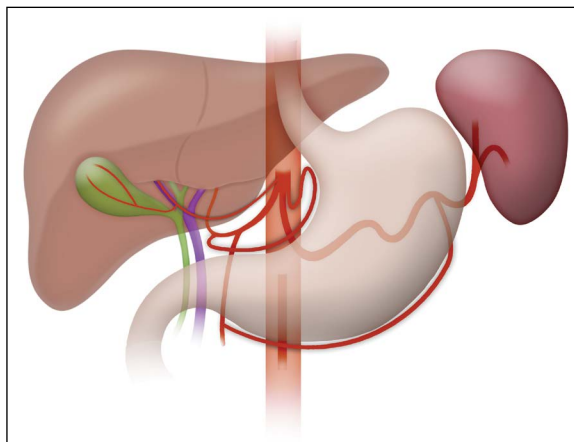
Figure 5. Type I, subtype B — accessory right hepatic artery originating from four-branch coeliac trunk.
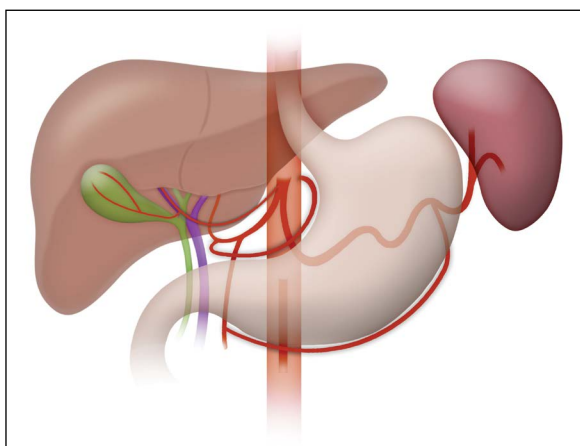
Figure 4. Type I, subtype A — accessory right hepatic artery branching from trifurcation variation of coeliac trunk.
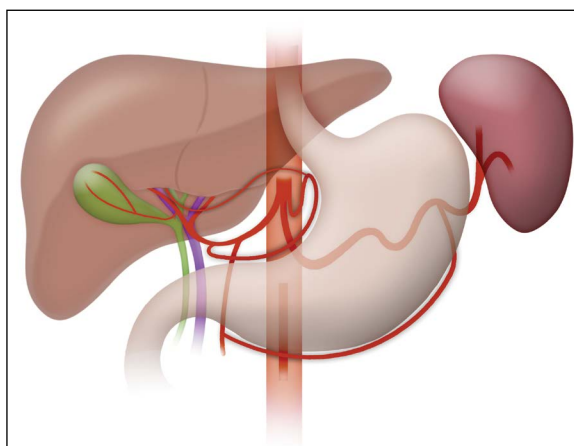
Figure 6. Type I, subtype C — accessory right hepatic artery arising from left gastric artery.

One of them is the case of trifurcation variation of CT that contains aRHA (Fig. 4). CHA, the splenic artery (SA) and aRHA originate from the common arterial trunk and LGA arises directly from the abdominal aorta [34]. The second one is the case of a four-branch trunk (Fig. 5). The CT gives off three basic arteries, i.e. CHA, SA, LGA, and an additional fourth branch, i.e. aRHA [8].

Another unusual phenomenon is the branching of aRHA from LGA (Fig. 6). Such an anatomic variation was discovered in a female who died at the age of 92 years. An aHA arising from LGA and reaching the left lobe of the liver is definitely more frequent. In the described case, LGA branches off CT. After running a short course, it divides into three branches. Two of them are abnormal large gastric arteries and the third one is aRHA. In this study the course of this vessel

was carefully explored. It has been confirmed that it supplies the right lobe of the liver [37].

Also, the presence of aRHA arising from the right renal artery (RRA) (Fig. 7), was identified on renal computerised tomographic angiogram by Darsan et al. [10]. There were two reported cases of subjects with the anatomical variation. However, the courses of accessory vessels were different. In the first case a 46-year-old female had aRHA that branched from RRA near its origin from the abdominal aorta. Then, it passed aloft behind the inferior vena cava and ramified in the right lobe of the liver. In the second case involving a 50-year-old male, aRHA branched from RRA close to the renal hilum. Then, it passed along the right crus of diaphragm. The aRHA also supplied the right lobe of the liver [10].

In the literature there are also cases presenting aRHA that originates from CHA (Fig. 8). The case of
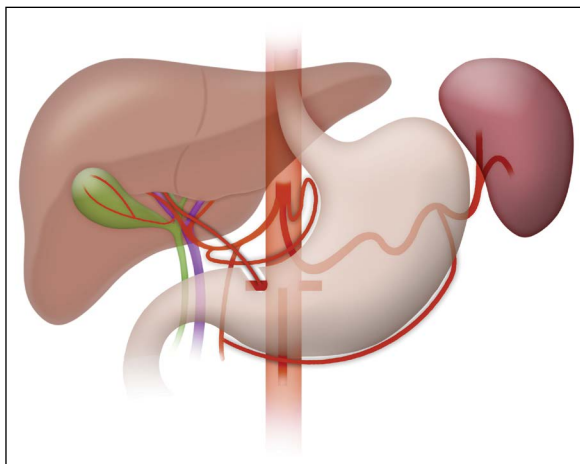
Figure 7. Type IV — accessory right hepatic artery originating from right renal artery.
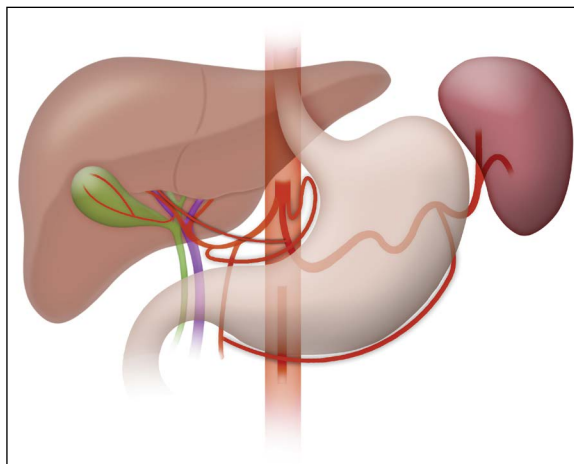
Figure 9. Type I, subtype E — accessory right hepatic artery branching from splenic artery.
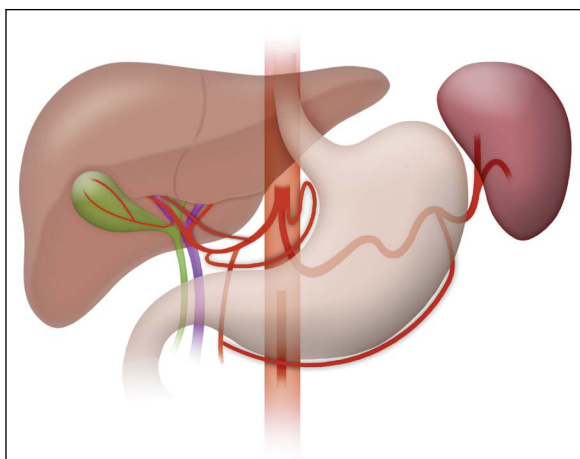
Figure 8. Type II, subtype A — accessory right hepatic artery originating from common hepatic artery.
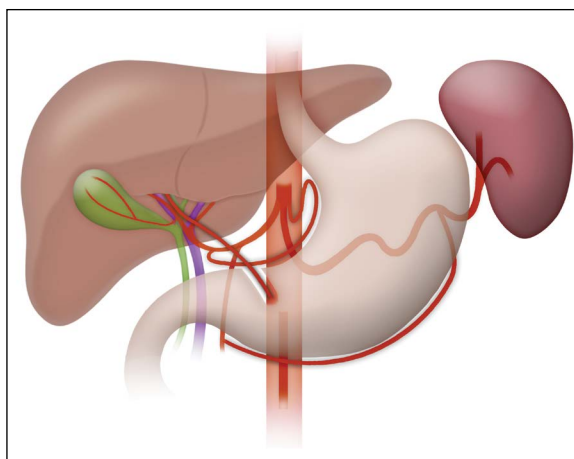
Figure 10. Type V — accessory right hepatic artery arising from abdominal aorta.

a 65-year-old Caucasian female shows this kind of an abnormality. The CHA arose from the coeliac trunk, which is a typical condition. However, after a course of 9 mm it branched off aRHA. The vessel passed behind the portal vein and supplied the right lobe of the liver [40].

The occurrence of aRHA arising from the SA (Fig. 9) was also reported in the literature by Caruso et al. [6]. In the case of a 67-year-old cadaveric organ donor, aRHA crossed downward and parallel to CHA, after branching from SA. Then it passed behind the gastroduodenal artery and the common bile duct. Ultimately, aRHA ran along the right side of the portal vein and entered the right lobe of the liver [6].

There also occur cases of aRHA branching off directly from the periphery of the abdominal aorta (Fig. 10) [12].

The occurrence of an aLHA is less prevalent than the aRHA [35]. In the literature, the most commonly described kind of variation is aLHA arising from LGA [12, 14, 20, 38] (Fig. 11). It is the type II according to the Hiatt's classification [22]. During dissection of the cadaver of a 94-year-old man, such an abnormality was identified. The aLHA originated from the branching area of LGA and then it ran upwards supplying blood to the left liver lobe [38].

In some individuals, aLHA branches off from SMA (Fig. 12) [12, 20].

A rare occurrence of aLHA leading from CHA (Fig. 13) has also been reported. In the case of a 55-year-old male, aLHA was extending opposite to GDA and ran upwards and medially to PHA [35].

Another interesting phenomenon are patients in whom both aHA occur simultaneously in addition to
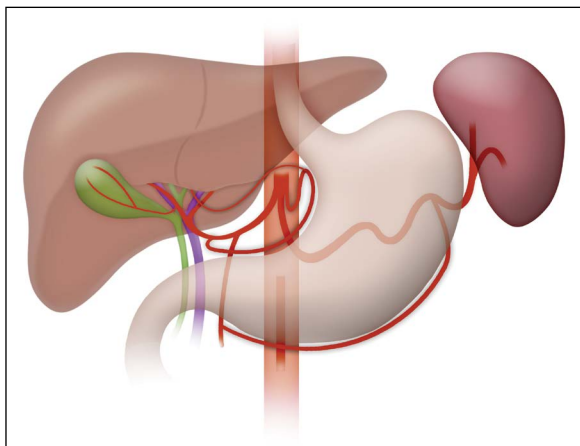
Figure 11. Type I, subtype D — accessory left hepatic artery branching from left gastric artery.
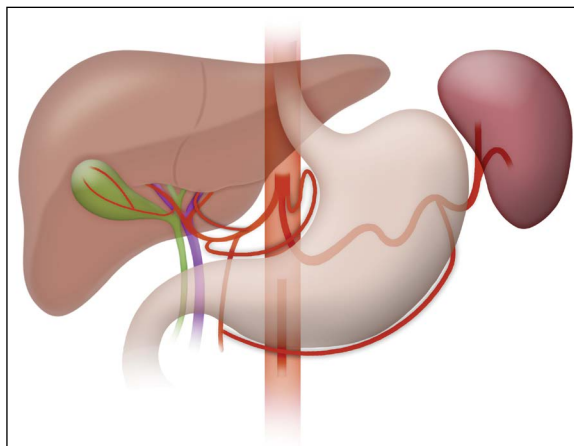
Figure 13. Type II, subtype B — accessory left hepatic artery arising from common hepatic artery.
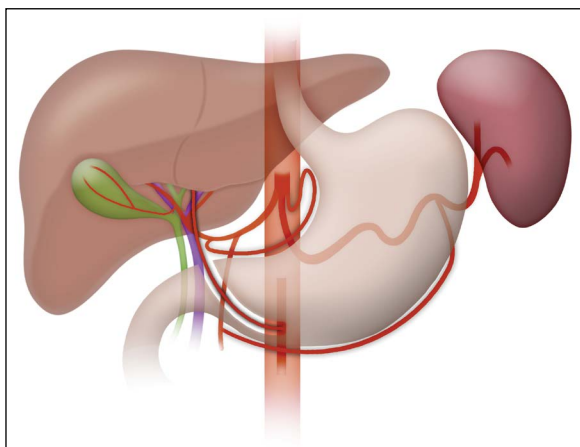
Figure 12. Type III, subtype B — accessory left hepatic artery branching from superior mesenteric artery.
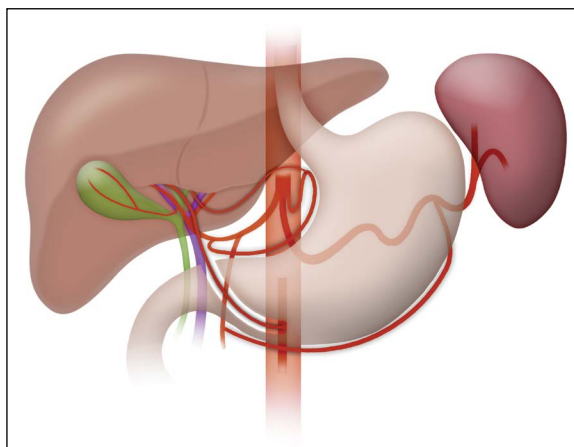
Figure 14. Type VI — co-occurrence of accessory right hepatic artery and accessory left hepatic artery.

the normal arterial supply (Fig. 14). In the case of an adult male cadaver, a triple arterial blood supply to the liver was observed. There were also reported cases of aLHA arising from the LGA and running upwards in the hepatogastric ligaments. At the same time, aRHA originated from SMA and ran behind the common bile duct in the hepatoduodenal ligament [11]. Such arterial anomalies result from differences in embryonic development. However, it may cause complications associated with diagnostic and surgical procedures in the epigastric region [11]. Similarly, we identified a case of a 67-year-old female with both aHA, which is an example of type IV in Hiatt's classification [22]. The aLHA arose from LGA, whereas the aRHA originated from SMA, crossed the right posterior portal vein and distributed blood to the right anterior region of the liver to supply segments V and VIII [28]. Another

unusually rare case of coexistence of aLHA and aRHA was noticed during a dissection of a human cadaver. The aLHA arose from CHA, supplying the stomach and the left liver lobe. The aRHA originated from GDA, running behind the cystic duct and then into the liver [24].

We proposed a new classification of aHA origins with a division into types and subtypes including all departures described in the literature (Table 3). This classification does not focus on the physiological significance of these arteries. Therefore, we do not divide them into accessory and replaced ones. Nevertheless, they are classified into right and left arteries depending on which part of the liver they supply. It is not a classification that serves didactic purposes; however, it is intended for clinicians in whose work liver vascularisation plays a key role. Therefore, it

Table 3. New classification system based on the available literature by Malicki et al. (current study)

Type	Description
I	aHA from CT and its branches (except for the branches associated with the CHA)
A	aRHA from trifurcation variation of CT
B	aRHA from four-branch CT
C	aRHA from LGA
D	aLHA from LGA
E	aRHA from SA
II	aHA from CHA and its branches
A	aRHA from CHA
B	aLHA from CHA
C	aRHA from LHA
D	aRHA from GDA
III	aHA from SMA
A	aRHA from SMA
B	aLHA from SMA
IV	aRHA from RRA
V	aRHA from AA
VI	Co-occurrence of aRHA and aLHA

Abbreviations — see text

avoids a complex division in order to create a clear and easy to read set of information. Our aim is to collect knowledge of all possible variations, which is essential in surgical specialties.

The classification includes six types in total. We distinguish type I in which aHA originates from CT and its branches, except for the branches associated with CHA. The arteries extending from CHA represent a separate category, i.e. type II to reduce the number of subtypes. This results in a classification that is readable for an analysis by researchers. Most of the types are related to aRHA. Only three of them refer to aLHA. However, the last type involves co-occurrence of both accessory arteries.

CLINICAL SIGNIFICANCE OF THE ACCESSORY HEPATIC ARTERY

Accessory hepatic arteries are frequently smaller than basic arterial hepatic vessels [40]. Nevertheless, they are functionally relevant [40]. We reviewed a case study that support this statement [15].

A 31-year-old male suffered in a motor vehicle collision. A CT scan of the chest, abdomen and pelvis demonstrated internal injuries. The most important one, in the context of the issue discussed in this article, was a pancreatic head haematoma which triggered interruption of arterial flow in the CHA. The examination also showed the presence of aLHA [15]. During surgical intervention it was observed that the liver parenchyma was still viable. The aLHA developed a rich net of collateral arterial vessels with the inferior phrenic artery. The additional source of liver blood supply was high significant in the case. Therefore, any major signs of acute liver ischaemia were not noticed. Despite extensive injuries, the patient suffered only temporary and limited ischaemic changes [15]. After one month following the accident, angiography, computed tomography and magnetic resonance imaging were performed. An enlargement of aLHA becoming the dominant arterial vessel was observed.

We can use this rare case as an example of "in vivo" presentation of clinical significance of additional hepatic artery occurrence. It has also been suggested that the well-known liver resilience to arterial ischaemia is a result of occurrence of other possible liver arterial flow sources [15]. It is obvious that a variable course of such vessels and functional significance cause complications during various abdominal procedures. Vessel damage may lead to dangerous bleeding. That is why it is so important to identify additional hepatic arteries preoperatively. It allows you to plan a correct procedure which often determines the success of a surgery [47].

However, it has been reported that the presence of aHA can be beneficial in the context of rare surgeries. Paloyo et al. [36] presented a case of a 64-year-old male. The patient underwent orthotopic liver transplantation. Interestingly, he suffered from portomesenteric vein thrombosis. It affected the portal vein, too. Such a pathological condition is a contraindication against liver transplantation. However, current achievements in surgical techniques can solve this problem. There are various options such as thromboendovenectomy, portocaval hemitransposition, renoportal anastomosis or arterialisation of PV. Thromboendovenectomy was performed as a first-choice procedure. Unfortunately, PV flow was still marginal. Another method had to be used in this case. Based on preoperative computed tomography the presence of aRHA branching from SMA was identified [36]. Thanks to this abnormal condition, PV arterialisation could be performed. The aRHA was accessible. Surgeons created end-to-end anastomosis between the additional hepatic artery and the recipient's PV. It was a highly effective and easy method

of increasing portal flow. Doppler ultrasonography confirmed turbulent flow and increased pulsatility. Four years following liver transplantation, the patient had normal liver function. It is an extremely rare use of the presence of an aHA in order to facilitate a surgical procedure. Nevertheless, it shows that anatomical variations are not always an obstacle for surgeons only [36].

An aHA can be associated with various pathologic liver conditions. Vascular variants trigger many clinical syndromes [13]. In the present study, we focus on disorders related to liver arterial flow.

THROMBOSIS

Hepatic artery thrombosis frequently occurs as a complication following liver transplantation. Other surgeries such as Whipple procedure may also lead to this kind of thrombosis [13]. It is a life-threatening condition. It has been estimated that this disorder occurs in 2.5–9% of adults and in 9–15% of paediatric population [18].

There is no evidence in the literature that hepatic arterial abnormalities have an impact on the frequency of hepatic artery thrombosis incidence. However, it is clear that the presence of accessory arteries increase the number of anastomosis procedures that have to be performed during transplantation. It makes the technical aspect of the surgery more difficult. Despite this fact, it has been suggested that liver with vascular variations can be transplanted without increased risk [17]. Thrombosis complications require revascularisation. Unfortunately, this method often fails. It results in necessary re-transplantation [18]. Most often, early hepatic artery thrombosis is recognised during a routine postoperative ultrasound examination. This form of the disease is asymptomatic. If the thrombosis is not diagnosed in time, various complications can develop. The most significant one is liver parenchyma and duct ischaemia [21]. Interestingly, development of collateral arterial vessels can prevent liver failure. It has been reported that such patients are in good condition despite diagnosed irreversible hepatic artery thrombosis [17]. Prevention strategies can also play an important role. According to previous studies, implementation of acetylsalicylic acid therapy following liver transplantation may reduce the risk for occurrence of the disorder. The introduction of microvascular surgery is useful, too. An early diagnosis gives the chance for successful treatment.

Therefore, the use of Doppler ultrasonography may be essential [9].

STENOSIS

Hepatic artery stenosis (HAS) is one of the common complications following orthotopic liver transplantation. According to previous studies, the frequency of this disorder ranges from 3.5% to 11% [26, 29]. We have not reviewed any papers containing a case report of the development of stenosis in relation to aHA. However, we speculate that this is a potential phenomenon as there are cases where this artery replaces the classic hepatic artery and becomes a significant provider of blood for the liver. Presumably, in a patient with aHA who has undergone liver transplantation, the vessel stenosis may occur as a classic post-operative complication following this type of surgery.

Most often, HAS is asymptomatic. However, it may result in hepatic artery thrombosis. It can also lead to liver ischaemic and biliary strictures [27, 29]. There are various well-known risk factors. The most relevant one, in the context of the analysed issue, is complex donor hepatic artery anatomy. It is also related to a prolonged operative time [27]. The choice of treatment method is a matter of discussion in the literature. Surgical management such as aorto-hepatic bypass or re-anastomosis following the resection of a stenotic segment is always an option for HAS. However, achievements in the recent years have made endovascular procedures a golden standard nowadays. Interventional radiology offers less invasive medical procedures and uses local anaesthesia only. Therefore, these techniques have advantages over conventional vascular surgery. Two main endovascular methods are percutaneous transluminal angioplasty and stenting. As for their efficiency, there are no significant differences between them. Nevertheless, using percutaneous transluminal angioplasty results in more common HAS recurrence than following stenting. That is why it was suggested that stenting could be a first-line treatment [29]. However, according to Pulitano et al. [41] study, endovascular treatment is given in the case of graft impairment or ischaemic biliary strictures. This kind of therapy is beneficial because it may reduce further graft damage. Endovascular methods should not be performed in asymptomatic patients or those diagnosed at a late stage of the disease [41].

ARTERIOPORTAL SHUNTS

It is the most common intrahepatic vascular shunt. We can also distinguish other types such as arteriovenous, portosystemic, portoportal or venovenous shunts. It is a kind of pathological anastomosis between the portal vein and the hepatic artery. It provides direct communication between these hepatic vessels. According to the laws of physics, oxygenated blood flows into the portal vein under high pressure. This process facilitates detection of this disorder by dynamic contrast-enhanced computed tomography or magnetic resonance imaging. The scan is characterised by an occurrence of a wedge-shaped geographic region. The arterioportal shunt is frequently a result of iatrogenic trauma such as liver biopsy. It may also be a concomitant disorder of haemangiomas or hepatocellular carcinoma. Most often such a shunt is asymptomatic [4, 13]. In the literature, there is no evidence proving an association between the presence of arterioportal shunts and the occurrence of aHA. However, this condition of aHA is probably possible. Since direct communication between the classical artery and portal vein is possible, a similar anastomosis between the artery and portal vein may be created in patients with aHA.

ANEURYSM

We can define aneurysm as a pathological dilatation of a blood vessel. However, this basic definition is too general. Therefore, a better classification is required. The exact pathophysiology of aneurysm is still unclear. Nevertheless, many risk factors are well-known [23]. Among them the most important ones are obesity, atherosclerosis, hypertension, peripheral artery disease, peptic ulcer disease. It has also been suggested that tobacco and alcohol consumption are closely related to aneurysm development [39].

Hepatic artery aneurysm (HAA) is a rare clinical condition. It has been estimated that HAA accounts for 20% of visceral aneurysms. It makes HAA the second most common visceral aneurysm following splenic artery aneurysm (SAA) [1].

Development of aHA aneurysm has been also reported. However, it is extremely rare [42]. Serena et al. [42] described a case of a 71-year-old Caucasian female who presented with aLHA mycotic pseudoaneurysm. Probably, the aetiological factor of this disorder was *Clostridium difficile*. Interestingly, the location of pseudoaneurysm precluded open surgery or percutaneous thrombin injection. Therefore, coil

of this lesion was performed. Antibiotic therapy was also introduced [42].

Aneurysms have been divided into two main types. The first group are true aneurysms which have a wall consisting of all layers of vascular structure. They are related to arterial fibrodysplasia, polyarteritis nodosa, vasculitis, systemic lupus erythematosus. The second type are pseudoaneurysms that have a fibrous sac without the endothelium or vascular wall structure. The other term for this type is "false aneurysm". It develops as a result of blunt or penetrating injuries. However, the most common cause is iatrogenic trauma such as biopsy [4, 13, 23]. Interestingly, an infection may also result in this disorder. Mycotic aneurysms have been described in the literature [42]. True aneurysms are most often asymptomatic. Sometimes, patients may complain of abdominal pain. Therefore, these lesions are identified accidentally on imaging tests.

Hepatic artery aneurysm is a severe disorder. Rupture of HAA is a life-threatening condition. It can affect the peritoneal cavity, hepatobiliary tract, stomach or the duodenum. The frequency of HAA rupture ranges from 20% to 80% [1].

There are plenty of treatment strategies. An open repair procedure is surgical excision of an aneurysm and reconstruction of liver vascularisation. An arterial by-pass may be required [46]. Obviously, there are other less invasive techniques such as trans-arterial embolisation or covered stent placement [39]. There are no significant differences in overall mortality and post-operative complications between the traditional and endovascular treatment methods. However, the latter reduces the time of hospitalisation. Furthermore, it is beneficial for elderly patients since because of their age surgery may be contraindicated in some individuals. Therefore, endovascular treatment is recommended [16]. Currently, an aneurysm which has a diameter greater than 2 cm and non-atherosclerotic origin are main symptoms that predispose to intervention [33].

HEPATOCELLULAR CARCINOMA

Accessory hepatic arteries may also play an important role in cancer development. They can supply tumours. According to previous studies, this type of cancer has almost exclusively arterial vascularisation. The knowledge of liver vascular abnormalities is also essential for proper performance of chemoembolisation. It is a highly recommended treatment approach.

The other options are only surgical hepatic resection or liver transplantation [7].

CONCLUSIONS

The functional importance and variable courses of aHA create a risk of complications during abdominal procedures. Their occurrence may also be associated with development of pathological conditions. Therefore, preoperative diagnosis of these arteries plays an important role. It enables radiologists and surgeons to obtain all significant information and properly plan the surgical procedure in advance.

Conflict of interest: None declared

REFERENCES

1. Abdallah FF, Serracino-Inglott F, Ananthakrishnan G. Giant hepatic aneurysm presenting with hematemesis successfully treated with an endovascular technique. Vasc Endovascular Surg. 2017; 51(5): 331–334, doi: 10.1177/1538574417707145, indexed in Pubmed: 28478708.
2. Abdel-Misih SRZ, Bloomston M. Liver anatomy. Surg Clin North Am. 2010; 90(4): 643–653, doi: 10.1016/j.suc.2010.04.017, indexed in Pubmed: 20637938.
3. Abdullah SS, Mabrut JY, Garbit V, et al. Anatomical variations of the hepatic artery: study of 932 cases in liver transplantation. Surg Radiol Anat. 2006; 28(5): 468–473, doi: 10.1007/s00276-006-0121-0, indexed in Pubmed: 16642277.
4. Albers BK, Khanna G. Vascular anomalies of the pediatric liver. Radiographics. 2019; 39(3): 842–856, doi: 10.1148/rg.2019180146, indexed in Pubmed: 31059404.
5. Bhargava P, Vaidya S, Kolokythas O, et al. Pictorial review. Hepatic vascular shunts: embryology and imaging appearances. Br J Radiol. 2011; 84(1008): 1142–1152, doi: 10.1259/bjr/82649468, indexed in Pubmed: 22101582.
6. Caruso F, Dondossola D, Fornoni G, et al. Right hepatic artery from splenic artery: the four-leaf clover of hepatic surgery. Surg Radiol Anat. 2016; 38(7): 867–871, doi: 10.1007/s00276-016-1617-x, indexed in Pubmed: 26769020.
7. Cazejust J, Bessoud B, Colignon N, et al. Hepatocellular carcinoma vascularization: from the most common to the lesser known arteries. Diagn Interv Imaging. 2014; 95(1): 27–36, doi: 10.1016/j.diii.2013.04.015, indexed in Pubmed: 23978434.
8. Chanasong R, Putiwat P, Roboon J, et al. Accessory hepatic artery arising from celiac trunk: an incidence in a Thai cadaver. Int J Morphol. 2014; 32(4): 1136–1139, doi: 10.4067/s0717-95022014000400002.
9. Compagnon P, Toso C. Selective retransplantation after late hepatic artery thrombosis. Transpl Int. 2019; 32(5): 470–472, doi: 10.1111/tri.13411, indexed in Pubmed: 30779232.
10. Darsan L, Vishal V, Cardoza F. Accessory right hepatic artery originating from proximal and distal right renal artery in two subjects. Indian J Urol. 2019; 35(4): 305–306, doi: 10.4103/iju.IJU_86_19, indexed in Pubmed: 31619873.
11. Dolenšek J. Triple arterial blood supply to the liver and double cystic arteries. Folia Morphol. 2017; 76(3): 523––526, doi: 10.5603/FM.a2017.0008, indexed in Pubmed: 28150275.
12. Egorov VI, Yashina NI, Fedorov AV, et al. Celiaco-mesenterial arterial aberrations in patients undergoing extended pancreatic resections: correlation of CT angiography with findings at surgery. JOP. 2010; 11(4): 348–357, indexed in Pubmed: 20601809.
13. Elsayes KM, Shaaban AM, Rothan SM, et al. A comprehensive approach to hepatic vascular disease. Radiographics. 2017; 37(3): 813–836, doi: 10.1148/rg.2017160161, indexed in Pubmed: 28430541.
14. Erbay N, Raptopoulos V, Pomfret EA, et al. Living donor liver transplantation in adults: vascular variants important in surgical planning for donors and recipients. AJR Am J Roentgenol. 2003; 181(1): 109–114, doi: 10.2214/ajr.181.1.1810109, indexed in Pubmed: 12818839.
15. Fernandes E, Pedrazzani C, Gerena M, et al. Traumatic common hepatic artery injury causing isolated right hepatic ischemia due to a left accessory artery. A case report. Int J Surg Case Rep. 2017; 39: 56–59, doi: 10.1016/j.ijscr.2017.07.061, indexed in Pubmed: 28806621.
16. Ferrara D, Giribono AM, Viviani E, et al. Endovascular management of a large hepatic artery aneurysm. Clin Ter. 2017; 168(3): e178–e180, doi: 10.7417/T.2017.2001, indexed in Pubmed: 28612892.
17. Fouzas I, Papanikolaou C, Katsanos G, et al. Hepatic artery anatomic variations and reconstruction in liver grafts procured in greece: the effect on hepatic artery thrombosis. Transplant Proc. 2019; 51(2): 416–420, doi: 10.1016/j.transproceed.2019.01.078, indexed in Pubmed: 30879555.
18. Fouzas I, Sklavos A, Bismpa K, et al. Hepatic artery thrombosis after orthotopic liver transplantation: 3 patients with collateral formation and conservative treatment. Transplant Proc. 2012; 44(9): 2741–2744, doi: 10.1016/j.transproceed.2012.09.002, indexed in Pubmed: 23146510.
19. Garg S, Kumar KH, Sahni D, et al. Anatomy of the hepatic arteries and their extrahepatic branches in the human liver: a cadaveric study. Ann Anat. 2020; 227: 151409, doi: 10.1016/j.aanat.2019.07.010, indexed in Pubmed: 31400446.
20. Hanif F, Farooq U, Malik AA, et al. Hepatic artery variations in a sample of pakistani population. J Coll Physicians Surg Pak. 2020; 30(2): 187–191, doi: 10.29271/jcpsp.2020.02.187, indexed in Pubmed: 32036828.
21. Heaton ND. Hepatic artery thrombosis: conservative management or retransplantation? Liver Transpl. 2013; 19 (Suppl 2): S14–S16, doi: 10.1002/lt.23739, indexed in Pubmed: 24019107.
22. Hiatt JR, Gabbay J, Busuttil RW. Surgical anatomy of the hepatic arteries in 1000 cases. Ann Surg. 1994; 220(1): 50–52, doi: 10.1097/00000658-199407000-00008, indexed in Pubmed: 8024358.
23. Inston N, Mistry H, Gilbert J, et al. Aneurysms in vascular access: state of the art and future developments. J Vasc Access. 2017; 18(6): 464–472, doi: 10.5301/jva.5000828, indexed in Pubmed: 29099536.

24. Jin W, Dong M, Pan J, et al. Rare combined variations of accessory left hepatic artery and accessory right hepatic artery: a case report and literature review. Surg Radiol Anat. 2020; 42(4): 443–447, doi: 10.1007/s00276-019-02396-4, indexed in Pubmed: 31811353.

25. Koops A, Wojciechowski B, Broering DC, et al. Anatomic variations of the hepatic arteries in 604 selective celiac and superior mesenteric angiographies. Surg Radiol Anat. 2004; 26(3): 239–244, doi: 10.1007/s00276-004-0229-z, indexed in Pubmed: 14968265.

26. Lee DD, Paz-Fumagalli R, Croome KP, et al. Hepatic artery stenosis after liver transplant: Donation after cardiac death donor vs donation after brain death donor grafts. Clin Transplant. 2018; 32(11): e13413, doi: 10.1111/ctr.13413, indexed in Pubmed: 30240491.

27. Lee D, Chung BH, Heo SH, et al. Case report of a large common hepatic artery aneurysm. Ann Vasc Surg. 2018; 52: 316.e11–316.e13, doi: 10.1016/j.avsg.2018.04.011, indexed in Pubmed: 29886208.

28. Li X, Zhang X, Lu Q, et al. An accessory right hepatic artery derived from the superior mesenteric artery for anterior right liver lobe supply: a case report. Surg Radiol Anat. 2019; 41(8): 969–971, doi: 10.1007/s00276-018-2173-3, indexed in Pubmed: 30580394.

29. Magand N, Coronado JL, Drevon H, et al. Primary angioplasty or stenting for hepatic artery stenosis treatment after liver transplantation. Clin Transplant. 2019; 33(12): e13729, doi: 10.1111/ctr.13729, indexed in Pubmed: 31630451.

30. Martins AC. Retroportal accessory right hepatic artery arising from the left hepatic artery: anatomy and surgical implications. HPB (Oxford). 2010; 12(9): 654–655, doi: 10.1111/j.1477-2574.2010.00204.x, indexed in Pubmed: 21158205.

31. Michels NA. Newer anatomy of the liver and its variant blood supply and collateral circulation. Am J Surg. 1966; 112(3): 337–347, doi: 10.1016/0002-9610(66)90201-7, indexed in Pubmed: 5917302.

32. Molmenti EP, Klein AS, Henry ML. Procurement of liver and pancreas allografts in donors with replaced/accessory right hepatic arteries. Transplantation. 2004; 78(5): 770–771, doi: 10.1097/01.tp.0000132785.96091.d9, indexed in Pubmed: 15371686.

33. Nathan DP, Wang GJ, Woo EY, et al. Open and endovascular repair of hepatic artery aneurysm: two case reports and review of the literature. Vascular. 2011; 19(1): 42–46, doi: 10.1258/vasc.2010.cr0208, indexed in Pubmed: 21489926.

34. Olewnik Ł, Wysiadecki G, Polguj M, et al. Types of coeliac trunk branching including accessory hepatic arteries: a new point of view based on cadaveric study. Folia Morphol. 2017; 76(4): 660–667, doi: 10.5603/FM.a2017.0053, indexed in Pubmed: 28612916.

35. Pai RS, Hunnargi AS, Srinivasan M. Accessory left hepatic artery arising from common hepatic artery. Indian J Surg. 2008; 70(2): 80–82, doi: 10.1007/s12262-008-0021-0, indexed in Pubmed: 23133027.

36. Paloyo S, Nishida S, Fan Ji, et al. Portal vein arterialization using an accessory right hepatic artery in liver transplantation. Liver Transpl. 2013; 19(7): 773–775, doi: 10.1002/lt.23653, indexed in Pubmed: 23554089.

37. Panagouli E, Venieratos D. Right accessory hepatic artery arising from the left gastric artery: a case report. Rom J Morphol Embryol. 2011; 52(3 Suppl): 1143–1145, indexed in Pubmed: 22119839.

38. Paraskevas GK, Raikos A. Multiple aberrant coeliac trunk ramifications. Singapore Med J. 2011; 52(7): e147–e149, indexed in Pubmed: 21808947.

39. Polat E, Ozogul YB, Ercan M, et al. Management of hepatic artery aneurysms. Bratisl Lek Listy. 2012; 113(11): 676–679, doi: 10.4149/bll_2012_154, indexed in Pubmed: 23137209.

40. Polguj M, Gabryniak T, Topol M. The right accessory hepatic artery; a case report and review of the literature. Surg Radiol Anat. 2010; 32(2): 175–179, doi: 10.1007/s00276-009-0536-5, indexed in Pubmed: 19669076.

41. Pulitano C, Joseph D, Sandroussi C, et al. Hepatic artery stenosis after liver transplantation: is endovascular treatment always necessary? Liver Transpl. 2015; 21(2): 162–168, doi: 10.1002/lt.24043, indexed in Pubmed: 25378262.

42. Serena TJ, Antypas E, Malay N, et al. Endovascular intervention of a mycotic pseudoaneurysm of accessory left hepatic artery arising from the left gastric artery presenting secondary to clostridium difficile colitis: a case report. Cureus. 2020; 12(4): e7802, doi: 10.7759/cureus.7802, indexed in Pubmed: 32461869.

43. Si-Tayeb K, Lemaigre FP, Duncan SA. Organogenesis and development of the liver. Dev Cell. 2010; 18(2): 175–189, doi: 10.1016/j.devcel.2010.01.011, indexed in Pubmed: 20159590.

44. Sureka B, Sharma N, Khera PS, et al. Hepatic vein variations in 500 patients: surgical and radiological significance. Br J Radiol. 2019; 92(1102): 20190487, doi: 10.1259/bjr.20190487, indexed in Pubmed: 31271536.

45. Tigga SR, Saluja S, Budhiraja V, et al. Variant anatomy of the hepatic vasculature: importance in hepatobiliary resections. J Clin Diagn Res. 2017; 11(6): AD01–AD03, doi: 10.7860/JCDR/2017/27193.10061, indexed in Pubmed: 28764144.

46. Wyżgowski P, Grzela T, Przybył M, et al. Rare case of hepatic artery pseudoaneurysm. Pol Przegl Chir. 2016; 88(3): 163–165, doi: 10.1515/pjs-2016-0046, indexed in Pubmed: 27428839.

47. Yamashita K, Hashimoto D, Itoyama R, et al. Accessory right hepatic artery branched from gastroduodenal artery. Surg Case Rep. 2015; 1: 90, doi: 10.1186/s40792-015-0092-7, indexed in Pubmed: 26435909.

48. Yu YD, Kim DS, Byun GY, et al. Liver abscess developed after cadaveric liver transplantation due to ligation of an accessory right hepatic artery of the donor graft. J Korean Surg Soc. 2012; 83(4): 246–249, doi: 10.4174/jkss.2012.83.4.246, indexed in Pubmed: 23091798.

REVIEW ARTICLE

VIA MEDICA

Morphological and clinical picture of the morphea in the oral cavity

M. Pedowska[1], M. Ptasiewicz[1], J. Szumiło[2], R. Chałas[1]

[1]Department of Oral Medicine, Medical University of Lublin, Poland
[2]Department of Clinical Pathomorphology, Medical University of Lublin, Poland

There are several types of morphea with different levels of connective tissue involvement and morphological manifestations.

In this mini review, it was pointed out the most important morphological and clinical aspects of localised scleroderma in the oral cavity. The case presented in this article supports the scientific information and is described with details. The morphea of mucous membrane which was clinically suspected, was proved by histopathological examination of the sample.

The unusual location of the local findings posed a diagnostic challenge. The case history should be significant due to the low number of studies. The special attention should be taken to match the clinical with pathomorphological picture in localised scleroderma diagnosis and treatment when the involvement of skin and oral mucosa is. (Folia Morphol 2022; 81, 3: 544–550)

Key words: linear scleroderma, oral cavity, oral mucosa

INTRODUCTION

Scleroderma is the disease of connective tissue which primarily affects the mucous membrane or skin with their thickening and hardening. There are two types of scleroderma listed in the literature: the first type is morphea — localised form and the second type is systemic sclerosis or systemic scleroderma [5].

Morphea is a disorder which generally affects skin but may also influence the muscles and bone structure. The systemic sclerosis mostly involves the internal organs, such as the heart, oesophagus, kidneys and lungs. The severity and outcomes of systemic scleroderma vary. Microscopic appearance of scleroderma depends on the stage of the disease. For a correct histopathological diagnosis, the skin sample should contain subcutaneous tissue, what is related to the fact that morphological anomalies are best visible in the transition area between the dermis and the subcutaneous tissue.

Early lesions are difficult to diagnose. Clinically, they are described as discoloured, pale macula. Histology is not characteristic. In the early stage of the disease, periadnexal and perivascular lymphohistiocytic inflammatory infiltration is found histologically, as well as a denser, homogenized collagen. In the area of blood vessels, this collagen is more eosinophilic. This is the cause of periadnexal fat reduction or disappearance. The collagen formed at this early stage can penetrate into adipose tissue as pseudopods and may be followed by an inflammatory infiltrate. A tumefied endothelium with decreased lumen may be visible on dermis and subcutaneous tissue [15].

More advanced stages show no clinical signs of inflammation, but the fibrosis of the dermis is evident and progressively spreads over the adipose tissue.

The histological pictures and diagnosis of more advanced lesions are more foreseeable. At this stage, the dermal collagen is eosinophilic and homogenized. There is no inflammatory infiltrate that already shows atrophy. The vessels of the subcutaneous tissue show a thickened wall and significantly decreased lumen size. The destruction of adipose tissue clinically manifests as the depression of the skin and replacement of adipose tissue by sclerotic collagen is best visible when compared with a contralateral normal skin [5].

Aetiology and pathogenesis

The aetiology of scleroderma is not fully known. Some environmental factors like silica or organic solvents may play an important role. It may be also triggered by viral or bacterial (*Borelia burgdorferi*) infections [14].Genetic factors have been also implicated [1]. Some forms of morphea are activated by trauma or associated with an autoimmune process.

The pathogenesis of localised and systemic scleroderma appears to be similar and complex. It may involve such syndromes as the facial tissues and the ipsilateral brain parenchyma, which contains progenitor cells. The proposed explanation for cortical dysgenesis as a cause of scleroderma development is put forward. It is a developmental defect that affects the rostral neural tube unilaterally. It is sometimes characterised as a neurocutaneous syndrome in which cutaneous manifestations are strictly connected with primary brain malformations.

A clone of vulnerable cells would develop lesions following the Blaschko's lines. According to these hypothesis there is a possibility that genetic mosaicism is a determining factor for the linear distribution of the sclerosis process. This theory would explain why multiple frontoparietal lesions are observed [2].

Since some skin lesions are seen on the area supplied with trigeminal nerve branches, the disruption of sympathetic fibres is also regarded as an aetiological factor [16]. Overall, inflammation with probable autoimmune factors and embryological disease such as genetic mosaicism appears to be more clearly associated with localised scleroderma aetiopathogenesis.

Three primary mechanisms contribute to the development of scleroderma: autoimmune phenomena, excess fibrosis and vascular anomalies. Those anomalous interactions between endothelial cells, fibroblasts, and lymphocytes (B and T) lead to microcirculatory vascular involvement. The endothelial cells generate great amounts of endothelin 1, causing vasoconstriction and fibroblast activation. Furthermore, fibroblasts and activated endothelial cells produce reactive oxygen species that accelerate vascular remodelling, leading to obliteration of small vessels. Activated fibroblasts readily differentiate into myofibroblasts, which have an increased ability to synthesize collagen [3].

Epidemiology

Scleroderma is not a common disease. Its prevalence varies according to gender, ethnicity and geographical area. Although systemic scleroderma is rare in children and the elderly, it can occur at any age. The disease is most common in people aged 30–50 years. As with many other autoimmune diseases, women are at greater risk than men (F:M = 4.6:1). Taking the United States as an example, the overall incidence rate among adults is approximately 20 per million per year. This rate has increased between 1944 and 1973, but has been relatively stable since that time.

Localised scleroderma is relatively rare with around 0.3 to 3 cases per 100,000 inhabitants annually. Prevalence is similar in children and adults. Ninety per cent of children are diagnosed between the ages of 2 and 14, whereas for adults the peak incidence is in their fifth decade. It is more common in Caucasian women (F:M = 2–4:1) [23].

Morphea

There are several subtypes of morphea distinguished in the literature with different clinical manifestations and levels of connective tissue involvement. Each subtype may affect the face with varying intensity. Subtypes are not exclusive, different ones may be seen in the same patient. The subtypes may transform and coexist [15].

The most widely used classification of morphea is Mayo Clinic Classification [23], which distinguished: generalised morphea; plaque morphea; bullous morphea; linear scleroderma — with subtypes involving the head and face, linear scleroderma "en coup de saber", progressive facial hemiatrophy with Parry-Romberg syndrome and deep morphea [17]. Laxer and Zulian include five subtypes of morphea: circumscribed (superficial or deep), linear (superficial or deep), generalised, pansclerotic, or mixed [4]. A group of experts at the European Dermatology Forum proposed a classification of localised scleroderma (LS) that takes into account the extent and depth of fibrosis and includes the main five types as follow:

1. Limited type; 2. Generalised type; 3. Linear type; 4. Deep type; 5. Mixed type, with some subtypes inside of every group. The authors consider eosinophilic fasciitis (Shulman syndrome) as a separate type within the spectrum of LS [8].

Plaque morphea is the most common form in adults and it is described as well-demarcated oval or round areas of hard and shiny mucous membrane or skin. In the very early stage, a violaceous halo around the plaque ("purple ring") is sometimes observed. It can involve the skin and subcutaneous of several anatomical regions, usually on the trunk and proximal extremities [3]. Bullous type of morphea is rare and it is a mixture of such lesions as: blisters, erosions, and the more common plaques. In deep morphea, a single lesion is observed, usually on the upper trunk, near the spine. The skin over it may look normal, atrophic, or may be hardened with depression. Typically, the dermis, adipose tissue and muscles are affected. Associations with vaccine administration or intramuscular injection of vitamin K have been reported in some cases [24].

In generalised morphea plaques and spots are observed in more than 2 places on the body. It is more frequent in women than in men. In some cases, exercise has been described as the trigger. Lesions are usually multiple (> 4), more than 3 cm in dimension, ill-defined, pigmented, indurated, and adhered to deep planes. Plaques are formed mainly on the trunk and limbs. Hardening is relatively quick within a few months, but no signs of acute inflammation such as swelling and erythema may be observed [13].

Linear scleroderma is described as a linear induration, usually single and unilateral, involving the dermis, subcutaneous tissue, muscle, and underlying bone. The lesions are seen mostly on the extremities, face, or scalp. They often follow Blaschko's lines. Growth disturbance and ankylosis may be found in cases in which muscles and bone are affected. Close to 67% of patients with linear scleroderma are children before 18 years of age. It affects males and females equally. In almost one-half of patients with linear scleroderma, a combination with another subtype of localised scleroderma is observed — so--called mixed morphea. Localised facial scleroderma associated with linear sclerosis or plaque morphea elsewhere (most often on the torso) is typical for children. Changes located on the scalp can cause alopecia with a linear distribution and the affected area is often atrophic or depressed. The skin which covers the lesion is smooth, shiny, hard, and sometimes pigmented. It tends to deform the bone and it is usually unilateral, affecting the parietal region. It can extend to the cheek and nose areas as well as the upper lip [6].

Linear scleroderma "en coup de sabre" is a slowly progressive disease limited to the hemiface. In this type of scleroderma, stiffness and contractions of the affected area are noticeable first, followed by the area of linear alopecia, extending from the parietal area to the scalp. The depressed area/line often covers the area of the upper lip and nose, even reaching to the gingiva, spacing and changing the position of the teeth. Sometimes the lesions include the maxilla and mandible bones, which results in occlusal abnormalities, delayed teeth eruption or atrophy of roots [18]. Children commonly have this particular form of linear scleroderma, but female individuals are more often affected (F:M = 3:1).

Parry-Romberg syndrome, known as progressive facial hemiatrophy, is a rare disorder. It develops in the first and second decade of life, commonly affects the dermatomes of one or multiple branches of the trigeminal nerve. In the affected areas of the scalp, scarring alopecia, hardening of the skin and changes in its colour, such as depigmentation and hyperpigmentation, may be observed. These changes precede the atrophy of the subcutaneous tissue, skin, muscles and the underlying bone structures. This atrophy is usually unilateral [21]. The disease progresses slowly, becomes self-limited and stationary over time. The process usually takes 2 to 20 years. Progressive facial hemiatrophy may clinically resemble linear scleroderma. They may coexist in approximately 20–37% cases. In most cases, dermatitis and hardening of the skin are minor or absent, usually below the eye region. Linear scleroderma and progressive facial hemiatrophy are sometimes regarded as a spectrum of the same disease [7].

Introduction to the clinical presentation

Morphea is a form of linear scleroderma which can involve the head and neck region. The disease results in excessive deposition of collagen, sclerosis, and atrophy of the involved areas. The lesions may clinically present as hyper- or hypopigmented areas or ivory, atrophic plaques.

The progression of the disease may lead to the damage of skin, subcutaneous tissues, muscles, nerves, and bone resorption [11]. Histopathologic
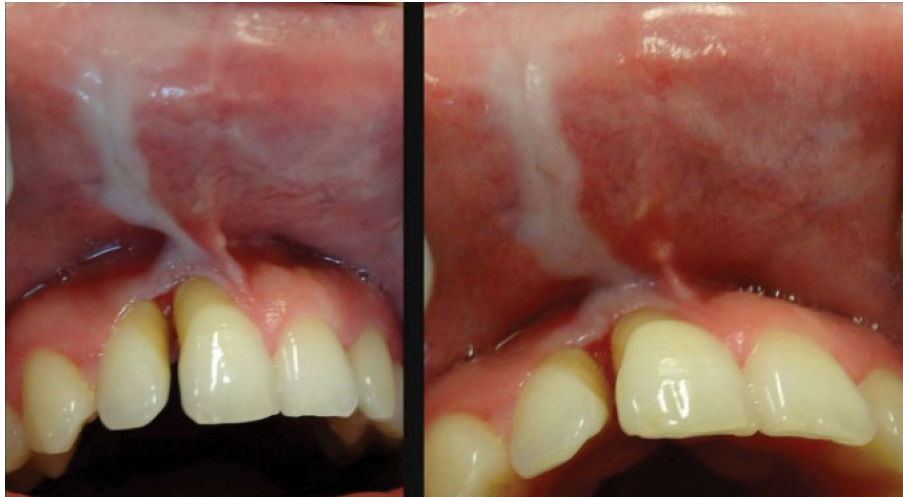
Figure 1. The lesion in the oral cavity before the diagnosis and the treatment. The white, hard, unpainful, unmovable lesion between upper incisors reaching the vestibulum and upper lip.

evaluation usually shows homogenisation and thickening of the dermal collagen, similar to scar formation. Typically, linear morphea has no systemic involvement.

PRESENTATION OF THE CASE

A 35-year-old military pilot presented in the Outpatient Clinic of the University Dentistry Centre to diagnose a white linear discoloration on the upper alveolar ridge. The patient reported a 6-month history of the lesion localised between teeth 11 and 12 and the upper lip. The white discoloration was noticed by him while military service in Afghanistan. Later on, the general dentist referred the patient to cover the gingival recessions of teeth 11, 12 to a dental surgeon. The clinical and radiological (radiography and cone-beam computer tomography) analysis let to diagnose the bone resorption localised between and above the apexes of the incisors of the 1st quadrant. The dental surgeon advised the bone regeneration and referred the patient for further treatment to the Department of Oral Medicine, Medical University of Lublin. During the clinical examination, the white patch and a white line on the upper lip leading to the vestibulum and teeth 11, 12 were noticed (Fig. 1). The pull syndrome was positive, the attached gingivae were missing, roots were exposed 6 and 7 mm. The 1st degree mobility of teeth 11 and 12 was diagnosed, the teeth were checked for vitality, and the test was positive. The bleeding on probing and pocket depth was measured while routine dental examination. There were no signs of gingivitis or
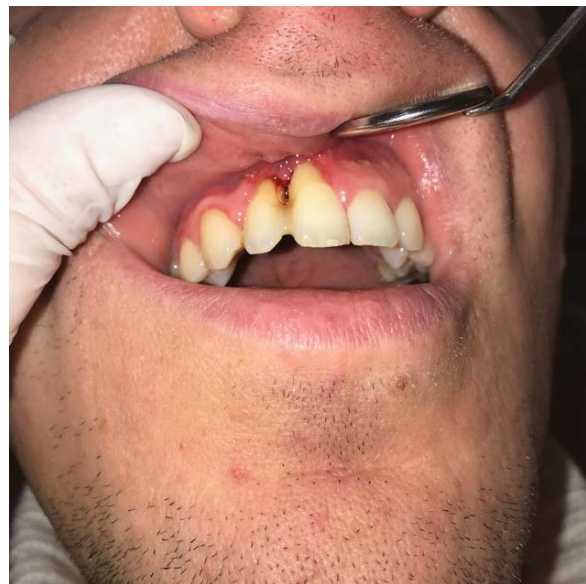
Figure 2. The situation in the oral cavity after the biopsy and the dental treatment. The lesion has been removed for the biopsy, the healing process and scaring is visible.

periodontitis diagnosed in the oral cavity. The patient was referred to the general practitioner and rheumatologist to check-up. The blood tests were without significant changes. The unusual location of the local findings posed a diagnostic challenge. Discolorations continue to progress and the morphea was clinically suspected. The biopsy of the lesion was performed (Fig. 2). Histopathologic evaluation revealed atrophic, partly hyperplastic stratified squamous epithelium and dense, homogenised, deeply penetrating collagen bundles (confirmed by van Gieson stain) with
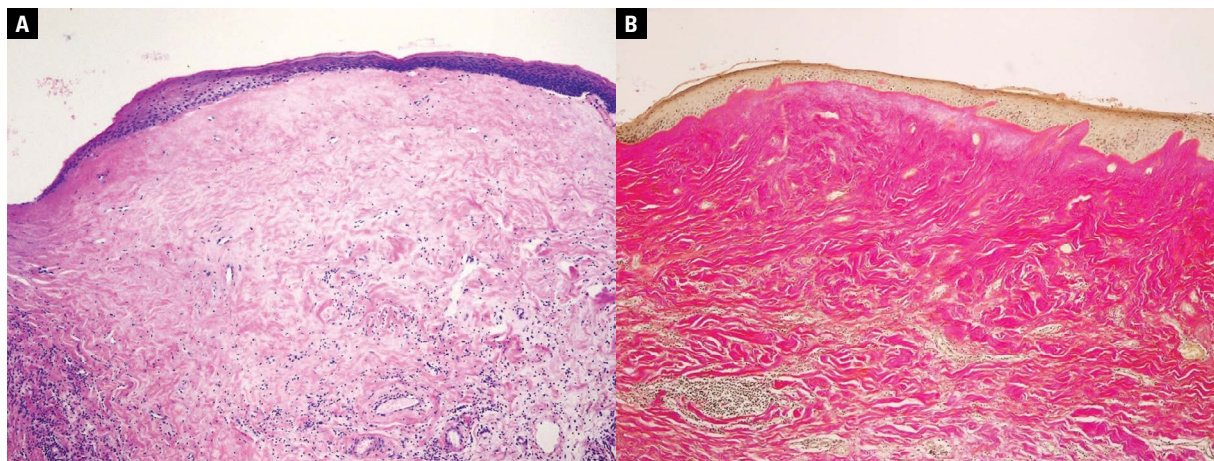
Figure 3. A. Microscopic appearance of the oral morphea. Dense, homogenised collagen bundles with small number of fibroblast and sparse, dispersed and perivascular lymphocytic infiltration in the deeper part of the mucosa; haematoxylin and eosin stain; objective magnification 5×; **B.** Microscopic appearance of the oral morphea. Dense, homogenised collagen bundles with small number of fibroblast and sparse, dispersed and perivascular lymphocytic infiltration in the deeper part of the mucosa; van Gieson stain; objective magnification 5×.

Figure 4. Coexisting lesion on the skin of the cheek before the treatment. The flat, hard, hyperpigmented lesion on the skin of the cheek. Based on the clinical examination the lesion is qualified as the progression of the morphea.
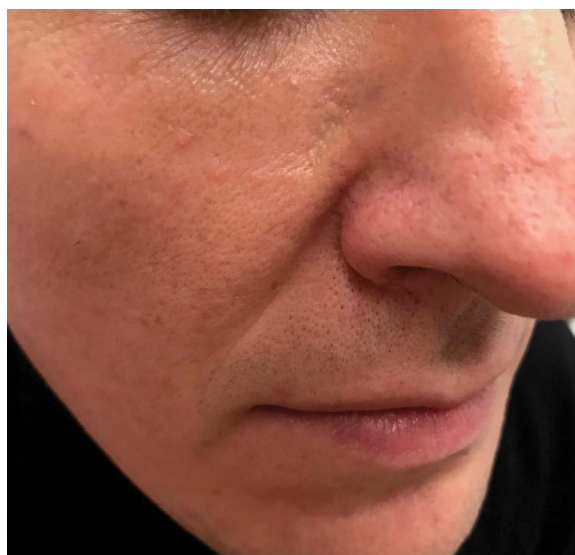
Figure 5. Coexisting lesion on the skin of the cheek after the 8 weeks of the topical tacrolimus therapy. The lesion is limited after local treatment, became softer in palpation and paler.

a small number of fibroblasts and sparse, dispersed and perivascular inflammatory infiltration composed mostly of lymphocytes located in the deeper part of the lesion (Fig. 3A, B). After the results of the biopsy, the diagnosis of linear morphea was confirmed.

Due to the toothache of teeth number 11, 12 and the progressing mobility of the incisors, the root canal treatment was performed and the teeth were splinted. The intraoral lesion was treated with 0.1% tacrolimus ointment under occlusive dressing applied twice per day topically. The treatment was administered for 4 months. The patient was observed on control visits every 2–3 months. During the therapy, the intraoral lesion was reduced and softened. After 2 years of observation, a new plaque-like, hyperpig-

mented lesion, located on the right side of the nose was observed (Fig. 4). The patient was referred to the dermatologist, the topical treatment of the lesion with the use of 0.1% tacrolimus was continued. The lesion reduced the size and pigmentation after 3 months of local treatment (Fig. 5).

The patient is under periodontal and dermatological control, and the teeth localised in the lesion are still functioning without mobility. Further dental treatment will be focused on possible tissue and bone regeneration with the use of autogenic growth factors and stem cells.

DISCUSSION

Localised scleroderma is a rare disorder of the immune system and connective tissue with unknown aetiology, but environmental triggers, autoimmune phenomena, and genetic factors may contribute a role in the disease development [19]. The disease may attack the skin but also can extend to muscles. It must also be considered regarding local bone loss and gingival recession. Severe course of morphea is a potential cause of deformation and impairment. In almost all cases, the sclerosis process involves the skin alone. Involvement of the oral mucosa and teeth in case of morphea has been rarely reported. Tang et al. [22] in 2012 presented 25 cases described in literature and associated with oral and dental manifestations. Our case with the described symptoms falls into this group too. The differential diagnosis of morphea should include chemical or physical burns and trauma. Initial clinical state can be difficult to diagnose, so the case history is significant. When the lesion is intraoral and affects the gingiva and alveolar ridge, dental care is necessary. Because of the low number of case reports published by now, the careful studying them before early diagnosis can allow to perform proper dental treatment and save the teeth located in the lesion.

At present, there is no agreement how to treat localized scleroderma. Various therapeutic strategies have been presented in the studies based on clinical cases which include: topical or oral vitamin D, D-penicillamine, phenytoin, cyclosporine, corticosteroids, methotrexate and interferon administration as well as psoralen-UVA photochemotherapy [20]. In the initial, inflammatory phase, topical use of strong corticosteroids is recommended. Local treatment is used in cases of more limited and superficial lesions [10]. The efficacy of the treatment of localised scleroderma is difficult to estimate due to the low number of described case reports.

There is no standard modality for the treatment of intraoral scleroderma, either. Topical calcineurin inhibitors such as 0.1% tacrolimus ointment can effectively reduce skin thickening, hyperpigmentation, hardness, erythema, and contraction. Topical and intralesional corticosteroid therapy, according to the German guidelines applied for 1 or 3 months, has also shown positive effects. Relatively good results were obtained with topical treatment with a vitamin D analogue in combination with phototherapy using low-dose ultraviolet A1 and 0.005% calcipotriol ointment applied twice per day [9].

The diagnosis of morphea basis on the rapid and advanced progression of skin lesions. The systemic treatment may be required and drugs of first choice are methotrexate and steroids [12]. Therefore, disease activity and subtype must be assessed before starting treatment.

CONCLUSIONS

In conclusion, because of unique cases of morphea limited to the oral mucosa, both dentists and medical doctors should be familiar with the clinical presentation of morphea and consider its morphology especially in the presence of isolated whitish lines of plaques of the oral mucosa.

Its proper differentiation and careful observation are important to avoid significant local complications. Most of the patients with intraoral lesions were diagnosed until now in an advanced stage by dermatologists or rheumatologists and not by dentists. Therefore, special attention should be taken to the involvement of skin and oral mucosa in localized scleroderma recognition and treatment.

Conflict of interest: None declared

REFERENCES

1. Albuquerque JV, Andriolo BNg, Vasconcellos MRa, et al. Interventions for morphea. Cochrane Database Syst Rev. 2019; 7: CD005027, doi: 10.1002/14651858.CD005027. pub5, indexed in Pubmed: 31309547.
2. Asano Y, Fujimoto M, Ishikawa O, et al. Diagnostic criteria, severity classification and guidelines of localized scleroderma. J Dermatol. 2018; 45(7): 755–780, doi: 10.1111/1346-8138.14161, indexed in Pubmed: 29687475.
3. Bielsa Marsol I. Update on the classification and treatment of localized scleroderma. Actas Dermosifiliogr. 2013; 104(8): 654–666, doi: 10.1016/j.adengl.2012.10.012, indexed in Pubmed: 23948159.
4. Careta MF, Romiti R. Localized scleroderma: clinical spectrum and therapeutic update. An Bras Dermatol. 2015; 90(1): 62–73, doi: 10.1590/abd1806-4841.20152890, indexed in Pubmed: 25672301.
5. Distler O, Cozzio A. Systemic sclerosis and localized scleroderma — current concepts and novel targets for therapy. Semin Immunopathol. 2016; 38(1): 87–95, doi: 10.1007/s00281-015-0551-z, indexed in Pubmed: 26577237.
6. Figueiroa Careta M, Romiti R. Localized scleroderma: clinical spectrum and therapeutic update. An Bras Dermatol. 2015; 90(1): 62–73, doi: 10.1590/abd1806-4841.20152890, indexed in Pubmed: 25672301.
7. Khatri S, Torok KS, Mirizio E, et al. Autoantibodies in morphea: an update. Front Immunol. 2019; 10: 1487,

doi: 10.3389/fimmu.2019.01487, indexed in Pubmed: 31354701.

8. Knobler R, Moinzadeh P, Hunzelmann N, et al. European Dermatology Forum S1-guideline on the diagnosis and treatment of sclerosing diseases of the skin, Part 1: localized scleroderma, systemic sclerosis and overlap syndromes. J Eur Acad Dermatol Venereol. 2017; 31(9): 1401–1424, doi: 10.1111/jdv.14458, indexed in Pubmed: 28792092.

9. Kreuter A, Krieg T, Worm M, et al. German guidelines for the diagnosis and therapy of localized scleroderma. J Dtsch Dermatol Ges. 2016; 14(2): 199–216, doi: 10.1111/ddg.12724, indexed in Pubmed: 26819124.

10. Kurzinski KL, Zigler CK, Torok KS. Prediction of disease relapse in a cohort of paediatric patients with localized scleroderma. Br J Dermatol. 2019; 180(5): 1183–1189, doi: 10.1111/bjd.17312, indexed in Pubmed: 30315656.

11. Li S. Scleroderma in children and adolescents. Pediatr Clin North Am. 2018; 65(4): 757–781, doi: 10.1016/j.pcl.2018.04.002.

12. Liu XS, Gao Y, Zheng LiWu, et al. New alternative therapy for orofacial localized scleroderma. Oral Surg Oral Med Oral Pathol Oral Radiol Endod. 2010; 110(3): e15–e19, doi: 10.1016/j.tripleo.2010.04.004, indexed in Pubmed: 20634110.

13. Machan A, Oumakhir S, Khalidi M, et al. Radiation-induced morphea: autoimmunity as a risk factor. Neth J Med. 2019; 77(1): 29–31, indexed in Pubmed: 30774102.

14. Mazori DR, Wright NA, Patel M, et al. Characteristics and treatment of adult-onset linear morphea: a retrospective cohort study of 61 patients at 3 tertiary care centers. J Am Acad Dermatol. 2016; 74(3): 577–579, doi: 10.1016/j.jaad.2015.09.069, indexed in Pubmed: 26892661.

15. Mertens JS, Seyger MMB, Thurlings RM, et al. Morphea and eosinophilic fasciitis: an update. Am J Clin Dermatol. 2017; 18(4): 491–512, doi: 10.1007/s40257-017-0269-x, indexed in Pubmed: 28303481.

16. Noakes R. Assessing the response of morphea and limited scleroderma to tranilast: a small prospective study com-paring topical corticosteroids to a combination of topical corticosteroids and tranilast. Clin Cosmet Investig Dermatol. 2018; 11: 321–326, doi: 10.2147/CCID.S160923, indexed in Pubmed: 30013378.

17. Ozlu E, Karadag AS, Akdeniz N, et al. Morphea secondary to interferon beta1b injection: a case and review of the literature. Dermatol Online J. 2019; 25(4), indexed in Pubmed: 31046913.

18. Rongioletti F, Ferreli C, Atzori L, et al. Scleroderma with an update about clinico-pathological correlation. G Ital Dermatol Venereol. 2018; 153(2): 208–215, doi: 10.23736/S0392-0488.18.05922-9, indexed in Pubmed: 29368844.

19. Sartori-Valinotti JC, Tollefson MM, Reed AM. Updates on morphea: role of vascular injury and advances in treatment. Autoimmune Dis. 2013; 2013: 467808, doi: 10.1155/2013/467808, indexed in Pubmed: 24319593.

20. Shalaby SM, Bosseila M, Fawzy MM, et al. Fractional carbon dioxide laser versus low-dose UVA-1 phototherapy for treatment of localized scleroderma: a clinical and immuno-histochemical randomized controlled study. Lasers Med Sci. 2016; 31(8): 1707–1715, doi: 10.1007/s10103-016-2041-5, indexed in Pubmed: 27510285.

21. Sommer A, Gambichler T, Bacharach-Buhles M, et al. Clinical and serological characteristics of progressive facial hemiatrophy: a case series of 12 patients. J Am Acad Dermatol. 2006; 54(2): 227–233, doi: 10.1016/j.jaad.2005.10.020, indexed in Pubmed: 16443052.

22. Tang MM, Bornstein MM, Irla N, et al. Oral mucosal morphea: a new variant. Dermatology. 2012; 224(3): 215–220, doi: 10.1159/000337554, indexed in Pubmed: 22538799.

23. Tratenberg M, Gutwein F, Rao V, et al. Localized scleroderma: a clinical review. Curr Rheumatol Rev. 2017; 13(2): 86–92, doi: 10.2174/1573397112666160907105434, indexed in Pubmed: 27604889.

24. Vigneron C, Bauer N, Waisse W, et al. Morphée du sein radio-induite : une complication méconnue. Cancer/ /Radiothér. 2014; 18(1): 64–67, doi: 10.1016/j.canrad.2013.09.006.

VIA MEDICA

R E V I E W   A R T I C L E

"False" foramina and fissures of the skull: a narrative review with clinical implications

C. Werner[1], M. Mathkour[2, 3], J. Koueik[4], Ł. Olewnik[5], A. Aysenne[1], M. Loukas[6, 7], J. Iwanaga[1, 8, 9], A.S. Dumont[1], R.S. Tubbs[1, 6, 8, 10–13]

[1]Department of Neurosurgery, Tulane Centre for Clinical Neurosciences, Tulane University School of Medicine, New Orleans, LA, United States
[2]Tulane University and Ochsner Clinic Neurosurgery Programme, Tulane University School of Medicine, New Orleans LA, United States
[3]Neurosurgery Division, Surgery Department, Jazan University, Jazan, Kingdom of Saudi Arabia
[4]Department of Neurological Surgery, University of Wisconsin, Madison, WI, United States
[5]Department of Anatomical Dissection and Donation, Medical University of Lodz, Poland
[6]Department of Anatomical Sciences, St. George's University, St. George's, Grenada
[7]Department of Anatomy, University of Warmia and Mazury, Olsztyn, Poland
[8]Department of Neurology, Tulane Centre for Clinical Neurosciences, Tulane University School of Medicine, New Orleans, LA, United States
[9]Division of Gross and Clinical Anatomy, Department of Anatomy, Kurume University School of Medicine, Kurume, Fukuoka, Japan
[10]Department of Structural and Cellular Biology, Tulane University School of Medicine, New Orleans, LA, United States
[11]Department of Surgery, Tulane University School of Medicine, New Orleans, LA, United States
[12]Department of Neurosurgery and Ochsner Neuroscience Institute, Ochsner Health System, New Orleans, LA, United States
[13]University of Queensland, Brisbane, Australia

"False" foramina and fissures of the skull are described as openings formed between the adjacent edges of two or more bones and not conduits directly through a single bone. Trauma and metabolic disorders appear to affect these foramina and fissures differently when compared to the "true" foramina and fissures. Therefore, the aim of this paper is to provide a narrative review of the current literature about "false" foramina and fissures of the skull and skull base with a focus on their clinical significance. (Folia Morphol 2022; 81, 3: 551–558)

Key words: pseudo, foramina, fissures, skull base, calvaria

INTRODUCTION

The skull and skull base are the most complex bony structures in the human body. They must provide numerous passageways for arteries, veins, and nerves to enter and exit from the brain and surrounding intracranial structures. Many of the foramina that allow the passage of neurovascular structures are entirely contained within a single bone. The foramen rotundum and foramen spinosum located within the sphenoid bone are two examples [53]. However, additional "false" or pseudoforamina and fissures are openings formed between the adjacent edges of two or more bones. With similar logic, we have previously reviewed the so-called "false" ligaments that do not connect two bones together but rather begin and end on the same bone (e.g. suprascapular ligament) [50]. With similar logic, we here describe a "false" foramen as an opening or passage not within a single bone but

Address for correspondence: J. Iwanaga, DDS, PhD, Department of Neurosurgery, Tulane Centre for Clinical Neurosciences,
131 S. Robertson St. Suite 1300, New Orleans, LA 70112, USA, tel: 5049885565, fax: 5049885793, e-mail: iwanagajoeca@gmail.com

rather created by the approximation of two nearby bones. An example of such a foramen is the jugular foramen, which is situated between the temporal and occipital bones. As most medical dictionaries define a foramen as an opening through "a bone", the present article identifies and provides a narrative review of the "false" foramina and fissures of the skull and skull base with a focus on their distinction from "true" foramina and their clinical significance. The term "false foramen" has been used by other authors [3, 7, 13]. However, the definition of false skull foramina has been loose, so that our review is the first attempt to establish a true definition and review the topic. Moreover, the notion of a false foramen does have significant clinical implications. Skull base fractures are more likely to injure structures traveling in a "true" skull base foramen than a "false" foramen as fractures are less likely to cross a foramen created between two adjacent bones. Therefore, the neurovascular structures contained within these passages are somewhat more protected. The present article identifies and provides a narrative review of the "false" foramina and fissures of the skull and skull base, focusing on their distinction from "true" foramina. The clinical significance of this distinction is also discussed.

REVIEW

Bony anatomy of the skull

The superior region of the skull, also known as the calvaria, is formed from parts of the frontal, occipital, and parietal bones [48]. The skull base or basicranium is formed from the inferior parts of those bones in addition to parts of the ethmoid, sphenoid, and temporal bones [44]. Inferior to the anterior region of the skull base, the facial skeleton or viscerocranium consists of 14 bones: the inferior nasal turbinate bones (2), lacrimal bones (2), mandible (1), maxillae (2), nasal conchae bones (2), palatine bones (2), vomer (1), and zygomatic bones (2) [30]. Most skull bones are joined together by fibrous sutures that normally close during the first through sixth decades of life [20, 32].

The skull base is typically divided into anterior, middle, and posterior parts for convenience of organization. The anterior skull base consists mainly of the frontal and ethmoid bones in addition to parts of the sphenoid bone, and its posterior borders are the lesser wings of the sphenoid [45]. The inferior depression known as the anterior cranial fossa houses the frontal lobes of the cerebral hemispheres and allows for the passage of cranial nerve (CN) I fibres through the cribriform plate foramina. The named foramina include the foramen cecum and the anterior and posterior ethmoidal foramina, which transmit the anterior and posterior ethmoidal arteries and nerves, and ethmoidal veins.

The middle cranial fossa is formed from the occipital, sphenoid, and temporal bones, the body of the sphenoid forming its anterior border and the basilar part of the occipital bone (anterior to the foramen magnum) its posterior border [29]. The middle cranial fossa contains many foramina and fissures: the optic foramen (canal), superior orbital fissure, foramen rotundum, foramen ovale, foramen spinosum, foramen lacerum, the hiatuses of the greater and lesser petrosal nerves, and the carotid canal. These constitute passages for CN II–VI or their major branches, the internal carotid artery (ICA), and numerous smaller arteries, nerves, and veins.

The posterior skull base is formed from the sphenoid, temporal, and occipital bones and houses the cerebellum, pons, and medulla oblongata. The anterior borders of the posterior cranial fossa are the dorsum sellae, parts of the body of the sphenoid, and parts of the basilar part of the occipital bone [44]. The foramen magnum is the most significant passageway in the posterior cranial fossa and transmits the medulla oblongata, which continues inferiorly as the spinal cord, and the spinal and vertebral arteries [49]. In addition, the spinal part of the accessory nerve traverses this foramen. Additional named passageways include the internal acoustic meatus, jugular foramen, and hypoglossal canal, which are passages for CN VII–XII and important vasculature, including the internal jugular vein [45]. Variant skull foramina include the orbitomeningeal, retromolar, and sphenoidal emissary foramina [27, 28, 31, 36].

False foramina and fissures of the anterior skull

"False" foramina and fissures can be found in all three fossae of the skull base. A complete list is given in Table 1.

The **foramen cecum** (Fig. 1) is a small notch formed at the junction between the frontal crest of the frontal bone and the ethmoid bone [45]. It normally closes via ossification during the first few years of life; however, foramen cecum patency has been reported in adults and can manifest as a nasoethmoidal encephalocele or dermoid cyst secondary

Table 1. Summary of calvarial and skull base false foramina and fissures

Skull location	Name	Surrounding bones	Contained structures
Anterior	Foramen cecum	Frontal, ethmoid	Emissary vein
	Sphenopalatine foramen	Sphenoid, palatine	Sphenopalatine artery and vein, posterior superior lateral nasal nerve, nasopalatine nerves
	Palatovaginal canal	Sphenoid, palatine	Pharyngeal branch of maxillary artery, pharyngeal nerve
	Vomerovaginal canal	Sphenoid, vomer	None
Middle	Foramen lacerum	Sphenoid, temporal, occipital	Meningeal branch of ascending pharyngeal artery, greater petrosal nerve, deep petrosal nerve, vidian nerve
	Superior orbital fissure	Sphenoid	Cranial nerve III–VI branches, ophthalmic veins, branches of middle meningeal and lacrimal arteries
	Inferior orbital fissure	Sphenoid, maxilla, zygomatic bone	Cranial nerve V branches, infraorbital artery
Posterior	Jugular foramen	Temporal, occipital	Inferior petrosal sinus, sigmoid sinus, cranial nerve IX–XI, meningeal branches of ascending pharyngeal artery and occipital arteries
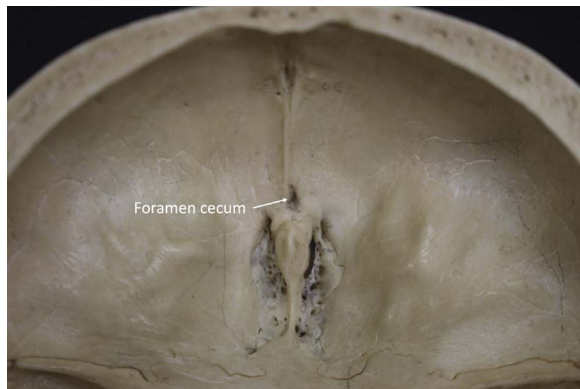
Figure 1. Superior view of the foramen cecum.
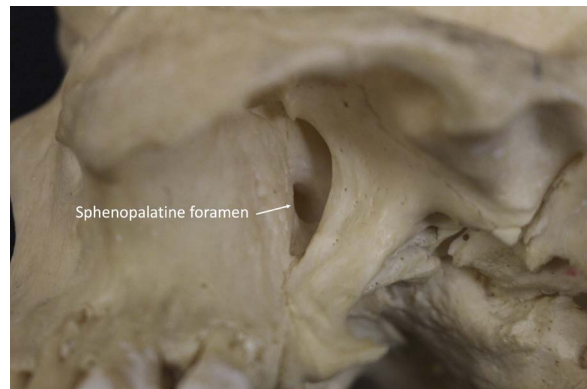
Figure 2. Inferolateral view of the left sphenopalatine foramen.

to dural extension of a dermoid sinus [2, 30]. It can transmit an emissary vein that runs from the nasal cavity to the superior sagittal sinus, thus paranasal sinus infections can spread to the intracranial cavity and cause meningitis and brain abscesses [45].

The **sphenopalatine foramen** (Fig. 2) is formed at the junction of the sphenopalatine notch of the palatine bone and the body of the sphenoid and leads from the pterygopalatine fossa to the nasal cavity [45]. While it is historically described as culminating in the posterior part of the middle nasal concha of the superior meatus, more recent anatomical studies have classified it on the basis of its openings to the superior and middle meatuses [52]. It transmits the sphenopalatine artery and vein, the posterior superior lateral nasal nerve, and the nasopalatine nerves [45]. The sphenopalatine foramen is clinically significant primarily in regard to epistaxis arising from the sphenopalatine artery, and anatomical variations can affect surgical planning and the outcome of proce-
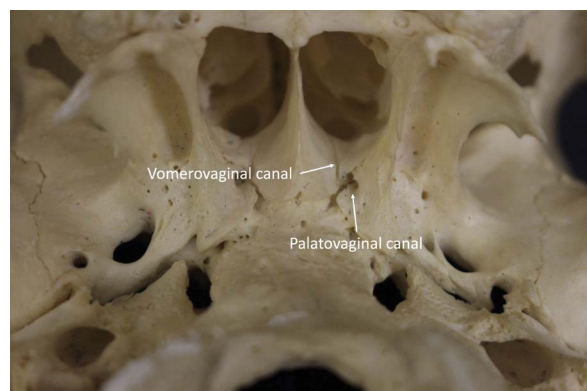
Figure 3. Inferior view of the left vomerovaginal and palatovaginal canals.

dures such as sphenopalatine artery ligation [41]. It is also used as a target for pterygopalatine ganglion aesthetic blockade [22].

The **palatovaginal canal** (Fig. 3) is a passage from the pterygopalatine fossa to the roof of the pharynx

Figure 4. Superolateral view of the right foramen lacerum.
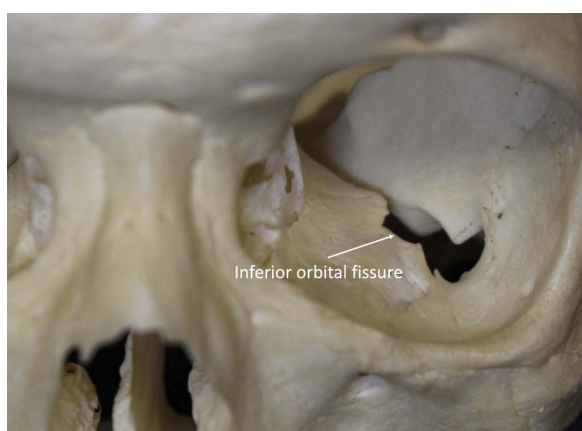
Figure 5. Anterior view of the left inferior orbital fissure.
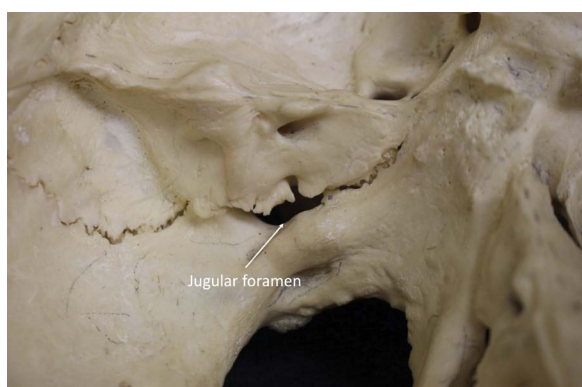
Figure 6. Superomedial view of the left jugular foramen.

located between the vaginal process from the medial plate of the pterygoid process of the sphenoid bone and the sphenoidal process of the palatine bone [45]. The major structures it contains are the pharyngeal branches of the maxillary artery and the maxillary division of CN V. Additionally, anatomical variants of the sphenopalatine vasculature can trav-

el through the palatovaginal canal and complicate epistaxis treatment [40]. Neoplastic spread through the palatovaginal canal has also been reported in the literature [40].

Medially, the **vomerovaginal canal** (Fig. 3), if present, is located between the alae of the vomer and the vaginal processes of the sphenoid bone bilaterally. It leads into the anterior end of the palatovaginal canal [45]. It is an inconstant canal and no major structures pass through it [35].

False foramina and fissures of the middle skull

The triangular-shaped **foramen lacerum** (Fig. 4) is located posteromedial to the foramen ovale and is formed by the body and roots of the pterygoid process and the greater wing of the sphenoid bone anteriorly, the apex of the petrous part of the temporal bone posterolaterally, and the basilar part of the occipital bone medially [45]. A meningeal branch of the ascending pharyngeal artery, the vidian artery and nerve (formed within the foramen by the greater petrosal and deep petrosal nerves), and an emissary vein pass through it. The lacerum segment of the ICA traverses it superiorly but does not pass through it [32]. Normally, the inferior foramen lacerum fills with cartilage after birth. Partial occlusion has been reported and used to classify different foramen types, some of which necessitate alternative routes for structures that normally traverse the foramen such as the greater petrosal nerve [43]. The greater petrosal nerve, deep petrosal nerve, or vidian structures can also be compressed in cases of postnatal obliteration, leading to autonomic neuropathy. The foramen lacerum can provide a passageway for tumours to pass through the skull base, particularly if it is incompletely obliterated [38].

The **inferior orbital fissure** (Fig. 5) is located in the floor of the orbit and is formed from the greater wing of the sphenoid bone superiorly, the maxilla and orbital process of the palatine bone inferiorly, and the zygomatic bone laterally [45]. Branches of the maxillary division of CN V are the major structures that pass through it. It is an important landmark for endonasal endoscopic and orbital surgeries [10, 37]. The fissure ends at the infraorbital foramen on the face [42].

False foramina and fissures of the posterior cranial fossa

The irregularly-shaped **jugular foramen** (Fig. 6) is located at the posterior end of the petro-occipital suture and is formed anteriorly by the jugular fossa

of the petrous portion of the temporal bone and posteriorly by the jugular process of the occipital bone [15, 16, 45]. Historically, this foramen was divided into two compartments by the bony jugular spine: a pars nervosa that contained CN IX, the inferior petrosal sinus, and a meningeal branch of the ascending pharyngeal artery; and a pars venosa that contained the sigmoid sinus and CNs X and XI [24, 45]. Recent anatomical studies have yielded a three compartment classification: an anterior portion that transmits the inferior petrosal sinus, an intermediate portion that transmits CNs IX–XI, and a posterior portion that transmits the sigmoid sinus and meningeal branches of both the ascending pharyngeal and occipital arteries [24, 25]. These compartments are separated by dural septa that connect opposing intrajugular processes of the temporal and occipital bones [29]. The jugular foramen is a common site of skull base tumours including paragangliomas (globus jugulare tumours), schwannomas, and meningiomas [13].

Developmental differences and similarities

The skull is a developmentally complex structure to which both the neural crest and mesoderm contribute. It undergoes both intramembranous and endochondral ossification [31]. The palatine and maxillary bones are neural crest-derived intramembranous bones, and the occipital bone is a mesodermal endochondral bone [33]. Therefore, both bone ossification patterns form "false" foramina: the infraorbital fissure is formed from the maxillary bone and the jugular foramen from the occipital bone. The various ossification patterns of the foramen lacerum are possible owing to its formation within the endochondral bones [43]. Likewise, both ossification patterns form "true" foramina such as the palatine foramina (within the palatine bone) and hypoglossal canal (within the occipital bone).

Studies on chick embryo models examining the development of the jugular foramen and hypoglossal canal have shown that mesenchymal tissue first surrounds the contained blood vessel [33]. The mesenchyme is less dense than surrounding mesenchyme, which forms the cartilage of the non-foraminal bone. Next, the mesenchymal cells adjacent to the blood vessel and nerves change morphology to resemble perichondral cells. At this stage, the jugular "false" foramen appears different from the hypoglossal "true" foramen in that its shape conforms better to the contained blood vessel. However, no studies have

examined the clinical significance of this difference. It is currently under debate whether blood vessels, nerves, or both are primarily responsible for directing the formation of foramina, and further studies could provide more information on developmental differences between "true" and "false" foramina. A better understanding of this embryology might lead to an improved understanding of patients who are prone to developing stenosis of various skull base foramina such as patients with achondroplasia and stenosis or narrowing of the jugular foramen.

Skull fractures involving foramina and fissures

Traumatic skull base injuries can pose significant challenges to surgeons because of their complex anatomy and symptomatology. The orbit is a common place for fractures owing to its relative weakness [25]. Fractures of the superior orbital fissure can result in superior orbital fissure syndrome [54]. Typical symptoms include diplopia, extraocular muscle weakness, exophthalmos, and ptosis [54]. Crush injury and fracture of the petrous part of the temporal bone can lead to avulsion of the petrous part of the temporal bone backwards with inward rotation of the apex and can cause severe distortion of the foramen lacerum [23]. This can damage nearby structures such as the ICA. Additionally, CN VI can be stretched, so patients with fractures in this region typically present with abducens nerve palsy [26].

Fractures of the posterior skull base are less common but identifiable when patients present with deficits in multiple cranial nerves [17]. Jugular foramen fractures presenting with lower cranial nerve deficits have been reported in the setting of occipital bone fracture with subsequent direct nerve injury or delayed ischaemia-related oedema [1, 47]. Rarely, severe trauma to the occiput can cause a fracture that courses from the jugular foramen, across the petrous part of the temporal bone, and through the foramina spinosum to the foramen lacerum and the foramen magnum [25]. However, skull base fractures are more likely to injure structures travelling in a "true" skull base foramen than a "false" foramen as fractures are unlikely to cross a foramen created between two adjacent bones unless there is significant blunt trauma to the region that affects multiple bones. Therefore, the neurovascular structures contained within these passages are somewhat more protected.

Severe basilar fractures can involve these "false" foramina because unions of multiple bones are inher-

ently weak points in the skull base [51]. Moreover, most cranial nerves are carried by these foramina, so fractures of the "true" foramina could be underreported because the resulting neurological deficits are inconspicuous. Hypothetically, the true foramina might offer additional protection to the nerves and vessels that traverse them and future studies might address this difference.

Disorders of bone and cartilage

Paget's disease (PD) is a chronic bone disorder characterised by increased cellular turnover that can involve bones of the skull [8]. PD of the skull frequently results in areas of localised or diffuse thickening and interspersed areas of osteoporotic lesions [39]. The most common neurological symptom is hearing loss, which is thought to be due to loss of bone mineral density in the cochlear capsule, not to internal acoustic meatus narrowing (stenosis) secondary to sclerosis [34]. To the best of our knowledge, there are no reported cases of "false" foramina narrowing in the setting of PD of the skull. However, optic neuropathy due to optic canal sclerosis has been reported [12].

Fibrous dysplasia is another chronic bone disorder that often affects craniofacial bones including the ethmoid, sphenoid, frontal, and temporal bones [19]. It is thought to involve abnormal growth and differentiation of marrow stromal cells resulting in abundant expansile fibrous tissue deposition in place of normal bone, causing structural defects [19]. In contrast to PD, fibrous dysplasia causes conductive hearing loss due to external acoustic meatus stenosis [6]. Narrowing of the optic canal and jugular foramen has also been reported [4, 46]. While there have been no studies directly examining the histopathology of PD or fibrous dysplasia in cranial foramina, differences in which foramina are affected could be due to pathophysiology instead of differences between "true" and "false" foramina. However, multiple bones provide multiple sites for the initiation of bony expansion; the jugular foramen can become stenotic from either temporal or occipital bone overgrowth, while the hypoglossal canal must become stenotic from occipital bone overgrowth.

As both intramembranous and endochondral ossification are involved in the formation of both "true" and "false" foramina, it is unlikely that cartilaginous disorders would preferentially affect one type of foramen. In one such disorder, achondroplasia, cartilage cannot be fully converted to bone and the foramen

magnum is commonly stenotic at birth. The narrowing of the jugular foramen increases intracranial venous pressures and in turn alters the cerebrospinal fluid dynamics, frequently resulting in hydrocephalus in this particular patient population. Notably, studies suggest that this stenosis results partly from premature closure of the posterior intraoccipital synchondroses [18]. Abnormalities in other skull base synchondroses could in principle affect the "false" foramina formed from them [5]. For example, the spheno-occipital synchondrosis, which forms part of the foramen lacerum border, can close prematurely, preventing normal foramen expansion and causing constriction of neurovascular structures [11].

CONCLUSIONS

In this review we have explored all the cranial foramina and fissures that are formed from parts of more than one bone. These "false" foramina share similarities with the "true" neurovascular passageways formed within a single bone, but also differ from them. Future study on the developmental differences between the two foramen types is warranted in order to elucidate their clinical significance further. Additionally, how anatomical variations and various mechanisms for skull base fracture affect the true versus false skull base foramina should be studied in patient cohorts [9, 14, 41].

Acknowledgements

Conflict of interest: None declared

REFERENCES

1. Alberio N, Cultrera F, Antonelli V, et al. Isolated glossopharyngeal and vagus nerves palsy due to fracture involving the left jugular foramen. Acta Neurochir (Wien). 2005; 147(7): 791–794, doi: 10.1007/s00701-005-0547-x, indexed in Pubmed: 15891807.

2. Amir R, Dunham ME. Bilateral choanal atresia associated with nasal dermoid cyst and sinus: a case report and review of the literature. Int J Pediatr Otorhinolaryngol. 2001; 58(1): 81–85, doi: 10.1016/s0165-5876(00)00463-8, indexed in Pubmed: 11249985.

3. Beshtawi K, Qirresh E, Parker M, et al. Custom focal trough in cone-beam computed tomography reformatted

panoramic versus digital panoramic for mental foramen position to aid implant planning. J Clin Imaging Sci. 2020; 10: 34, doi: 10.25259/JCIS_150_2019, indexed in Pubmed: 32547837.

4. Brown EW, Megerian CA, McKenna MJ, et al. Fibrous dysplasia of the temporal bone: imaging findings. AJR Am J Roentgenol. 1995; 164(3): 679–682, doi: 10.2214/ajr.164.3.7863893, indexed in Pubmed: 7863893.

5. Cendekiawan T, Wong R, Rabie A. Relationships between cranial base synchondroses and craniofacial development: a review. Open Anat J. 2010; 2(1): 67–75, doi: 10.2174/1877609401002010067.

6. Chinski A, Beider B, Cohen D. Fibrous dysplasia of the temporal bone. Int J Pediatr Otorhinolaryngol. 1999; 47(3): 275–281, doi: 10.1016/s0165-5876(98)00184-0, indexed in Pubmed: 10321784.

7. Coquet T, Lefranc M, Chenin L, et al. Unilateral duplicated abducens nerve coursing through both the sphenopetro-clival venous gulf and cavernous sinus: a case report. Surg Radiol Anat. 2018; 40(7): 835–840, doi: 10.1007/s00276-018-2003-7, indexed in Pubmed: 29541802.

8. Cundy T, Reid IR. Reprint: Paget's disease of bone. Clin Biochem. 2012; 45(12): 970–975, doi: 10.1016/j.clinbio-chem.2012.06.011, indexed in Pubmed: 22728011.

9. Cvetko E, Bosnjak R. Unilateral absence of foramen spi-nosum with bilateral ophthalmic origin of the middle meningeal artery: case report and review of the literature. Folia Morphol. 2014; 73(1): 87–91, doi: 10.5603/FM.2014.0013, indexed in Pubmed: 24590529.

10. De Battista JC, Zimmer LA, Theodosopoulos PV, et al. Anatomy of the inferior orbital fissure: implications for endoscopic cranial base surgery. J Neurol Surg B Skull Base. 2012; 73(2): 132–138, doi: 10.1055/s-0032-1301398, indexed in Pubmed: 23542710.

11. Di Ieva A, Bruner E, Haider T. Skull base embryology: a multidisciplinary review. Childs Nerv Syst. 2014; 30: 991–1000.

12. Eretto P, Krohel GB, Shihab ZM, et al. Optic neuropathy in Paget's disease. Am J Ophthalmol. 1984; 97(4): 505–510, doi: 10.1016/s0002-9394(14)76136-7, indexed in Pubmed: 6720822.

13. Fayad JN, Keles B, Brackmann DE. Jugular foramen tumors: clinical characteristics and treatment outcomes. Otol Neurotol. 2010; 31(2): 299–305, doi: 10.1097/MAO.0b013e3181be6495, indexed in Pubmed: 19779386.

14. Ghosh S, Narayan R. Fractures involving bony orbit: A comprehensive review of relevant clinical anatomy. Trans Res Anat. 2021; 24: 100125, doi: 10.1016/j.tria.2021.100125.

15. Gkasdaris G, Tripsianis G, Kotopoulos K, et al. Clinical anatomy and significance of the thoracic intervertebral foramen: A cadaveric study and review of the literature. J Craniovertebr Junction Spine. 2016; 7(4): 228–235, doi: 10.4103/0974-8237.193266, indexed in Pubmed: 27891032.

16. Gul B, Samanci C, Uluduz DU, et al. Does measurement of the jugular foramen diameter on MRI help to differentiate transverse sinus thrombosis from unilateral transverse sinus hypoplasia? Radiol Med. 2021; 126(3): 430–436, doi: 10.1007/s11547-020-01265-0, indexed in Pubmed: 32857273.

17. Gutierrez S, Warner T, McCormack E, et al. Lower cranial nerve syndromes: a review. Neurosurg Rev. 2021; 44(3): 1345–1355, doi: 10.1007/s10143-020-01344-w, indexed in Pubmed: 32638140.

18. Hecht JT, Nelson FW, Butler IJ, et al. Computerized tomography of the foramen magnum: achondroplastic values compared to normal standards. Am J Med Genet. 1985; 20(2): 355–360, doi: 10.1002/ajmg.1320200219, indexed in Pubmed: 3976726.

19. Hullar TE, Lustig LR. Paget's disease and fibrous dysplasia. Otolaryngol Clin North Am. 2003; 36(4): 707–732, doi: 10.1016/s0030-6665(03)00028-8, indexed in Pubmed: 14567061.

20. Idriz S, Patel JH, Ameli Renani S, et al. CT of normal developmental and variant anatomy of the pediatric skull: distinguishing trauma from normality. Radiographics. 2015; 35(5): 1585–1601, doi: 10.1148/rg.2015140177, indexed in Pubmed: 26207580.

21. Iwanaga J, Singh V, Ohtsuka A, et al. Acknowledging the use of human cadaveric tissues in research papers: Recommendations from anatomical journal editors. Clin Anat. 2021; 34(1): 2–4, doi: 10.1002/ca.23671, indexed in Pubmed: 32808702.

22. Iwanaga J, Wilson C, Simonds E, et al. Clinical anatomy of blockade of the pterygopalatine ganglion: literature review and pictorial tour using cadaveric images. Kurume Med J. 2018; 65(1): 1–5, doi: 10.2739/kurumemedj.MS651001, indexed in Pubmed: 30158355.

23. Katsuno M, Yokota H, Yamamoto Y, et al. Bilateral traumatic abducens nerve palsy associated with skull base fracture--case report. Neurol Med Chir (Tokyo). 2007; 47(7): 307–309, doi: 10.2176/nmc.47.307, indexed in Pubmed: 17652916.

24. Katsuta T, Rhoton AL, Matsushima T. The jugular foramen: microsurgical anatomy and operative approaches. Neurosurgery. 1997; 41(1): 149–201; discussion 201, doi: 10.1097/00006123-199707000-00030, indexed in Pubmed: 9218307.

25. Katzen JT, Jarrahy R, Eby JB, et al. Craniofacial and skull base trauma. J Trauma. 2003; 54(5): 1026–1034, doi: 10.1097/01.TA.0000066180.14666.8B, indexed in Pubmed: 12777923.

26. Khan N, Zumstein B. Transverse clivus fracture: case presentation and significance of clinico-anatomic correlations. Surg Neurol. 2000; 54(2): 171–177, doi: 10.1016/s0090-3019(00)00284-6, indexed in Pubmed: 11077100.

27. Lai PF, Wu X, Lan SH, et al. Anatomical study of a surgical approach through the neck to the jugular foramen under endoscopy. Surg Radiol Anat. 2021; 43(2): 251–260, doi: 10.1007/s00276-020-02574-9, indexed in Pubmed: 32959079.

28. Leonel LC, Peris-Celda M, de Sousa SD, et al. The sphenoidal emissary foramen and the emissary vein: Anatomy and clinical relevance. Clin Anat. 2020; 33(5): 767–781, doi: 10.1002/ca.23504, indexed in Pubmed: 31625185.

29. Linn J, Peters F, Moriggl B, et al. The jugular foramen: imaging strategy and detailed anatomy at 3T. Am J Neuroradiol. 2009; 30(1): 34–41, doi: 10.3174/ajnr.A1281, indexed in Pubmed: 18832666.

30. Lowe LH, Booth TN, Joglar JM, et al. Midface anomalies in children. Radiographics. 2000; 20(4): 907–22; quiz 1106, doi: 10.1148/radiographics.20.4.g00jl07907, indexed in Pubmed: 10903683.

31. Macchi V, Regoli M, Bracco S, et al. Clinical anatomy of the orbitomeningeal foramina: variational anatomy of the canals connecting the orbit with the cranial cavity. Surg Radiol Anat. 2016; 38(2): 165–177, doi: 10.1007/s00276-015-1530-8, indexed in Pubmed: 26233593.

32. Mancall EL, Brock DG. Gray's Clinical Neuroanatomy E-Book. Elsevier Health Sciences 2011.

33. McGonnell IM, Akbareian SE. Like a hole in the head: Development, evolutionary implications and diseases of the cranial foramina. Semin Cell Dev Biol. 2019; 91: 23–30, doi: 10.1016/j.semcdb.2018.08.011, indexed in Pubmed: 30385045.

34. Monsell EM. The mechanism of hearing loss in Paget's disease of bone. Laryngoscope. 2004; 114(4): 598–606, doi: 10.1097/00005537-200404000-00002, indexed in Pubmed: 15064610.

35. Narayan R, Verma M. Cranial base. Encyclopedia of Animal Cognition and Behavior. 2019: 1–13, doi: 10.1007/978-3-319-47829-6_1278-1.

36. Ngeow WC, Chai WL. The clinical significance of the retromolar canal and foramen in dentistry. Clin Anat. 2021; 34(4): 512–521, doi: 10.1002/ca.23577, indexed in Pubmed: 32020669.

37. Ozer MA, Celik S, Govsa F. A morphometric study of the inferior orbital fissure using three-dimensional anatomical landmarks: application to orbital surgery. Clin Anat. 2009; 22(6): 649–654, doi: 10.1002/ca.20829, indexed in Pubmed: 19670289.

38. Phelps PD, Beale DJ. The foramen lacerum: a route of access to the cranial cavity for malignant tumours below the skull base. Clin Radiol. 1992; 46(3): 179–183, doi: 10.1016/s0009-9260(05)80441-6.

39. Poppel MH, Jacobson HG, Duff BK, et al. Basilar impression and platybasia in Paget's disease. Radiology. 1953; 61(4): 639–644, doi: 10.1148/61.4.639, indexed in Pubmed: 13100676.

40. Rumboldt Z, Castillo M, Smith JK. The palatovaginal canal: can it be identified on routine CT and MR imaging? Am J Roentgenol. 2002; 179(1): 267–272, doi: 10.2214/ajr.179.1.1790267, indexed in Pubmed: 12076948.

41. Scanavine A, Navarro J, Megale Sd, et al. Anatomical study of the sphenopalatine foramen. Braz J Otorhinolaryngol. 2009; 75(1): 37–41, doi: 10.1016/s1808-8694(15)30829-6.

42. Shin KJ, Shin HJ, Lee SH. Location of the infraorbital foramen with reference to soft tissue landmarks for regional nerve blocks during midface surgery. Clin Anat. 2020; 33(8): 1159–1163, doi: 10.1002/ca.23556, indexed in Pubmed: 31894604.

43. Singh R, Kumar R. Variations in the morphology of foramen lacerum. J Craniofac Surg. 2020; 31(6): 1848–1850, doi: 10.1097/SCS.0000000000006521, indexed in Pubmed: 32487831.

44. Skrzat J, Walocha J, Zawiliński J. Accessory spine of the foramen ovale. Folia Morphol. 2012; 71(4): 263–266, indexed in Pubmed: 23197146.

45. Standring S. Gray's anatomy 42nd ed. Elsevier, London 2020.

46. Taşar M, Ors F, Yetişer S, et al. Multiple globoid meningiomas associated with craniomandibular fibrous dysplasia: case report. Clin Imaging. 2004; 28(1): 20–22, doi: 10.1016/S0899-7071(03)00008-1, indexed in Pubmed: 14996442.

47. Toledo-Gotor C, Gorría N, Oscoz M, et al. Posttraumatic delayed jugular foramen syndrome in a toddler. Neuropediatrics. 2021; 52(5): 403–405, doi: 10.1055/s-0040-1722684, indexed in Pubmed: 33511597.

48. Tubbs RS, Bosmia AN, Cohen-Gadol AA. The human calvaria: a review of embryology, anatomy, pathology, and molecular development. Childs Nerv Syst. 2012; 28(1): 23–31, doi: 10.1007/s00381-011-1637-0, indexed in Pubmed: 22120469.

49. Ulcay T, Kamaşak B, Görgülü Ö, et al. A golden ratio for foramen magnum: an anatomical pilot study. Folia Morphol. 2022; 81(1): 220–226, doi: 10.5603/FM.a2021.0018, indexed in Pubmed: 33634836.

50. Vetter M, Oskouian RJ, Tubbs RS. "False" ligaments: a review of anatomy, potential function, and pathology. Cureus. 2017; 9(11): e1853, doi: 10.7759/cureus.1853, indexed in Pubmed: 29372127.

51. Wani A, Ramzan A, Raina T, et al. Skull base fractures: An institutional experience with review of literature. Indian J Neurotr. 2013; 10(2): 120–126, doi: 10.1016/j.ijnt.2013.05.009.

52. Wareing MJ, Padgham ND. Osteologic classification of the sphenopalatine foramen. Laryngoscope. 1998; 108(1 Pt 1): 125–127, doi: 10.1097/00005537-199801000-00024, indexed in Pubmed: 9432081.

53. Worku M, Clarke E. Morphometric analysis of the foramen spinosum and variations of its shape, number, and relation to the spine of the sphenoid bone. Transl Res Anat. 2021; 24: 100124, doi: 10.1016/j.tria.2021.100124.

54. Zachariades N, Vairaktaris E, Papavassiliou D, et al. The superior orbital fissure syndrome. J Maxillofac Surg. 1985; 13(3): 125–128, doi: 10.1016/s0301-0503(85)80031-x, indexed in Pubmed: 3860588.

ORIGINAL ARTICLE

VM VIA MEDICA

Morphologic characterisation of the posterior inferior cerebellar artery. A direct anatomic study

L.E. Ballesteros-Acuña[1], H.Y. Estupiñán[1, 2] , F.A. Gómez-Torres[1]

[1]Department of Basic Sciences, Medicine School, Universidad Industrial de Santander, Bucaramanga, Colombia
[2]Department of Laboratory Medicine, Clinical Research Centre, Karolinska Institute, Karolinska University Hospital Huddinge, Huddinge, Sweden

Background: The number of studies on the cerebellar arteries has increased. The purpose of this study was to determine the morphological expression of posterior inferior cerebellar artery in a sample of Colombian population.
Materials and methods: One hundred eighty-six posterior inferior cerebellar arteries of fresh cadavers were studied. In each specimen, vertebral arteries were injected with 100 mL of semi-synthetic resin, dyed with mineral red.
Results: In the 93 blocks of brainstem and cerebellum evaluated, 174 (93.5%) posterior inferior cerebellar arteries were found. Also, there were 12 (6.5%) ageneses. There was single posterior inferior cerebellar artery in 159 (91.4%) samples and duplicate in 10 (5.7%), while 5 (2.9%) specimens showed hypoplasia. The posterior inferior cerebellar artery originated from the vertebral artery in 121 (69.5%) samples and from the basilar artery in 42 (24.1%) samples; while in 11 (6.4%) it originated in a common trunk with the anterior inferior cerebellar artery. In 101 (83.5%) cases, the posterior inferior cerebellar artery originated from the intracranial segment of the vertebral artery, while 20 (16.5%) samples originated from the extracranial segment. The calibres of posterior inferior cerebellar artery in its proximal and distal segments were 1.45 ± 0.37 mm and 1.33 ± 0.31 mm, respectively.
Conclusions: This study, carried out in cadaveric material, provides relevant qualitative and morphometric information of the posterior inferior cerebellar artery, useful for the diagnosis and clinical management, as well as for the surgical approaches that may compromise this structure. (Folia Morphol 2022; 81, 3: 559–566)

Key words: cerebellar irrigation, anatomical variation, hypoplasic agenesis, vertebro-basilar junction

INTRODUCTION

Usually, the intracranial segment of vertebral artery (VA), at its distal portion, gives rise to its last branch, the posterior inferior cerebellar artery (PICA). PICA can also originate independently from basilar artery (BA), or as a common trunk with the anterior inferior cerebellar artery (AICA). PICA irrigates the posterior inferior portion of cerebellum, the spinal dorsal territory in association with posterior spinal

arteries and the spinal lateral surface in association with AICA [3, 9, 19].

Posterior inferior cerebellar artery varies in its morphological expression related to its origin, trajectory, calibres, duplications, common trunks with AICAs, agenesis and hypoplasia. In the latter scenario, another cerebellar artery modifies its trajectory to supply PICA regions, which determines dynamic balances in irrigated areas by PICA and AICA, so that when most of the inferior surface of the cerebellum is supplied by PICA, AICA's territory is lesser than PICA's or vice versa [7, 21]. Many authors agree to divide the trajectory of the PICA in anterior, lateral medullary, televelotonsilar and cortical spinal segments, which is very useful from the topographic and surgical point of view [19, 21].

Posterior inferior cerebellar artery originated from the VA in 57.1–85% of cases, with lower incidences from the BA, internal carotid and posterior meningeal artery. PICA can present itself duplicated in 0.9% to 10% [14, 17, 19, 20]. Some authors described the presence of a main trunk in 75–92% cases that bifurcates into the rostral or medial and lateral or caudal branches [9, 10, 25]. In cases of absence of the PICA, other cerebellar arteries irrigate its territories [9, 17, 20]. PICA has the most variable trajectory of the cerebellar arteries and the most complex relationship with cranial nerves. In its trajectory, it courses above the glossopharyngeal nerve in a range of 14–27.5% cases, and between the roots of the accessory nerve in 20–38% of cases; while in 5–23.8% of cases crosses the fibres of the apparent origin of the vagus nerve and in 21.4–32.5% of cases passes between the vagus and accessory nerves [9, 11, 19, 22].

The relevance of PICA is related to the possibility of thromboembolic occlusions with consequent effects ranging from silent occlusion to infarct of the cerebellum or medulla oblongata with oedema, haemorrhage, and death [9, 22]. Moreover, this artery could be affected by neurovascular compression syndromes such as glossopharyngeal neuralgia and hemifacial spasm [2, 13].

The anatomical characteristics of PICA have been evaluated in some population groups through the infusion of its vascular beds, classic dissection, or imaging studies [1, 4, 5, 9, 10, 14, 17, 19, 22]. The variant expressions of PICA with its great functional and clinical significance, makes the morphological study of these structures necessary in samples of population groups such as the mestizo (Caucasian and Native American descent), predominant in Latin America. For this rea-

son, the work done supplies in a relevant fashion new reference information in our mestizo population.

MATERIALS AND METHODS

Posterior inferior cerebellar artery of 93 unclaimed bodies were studied, who underwent autopsy at the Institute of Legal Medicine and Forensic Sciences in Bucaramanga, Colombia. The inclusion criteria of the evaluated sample were mestizo (Caucasian and Native American descent) and men aged between 18 and 75 years old. The exclusion criteria included death due to traumatic brain injury or pathologies related to the encephalon. The ethics committee of the "Universidad Industrial de Santander" approved this investigation; the study complied with Resolution 008430 of 1993, Decree 2164 of 1992 and Law 10 of 1990 of the local Ministry of Health and with the principles of the Declaration of Helsinki (1964) and all subsequent revisions.

Each cadaveric specimen was subjected to bilateral channelling of the proximal segments of the vertebral arteries; through these vessels it was performed a lavage and presetting of the brain with formaldehyde 3%. Thereafter, the vertebral arteries were injected with 100 mL of semi-synthetic resin (a mixture of Palatal E210® BASF 80 mL and Styrene 20 mL) dyed with mineral red. After 30 minutes, once obtained the resin polymerisation, the exeresis of the encephalon was performed. Then, the anatomical pieces were subjected to a formaldehyde 10% fixation for 15 days.

Afterwards, the block resection of brainstem and cerebellum was performed and the leptomeninges were released using microdissection instruments, procedure that made possible the identification of the vertebrobasilar system and each of its structures. The different morphological expressions of PICAs were recorded in relation to their presence, level of origin, calibres, trajectories, anastomosis and relations to cranial pairs according to the criteria or patterns determined by Rhoton [20]. A difference equal or greater than 0.5 mm was established as criteria for left or right-side arterial dominance [18]. A digital calibrator (Mitotuyo®) was used for all morphometric evaluations of these vessels.

Digital photographs were taken from all pieces with a professional camera Canon® T2i. The obtained data was registered in Excel spreadsheets and statistical analyses were carried out using Stata 8.0 software. For data analysis, the continuous variables were described using means and deviations and the
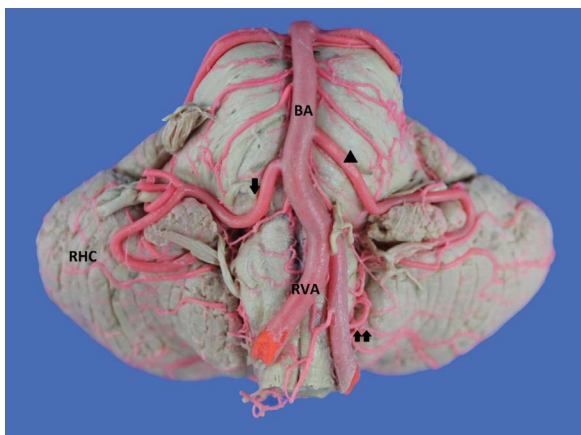
Figure 1. Front view of cerebellum. A hypoplastic left posterior inferior cerebellar artery and agenesic right one is observed. Bilateral dominance of the anterior inferior cerebellar artery; BA — basilar artery; RVA — right vertebral artery; RHC — right cerebellar hemisphere; triangular asterisk — left antero inferior cerebellar artery; arrow — right inferior anterior cerebellar artery; double arrow — hypoplastic left posterior inferior cerebellar artery.
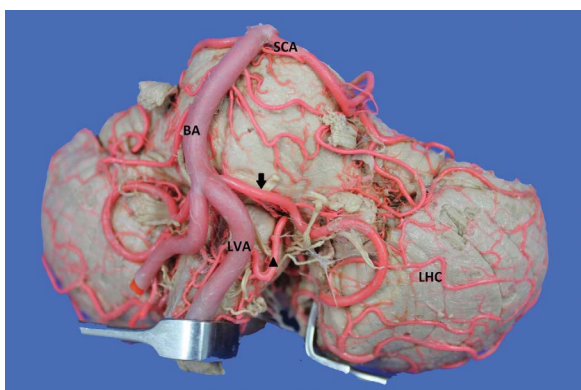
Figure 2. Front view of left cerebellar hemisphere. Posterior inferior cerebellar artery is duplicated with its origin in the vertebro-basilar junction (larger calibre) and vertebral artery; BA — basilar artery; LVA — left vertebral artery; LHC — left cerebellar hemisphere; SCA — superior cerebellar artery; arrow — inferior posterior cerebellar artery originating from the proximal segment of the basilar artery; triangular asterisk — left inferior cerebellar artery originating from the basilar artery.

Figure 3. Front view of right cerebellar hemisphere. Posterior and anterior inferior cerebellar arteries' trunks emerging from the basilar artery (BA). Additionally, a hypoplastic posterior inferior cerebellar artery originating from the vertebral artery; P — pons; arrow — trunk emerging from the basilar artery; triangular asterisk — inferior anterior cerebellar artery; double triangular asterisk — inferior posterior cerebellar artery; HPICA — hypoplastic posterior inferior cerebellar artery; SCA — superior cerebellar artery.
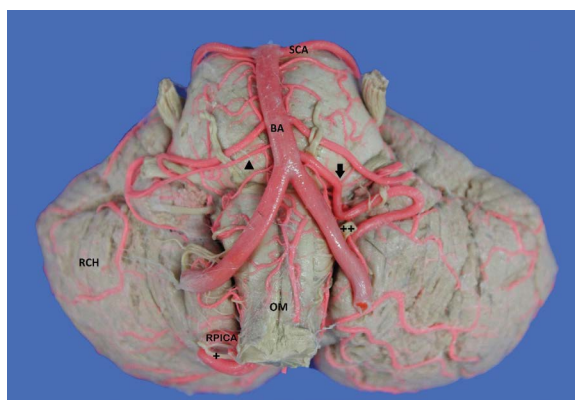
Figure 4. Anterior view of cerebellum. Left posterior inferior cerebellar artery originated from basilar artery (BA), its curse between the vagus and accessory nerves. Right posterior inferior cerebellar artery is originating from the vertebral artery's extraspinal segment relating to the spinal root of accessory nerve; RCH — right cerebellar hemisphere; OM — medulla oblongata; SCA — superior cerebellar artery; arrow — left posterior inferior cerebellar artery; RPICA — right posterior inferior cerebellar artery; +: spinal root of the accessory nerve; ++: vagus nerve.

nominal variables were described using its ratios. Statistical tests included χ^2 and t-test, accepting a significance level of $p \leq 0.05$.

RESULTS

In the 93 blocks of brainstem and cerebellum evaluated, 174 (93.5%) PICA were found, 88 on the right side and 86 on the left side. Also, there were 12 (6.5%) ageneses (Fig. 1). There was single PICA in 159 (91.4%) samples and duplicate in 10 (5.7%) samples (Fig. 2), all without statistically significant difference in relation to either presentation side (p = 0.17). Five (2.9%) specimens showed hypoplasic PICAs.

In 121 (69.5%) cases, PICA originated from the VA, while in 42 (24.1%) cases it emerged from the BA. A common trunk between PICA and AICA was observed from the VA in 7 (4.1%) samples (Fig. 3) and from the BA in 4 (2.3%) samples of blocks of brainstem and cerebellum (Fig. 4). Of the arteries with their
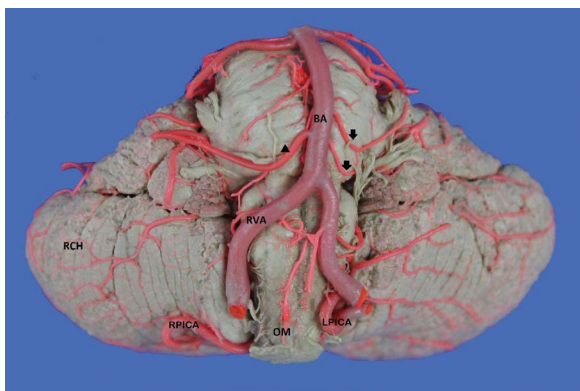
Figure 5. Anterior view of cerebellum. Bilateral origin of posterior inferior cerebellar artery from the vertebral artery's extraspinal segment. The lower loop of the tonsillomedullary segment is related with the tonsils' inferior surface; BA — basilar artery; OM — medulla oblongata; RCH — right cerebellar hemisphere; RVA — right vertebral artery; RPICA — right posterior inferior cerebellar artery; LPICA — left posterior inferior cerebellar artery; double arrow — double left anterior inferior cerebellar artery; triangular asterisk — anterior inferior cerebellar artery.

Table 1. Length and calibre of the segments of the inferior posterior cerebellar artery. Expressed in millimetres

	Anterior medullary	Lateral medullary	Tonsil-lomedullary	Televelo-tonsillar
Total length	3.39 ± 1.70	8.56 ± 2.63	21.06 ± 7.22	16.41 ± 8.36
Right	3.19 ±1.43	8.41 ± 2.70	21.65 ± 6.87	16.55 ± 7.24
Left	3.53 ± 1.86	8.61 ± 2.74	20.64 ± 7.49	16.03 ± 8.90
Total calibre	1.45 ± 0.37	1.44 ± 0.31	1.33 ± 0.31	1.32 ± 0.40
Right	1.46 ± 0.37	1.42 ± 0.26	1.34 ± 0.24	1.27 ± 0.22
Left	1.45 ± 0.32	1.46 ± 0.35	1.32 ± 0.33	1.34 ± 0.54

origin in the VA, 101 (83.5%) were of the V4 segment and 20 (16.5%) of the V3 segment (Fig. 5). PICAs which originated from the VA did so at 16.65 ± 6.16 mm from the vertebro-basilar junction, while the distance to that point from those originating from the BA was 12.25 ± 4.59 mm, with no statistically significant differences in relation to the either presentation side (p = 0.67). In 63 (36.2%) samples, the PICA originated from the posterior lateral surface of the VA and BA, from lateral surface in 68 (39.1%) samples, from posterior and posterior medial surface in 37 (21.3%) samples and 6 (3.4%) specimens, respectively.

Posterior inferior cerebellar artery distributed through the periphery of the medulla oblongata and the cerebellar vermis and then divided into four segments with variable length, between 1.95 to 39.23 mm.

The segments with a short length were the anterior and lateral medullary, while the tonsillomedullary segment with its sinuous trajectory presented greater length. PICA presented a calibre of 1.45 ± 0.37 mm; there was no statistically significant difference in relation to either side (p = 0.27). A reduction of 7.6% was observed between the calibre of the medullary (mesencephalic pons) and the tonsillomedullary (mesencephalic cerebellum) segments (Table 1).

Right PICAs' calibre was higher than the left side in 74 (42.5%) samples. The left branch presented a dominant calibre in 70 (40.2%) cases; there was no difference in calibre in 30 (17.2%) cases. In 141 (81%) samples, there was a bifurcation between the lateral and medial branches, while in 33 (19%) PICAs the branches emerged in form of a cluster, this presents a statistically significant difference (p = 0.02).

Lateral branches presented a calibre of 1.08 ± ± 0.18 mm and the medial 0.96 ± 0.19 mm (p = 0.07). From these branches, collaterals emerged for the cerebellar cortex, vermis and the fourth ventricle branches. A pair of cortical arteries emerged in 69 (48.9%) cases from the lateral branch and three collateral arteries were observed as part of 67 (47.5%) medial branches (Table 2).

The lower loop of the tonsillomedullary segment related to the tonsil on 148 (85.1%) samples. In relation to the upper surface of the tonsil, it was found in 38 (25.6%) cases, with the lower segment in 56 (37.9%) and with the middle segment in 54 (36.5%) sample blocks of brainstem and cerebellum. In 26 (14.9%) cases the lower loop of the third segment was below the cerebellar tonsil and corresponded to the arteries that originated from V3 or from the lower part of V4 (Fig. 5).

The distance between the bifurcation point and the origin of PICA was variable; thus, it was classified in four groups every 20 mm: group 1 — 2 (1.4%) samples with a length of up to 20 mm; group 2 — 41 (29.1%) samples with a length between 21 and 40 mm; group 3 — 75 (53.2%) samples with a length between 41 and 60 mm; group 4 — 23 (16.3%) samples with a length equal or above 60 mm.

We observed a variable course of PICAs with different contact points on the cranial nerves. PICA presented the following relationships to cranial nerve pairs: above glossopharyngeal in 18 (10.1%) samples (Fig. 2); between glossopharyngeal and vagus in 12 (7.2%); between vagus and accessory 49 (28.3%) (Fig. 4); posterior to roots of the accessory nerve in 44 (25.4%)

Table 2. Collateral distribution by lateral and medial branch of the inferior posterior cerebellar artery

Lateral branch	Medial branch
1 cortical: 6 (4.3%)	1 collateral: 15 (10.6%) arteries:
	11 vermian
	4 cortical
2 cortical: 69 (48.9%)	2 collateral: 31 (22%):
	20 cortical and vermian
	7 double vermian
	2 vermian and televelo
	2 vermian and amygdala
3 cortical: 56 (39.7%)	3 collateral: 67 (47.5%):
	65 cortical, vermian and televelo
	2 amygdala, vermian and televelo
4 cortical: 10 (7.1%)	4 collateral: 15 (10.6%):
	8 cortical, vermian and televelo, more contralateral cortical
	7 cortical, vermian and televelo, more vermian contralateral
	5 collateral: 8 (5.7%):
	6 cortical, vermian and televelo, more cortical and contralateral vermian
	2 cortical, vermian and televelo, televelo and contralateral vermian
	6 collateral: 5 (3.5%):
	5 cortical, vermian and televelo, more cortical, vermian and contralateral televelo

samples (Fig. 4); through the roots of the vagus and accessory nerves in 14 (8%) and 37 (21%) samples, respectively. Hypoglossal contact was observed in 91 (52.3%) cases, 52 (57.1%) run below to the cranial pair, 8 (8.8%) above and 31 (34.1%) samples were distributed between the roots of the pair.

DISCUSSION

Of the cerebellar arteries, the PICA is the one that presents the greatest variability. The incidence of agenesis observed in this series (6.5%) is in accordance with some previous reports [10, 20]. Special attention is drawn to the high incidence (35.6%) reported by Akgun et al. [1] and no case of agenesis is reported in other studies [9, 14]. The presence of duplicate PICA reported in the literature in a range of 2.5–10% [14, 18, 20, 24, 26] is concordant with our findings, while Macchi et al. [10] do not report

duplications. In other studies, PICA hypoplasia has been reported in a range of 5–16% [9, 20], a figure that is higher than that found in our series.

The origin of the PICA from the VA has been reported in a range of 72–85% [9, 10, 14, 19, 20, 26], while in this study a lower incidence was found, concordant with Akgun et al. [1], whereas the origin of the PICA from the extradural segment of the VA that has been reported in 10–16.7% is concordant with what was observed in this study [1, 18, 19]. High incidence of extradural origin of the PICA reported by Macchi et al. [10] (32.5%) and the non-report of Ucerler et al. [26] of this morphological expression is highlighted.

The significant incidence of PICA that emerges from BA should be considered; our findings are consistent with the reports of Mercier et al. [14] and Macchi et al. [10]. Other authors report this origin in a range of 7.4–12.5% [1, 24, 27]. A PICA variable that besides being visually attractive is accompanied by marked clinical implications that determine its obstruction or injury, for its extensive irrigated territory, is the presence of PICA–AICA trunk, reported by some authors in 12.5–22% [4, 10, 14], whereas our observations (6.4%) are concordant with Ucerler et al. [26]. The distance of the emergence of the PICA in relation to the vertebro-basilar junction, indicated in previous studies in 16–16.9 mm, and without significant differences in relation to the presentation side, is concordant with that found in this series. Pai et al. [17] report a distance of 12 mm. In this study, a calibre of the anterior segment of the PICA of 1.45 mm was reported, similar to the figures most reported in literature [9, 18], while other authors denote this calibre in a range of 1.67–2 mm [1, 3, 7, 9, 16, 20].

The large qualitative and morphometric variability observed in the various PICA studies is probably due to factors such as the size of the samples, the different measurement methodologies and the phenotypic expressions of each population group evaluated.

The bifurcation of the PICA in lateral and medial branches, close to the televelotonsilar fissure has been reported with high incidence in a range in which our findings are located, of 78–92.5% [9, 10, 20, 27]. In agreement with what is reported in literature, we find that the lateral branch is greater than the medial one and its calibre slightly higher than a millimetre; It supplies the middle and lateral segments of the occipital surface of the cerebellar hemisphere. Some previous studies [9, 19, 20] indicate that the lateral

branch provides between one and several cortical branches, while in our observations we recorded the presence of one to five cortical branches, the most frequent expression being the presence of two branches cortical (48.9%). In the same sense, a medial branch that supplies the vermis and the medial portion of the cerebellar hemisphere is recorded. In this study we report as the most frequent scenario (47.5%) that the medial branch provides cortical, vermian and televelar branches.

The location of the caudal loop of the tonsillar medullary segment below the lower pole of the tonsil occurs when the PICA emerges from the extradural portion of the VA or from the proximal part of the intracerebral segment of this artery; this condition, observed in our study at 14.9%, is consistent with previous studies that report it in a range of 12.5–27.5% [9, 10, 26]. We also find this loop at the level of the pole or segment lower tonsil in a slightly higher percentage (37.9%), as reported by some authors [9, 10, 26]. In other cases, we recorded the location of the loop in the middle and upper segments of the medial wall of the tonsil (62.1%), incidence slightly higher than that reported by Lister et al. [9], while other studies [10, 26] report this expression in a range of 30–45%.

The location and extent of the infarctions originated by PICA occlusion are mainly determined by the nature of its aetiology (atheromatosis vs. embolism), haemodynamic factors, the anatomic variations of the vessels and the arterio-arterial anastomosis characteristics. The anatomical variations mainly comprise the origin, the branching pattern, irrigated areas, and parent vessel sizes. For example, people with an aberrant origin of the PICA and/or hypoplasia of the VA have a greater chance of having a cerebellar infarction and if it happens, it is expected to be larger and extensive infarcts than individuals with a usual pattern of the arterial anatomy in the posterior fossa. The syndrome associated with lateral medullary infarction may be caused by occlusion of PICA or VA, but it is most commonly attributed to occlusion of the VA [12, 15, 16, 20, 27, 28].

The syndrome originated by the PICA occlusion is known as the lateral medullary syndrome. This syndrome is characterized by the presence of: anaesthesia and thermoanalgesia in the hemibody caused by damage to the spinothalamic tract; Ipsilateral Horner syndrome determined by the affectation of the oculosympathetic fibres in the lateral medullary reticular substance; dysphagia, dysarthria and dysphonia as a result of ipsilateral paresis of the palate, pharynx, and vocal cords caused by an injury of the ambiguous nucleus; facial ipsilateral hypoesthesia, caused by lesions on the trigeminal tract; ataxia, dizziness, nystagmus, and ipsilateral cerebellar signs caused by damage to the vestibular nuclei and arqui and paliocerebellum; emesis explained by the involvement of the nucleus of the solitary tract; nystagmus and diplopia caused by an injury to the spinal cord and the medial longitudinal fasciculus; facial paralysis caused by damage to the seventh cranial nerve motor nucleus [6, 8, 16, 20, 28].

Cerebral revascularisation in the posterior circulation is well recognised as an important factor in the treatment of aneurysms that arise at the origin of the PICA, most commonly in the posterior fossa below the basilar apex, and less frequently in the distal segments [9]. The revascularisation is also used in the treatment of complex and giant intracranial tumours involving the pontocerebellar angle, occipital foramen, cervicocranial junction, clivus, jugular foramen, fourth ventricle, cerebellum and arteriovenous malformations; lesions that involve major vessels of this anatomical region. In these procedures the PICA and AICA are anastomosed end-to-end, end-to-side, or side to side to the contralateral equivalent arteries or extracranial arteries, such as the superficial temporal artery and occipital artery to achieve the neural parenchyma revascularisation [1, 7, 20, 23]. Although bypass procedures can reduce mortality and morbidity, knowledge of the anatomical characteristics of the vasculature plays an important role in preoperative planning and appropriate locations for anastomosis [1, 20].

Our findings are consistent with that reported in previous studies [9, 10, 19, 20, 22] that record the relationship of the PICA with the nerves that emerge from the medulla oblongata, being the most frequent scenario the course of the artery between pairs X and XI (21–31%), followed by the course of the artery between the fibres of the XI pair (10–27%). The trajectory of the PICA over the IX pair is reported as the lowest incidence (4.8–17%). Our study is consistent with the majority of reports [10, 14, 20] that indicate that the path of the PICA with the highest incidence in its relationship with the hypoglossal nerve is the one which passes under the nerve (47.5–57.1%), while Lister et al. [9] reports as the most frequent trajectory that of the PICA coursing between the fibres of

the referred nerve. The dimensions of the segments of the PICA, anterior medulla (4.4 mm), medullary lateral (15.4 mm), tonsilomedullary (24.5 mm) and televelotonsilar (13.3 mm) reported by Lister et al. [9] are similar to those recorded in this series.

The IX–XII cranial nerves are usually in contact with the posterior surface of the VA, however, with the exception of the IX, the compression syndromes associated with these nerves are rare, although the sensorial distributions of these nerves are limited compared to the trigeminal nerve. The contacts between the cranial nerves and the VA become symptomatic when occurs an elongation or tortuosity of the proximal segments of the PICA, caused by age and arteriosclerosis. The vascular contact itself might not be enough to change the myelin structure in the root entry zone. Therefore, the presence of vascular indentation in patients with spasm of these nerves could strengthen the change in the myelin sheath in root entry zone that produces symptoms [2, 13, 25]. The compression of the glossopharyngeal and vagus nerves can cause severe episodic pain lasting from a few seconds to minutes, at the level of the palatine tonsil, larynx, tongue and ear, structures innervated by somatosensory elements of these nerves emerging through the retro-olive grove [13].

CONCLUSIONS

This study, carried out in cadaveric material, provides relevant qualitative and morphometric information of the PICA, useful for the diagnosis and clinical management, as well as for the surgical approaches that may compromise this structure.

Acknowledgements

Conflict of interest: None declared

REFERENCES

1. Akgun V, Battal B, Bozkurt Y, et al. Normal anatomical features and variations of the vertebrobasilar circulation and its branches: an analysis with 64-detector row CT and 3T MR angiographies. Sci World J. 2013; 2013: 620162, doi: 10.1155/2013/620162, indexed in Pubmed: 24023533.
2. Chung SS, Chang JW, Kim SH, et al. Microvascular decompression of the facial nerve for the treatment of hemifacial spasm: preoperative magnetic resonance imaging related to clinical outcomes. Acta Neurochir (Wien). 2000; 142(8): 901–907, doi: 10.1007/s007010070076, indexed in Pubmed: 11086829.
3. Fine AD, Cardoso A, Rhoton AL. Microsurgical anatomy of the extracranial-extradural origin of the posterior inferior cerebellar artery. J Neurosurg. 1999; 91(4): 645–652, doi: 10.3171/jns.1999.91.4.0645, indexed in Pubmed: 10507387.
4. Hou K, Li G, Luan T, et al. Anatomical study of anterior inferior cerebellar artery and its reciprocal relationship with posterior inferior cerebellar artery based on angiographic data. World Neurosurg. 2020; 133: e459––e472, doi: 10.1016/j.wneu.2019.09.047, indexed in Pubmed: 31526888.
5. Isaji T, Yasuda M, Kawaguchi R, et al. Posterior inferior cerebellar artery with an extradural origin from the V segment: higher incidence on the nondominant vertebral artery. J Neurosurg Spine. 2018; 28(2): 154–159, doi: 10.3171/2017.5.SPINE161286, indexed in Pubmed: 29192876.
6. Kase CS, Norrving B, Levine SR, et al. Cerebellar infarction. Clinical and anatomic observations in 66 cases. Stroke. 1993; 24(1): 76–83, doi: 10.1161/01.str.24.1.76, indexed in Pubmed: 8418555.
7. Kawashima M, Rhoton AL, Tanriover N, et al. Microsurgical anatomy of cerebral revascularization. Part II: posterior circulation. J Neurosurg. 2005; 102(1): 132–147, doi: 10.3171/jns.2005.102.1.0132, indexed in Pubmed: 15658105.
8. Kim HA, Yi HA, Lee H. Recent advances in cerebellar ischemic stroke syndromes causing vertigo and hearing loss. Cerebellum. 2016; 15(6): 781–788, doi: 10.1007/s12311-015-0745-x, indexed in Pubmed: 26573627.
9. Lister R, Rhoton A, Matsushima T, et al. Microsurgical anatomy of the posterior inferior cerebellar artery. Neurosurgery. 1982; 10(2): 170–199, doi: 10.1227/00006123-198202000-00004.
10. Macchi V, Porzionato A, Parenti A, et al. The course of the posterior inferior cerebellar artery may be related to its level of origin. Surg Radiol Anat. 2004; 26(1): 60–65, doi: 10.1007/s00276-003-0190-2, indexed in Pubmed: 14658014.
11. Macchi V, Porzionato A, Guidolin D, et al. Morphogenesis of the posterior inferior cerebellar artery with three-dimensional reconstruction of the late embryonic vertebrobasilar system. Surg Radiol Anat. 2005; 27(1): 56–60, doi: 10.1007/s00276-004-0303-6, indexed in Pubmed: 15645157.
12. Marinković S, Kovacević M, Gibo H, et al. The anatomical basis for the cerebellar infarcts. Surg Neurol. 1995; 44(5): 450–460, doi: 10.1016/0090-3019(95)00195-6, indexed in Pubmed: 8629230.
13. Matsushima T, Goto Y, Ishioka H, et al. Possible role of an endovascular provocative test in the diagnosis of glossopharyngeal neuralgia as a vascular compression syndrome. Acta Neurochir (Wien). 1999; 141(11): 1229–1232, doi: 10.1007/s007010050423, indexed in Pubmed: 10592125.
14. Mercier PH, Brassier G, Fournier HD, et al. Vascular microanatomy of the pontomedullary junction, posterior inferior cerebellar arteries, and the lateral spinal arteries. Interv Neuroradiol. 2008; 14(1): 49–58, doi: 10.1177/159101990801400107, indexed in Pubmed: 20557786.

15. Min WK, Kim YS, Kim JY, et al. Atherothrombotic cerebellar infarction: vascular lesion-MRI correlation of 31 cases. Stroke. 1999; 30(11): 2376–2381, doi: 10.1161/01.str.30.11.2376, indexed in Pubmed: 10548674.

16. Murakami T, Nakayasu H, Doi M, et al. Anterior and posterior inferior cerebellar artery infarction with sudden deafness and vertigo. J Clin Neurosci. 2006; 13(10): 1051–1054, doi: 10.1016/j.jocn.2005.12.045, indexed in Pubmed: 17074488.

17. Pai BS, Varma RG, Kulkarni RN, et al. Microsurgical anatomy of the posterior circulation. Neurol India. 2007; 55(1): 31–41, doi: 10.4103/0028-3886.30424, indexed in Pubmed: 17272897.

18. Pekcevik Y, Pekcevik R. Variations of the cerebellar arteries at CT angiography. Surg Radiol Anat. 2014; 36(5): 455–461, doi: 10.1007/s00276-013-1208-z, indexed in Pubmed: 24061702.

19. Person H, Vallée B, Lefèvre C, et al. Arterial and neural relations at the posterior and lateral aspects of the medullo-spinal junction. Surg Radiol Anat. 1998; 20(3): 177–184, doi: 10.1007/BF01628892, indexed in Pubmed: 9706676.

20. Rhoton AL. The cerebellar arteries. Neurosurgery. 2000; 47(3 Suppl): S29–S68, doi: 10.1097/00006123-200009001-00010, indexed in Pubmed: 10983304.

21. Rodríguez-Hernández A, Rhoton AL, Lawton MT. Segmental anatomy of cerebellar arteries: a proposed nomenclature. Laboratory investigation. J Neurosurg. 2011; 115(2): 387–397, doi: 10.3171/2011.3.JNS101413, indexed in Pubmed: 21548748.

22. Rusu MC, Popa E, Jianu AM, et al. The vascular layers on the rostral ventrolateral medulla. Rom J Morphol Embryol. 2012; 53(4): 951–956, indexed in Pubmed: 23303018.

23. Shrontz C, Dujovny M, Ausman JI, et al. Surgical anatomy of the arteries of the posterior fossa. J Neurosurg. 1986; 65(4): 540–544, doi: 10.3171/jns.1986.65.4.0540, indexed in Pubmed: 3760965.

24. Songur A, Gonul Y, Ozen OA, et al. Variations in the intracranial vertebrobasilar system. Surg Radiol Anat. 2008; 30(3): 257–264, doi: 10.1007/s00276-008-0309-6, indexed in Pubmed: 18253692.

25. Thomas KL, Vilensky JA. The anatomy of vascular compression in trigeminal neuralgia. Clin Anat. 2014; 27(1): 89–93, doi: 10.1002/ca.22157, indexed in Pubmed: 23381734.

26. Ucerler H, Saylam C, Cagli S, et al. The posterior inferior cerebellar artery and its branches in relation to the cerebellomedullary fissure. Clin Anat. 2008; 21(2): 119–126, doi: 10.1002/ca.20581, indexed in Pubmed: 18189278.

27. Urban PP. Speech motor deficits in cerebellar infarctions. Brain Lang. 2013; 127(3): 323–326, doi: 10.1016/j.bandl.2013.10.001, indexed in Pubmed: 24189047.

28. Venti M. Cerebellar infarcts and hemorrhages. Front Neurol Neurosci. 2012; 30: 171–175, doi: 10.1159/000333635, indexed in Pubmed: 22377889.

V M
VIA MEDICA

O R I G I N A L   A R T I C L E

Optic nerve sheath diameter measurement: a means of detecting increased intracranial pressure in pseudotumor cerebri patients

T. Ertekin[1], M.G. Boyaci[2], A. Bilir[1], A. Yucel[3], A. Ertekin[4], O. Turamanlar[1], R. Duman[5]

[1]Department of Anatomy, School of Medicine, Afyonkarahisar Health Sciences University, Afyonkarahisar, Turkey
[2]Department of Neurosurgery, School of Medicine, Afyonkarahisar Health Sciences University, Afyonkarahisar, Turkey
[3]Department of Radiology, School of Medicine, Afyonkarahisar Health Sciences University, Afyonkarahisar, Turkey
[4]Department of Emergency Medicine, School of Medicine, Afyonkarahisar Health Sciences University, Afyonkarahisar, Turkey
[5]Department of Opthalmology, Bursa Yüksek İhtisas Training and Research Hospital, Bursa, Turkey

Background: Pseudotumor cerebri (PTC) occurs when the pressure inside the skull increases for no obvious reason. The aim of this study was to investigate three different methods: the optic nerve sheath diameter (ONSD) method, ONSD/eyeball transverse diameter (ETD) index, and ONSD/orbital transverse diameter (OTD) index for the initial detection of elevated intracranial pressure in patients with PTC.
Materials and methods: A retrospective study of magnetic resonance data from adult PTC patients (n = 42) and control group (n = 40) was performed. ONSD and OTD measurements were made 3 mm and 10 mm posterior to the globe, after intracranial pressure was measured with lumbar puncture. The sensitivity, specificity, and overall accuracy of the findings on magnetic resonance imaging were calculated.
Results: The optic nerve sheath was enlarged in the PTC group compared with the control group. It showed 97% sensitivity and 100% specificity and 79% sensitivity and 87.5% specificity for 3 mm and 10 mm, respectively. The ONSD//ETD and ONSD/OTD indices were increased in the PTC group compared with the control group. For 3 mm posterior to the globe, the ONSD/ETD index had 90.5% sensitivity and 92% specificity, and the ONSD/OTD index had 86% sensitivity and 95% specificity. For 10 mm posterior to the globe, the sensitivity and specificity of the ONSD/ETD and ONSD/OTD indices were 86% and 80% and 74% and 82.5%, respectively.
Conclusions: According to our study, the ONSD method and the ONSD/ETD and ONSD/OTD indices are reliable diagnostic markers for PTC. These noninvasive techniques may be useful in monitoring the invasive intracranial catheter and have wide potential clinical applications in district hospitals, emergency departments and intensive care units. (Folia Morphol 2022; 81, 3: 567–573)

Key words: intracranial pressure, neurosurgery, optic nerve, pseudotumor cerebri, radiology

Address for correspondence: Dr. A. Bilir, Afyonkarahisar Health Sciences University, School of Medicine, Department of Anatomy, Afyonkarahisar, Turkey, tel: +90 272 246 28 42, fax: +90 272 228 14 29, e-mail: fztabdulkadirbilir@gmail.com

INTRODUCTION

Pseudotumor cerebri (PTC), also known as idiopathic intracranial hypertension, is a disorder that is described by the presence of pathologically increased intracranial pressure (ICP) in nonexistence of enlarged ventricles, intracranial mass lesions, and computed tomography (CT) and magnetic resonance (MR) imaging (MRI) findings associated with high ICP [1, 20, 25].

Intracranial pressure is detected by invasive placement into the ventricles or cerebral parenchyma with an intracranial catheter. This procedure is considered the gold standard. This method gives ICP results expressed in millimetres of mercury. Doctors tend to use noninvasive methods before applying invasive methods, and noninvasive methods are predominantly qualitative (e.g., papilledema, optic nerve sheath diameter [ONSD], tympanic membrane displacement) or provide imprecise readings [2, 18, 19, 21].

In this measurement method, the optic nerve sheath dilates due to more cerebrospinal fluid entering between the optic nerve and the dura mater. This is considered an indication of increased intracranial pressure [13, 14, 27].

Researchers have been mostly satisfied with the ONSD method and determined the correlation with the ICP measured by the invasive method, but some uncertainties and inconsistencies have remained regarding the accuracy of the method. Although multiple protocols and thresholds are suggested for the ONSD method, there is no generally accepted protocol or standardization. While ICP values greater than 20 mmHg are considered pathological, no quantitative link has been established between ICP and ONSD beyond this value. But different researchers determined a normal/abnormal cutoff value of ONSD that varied from 4.8 to 7.3 mm [4, 9, 15, 17, 30].

Another thought-provoking point with the ONSD method is that ONSD measurements of normal and sick individuals in the same studies often have large standard deviations (SD) overlapping each other. To overcome this situation, researchers have proposed and attempted to apply different indices on various imaging techniques, such as the ratio of optic nerve diameter to ONSD or the ratio of ONSD to eyeball transverse diameter (ETD) [6, 27]. The clinical application of the ONSD/ETD index has been described for patients with traumatic brain injury [28].

Our aim was to implement three different methods (the ONSD method, ONSD/ETD index, ONSD/orbital transverse diameter [OTD] index) for the initial detection of elevated ICP in patients with PTC. We investigated the applicability and reliability of the three methods in PTC patients.

MATERIALS AND METHODS

Study design and setting, inclusion and exclusion criteria

In this study, we retrospectively analysed the MR scan data of 82 adult patients (over 18 years old) who were admitted to the Radiology Department from January 2014 to December 2016. The present study was approved by the ethical committee of Afyonkarahisar Health Science University, Turkey (2017/7-193). In our study, we included patients who presented to the Neurosurgery Department in various combinations with complaints of headache, nausea, vomiting, visual impairment, diplopia, and dizziness and were directed to MR scans of the cranial region. The patients appeared to have negative MRI scans.

Control group

The control group was composed of patients older than 18 years who underwent MRI for various reasons (e.g., seizures, head injury, headache, and hearing loss), and the clinical results of these patients were evaluated as normal by a neuroradiologist. Patients whose signs and symptoms showed increased ICP were excluded from the control group. In addition, patients with a history of intracranial neoplasm, cranial deformity, and any orbital- or optic-related disorders were not included in the control group.

PTC group

For this group, severe headache of unknown cause and normal MRI scans were the primary inclusion criteria; among these, we selected patients who were diagnosed with PTC (International Classification of Diseases Ninth revision Clinical Modification; 348.2 Benign Intracranial Hypertension) by a neurologist. All patients diagnosed with PTC were examined by an ophthalmologist and a neuroradiologist. Patients determined to have any ophthalmological or neuroophthalmological diseases were excluded from the study.

Data sources and measurements

All MRI were performed on the Magnetom Aera 1.5T system (Siemens Healthcare, Erlangen, Germany). Brain MRIs were performed with a 24-channel head coil. The sequences analysed consisted of 5-mm
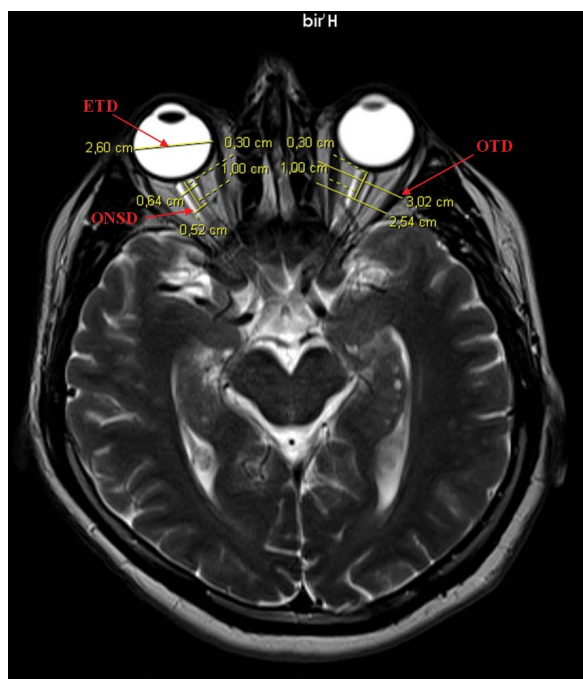
Figure 1. Axial T2W magnetic resonance imaging of the both orbit demonstrating the measurement techniques: On the left side, orbital transverse diameter (OTD) (medial orbital wall to lateral orbital wall); on the right side, eyeball transverse diameter (ETD) (retina to retina) and optic nerve sheath diameter (ONSD) measurements 3 mm and 10 mm behind the globe were showed.

sections, and T2W axial images were used for measurements. The left and right ETD (i.e., retina to retina), OTD (i.e., medial orbital wall to lateral orbital wall), and ONSDs were measured by the computer programme on the same MRI (Fig. 1). The measurements were made digitally via PACS. Theoretical and practical orbital anatomy and measurement technique training on MRI were given to the researchers who made the measurements. MRI of patients in the control group and the PTC group were randomly mixed, so the measurements were blinded. The parts of interest of the MRI were enlarged 3–4 times for better measurement. ONSD and OTD measurements were made from 3 mm and 10 mm behind the globe (Fig. 1). The researchers took care to use the same window, brightness, and contrast when taking all measurements. Intra-evaluator and inter-evaluator consistency were analysed statistically by the intraclass correlation coefficients (ICCs) between the two evaluators. The same methodological procedures were applied by both evaluators (A.B. and T.E.) when making measurements. ICP was measured invasively in a neurosurgical intensive care unit with lumbar puncture (LP).

Statistical analysis

Statistical analysis was performed by using the Statistical Package for the Social Sciences, version 19.0 (SPSS, Chicago, Illinois). All values are presented as the mean, SD, minimum, and maximum. The distribution of the data was evaluated by the Kolmogorov-Smirnov test. A nonparametric Mann–Whitney U test was used to determine the differences between two groups. Correlation analysis was performed with gender and age groups. Subsequently, a receiver operating characteristic (ROC) curve was generated to determine optimal cutoff values. The results were evaluated at a 95% confidence interval, and $p < 0.05$ was considered statistically significant.

RESULTS

Forty-two patients were included in the PTC group (mean age 42.49 ± 9.15), while 40 patients were included in the control group (mean age 44.03 ± 6.81). The patients in the control group were neurosurgery patients without invasive ICP results and clinical and radiological findings suggestive of normal ICP.

First, evaluator 1 measured five parameters two times. The coherence between the first and second measurements (intra-evaluator coherence) was evaluated by ICC, and the results showed an ICC value of $0.90 \leq 0.99$ ($p < 0.001$) for correlations in all parameters. Regarding comparisons of inter-evaluator measures, a strong ICC was also seen for each variable (ICC: $0.75 \leq 0.99$; $p < 0.001$).

Comparison of the groups

Measurements made 3 mm posterior of the globe

When the study group and the control group were compared, the right and left ONSDs were found to be significantly higher in the PTC group ($p \leq 0.001$). The enlargement was bilateral, and no correlation with age was found ($p = 0.68$). Mean ONSD led to a significant prediction of PTC (area under the curve [AUC] = 0.988, $p \leq 0.001$). The optimal cutoff value was calculated as 4.99 mm with 97% sensitivity and 100% specificity. The ONSD/ETD index correlated with ICP (i.e., ICP↑, ONSD↑), and with a cutoff value of 0.21, the sensitivity of the index was 90.5%, and the specificity was 92% for measurements (AUC = 0.977, $p \leq 0.001$). There was no correlation between the ONSD/ETD ratio and the gender or age of the patients ($p > 0.05$). Similarly, the ONSD/OTD index correlated with ICP, and with a cutoff value of 0.17 the ONSD/

Table 1. Measurements made from 3 mm posterior of the globe

Measurements	Control group (n = 40)		PTC group (n = 42)		P
	Mean ± SD	Min–Max	Mean ± SD	Min–Max	
ONSD	4.444 ± 0.397	3.48–4.97	5.752 ± 0.678	4.48–7.42	p ≤ 0.001
ONSD/ETD	0.187 ± 0.018	0.14–0.22	0.246 ± 0.031	0.2–0.32	p ≤ 0.001
ONSD/OTD	0.155 ± 0.0181	0.11–0.2	0.207 ± 0.039	0.15–0.39	p ≤ 0.001
ICP	–	–	28.523 ± 7.002	16–41	–

ETD — eyeball transverse diameter; ICP — intracranial pressure; ONSD — optic nerve sheath diameter; OTD — orbital transverse diameter; PTC — pseudotumour cerebri; SD — standard deviation; min — minimum; max — maximum
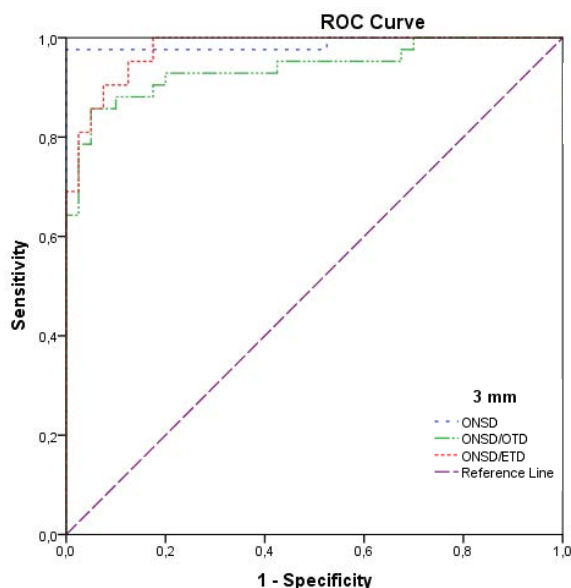
Figure 2. Receiver operating characteristic (ROC) analysis of ONSD, ONSD/ETD index and ONSD/OTD index for distance from 3 mm posterior of the globe; ETD — eyeball transverse diameter; ONSD — optic nerve sheath diameter; OTD — orbital transverse diameter.
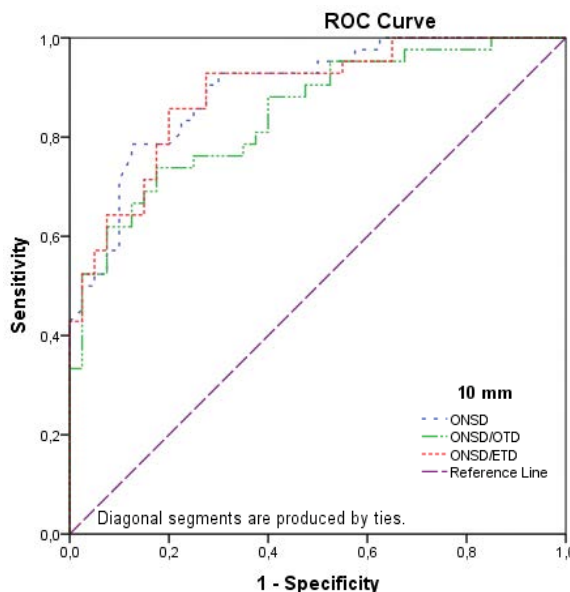
Figure 3. Receiver operating characteristic (ROC) analysis of ONSD, ONSD/ETD index and ONSD/OTD index for distance from 10 mm posterior of the globe; ETD — eyeball transverse diameter; ONSD — optic nerve sheath diameter; OTD — orbital transverse diameter.

Table 2. Measurements made from 10 mm posterior of the globe

Measurements	Control group (n = 40)		PTC group (n = 42)		P
	Mean ± SD	Min–Max	Mean ± SD	Min–Max	
ONSD	3.727 ± 0.452	3.05–4.77	4.782 ± 0.797	3.54–6.9	p ≤ 0.001
ONSD/ETD	0.156 ± 0.019	0.13–0.21	0.204 ± 0.036	0.14–0.29	p ≤ 0.001
ONSD/OTD	0.170 ± 0.025	0.12–0.23	0.227 ± 0.064	0.14–0.52	p ≤ 0.001
ICP	–	–	28.523 ± 7.002	16–41	–

ETD — eyeball transverse diameter; ICP — intracranial pressure; ONSD — optic nerve sheath diameter; OTD — orbital transverse diameter; PTC — pseudotumour cerebri; SD — standard deviation; min — minimum; max — maximum

/OTD index had a specificity of 86% and a sensitivity of 95% (AUC = 0.939, p ≤ 0.001) (Table 1, Fig. 2).

Measurements made 10 mm posterior of the globe

We determined the mean ONSDs for the control and PTC groups to be 4.78 mm and 3.72 mm, respectively. The difference was statistically significant (p ≤ 0.001). The optimal cutoff value was 4.21 mm with 79% sensitivity and 87.5% specificity (AUC = 0.894, p ≤ 0.001). The sensitivity and specificity of the ONSD//ETD and ONSD/OTD indices were 86% and 80% and 74% and 82.5%, respectively. The optimal cutoff values were calculated as 0.17 (AUC = 0.889, p ≤ 0.001) and 0.19 (AUC = 0.846, p ≤ 0.001) (Table 2, Fig. 3).

Table 3. Measurements of the bilateral ONSDs and two indices for the control and PTC group

Measurements		Control group (n = 40) Mean ± SD		PTC group (n = 42) Mean ± SD	
		Right	Left	Right	Left
ONSD	3 mm	4.473 ± 0.391	4.416 ± 0.415	5.719 ± 0.69	5.785 ± 0.708
	10 mm	3.737 ± 0.509	3.717 ± 0.450	4.780 ± 0.761	4.783 ± 0.868
ONSD/ETD	3 mm	0.187 ± 0.019	0.186 ± 0.019	0.245 ± 0.033	0.247 ± 0.032
	10 mm	0.156 ± 0.022	0.156 ± 0.019	0.205 ± 0.036	0.204 ± 0.038
ONSD/OTD	3 mm	0.155 ± 0.018	0.155 ± 0.019	0.205 ± 0.038	0.209 ± 0.041
	10 mm	0.170 ± 0.029	0.171 ± 0.024	0.228 ± 0.064	0.226 ± 0.066

ETD — eyeball transverse diameter; ICP — intracranial pressure; ONSD — optic nerve sheath diameter; OTD — orbital transverse diameter; PTC — pseudotumour cerebri; SD — standard deviation

In addition, the increase in ONSD was found to be statistically significant for both the right and left sides in the measurements made from both distances in the patient group (from 3 mm and 10 mm, p ≤ 0.001). This result is an indirect indication of a significant increase in ICP in the patient group.

The distribution of the bilateral ONSDs and two indices of the patients for the control and PTC groups are shown in Table 3. There was no significant difference between measurements of ONSD and calculations for two indices between the right and left sides (p > 0.05).

DISCUSSION

One of the most accurate and simplest invasive methods for measuring ICP is LP. This indirect and imprecise procedure is still commonly used, but the invasive nature of the method, the need for a doctor to perform the procedure, technical difficulties, and unwanted complications such as bleeding and infection are risk factors for this method [23].

Because of these risk factors, researchers have sought noninvasive approaches to determine ICP. Different methods of measuring ONSD have been previously shown in many studies: in postmortem samples (direct measurement) and in patients with increased intracranial pressure by noninvasive ultrasound, CT, or MRI [6, 12, 15, 16]. It has been determined that indirect measurement of ICP using ONSD measurements on MRI is reliably associated with invasive ICP measurement [10, 14].

An increase in ICP appears in the majority of cranial pathologies [7]. Different thresholds have been defined to show the increase in ICP in various populations. Previous studies reported a direct relationship between increased ICP and ONSD in patients with

traumatic and nontraumatic brain injuries [3, 8, 14, 22, 24, 26]. Similarly, in our study, we verified recent results, showing that a linear regression model demonstrates a strong correlation between ICP and ONSD.

We can address the discussion from two sides: First, what are the results of ONSD measurements in patients with PTC and are they compatible with the literature? Second, what is the methodological comparison of the measurements we used in the study?

Optic nerve sheath diameter is calculated by various radiological methods in the literature, but as a result of those studies, the researchers did not introduce generally accepted protocols to standardise the use of the ONSD technique. Some authors reported ONSD readings taken from different distances from the globe. Therefore, there may be differences between our results and those results [11, 13–15].

In the study comparing different location points far from the eyeball for ONSD measurements, it was found that the most stable results were obtained when the diameter was measured at a distance of 10 mm from the globe [27]. In the present study, we measured ONSD distances from 3 mm and 10 mm posterior to the globe on MRI. We found that the ONSD measurement in patients with PTC was significantly greater than that in the control group at both distances. Moreover, in the ROC analysis to analyse the predictive value of measurements for PTC diagnosis, the diagnostic accuracy of ONSD at 3 mm was slightly higher than that found for ONSD at 10 mm. We detected positive and statistically significant correlations between the LP pressure and ONSD measures for both the 3 mm (r = 0.708, p ≤ 0.001) and 10 mm (r = 0.572, p ≤ 0.001) distances.

On the other hand, in the literature an individual approach is recommended for the application of the ONSD method. Although ONSD and LP are related in a single patient, they can differ significantly from patient to patient. While 6.6 mm ONSD was measured at 5 mmHg ICP in one patient, 7 mm ONSD was measured at 30 mmHg ICP in the other patient. It should be noted that ONSD measurements depend on the elasticity, extensibility, and thickness of the dura mater exhibiting individual variations [5, 29]. Therefore, ICP assessment based on ONSD measurement in clinical examination should only be considered individually, evaluating the first and subsequent ONSD and ICP results together and making specific calculations for a particular patient.

In patients with PTC, the ONSD/ETD ratio was significantly greater than that in the control group, and it showed a positive correlation with ICP. Furthermore, their sensitivity and specificity were high for both indices calculated from 3 mm and 10 mm posterior of the globe. In the literature, only one study was performed related to ONSD/ETD and ICP in cases with hypertension. The authors found that the ONSD/ETD ratio was 0.29 ± 0.04 against 0.19 ± ± 0.02 in healthy adults and that the ONSD/ETD index correlated well with ICP both during the development of the pathology (i.e., ICP↑, ONSD↑) and during recovery (i.e., ICP↓, ONSD↓) [3]. As far as we know, there is no study investigating the relationship between the ONSD/OTD index and ICP in patients with PTC and other patient groups. The ONSD/ETD index correlated with ICP in patients with PTC, and its sensitivity and specificity were high. Furthermore, the ONSD/OTD index calculation 3 mm distance from the globe showed greater sensitivity and specificity than the index calculated 10 mm distance later.

The SD is a number that measures the spread of a data distribution. A high SD means that the numbers are spread out more. A low SD across studies indicates that the data points are close to the mean. ONSDs reported in the same studies have wide SDs that often overlap in the control and patient groups. To improve this situation, researchers have suggested indices such as ONS/ONSD and ONSD/ETD; these indices have insignificant SD [6, 27]. In our study, while the SD of the ONSD measurements varied from 0.39 to 0.79 at various locations, the SDs of the ONSD/ /ETD and ONSD/OTD indices were 0.018–0.064 and 0.018–0.038, respectively, which ensured very precise normative data.

Limitations of the study

We have two potential limitations. The first is the number of patients, and the second is the slice thickness of the MRI. Although the methodology of our study was well-founded, it consisted of a relatively small number of PTC patients. Future studies would be useful with more PTCs that could validate the results of our study. In the MRI technique, we used in our study, our slice thickness varied between 3 and 4 mm. The use of scanners with thinner sections may be useful for more accurate analysis of the optic nerve.

CONCLUSIONS

Our study shows that MRI findings, including ONSD, ONSD/ETD and ONSD/OTD indices, are reliable neuroradiological measures to diagnose PTC in patients. In cases with high ICP, ONSD and ONSD/ETD and ONSD/OTD ratios provide readings corresponding to ICP readings in millimetres of mercury. The use of these methods in clinical practice may help provide early accurate diagnosis and early treatment, but the limitations of these methods should be taken into account.

Other imaging modalities, such as orbital MRI or MR venography, may be added to routine clinical examinations to more accurately diagnose, detail the findings and investigate new features of PTC.

Conflict of interest: None declared

REFERENCES

1. Ambika S, Arjundas D, Noronha V, et al. Clinical profile, evaluation, management and visual outcome of idiopathic intracranial hypertension in a neuro-ophthalmology clinic of a tertiary referral ophthalmic center in India. Ann Indian Acad Neurol. 2010; 13(1): 37–41, doi: 10.4103/0972-2327.61275, indexed in Pubmed: 20436745.
2. Baheti NN, Nair M, Thomas SV. Long-term visual outcome in idiopathic intracranial hypertension. Ann Indian Acad Neurol. 2011; 14(1): 19–22, doi: 10.4103/0972-2327.78044, indexed in Pubmed: 21633609.
3. Bekerman I, Sigal T, Kimiagar I, et al. The quantitative evaluation of intracranial pressure by optic nerve sheath diameter/eye diameter CT measurement. Am J Emerg Med. 2016; 34(12): 2336–2342, doi: 10.1016/j.ajem.2016.08.045, indexed in Pubmed: 27717720.
4. Caffery TS, Perret JN, Musso MW, et al. Optic nerve sheath diameter and lumbar puncture opening pressure in nontrauma patients suspected of elevated intracranial pressure. Am J Emerg Med. 2014; 32(12): 1513–1515, doi: 10.1016/j.ajem.2014.09.014, indexed in Pubmed: 25284485.
5. Chauvet D, Carpentier A, Allain JM, et al. Histological and biomechanical study of dura mater applied to the

technique of dura splitting decompression in Chiari type I malformation. Neurosurg Rev. 2010; 33(3): 287–295, doi: 10.1007/s10143-010-0261-x, indexed in Pubmed: 20440557.

6. Chen H, Ding GS, Zhao YC, et al. Ultrasound measurement of optic nerve diameter and optic nerve sheath diameter in healthy Chinese adults. BMC Neurol. 2015; 15: 106, doi: 10.1186/s12883-015-0361-x, indexed in Pubmed: 26148482.

7. Dunn LT. Raised intracranial pressure. J Neurol Neurosurg Psychiatry. 2002; 73(suppl 1): i23–i27, doi: 10.1136/jnnp.73.suppl_1.i23.

8. Fraunfelder FT, Samples J, Fraunfelder FW. Possible optic nerve side effeects associated with nonsteroidal anti-inflammatory drugs. J Toxicol: Cutaneous Ocular Toxicol. 2008; 13(4): 311–316, doi: 10.3109/15569529409037531.

9. Geeraerts T, Launey Y, Martin L, et al. Ultrasonography of the optic nerve sheath may be useful for detecting raised intracranial pressure after severe brain injury. Intensive Care Med. 2007; 33(10): 1704–1711, doi: 10.1007/s00134-007-0797-6, indexed in Pubmed: 17668184.

10. Geeraerts T, Newcombe VFJ, Coles JP, et al. Use of T2-weighted magnetic resonance imaging of the optic nerve sheath to detect raised intracranial pressure. Crit Care. 2008; 12(5): R114, doi: 10.1186/cc7006, indexed in Pubmed: 18786243.

11. Görkem SB, Doğanay S, Canpolat M, et al. MR imaging findings in children with pseudotumor cerebri and comparison with healthy controls. Childs Nerv Syst. 2015; 31(3): 373–380, doi: 10.1007/s00381-014-2579-0, indexed in Pubmed: 25358812.

12. Hassen GW, Bruck I, Donahue J, et al. Accuracy of optic nerve sheath diameter measurement by emergency physicians using bedside ultrasound. J Emerg Med. 2015; 48(4): 450–457, doi: 10.1016/j.jemermed.2014.09.060, indexed in Pubmed: 25497897.

13. Helmke K, Hansen HC. Fundamentals of transorbital sonographic evaluation of optic nerve sheath expansion under intracranial hypertension. I. Experimental study. Pediatr Radiol. 1996; 26(10): 701–705, doi: 10.1007/BF01383383, indexed in Pubmed: 8805599.

14. Kimberly HH, Shah S, Marill K, et al. Correlation of optic nerve sheath diameter with direct measurement of intracranial pressure. Acad Emerg Med. 2008; 15(2): 201–204, doi: 10.1111/j.1553-2712.2007.00031.x, indexed in Pubmed: 18275454.

15. Legrand A, Jeanjean P, Delanghe F, et al. Estimation of optic nerve sheath diameter on an initial brain computed tomography scan can contribute prognostic information in traumatic brain injury patients. Crit Care. 2013; 17(2): R61, doi: 10.1186/cc12589, indexed in Pubmed: 23536993.

16. Liu D, Kahn M. Measurement and relationship of subarachnoid pressure of the optic nerve to intracranial pressures in fresh cadavers. Am J Ophthalmol. 1993; 116(5): 548–556, doi: 10.1016/s0002-9394(14)73195-2, indexed in Pubmed: 8238213.

17. Lochner P, Mader C, Nardone R, et al. Sonography of the optic nerve sheath beyond the hyperacute stage of intracerebral hemorrhage. J Ultrasound. 2014; 17(3): 225–228, doi: 10.1007/s40477-014-0069-6, indexed in Pubmed: 25177397.

18. McMahon CJ, McDermott P, Horsfall D, et al. The reproducibility of transcranial Doppler middle cerebral artery velocity measurements: implications for clinical practice. Br J Neurosurg. 2007; 21(1): 21–27, doi: 10.1080/02688690701210539, indexed in Pubmed: 17453770.

19. Pal A, Sengupta P, Biswas D, et al. Pattern of idiopathic intracranial hypertension in Indian population. Ann Indian Acad Neurol. 2019; 22(1): 47–51, doi: 10.4103/aian.AIAN_116_18, indexed in Pubmed: 30692759.

20. Pearce JMS. From pseudotumour cerebri to idiopathic intracranial hypertension. Pract Neurol. 2009; 9(6): 353–356, doi: 10.1136/jnnp.2009.194837, indexed in Pubmed: 19923117.

21. Raboel PH, Bartek J, Andresen M, et al. Intracranial pressure monitoring: invasive versus non-invasive methods: a review. Crit Care Res Pract. 2012; 2012: 950393, doi: 10.1155/2012/950393, indexed in Pubmed: 22720148.

22. Raffiz M, Abdullah JM. Optic nerve sheath diameter measurement: a means of detecting raised ICP in adult traumatic and non-traumatic neurosurgical patients. Am J Emerg Med. 2017; 35(1): 150–153, doi: 10.1016/j.ajem.2016.09.044, indexed in Pubmed: 27852525.

23. Rickert K, Sinson G. Intracranial pressure monitoring. Oper Tech Gen Surg. 2003; 5(3): 170–175, doi: 10.1016/s1524-153x(03)70010-4.

24. Sekhon MS, Griesdale DE, Robba C, et al. Optic nerve sheath diameter on computed tomography is correlated with simultaneously measured intracranial pressure in patients with severe traumatic brain injury. Intensive Care Med. 2014; 40(9): 1267–1274, doi: 10.1007/s00134-014-3392-7, indexed in Pubmed: 25034476.

25. Spennato P, Ruggiero C, Parlato RS, et al. Pseudotumor cerebri. Childs Nerv Syst. 2011; 27(2): 215–235, doi: 10.1007/s00381-010-1268-x, indexed in Pubmed: 20721668.

26. Tayal VS, Neulander M, Norton HJ, et al. Emergency department sonographic measurement of optic nerve sheath diameter to detect findings of increased intracranial pressure in adult head injury patients. Ann Emerg Med. 2007; 49(4): 508–514, doi: 10.1016/j.annemergmed.2006.06.040, indexed in Pubmed: 16997419.

27. Vaiman M, Gottlieb P, Bekerman I. Quantitative relations between the eyeball, the optic nerve, and the optic canal important for intracranial pressure monitoring. Head Face Med. 2014; 10: 32, doi: 10.1186/1746-160X-10-32, indexed in Pubmed: 25130267.

28. Vaiman M, Sigal T, Kimiagar I, et al. Noninvasive assessment of the intracranial pressure in non-traumatic intracranial hemorrhage. J Clin Neurosci. 2016; 34: 177–181, doi: 10.1016/j.jocn.2016.06.008, indexed in Pubmed: 27612672.

29. Van Noort R, Martin TR, Black MM, et al. The mechanical properties of human dura mater and the effects of storage media. Clin Phys Physiol Meas. 1981; 2(3): 197–203, doi: 10.1088/0143-0815/2/3/003, indexed in Pubmed: 7338023.

30. Zaidi SJ, Yamamoto LG. Optic nerve sheath diameter measurements by CT scan in ventriculoperitoneal shunt obstruction. Hawaii J Med Public Health. 2014; 73(8): 251–255, indexed in Pubmed: 25157326.

VIA MEDICA

O R I G I N A L   A R T I C L E

Anatomical study of the anterior interosseous nerve

A. Jeon[1], M. Lee[2], D.W. Kim[3], O.-Y. Kwon[3], J.-H. Lee[4]

[1]Department of Anatomy/Catholic Institute for Applied Anatomy, College of Medicine,
The Catholic University of Korea, Seoul, Korea
[2]School of Music and Arts, College of Music and Arts, Dankook University, Jukjeon, Korea
[3]Department of Anatomy and Cell Biology, College of Medicine, Chungnam National University, Daejeon, Korea
[4]Anatomy Laboratory, College of Sports Science, Korea National Sport University, Seoul, Korea

Background: The aim of this study is to investigate the location of nerves that innervate the flexor digitorum profundus (FDP), the flexor pollicis longus (FPL) and the pronator quadratus muscles. It also investigates the change in nerve location with hand movement.

Materials and methods: We studied 30 adult cadavers (17 males and 13 females) with a mean age of 69.5 years (range: 60–95 years). The reference line was from the humeral epicondylar line to the styloid process line of both the radius and ulnar bones. This study measured the anterior interosseous nerve (AIN) branch outpoint and the innervated muscle nerve entry point to the muscle belly. It also examines nerve position changes as related to making a fist.

Results: The reference line mean distance was 24.1 ± 1.2 cm. The median nerve branched into the AIN at 18.0 ± 4.0%. We found the most densely distributed section of the nerves' entry point to the muscle belly to be at a distance of 30% to 40% for the FDP and from 30% to 40% for the FPL. Except for the FPL, the nerve branch outpoints and the FDP moved by 3.0%, depending upon hand movements.

Conclusions: The results of this study show that it will be necessary to consider the anatomy of the nerve location as it enters the muscle belly as well as how it changes with movement. (Folia Morphol 2022; 81, 3: 574–578)

Key words: anterior interosseous nerve, flexor digitorum profundus, flexor pollicis longus, pronator quadratus, nerve position change

INTRODUCTION

The anterior interosseous nerve (AIN) is a branch of the median nerve that supplies the deep muscle of the anterior forearm compartment. AIN syndrome, not common, was first described in 1952 [7]. AIN syndrome usually causes motor weakness of the thumb and index finger pincer movements and sometimes is accompanied by wrist pain. However, abnormalities resulting AIN syndrome sensation can vary, depending upon the situation [10, 14].

The treatment options for AIN syndrome can be either surgical or nonsurgical, but we usually consider the surgical option if nonsurgical options have not previously been done within 4 to 6 months [8]. The anatomical aspect, even if there is an abnormality in the muscles and pain innervated by AIN, the observation range should be kept in mind for a wide

region from the brachial plexus to the forearm. This above reason will seriously think about the possible entrapment spot, and will apply specifically for the conservative nonsurgical treatment. When treating with conservative treatment, the faster the treatment period will be more effective. An earlier report shows that manual reduction of an AIN injury is effective in bringing about recovery [9]. However, a more useful therapeutic approach is possible after understanding how muscle movements can affect the anatomical location of both the nerves and muscles.

Nerve transfer has become a vital method in the reconstruction of hand function, especially in the reconstruction of the intrinsic muscles of the hand following injury to the ulnar or median nerve. The AIN is a common donor site for the ulnar nerve or the branch of the median nerve, resulting in a good clinical outcome [4–6].

The aim of this study is to investigate the location of nerves that innervate the flexor digitorum profundus (FDF), the flexor pollicis longus (FPL) and the pronator quadratus muscles. It also investigates how movement changes nerve location.

MATERIALS AND METHODS

We studied 30 unembalmed adult cadavers (17 males and 13 females) with a mean age of 69.5 years (range: 60–95 years). The specimens chosen had no history of forearm fracture or arm surgery.

For the measurements, on the anterior view, we identified the most prominent point of the medial epicondyle of the humerus (MEH), and of the lateral epicondyle of the humerus (LEH) before doing the dissection. On the distal view, we also identified the most distal point of the styloid process of the radius (SPR) and of the ulna (SPU). A line connecting the midpoints of the MEH and the LEH, as well as the midpoint of the SPR and the SPU, was used as a starting point reference line from proximal to distal (Fig. 1).

All experiments were conducted in the anatomy laboratory of the medical school. With the body in a supine position, we first dissected the skin and fat tissue to expose the pronator teres muscle. We attempted to locate the median nerve and carefully traced it distally to find the AIN. After finding the AIN, we carefully dissected it to examine the nerve branches around it in detail. In addition, in order to examine the AIN, the insertion site of pronator teres was cut and observed. We investigated the
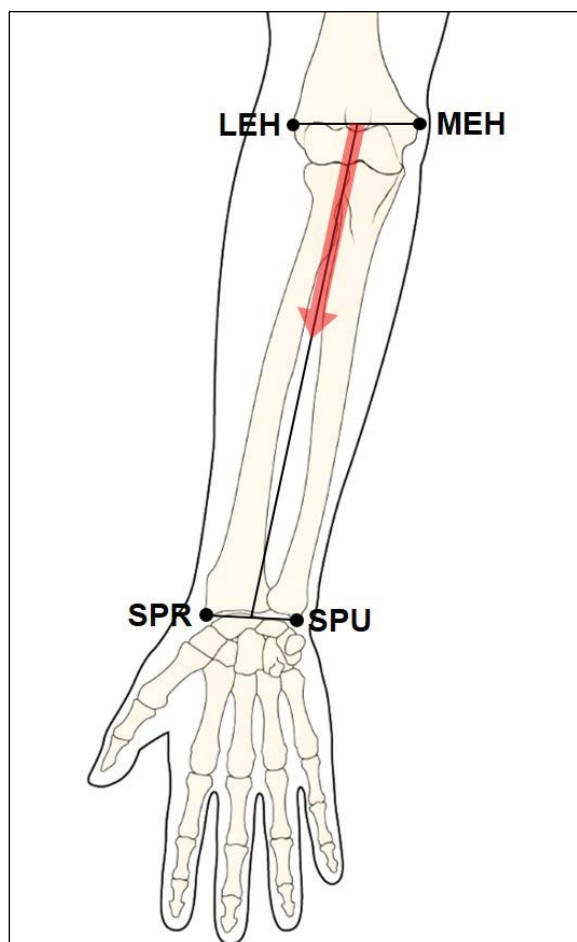
Figure 1. Illustration showing the reference line; LEH — lateral epicondyle of humerus; MEH — medial epicondyle of humerus; SPR — styloid process of radius; SPU — styloid process of ulna; red arrow — measuring direction.

target muscle type, the AIN nerve branch number that innervated each muscle, and the morphological location of nerves entering the muscle belly (Fig. 2). The measuring variables are as follow:
— the reference line length;
— the location of the point where the AIN divides from the median nerve;
— the location of the branch nerve outpoints that innervate the FPL and the FDF;
— the crossing point of the AIN with the superior border of pronator quadratus.

Additionally, to examine how movement changes nerve position, we performed the following steps on three unembalmed cadavers (Fig. 3).
1. After dissection, we measured the nerve entry point to the FPL and FDP when the palm was open;
2. After dissection, we measured the median branch outpoint to the AIN;

Figure 2. Photographs of the dissected forearm of fixed specimen; PQ — pronator quadrates; FPL — flexor pollicis longus; FDP — flexor digitorum profundus; AIN — anterior interosseous nerve; SUP — superior; LAT — lateral; arrow — nerve entering point to the muscle belly.
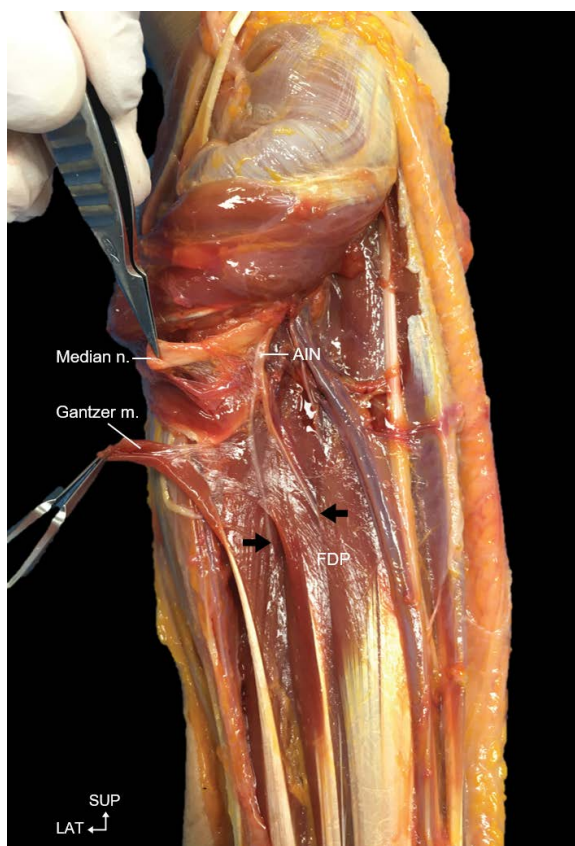
Figure 3. Photographs of the dissected forearm of unembalmed specimen; FDP — flexor digitorum profundus; SUP — superior; LAT — lateral; arrow — nerve entering point to the muscle belly.

3. The measured points were marked with a thumb-tack;
4. With the closed hand fist position, we measured the median branch outpoint to the AIN;
5. After opening the fist, we measured the degree of change in the nerve position.

A single observer took all measurements with a measuring tape and digital callipers (resolution 0.01 mm, CD-20PSX, Mitutoyo, Japan). Data was analysed using SPSS software version 23.0 (IBM SPSS Inc., Chicago, IL, USA). Comparisons between male and female cadavers were performed using the t-test. P values of less than 0.05 were considered statistically significant. The present study was conducted in accordance with the Declaration of Helsinki

RESULTS

The mean distance of the reference line was 24.1 ± 1.2 cm. The median branched into the AIN at 18 ± 4.0%. No significant distant differences were found in the reference line between males and females or between the right and left forearm (p ≥ 0.05).

We investigated the nerve entry points to the muscle belly in this study. For the FPL, the number of nerve entry points ranged from 2 to 5, and the distribution ratio was 31.0%, 37.9%, 24.1% and 7.0%. This study had 10 sections, based on reference length, and it examined which sections were densely distributed. After checking the raw data, we found the most densely distributed section was distance from 40% to 50% and distance from 30% to 60% sections was distributed about 94.8% (Table 1).

For the FDP, the number of nerve points ranged from 2 to 5, and the distribution ratio was 25.0%, 46.4%, 21.4% and 7.2%. Additionally, this study was divided into 10 sections, based on the reference length, and it examined which sections were densely distributed. After checking the raw data, we found the most densely distributed sections had a distance of 30% to 40% (Table 2).

The branch outpoint from the median nerve in the open palm position was 26.8 ± 1.9%. Howev-

Table 1. The mean value of the distributed frequency of nerve entry points to the flexor pollicis longus muscle belly

Structures	Mean ± SD [cm]	Distributed frequency (%)
Section 3 (20–30%)	26.0 ± 0.2	1.4
Section 4 (30–40%)	36.2 ± 2.2	25.2
Section 5 (40–50%)	45.2 ± 3.5	58.8
Section 6 (50–60%)	53.1 ± 2.7	10.8
Section 7 (60–70%)	64.0 ± 0.1	2.6
Section 8 (70–80%)	71.5 ± 0.1	1.2

SD — standard deviation

Table 2. The mean value of the distribution frequency of nerve entry points to the flexor digitorum profundus muscle belly

Structures	Mean ± SD [cm]	Distributed frequency (%)
Section 3 (20–30%)	27.2 ± 1.6	9.3
Section 4 (30–40%)	35.1 ± 2.7	60.1
Section 5 (40–50%)	43.0 ± 2.3	11.9
Section 6 (50–60%)	54.9 ± 3.3	11.7
Section 7 (60–70%)	62.3 ± 2.1	7.0
Section 8 (70–80%)	–	–

SD — standard deviation

Table 3. Nerve position change in accordance with muscle contraction (unit: %)

	Variable					
	A	**B**	**C**	**D**	**E**	**F**
Value	26.8 ± 1.9	29.9 ± 3.1	39.1 ± 2.7	44.3 ± 2.7	45.1 ± 3.0	45.4 ± 4.3

A — branch outpoint from median nerve in an open hand position; B — branch outpoint from median nerve in a closed fist hand position; C — nerve entry point of the flexor digitorum profundus muscle belly in an open hand position; D — nerve entry point of the flexor digitorum profundus muscle belly in a closed fist position; E — nerve entry point of the flexor pollicis longus muscle belly in a palm opened position; F — nerve entry point in the flexor pollicis longus muscle belly in a fist closed position
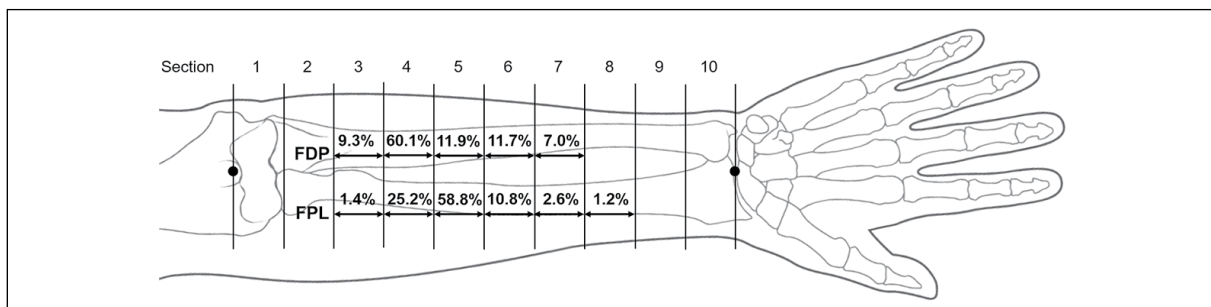
Figure 4. Degree of nerve distribution to enter the muscle belly on the reference line; FDP — flexor digitorum profundus; FPL — flexor pollicis longus.

er, after making a fist, the nerve change point was 29.9 ± 3.1%. So, except for the FPL, the nerve outpoint branch and FDP were moved 3.0% in accordance with hand movement (Table 3). The crossing point of the AIN with superior border of pronator quadratus was located at 76.1 ± 4.9% from the reference line. And the Gantzer muscle was found in 16 out of 60 specimens (Figs. 2, 3).

DISCUSSION

The AIN branched out under the pronator teres from the median nerve. This location might have caused AIN entrapment from the position where the nerves are divided. It is thought that the condition of the surrounding muscles, like a pronator teres, will cause nerve pressure. In this study, the median nerve runs to the anterior aspect of the hand and then branches out to the AIN at 4.4 ± 1.1 cm from the reference line. Previous studies have reported that the AIN branches out between 2.3 and 8.0 cm in Sunderland [11], 5.4 cm in Tubbs et al. [13], 8.0 cm in Benzel [1], 4.5 cm in Vincelet et al. [15] and 5.2 cm in Caetano et al. [3]. A number of cases reported about 5.0 cm regardless of population. The branch outpoint will become reference material for the treatment of AIN syndrome.

The integrated trigger point hypothesis postulates that motor endplates release excessive acetylcholine in myofascial pain, which is evidenced histopathologically by the presence of sarcomere shortening [2]. Target muscle and nerve production of abnormal acetylcholine is appropriately stimulated. At this time, the effect can be expected by treatment the nerve entered point of muscle belly. The recommended site

of recovery is 40.0–50.0% for the FPL and 30.0–40.0% for the FDP in this study (Fig. 4). The nerve entry point to the muscle belly is reported in this study. The information on the muscle belly nerve entry point can be used as helpful data for muscle and nerve relaxation during the clinical approach.

Clinically, the Gantzer muscle can also cause AIN syndrome [12]. Other anatomical studies have also indicated a relation between the Gantzer muscle and AIN syndrome [3]. The Gantzer muscle was found in 16 out of 60 specimens from all 8 cadavers and on both sides. In all cases found, this was independently innervated, and the AIN passed under the Gantzer muscle. This locational cause can affect the AIN syndrome according Gantzer muscle existence.

In 3 out of 60 specimens, the flexor digitorum superficialis was innervated by a branch of the AIN. Although it was difficult to find previous studies, this will provide reference material for muscle analysis related to AIN syndrome. One of the limitations of this study is our inability to examine more specimens. The fact that there was a 5.0% variation in FDP muscle nerve position related to whether the hand is open or closed into a fist is considered to be meaningful for the anatomical study of nerve position changes as related to movement.

CONCLUSIONS

The results of this study found that nerve location entered muscle belly and also nerve location related to movement with anatomical various investigation will be considered to treat in clinical practice.

Acknowledgements

Conflict of interest: None declared

REFERENCES

1. Benzel EC. Practical approaches to peripheral nerve surgery. American Association of Neurological Surgeons. 1992: 51–63.
2. Bron C, Dommerholt JD. Etiology of myofascial trigger points. Curr Pain Headache Rep. 2012; 16(5): 439–444, doi: 10.1007/s11916-012-0289-4, indexed in Pubmed: 22836591.
3. Caetano EB, Vieira LA, Sabongi Neto JJ, et al. Anterior interosseous nerve: anatomical study and clinical implications. Rev Bras Ortop. 2018; 53(5): 575–581, doi: 10.1016/j.rboe.2018.07.010, indexed in Pubmed: 30245997.
4. Dunn JC, Gonzalez GA, Fernandez I, et al. Supercharge end-to-side nerve transfer: systematic review. Hand (NY). 2021; 16(2): 151–156, doi: 10.1177/1558944719836213, indexed in Pubmed: 30924361.
5. Frank K, Englbrecht M, Koban KC, et al. Nerve transfer of the anterior interosseous nerve to the thenar branch of the median nerve - an anatomical and histological analysis. J Plast Reconstr Aesthet Surg. 2019; 72(5): 751–758, doi: 10.1016/j.bjps.2018.12.017, indexed in Pubmed: 30600157.
6. Head LK, Zhang ZZ, Hicks K, et al. Evaluation of intrinsic hand musculature reinnervation following supercharge end-to-side anterior interosseous-to-ulnar motor nerve transfer. Plast Reconstr Surg. 2020; 146(1): 128–132, doi: 10.1097/PRS.0000000000006903, indexed in Pubmed: 32590654.
7. Kiloh LG, Nevin S. Isolated neuritis of the anterior interosseous nerve. Br Med J. 1952; 1(4763): 850–851, doi: 10.1136/bmj.1.4763.850, indexed in Pubmed: 14916168.
8. Kodama N, Ando K, Takemura Y, et al. Treatment of spontaneous anterior interosseous nerve palsy. J Neurosurg. 2020; 132(4): 1243–1248, doi: 10.3171/2018.11.JNS181609, indexed in Pubmed: 32539243.
9. Li HM, Liu XJ. [Manual reduction of children's Monteggia fractures associated with anterior interosseous nerve injury]. Zhongguo Gu Shang. China J Orthopaedics Traumatology. 2014; 27(10): 862–865, indexed in Pubmed: 25739256.
10. Nakano KK, Lundergran C, Okihiro MM. Anterior interosseous nerve syndromes. Diagnostic methods and alternative treatments. Arch Neurol. 1977; 34(8): 477–480, doi: 10.1001/archneur.1977.00500200037007, indexed in Pubmed: 196582.
11. Sunderland S. The intraneural topography of the radial, median and ulnar nerves. Brain. 1945; 68: 243–299, doi: 10.1093/brain/68.4.243, indexed in Pubmed: 20982793.
12. Tabib W, Aboufarah F, Asselineau A. Compression of the anterior interosseous nerve by Gantzer's muscle. Chirurgie de la Main. 2001; 20(3): 241–246, doi: 10.1016/s1297-3203(01)00041-5, indexed in Pubmed: 11496612.
13. Tubbs RS, Custis JW, Salter EG, et al. Quantitation of and superficial surgical landmarks for the anterior interosseous nerve. J Neurosurg. 2006; 104(5): 787–791, doi: 10.3171/jns.2006.104.5.787, indexed in Pubmed: 16703884.
14. Ulrich D, Piatkowski A, Pallua N. Anterior interosseous nerve syndrome: retrospective analysis of 14 patients. Arch Orthop Trauma Surg. 2011; 131(11): 1561–1565, doi: 10.1007/s00402-011-1322-5, indexed in Pubmed: 21611763.
15. Vincelet Y, Journeau P, Popkov D, et al. The anatomical basis for anterior interosseous nerve palsy secondary to supracondylar humerus fractures in children. Orthop Traumatol Surg Res. 2013; 99(5): 543–547, doi: 10.1016/j.otsr.2013.04.002, indexed in Pubmed: 23916783.

VIA MEDICA

O R I G I N A L   A R T I C L E

Reference luminal diameters of the carotid arteries among healthy Nigerian adults

S.P.K. Kpuduwei[1, 2, 3], E.K. Kiridi[4], H.B. Fawehinmi[1], G.S. Oladipo[1]

[1]Department of Anatomy, University of Port Harcourt, Port Harcourt, Nigeria
[2]Department of Surgery, Federal Medical Centre, Yenagoa, Nigeria
[3]Division of Neurosurgery, Department of Surgery, National Hospital Abuja, Nigeria
[4]Department of Radiology, Niger Delta University, Wilberforce Island, Bayelsa State, Nigeria

Background: The carotid arteries serve as major blood supply to the head and neck region of the body. Understanding their structure and function in the pathogenesis of stroke and in interventional neuroradiology due to luminal stenosis, atherosclerosis and wall stiffness is paramount. Doppler ultrasound scan plays key role in the early diagnosis of the pathologies of the arteries as it is an affordable, accessible, reliable and non-invasive clinical tool. Knowing normal average diameter of the carotid arteries among healthy individuals is important in making correct clinical diagnosis in any population. The aim of the study was to determine mean diameters of the carotid arteries among healthy adult Nigerians for reference.

Materials and methods: This was a prospective study involving 104 healthy Nigerians within the ages of 18 and 65 years who had their carotid arteries scanned on both sides and each diameter was measured. A 95% confidence level was used; a p-value of < 0.05 was significant.

Results: Of the studied population, 62 were males and 42 were females, and the average age of the subjects was 28.32 ± 9.09 years. From this study, the average luminal diameter of the common carotid artery = 0.61 ± 0.08 cm, internal carotid artery = 0.60 ± 0.08 cm and external carotid artery = 0.49 ± 0.10 cm. The results showed that although, there are differences in measurements between the two sexes (males slightly higher than females in common carotid artery) and between right and left sides (with right side slightly higher), they are not statistically significant.

Conclusions: This sonographic study on healthy Nigerian adults has given us normal reference values of the luminal diameters of the carotid arteries among Nigerians, which clinicians can make reference to, when assessing carotid artery diameters of patients in Nigeria. (Folia Morphol 2022; 81, 3: 579–583)

Key words: carotid artery, luminal diameter, ultrasound scan, reference values, Nigerians

---

Address for correspondence: Dr. S.P.K. Kpuduwei, MD, MSc, MWACS, Department of Anatomy, University of Port Harcourt, Port Harcourt, Nigeria, tel: +234-8035382152, e-mail: dr.kpuduwei@gmail.com

INTRODUCTION

Blood supply to the brain is one of the key reasons why neurosurgeons and neurologists are interested in the structure and function of the carotid arteries, especially the internal carotid artery. The carotid arteries also play cardinal role in regulating the volume and pressure of blood that reaches the head and neck in addition to supplying oxygenated blood, as they are known to be influenced by cardiac outputs and blood pressure. However, the internal carotid artery (ICA) also serves as a gateway for vascular interventions in the brain, in addition to supplying blood to the cerebrum [8, 13, 23]. Stroke is global killer and the relationship between carotid artery diameter and cardiovascular risk for cerebrovascular events with the attendant compensatory dilation in atherosclerosis has been established [10, 20]. Interestingly, the carotid artery is also known to suffer several disease conditions that may affect its major function [14]. Atherosclerosis, luminal stenosis, wall stiffness may all affect its effective diameter, elasticity, and the velocity and volume of blood it can supply to the brain [25].

Ultrasonography is currently the first and preferred mode of assessment of the carotid arteries by clinicians because it is easily affordable, accessible, reliable with little or no complications as a non-invasive method with ease for follow-up [12, 17, 19, 24]. However, it would be difficult to state the exact degree of stenosis or dilation of the carotid arteries without normal reference values in the patient's environment, as there are indications to show racial variations in the size of the arteries [7]. In Nigeria, most clinicians use reference values in foreign texts to deduce their conclusion on the status of the luminal diameters of the carotid arteries, especially when there are no obvious atherosclerotic plagues to suggest pathology. This is partly because there is no existing established data of normal standardized reference values from healthy Nigerian subjects.

The aim of this study was to determine the mean luminal diameters of the carotid arteries in healthy adults to serve as normal reference values for clinical diagnostics among Nigerian patients.

MATERIALS AND METHODS

One hundred and four (104) healthy Nigerian adults between the ages of 18 and 65 years were sampled in this prospective cross-sectional study. The study was approved by the Ethics Committee of the University of Port Harcourt. Adequate consent from all participants was obtained. Subjects with history and overt signs of cardiovascular, cerebrovascular and metabolic disorders were excluded. Using ultrasound scan machine "EcoMed" version VERTU-3 Portable USG with linear transducer and frequency of 7.0 MHz, all participants were scanned by experienced radiologist. Sonographic measurements of luminal diameter for common carotid artery (CCA), ICA and external carotid artery (ECA) on both right and left sides about 1 cm from the carotid bifurcation in grayscale and B-mode were made. The measurements were done according to the recommendations of the Japan Society of Ultrasonics in Medicine and the American Society of Echocardiography using two-dimensional (2D) ultrasound images in end-diastolic phase. The diameter was basically obtained as the distance between one intimal layer and its opposite intimal layer [18, 22]. All measurements were in centimetres (cm).

Statistical analysis

The data acquired was analysed using the IBM SPSS version 23.0 from which, mean, standard deviation and T-test based on age and sex were calculated. Using a 95% confident level, p-value of < 0.05 was significant. Figure 1 shows a measured carotid artery.

RESULTS

Out of the total 104 subjects, the males were 62 and females 42. The average age of the subjects was 28.32 ± 9.09 years. The average height, weight, body mass index and blood pressure of the subjects were 1.72 ± 0.06 m, 67.65 ± 12.42 kg, 22.84 ± 4.15 kg/m² and $113.92 \pm 13.46/73.40 \pm 9.84$ mmHg, respectively. As shown in the Table 1, the results of this study showed that there are differences in measurements between the two sexes (males slightly higher than females in CCA and females higher than males in ICA and ECA) and between right and left sides (with right side slightly higher); however, they are not statistically significant. The right diameter measurements for CCA are, males = 0.63 ± 0.09, females = 0.61 ± 0.07; for ICA, males = 0.60 ± 0.09, females = 0.61 ± 0.10; for ECA, males = 0.49 ± 0.08, females = 0.51 ± 0.09. The left diameter measurements for CCA, males = 0.60 ± 0.09, females = 0.59 ± 0.06; for ICA, males = 0.60 ± 0.07, females = 0.61 ± 0.07; for ECA, males = 0.47 ± 0.14, females = 0.49 ± 0.07. From this study, the average luminal diameter for both sexes for the CCA = 0.61 ± 0.08 cm, ICA = 0.60 ± 0.08 cm and ECA = 0.49 ± 0.10 cm. Reference range of values for the diameters of the carotid arteries within which diameters can be said to be normal were
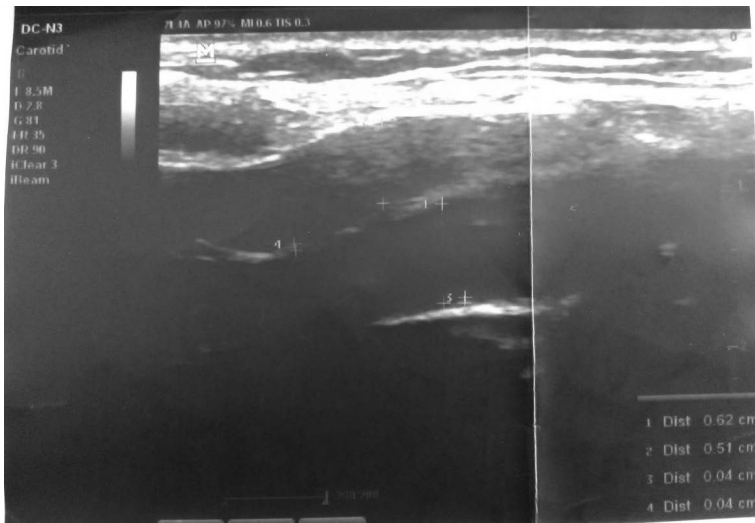
Figure 1. Doppler scan of carotid arteries with measurements.

Table 1. Descriptive statistics of the measured dimensions of the carotid arteries

Carotid artery diameter [cm]	Male (n = 62)			Female (n = 42)		
	Min	Max	Mean ± SD	Min	Max	Mean ± SD
Right						
CCA diameter	0.46	0.83	0.63 ± 0.09	0.43	0.77	0.61 ± 0.07
ICA diameter	0.35	0.81	0.60 ± 0.09	0.27	0.79	0.61 ± 0.10
ECA diameter	0.31	0.71	0.49 ± 0.08	0.33	0.79	0.51 ± 0.09
Left						
CCA diameter	0.42	0.77	0.60 ± 0.09	0.47	0.70	0.59 ± 0.06
ICA diameter	0.39	0.73	0.60 ± 0.07	0.43	0.81	0.61 ± 0.07
ECA diameter	−0.43	0.71	0.47 ± 0.14	0.26	0.66	0.49 ± 0.07

Min — minimum; Max — maximum; SD — standard deviation; CCA — common carotid artery; ICA — internal carotid artery; ECA — external carotid artery

Table 2. Reference value ranges for the diameters of the carotid arteries

Parameter (cm)	Male	Female	Total
Common carotid artery diameter	0.46–0.74	0.44–0.79	0.45–0.76
Internal carotid artery diameter	0.45–0.76	0.44–0.75	0.44–0.75
External carotid artery diameter	0.34–0.65	0.26–0.69	0.30–0.67

calculated using the formulae according to Kirkwood and Sterne (2003) [6]; Lawless and Fredette (2005) [11] below and are represented in Table 2.

$$LOWER\ LIMIT\ =\ m - t_{0.975,\infty} \times \sqrt{\frac{n+1}{n}} \times S.D$$

$$UPPER\ LIMIT\ =\ m + t_{0.975,\infty} \times \sqrt{\frac{n+1}{n}} \times S.D$$

where, $t_{0.975,\infty} = 1.96$, n — sample size, S.D — standard deviation [6, 11].

DISCUSSION

Carotid artery lumen plays an important role in clinical practice in the cardiovascular as well as vascular neurosurgical sectors. The importance of normal reference values to guide diagnostic and operative work up in-patient care cannot be overemphasized. The lack of Nigerian data with normal anatomical range of values for carotid artery diameters is one major problem this research has solved. Relying solely on foreign data is not desirable as there are known and established racial or demographic differences [7, 9, 16] that would also affect clinical decision-making in patient care in Nigeria. More so, the carotid arteries are not all the same in calibre and morphology [2, 21]. Furthermore, from our study, the proximity in diameter of the lumen of the internal carotid artery (0.60 cm) to that of the common carotid artery (0.61 cm) confirms that the former is a direct branch of the later as noted in embryology of the vessels as

they both developed from the same third aortic arch. Whereas, a wide difference is noted between the CCA and the ECA (0.49 cm), which developed from a different source (ventral pharyngeal artery) [3].

Review of similar studies in Sweden, by Jensen-Urstad et al. [5] noted the mean CCA in Swedish males and females as 0.63 ± 0.6 cm and 0.56 ± 0.5 cm, respectively with significant difference between the two sexes. However, in our index Nigerian study mean CCA diameter for males and females were 0.62 ± ± 0.09 cm and 0.60 ± 0.07 cm, respectively, where we find close values with that of the Swedish study only in the males but noted higher values in our females in comparison to that of the Swedish. In the United States, one study by Krejza et al. [9] gave normal values of diameter of CCA of males and females as 0.65 ± 0.98 cm and 0.61 ± 0.80 cm, respectively. In another study by Hwaung et al. [4], mean total values for the females (0.62 ± 0.88 cm) were higher than those for the males (0.57 ± 0.79 cm) in same country. This is similar to our study with the diameters of ICA and ECA, where the values for females were higher than those of males. Although there was significant difference between the sexes with reference to the diameters of the carotid in the study by Hwaung et al. [4], we did not record the same significance.

Whereas our values for CCA in the males were lower than those from Sweden and those from one study in the United States, we had higher values for CCA in our females in comparison to those from Sweden [5, 9]. We also had higher values in our males compared with those of the second study from United States with relatively lower values in our females to theirs [4]. Our values were higher on both sides for the values published from an Iraqi study [17], where diameter of right CCA = 0.60 ± 0.7 cm and left CCA = 0.58 ± 0.7 cm.

In a Nigerian study, Agunloye and Owolabi [1] worked on two cohort groups of patients. The 'controls' were hypertensive patients without any form of cerebrovascular accident and the 'cases' were hypertensive patients with any form of cerebrovascular accident. The results of the CCA diameters obtained for the 'controls' (right CCA = 0.59 ± 0.07 cm and left CCA = 0.58 ± 0.12 cm) [1] were similar to those of our index study but slightly lower (0.62 ± 0.08 cm and 0.59 ± 0.08 cm, respectively). One would have expected their values to be higher than normal healthy subjects as in our study based on the hypertensive factor [15, 20]; however, this was not the case. It may be that the degree of hypertension in the 'control' group at that time had not affected the diameter of the subjects just as there were no clinical signs or symptoms of stroke. This is an important point to note as the values of carotid artery diameter from the 'case' group, which were those hypertensives patients with any form of cerebrovascular event (right CCA = 0.66 ± 0.10 cm and left CCA = 0.63 ± 0.10 cm) were much higher than values from our study.

Since we were dealing with apparently healthy population with the aim of providing reference values, it was important to restrict the extremes of age. We believe the age bracket and body size of the subjects could have also played key roles in determining the diameter of the carotid arteries in our index study as they were mostly young adults with normal body size and blood pressure with no obvious clinical co-morbidities, where age and weight related changes have not become evident. This select population was important for the inclusion criteria as laboratory serum investigations which were termed invasive were not also intended.

Limitations of the study

The study did not include laboratory work up of the subjects, such as serum cholesterol, as the were no intents or consent for invasive investigations of the subjects.

CONCLUSIONS

This sonographic study on healthy Nigerian adults has given us normal reference values for the luminal diameters of the carotid arteries (CCA, ICA and ECA), which clinicians can refer to, when assessing carotid artery diameters of patients in Nigeria for clinical decision making. It also establishes that, although there are notable differences in values from different populations across countries, the Nigerian population has peculiar carotid artery diameter values, having higher values than some countries and lower for others, which needed to be established as the largest black nation in the world. It is also possible to infer the embryological relation between the CCA and the ICA based on their proximity in luminal size from our study.

Conflict of interest: None declared

REFERENCES

1. Agunloye AM, Owolabi MO. Exploring carotid sonographic parameters associated with stroke risk among hypertensive stroke patients compared to hypertensive controls. J Ultrasound Med. 2014; 33(6): 975–983, doi: 10.7863/ultra.33.6.975, indexed in Pubmed: 24866604.

2. Al-Rafiah A, EL-Haggagy AA, Aal IHA, et al. Anatomical study of the carotid bifurcation and origin variations of the ascending pharyngeal and superior thyroid arteries. Folia Morphol. 2011; 70(1): 47–55, indexed in Pubmed: 21604253.

3. Dungan DH, Heiserman JE. The carotid artery: embryology, normal anatomy, and physiology. Neuroimaging Clin N Am. 1996; 6(4): 789–799, indexed in Pubmed: 8824131.

4. Hwaung P, Heo M, Bourgeois B, et al. Greater height is associated with a larger carotid lumen diameter. Medicines. 2019; 6(2): 57, doi: 10.3390/medicines6020057.

5. Jensen-Urstad K, Jensen-Urstad M, Johansson J. Carotid artery diameter correlates with risk factors for cardiovascular disease in a population of 55-year-old subjects. Stroke. 1999; 30(8): 1572–1576, doi: 10.1161/01.str.30.8.1572.

6. Kirkwood B, Sterne J. Essential Medical Statistics. 2nd Ed. lackwell Publishing Ltd 2003: 56–57.

7. Koskinen SM, Soinne L, Valanne L, Silvennoinen H. The normal internal carotid artery: a CTA study. In: European Society of Radiology. 2014 [Internet]. www.myESR.org.

8. Kpuduwei SPK. Clinical Basis for the Knowledge of Anatomy of Carotid Artery: A Review Article. Yenagoa Med J. 2020; 2(3): 23–28.

9. Krejza J, Arkuszewski M, Kasner SE, et al. Carotid artery diameter in men and women and the relation to body and neck size. Stroke. 2006; 37(4): 1103–1105, doi: 10.1161/01.STR.0000206440.48756.f7, indexed in Pubmed: 16497983.

10. Labropoulos N, Zarge J, Mansour MA, et al. Compensatory arterial enlargement is a common pathobiologic response in early atherosclerosis. Am J Surg. 1998; 176(2): 140–143, doi: 10.1016/s0002-9610(98)00135-4, indexed in Pubmed: 9737619.

11. Lawless JF, Fredette M. Frequentist prediction intervals and predictive distributions. Biometrika. 2005; 92(3): 529–542, doi: 10.1093/biomet/92.3.529.

12. Manterola HL, Lo Vercio L, Díaz A, et al. Validation of an open-source tool for measuring carotid lumen diameter and intima-media thickness. Ultrasound Med Biol. 2018; 44(8): 1873–1881, doi: 10.1016/j.ultrasmedbio.2018.04.001, indexed in Pubmed: 29773245.

13. Meng L, Hou W, Chui J, et al. Cardiac output and cerebral blood flow: the integrated regulation of brain perfusion in adult humans. Anesthesiology. 2015; 123(5): 1198–1208, doi: 10.1097/ALN.0000000000000872, indexed in Pubmed: 26402848.

14. Onaizah O, Poepping TL, Zamir M. A model of blood supply to the brain via the carotid arteries: Effects of obstructive vs. sclerotic changes. Med Eng Phys. 2017; 49: 121–130, doi: 10.1016/j.medengphy.2017.08.009, indexed in Pubmed: 28917828.

15. Päivänsalo M, Merikanto J, Jerkkola T, et al. Effect of hypertension and risk factors on diameters of abdominal aorta and common iliac and femoral arteries in middle-aged hypertensive and control subjects. Atherosclerosis. 2000; 153(1): 99–106, doi: 10.1016/s0021-9150(00)00374-9.

16. Ranadive SM, Yan H, Lane AD, et al. Aerobic exercise training and arterial changes in african americans versus caucasians. Med Sci Sports Exerc. 2016; 48(1): 90–97, doi: 10.1249/MSS.0000000000000742, indexed in Pubmed: 26225767.

17. Rashid SA, Mahmud SA. Correlation between carotid artery intima-media thickness and luminal diameter with body mass index and other cardiovascular risk factors in adults. Sultan Qaboos Univ Med J. 2015; 15(3): e344––e350, doi: 10.18295/squmj.2015.15.03.007, indexed in Pubmed: 26357554.

18. Roman MJ, Naqvi TZ, Gardin JM, et al. Emile mohler. American association echocardiographers- clinical-app-of-non-invasive-vasc-us-in-cv-risk-stratification.pdf. J Am Soc Echocardiogr. 2006; 19: 943–954.

19. Saba L, Banchhor SK, Araki T, et al. Intra- and inter-operator reproducibility of automated cloud-based carotid lumen diameter ultrasound measurement. Indian Heart J. 2018; 70(5): 649–664, doi: 10.1016/j.ihj.2018.01.024, indexed in Pubmed: 30392503.

20. Sedaghat S, van Sloten TT, Laurent S, et al. Common carotid artery diameter and risk of cardiovascular events and mortality: pooled analyses of four cohort studies. Hypertension. 2018; 72(1): 85–92, doi: 10.1161/HYPERTENSIONAHA.118.11253, indexed in Pubmed: 29785959.

21. Sheikh-Bahaei N, Matys T, Gillard JH. Anatomy of the neck arteries. In: Neurovascular Imaging: From Basics to Advanced Concets. Sringer, New York 2016: 87–94.

22. Terminology and Diagnostic Criteria Committee, Japan Society of Ultrasonics in Medicine. Standard method for ultrasound evaluation of carotid artery lesions. J Med Ultrasonics. 2009; 36(4): 219–226, doi: 10.1007/s10396-009-0238-y.

23. Tolezani EC, Costa-Hong V, Correia G, et al. Determinants of functional and structural properties of large arteries in healthy individuals. Arq Bras Cardiol. 2014; 103(5): 426–432, doi: 10.5935/abc.20140124, indexed in Pubmed: 25211201.

24. Wikstrand J. Methodological considerations of ultrasound measurement of carotid artery intima-media thickness and lumen diameter. Clin Physiol Funct Imaging. 2007; 27(6): 341–345, doi: 10.1111/j.1475-097X.2007.00757.x, indexed in Pubmed: 17944655.

25. Woldeyes DH. Anatomical variations of the common carotid artery bifurcations in relation to the cervical vertebrae in ethiopia. Anat Physiol Curr Res. 2014; 4(3): 1–3.

ORIGINAL ARTICLE

VIA MEDICA

Morphologic comparison of blood vessels used for coronary artery bypass graft surgery

M. Garnizone, E. Vartina, M. Pilmane

Department of Morphology, Institute of Anatomy and Anthropology, Riga Stradins University, Riga, Latvia

Background: The aim of this study was to evaluate morphologic features of healthy saphenous vein and internal thoracic artery, blood vessels used in coronary artery bypass graft (CABG) surgery, and compare results.

Materials and methods: Ten specimens of saphenous veins and ten of internal thoracic arteries used for CABG were obtained from 20 patients. Histological routine and immunohistochemical staining was performed with: endothelin (ET), tissue inhibitor of metalloproteinase 2 (TIMP2), metallomembranoproteinase 2 (MMP2), transforming growth factor beta (TGFβ), hepatocyte growth factor (HGF), vascular endothelial growth factor (VEGF), protein gene product 9.5 (PGP9.5), vascular cell adhesion molecule (VCAM), intercellular adhesion molecule (ICAM). A semiquantitative evaluation method was used.

Results: There was found: a moderate number of endothelin-positive cells in both blood vessel types; a moderate number of MMP2-positive cells and moderate in number to numerous TIMP2-positive cells in veins. In arteries — occasionally marked positive MMP2 cells and negative TIMP2; moderate in number to numerous VEGF-positive endothelial cells on small blood vessels in vein wall and occasionally in artery wall; numerous TGFβ-positive structures in veins and abundance of VCAM- and ICAM-positive cells, few in arteries; few HGF-positive structures in veins, negative in arteries; In veins, few PGP9.5-positive nerve fibres, in arteries — moderate. Moderate TUNEL reaction-positive apoptotic cells in veins and few to moderate in arteries.

Conclusions: Vena saphena magna grafts are characterised by increased plasticity when it comes to modelling. Number of VEGF, VCAM and ICAM found in vena saphena magna proves the possible tendency of graft failure on basis of local blood supply intensification. Appearance of endothelin positive cells indicate the similar homeostasis condition in endotheliocytes in both — vein and artery grafts. (Folia Morphol 2022; 81, 3: 584–593)

Key words: immunohistochemistry, saphenous vein, internal thoracic artery

INTRODUCTION

Arteries (*arteria thoracica interna*) and veins (*vena saphena magna*) are often used for coronary artery bypass graft (CABG) surgery. Morphologic architecture of relatively healthy blood vessel wall is known; however, qualitative data on morphologic features

Address for correspondence: Dr. M. Garnizone, Department of Morphology, Institute of Anatomy and Anthropology, Riga Stradins University, Kronvalda bulvaris 9, Riga, Latvia, tel: +37167320862, e-mail: marika.garnizone@gmail.com

and possible changes in blood vessels actually used in CABG surgery is lacking. Therefore, it was important to conduct a morphologic study and a comparison of both blood vessel types that might lead us to reasons that influence grafts post-operative sustainability.

There are differences and similarities in morphologic characterisation of blood vessel wall; it is composed of three layers, the intima, media, and adventitia. In arteries the internal elastic layer further separates the intima and media, and the external elastic layer separates the media and adventitia [14, 45].

The intimal luminal surface is lined by the endothelium which is a continuous layer of flat polygonal endothelial cells in direct contact with blood flow. In venous system these cells produce vasorelaxants, such as prostacyclin and nitric oxide, that prevent platelet activation, adhesion, and aggregation. Nitric oxide also negatively affects the expression of chemical mediator secretion and inflammatory cell adhesion molecules including intercellular adhesion molecule-1 (ICAM-1) and vascular cell adhesion molecule-1 (VCAM-1) [9, 37, 45].

In arteries, the thickness of the intima increases with age (phlebosclerosis). The earliest signs of atherosclerosis appear in the areas of sheer stress and increased intimal thickness [9, 17, 40]. In case of inflammation, the glycocalyx is sheared off, permitting the attachment of leukocytes and the transport of water from microvessels, and possibly initiating the development of atherosclerotic lesions [43].

Intimal layer in arteries ends with internal elastic lamina that may function as a barrier to macromolecular accumulation in the vascular wall. Structural defects within the internal elastic lamina are directly implicated in the onset of intimal thickening in human arteries [42].

Media is a porous heterogeneous medium consisting of an extracellular matrix with embedded smooth muscle cells (SMC). In larger veins, such as the saphenous vein, there are coarse bundles of irregular muscle, partially organized into longitudinal and circular layers [17, 22, 45]. Arteries are classified as either elastic or muscular according to the proportion of cellular and fibrous components in this layer or transitional if they have features of both elastic and muscular arteries [50]. The internal thoracic artery is an artery of the transitional (mixed) type. The nonfenestrated internal elastic lamina of the internal thoracic artery may inhibit cellular migration, perhaps preventing the initiation of intimal hyperplasia and the initiation of atherosclerosis [5].

Nonparallel branching elastin strands in media increase the capacity to change diameter under neurohumoural stimulation. However, in general it is less well developed in veins than that of the arterial system. This thin media in veins may contribute to the development of varicosities in lower extremities [17, 22, 45]. The tunica media contains extracellular connective elements (elastin, collagen types I and III, proteoglycans, and glycosaminoglycans). Transforming growth factor beta (TGFβ) downregulates smooth muscle cell mitogenesis and stabilizes the extracellular matrix against smooth muscle cell migration. In addition, heparin and heparin-like molecules neutralise fibroblast growth factor to downregulate cell proliferation. This process is important because these factors keep the normal vessel wall in a state of low cell turnover with low rates of proliferation and apoptosis. Injury or changes to the environment, as when veins are exposed to arterial flow, can increase rates of proliferation or apoptosis [2, 6, 45].

Adventitia extends from the external elastic lamina to an ill-defined boundary usually contiguous with the perivascular connective tissue. The adventitia varies in thickness and organization. It is generally the thickest layer in large veins. Bundles of longitudinally oriented SMC are interspersed with collagen and elastic fibres in this layer. Compared with *vasa vasorum* of corresponding arteries, *vasa vasorum* are much more extensive in venous adventitia and penetrate into deeper regions of the adventitia as well. Lower oxygen tension in venous blood is a possible explanation for this phenomenon. In thick-walled arteries, mural stresses and deformations may affect the *vasa vasorum* [6, 37, 45].

In general, veins have thinner walls than their corresponding arteries because their cellular and fibrous components are typically more limited than those of the arterial system. This wall composition leads to the properties of veins as "capacitance vessels" and arteries as "resistance vessels." It should be noted that the composition of vein walls is also different, with a relative abundance of collagen fibres, particularly in large veins, and a relative paucity of elastic fibres — as might be assumed from the diminished internal and external elastic laminae. Researchers have increasingly recognized the vein graft tunica adventitia as an important repository of progenitor cells, which subsequently can migrate and proliferate, and as a source of vascular wall inflammatory cells, cytokines, and chemokines [20, 31, 45, 51].

Specific factors for blood vessel wall

Endothelin-1 (ET-1) is the endogenous agonist for ET receptors [47]. ET-1 carries out its effects through two types of membrane G-protein-coupled receptors (ETA and ETB). ETB receptor function seems to differ between a similarly sized arterial and venous pair [39]. Many important functions are mediated by the activation of these receptors, such as cardiovascular remodelling, vasoconstriction, cell proliferation and differentiation, production of extracellular matrix, and water and sodium secretion control. ET receptors can be found on vascular SMC, adventitial fibroblasts, and mostly endothelial cells [1, 46, 48].

Matrix metalloproteinases (MMPs) are a family of endopeptidases whose primary function is the cleavage and degradation of extracellular matrix components that are involved in wound healing, tissue repair and remodelling in response to injury and vasoconstriction. It is believed that MMPs are induced in the vessel wall in response to increased blood flow and are involved significantly in arterial wall remodelling. MMPs are produced by SMC and macrophages to actively modify the matrix. Activities of those proteins are regulated by tissue inhibitors of metalloproteinases (TIMPs). In addition to an inhibitory role against metalloproteinases, they also directly suppress the proliferation of endothelial cells maintaining tissue homeostasis by suppressing the proliferation of quiescent tissues in response to angiogenic factors, and by inhibiting protease activity in tissues undergoing remodelling of the extracellular matrix [33, 35, 45, 48].

Encoded transforming growth factor beta protein regulates cell proliferation, differentiation and growth, and can modulate expression and activation of other growth factors. TGFβ critically regulates the development of neointima formation following vascular injury [23, 28–30].

Hepatocyte growth factor (HGF) is an angiogenic, cardioprotective factor important for tissue and vascular repair. High levels of HGF are associated with chronic inflammatory diseases, such as coronary artery disease (CAD) and are suggested as a marker of the ongoing atherosclerotic event in patients with CAD. Pleiotropic growth factor has potential angiogenic, anti-apoptotic, antifibrotic and anti-inflammatory benefits [28, 30].

Vascular endothelial growth factor (VEGF) is a secreted glycoprotein believed to be a multifunctional regulator of endothelial cell growth whose biological activities are mediated via receptors which are expressed predominantly on vascular endothelial cells. It induces proliferation and migration of vascular endothelial cells and is essential for both physiological and pathological angiogenesis. Stretch-induced modulation of genes involved in myogenic differentiation contributes to the vascular remodelling that underlies pathologic complications, such as neointima development and atherosclerosis, of the vein grafts [7, 13, 22, 41].

Protein gene product 9.5 (PGP9.5) is also known as ubiquitin C-terminal hydrolase 1 (UCHL-1). It is highly specific to be expressed in neurons and in cells of the diffuse neuroendocrine system. Originally isolated as a neuron-specific protein, it also plays important roles in the nonlysosomal proteolytic pathway. In the vascular system PGP9.5-immunoreactivity occurs in an extensive plexus of fine perivascular nerve fibres and fascicles running around and along both arteries and veins, mainly at the adventitial-medial border [18, 24].

Vascular cell adhesion molecule-1 encodes a cell surface protein expressed by cytokine-activated endothelium. It is not expressed under baseline conditions but is rapidly induced by proatherosclerotic conditions [27].

Intercellular adhesion molecule-1 is a member of the immunoglobulin superfamily of adhesion receptors. It is a cell surface protein which is typically expressed on endothelial cells and cells of the immune system and is involved in the binding of a cell to another cell or to the extracellular matrix. Levels of endothelial ICAM-1 expression greatly increase after stimulation by cytokines (e.g., IL-1, TNF-α, IFN-γ), or bacterial endotoxin. They have roles in cell proliferation, differentiation, motility, trafficking, apoptosis and tissue architecture [8, 12].

Increased shear stress upregulates ICAM-1, steady shear stress upregulates VCAM-1, and oscillatory stress decreases levels of both molecules [45].

Terminal deoxynucleotidyl transferase (TdT) dUTP nick-end labelling (TUNEL) assay has been designed to detect apoptotic cells that undergo extensive DNA degradation during the late stages of apoptosis [26].

The aim of this study was to evaluate morphologic features of healthy saphenous vein and healthy internal thoracic artery used in CABG surgery and compare results.

MATERIALS AND METHODS

Twenty blood vessel samples were acquired in Pauls Stradins Clinical University Hospital, Heart Sur-

gery Centre from patients who were admitted to the hospital for CABG surgery. Patients' records were retrieved and analysed according to a predetermined protocol.

Ten specimens of saphenous veins used for CABG were obtained from 10 patients (7 males and 3 females, age ranged from 55 to 81 years old) and ten specimens of internal thoracic arteries used for CABG were obtained from 10 patients (8 males and 2 females, age ranged from 54 to 75 years old).

Hospitals Ethics Committee and local Committee of Ethics at Riga Stradins University approved the research on 22nd February of 2018. Before the surgery all patients were informed about the procedure of collecting the sample, possible risks and agreed on the procedure by signing patient's consent.

Data on vascular risk factors (age, sex, body mass index, smoking habits, physical activities, pregnancies, use of hormonal drugs) were collected from all patients.

Methods

During the surgery, after obtaining a blood vessel used as bypass, a size of 2–3 cm tissue samples from that blood vessel were removed for the study and taken to the laboratory.

Tissue samples delivered to the laboratory were immersed for 24 hours in Stefanini liquid — a mixture consisting of 2% formaldehyde and 0.2% picric acid in 0.1-M phosphate buffer (pH 7.2) for fixation [44]. Afterwards they were washed for 12 hours in phosphate buffer (pH 7). Then, tissue samples were embedded in paraffin and using microtome cut into 3–4 μm thick sections. Xylene was used to clear off paraffin, and alcohol 96° to dehydrate tissue sections. The slides were prepared for histological routine staining and immunohistochemical staining using the HiDef Detection™ HRP Polymer System to identify the following markers in tissue samples: ET (mouse, ab-2786, 1:250, Abcam), MMP2 (mouse, sc-53630, 1:100, Santa Cruz Biotechnology, Inc.), TIMP2 (mouse, sc-21735, 1:200, Santa Cruz Biotechnology, Inc.), TGFβ (rabbit, sc-82, 1:100, Santa Cruz Biotechnology, Inc.), HGF (goat, f-21, 1:300, RD Systems), VEGF (rabbit, orv-191500, 1:100, Biorbyt), PGP9.5 (rabbit, 439273a, 1:200, Invitrogen), VCAM (goat, cd-106, 1:200, RD Systems), ICAM (goat, cd-54, 1:300, RD Systems).

Next step included rinsing of tissue samples in wash buffer (TRIS) (Lot 0713513, Diapath S.p.A., Italy) twice for 5 minutes, then placing them in a microwave oven for up to 20 minutes in boiling

EDTA buffer (Lot 0713311, Diapath S.p.A., Italy) and then cooling down until 65°C (approximately 20 minutes). The specimen was placed in a TRIS wash buffer, and blocking with peroxidase block (Lot 1213603A, Cell Marque, USA) was performed for 10 minutes. After rinsing twice for 5 minutes it was once more rinsed in TRIS for 5 minutes.

Different staining systems were used, taking into account the origin of the antibodies.

When obtained from goat, LSAB system (Santa Cruz Biotechnology, Inc., USA) was used. Primary antibody was introduced for 2 hours. Before and after incubation with secondary antibody (biotin) for 30 minutes, it was washed in TRIS for 5 minutes. Next step was incubation with horseradish peroxidase-streptavidin complex for 30 minutes followed by washing with TRIS for 5 more minutes.

When obtained from mouse or rabbit, the EnVision staining system (Lot 1528902C, Cell Marque, USA) was used. Primary antibody was introduced for 1 hour. Before and after the EnVision+/binding for 30 minutes, it was washed in TRIS twice, each for 5 minutes.

To stain any of these tissues, they were covered with 3,3'-diaminodbenzidine sensitive colorimetric substrate and left in room temperature for 10 minutes and then washed in distilled water for 5 minutes. At this point positive structures stained brown. To stain negative structures, haematoxylin (Mayer's haematoxylin, Bio Optica Milano S.p.A., Italy) was used for 2 minutes.

To detect and quantify apoptotic cell death at single cell level in cells and tissues *in situ* Cell Detection Kit was used. Dewaxation and rehydration of paraffin embedded tissue according to standard protocol by heating at 60°C followed by washing in xylene and rehydration through a graded series of ethanol and double distilled water. In next phase incubation of tissue sections for 15–30 minutes at +21°C to +37°C with proteinase K takes place. TUNEL mixture is prepared immediately before use and is kept on ice until use. Meanwhile slides are rinsed twice with phosphate buffered saline (PBS) and area around the sample is dried. TUNEL reaction mixture is added on the sample. It is covered with a lid and left for incubation for 60 minutes at +37°C in a humidified atmosphere in the dark. Reaction is finished with rinsing it with PBS.

For the analysis of the positive structures detected by immunohistochemistry, a semiquantitative evalu-
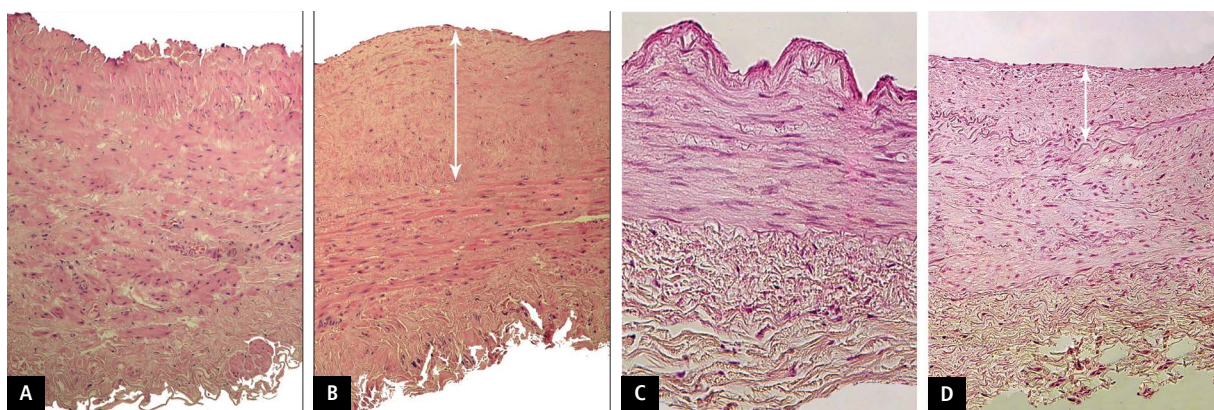
Figure 1. Note a classic picture of *vena saphena magna* wall with three intact layers — tunica intima, tunica media and tunica adventitia (**A**), with one exception (**B**) of hyperplasia of tunica intima (arrow), where it is thick and wider than tunica media; haematoxylin and eosin, ×100. In comparison, note a classic picture of *arteria thoracica interna* wall with three layers — tunica intima, tunica media and tunica adventitia (**C**) and atheromatous deposit in tunica intima (arrow), which was found in half of the *arteria thoracica interna* specimens (**D**); haematoxylin and eosin, ×200.

Table 1. Median values of immunohistochemical evaluation results

Blood vessel	Endothelin	MMP2	TIMP2	TGFβ	HGF	VEGF	PGP9.5	VCAM	ICAM	TUNEL
Vena saphena magna	++	++	++/+++	+++	+	++/+++	+	++++	++++	++
Arteria thoracica interna	++	0/+	0	+	0	0/+	++	+	+	+/++

MMP2 — metallomembranoproteinase 2; TIMP2 — tissue inhibitor of metalloproteinase 2; TGFβ — transforming growth factor beta; HGF — hepatocyte growth factor; VEGF — vascular endothelial growth factor; PGP9.5 — protein gene product 9.5; VCAM — vascular cell adhesion molecule; ICAM — intercellular adhesion molecule; TUNEL — terminal deoxynucleotidyl transferase (TdT) dUTP nick-end labelling

ation method was used [38]. The designations were as follows: 0 — negative reaction; 0/+ — occasionally marked structures in the view field; + — a few positive structures in the view field; +/++ — a few to moderate number of positive structures in the view field; ++ — a moderate number of positive structures found in the view field; ++/+++ — moderate to numerous positive structures; +++ — numerous positive structures in the view field; ++++ — abundance of positive structures in view field. Ten view fields for each slide were analysed at magnification of ×200 by semiquantitative method. The evaluation was performed with Leica microscope by two independent researchers with following comparison of the results later. Median of the results for each slide was then processed further. IBM SPSS programme was used for statistical analysis. Spearman correlation test was performed for finding correlations. For statistical comparison Mann-Whitney U test was performed.

RESULTS

Routine morphology

Vein wall as well as arterial wall was composed of three tunicae evaluated in routine staining. The first tunica from the luminal side was the intima, which was fully or partially covered with endothelial cells. Tunica intima in all vein specimens was thinnest from all the layers (Fig. 1A) with one exception, where tunica intima was thick, wider than tunica media (Fig. 1B). Even though arterial specimens also showed all three tunicae (Fig. 1C) in half of the specimens tunica intima revealed atheromatous deposits (Fig. 1D). The media in veins was thick and filled with SMC with one exception, where tunica media was thin. Tunica media in all arteries was thick and filled with SMC. Tunica adventitia in both arteries and veins consisted of bundles of collagen fibres, fibroblasts, vasa vasorum from which few were sclerotic in all vein specimens and only in two artery specimens.

Immunohistochemistry results

A moderate number of (++) endothelin-positive endothelial cells were found in veins as well as in arteries (Table 1).

A moderate number of (++) MMP2-positive endothelial cells, SMC and fibroblasts (Fig. 2A) and variable — mainly moderate to numerous (++/+++) TIMP2-positive endothelial cells, SMC and fibroblasts
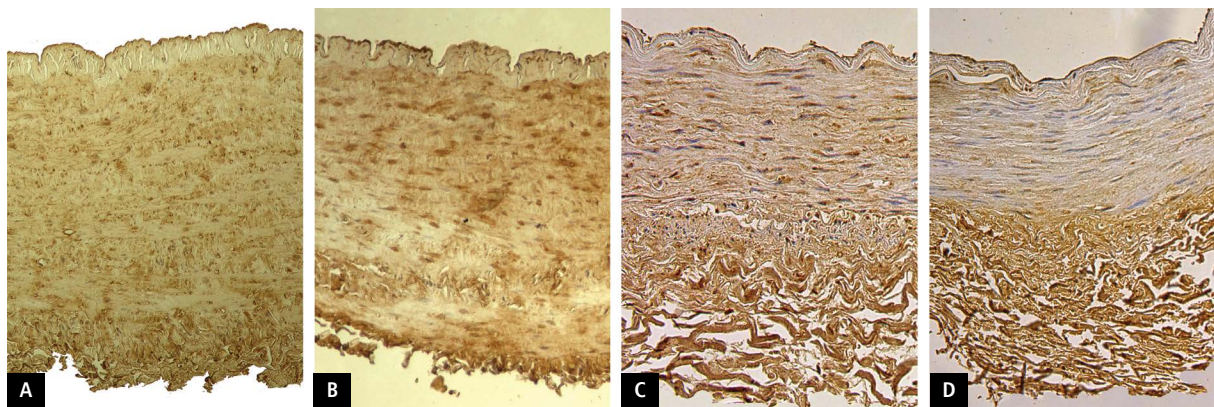
Figure 2. Throughout all layers of *vena saphena magna* there can be seen moderate (++) metallomembranoproteinase 2 (MMP2)-positive endothelial cells, smooth muscle cells and fibroblasts (**A**), MMP2 immunohistochemical staining, ×100 and numerous (+++) tissue inhibitor of metalloproteinase 2 (TIMP2)-positive endothelial cells, smooth muscle cells and fibroblasts (**B**), TIMP2 immunohistochemical staining, ×200. In comparison, throughout all layers of *arteria thoracica interna* there can be seen few (+) MMP2-positive endothelial cells, smooth muscle cells and fibroblasts (**C**), MMP2 immunohistochemical staining, ×200 and occasionally marked (0/+) TIMP2-positive endothelial cells, smooth muscle cells and fibroblasts (**D**), TIMP2 immunohistochemical staining, ×200.

(Fig. 2B) were found in veins. Despite variability, in all cases positive structures were evaluated as equal with both MMP2 and TIMP2 with one exception, where MMP2-positive structures were evaluated as moderate (++), but TIMP2-positive structures were evaluated as few (+). Comparing to arteries — variable, but mostly occasionally marked (0/+) MMP2-positive endothelial cells, SMC and fibroblasts (Fig. 2C) and variable, but mostly negative (0) TIMP2 reaction on endothelial cells, SMC and fibroblasts (Fig. 2D) were found. In all cases there were more positive structures for MMP2 than TIMP2 with one exception, where they were evaluated as equal.

Moderate in number to numerous (++/+++) VEGF-positive endothelial cells were found on small blood vessels in vein wall (Fig. 3A); however, only occasionally (0/+) VEGF-positive endothelial cells were found on small blood vessels in artery wall (Fig. 3B).

All vein specimens were rich with TGFβ, VCAM and ICAM: numerous (+++) TGFβ structures, abundance (++++) of VCAM- and ICAM-positive endothelial cells were also found. All arterial specimens had few (+) TGFβ-, VCAM- and ICAM-positive structures.

Hepatocyte growth factor expression was not characteristic in veins or in arteries: only few (+) positive structures were found in tunica intima of veins and in arteries no (0) positive structures were found.

In tunica adventitia of veins few (+) PGP9.5-positive nerve fibres were found, comparing to the same layer of arteries that was slightly more innervated, where moderate (++) PGP9.5-positive nerve fibres were found.
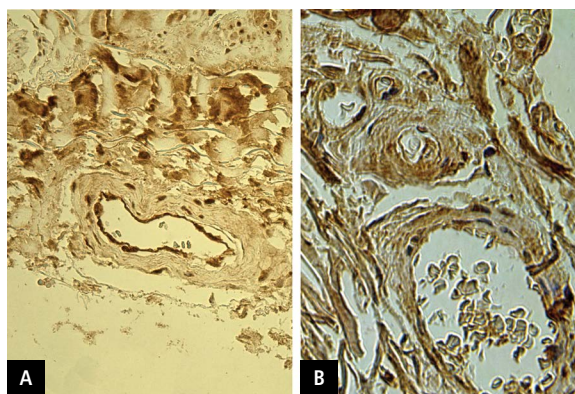
Figure 3. Note adventitial layer of *vena saphena magna* with abundance (++++) of vascular endothelial growth factor (VEGF)-positive endothelial cells found in small blood vessels (**A**) in comparison with adventitial layer of *arteria thoracica interna* with few (+) VEGF-positive endothelial cells found in small blood vessels (**B**), VEGF immunohistochemical staining, ×400.

A moderate number of (++) TUNEL reaction-positive apoptotic cells were found in veins and few to a moderate number of (+/++) TUNEL reaction-positive apoptotic cells were found in arteries.

There was a significant difference in the number of MMP2-, TIMP2-, TGFβ-, VCAM-, ICAM- and HGF-positive structures between arteries and veins (U = 0.000, p < 0.001).

There was also found significant difference in the number of VEGF-positive structures between arteries and veins (U = 4.000, p < 0.001) and significant difference in the number of TUNEL reaction-pos-

itive apoptotic cells between arteries and veins (U = 12.000, p = 0.003).

Results for endothelin- and PGP9.5-positive structures did not show significant difference between arteries and veins.

There was a significant correlation between the number of HGF-positive structures and the number of TIMP2-positive structures in veins. The correlation level is medium positive (r = 0.731; p = 0.016).

DISCUSSION

Saphenous vein grafts remain the most commonly implanted surgical conduits during CABG, yet they are prone to accelerated atherosclerosis and subsequent failure [19]. Internal thoracic artery grafts exhibit a striking absence of occlusive lesions, and has far superior patency rates compared to the saphenous veins following CAGB surgery. The reason for these unique artery qualities has not been clearly determined, but is most likely multifactorial [4].

Even though our study showed the amount of endothelin expressed in veins and arteries were similar, reasons behind this result may be different. As saphenous vein grafts are exposed to arterial blood flow and pressure, they might generally exhibit unfavourable vascular remodelling afterwards [4, 11]. Studies have suggested that competitive flow is an important factor in early internal thoracic artery graft failure. Flow competition from minimally diseased native coronary vessels has been implicated in the failure of these grafts, but it was not thought to affect saphenous vein graft patency [34, 36]. In a study (Meng et al., 2013 [34]) that established a swine model of CABG with a left internal mammary artery graft to the left anterior descending coronary artery, in order to investigate the influence of competitive flow on left internal mammary artery graft flow, it was found that plasma concentration of the endothelin in left internal mammary artery after grafting was significantly higher than that before grafting [34]. This shows that changes of blood flow in both types of blood vessels used as CABG impact the patency of a graft.

Expression levels of MMPs and TIMPs should always be evaluated together as MMPs are involved in tissue repair and remodelling, but activities of those proteins are regulated by TIMPs by inhibition and also suppression of the proliferation of endothelial cells maintaining tissue homeostasis [33, 35]. The extracellular matrix is a dynamic structure that requires constant synthesis and degradation by MMPs [15, 16]. We found that in saphenous vein grafts the number of MMP- and TIMP2-positive structures was moderate to numerous and mostly equal and this might be the basic level of expression of these factors in the vein. Or this could be explained by sudden change in blood flow and pressure requiring active change of extra cellular matrix as normally venous blood pressure is lower and does not require such levels of these proteins. In internal thoracic arteries both proteins were found to be variable, but MMP2 were mostly occasionally marked positive, but TIMP2 mostly negative. To provide constant change of extracellular matrix in higher blood pressure, expression of these proteins in internal thoracic artery grafts should be expected high to maintain a normal architecture of an arterial wall. Since in half of arterial specimen an atheromatous plaque was observed in routine staining, which indicate a failure of maintaining such architecture. Furthermore, our study shows almost an absence of TIMP2 that normally would supress enzymes that degrade internal elastic membrane, resulting in vascular SMC and collagen fibres entering tunica intima, which was described as intimal hyperplasia.

We found numerous TGFβ-positive structures in saphenous vein wall, but all arterial specimens had few TGFβ-positive structures. TGFβ is a signalling family with essential functions in the physiologic homeostasis of the vascular endothelium and smooth muscle, as well as other tissues. TGFβ family includes a structurally diverse set of more than 33 cytokines that regulate the differentiation, proliferation, migration and survival of diverse cell types [53]. As Yuan et al. (2011) [52] states, severe vascular wall degeneration and collagen deposition together with overexpressed TGFβ signalling cytokines may provide preliminary evidence for the failure of the saphenous vein grafts. This might indicate internal thoracic artery grafts longer durability.

Allen et al. (1998) [3] states that adhesion molecules can increase the binding of leukocytes to the vascular endothelium, which is thought to be an important factor in the early development of atherosclerosis. Also harvesting the vein graft is known to activate the graft endothelium [21]. Our study showed abundance of VCAM- and ICAM-positive endothelial cells in saphenous vein grafts, although arterial specimens had only few VCAM- and ICAM-positive structures, which implies higher possibility for vein graft failure.

Physiological remodelling of blood vessels before and after birth has been shown to be the result of a balance between apoptosis and cell proliferation. The role of apoptosis has been investigated in vessel remodelling that occurs as arteries adapt to changes in cardiovascular function after birth [32]. Cho et al. (1995) [10] have demonstrated that apoptosis significantly contributes to postpartum arterial remodelling and that changes in cell death rates alone may be sufficient to induce profound changes in the vessel wall mass.

Use of TUNEL reaction for detection of apoptotic cardiomyocytes in patients who underwent CABG surgery had been done before by Kovacević et al. (2007) [25]. However, apoptosis in myocytes of grafts haven't been researched. Our study shows that there is a significant difference in the number of apoptotic cells between arteries and veins. As moderate number of TUNEL reaction-positive apoptotic cells were found in veins and less TUNEL reaction-positive apoptotic cells were found in arteries, which suggests higher plasticity of vein wall in comparison to arterial wall.

Vascular endothelial growth factor plays a fundamental role in physiological and pathological angiogenesis and also induces endothelium-derived vasorelaxation [49]. More VEGF-positive endothelial cells were found on small blood vessels in vein wall than on small blood vessels in artery wall. This might indicate that more active angiogenesis takes place in the wall of a vein graft.

It is known that extensive plexus of fine perivascular nerve fibres and fascicles is located around and along both arteries and veins, mainly at the adventitial-medial border [18]. This shows that only the fascicles of nerve fibres enter the wall of a blood vessel. That explains why we found only few PGP9.5-positive nerve fibres in veins, and the same layer of arteries was slightly more innervated. These results did not significantly differ between arteries and veins.

CONCLUSIONS

Vena saphena magna grafts are characterised by relatively higher number of MMP2-, TIMP2-, HGF- and TGFβ-positive structures than the artery graft, which suggest more seemingly an increase of plasticity when it comes to modelling of the vein grafts.

Notably higher expression of VEGF, VCAM and ICAM in *vena saphena magna*, but not *arteria thoracica interna* graft proves the possible tendency of graft failure on the basis of local blood supply intensification.

Arteria thoracica interna graft is characterised by moderate neuropeptide-containing innervation, which is much more indistinct in the *vena saphena magna* graft, while similar appearance of endothelin-positive and apoptotic cells indicate the similar homeostasis condition in endotheliocytes and equal expression of programmed cell death ligands in both — vein and artery grafts.

Conflict of interest: None declared

REFERENCES

1. Abraham D, Dashwood M. Endothelin: role in vascular disease. Rheumatology (Oxford). 2008; 47 (Suppl 5): v23–v24, doi: 10.1093/rheumatology/ken282, indexed in Pubmed: 18784133.
2. Airhart N, Curci JA. Arterial Aneurysms. In: Cronenwett JL, Johnston KW (ed). Rutherford's Vascular Surgery 8th ed. Elsevier, London, UK 2014: 113–131.
3. Allen S, Khan S, Tam Sp, et al. Expression of adhesion molecules by lp(a): a potential novel mechanism for its atherogenicity. FASEB J. 1998; 12(15): 1765–1776, doi: 10.1096/fasebj.12.15.1765, indexed in Pubmed: 9837867.
4. Anstadt MP, Franga DL, Portik-Dobos V, et al. Native matrix metalloproteinase characteristics may influence early stenosis of venous versus arterial coronary artery bypass grafting conduits. Chest. 2004; 125(5): 1853–1858, doi: 10.1378/chest.125.5.1853, indexed in Pubmed: 15136400.
5. Baron SJ, Mick S, Shekar PS, Mauri I. Cardiovascular therapeutics: a companion to Braunwald's heart disease. In: Antman EM, Sabatine MS (ed). 4th Ed. W.B. Saunders 2013: 214–239.
6. Berceli SA. Autogenous Grafts. In: Cronenwett JL, Johnston KW (ed). Rutherford's Vascular Surgery. 8th ed. Elsevier, London, UK 2014: 1382–1401.
7. Breier G, Albrecht U, Sterrer S, et al. Expression of vascular endothelial growth factor during embryonic angiogenesis and endothelial cell differentiation. Development. 1992; 114(2): 521–532, doi: 10.1242/dev.114.2.521, indexed in Pubmed: 1592003.
8. Broide DH, Sriramarao P. Cellular Adhesion in Inflammation. In: Franklin Adkinson JrN (ed). Middleton's Allergy: Principles and Practice 8th ed. Elsevier, Philadelphia, USA 2013: 81–94.
9. Buratto E, Shi WY, Konstantinov IE. An intima affair adds to the dominion of the internal thoracic artery in coronary artery bypass grafting. J Thorac Cardiovasc Surg. 2016; 151(6): 1709–1710, doi: 10.1016/j.jtcvs.2016.02.052, indexed in Pubmed: 27016792.
10. Cho A, Courtman DW, Langille BL. Apoptosis (programmed cell death) in arteries of the neonatal lamb. Circ Res. 1995; 76(2): 168–175, doi: 10.1161/01.res.76.2.168, indexed in Pubmed: 7834826.
11. Cox J, Chiasson D, Gotlieb A. Stranger in a strange land: The pathogenesis of saphenous vein graft stenosis with

emphasis on structural and functional differences between veins and arteries. Prog Cardiovasc Dis. 1991; 34(1): 45–68, doi: 10.1016/0033-0620(91)90019-i.

12. Danik JS, Paynter NP, Ridker PM. Genomic Biomarkers in Human Population Studies. In: Ginsburg GS, Huntington WF (ed). Genomic and Personalized Medicine 2nd ed. Academic Press, UK, London 2012: 247–262.

13. Dvorak HF, Brown LF, Detmar M, et al. Vascular permeability factor/vascular endothelial growth factor, microvascular hyperpermeability, and angiogenesis. Am J Pathol. 1995; 146(5): 1029–1039, indexed in Pubmed: 7538264.

14. Freischlag JA, Heller JA. Venous disease. In: Townsend CM, Beauchamp RD, Evers BM, Mattox KL (ed). Sabiston Textbook of Surgery. 20th ed., Elsevier, Philadelphia, USA 2016: 1827–1847.

15. Galis ZS, Johnson C, Godin D, et al. Targeted disruption of the matrix metalloproteinase-9 gene impairs smooth muscle cell migration and geometrical arterial remodeling. Circ Res. 2002; 91(9): 852–859, doi: 10.1161/01.res.0000041036.86977.14, indexed in Pubmed: 12411401.

16. Galis Z, Khatri J. Matrix metalloproteinases in vascular remodeling and atherogenesis. Circulation Res. 2002; 90(3): 251–262, doi: 10.1161/res.90.3.251.

17. Gallagher PJ, van der Wal AC. Cardiovascular system. In: Cross S (ed). Underwood's Pathology: A Clinical Approach. 6th ed. Elsevier, London, UK 2013: 242–283.

18. Gulbenkian S, Wharton J, Polak JM. The visualisation of cardiovascular innervation in the guinea pig using antiserum to protein gene product 9.5 (pgp 9.5). J Autonomic Nervous System. 1987; 18(3): 235–247, doi: 10.1016/0165-1838(87)90122-6.

19. Halabi AR, Alexander JH, Shaw LK, et al. Relation of early saphenous vein graft failure to outcomes following coronary artery bypass surgery. Am J Cardiol. 2005; 96(9): 1254–1259, doi: 10.1016/j.amjcard.2005.06.067, indexed in Pubmed: 16253593.

20. Havelka GE, Kibbe MR. The vascular adventitia: its role in the arterial injury response. Vasc Endovascular Surg. 2011; 45(5): 381–390, doi: 10.1177/1538574411407698, indexed in Pubmed: 21571779.

21. Hinokiyama K, Valen G, Tokuno S, et al. Vein graft harvesting induces inflammation and impairs vessel reactivity. Ann Thorac Surg. 2006; 82(4): 1458–1464, doi: 10.1016/j.athoracsur.2006.05.038, indexed in Pubmed: 16996954.

22. Hocking KM, Brophy C, Rizvi SZ, et al. Detrimental effects of mechanical stretch on smooth muscle function in saphenous veins. J Vasc Surg. 2011; 53(2): 454–460, doi: 10.1016/j.jvs.2010.09.010, indexed in Pubmed: 21146345.

23. Kanzaki T, Tamura K, Takahashi K, et al. In vivo effect of TGF-beta 1. Enhanced intimal thickening by administration of TGF-beta 1 in rabbit arteries injured with a balloon catheter. Arterioscler Thromb Vasc Biol. 1995; 15(11): 1951–1957, doi: 10.1161/01.atv.15.11.1951, indexed in Pubmed: 7583576.

24. Kon Y, Endoh D, Iwanaga T. Expression of protein gene product 9.5, a neuronal ubiquitin C-terminal hydrolase, and its developing change in Sertoli cells of mouse testis. Mol Reprod Develop. 1999; 54(4): 333–341, doi: 10.1002/(sici)1098-2795(199912)54:4<333::aid-mrd3>3.0.co;2-8.

25. Kovacević M, Simić O, Jonjić N, et al. Apoptosis and cardiopulmonary bypass. J Card Surg. 2007; 22(2): 129–134, doi: 10.1111/j.1540-8191.2006.00355.x, indexed in Pubmed: 17338746.

26. Kyrylkova K, Kyryachenko S, Leid M, et al. Detection of apoptosis by TUNEL assay. Methods Mol Biol. 2012; 887: 41–47, doi: 10.1007/978-1-61779-860-3_5, indexed in Pubmed: 22566045.

27. Ley K, Huo Y. VCAM-1 is critical in atherosclerosis. J Clin Invest. 2001; 107(10): 1209–1210, doi: 10.1172/JCI13005, indexed in Pubmed: 11375406.

28. Lönn J, Starkhammar Johansson C, Kälvegren H, et al. Hepatocyte growth factor in patients with coronary artery disease and its relation to periodontal condition. Results Immunol. 2011; 2: 7–12, doi: 10.1016/j.rinim.2011.12.002, indexed in Pubmed: 24371561.

29. Low EL, Baker AH, Bradshaw AC. Dissecting transforming growth factor-beta signalling pathways in primary human vascular smooth muscle cells. Atherosclerosis. 2015; 241(1): e77, doi: 10.1016/j.atherosclerosis.2015.04.269.

30. Lu F, Zhao X, Wu J, et al. MSCs transfected with hepatocyte growth factor or vascular endothelial growth factor improve cardiac function in the infarcted porcine heart by increasing angiogenesis and reducing fibrosis. Int J Cardiol. 2013; 167(6): 2524–2532, doi: 10.1016/j.ijcard.2012.06.052, indexed in Pubmed: 22981278.

31. Maiellaro K, Taylor WR. The role of the adventitia in vascular inflammation. Cardiovasc Res. 2007; 75(4): 640–648, doi: 10.1016/j.cardiores.2007.06.023, indexed in Pubmed: 17662969.

32. Mallat Z, Tedgui A. Apoptosis in the vasculature: mechanisms and functional importance. Br J Pharmacol. 2000; 130(5): 947–962, doi: 10.1038/sj.bjp.0703407, indexed in Pubmed: 10882378.

33. Martinez-Lemus L, Galiñanes E. Matrix metalloproteinases and small artery remodeling. Drug Discovery Today: Disease Models. 2011; 8(1): 21–28, doi: 10.1016/j.ddmod.2011.06.002.

34. Meng X, Fu Q, Sun W, et al. Competitive flow arising from varying degrees of coronary artery stenosis affects the blood flow and the production of nitric oxide and endothelin in the internal mammary artery graft. Eur J Cardiothorac Surg. 2013; 43(5): 1022–1027, doi: 10.1093/ejcts/ezs507, indexed in Pubmed: 23002187.

35. Nagase H, Visse R, Murphy G. Structure and function of matrix metalloproteinases and TIMPs. Cardiovasc Res. 2006; 69(3): 562–573, doi: 10.1016/j.cardiores.2005.12.002, indexed in Pubmed: 16405877.

36. Nordgaard H, Nordhaug D, Kirkeby-Garstad I, et al. Different graft flow patterns due to competitive flow or stenosis in the coronary anastomosis assessed by transit-time flowmetry in a porcine model. Eur J Cardiothorac Surg. 2009; 36(1): 137–142, doi: 10.1016/j.ejcts.2009.02.036, indexed in Pubmed: 19376731.

37. Ovalle WK, Nahirney PC. Cardiovascular system. In:, Nahirney PC (ed). Netter's Essential Histology. 2nd ed. Elsevier, London, UK 2013: 187–209.

38. Pilmane M, Luts A, Sundler F. Changes in neuroendocrine elements in bronchial mucosa in chronic lung disease in adults. Thorax. 1995; 50(5): 551–554, doi: 10.1136/thx.50.5.551, indexed in Pubmed: 7541167.

39. Schiffrin EL. Role of endothelin-1 in hypertension. Hypertension. 1999; 34: 876–881, doi: 10.1161/HYPERTENSIONAHA.108.117366.

40. Schwartz SM, deBlois D, O'Brien ER. The intima. Soil for atherosclerosis and restenosis. Circ Res. 1995; 77(3): 445–465, doi: 10.1161/01.res.77.3.445, indexed in Pubmed: 7641318.

41. Shyu KG, Chang ML, Wang BW, et al. Cyclical mechanical stretching increases the expression of vascular endothelial growth factor in rat vascular smooth muscle cells. J Formos Med Assoc. 2001; 100(11): 741–747, indexed in Pubmed: 11802532.

42. Sims F. The initiation of intimal thickening in human arteries. Pathology. 2000; 32(3): 171–175, doi: 10.1080/pat.32.3.171.175.

43. Smith M, Long D, Damiano E, et al. Near-Wall μ-PIV reveals a hydrodynamically relevant endothelial surface layer in venules in vivo. Biophysical J. 2003; 85(1): 637–645, doi: 10.1016/s0006-3495(03)74507-x.

44. Stefanini M, De Martino C, Zamboni L. Fixation of ejaculated spermatozoa for electron microscopy. Nature. 1967; 216(5111): 173–174, doi: 10.1038/216173a0, indexed in Pubmed: 4862079.

45. Sumpio B, Chin J. Vessel Wall Biology. In: Sidawy AN, Perler BA (ed). Rutherford's Vascular Surgery and Endovascular Therapy. 9th ed. Elsevier, Philadelphia, USA 2018: 30–43.

46. Trindade M, Oigman W, Fritsch Neves M. Potential role of endothelin in early vascular aging. Curr Hypertens Rev. 2017; 13(1): 33–40, doi: 10.2174/1573402113666170414165735, indexed in Pubmed: 28413991.

47. Tykocki NR, Gariepy CE, Watts SW. Endothelin ET(B) receptors in arteries and veins: multiple actions in the vein. J Pharmacol Exp Ther. 2009; 329(3): 875–881, doi: 10.1124/jpet.108.145953, indexed in Pubmed: 19297422.

48. Velazquez O, Wang B. Cells of the Vascular System. In: Cronenwett JL, Johnston KW (ed). Rutherford's Vascular Surgery 8th ed. Elsevier, London, UK 2014: 49–65.

49. Wei W, Chen ZW, Yang Q, et al. Vasorelaxation induced by vascular endothelial growth factor in the human internal mammary artery and radial artery. Vascul Pharmacol. 2007; 46(4): 253–259, doi: 10.1016/j.vph.2006.10.009, indexed in Pubmed: 17174609.

50. Wolinsky H, Glagov S. A lamellar unit of aortic medial structure and function in mammals. Circ Res. 1967; 20(1): 99–111, doi: 10.1161/01.res.20.1.99, indexed in Pubmed: 4959753.

51. Yu P, Nguyen BT, Tao M, et al. Lack of interleukin-1 signaling results in perturbed early vein graft wall adaptations. Surgery. 2013; 153(1): 63–69, doi: 10.1016/j.surg.2012.06.005, indexed in Pubmed: 22853857.

52. Yuan SM, Wang YQ, Shen Yi, et al. Transforming growth factor-beta in graft vessels: histology and immunohistochemistry. Clinics (Sao Paulo). 2011; 66(5): 895–901, doi: 10.1590/s1807-59322011000500029, indexed in Pubmed: 21789397.

53. Yung LM, Nikolic I, Paskin-Flerlage SD, et al. A selective transforming growth factor-beta ligand trap attenuates pulmonary hypertension. Am J Respir Crit Care Med. 2016; 194(9): 1140–1151, doi: 10.1164/rccm.201510-1955OC, indexed in Pubmed: 27115515.

VM
VIA MEDICA

ORIGINAL ARTICLE

Green tea extract modulates lithium-induced thyroid follicular cell damage in rats

S.M. Zaki[1, 2], G.H.A. Hussein[3], G.M. Helal[4], S.F. Arsanyos[2], W.A. Abd Algaleel[2]

[1]Department of Anatomy, Fakeeh College for Medical Sciences, Jeddah, Saudi Arabia
[2]Department of Anatomy and Embryology, Faculty of Medicine, Cairo University, Egypt
[3]Department of Anatomy and Embryology, Faculty of Medicine, Beni Suef University, Egypt
[4]Department of Medical Biochemistry, Faculty of Medicine, Mansoura University, Egypt

Background: The aim of the current work was to clarify the modulation role of green tea extract (GTE) over structural and functional affection of the thyroid gland after long term use of lithium carbonate (LC). The suggested underlying mechanisms participating in thyroid affection were researched.

Materials and methods: Twenty-four Sprague-Dawley adult albino rats were included in the work. They were divided into three groups (control, LC, and concomitant LC + GTE). The work was sustained for 8 weeks. Biochemical assays were performed (thyroid hormone profile, interleukin 6 [Il-6]). Histological, histochemical (Periodic Acid Schiff [PAS]) and immunohistochemical (caspase-3, tumour necrosis factor alpha [TNF-α], proliferating cell nuclear antigen [PCNA]) evaluations were done. Oxidative/antioxidative markers (malondialdehyde [MDA]/gluthathione [GSH], super-oxide dismutase [SOD]) and Western blot evaluation of the Bcl2 family were done.

Results: Lithium carbonate induced hypothyroidism (decreased T3, T4/increased thyroid-stimulating hormone [TSH]). The follicles were distended, others were involuted. Some follicles were disorganised, others showed detached follicular cells. Apoptotic follicular cells were shown (BAX and caspase-3 increased, Bcl2 decreased, BAX/Bcl2 ratio increased). The collagen fibres' content and proinflammatory markers (TNF-α and IL-6) increased. The proliferative nuclear activity was supported by increased expression of PCNA. Oxidative stress was established (increased MDA/decreased GSH, SOD). With the use of GTE, the thyroid hormone levels increased, while the TSH level decreased. Apoptosis was improved as BAX decreased, Bcl2 increased, and BAX/Bcl2 ratio was normal. The collagen fibres' content and proinflammatory markers (TNF-α and IL-6) decreased. The expression of PCNA and caspase-3 were comparable to the control group. The oxidative markers were improved (decreased MDA/increased GSH, SOD).

Conclusions: In conclusion, prolonged use of LC results in hypothyroidism, which is accompanied by structural thyroid damage. LC induced thyroid damage through oxidative stress that prompted sterile inflammation and apoptosis. With the use of GTE, the thyroid gland regained its structure and function. The protecting role of GTE is through antioxidant, antifibrotic, anti-inflammatory, and antiproliferative effects. (Folia Morphol 2022; 81, 3: 594–605)

Key word: lithium carbonate, green tea extract, thyroid damage, oxidative stress, inflammation, apoptosis

Address for correspondence: Dr. S.M. Zaki, Department of Anatomy, Fakeeh College for Medical Sciences, Jeddah, Saudi Arabia,
e-mail: zakysherif1@gmail.com

INTRODUCTION

Lithium and its salts such as lithium carbonate (LC) are commonly used for the treatment of numerous psychiatric illnesses [11]. It is used in the therapy of mood instability (bipolar disorder) and has a prospective role in the therapy of mania and depression [23]. It precludes mood swings in patients with manic-depressive disorder [7]. Although it is a unique drug, prolonged treatment with therapeutic levels may cause multisystem toxicity [25]. It can disturb the function of the heart, liver, kidney, testes, and gastrointestinal system. Additionally, it can induce diabetes insipidus, acneform eruptions, renal toxicity, and brain damage [15, 28, 43, 45].

The concentration level of lithium in the thyroid gland is 3–4 times that in plasma [5]. Lithium influences the function of the thyroid gland, either directly or indirectly via the hypothalamic-pituitary-thyroid axis [27]. It interferes with thyroid functions at the stage of hormonal secretion [13]. It competes for iodide transport, increases thyroidal radioiodine retention, and decreases deiodination from T4 to T3 [27]. It may cause hypothyroidism, goitre, or infrequently thyrotoxicosis [13]. Some researchers reported lithium-induced hypothyroidism was associated with oxidative stress [49]. Furthermore, others described the alteration of the thyroid gland at the cellular and subcellular levels [51].

Green tea (GT) is one of the common beverages in the globe. Its chief components are the polyphenol (catechins) [44]. GT catechins are epigallocatechin, epigallocatechin-3-gallate (EGCG), epicatechin, and epicatechin-3-gallate [12]. Moreover, GT contains caffeine, quercetin, chlorogenic acid, garlic acid, myricetin, and kaempferol [44]. GT polyphenols have protective roles against neurodegenerative diseases, cancer, heart disease, lung damages, and diabetes [21, 44].

The mechanism through which LC induces thyroid damage at the cellular level is not clearly understood and not enough studied. Furthermore, no works have investigated the protective role of green tea extract (GTE) over such damage. So, the present work intended to clarify the modulation role of GTE over structural and functional affection of thyroid gland after long term use of LC. The suggested underlying mechanisms participating in thyroid affection were investigated.

MATERIALS AND METHODS

Animals

Twenty-four Sprague-Dawley adult albino rats were included in the work. They were housed in a dark/light cycle (12/12 h), humidity (50–60%) and temperature (25 ± 1°C). The study was completed in the Experimental Animal Centre, Faculty of Medicine, Cairo University, Egypt.

Experimental design

The rats were distributed into three groups (8 in each group): control, LC, and GTE (concomitant LC + GTE).

Ethical approval

All relevant international, national, and/or institutional guidelines for the care and use of animals were followed. The study was permitted by the Ethics Committee, Faculty of Medicine, Cairo University, Egypt.

Test materials

Lithium carbonate was obtained in the form of tablets (400 mg) (Nile Co. for Pharmaceuticals and Chemical Industries, Egypt). Tablets were liquefied in distilled water and given through an intragastric tube in a dose of 30 mg/kg/day for 8 weeks [10].

Green tea extract was obtained in the form of tablets (200 mg) (Techno-med Group Co., Egypt). Tablets were melted in distilled water and given orally in a dose of 150 mg/kg/day for 8 weeks [19].

General health profile

Food and water intake, motility, and health condition were recorded daily. Bodyweight (BW) was documented at the start and end of the study.

Biochemical assay

The serum levels of total T3 (TT3), free T3 (FT3), total T4 (TT4), free T4 (FT4) and thyroid-stimulating hormone (TSH) were determined by radioimmunoassay (xh6080, Xi'an). The inflammatory marker interleukin 6 (IL-6) was assessed by the commercially ELISA kits according to manufacturer's instructions.

Tissue sampling

Thyroid was dissected and fixed in 10% formalin saline. The tissue was sectioned every 10th section (5 μm thick). The thyroid tissue extract was prepared according to Gordon et al. [14].

Light microscopic study

Haematoxylin and eosin (H&E) and Masson's trichrome stained sections were prepared according to Suvarna et al. [45].

Histochemical evaluation (PAS stain)

Histochemical evaluation (Periodic Acid-Schiff [PAS]-stained) sections were prepared according to Suvarna et al. [45].

Immunohistochemistry [41]

Paraffin sections were prepared. Then, suitable quantity of serum was added to the sections for 30 min.

Caspase-3. The sections were incubated with anti-active caspase-3 antibody (cataloque number: ab13847, Abcam, Cambridge, UK), then followed with biotinylated secondary antibody (LSAB kit, Dako Carpentaria, CA, USA). After that, they were incubated with streptavidin HRP (LSAB kit, Dako, Carpentaria, CA, USA), and then with 3'-diaminobenzidine (0.05% DAB).

Tumour necrosis factor alpha (TNF-α). The sections were incubated with the primary monoclonal anti-TNF-α antibody (52B83) using dilutions 1:5000 for 36 h at 4°C. Then, they were incubated with biotinylated secondary antibodies for 5 h and then with Avidin-Biotin-Peroxidase Complex (ABC). Finally, the immune reaction was visualised with 0.05% DAB.

PCNA immunostaining. Proliferating cell nuclear antigen (PCNA) is a helper protein of DNA polymerase enzymes and is used as a typical marker for proliferating cells [38]. The immunostaining essential pretreatment was done by boiling for 10 min in 10 mmol/L citrate buffer (catalogue number AP 9003) (pH 6) for antigen retrieval. Then, the sections were incubated with the primary antibody (a rabbit polyclonal antibody) (catalogue number ab15497, Abcam, Cambridge, UK). Immunostaining was finalised by using the Ultra-vision detection system (catalogue number TP-015-HD). The small intestine was used as a positive-control section. The positive reaction appeared as brown nuclear colouration [38].

Oxidative/antioxidative markers

Thyroid lipid peroxidation. Malondialdehyde (MDA) was measured using the method of Buege [8]. Briefly, 100 μL serum was diluted with distilled water to 500 μL. One mL of TBA–HCl reagent was added to the diluted sample. The reaction mixture was centrifuged, and the supernatant was taken. The optical density was measured spectrophotometrically at 532 nm. The concentration of MDA in the sample was got by plotting the obtained absorbance against the standard graph.

Thyroid superoxide dismutase (SOD). SOD was measured according to the modified Misra and Fridovich's method [35]. Ten μL of bovine catalase and 1965 μL of Na2CO3 buffer were added to 5 μL of 10% thyroid homogenate. Then, the mixture was added to 20 μL of 30 mM epinephrine in 0.05% ethanoic acid. The activity of SOD was determined at 37°C at 480 nm in a spectrophotometer (Model BL 158, ELICO) at 0 minutes and after 3 minutes. The activity of SOD was expressed as the quantity of the enzyme that impedes the oxidation of epinephrine by 50% = 1 U/μg/mg tissue protein.

Thyroid glutathione (GSH). The measurement of GSH was constructed on the reduction of DTNB with GSH to produce a yellow compound. The reduced chromogen was measured at 405 nm. The concentration of the GSH was calculated using the standard curve and expressed/mg of tissue protein [48].

Morphometric analysis

The content of collagen fibres and the optical density of PAS in colloids and follicular basement membranes were assessed. Adding, the immune expression of TNF-α, caspase-3 positive follicular cell nuclei (%), and the PCNA positive follicular cell nuclei (%) were evaluated using the Leica LAS V3.8 image analyser computer system (Switzerland).

Western blot

The homogenised thyroid tissue was added to the ReadyPrep™ protein extraction kit (Bio-Rad Inc., catalogue number 163-2086). Twenty μg protein concentration was loaded with an equal volume of 2× Laemmle sample buffer. Primary antibodies of Bcl2 and Bcl-2-associated X protein (BAX) (Santa Cruz Biotechnology, Inc., catalogue numbers: sc-7382 and sc-7480) were diluted in TBST and incubated overnight against the blotted target protein followed by incubation with the HRP-conjugated secondary antibody (Goat anti-rabbit IgG-HRP-1 mg Goat Novus Biologicals) solution for 1 h at RT. The chemiluminescent substrate (Clarity™ Western ECL substrate Bio-Rad, catalogue number 170-5060) was applied to the blot.

Statistical analysis

Statistical evaluation was performed using SPSS version 21 (IBM Corporation, Somers, NY, USA) statistical software. Data were stated as means ± standard

Table 1. Body weight (BW) in the different groups at the end of study

Group	BW [g] Mean ± SD	Versus group	P value
Control	200 ± 22.5		
LC-treated	245.5 ± 30.8	Control	0.01*
		GET-treated	0.03*
GTE-treated	215.6 ± 18.4	Control	0.1
		LC-treated	0.03*

*P-value significant; the BW at the beginning of the study was 160.5 ± 17.1 g; BW — bodyweight; GTE — green tea extract; LC — lithium carbonate; SD — standard deviation

deviation. Statistical analysis was done by mean of ANOVA tracked by Bonferroni pairwise comparisons.

RESULTS

The general health data

The water and food consumption and health condition were relatively exceptional in all groups. At the beginning of the study, the BW was 160.5 ± ± 17.1 g. By the end of the experiment, the BW of the LC group increased by 21% compared to the control group. Simultaneous administration of GTE along with LC ameliorates the weight gain (12% decrease) as compared to the LC group. BW of the control and GTE groups were similar (Table 1).

Hormonal results

The LC group exhibited a significant decrease in TT3, TT4 (29, 32%) and FT3, FT4 (53, 50%) compared to the control group. Adding, the TSH level in this group increased by 161% compared to the control group (Table 2).

With the use of GTE, the serum level of TT3, TT4, FT3, FT4 increased by 16%, 23%, 28%, 22% compared to the control group. Moreover, the TSH level in this

group decreased (45%) compared to the LC group; however, its' level was still higher (41%) than that of the control group (Table 2).

Histopathology of the thyroid gland

The follicles of the control group were lined by cubical cells and contained acidophilic homogenous colloid (Fig. 1A).

The follicles in the LC group showed variable activities; some follicles were distended, while others were involuted. The distended follicles were lined by flat cells. Moreover, some follicles were disorganised with wide interfollicular spaces. Furthermore, some follicles had detached follicular cells inside the colloid. The follicular cells were mostly vacuolated. Finally, congested-capillary vessels were detected (Fig. 1B–E). With the use of GTE, the thyroid architecture looked almost normal (Fig. 1F).

Content of collagen fibres

The fibres' content increased 2-fold in the LC group compared to the control group. Much advance was perceived in the GTE group as its fibres' content was 1-fold compared to the control group. The fibres' content in the GTE group was 37% lower compared to the LC group (Fig. 2, Table 3).

Histochemistry of the thyroid gland

In the control group, the follicular cells displayed strong PAS reactions in colloids and basal laminae (Fig. 3A, Table 3). The basal laminae of the follicular cells in the LC group revealed weak PAS reactions. The colloids revealed moderate PAS reactions, while the reactions were absent in the vacuoles of colloids. The disrupted basement membranes displayed discontinuous PAS reaction. The reaction was 64% lower than in the LC group (Fig. 3B, C, Table 3). After the

Table 2. Thyroid function tests at the end of the study

Group		TSH	TT3 [ng/mL]	FT3 [pmol/L]	TT4 [µg/dL]	FT4 [pmol/L]
Control	Mean ± SD	3.6 ± 0.3	6.2 ± 0.5	16.7 ± 0.8	21.2 ± 1.0	32.9 ± 3.2
LC-treated	Mean ± SD	9.4 ± 1.3	4.4 ± 0.2	7.7 ± 1.2	14.4 ± 1.7	16.3 ± 3.0
	Versus control	< 0.001*	< 0.001*	< 0.001*	< 0.001*	< 0.001*
	Versus GTE-treated	< 0.001*	0.01*	< 0.001*	0.055	0.002*
GTE-treated	Mean ± SD	5.1 ± 0.3	5.2 ± 0.4	12.0 ± 0.8	17.2 ± 2.1	25.4 ± 3.0
	Versus control	< 0.001*	0.002*	< 0.001*	0.007*	0.007*
	Versus LC-treated	< 0.001*	0.01*	< 0.001*	0.055	0.002*

*p-value significant; GTE — green tea extract; LC — lithium carbonate; SD — standard deviation; FT3 — free T3; FT4 — free T4; TT3 — total T3; TT4 — total T4; TSH — thyroid-stimulating hormone
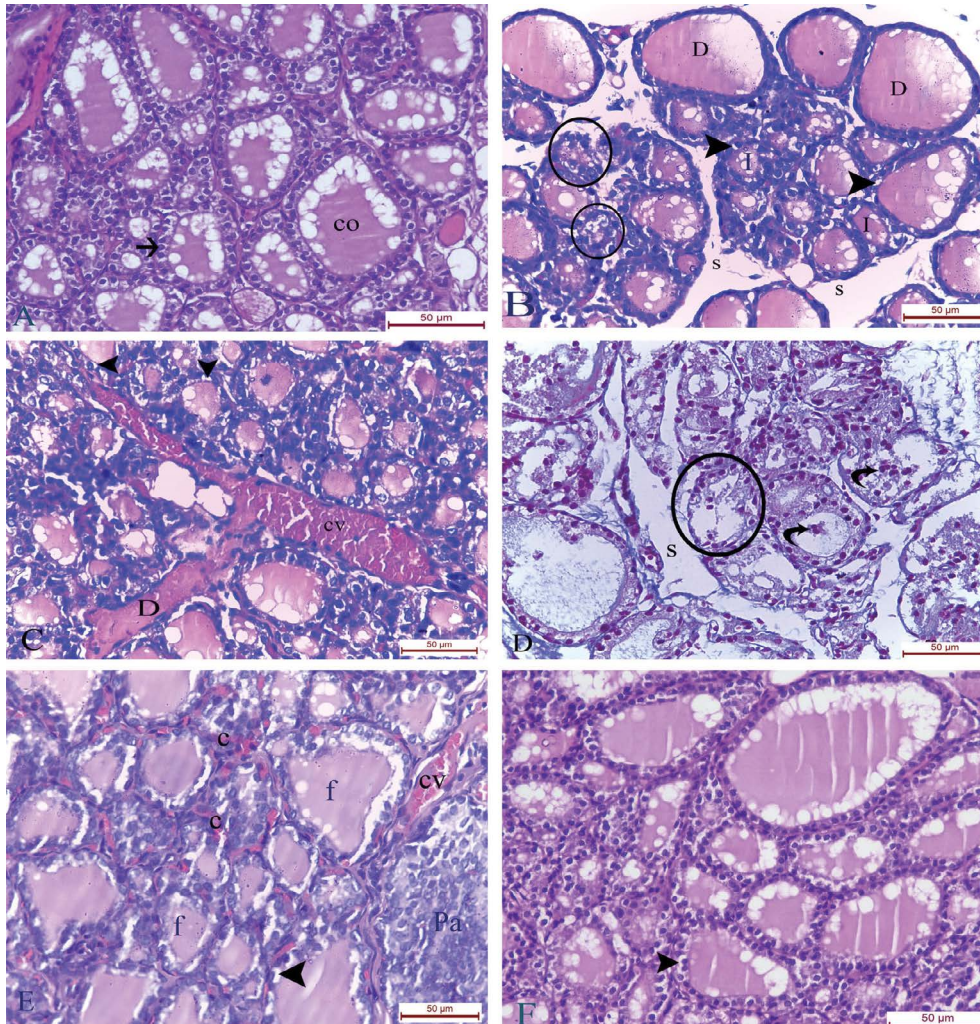
Figure 1. A. Normal follicles of the control rats. Note simple cuboidal follicular cells (arrows) surrounding homogenous acidophilic colloid (co); **B–E.** Thyroid follicles of lithium carbonate group; **B.** Some follicles are distended (D), others are involuted (I). Note damaged and disorganised follicles (encircled) with a large interfollicular space (S). Note follicular cells with vacuolated cytoplasm (arrowheads); **C.** Markedly distended thyroid follicle (D). Note congested-capillary vessel (CV) and follicular cells with vacuolated cytoplasm (arrowheads); **D.** Loss of normal thyroid architecture. Most of the follicles have shredded epithelial lining (curved arrows) and have no colloid. Note disorganized follicles (encircled) with a large interfollicular space (S); **E.** Thyroid follicles (F) with vacuolated cells (arrowheads). Note congested-capillary vessel (CV), interfollicular spaces with extravasated blood (c). Notice part of the parathyroid gland (Pa); **F.** Nearly normal thyroid architecture of the green tea extract rats. Note follicular cells with vacuolated cytoplasm (arrowheads). Haematoxylin and eosin ×400.

concomitant treatment with GTE, the PAS reaction was strong in colloids and basement membranes. The reaction was comparable to the control group and was > 1-fold higher than that of the LC group (Fig. 3D, Table 3).

Immunohistochemistry of the thyroid gland

The control group displayed positive PCNA follicular cell nuclei (Fig. 4A). The LC group displayed an increased number of positive PCNA follicular cell nuclei (6.5-fold higher compared to the control group) (Fig. 4B, C, Table 3). The use of GTE was related to a 2-fold increase in the number of positive PCNA follicular cell nuclei com-

pared to the LC group. The expressions in the control and GTE groups were identical (Fig. 4D, Table 3).

The control group displayed weak caspase-3 expression of the follicular cell nuclei (Fig. 5A). The LC group showed strong expression in the follicular cell nuclei (2-fold higher compared to the control group) (Fig. 5B, C, Table 3). The administration of GTE was related to a 1-fold increase in the expression in the cell nuclei compared to the LC group. The expressions in the control and GTE groups were similar (Fig. 5D, Table 3).

The control group showed weak expression of TNF-α of the follicular cells (Fig. 6A). The expression
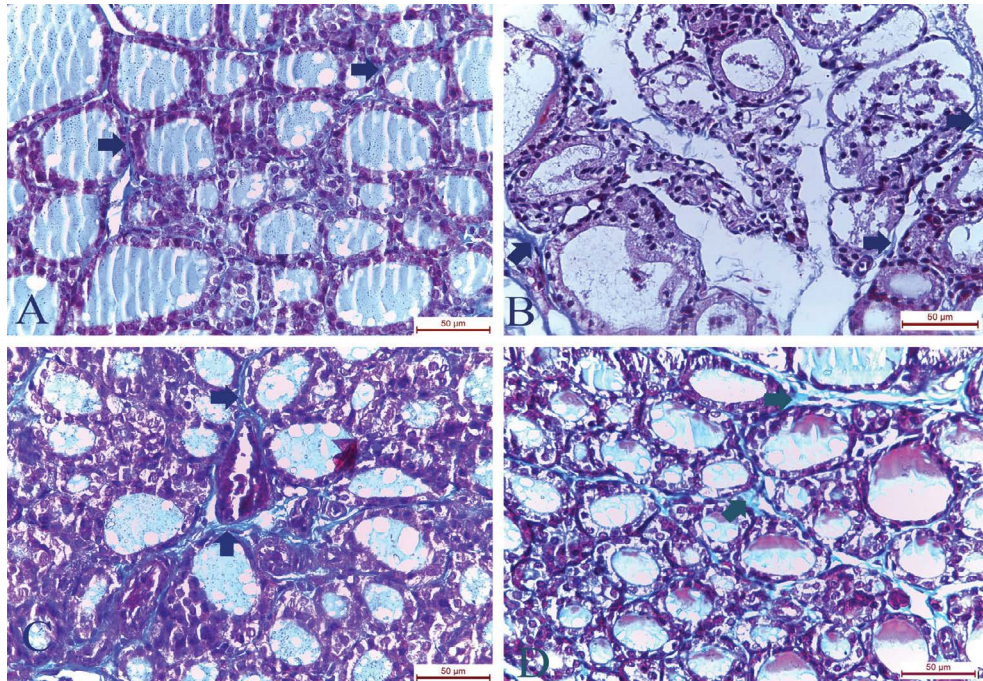
Figure 2. A. The collagen fibres (arrows) between thyroid follicles in the control; **B, C.** Increased collagen fibres (arrows) between thyroid follicles in the lithium carbonate rats; **C.** Negligible collagen fibres (arrows) between thyroid follicles in the green tea extract rats. Masson's trichrome ×400.

Table 3. Collagen fibres, Periodic Acid Schiff (PAS) reaction, apoptotic and proliferative markers

Group		Content of collagen fibres	Optical density of PAS reaction	Caspase-3 positive cells (% of total cells)	PCNA positive cells (% of total cells)	BAX	Bcl2	BAX/Bcl2 ratio
Control	Mean ± SD	18.2 ± 5.9	0.31 ± 0.06	4.0 ± 1.6	12.8 ± 1.9	0.83 ± 0.05	2.73 ± 0.16	0.27 ± 0.05
LC-treated	Mean ± SD	55.2 ± 8.2	0.11 ± 10.06	30.0 ± 7.9	38.8 ± 6.3	2.44 ± 0.16	1.11 ± 0.05	2.42 ± 0.39
	Versus control	< 0.001*	< 0.001*	< 0.001*	< 0.001*	< 0.001*	< 0.001*	< 0.001*
	Versus GTE-treated	0.003*	0.005*	< 0.001*	< 0.001*	< 0.001*	< 0.001*	< 0.001*
GTE-treated	Mean ± SD	37.4 ± 5.0	0.24 ± 0.04	12.6 ± 2.8	23.2 ± 3.3	1.31 ± 0.07	2.32 ± 0.706	0.54 ± 0.03
	Versus control	0.002*	0.144	0.052	0.007*	< 0.001*	< 0.001*	0.259
	Versus LC-treated	0.003*	0.005*	< 0.001*	< 0.001*	< 0.001*	< 0.001*	< 0.001*

*p-value significant; BAX — Bcl-2-associated X protein; GTE — green tea extract; LC — lithium carbonate; PCNA — proliferating cell nuclear antigen; SD — standard deviation

in the LC group was strong (2-fold higher compared to the control group) (Fig 6B, C, Table 4). The use of GTE was related to a 1-fold increase in the expression in the follicular cell compared to the LC group. The expressions in the control and GTE groups were similar (Fig. 6D, Table 4).

Western blot evaluation of BAX and Bcl2 (Fig. 7, Table 3)

The expression of BAX in the LC group increased by 190% (about 2-fold) compared to the control group. The expression in the GTE group was 46% lower compared to the LC group, but still higher (57%) compared to the control group.

The expression of Bcl2 in the LC group decreased by 59% compared to the control group. The expression in the GTE group was 1-fold higher compared to the LC group, but 15% lower compared to control group.

The BAX/Bcl2 ratio was 8-fold higher compared to the control group. The ratios of the control and GTE groups were comparable.
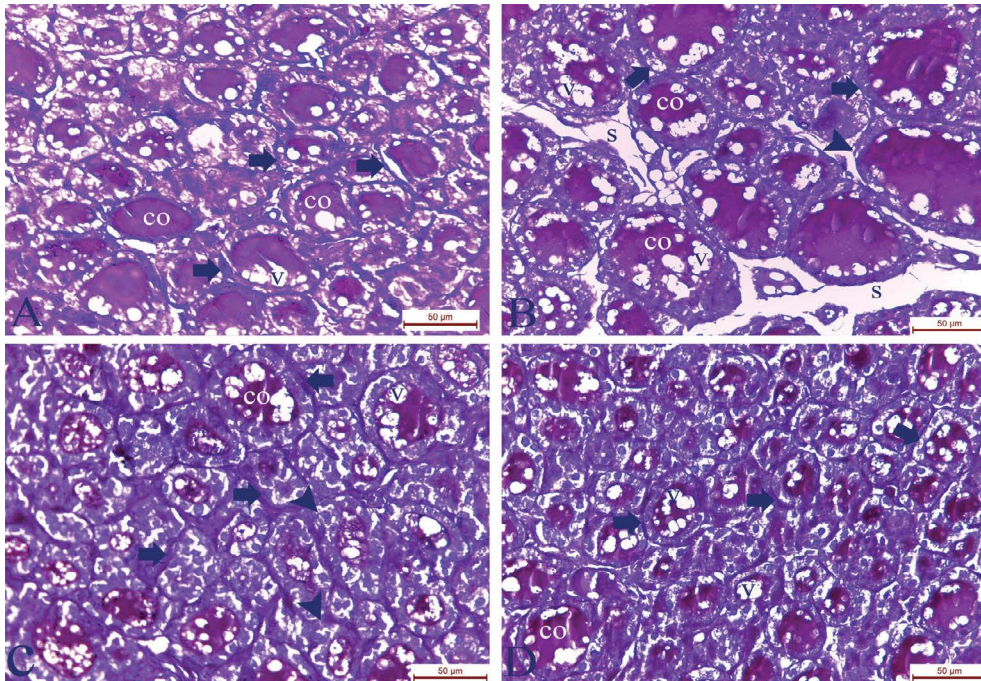
Figure 3. A. Strong Periodic Acid Schiff (PAS)-positive reaction in the colloid (co) and basement membranes (arrows) of the follicles with a negative reaction in the peripheral vacuoles of colloids (v) in the control group; **B, C.** Weak PAS reaction in the basement membranes (arrows) of the follicles in the lithium carbonate group. The PAS reaction was moderate in colloids (co), while it was absent in peripheral vacuoles of colloids (v). Note discontinuous PAS-positive reaction in the disrupted basement membranes (arrowheads); **D.** Strong PAS-positive reaction in colloids (co) and basement membranes (arrows) of the follicles with a negative reaction in the minute peripheral vacuoles of colloids (v) in the green tea extract group. PAS ×400.
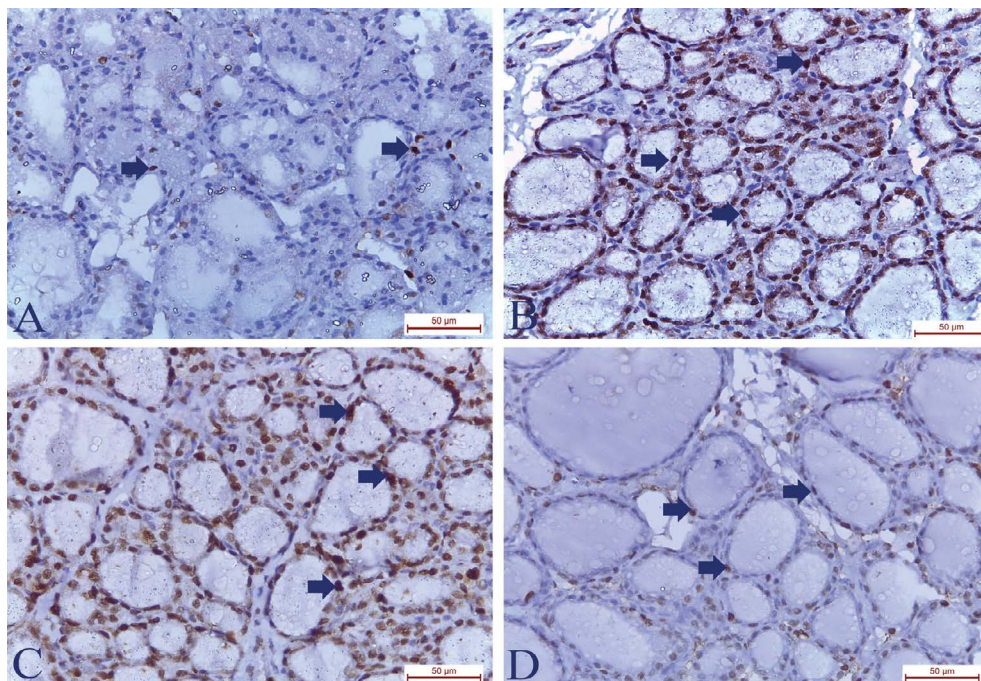
Figure 4. A. The number of proliferating cell nuclear antigen (PCNA) positive cells (arrows) in the control rats; **B, C.** Apparent increase in the number of PCNA positive cells (arrows) in the lithium carbonate rats; **D.** Slight increase in the number of PCNA positive cells (arrows) in the green tea extract rats. PCNA ×400.
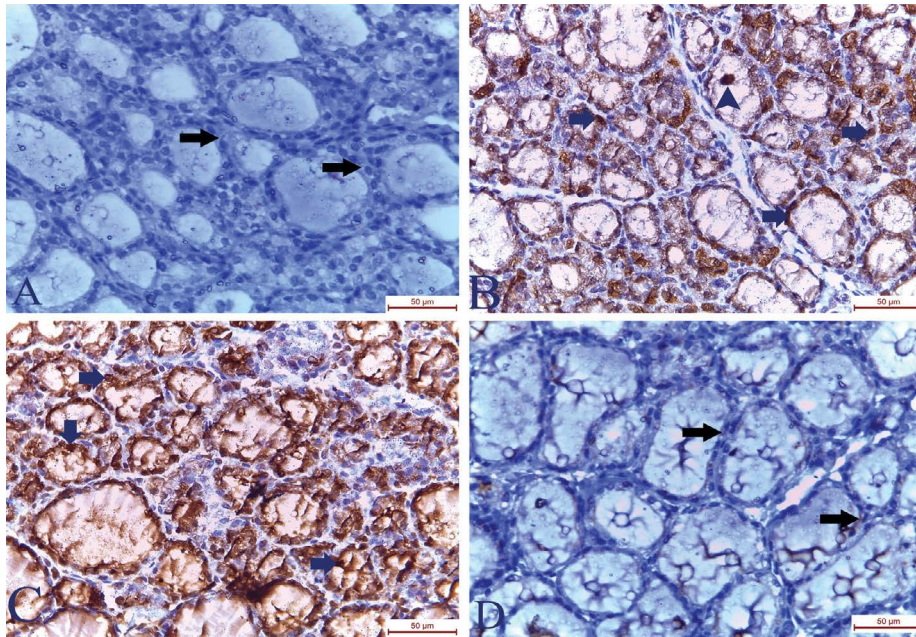
Figure 5. A. Control group exhibited weak caspase-3 expression in the follicular cell nuclei (arrows); **B, C.** The lithium carbonate group showed strong expression in the follicular cell nuclei (arrows); **D.** Slight expression in the follicular cell nuclei (arrows) in the green tea extract group. Caspase-3 $\times 400$.
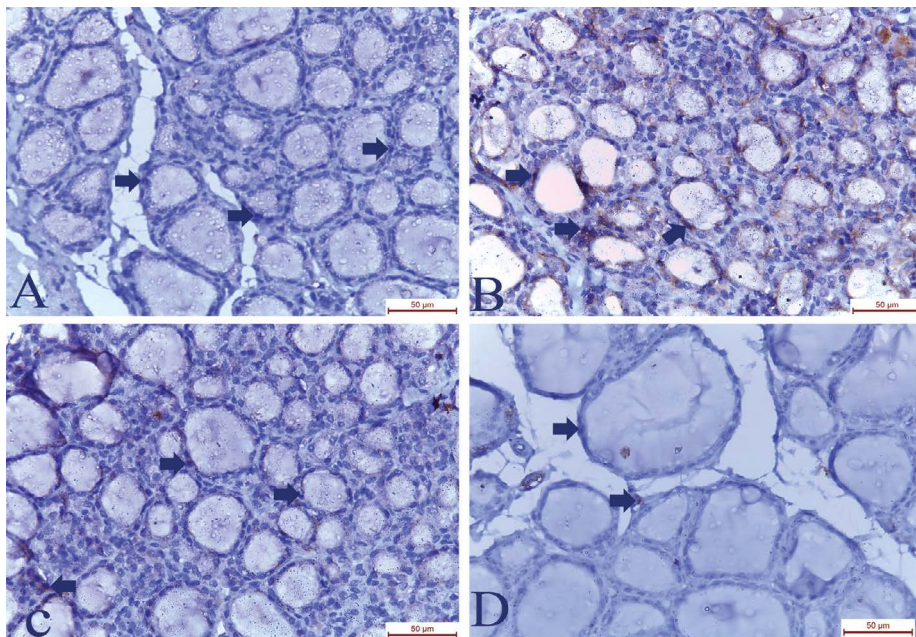
Figure 6. A. Control group displayed weak expression of tumour necrosis factor alpha (TNF-α) in the follicular cell nuclei (arrows); **B, C.** The lithium carbonate group showed increased expression of TNF-α in the follicular cell nuclei (arrows); **D.** Slight increase in the expression of TNF-α in the follicular cell nuclei (arrows) in the green tea extract group. TNF-α $\times 400$.

Proinflammatory and oxidative markers assessment (Table 4)

Interleukin 6 of the LC group was 5-fold higher compared to the control group. With the use of GTE, IL-6 became 2.5-fold higher compared to the control group.

Malondialdehyde of the LC group was 171% higher compared to the control group. With the use of GTE, MDA became 49% lower compared to the LC group; however, it was 47% higher compared to the control group.

Table 4. Inflammatory and oxidative/antioxidative markers

Group		MDA [nmol/mg tissue protein]	GSH [μg/mg tissue protein]	SOD [nmol/mg tissue protein]	IL-6 [pg/mg tissue protein]	TNF-alpha [pg/mg tissue protein]
Control	Mean ± SD	1.53 ± 0.16	1.89 ± 0.05	7.1 ± 0.46	82.0 ± 7.81	64.6 ± 10.04
LC-treated	Mean ± SD	4.16 ± 0.41	0.7 ± 0.14	2.98 ± 0.4	374.0 ± 24.65	388.0 ± 16.84
	Versus control	< 0.001*	< 0.001*	< 0.001*	< 0.001*	< 0.001*
	Versus GTE-treated	< 0.001*	< 0.001*	< 0.001*	< 0.001*	< 0.001*
GTE-treated	Mean ± SD	2.25 ± 0.09	1.55 ± 0.12	5.9 ± 0.3	158.8 ± 14.7	243.00 ± 30.02
	Versus control	0.003*	0.01*	0.01*	< 0.001*	< 0.001*
	Versus LC-treated	< 0.001*	< 0.001*	< 0.001*	< 0.001*	< 0.001*

*p-value significant; GSH — gluthathione; GTE — green tea extract; IL-6 — interleukin 6; LC — lithium carbonate; MDA — malondialdehyde; SD — standard deviation; SOD — superoxide dismutase; TNF-alpha — tumour necrosis factor alpha
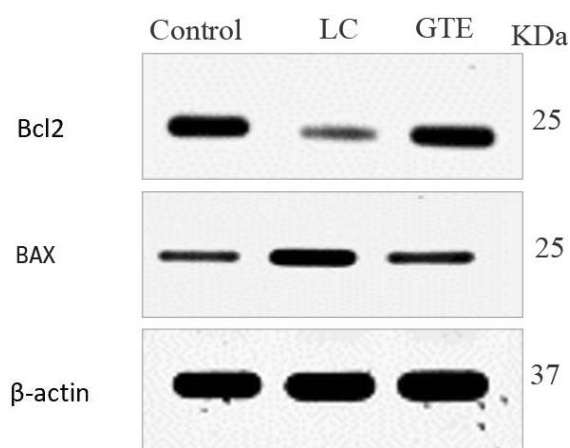
Figure 7. Western blot assay of Bcl-2-associated X protein (BAX) and Bcl2. BAX was higher in the lithium carbonate (LC) group compared to the control. Bcl2 was lower in the green tea extract (GTE) group compared to the control. Beta-actin was used as a control.

Glutathione and SOD of the LC group decreased by 62, 42% compared to the control. With the use of GTE, the antioxidant markers increased by 121 (97%) compared to the LC group; however, both markers were 17, 16% higher than in the control group.

DISCUSSION

Under our experimental condition, hypothyroidism induced by lithium was confirmed by a decrease in the level of thyroid hormones (TT3, TT4, FT3, FT4). LC influences its effects over the thyroid hormones either directly or indirectly via the hypothalamic-pituitary-thyroid axis [27].

Moreover, an increase in serum level of TSH occurs mostly secondary to the decreased thyroid hormone secretion. TSH is a thyrotropin hormone that is secreted from the pituitary gland and stimuluses the formation of T3 and T4 [17]. It is the key indicator of thyroid dysfunction [3]. The resultant hypersecretion of TSH specifies the commencement of hypothyroidism as described formerly in patients treated with LC [24]. The diagnostic characteristic of TSH emerges from the inverse linear relations between the serum TSH and FT4 level as tiny changes in T4 levels induces enormous changes in serum TSH [2, 3].

By the end of the work, the BW of the LC rats increased by 21% compared to the control group. The weight gain is typically related to low basal metabolic rates consequence to the hypothyroidism induced by LC [31].

The prolonged take of LC is associated with thyroid damage. The colloids are extensively vacuolated and depleted. The follicles either distended or involuted. Moreover, some follicles are disorganised with wide interfollicular spaces and detached follicular cells. Additional, the follicular cells show vacuolations.

The observed thyroid damage in the LC group is mostly multifactorial. Oxidative stress is one of the pathogenic mechanisms through which LC can induce thyroid damage at the cellular level. Many researchers proved the oxidative stress role of LC over many organs such as heart, kidney, and testis [34, 39]. Oxidative stress is a shift in the balance between oxidants and antioxidants in favour of oxidants [6]. With the prolonged use of LC, the oxidant marker (MDA) became high (171%), while the antioxidant markers (GSH and SOD) became low (62%, 42%).

The resulting oxidative stress of LC creates oxygen free radical (ROS) that reacts with numerous biomolecules in the cell, leading eventually to oxidative damage [32]. ROS is scavenged by several cellular defence mechanisms involving non-enzymatic (GSH) and enzymatic (SOD) scavenger mechanisms. SOD catalyses the dismutation of O_2^- to H_2O_2 and O_2 [22], while GSH offers protection against free radicals, per-

oxides, and toxic compounds [33]. Prolonged use of LC decreased the activities of the free radical scavenging enzymes SOD and GSH. This results in augmented production of the O_2^- and H_2O_2, which in turn leads to the production of OH^- [18]. The generation of OH^- takes part in the observed thyroid toxic damage [18].

Higher lipid peroxidation (higher MDA), noticed in the LC group, led to distraction of the follicular basement membranes' integrity, and the cytoplasmic enzyme's leakage [9]. Many researchers believed that MDA's level is sufficient proof of oxidative stress [26]. So finally, the increased MDA content indicates severe oxidative stress and increased lipid peroxidation.

Sterile inflammation (inflammation in the absence of infection) is the second pathogenic mechanisms through which LC induced thyroid damage at the cellular level. Inflammation was evident by the increase in the pro-inflammatory cytokines (a 2-fold elevation in TNF-α and 5-fold increase in IL-6). TNF-α is accountable for the pathogenesis of increases in ROS and oxidative stress [26]. It controls the growth, proliferation, differentiation, and viability of activated leukocytes [36]. Furthermore, TNF-α elicits the cellular release of cytokines, chemokines, or inflammatory mediators [36]. So, extreme TNF-α secretion results in thyroid injury indirectly through inducing oxidative stress, and directly through inducing apoptosis. The resultant fibrosis was consequent to oxidative stress and inflammation.

Congestion in the vasculature of the thyroid gland was a constant feature in the LC group. It is caused as a result of the increased demand for blood to feed the follicular cells or as a result of the increased thyroid gland's size [10]. Furthermore, congestion can be part of the previously stated inflammatory process that accompanies LC toxicity. Moreover, prolonged elevation of TSH induces neovascularisation and increases the stromal vascularity as TSH acts as a growth factor for the thyroid tissue [20].

Apoptosis is also a main pathogenic mechanism through which LC induced thyroid damage at the cellular level. Apoptosis is induced by higher levels of MDA and TNF-α [6, 26]. Apoptosis enhances the release of cytokines and ROS, which lastly damages thyroid gland [26].

The framework of the apoptotic signal pathway finally converges into a common mechanism driven by caspases [47]. Caspase-3 is the principal destroyer of apoptosis, thus sponsoring cell survival [30]. Caspase-3 of the LC group was 2-fold higher com-

pared to the control. The caspase mechanism is negatively regulated by Bcl2 family unit [1]. This family is classified into a family containing Bcl2, a second family containing BAX, and a third family including Bik and Bid [50]. The Bcl2 exerts anti-apoptotic effect by impeding a step that leads to the activation of caspases, while BAX exerts proapoptotic activity [50]. With the use of LC, the expression of BAX increased 2-fold, while the expression of Bcl2 decreased by 59%. The BAX/Bcl2 ratio increased 8-fold. This ratio describes the accountability of the cell for apoptosis [50].

With prolonged exposure to LC, some follicular cells may pass into irreparable damage and undergo terminal growth arrest or apoptosis. However, other follicular cells may acquire an intrinsic mechanism of death resistance and finally lead to hyperplasia instead of apoptosis. Such hyperplasia was furtherly confirmed morphometrically by a significant increase in the number of PCNA positive follicular cell nuclei (6.5-fold). PCNA is directly correlated with the proliferative state of various tissues [52, 54].

Green tea extract has a perfect influence on thyroid damage induced by LC. The beneficial impacts of GTE are ascribed to the polyphenolic compounds, particularly the catechins, which constitute 30% of the dry weight of green tea leaves [16].

With the use of GTE, the level of thyroid hormones increased, while the TSH level decreased. However, the hormonal levels were still away from the control group. BW in the GTE group was comparable to the control group. Weight improvement is mostly explained by increased basal metabolic rates as a consequence of regaining normal thyroid function.

Besides, the expression of PCNA in the GTE group was like the control group. This is mostly attributed to the antiproliferative property of GTE [29].

Apoptosis was considerably improved in the GTE group as the expression of caspase-3 and BAX/Bcl2 ratio was comparable to the control. Moreover, the expression of BAX decreased, while that of Bcl2 increased. Such protective role of GTE could be explained by its antioxidant effect (decreased MDA/increased GSH, SOD). The antioxidant effect of GTE was documented in many studies [40, 42]. Catechins and theaflavins of GT are responsible for such antioxidant activity [4].

Besides, we proved the antifibrotic and anti-inflammatory role of GTE as the collagen fibres content and proinflammatory markers (TNF-α and IL-6) decreased compared to the LC group. The anti-inflam-

matory and antifibrotic roles of GTE were proved in many literature reports [37, 53].

There seem to be two major effects of lithium salts in bipolar disorder, i.e. inhibitory action on inositol monophosphatase and inhibition of glycogen synthase kinase-3 activity. No reports in the literature documented any effect of GTE on these enzymes. So, GTE has no harm interfering with lithium action on the brain.

CONCLUSIONS

In conclusion, prolonged use of LC results in hypothyroidism, which is accompanied by structural thyroid damage. LC induced thyroid damage through oxidative stress that prompted sterile inflammation and apoptosis. With the use of GTE, the thyroid gland regained its structure and function. The protective role of GTE is through its antioxidant, anti-inflammatory, antiproliferative and antifibrotic effects.

Conflict of interest: None declared

REFERENCES

1. Adams JM, Cory S. The Bcl-2 protein family: arbiters of cell survival. Science. 1998; 281(5381): 1322–1326, doi: 10.1126/science.281.5381.1322, indexed in Pubmed: 9735050.
2. Baloch Z, Carayon P, Conte-Devolx B, et al. Laboratory medicine practice guidelines. Laboratory support for the diagnosis and monitoring of thyroid disease. Thyroid. 2003; 13(1): 3–126, doi: 10.1089/105072503321086962, indexed in Pubmed: 12625976.
3. Benhadi N, Fliers E, Visser TJ, et al. Pilot study on the assessment of the setpoint of the hypothalamus-pituitary-thyroid axis in healthy volunteers. Eur J Endocrinol. 2010; 162(2): 323–329, doi: 10.1530/EJE-09-0655, indexed in Pubmed: 19926783.
4. Benzie IFF, Wachtel-Galor S. Herbal Medicine. Biomolecular Clinical Aspects. 2011, doi: 10.1201/b10787.
5. Berens SC, Wolff J, Murphy DL. Lithium concentration by the thyroid. Endocrinology. 1970; 87(5): 1085–1087, doi: 10.1210/endo-87-5-1085, indexed in Pubmed: 4098397.
6. Birben E, Sahiner UM, Sackesen C, et al. Oxidative stress and antioxidant defense. World Allergy Organ J. 2012; 5(1): 9–19, doi: 10.1097/WOX.0b013e3182439613, indexed in Pubmed: 23268465.
7. Bjelakovic G, Nikolova D, Gluud LL, et al. Mortality in randomized trials of antioxidant supplements for primary and secondary prevention: systematic review and meta-analysis. JAMA. 2007; 297(8): 842–857, doi: 10.1001/jama.297.8.842, indexed in Pubmed: 17327526.
8. D'souza D, Subhas BG, Shetty SR, et al. Estimation of serum malondialdehyde in potentially malignant disorders and post-antioxidant treated patients: A biochemical study. Contemp Clin Dent. 2012; 3(4): 448–451, doi: 10.4103/0976-237X.107438, indexed in Pubmed: 23633807.
9. Dhouib H, Jallouli M, Draief M, et al. Oxidative damage and histopathological changes in lung of rat chronically exposed to nicotine alone or associated to ethanol. Pathol Biol (Paris). 2015; 63(6): 258–267, doi: 10.1016/j.patbio.2015.10.001, indexed in Pubmed: 26586280.
10. El-Mahalaway AM, El-Azab NEE. Impacts of resveratrol versus platelet-rich plasma for treatment of experimentally

11. lithium-induced thyroid follicular cell toxicity in rats. A histological and immunohistochemical study. Ultrastruct Pathol. 2019; 43(1): 80–93, doi: 10.1080/01913123.2019.1593270, indexed in Pubmed: 30982377.
12. Focosi D, Azzarà A, Kast RE, et al. Lithium and hematology: established and proposed uses. J Leukoc Biol. 2009; 85(1): 20–28, doi: 10.1189/jlb.0608388, indexed in Pubmed: 18809733.
13. Galati G, Lin A, Sultan AM, et al. Cellular and in vivo hepatotoxicity caused by green tea phenolic acids and catechins. Free Radic Biol Med. 2006; 40(4): 570–580, doi: 10.1016/j.freeradbiomed.2005.09.014, indexed in Pubmed: 16458187.
14. George J, Joshi SR. Drugs and thyroid. J Assoc Physicians India. 2007; 55: 215–223.
15. Gordon J, Crutchfield F, Jennings A, et al. Preparation of lipid-free tissue extracts for chromatographic determination of thyroid hormones and metabolites. Arch Biochem Biophys. 1982; 216(2): 407–415, doi: 10.1016/0003-9861(82)90229-6.
16. Gosselin RE, Smith RP, Hodge HC. Clinical toxicology of commercial products. Williams & Wilkins, Baltimore 1984.
17. Graham H. Green tea composition, consumption, and polyphenol chemistry. Prev Med. 1992; 21(3): 334–350, doi: 10.1016/0091-7435(92)90041-f.
18. Grossmann M, Weintraub BD, Szkudlinski MW. Novel insights into the molecular mechanisms of human thyrotropin action: structural, physiological, and therapeutic implications for the glycoprotein hormone family. Endocr Rev. 1997; 18(4): 476–501, doi: 10.1210/edrv.18.4.0305, indexed in Pubmed: 9267761.
19. Halliwell B, Gutteridge JM. Free radicals and antioxidant protection: mechanisms and significance in toxicology and disease. Hum Toxicol. 1988; 7(1): 7–13, doi: 10.1177/096032718800700102, indexed in Pubmed: 3278973.
20. Hamdy MA, El-Maraghy SA, Kortam MA. Modulatory effects of curcumin and green tea extract against experimentally induced pulmonary fibrosis: a comparison with N-acetyl cysteine. J Biochem Mol Toxicol. 2012; 26(11): 461–468, doi: 10.1002/jbt.21447, indexed in Pubmed: 23132788.
21. Hassanin KMA, Abd El-Kawi SH, Hashem KS. The prospective protective effect of selenium nanoparticles against chromium-induced oxidative and cellular damage in rat thyroid. Int J Nanomedicine. 2013; 8: 1713–1720, doi: 10.2147/IJN.S42736, indexed in Pubmed: 23658489.
22. Higdon JV, Frei B. Tea catechins and polyphenols: health effects, metabolism, and antioxidant functions. Crit Rev Food Sci Nutr. 2003; 43(1): 89–143, doi: 10.1080/10408690390826464, indexed in Pubmed: 12587987.
23. Husain K, Somani SM. Interaction of exercise training and chronic ethanol ingestion on testicular antioxidant system in rat. J Appl Toxicol. 1998; 18(6): 421–429, doi: 10.1002/(sici)1099-1263(199811/12)18:6<421::aid-jat532>3.0.co;2-r.
24. Kalantari H, Salimi A, Rezaie A, et al. Evaluation of sub-acute oral toxicity of lithium carbonate microemulsion (nano size) on liver and kidney of mice. Jundishapur J Nat Pharm Prod. 2015; 10(1): e22312, doi: 10.17795/jjnpp-22312, indexed in Pubmed: 25866723.
25. Kleiner J, Altshuler L, Hendrick V, et al. Lithium-Induced Subclinical Hypothyroidism. J Clin Psychiatry. 1999; 60(4): 249–255, doi: 10.4088/jcp.v60n0409.
26. Kumarguru BN, Natarajan M, Nagarajappa AH. The pathology of lithium induced nephropathy: a case report and review, with emphasis on the demonstration of mast cells. J Clin Diagn Res. 2013; 7(2): 374–377, doi: 10.7860/JCDR/2013/4448.2774, indexed in Pubmed: 23543788.
27. Kurt A, Tumkaya L, Turut H, et al. Protective effects of infliximab on lung injury induced by methotrexate. Arch

Bronconeumol. 2015; 51(11): 551–557, doi: 10.1016/j.arbr.2015.05.012.

27. Lazarus JH. Lithium and thyroid. Best Pract Res Clin Endocrinol Metab. 2009; 23(6): 723–733, doi: 10.1016/j.beem.2009.06.002, indexed in Pubmed: 19942149.

28. Lazarus JH, Bennie EH. Effect of lithium on thyroid function in man. Acta Endocrinol (Copenh). 1972; 70(2): 266–272, doi: 10.1530/acta.0.0700266, indexed in Pubmed: 5068104.

29. Li MJ, Yin YC, Wang J, et al. Green tea compounds in breast cancer prevention and treatment. World J Clin Oncol. 2014; 5(3): 520–528, doi: 10.5306/wjco.v5.i3.520, indexed in Pubmed: 25114865.

30. Ma J, Zou C, Guo L, et al. Novel death defying domain in met entraps the active site of caspase-3 and blocks apoptosis in hepatocytes. Hepatology. 2014; 59(5): 2010–2021, doi: 10.1002/hep.26769, indexed in Pubmed: 24122846.

31. Mackowiak P, Ginalska E, Nowak-Strojec E, et al. The influence of hypo- and hyperthyreosis on insulin receptors and metabolism. Arch Physiol Biochem. 1999; 107(4): 273–279, doi: 10.1076/1381-3455(199908)107:04;1-q;ft273.

32. McCord JM. Human disease, free radicals, and the oxidant/antioxidant balance. Clin Bioch. 1993; 26(5): 351–357, doi: 10.1016/0009-9120(93)90111-i.

33. Meister A. Glutathione, ascorbate, and cellular protection. Cancer Res. 1994; 54(7 Suppl): 1969s–1975s, indexed in Pubmed: 8137322.

34. Mezni A, Aoua H, Khazri O, et al. Lithium induced oxidative damage and inflammation in the rat's heart: Protective effect of grape seed and skin extract. Biomed Pharmacother. 2017; 95: 1103–1111, doi: 10.1016/j.biopha.2017.09.027, indexed in Pubmed: 28922729.

35. Misra H, Fridovich I. The role of superoxide anion in the autoxidation of epinephrine and a simple assay for superoxide dismutase. J Biol Chem. 1972; 247(10): 3170–3175, doi: 10.1016/s0021-9258(19)45228-9.

36. Nair MP, Mahajan S, Reynolds JL, et al. The flavonoid quercetin inhibits proinflammatory cytokine (tumor necrosis factor alpha) gene expression in normal peripheral blood mononuclear cells via modulation of the NF-kappa beta system. Clin Vaccine Immunol. 2006; 13(3): 319–328, doi: 10.1128/CVI.13.3.319-328.2006, indexed in Pubmed: 16522772.

37. Ohishi T, Goto S, Monira P, et al. Anti-inflammatory Action of Green Tea. Antiinflamm Antiallergy Agents Med Chem. 2016; 15(2): 74–90, doi: 10.2174/1871523015666160915154443, indexed in Pubmed: 27634207.

38. Oktay K, Schenken RS, Nelson JF. Proliferating cell nuclear antigen marks the initiation of follicular growth in the rat. Biol Reprod. 1995; 53(2): 295–301, doi: 10.1095/biolreprod53.2.295, indexed in Pubmed: 7492681.

39. Ossani GP, Uceda AM, Acosta JM, et al. Role of oxidative stress in lithium-induced nephropathy. Biol Trace Elem Res. 2019; 191(2): 412–418, doi: 10.1007/s12011-018-1617-2, indexed in Pubmed: 30600502.

40. Peluso I, Serafini M. Antioxidants from black and green tea: from dietary modulation of oxidative stress to pharmacological mechanisms. Br J Pharmacol. 2017; 174(11): 1195–1208, doi: 10.1111/bph.13649, indexed in Pubmed: 27747873.

41. Ramos-Vara JA, Kiupel M, Baszler T, et al. Suggested guidelines for immunohistochemical techniques in veterinary diagnostic laboratories. J Vet Diagn Invest. 2008; 20(4): 393–413, doi: 10.1177/104063870802000401, indexed in Pubmed: 18599844.

42. Roychoudhury S, Agarwal A, Virk G, et al. Potential role of green tea catechins in the management of oxidative stress-associated infertility. Reprod Biomed Online. 2017; 34(5): 487–498, doi: 10.1016/j.rbmo.2017.02.006, indexed in Pubmed: 28285951.

43. Singer I, Rotenberg D, Puschett JB. Lithium-induced nephrogenic diabetes insipidus: in vivo and in vitro studies. J Clin Invest. 1972; 51(5): 1081–1091, doi: 10.1172/JCI106900, indexed in Pubmed: 4341501.

44. Singhal K, Raj N, Gupta K, et al. Probable benefits of green tea with genetic implications. J Oral Maxillofac Pathol. 2017; 21(1): 107–114, doi: 10.4103/0973-029X.203758, indexed in Pubmed: 28479696.

45. Suvarna SK, Layton C, Bancroft JD. Bancroft's theory and practice of histological techniques. Elsevier, Oxford 2019.

46. Thakur S, Thakur S, Chaube S, et al. Subchronic supplementation of lithium carbonate induces reproductive system toxicity in male rat. Reprod Toxicol. 2003; 17(6): 683–690, doi: 10.1016/s0890-6238(03)00107-2.

47. Thornberry NA, Lazebnik Y. Caspases: enemies within. Science. 1998; 281: 1312–1316.

48. Tipple TE, Rogers LK. Methods for the determination of plasma or tissue glutathione levels. Methods Mol Biol. 2012; 889: 315–324, doi: 10.1007/978-1-61779-867-2_20, indexed in Pubmed: 22669674.

49. Toplan S, Dariyerli N, Ozdemir S, et al. Lithium-induced hypothyroidism: oxidative stress and osmotic fragility status in rats. Biol Trace Elem Res. 2013; 152(3): 373–378, doi: 10.1007/s12011-013-9629-4, indexed in Pubmed: 23408263.

50. Tsujimoto Y. Role of Bcl-2 family proteins in apoptosis: apoptosomes or mitochondria? Genes Cells. 1998; 3(11): 697–707, doi: 10.1046/j.1365-2443.1998.00223.x, indexed in Pubmed: 9990505.

51. Valle FC, Hayashi H, Prates JC, et al. Cellular and subcellular alterations of the thyroid gland in rats caused by lithium carbonate. Bull Assoc Anat (Nancy). 1993; 77: 39–43.

52. Velický J, Titlbach M, Lojda Z, et al. Expression of the proliferating cell nuclear antigen (PCNA) in the rat thyroid gland after exposure to bromide. Acta Histochem. 1997; 99(4): 391–399, doi: 10.1016/s0065-1281(97)80032-3.

53. Wang L, Yang G, Yuan Li, et al. Green tea catechins effectively altered hepatic fibrogenesis in rats by inhibiting ERK and Smad1/2 phosphorylation. J Agric Food Chem. 2019; 67(19): 5437–5445, doi: 10.1021/acs.jafc.8b05179, indexed in Pubmed: 30424599.

54. Zhong W, Peng J, He H, et al. Ki-67 and PCNA expression in prostate cancer and benign prostatic hyperplasia. Clin Invest Med. 2008; 31(1): E8–EE15, doi: 10.25011/cim.v31i1.3136, indexed in Pubmed: 18312749.

ORIGINAL ARTICLE

Morphological examination of the accessory sex glands of the Barki bucks (*Capra hircus*)

M.A.M. Alsafy[1] , M.M.A. Abumandour[1], A.A. Karkoura[1], R. El-Bakary[1], M.A. Seif[2], K. Roshdy[3]

[1]Department of Anatomy and Embryology, Faculty of Veterinary Medicine, Alexandria University, Alexandria, Egypt
[2]Department of Anatomy and Embryology, Faculty of Veterinary Medicine, Matrouh University, Matrouch, Egypt
[3]Department of Histology and Cytology, Faculty of Veterinary Medicine, Alexandria University, Alexandria, Egypt

Background: The present investigation was prepared to describe the accessory sex glands of the Barki bucks grossly and by light microscopy.
Materials and methods: There are four sex glands: ampullary, vesicular, prostate, and bulbourethral. The ampullary gland is an enlargement of the terminal part of the ductus deferens, its glandular part has branched tubuloalveolar glands, and its secretory alveoli lined with a pseudo-stratified epithelium composed of cuboidal to columnar cells. The vesicular gland takes the appearance of a cluster of grapes and the left vesicular gland is enlarged and higher than the right one. The vesicular gland is a lobulated tubuloalveolar gland with wide intralobular space and the gland contain a secretory unit which lined by pseudo-stratified columnar epithelium, and the interlobular ductules lined by the stratified epithelium, while the interlobular duct lined by simple cuboidal epithelium; moreover, the lining epithelium of secretory part consists of tall columnar cells. The prostate gland consists only of the disseminated part and is enclosed by a connective tissue capsule that was thin dorsally, thick laterally, and reduced in thickness ventrally. The prostatic acini are lined by simple cuboidal epithelium.
Results: The bulbourethral gland was similar in size to the walnut and surrounded by a capsule and there are interlobular connective tissue septa that divided the gland into lobes and lobules of different sizes. The bulbourethral gland contained secretory units lined by the tall simple columnar epithelium of mucous type with basely located nuclei and eosinophilic cytoplasm contains granular secretion.
Conclusions: The gross and microscopic examination of the four accessory sex glands gave valuable information in the future pathology diagnosis of the accessory sex glands of the Barki bucks. (Folia Morphol 2022; 81, 3: 606–613)

Key words: bucks, sex glands, gross morphology, light microscopy, computed tomography scan

INTRODUCTION

The ruminant anatomy was generally concentrated on the bovine especially ox with limited comparative points to the small ruminants, especially goat.

Goat is belonging to the Caprini of the Bovidae family in the sub-order Ruminantia of the order Artiodactyla. The goat is considered an important source of meat, milk, and hair in Egypt. The male goat is a very familiar

animal in Egyptian farms. There are about seven to ten goat breeds in Egypt: Zaraibi, Barki (*Sahrawi*), Wahati, Sharkawi, and Black Sinai [14]. The three major breeds in Egypt are: Ossimi, Rahmani, and Barki, which are characterised by fat-tailed, their fleece is coarse wool and they are small to medium in size [14].

The male genital systems have to be sound to ensure successful breeding. Ram and buck breeding soundness examination is important to assess the ability to impregnate females during the breeding season [6].

The purpose of the present work was to describe the anatomical position and appearance of the accessory sex glands as well as the microscopic structure of these glands, as there is little available published information about the accessory sex gland of the Barki (*Sahrawi*) bucks. The study of the accessory sex gland in bucks is very important due to its big role in the fertility rate consideration. Additionally, the obtained data were compared with the previous published anatomical data about the accessory sex glands.

MATERIALS AND METHODS

Animals and ethics

The present work was carried out on eight normal healthy Barki bucks weighing 25–30 kg and the aged between 1 and 2 years. The Barki bucks were collected from the goat farms in the Matrouh government and transported to the Anatomical Laboratory at the Anatomy and Embryology Department, Faculty of Veterinary Medicine, Alexandria University, Egypt.

This study followed the rules for the care and use of animals and was approved by the Animal Welfare and Ethics Committees, Faculty of Veterinary Medicine, Alexandria University, Egypt.

Gross morphology

Four Barki bucks were used in the gross morphological descriptions after their sedation with intramuscular injection of the 2% xylazine HCl (0.2 mg/kg of body weight) and atropine (0.04 mg/kg). Then, these bucks were anesthetised by intravenous injection of ketamine (5 mg/kg). The bucks were injected with heparin (1.000 IU) to obtain well bleeding and prevent the coagulation. Then, they were sacrificed by the well bleeding through the common carotid artery for injection of 10% formalin. The specimens were stored for 2 weeks in formalin 10%. The cadavers were injected via a needle in several sites of the body and on the pelvic cavity using the ordinary preservation solution (10% formalin, 2% phenol, and 1% glycerin).

Computed tomography scans

Two bucks were subjected to computed tomography (CT). After physical examination of animals, they were anesthetised by using the combination of ketamine hydrate 0.5–2 mg/kg of body weight and 2% xylazine HCl 1–3 mg/kg of body weight. The bucks' cadavers were taken freshly to the CT centre immediately and fixed in the sternal recumbence position and then, serially sectioned using the Hitachi CT scanner (CT-W450-10A, Hitachi, Japan) (scanning conditions: 120 KV and 200 MA, the width and level of the window [W/L]: 2000/250) to examine the accessory male sex reproductive glands. The section thickness was 0.5 cm, part interval in the cross-section from the level of the last lumbar to the fourth caudal vertebrae. The CT images photographed were helpful in the identification of the structures situated from the level of the fifth lumbar and the fourth caudal vertebra. To obtain the good resolution images in the bone windows, the CT machine was adapted with 200 Hounsfield units (HU) in the windows width and 1600 HU in the level of the windows. While in the soft tissue, we adapted the apparatus with 30 HU in the width of the window and 290 HU in the level of the windows.

Light microscopy

Two bucks were used for light microscopic examination. The accessory sex glands were removed from the freshly slaughtered male bucks and were put in 10% normal buffer formalin solution and transported to the histological lab for the histological preparation of the slides (cutting and staining) to allow the examination of the slides under the light microscope to know the characteristic points of each gland. Then, the samples were put in 70% alcohol solution. Next, they were rapidly dehydrated through ascending grades of ethyl alcohol series (30, 50, 70, 90, and 100% for two changes) for a half-hour in each. Then, they were cleared by putting in xylene and embedded in paraffin wax. Samples sections of 5 μm were cut by Leica rotatory microtome and mounted on the glass slides. Finally, the paraffin sections were used for ordinary staining by Harris haematoxylin and eosin (H&E) stain. The histological techniques were carried according to Suvarna et al. [38].
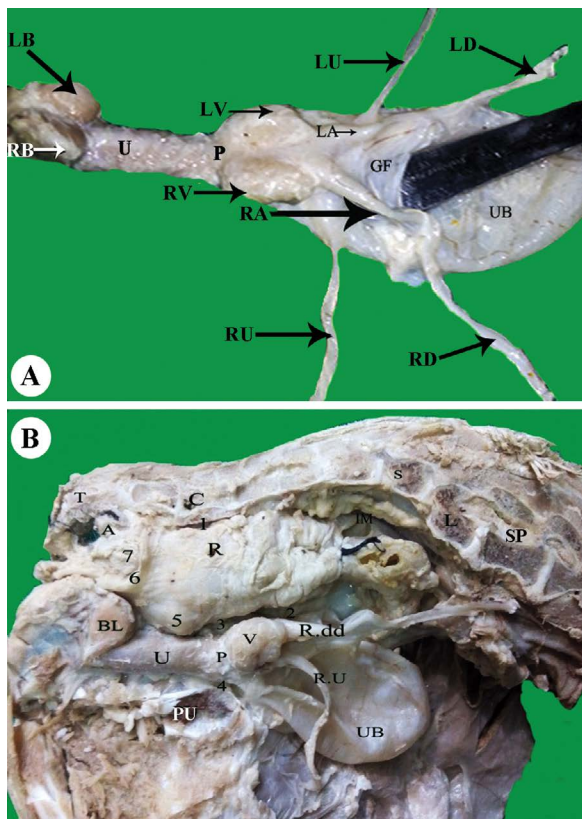
Figure 1. Morphological appearance of the position of the accessory sex reproductive glands of the buck; **A.** Isolated genital organs with the accessory sex reproductive glands of the buck; UB — urinary bladder; LD-RD — left and right ductus deference; GF — genital fold; LU-RU — left and right ureter; LA-RA — ampulla of ductus deference; LV-RV — left and right vesicular gland; P — prostate gland; U — urethra; LB-RB — left and right bulbo urethral gland; **B.** Left side of the pelvic cavity showing the topography of the accessory sex reproductive glands of the buck; 1 — pararectal fossa; 2 — vesicogenital pouch; 3 — rectogenital pouch; 4 — pubovesical pouch; 5 — ampulla recti; 6 — muscle sphincter ani internus; 7 — muscle sphincter ani externus; R — rectum, R.dd — right ampulla of ductus deference; R.U — right ureter; UB — urinary bladder; U — urethra; IM — mesorectum; V — vesicular gland; P — prostate gland; BL — bulbourethral gland; L — lumbar vertebrae; S — sacral vertebrae; C — caudal vertebrae.

The nomenclature used in this study is adapted to Nomina Anatomica Veterinaria [29].

RESULTS

In all examined bucks, there were four accessory sex glands (*Glandulae genitales accessoriae*): the paired ampulla of the ductus deferens (ampullary gland), the paired vesicular gland (*Glandula vesicularis*), the prostate (*Glandula prostatica*), and the paired bulbourethral gland (*Glandula bulbourethralis*). All accessory sex glands were located along the pelvic urethra and their ducts opened and empty their secretion into the urethra.
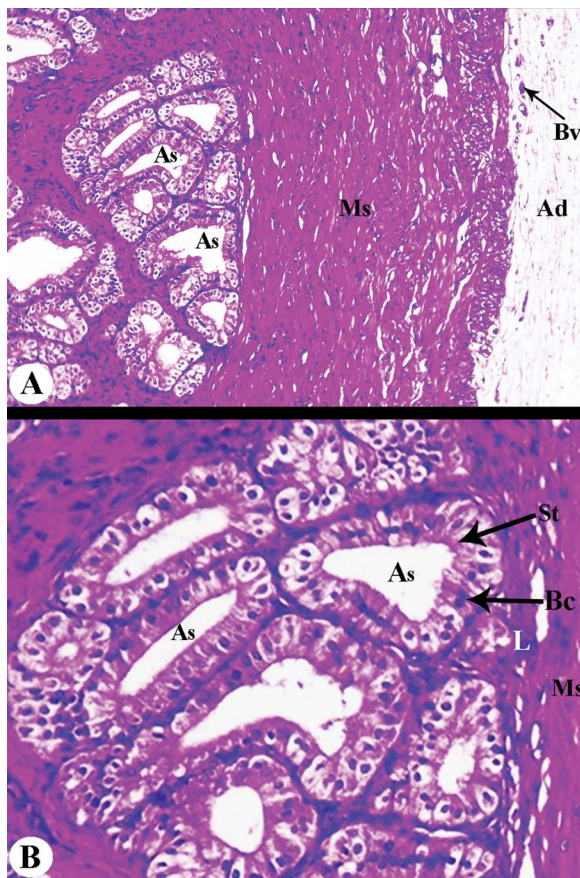
Figure 2. A, B. Micrograph of the ampullary gland of the adult buck showing; As — alveoli; Ms — tunica muscularis; Ad — tunica adventitia; Bv — blood vessels; St — pseudo-stratified epithelium; Bc — basal cell; L — lamina propria; haematoxylin and eosin, ×160.

Ampullary gland (*Glandula ampulla ductus deferentis*)

The ampullary gland (Fig. 1A\LA and RA; Fig. 1B/R.dd; Fig. 6A/4) is a glandular enlargement of the terminal part of the ductus deferens. The length of the ampullary gland reaches 3.5 ± 0.4 cm and the width was 0.5 ± 0.12 cm. The ampullary glands were directed ventrocaudally on the dorsal surface of the urinary bladder and attached by the genital fold (Fig. 1A\GF).

The light microscopic examination showed that the gland (Fig. 2) consisted of the tunica mucosa, tunica muscularis, lamina propria and tunica adventitia, and some blood vessels. The glandular part contained branches of tubuloalveolar glands. The secretory alveoli were lined with a pseudo-stratified epithelium composed of cuboidal to columnar cells with some basal cells.

Vesicular gland (*Glandula vesicularis*)

In all investigated bucks, the paired vesicular gland (Fig. 1A\LV-RV; Fig. 1B/V; Fig. 6A/3) were located on
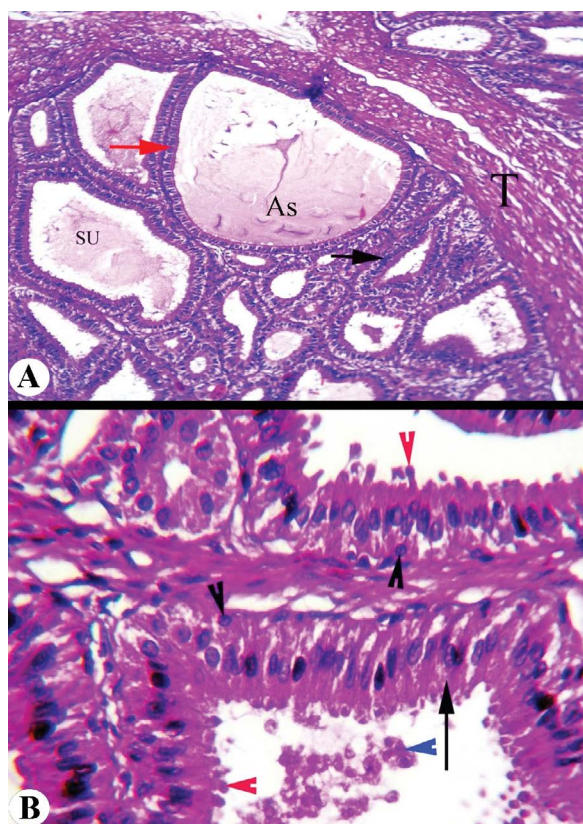
Figure 3. Cross-section micrograph of the vesicular gland of the mature buck showing; **A.** Secretory units (SU) lined by pseudo stratified columnar epithelium, intralobular ductules lined by stratified epithelium (black arrow) and intralobular duct lined by simple cuboidal epithelium (red arrow) with intraluminal eosinophilic secretion (As); haematoxylin and eosin, ×160; **B.** The lining epithelium of secretory part consists of tall columnar cells (arrow), apical blebs of granular end pieces (red arrowheads) and detached blebs in lamina (blue arrowheads), small and spherical basal cells (black arrowheads); haematoxylin and eosin, ×400.

the craniodorsal aspect of the neck of the urinary bladder (*Vesica urinaria*) and laterally to the ampullary glands. It could be identified by its appearance that looks like a cluster of grapes and it is important to note that the left vesicular gland was enlarged and higher than the right one in the same buck.

The light microscopic examination clarified that the vesicular gland (Fig. 3) is a lobulated tubulo-alveolar gland with wide intralobular space or sinuses for storage of a large number of secretions. The gland contained a secretory unit lined by pseudo-stratified columnar epithelium, and the interlobular ductules were lined by the stratified epithelium, while the interlobular duct was lined by simple cuboidal epithelium with intra-luminal eosinophilic secretion. The lining epithelium of the secretory part consisted of tall columnar cells, apical blebs of granular end pieces,

and detached blebs in lamina, small and spherical basal cells.

Prostate gland (*Glandula prostatica*)

In all examined bucks, the single prostate gland (Fig. 1/P; Fig. 6B/16) was located close to the junction of the vesicular gland at the pelvic region. It was constituted only from the disseminated part (*pars disseminate*). The pars disseminate surrounded the pelvic urethra which was covered by the urethra masculina.

The light microscopic examination showed that the prostate gland was enclosed by a connective tissue capsule (Fig. 4) that was thin dorsally, thick laterally, and reduced in thickness ventrally. The gland capsule was enveloped by a layer of skeletal muscle (muscle urethralis) that was surrounded by a layer of loose connective tissue trabeculae extending from the capsule and descending into the parenchyma of the gland forming interlobular connective tissue and divided the gland into lobules. The glandular substance consisted of numerous follicles, which opened into the elongated canal. The prostatic acini were lined by simple cuboidal epithelium.

Bulbourethral gland (*Glandula bulbourethralis*)

In all investigated bucks, the paired bulbourethral gland was similar in size to the walnut and located dorsal to the urethra in both sides of it, cranial to the ischial arch (Fig. 1A\LB-RB; Fig. 1B/BL; Fig. 6C/23). It was closely related to the bulb of the penis and in general, it appeared to be covered mostly by the bulbospongiosus muscle. The right and left bulbourethral glands appeared to be nearly equal in size and their shape similar to each other.

The light microscopic examination showed that the bulbourethral gland was surrounded by a white fibrous capsule and there were interlobular connective tissue septa that divided the gland into lobes and lobules of different sizes (Fig. 5). The gland contained secretory units lined by the tall simple columnar epithelium of mucous type with basely located nuclei and eosinophilic cytoplasm contained granular secretion.

DISCUSSION AND CONCLUSIONS

There are four accessory sex glands in most mammalian species: ampullary, seminal vesicle, prostate, and the bulbourethral glands in the Barki bucks as reported in horse [8, 12], bull [7, 12], spotted paca [5], *Gracilinanus microtarsus* [10], Arabian oryx [13], Elk (*Cervus canadensis*) [22], red deer (*Cervus elaphus*) [36].
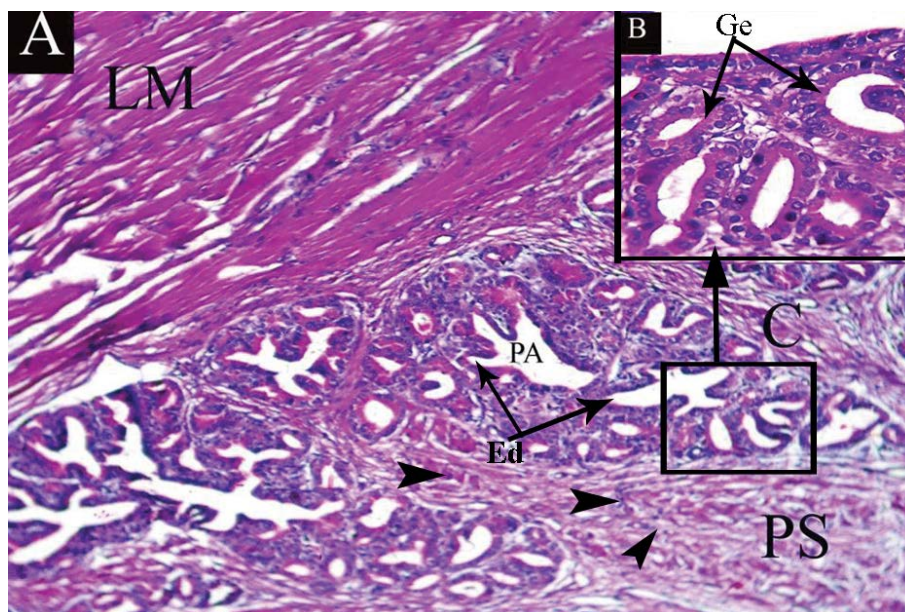
Figure 4. Histological micrograph of the prostate gland (pars dessiminata) from the mature buck; **A.** Lamina muscularis (LM), prostatic acini (PA), surrounded by fibrous capsule (C) and propria submucosa (PS) with smooth muscle bundles (black arrowheads), excretory ducts of the prostate gland (Ed); haematoxylin and eosin, ×160; **B.** Prostatic acini lined by simple cuboidal epithelium with glandular epithelium (Ge); haematoxylin and eosin, ×400.
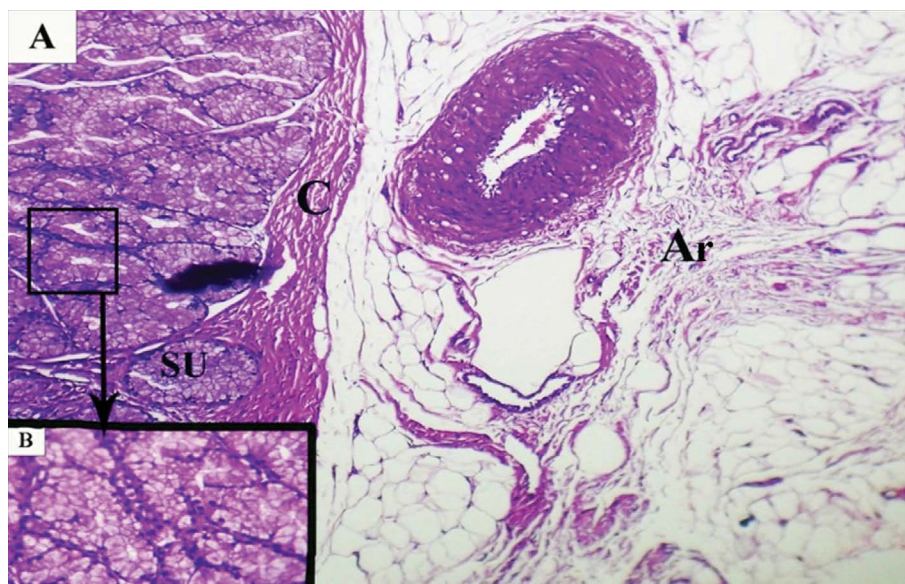
Figure 5. Histological cross section micrograph of the bulbourethral gland of the mature buck; **A.** Adventitia (Ar), capsule (C) and secretory unit (SU); haematoxylin and eosin, ×160; **B.** The lining epithelium of secretory unit is a tall simple columnar epithelium of mucous.

While, the presence of three accessory sex glands was reported in canine (prostate, bulbourethral glands and ampullary gland) [12], canine (prostate, seminal vesicle and ampullary gland) [32], in the pampas deer *Ozotoceros bezoarticus* (prostate, vesicular and the ampullary glands) [34], in the lesser anteater (prostate, seminal vesicle and bulbourethral glands). However, there are two accessory sex glands only, the prostate and vesicular gland, in the capybara [15]. Furthermore, El-Hagri [12] and Budras et al. [7] reported that the accessory sex glands were fully developed only in the bull.

The present investigation reported that the ampullary gland is a glandular enlargement of the terminal part of the ductus deferens, similar result mentioned by some authors [12, 16, 33, 37]. Furthermore, Frans-
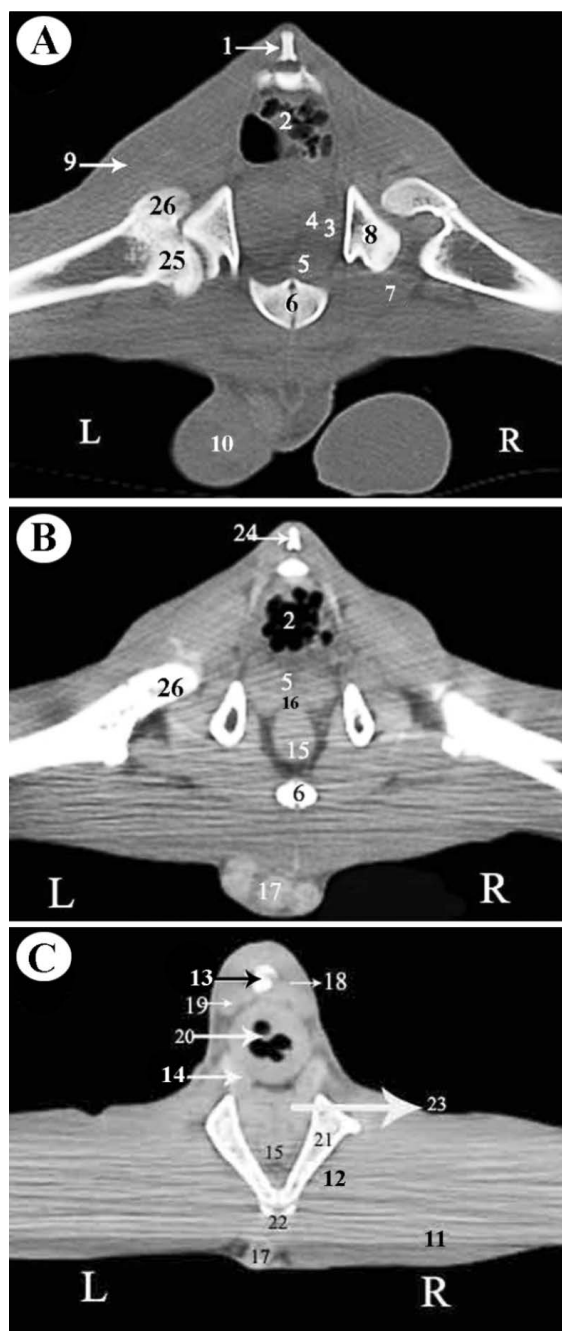
Figure 6. Computed tomography images of the male buck's pelvis; **A.** Transversal computed tomography scan at the level of the 3rd sacral vertebra; **B.** Transversal computed tomography scan at the level of the 5th sacral vertebra; **C.** Transversal computed tomography scan at the level of the 3rd caudal vertebra; 1 — 3rd sacral vertebra; 2 — rectum; 3 — vesicular gland; 4 — ampulla of ductus deference; 5 — neck of urinary bladder; 6 — pubic symphysis; 7 — ilio psoas muscle; 8 — right ilium shaft; 9 — superficial gluteal muscle; 10 — testis; 11 — right adductor muscle; 12 — external obturator muscle; 13 — 3rd caudal vertebra; 14 — muscle sphincter ani internus and externus; 15 — pelvic urethra; 16 — prostata; 17 — penis; 18 — right sacrocaudalis dorsalis lateralis muscle; 19 — right sacrocaudalis ventralis medialis and lateralis muscle; 20 — anal canal; 21 — right ischium; 22 — ischiatic arch; 23 — bulbo urethral gland; 24 — 5th sacral vertebra; 25 — head of femur; 26 — greater trochanter of femur; L — left side; R — right side.

don et al. [16] added that its size has a species variation among animal species; well-developed in stallion, bull and ram but, it is absent in the boar; however, Bacha and Bacha [4] and El-Hagri [12] mentioned that it is ill well-developed in the boar but absent in the tomcat and also do Nascimento Lima et al. [10] reported the absence of this gland in *Gracilinanus microtarsus*. The present histological observation of the ampullary was similar with Trautmann et al. [39] and Wrobel [41] that the gland consists of three layers: the tunica mucosa, tunica muscularis and tunica adventitia.

In all investigated bucks, the paired vesicular gland were located on the craniodorsal aspect of the urinary bladder and it could be easily identified by its appearance which looks like a cluster of grapes and also it's important to note that the left vesicular gland was enlarged and higher than the right one; similar findings were obtained by some authors [3, 12, 19]. The vesicular gland is the largest accessory sex gland in the bull [7, 12] and the spotted paca [5]. However, the vesicular gland was absent in the canines [12], *Gracilinanus microtarsus* [10] and some rodents [2, 20]. In the current histological study, the vesicular gland was a lobulated alveolar gland containing a secretory unit that lined by pseudo-stratified columnar epithelium, and the interlobular ductules were lined by the stratified epithelium, while the interlobular duct was lined by simple cuboidal epithelium; similar findings were obtained by some authors [3, 19, 27]. While it was lined by simple cuboidal epithelium as reported in the spotted paca [5], it was lined by a simple columnar epithelium as observed in Guinea pig [40], rat [35] and giant rat [21, 23].

Morphologically, the prostate gland may be single as present in our study and by some authors [12, 17–19, 26, 32] or paired as noted by Junqueira et al. [24]. In our work, we found that the single prostate gland has only the pars disseminate that is found in the pelvic urethra and surrounded by the urethral masculina; similar findings were obtained by some authors [12, 17, 18, 26, 32]. Pathak et al. [31] reported that there is an additional part named the corpus prostate present in some gaddi goats; however, this corpus prostate is not present in small ruminants in all published anatomical textbooks [11, 12, 18].

There is some variation in the portions of the prostate gland among animals species; the present study with and some other authors [12, 17, 18, 26, 32] noted the presence of only one portion called

disseminate part, while Gofur [19] in the Black Bengal buck mentioned that the single prostate gland has two portions: compact (external) and disseminate (internal) portion. On the other hand, Junqueira et al. [24] in rat noted that the paired prostate gland has a dorsal and ventral part. Also Neuhaus et al. [28] in the Guinea pig noted that the prostate gland has two portions: the large cranial lobe and the smaller caudal lobe. Moreover, Ojasti [30] in the capybara noted that the prostate gland consists of three parts: intermediate, dorsal and lateral lobes.

According to our histological studies, the prostate gland was enclosed by a connective tissue capsule, which was thin dorsally, thick laterally and reduced in thickness ventrally. The capsule was enveloped by a layer of skeletal muscle surrounded by a layer of skeletal muscle, similar to that reported by Gofur [19] and Pathak et al. [31]. In Guinea pig, the prostate is enveloped by a fibrous muscular layer [1] while in the spotted paca [5] this layer consists of smooth muscle fibre, similar to that observed in the prostate gland of the mouse [9, 25]. The present study noted that the prostatic acini were lined by simple cuboidal epithelium while in the spotted paca [5] it is simple columnar epithelium but pseudo-stratified in some regions.

Our study revealed that the paired bulbourethral gland is small in size similar to hazelnut, and lies dorsal to the pelvic urethra and more obvious as the gland surrounded by a white fibrous capsule; similar observations were noted by some authors [3, 7, 16, 19]. In the spotted paca, the bulbourethral gland presented at the terminal part of the rectum and dorsal to the urethra and caudal to the prostate gland [5]. The bulbourethral gland is absent in the canine and present in the feline, as noted by El-Hagri [12] and Bacha and Bacha [4]. The bulbourethral gland is surrounded by striated skeletal muscle, as noted by Borges et al. [5], Gude et al. [21] and Hebel and Stromberg [23]. Our work mentioned that the bulbourethral gland contains secretory units lined by the tall simple columnar epithelium of mucous type. The lining simple columnar epithelium was also noted by Hebel and Stromberg [23]. The bulbourethral gland appears to be covered mostly by the bulbospongiosus muscle and the gland itself is covered by a white fibrous capsule, similar to that noted by Budras et al. [7].

Conflict of interest: None declared

REFERENCES

1. Amiya PSH, Maiti BR. Quantitative studies of the reproductiveorgans of the male bandicoot rat: a common rodent pest. Anat Anzeiger. 1982; 151(5): 483–495.
2. Angulo J, Alvarez M. The genital tract of the male conga hutia, capromys pilorides (say). J Mammal. 1948; 29(3): 277, doi: 10.2307/1375394.
3. Archana P, Katiyar RS, Sharma DN, et al. Gerentological studies on the gross and histomorphology of the vesicular gland of gaddi goat (Copra hircus). Int J Morphol. 2009; 27(1), doi: 10.4067/s0717-95022009000100002.
4. Bacha Jr, Bacha LM. Color atlas of veterinary histology. John Wiley & Sons 2012.
5. Borges EM, Branco É, de Lima AR, et al. Morphology of accessory genital glands of spotted paca (Agouti paca Linnaeus, 1766). Anim Reprod Sci. 2014; 145(1-2): 75–80, doi: 10.1016/j.anireprosci.2013.12.014, indexed in Pubmed: 24461579.
6. Boukhliq R, El Al, Tibary A. Gross anatomy and ultrasonographic examination of the reproductive organs in rams and bucks. Revue Marocaine des Sciences Agronomiques et Vétérinaires. 2018; 6(2).
7. Budras KD, Habel RE, Wunsche A, Buda S. Bovine anatomy: An illustrated text. 1st ed. Schlutersche GmbH & Co. KG, Verlag und Druckerei, Hannover 2003: 289–291.
8. Budras KD, Sack WO, Rock S, Horowitz A, Berg R. Anatomy of the Horse, 6th ed. Schluetersche, Germany 2012.
9. Cagnon VH, Camargo AM, Rosa RM, et al. Ultrastructural study of the ventral lobe of the prostate of mice with streptozotocin induced diabetes (C57BL/6J). Tissue Cell. 2000; 32(4): 275–283, doi: 10.1054/tice.2000.0123, indexed in Pubmed: 11145010.
10. do Nascimento Lima JM, Santos AC, Viana DC, et al. Estudo morfológico dos órgãos genitais masculinos em Gracilinanus microtarsus. BJVRAS. 2013; 50(6): 447–456.
11. Dyce KM, Sack WO, Wensing CJG. Text book of Veterinary anatomy. WB Saunders Company, Philadelphia, London and Toronto 2010.
12. El-Hagri MAA. Splanchnology of Domestic Animals. 1st public organization for books and scientific publications, Giza: Cairo University Press. Springer, Berlin Heidelberg 1967: 23–30.
13. Eljarah A, Al-Zghoul MB, Jawasreh K, et al. Characterization of male reproductive anatomy of the endangered Arabian oryx (Oryx leucoryx). Theriogenology. 2012; 78(1): 159–164, doi: 10.1016/j.theriogenology.2012.01.032, indexed in Pubmed: 22444562.
14. Elshennawy M. Sheep development program in Egypt. In: Gabiña D. (ed.). Strategies for sheep and goat breeding (Cahiers Options Méditerraéennes; n. 11). CIHEAM, Zaragoza 1995: 27–32.
15. Fernandez D, Ferraz R, Melo A, et al. Análise histológica das glândulas uretrais da capivara (Hydrochoerus hydrochaeris). Pesq Vet Bras. 2010; 30(4): 373–377, doi: 10.1590/s0100-736x2010000400015.
16. Frandson RD, Wilke WL, Fails AD. Anatomy and physiology of farm animals. John Wiley & Sons 2009.
17. Garrett PD. Guide to ruminant anatomy based on the dissection of the goat. Low State University Press, AMES 1988.

18. Getty R. The Anatomy of the Domestic Animals. Vol. 1, 5th Ed. WB Saunders Company, Philadelphia, USA 1975.

19. Gofur M. Anatomy and histomorphometry of accessory reproductive glands of the Black Bengal buck. Eur J Anat. 2015; 19(2): 171–178.

20. Gottreich A, Hammel I, Yogev L, et al. Quantitative microscopic changes in the mole rat's accessory sex organs during an annual cycle. Anat Rec. 1996; 246(2): 231–237, doi: 10.1002/(SICI)1097-0185(199610)246:2<231::AID-AR10>3.0.CO;2-P, indexed in Pubmed: 8888965.

21. Gude WD, Cosgrove GE, Hirsch GP. Histological atlas of the laboratory mouse. Springer 1982: 17–19.

22. Haigh J. Reproductive anatomy and physiology of male wapiti and red deer. Current Therapy in Large Animal Theriogenology. 2nd Ed. Saunders Elsevier Inc, St. Louis, Missouri 2007: 932–936.

23. Hebel R, Stromberg MW. Anatomy and embryology of the laboratory rat. BioMed Verlag 1986.

24. Junqueira LCU, Martins EO, Luiz Carlos Uchôa Junqueira EO. Atlas de anatomia microscópica do rato. 1947.

25. Kawamura H, Nonogaki T, Yoshikawa K, et al. Morphological changes in mouse accessory sex glands following neonatal estrogen treatment. Ann Anat. 2000; 182(3): 269–274, doi: 10.1016/S0940-9602(00)80034-5, indexed in Pubmed: 10836100.

26. Kundu P. Anatomical studies on the accessory male sex glands (gross and microscopic) of the Indian goat (Jamunapari and cross Jamunapari). IJAH 1980: 151–153.

27. Menezes DJ, Assis Neto AC, Oliveira MF, et al. Morphology of the male agouti accessory genital glands (Dasyprocta prymnolopha Wagler, 1831). Pesq Vet Bras. 2010; 30(9): 793–797, doi: 10.1590/s0100-736x2010000900014.

28. Neuhaus J, Dorschner W, Mondry J, et al. Comparative anatomy of the male guinea-pig and human lower urinary tract: histomorphology and three-dimensional reconstruction. Anat Histol Embryol. 2001; 30(3): 185–192, indexed in Pubmed: 11447945.

29. Nomina Anatomica Veterinaria. 5th edition (revised version). Prepared by the International Committee on Veterinary Gross Anatomical Nomenclature (I.C.V.G.A.N.) and authorized by the General Assembly of the World Association of Veterinary Anatomists (W.A.V.A.) Knoxville, TN (U.S.A.) 2003 Published by the Editorial Committee

Hannover (Germany), Columbia, MO (U.S.A.), Ghent (Belgium), Sapporo (Japan). Springer 2012.

30. Ojasti J. Estudio biológico del chigüire o capibara. Fondo Nacional de Investigaciones Agropecuarias Caracas 1973.

31. Pathak A, Katiyar RS, Sharma DN, et al. Gross Anatomical, Histological and Histochemical Studies on the Postnatal Development of the Prostate Gland of Gaddi Goat. Int J Morphol. 2012; 30(2): 731–739, doi: 10.4067/s0717-95022012000200063.

32. Pérez W, Vazquez N, Ungerfeld R. Gross anatomy of the male genital organs of the pampas deer (Ozotoceros bezoarticus, Linnaeus 1758). Anat Sci Int. 2013; 88(3): 123–129, doi: 10.1007/s12565-013-0171-4, indexed in Pubmed: 23381482.

33. Raghavan D. Anatomy the of ox. Indian Council of Agricultural Research, New Delhi 1964.

34. Rossi LF, Luaces JP, Aldana Marcos HJ, et al. Anatomy and histology of the male reproductive tract and spermatogenesis fine structure in the lesser anteater (Tamandua tetradactyla, Myrmecophagidae, Xenarthra): morphological evidences of reproductive functions. Anat Histol Embryol. 2013; 42(4): 247–256, doi: 10.1111/ahe.12008, indexed in Pubmed: 23072214.

35. Sprando RL, Collins TF, Black TN, et al. Light microscopic observations on the reproductive tract of the male sand rat, Psammomys obesus. Tissue Cell. 1999; 31(1): 99–115, doi: 10.1054/tice.1999.0003, indexed in Pubmed: 10368991.

36. Stewart D. Male genitalia of red deer (Cervus elaphus). NZVJ. 1983; 31(7): 122.

37. Suri S, Sudhakar L, Bhardwaj R. Seasonal variation in the histomorphology and histochemistry of ampulla of vas deferens of gaddi goat and gaddi sheep. Int J Morphol. 2008; 26(1), doi: 10.4067/s0717-95022008000100022.

38. Suvarna SK, Layton C, Bancroft JD. Bancroft's Theory and Practice of Histological Techniques, Expert Consult: Online and Print, 7: Bancroft's Theory and Practice of Histological Techniques. Elsevier, Churchill Livingstone 2013.

39. Trautmann A, Fiebiger J, Habel RE, Biberstein EL. Fundamentals of the histology of domestic animals. Comstock 1957.

40. Wagner JE. The biology of the guinea pig. Academic Press 2014.

41. Wrobel K. Male reproductive system. In textbook of veterinary histology. Dellmann H (ed.). DP Lea & Febiger, Philadelphia 1993.

V M
VIA MEDICA

ORIGINAL ARTICLE

A potential role of mesenchymal stem cells derived from human umbilical cord blood in ameliorating psoriasis-like skin lesion in the rats

S.S. Attia, M. Rafla, N.E. El-Nefiawy, H.F. Abdel Hamid, M.A. Amin, M.A. Fetouh

Department of Anatomy and Embryology, Faculty of Medicine, Ain Shams University, Abbasia, Cairo, Egypt

Background: Psoriasis is a common autoimmune inflammatory skin disease, with no clear cause, treated with topical agents and phototherapy, conventional immunosuppressant drugs and biologic agents. Stem cell therapy has generated significant interest in regenerative medicine. The aim of this study was to use mesenchymal stem cell (MSC) therapy compared to the topical application of the standard conventional corticosteroid cream.

Materials and methods: Forty male adult albino rats were used, divided into four groups, 10 rats each: group I (control), group II (psoriasis-like lesions induced by usage of Aldara cream), group III (treated with betamethasone) and group IV (treated with MSCs). Specimens were stained with haematoxylin and eosin, Masson's trichrome, immune-histochemical technique for CD4, CD8 and CD31. Ultra-sections were prepared for transmission electron microscope (TEM) examination.

Results: Mesenchymal stem cells demonstrated efficacy in reduction of disease severity in the form of uniform epidermal thickness covered by a very thin keratin layer. Normally arranged layers of epidermal layers, with a clear border demarcation, were seen between the epidermis and the dermis with apparently intact basement membrane. TEM showed absence of gaps between the tightly connected cells of the basal layer and the resting basement membrane.

Conclusions: Application of MSCs raises hope for developing a new, safe and effective therapy for psoriatic patients, avoiding the side effects of betamethasone.
(Folia Morphol 2022; 81, 3: 614–631)

Key words: psoriasis, human umbilical cord blood-derived mesenchymal stem cells, rat, imiquimod cream, CD4, CD8, CD31, electron microscopy

INTRODUCTION

Psoriasis is a common autoimmune chronic inflammatory skin disease, with no clear cause, that affects 2–3% of the world's population and greatly impairs the quality of life of affected individuals. Psoriasis vulgaris or plaque psoriasis, the most prevalent disease type, it is characterised by well-demarcated, red, scaly plaques. Psoriasis-affected skin has a thickened epidermis with scaly patches, due to excessive proliferation and aberrant differentiation of kerat-

inocytes, and redness that is caused by increased dilatation of the dermal blood vessels, and infiltration of immune cells [1].

It is considered to be a systemic disease rather than one limited to the skin as in certain cases, the cutaneous immune response becomes no longer restricted to the skin and results in systemic inflammation leading to the development of comorbidities. The pathogenesis of psoriasis has an immunological basis. A central role is played by T helper (Th) 1 and Th17 lymphocytes and by cytokines. Th17 cells are involved not only in psoriasis but also in other autoimmune diseases; therefore, the involvement of the immune system in psoriasis is widely accepted now [25].

The treatment varies, depending on disease severity, from topical agents and phototherapy to conventional immunosuppressant drugs and biologic agents. However, they are expensive and several adverse reactions have been also reported [14]. Therefore, there is an unmet need for the development of a safe and effective therapy.

Stem cell therapy has evoked great expectations and showed significant interest in regenerative medicine. Mesenchymal stem cells (MSCs) are multipotent non-haematopoietic stromal cells. They can be isolated from bone marrow, umbilical cord blood and adipose tissue [19]. Because of their ability to modulate immune responses, MSCs are considered to be a therapeutic approach for the treatment of patients with systemic lupus erythematosus, rheumatoid arthritis, graft-versus-host disease, Crohn's disease, and multiple sclerosis [8, 10, 41].

Reviewing the literature, few recent animal studies that investigated the potential use of stem cell therapy, of different origins, in the treatment of psoriasis were found. Human embryonic MSCs, adult human MSCs, and human umbilical cord-derived MSCs were used by the authors respectively [21, 23, 36].

Here, the present study was conducted to examine the therapeutic scope of the human umbilical cord-derived mesenchymal stem cells (hUCB-MSCs) in the treatment of psoriasis using imiquimod (IMQ)-induced psoriasis rat model. Stem cell therapy was compared with the topical application of the standard conventional corticosteroid cream. hUCB-MSCs have been selected in the present study due to the lack of ethical considerations and the easy access to them following Lee et al. [23]. Light microscopic, immunohistochemical, transmission electron microscopic

(TEM) methods were utilised in this study in addition to morphometry and image analysis.

MATERIALS AND METHODS

Animals

Forty male adult albino rats weighing 180–200 g were obtained from Ain Shams University Faculty of Medicine research centre (MASRI). Rats were housed in stainless steel cages, 2 rats per cage, and were left for a week before any intervention to acclimatize to experimental conditions. The rats were exposed to 12 hours light/dark cycle and allowed free access to food and water (*ad libitum*) with suitable environmental conditions and good ventilation.

Ethical consideration

All the experimental protocols were carried out in accordance with the guidelines approved by the Committee of Animal Research Ethics, Faculty of Medicine Ain Shams University, which conforms to the legal requirements in Poland and EU Directive 2010/63/ /EU of the European Parliament and the Council of 22 September 2010 as well as the requirement of National Research Council 2011.

Materials
— Imiquimod (IMQ, 5% cream, Aldara®) in the form of sachets, each containing 250 mg of cream, purchased from MEDA pharmaceutical company, Sweden.
— Betamethasone cream (0.05% cream, Betamethasone®) purchased from AMRIYA PHARM.IND, pharmaceutical company, Egypt.
— Xanthan gum (vehicle of the Aldara cream) purchased from Sigma chemical company (Cairo, Egypt), in the form of white dry powder. Two grams of xanthan gum were dissolved in 100 mL of normal saline.

Isolation and culture of hUCB-MSCs

Isolation and culture of hUCB-MSCs were performed in the Stem Cell Unit, Faculty of Medicine, Cairo University. The umbilical cord blood (UCB) samples were obtained from the umbilical vein immediately after delivery, with the informed consent of the mother. The UCB samples were mixed with Hetasep solution (stem cell technologies) at a ratio of 5:1, and then incubated at room temperature to deplete erythrocyte counts. The supernatant was collected carefully, and mononuclear cells were obtained using

Ficoll density-gradient centrifugation at 2500 rpm for 20 minutes. The cells were washed twice in phosphate buffered saline (PBS). Cells were seeded at a density of 2×10^5 to 2×10^6 cells/cm² on plates in growth media that consisted of D-media and 10% foetal bovine serum. After 3 days, non-adherent cells were removed. The adherent cells formed colonies and grew rapidly, showing spindle-shaped morphology [22].

Induction of psoriasis-like skin inflammation

Psoriasis-like skin inflammation was induced according to the method of Chen et al. [7]. Briefly, rats received a daily topical dose of 62.5 mg of Aldara® cream (5%) containing 3.125 mg of imiquimod (IMQ) on the shaved back skin for 12 consecutive days to achieve the optimal inflammation. Every cream sachet is containing 250 mg of Aldara cream (2 mL) having 12.5 mg of IMQ; therefore, the required single dose will be quarter of a sachet (0.5 mL). IMQ application was in the middle portion of the median sagittal plane of the back of each animal.

Experimental groups

Rats were randomly divided into four groups, 10 rats each:
— **group I (control)**: subdivided into: **group IA (negative control)**: included 5 rats that didn't receive any treatment; **group IB (positive control)**: included 5 rats that received a daily topical dose of 0.5 mL of the vehicle of the cream (Xanthan gum in normal saline 200 mg/10 mL) on the shaved back skin for 12 consecutive days used as a control group;
— **group II (psoriasis)**: rats received a daily topical dose of 0.5 mL of Aldara® cream on the shaved back skin for 12 consecutive days;
— **group III (psoriasis + betamethasone)**: rats received a combination of treatments. A daily topical dose of 0.5 mL of Aldara® cream on the shaved back skin for 12 consecutive days. Then, on the 6th day Betamethasone® cream (0.05%) was applied twice daily till the 12th day [26];
— **group IV (psoriasis + hUCB-MSCs)**: rats received a combination of treatments. A daily topical dose of 0.5 mL of Aldara® cream on the shaved back skin for 12 consecutive days. Then, on the 6th day rats received one subcutaneous MSCs injection (2×10^6) cells per injection within 2 mL of the media) at the 4 corners around the edge of the inflamed area of the skin [23].

Specimen collection

On day 12 of the present experiment, animals were sacrificed using ether inhalation. Skin specimens were excised and some of them were fixed in 10% neutral formalin in water for 48 hours and processed for light microscopic examination, while other specimens were fixed immediately in 2.5% glutaraldehyde and processed for TEM examination.

Preparation of specimens for light microscopic examination

Serial paraffin sections of 5 μm thickness were cut and stained with haematoxylin and eosin (H&E) and Masson's trichrome [11] for light microscopic examination.

Immunohistochemistry technique

The immunohistochemical staining was carried out using the avidine-biotin technique [2]. Samples from back skin (3 mm diameter) were immersed in TissueTek (Bayer), snap-frozen in liquid nitrogen, and stored at –80°C until use. Six-micrometer cryosections of snap-frozen skin were cut using a cryostat (Jung Frigocut 2800 E; Leica). Sections were fixed in acetone (Fluka Chemie) containing 0.5% H_2O_2 for 10 minutes at room temperature. Staining was performed essentially as described by van der Fits et al. [39]. Slides were incubated overnight at 4°C, or for 1 hour at room temperature, with primary antibodies (Abs) against the following antigens (Ags) or cell types: CD4, CD8, CD31. This was followed by incubation for 30 minutes with biotin-linked secondary donkey-anti-rabbit, goat anti-hamster, or rabbit-anti-rat Abs and peroxidase-linked avidin (Dako).

Preparation of skin specimens for TEM [2]

The tissues were cut in slices 1 mm³ and fixed immediately in 2.5% buffered glutaraldehyde (pH 7.4) for 24 hours. The specimens were rinsed twice in phosphate buffer 20 minutes each. The specimens were post fixed in 1% osmic acid for 1 hour. Then tissues were washed twice in phosphate buffer, half an hour each. The specimen was put in a series of ascending grades of alcohol according to the following schedule: alcohol 50% for 10 minutes, alcohol 70% for 10 minutes, alcohol 80% for 10 minutes, alcohol 95% for 10 minutes, alcohol 100%, two changes 10 minutes each. Clearing was performed in propylene oxide for 20 minutes at room temperature. Infiltration was done using equal parts of propylene

oxide and Epon 812 and left in infiltration medium overnight. The sections were embedded in epoxy resin embedding media.

Semi thin sectioning

The block is cut into semithin sections (1 μm) with a glass knife, using an ultramicrotome. The sections are then stained with Toluidine Blue for 25 seconds and examined by light microscope Olympus model BX51. Images were captured by camera Olympus model E-PM2 with 4608 × 3072-pixel format to determine the ultrathin area.

Ultrathin sectioning

Ultrathin sections were made at 50–70 nm using ultra-microtome Sumy Electron Optics (SEO) model UMTP-6M at thickness 90 nm, mounted on copper grids (200 mesh).

Sections were stained with double stain (uranyl acetate 5% for 15 min followed by lead citrate for 8 min).

Electron micrographing

Finally, sections were examined by TEM SEO model PEM-100, Faculty of Agriculture, Cairo University at different magnification. The photos were taken at 75 kV. Photos were captured by CCD camera JENOPTIK model ProgRes MFcool.

Morphometric study and image analysis

Haematoxylin and eosin-stained sections were used to assess the following parameters:
— thickness of the epidermis;
— blood vessels count;
— inflammatory cells count.

"Image J" computer image analysis software version 1.40 g was used to measure the previously mentioned parameters. For each of the previous entries, measurements were taken from 6 microscopic fields per slide, 6 slides per rat and 6 rats per group.

Counting the number of inflammatory cells per microscopic field was performed using the (×40) objective lens. Thickness of the epidermis and number of blood vessels per microscopic field were done using the (×10) objective lens.

Statistical analysis

Statistical analysis was done using the SPSS software (Statistical Package for Social Studies, version 13.0). One-way analysis of variance (ANOVA) was employed to compare means in different groups with each other. Bonferroni *post hoc* test was used to detect significance between every two individual groups.

The significance of the data was determined by the probability (p value). P > 0.05 was considered non-significant. P ≤ 0.05 was considered significant and p ≤ 0.001 was considered highly significant [37]. Data was represented in tables and histograms, prepared by using MS Excel 2013.

RESULTS

Macroscopic results

At the end of the experiment macroscopic examination of the mid-back skin of the rats that was shaved at the beginning of the experiment revealed the following: in the control group heavy hair regrowth was observed after 12 days and the skin appeared normal. In group II where the skin was subjected to topical application of IMQ cream for 12 days, well demarcated erythema with overlying scale like flakes (scaling) was found and hair regrowth was greatly hindered. In group III, the skin area that was subjected to betamethasone cream preceded by IMQ cream application revealed hair regrowth, no erythema but still there were some scales on the skin surface. In group IV, the skin area that was injected by subcutaneous MSCs preceded by IMQ cream application showed normal appearance of the skin with hair regrowth. No erythema or scales were observed (Fig. 1).

Histological results
Group I (control)

Haematoxylin and eosin-stained sections from the control rats revealed the epidermis and dermis layers. The epidermis was composed of stratified squamous epithelium with uniform thickness and lies on a wavy basement membrane. The border between the epidermis and dermis was clearly demarcated. The epidermis appeared to be arranged into four layers and covered by keratin scales. It was composed of stratum basale; the cells of stratum basale were columnar in shape with basophilic cytoplasm. Above this layer, the stratum spinosum layer consisted of polyhedral acidophilic cells with rounded nuclei. The third layer, stratum granulosum, showed numerous basophilic granules (keratohyalin granules). Finally, the superficial stratum corneum appeared non-cellular and formed of acidophilic scales giving basket
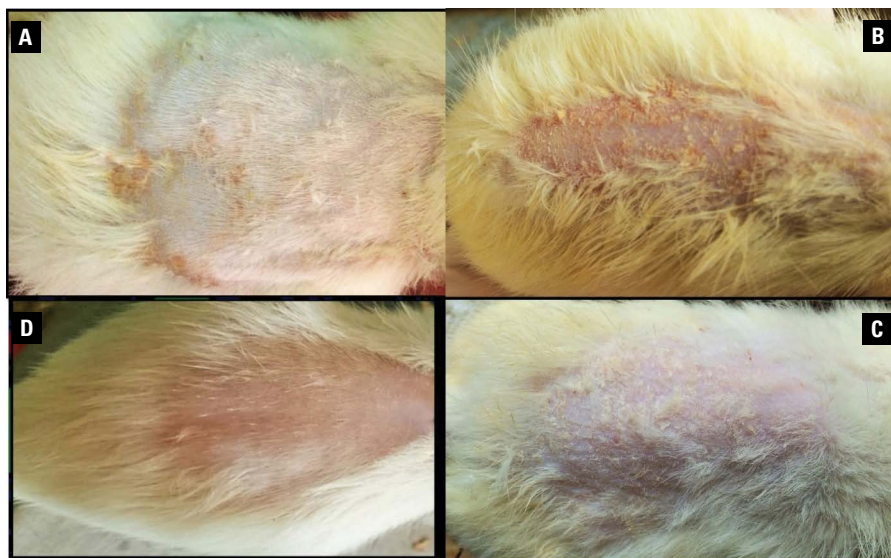
Figure 1. Gross appearance of: **A.** The normal control rat's skin showing heavy hair regrowth; **B.** The rat's skin that was treated with imiquimod (IMQ) cream for 12 days (group II). A well-demarcated erythema with overlying scale-like flakes (scaling) is observed. Note that hair regrowth is very weak; **C.** The rat's skin was topically treated by betamethasone cream preceded by IMQ cream application (group III) showing hair regrowth. No erythema is observed but still there are some scales on the skin surface; **D.** The rat's skin that received subcutaneous mesenchymal stem cells injection preceded by IMQ cream treatment (group IV) showing normal appearance of the skin with hair regrowth. No erythema or scales are observed.
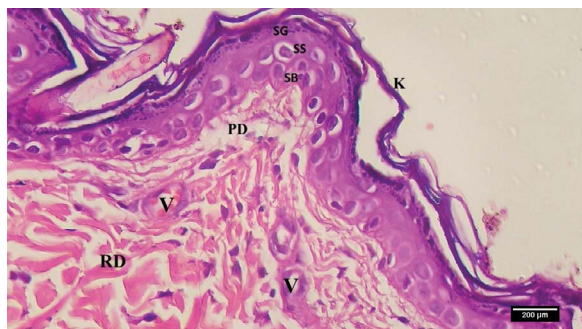

Figure 2. A light microscopic picture of a section in control rat's skin showing layers of the epidermis consisting of stratum basale (SB) which appears as basophilic columnar cells. Stratum spinosum (SS) appears as polyhedral acidophilic cells. Stratum granulosum (SG) appears containing numerous basophilic keratohyalin granules. Stratum corneum is the most superficial acellular layer and the covering acidophilic keratin scales (K) appears as a basket weave. Uniform thickness of the epidermis is obvious through the whole section. Note the papillary layer (PD) and reticular layer (RD) of the underling dermis showing collagen bundles and few blood vessels (V); H&E, ×400.

Figure 3. A light microscopic picture of a section in control rat's skin showing the papillary layer of dermis (PD) containing fine interlacing collagen fibres (arrow). The reticular layer of dermis (RD) contains thick wavy collagen fibres (C). The dermis apparently reveals few cellular elements (circle) and blood vessels (V). The epidermis is uniform in thickness with red keratin layer (K) is seen on top; Masson's trichrome, ×100.

weave appearance. The underlying papillary layer of dermis showed fine collagen fibres, patent capillaries and many connective tissue cells. The inner reticular layer of dermis was composed of dense connective tissue rich in thick collagen fibres (Fig. 2).

Masson's trichrome-stained sections showed the papillary dermis with fine interlacing collagen fibres just below the epidermis. Deeper dense and thick wavy collagen fibres appeared in the reticular dermis (Fig. 3).

Immunohistochemical staining with CD31 revealed few, sporadic positively stained new vascular endothelial cells in the wall of the dermal blood vessels mainly in the papillary layer. The blood vessels appeared with thin wall and patent lumen (Fig. 4).
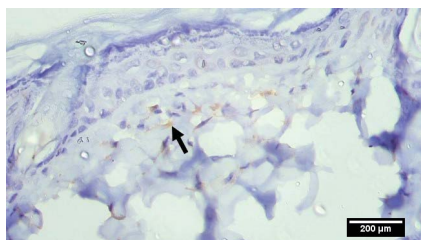
Figure 4. A light microscopic picture of an immunohistochemically stained sections with antibody for endothelial cells of the blood vessels in control rat's skin showing few, sporadic positively stained new vascular endothelial cells (arrow) in the wall of the dermal blood vessels mainly in the papillary layer; anti-CD31 antibody immune staining with Avidine-Biotin peroxidase method, ×400.
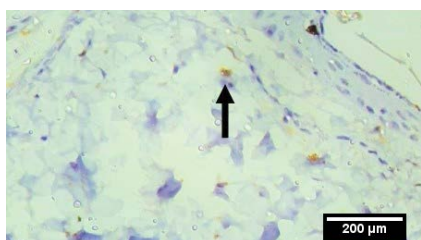

Figure 5. A light microscopic picture of an immunohistochemically stained sections with CD8 antibody in control rat's skin showing almost negative immune reaction with very few, sporadic positively stained cells (arrow) in the dermis (arrow); anti-CD8 immune staining with Avidine-Biotin peroxidase method, ×400.
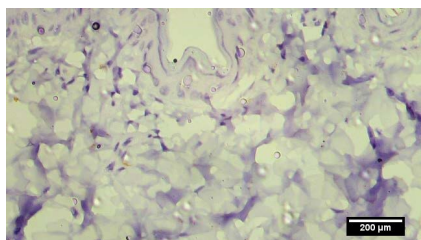

Figure 6. A light microscopic picture of an immunohistochemical stained sections of control rat's skin showing negative reaction for CD4 immune staining; anti-CD4 antibody immune staining with Avidine-Biotin peroxidase method, ×400.

Immunohistochemical staining with CD8 antibody revealed negative immune reaction with very few, sporadic positively stained cells in the dermis (Fig. 5). Immunohistochemical staining with CD4 antibody showed negative reaction (Fig. 6).

Group II (IMQ cream group)

Haematoxylin and eosin-stained sections from group II that was treated with IMQ ream for 12 days revealed apparent thickening of the epidermis (epidermal hyperplasia), elongation of the rete ridges and thinning of supra-papillary plates

Figure 7. A light microscopic picture of a rat's skin section of the group that was treated with imiquimod cream for 12 days (group II). The photo demonstrates epidermal hyperplasia (E). Elongation of the rete ridges (R), collections of immune cell infiltration (arrow) in the papillary dermis. Note thinning of the supra-papillary plates (p); H&E, ×100.

Figure 8. A light microscopic picture of a rat's skin section of the group that was treated with imiquimod cream for 12 days (group II) showing apparent proliferation of different layers of the epidermis with overcrowding of the cells at the basal layer (B). Mitotic figures are evident (curved arrow). Wide intercellular spaces between basal keratinocytes and gaps in the basement membrane underlying the epidermis and traversing inflammatory cells can be seen (arrowhead). There is no sharp demarcation between the epidermis and dermis (basement membrane is almost not visualised). Notice numerous blood vessels (V) and immune cell infiltration (arrow) in the underlying dermis; H&E, ×400.

(Fig. 7). The granular layer of the epidermis in which terminal differentiation begins was greatly reduced or absent, consequently a stratum corneum form incompletely differentiated keratinocytes that known as parakeratosis. Also, widening of the intercellular spaces between keratinocytes due to intercellular oedema known as spongiosis was seen. The basement membrane between epidermis and dermis appeared irregular and discontinuous at some area with traversing inflammatory cells into the epidermis (exocytosis). The underlying dermis showed increased angiogenesis and immune cell infiltration (Fig. 8).
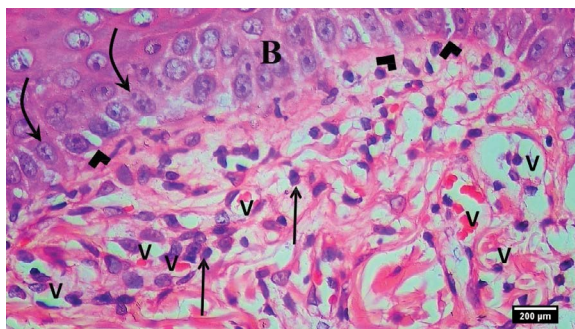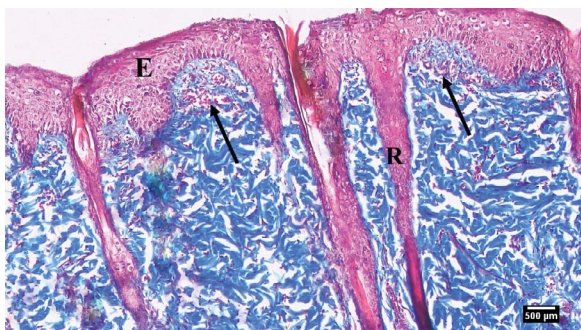
Figure 9. A light microscopic picture of a rat's skin section of the group that was treated with imiquimod cream for 12 days (group II) showing epidermal hyperplasia (E), elongation of the rete ridges (R). Numerous inflammatory cell infiltrate is seen in the dermis (arrow); Masson's trichrome, ×100.
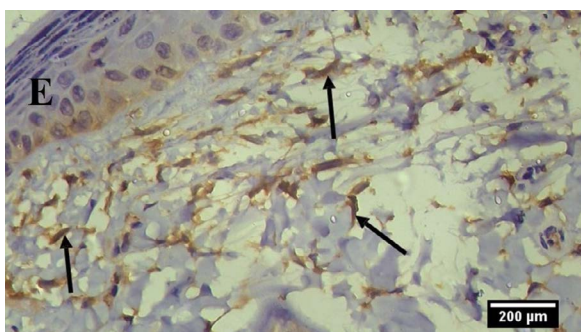

Figure 10. A light microscopic picture of an immunohistochemically stained sections with antibody for endothelial cells of the blood vessels in rat's skin section of the group that was treated with imiquimod cream for 12 days (group II). Plenty of positively stained new vascular endothelial cells (arrow) in the wall of the dermal blood vessels are seen mainly in the papillary layer of dermis. Notice also, the positive immune staining can be seen in some areas of the epidermis (E); anti-CD31 antibody immune staining with Avidine-Biotin peroxidase method, ×400.

Figure 11. A light microscopic picture of an immunohistochemically stained sections with CD8 antibody in rat's skin sections of the group that was treated with imiquimod cream for 12 days (group II). Positively immune stained CD8 cells can be seen in the papillary dermis (arrow). Positive cells are located mainly around and nearby blood vessels (V). CD8 positive immune stained cells can be visualised in the epidermis as well (E); anti-CD8 antibody immune staining with Avidine-Biotin peroxidase method, ×400.
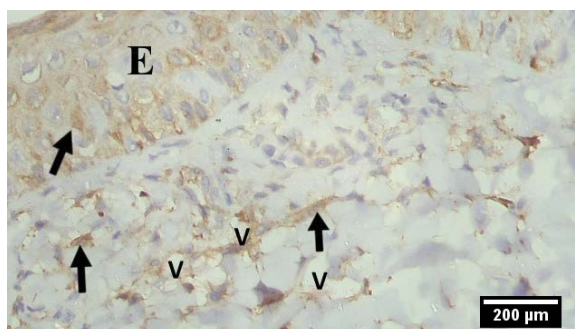
Figure 12. A light microscopic picture of an immunohistochemically stained sections with CD4 antibody in rat's skin sections of the group that was treated with imiquimod cream for 12 days (group II) showing positively immune stained CD4 cells in the papillary dermis (arrow). Positive cells are located mainly around and nearby blood vessels (V). CD4 positive immune stained cells can be visualised in the epidermis as well (E); anti-CD4 antibody immune staining with Avidine-Biotin peroxidase method, ×400.

Masson's trichrome-stained sections showed epidermal hyperplasia, elongation of the rete ridges. Also, numerous inflammatory cell infiltrate was seen particularly in the superficial dermis (Fig. 9).

Immunohistochemical staining with CD31 revealed plenty of positively stained new vascular endothelial cells in the wall of the dermal blood vessels mainly in the papillary layer of dermis. The positive immune staining also was seen in some areas of the epidermis (Fig. 10). Immunohistochemical staining with CD8 antibody revealed positively immune stained CD8 cells in the papillary dermis. CD8 positive immune stained cells were visualised in the epidermis as well (Fig. 11). Immunohistochemical staining for CD4 showed positively immune stained CD4 cells in the papillary dermis. Positive CD8 and CD4 cells were located mainly around and nearby blood vessels and both were visualized in the epidermis as well (Fig. 12).

Group III (IMQ + betamethasone group)

Haematoxylin and eosin-stained sections from the group that received betamethasone cream preceded by IMQ cream application revealed epidermis with uniform thickness covered with a thin layer of keratin. Elongation of the rete ridges into the underlying connective tissue of dermis also was seen. The epidermis was composed of 4 layers. Stratum basale was formed of crowded low columnar basophilic cells with basal oval nuclei that showed some mitotic figures. Above this layer, stratum spinosum was present and consisted of few acidophilic polygonal cells with frequent pyknotic nuclei and vac-

Figure 13. A light microscopic picture of a section in rat's skin of the group that received betamethasone cream preceded by imiquimod cream application (group III) showing the 4 layers of the epidermis. The photo displays crowded basal basophilic low columnar cells of stratum basale (SB) with some mitotic figures (short curved arrow). Note the large blood vessel containing many inflammatory cells that is located at the basal layer of the epidermis (V). Stratum spinosum (SS) appears as acidophilic polygonal cells with frequent pyknotic nuclei (double arrow) and vacuolations (arrowhead). Stratum granulosum (SG) appears as flat cells filled with many basophilic keratohyalin granules and apparently thick layer of acidophilic stratum corneum (SC). Notice that there is no sharp demarcation line between epidermis and dermis (no visible basement membrane) and travelling inflammatory cells into the epidermis is obvious (oblong shape). The underlying dermis demonstrates frequent blood vessels (V), and some collections of inflammatory cells (arrow); H&E, ×400.

Figure 14. A light microscopic picture of a section in rat's skin of the group that received betamethasone cream preceded by imiquimod cream application (group III) showing thick hypertrophied epidermis (E). The underlying papillary layer of dermis (PD) containing fine interlacing collagen fibres (arrow). The reticular layer of dermis (RD) contains thick wavy collagen fibres (C). Numerous transversely cut hair follicles (H) and sebaceous glands (S) are visible; Masson's trichrome, ×100.

uolations. Stratum granulosum consisted of 2 rows of spindle-shaped cells with basophilic granular cytoplasm. Finally, the stratum corneum appeared to be formed of acidophilic thick layer. No sharp demarcation line be-
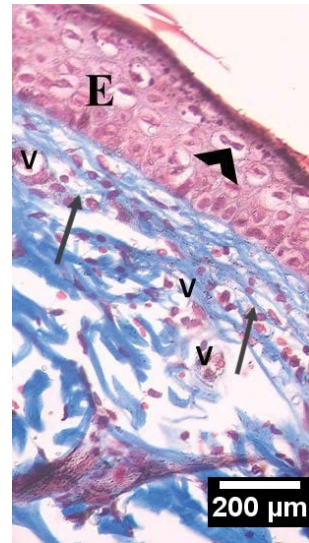
Figure 15. A higher magnification of Figure 14 showing the epidermis with crowded basal layer, many pyknotic nuclei (arrow head) in spongy layer. The underlying papillary dermis shows inflammatory cells (arrow) particularly localized around the dermal blood vessels (v); Masson's trichrome, ×400.

tween epidermis and dermis was seen with travelling inflammatory cells into the epidermis. The underlying dermis showed frequent blood vessels and some collections of inflammatory cells (Fig. 13).

Masson's trichrome-stained sections showed crowded basal layer in the epidermis with many pyknotic nuclei in spongy layer. The underlying papillary dermis showed inflammatory cells particularly localized around the dermal blood vessels (Figs. 14, 15).

Immunohistochemical staining with antibody for endothelial cells of the blood vessels CD31 antibody immune stained with Avidin-Biotin peroxidase method revealed moderate number of positively stained new vascular endothelial cells in the wall of the dermal blood vessels mainly in the papillary layer (Fig. 16). Immunohistochemical staining for CD8 antibody revealed few sporadic positively immune stained CD8 cells in the papillary dermis (Fig. 17). Immunohistochemical staining for CD4 antibody revealed positively immune stained CD4 cells in the papillary dermis. Positive cells were located mainly around and nearby blood vessels (Fig. 18).
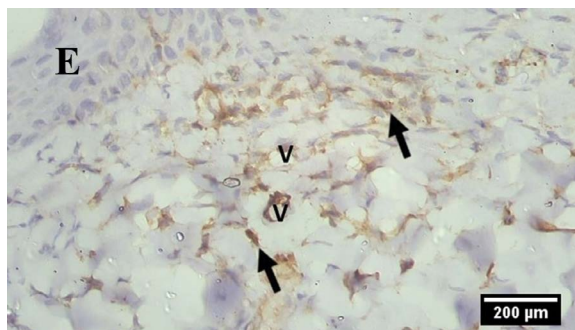
Group IV (IMQ + hUCB-MSCs)

Haematoxylin and eosin-stained sections from the group that received one subcutaneous umbilical cord derived MSCs injection preceded by IMQ cream revealed epidermis with uniform thickness that lied on a straight basement membrane and covered with
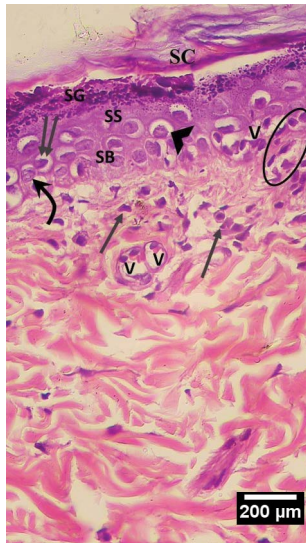
Figure 16. A light microscopic picture of an immunohistochemically stained sections with antibody for endothelial cells of the blood vessels in rat's skin of the group that received betamethasone cream preceded by imiquimod cream application (group III) showing moderate number of positively stained new vascular endothelial cells (arrow) in the wall of the dermal blood vessels mainly in the papillary layer. Also, positive immune stained cells are observed in the epidermis (arrowhead); anti-CD31 antibody immune staining with Avidine-Biotin peroxidase method, ×400.

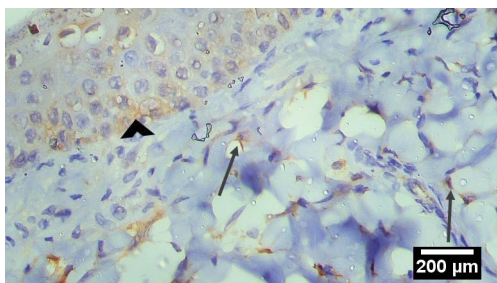**Figure 17.** A light microscopic picture of an immunohistochemically stained sections with CD8 antibody in rat's skin sections of group that received betamethasone cream preceded by imiquimod cream application (group III) showing few sporadic positively immune stained CD8 cells in the papillary dermis (arrow); anti-CD8 antibody immune staining with Avidine-Biotin peroxidase method, ×400.
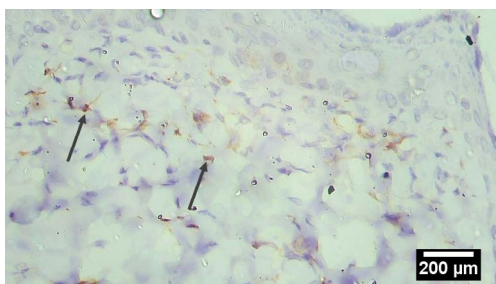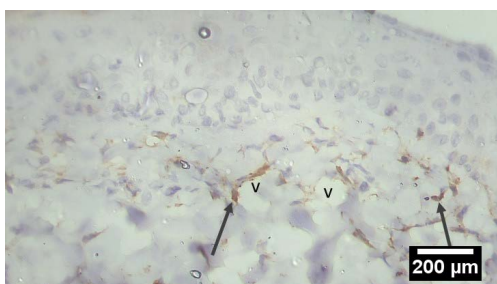

Figure 18. A light microscopic picture of an immunohistochemically stained sections with CD4 antibody in rat's skin sections of group that received betamethasone cream preceded by imiquimod cream application (group III) showing positively immune stained CD4 cells in the papillary dermis (arrow). Positive cells are located mainly around and nearby blood vessels (V); anti-CD4 antibody immune staining with Avidine-Biotin peroxidase method, ×400.

a very thin keratin layer. The layers of the epidermis consisted of stratum basale which appeared as basophilic columnar cells resting on a straight continuous

Figure 19. A light microscopic picture of a section of rat's skin of the group that received subcutaneous mesenchymal stem cells injection preceded by imiquimod cream application (group IV). The photo depicts layers of the epidermis consisting of stratum basale (SB) which appears as basophilic columnar cells resting on a straight continuous basement membrane, stratum spinosum (SS) appears as polyhedral acidophilic cells. Stratum granulosum (SG) appears containing numerous basophilic granules. Stratum corneum (SC) is the most superficial acellular layer. Some keratocytes show pyknotic nuclei (curved arrow), other reveal vacuolation (arrowhead). Uniform thickness of the epidermis is obvious through the whole section. Note the papillary layer (PD) and reticular layer (RD) of the underling dermis which demonstrate few blood vessels (V) and connective tissue cells (arrow); H&E, ×400.

basement membrane. Stratum spinosum appeared as polyhedral acidophilic cells. Stratum granulosum appeared containing numerous basophilic granules. Stratum corneum was the most superficial acellular layers. A clear border demarcation was seen between the epidermis and the dermis with apparently intact basement membrane. The underling dermis showed few blood vessels and connective tissue cells (Fig. 19).

Masson's trichrome-stained sections showed papillary layer of dermis containing fine interlacing collagen fibres. The reticular layer of dermis showed thick wavy collagen fibres. The sharp demarcation between the epidermis and dermis was evident (Fig. 20).

Immunohistochemical staining with CD31 revealed few, sporadic positively stained new vascular endothelial cells in the wall of the dermal blood vessels mainly in the papillary layer (Fig. 21). Immunohistochemical staining for CD8 and CD4 antibodies revealed negative immune reaction (Figs. 22, 23).

Using TEM, the epidermis of rat's skin of IMQ treated group II showed apparent proliferation of the epidermis with overcrowded basal layer which
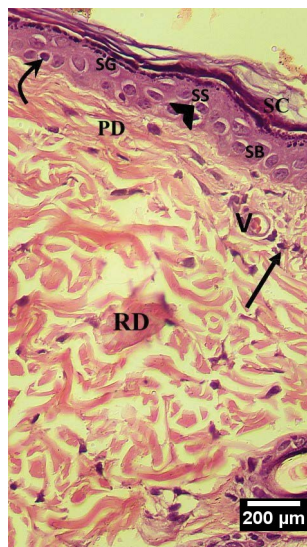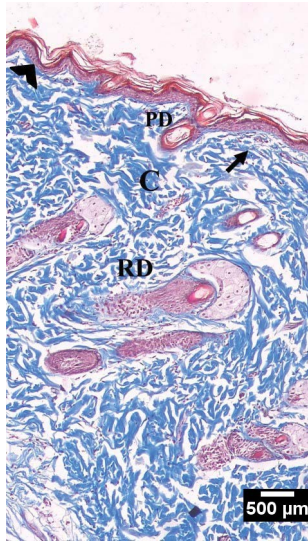
Figure 20. A light microscopic picture of a section in rat's skin of the group receiving subcutaneous mesenchymal stem cells injection preceded by imiquimod cream application (group IV) showing the papillary layer of dermis (PD) containing fine interlacing collagen fibres (arrow). The reticular layer of dermis (RD) contains thick wavy collagen fibres (C). Sharp demarcation between the epidermis and dermis is evident (arrowhead); Masson's trichrome, ×100.
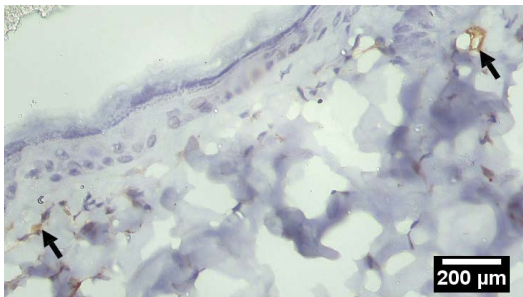

Figure 21. A light microscopic picture of an immunohistochemically stained sections with antibody for endothelial cells of the blood vessels in rat's skin of the group receiving subcutaneous mesenchymal stem cells injection preceded by imiquimod cream application (group IV) showing few, sporadic positively stained new vascular endothelial cells (arrow) in the wall of the dermal blood vessels mainly in the papillary layer; anti-CD31 antibody immune staining with Avidine-Biotin peroxidase method, ×400.

was loosely attached to the resting basement membrane. Wide intercellular spaces within the basal layer and large gaps between them and the underlying basement membrane were obviously seen. While in the MSCs-treated group IV, there were no gaps seen between the tightly connected cells of the basal layer and the resting basement membrane (Fig. 24). In IMQ-treated group, the stratum basale cells resting on a basement membrane appeared irregular in shape with tendency of mitosis and division of its dense nucleolus with wide intercellular spaces. The resting
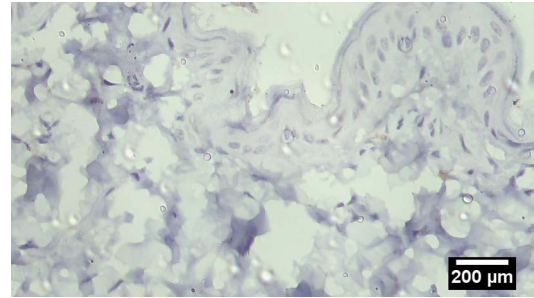
Figure 22. A light microscopic picture of an immunohistochemically stained sections with CD8 antibody in rat's skin of the group receiving subcutaneous mesenchymal stem cells injection preceded by imiquimod cream application (group IV) showing negative immune reaction; anti-CD8 antibody immune staining with Avidine-Biotin peroxidase method, ×400.
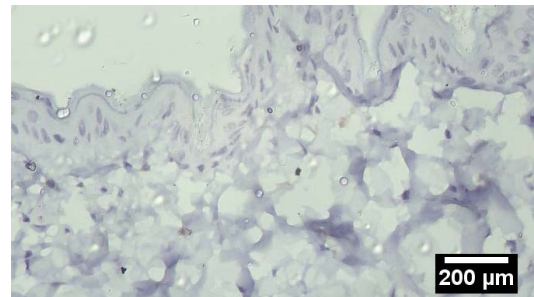
Figure 23. A light microscopic picture of an immunohistochemically stained sections with CD4 antibody in rat's skin of the group receiving subcutaneous mesenchymal stem cells injection preceded by imiquimod cream application (group IV) showing negative reaction for CD4 immune staining; anti-CD4 antibody immune staining with Avidine-Biotin peroxidase method, ×400.

basement membrane showed large gaps and absence of hemidesmosomes connecting it to the basal layer. While in MSCs-treated group the stratum basale cells appeared columnar in shape with elongated euchromatic nucleus and dense nucleolus. These cells have processes that were connected tightly together by desmosomes and were connected with the basement membrane by hemidesmosomes (Figs. 25, 26, 27).

Morphometric results and statistics

Thickness of the epidermis

Measuring of the epidermal thickness in H&E-stained sections under high power field of light microscope revealed highly statistically significant increase in the epidermal thickness in group II (IMQ-treated) and the betamethasone-treated group III compared to the control (group I) (p < 0.001). In MSCs-treated group IV, there was a highly significant decrease in the epidermal thickness as compared to group II (IMQ-treated) (p < 0.001) (Table 1, Fig. 28).
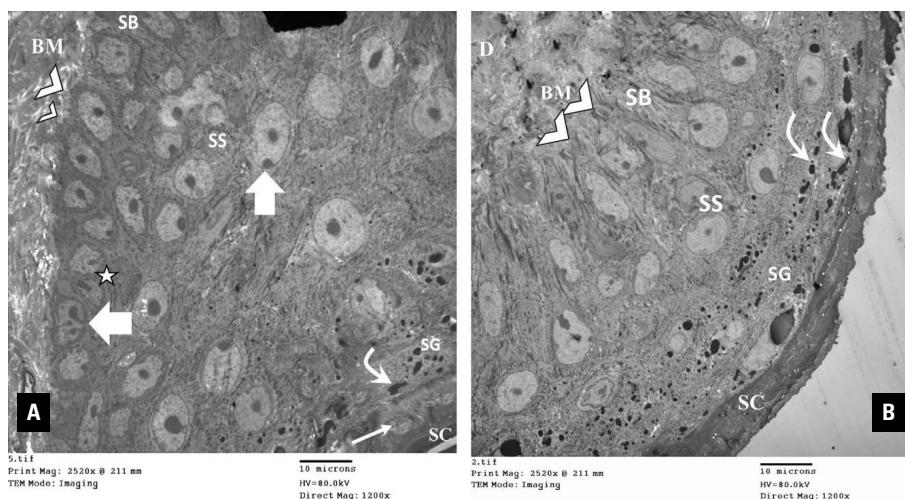
Figure 24. A. An electron photomicrograph of a section in the epidermis of rat's skin of the group that was treated with Aldara cream for 12 days showing apparent proliferation of different layers of the epidermis with overcrowding of the cells of the basal layer. Stratum basale (SB) cells resting on a loosely attached basement membrane (BM). The cells appear columnar in shape with elongated euchromatic nucleus and dense nucleolus; however, some cells appear irregularly in shape (asterisk). Notice the wide intercellular spaces within the basal layer and the large gaps (arrowhead) between them and the underlying basement membrane. In stratum spinosum (SS) keratinocytes are polygonal in shape with rounded euchromatic nucleus and electron dense nucleolus. Mitotic figures are evident (thick arrow). In stratum granulosum layer (SG), the cytoplasm of the cells contains few keratohyalin granules (curved arrow). Notice the superficial stratum corneum (SC) with many cytoplasmic and nuclear remnants (parakeratosis) (arrow); **B.** After receiving subcutaneous mesenchymal stem cells injection preceded by Aldara cream application showing stratum basale (SB) cells resting on a basement membrane (BM) separating it from the underlying dermis (D). the cells are connected with the basement membrane by hemidesmosomes (arrowhead). In stratum spinosum (SS) keratinocytes are polygonal in shape with rounded euchromatic nucleus and electron dense nucleolus. In stratum granulosum (SG) The cells have oblong euchromatic nucleus, the cytoplasm contains keratohyalin granules (curved arrow). Notice the superficial stratum corneum (SC) non-nucleated cells with electron dense patches of keratin; TEM ×1200.
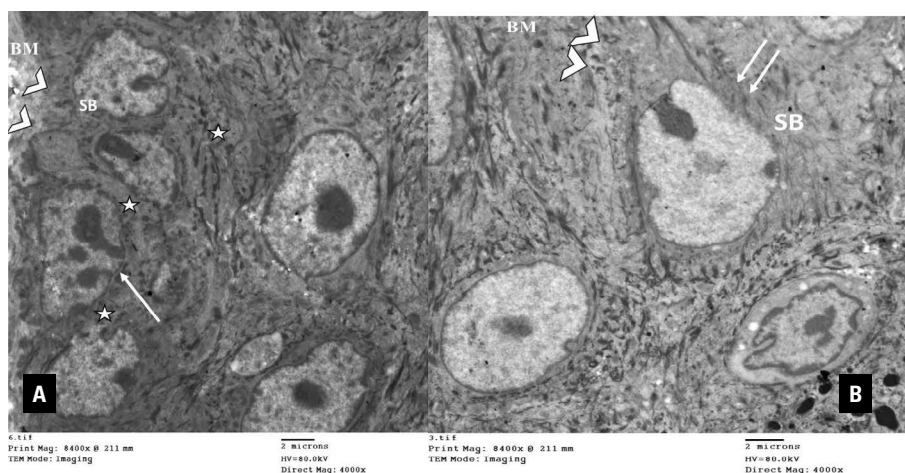
Figure 25. A. A higher magnification of a part of section of Figure 24A showing stratum basale (SB) cells resting on a basement membrane (BM). The cells appear irregular in shape with tendency of mitosis and division of its dense nucleolus (arrow). Notice the wide intercellular spaces between them (*). The resting basement membrane shows large gaps and absence of hemidesmosomes connecting it to the basal layer (arrowhead); **B.** After subcutaneous mesenchymal stem cells injection preceded by Aldara cream application showing stratum basale (SB) cells resting on a basement membrane (BM). The cells appear columnar in shape with elongated euchromatic nucleus and dense nucleolus. The cells have processes that are connected together by desmosomes (arrow) and are connected with the basement membrane by hemidesmosomes (arrowhead); TEM ×4000.

Blood vessels count

Counting the number of new blood vessels in H&E-stained sections under low power field of light microscope, revealed highly statistically significant increase in the number of new blood vessel formation in group II (IMQ-treated), significant increase in
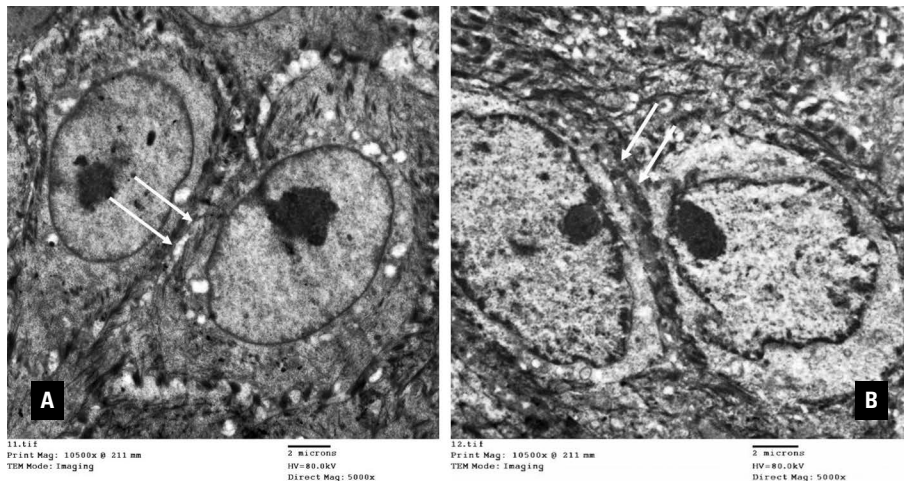
Figure 26. A. An electron photomicrograph of a section in the epidermis of rat's skin of the group that was treated with Aldara cream for 12 days showing stratum basale cells. The cells appear columnar in shape with elongated euchromatic nucleus and dense nucleolus. The cells show wide intercellular spaces where they lost their desmosomal connections (arrow); **B.** After receiving subcutaneous mesenchymal stem cells injection preceded by Aldara cream application showing stratum basale cells. The cells appear columnar in shape with elongated euchromatic nucleus and dense nucleolus; TEM ×5000.
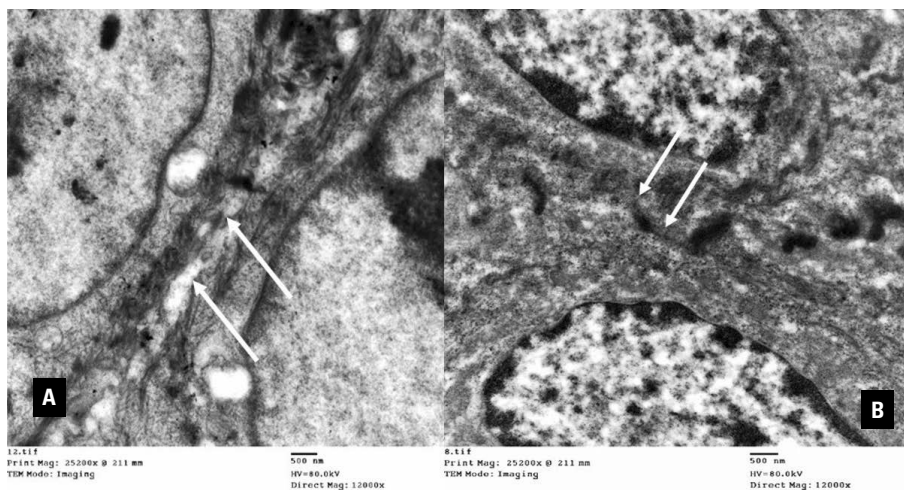
Figure 27. A. A higher magnification of a part of section of Figure 26A showing the wide intercellular spaces between the epidermal cells where they lost their desmosomal connections (arrow); **B.** After receiving subcutaneous mesenchymal stem cells injection preceded by Aldara cream application showing stratum basale cells. The cells have processes that are connected together tightly by desmosomes (arrow); TEM ×12000.

betamethasone-treated group III and non-significant increase in MSCs-treated group IV, compared to the control (group I). While in betamethasone-treated group III and MSCs-treated group IV, there was a highly significant decrease in the number of new blood vessel formation as compared to group II (IMQ-treated) ($p < 0.001$) (Table 1, Fig. 29).

Inflammatory cells count

The numbers of inflammatory cells in H&E-stained sections under high power field of light microscope, revealed highly statistically significant increase in the number of inflammatory cells in group II (IMQ-treated) and in betamethasone-treated group III and non-significant increase in MSCs-treated group IV compared to the control (group I). While in betamethasone-treated group III and MSCs-treated group IV, there was a highly significant decrease in the number of inflammatory cells as compared to group II (IMQ-treated) ($p < 0.001$) (Table 1 Fig. 30).

DISCUSSION

The current work was designed to investigate the possible effect of human umbilical cord-derived MSCs

Table 1. Histomorphometric parameters in the four study groups

Mean ± standard deviation of	Control group	IMQ--treated group	Betamethasone--treated group	MSCs--treated group
Epidermal thickness/high power field	0.5636 ± 0.23	6.28 ± 1.06 (p < 0.001)[a]	1.47 ± 0.28 (p < 0.001)[a] (p < 0.001)[d]	0.8 ± 0.3 (p = 0.05)[b] (p < 0.001)[d] (p < 0.001)[e]
Blood vessels count	12.2 ± 2.5	36.2 ± 5.11 (p < 0.001)[a]	17.2 ± 2.1 (p < 0.001)[a] (p < 0.001)[d]	15.4 ± 1.7 (p = 0.36)[c] (p < 0.001)[d] (p = 0.053)[f]
Inflammatory cells count	17.2 ± 0.81	92 ± 0.98 (p < 0.001)[a]	27.1 ± 3.1 (p < 0.001)[a] (p < 0.001)[d]	18.7 ± 3.27 (p = 0.07)[c] (p < 0.001)[d] (p < 0.001)[e]

[a]Highly significant increase in comparison with control group; [b]Significant increase in comparison with control group; [c]Non-significant increase in comparison with control group; [d]Highly significant decrease in comparison with IMQ-treated group; [e]Highly significant decrease in comparison with betamethasone-treated group; [f]Significant decrease in comparison with betamethasone-treated group; IMQ — imiquimod; MSC — mesenchymal stem cell
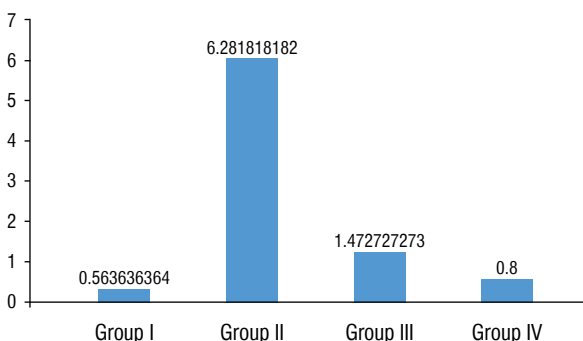
Figure 28. Mean thickness of the epidermis in micrometer.
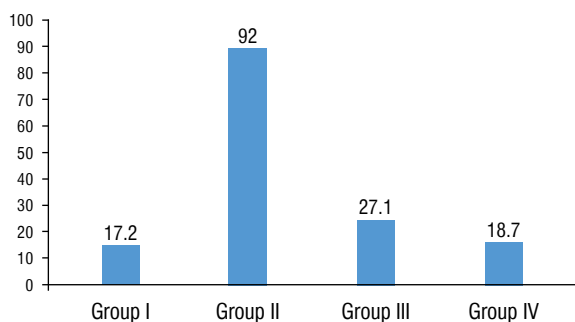
Figure 30. Mean inflammatory cells count.
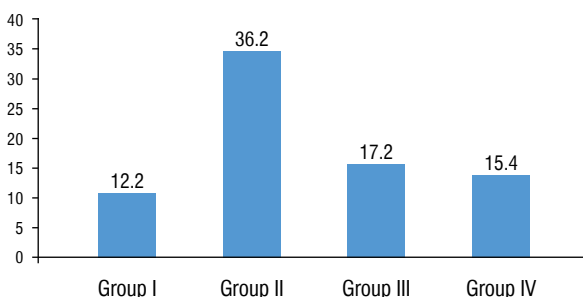
Figure 29. Mean blood vessels count.

versus conventional betamethasone cream treatment on imiquimod-induced psoriasis-like skin lesion in adult male albino rat model. Psoriasis appears to be a uniquely human disease, it exclusively affects human among all animals with two reported exceptions; a rhesus monkey [24] and a cynomolgus monkey [40].

This lack of a suitable animal model has greatly hindered research into the pathogenesis and treatment of psoriasis. Over the past decades, numerous mouse models have been identified by genetic engineering and xenografting (human psoriatic skin grafted to immuno-deficient mice) as an attempt to reproduce psoriasis. Extensive comparisons between these models have been made in different reviews [3, 9, 13]. However, not all these models reflect all clinical, histological and immunophenotypic characteristics of human psoriasis as described by Irfan et al. [16] who reported that imiquimod-induced psoriasis-like skin inflammation in mice model is considered to have the same and most closely resemblance with human psoriasis.

Jason et al. [18] added that the IMQ mouse model offers scientists several excellent advantages; easy to use, inexpensive, and needs short treatment duration to elicit acute skin inflammation.

Nestle and Nickoloff [29] defined several criteria for an ideal psoriasis model which are: 1) epidermal changes based on keratinocyte hyperproliferation and altered differentiation; 2) papillomatosis (regular and symmetrical extension of rete ridges, separated by elongated dermal papillae); 3) presence of inflammatory cells including T cells, dendritic cells, and neutrophils; 4) altered vascularity. In the present study, gross examination of the skin treated by IMQ cream (group II) showed signs of acute skin inflammation as erythema, scaling and thickening (induration) after 2–3 days from the start of experiment. These signs gradually worsened with continued treatment till the end of the experiment. Similar findings were described by van der Fits et al. [39]. The results presented in the current work showed that IMQ-induced skin inflammation clearly and consistently fulfils the previous criteria 1, 2, 3, 4.

These clinical features were explained by Bochenska et al. [3] who reported that the erythema represents the degree of vasodilatation in the dermis to which multiple cytokines (interleukin 1 [IL-1] and tumour necrosis factor alpha [TNF-α]) and compounds like (NO, phospholipase A2, metabolites and histamine) from various cellular sources (keratinocytes, dendritic cells, mast cells) contribute. Skin thickness or induration is the result of increased keratinocytes proliferation due to stimulation by proinflammatory cytokines as well as dermal infiltration by inflammatory cells. Scaling reflects abnormal keratinocyte differentiation and maturation due to increased proliferation and the abnormal cytokine medium. Hence, squamous keratinocytes aberrantly retain intact nuclei (parakeratosis) and release few extracellular lipids that normally cement adhesions of corneocytes. Therefore, poorly adherent stratum corneum is formed and this results in the characteristic scales of psoriasis, a phenomenon typical for psoriasis skin lesions.

While the naked eye observation of the betamethasone-treated group (group II) and MSCs-treated group (group IV) in the present study showed that the psoriatic erythema, scaling and thickening were highly reduced compared with the IMQ group. However, in group III there were still some scales on the skin surface. While in group IV no erythema or scales were observed with normal hair regrowth.

Examination of H&E-stained sections of IMQ-treated group of rats in the present study showed increased epidermal thickening (acanthosis) which was statistically highly significant compared to the control group. Also, retention of nuclei in the stratum corneum (parakeratosis) and absence of the granular layer was observed in contrast to the control group. These findings coincided with those of Sah et al. [36] and Chamcheu et al. [4] who added that these histological findings are interestingly mimicking those of human samples of patients with active psoriasis taken in the same study.

Also, in the present study examining H&E-stained sections of IMQ-treated group showed widening of the intracellular spaces between keratinocytes was obviously observed and this was due to the intercellular oedema known as spongiosis that was reported by Murphy et al. [27] who added that spongiosis was observed in the early stage while it became minimal or absent in the fully developed clinical plaque due to extension of inflammatory cells migration from the papillary capillaries via the thinned supra-papillary plates into the epidermis (exocytosis).

Exocytosis was observed in the H&E-stained sections of IMQ-treated group in the present study and confirmed by immunohistochemical staining of CD4 and CD8 cells as some inflammatory cells traversed into the epidermis through the irregular and discontinuous basement membrane.

Ghoreschi et al. [12] stated that the dermis of psoriatic skin is infiltrated predominantly by CD4-positive Th cells, which produce proinflammatory cytokines such as interferon (IFN)-c, TNF and IL-17. Also, elevated levels of IL-6, IL-8 and keratinocyte growth factor (transforming growth factor-alpha) are found in psoriatic lesions Thus, an intense cross-talk between immune cells and keratinocytes seems to establish an interactive cytokine network, responsible for the development of psoriasis.

In the present study, there was a statistical increase of the numbers of the inflammatory cells in the papillary dermis of the IMQ-treated group which was highly significant compared to the control group. It was found that the inflammatory infiltrate was largely composed of CD4 and CD8 T cells as confirmed by immunohistochemical staining using (CD4 and CD8) antibodies as markers for these cells which revealed positively immune stained CD4 and CD8 cells in the papillary dermis and they were visualized also in the epidermis.

Similar findings were described by Hawkes et al. [14] and Ogawa et al. [30] who stated that activated CD4 and CD8 lymphocytes were initially considered to be equally important in the inflammation associated with psoriasis because large numbers of activated CD4 and CD8 lymphocytes were identified in the skin and peripheral blood of psoriatic patients.

Disruption of the basement membrane and the impairment of the skin barrier function was described as a feature for psoriasis in the mouse model by Raychaudhuri et al. [34] and was confirmed recently by the study of Jabeen et al. [17] who evaluated the disruption of skin barrier in the IMQ-treated mouse model by measuring the trans-epidermal water loss which reached a significant high value after 4 days of IMQ application.

The electron microscopic examination of the IMQ-treated group in the current work confirmed the light microscopic observations and showed that the intercellular spaces especially within the basal layer were considerably widened losing the desmosomal contacts in between the basal keratinocytes. Also, the resting basement membrane showed large gaps and absence of hemidesmosomes connecting it to the basal layer.

The present ultrastructure findings coincided with Natsumi et al. [28] who reported that several gaps of lamina densa of the basement membrane were detected in IMQ psoriasis model mouse.

In the current study, H&E-stained sections of IMQ-treated group showed increased angiogenesis and immune cell infiltrations in the underlying dermis. These findings were obviously noticed and confirmed by Masson's trichrome stain.

In the present work, there was a statistical increase of the numbers of dermal blood vessels of the IMQ-treated group which was highly significant compared to the control group. This increased vascularisation was visualised also by immunohistochemical staining using (CD31) antibody as a marker for endothelial blood vessels which revealed plenty of positively stained new vascular endothelial cells in the wall of the dermal blood vessels mainly in the papillary layer of dermis. The positive immune staining also was seen in some areas of the epidermis.

On the other hand, close examination of H&E-stained sections of rats of betamethasone-treated group and MSCs-treated group in the present study showed some differences between them although both of them showed decrease in the epidermal thickening which was statistically highly significant compared to the IMQ group, but the thickness of the epidermis in betamethasone group was not uniform with some areas of apparent increased thickness with crowded basal layer and no sharp demarcation line between epidermis and dermis. However, the underlying dermis of the two groups showed a decrease in the newly formed blood vessels and the inflammatory cells, which was statistically highly significant compared to the IMQ group. This decreased vascularisation was visualized also by immunohistochemical staining using (CD31) antibody as a marker for endothelial blood vessels which revealed few, sporadic positively stained new vascular endothelial cells in the wall of the dermal blood vessels mainly in the papillary layer.

These findings were explained by Chen et al. [7] who reported that corticosteroids are potent anti-inflammatory agents that block several inflammatory pathways and induce apoptosis of inflammatory cells but could not promote the differentiation of keratinocytes and inhibit the proliferation of keratinocytes as well as suppressing cytokine production by T cells, dendritic cells and keratinocytes. Thus, the mechanism of action of corticosteroids allows it to be only used in combination therapy with other topical agents that may improve their efficacy and safety profile over longer periods.

In group IV (MSCs-treated group), sections stained by H&E showed uniform thickness of the epidermis lying on intact basement membrane where a clear border of demarcation was seen between the epidermis and dermis. These findings were confirmed by Masson's trichrome-stained sections and by the electron microscopic examination that showed no wide intercellular spaces between the epidermal basal layer where the cells connected tightly together by desmosomes and were connected with the basement membrane by hemidesmosomes.

These ultrastructure findings could be explained in view of the study of Shin et al. [38] who reported that the electron microscopic analysis revealed that subcutaneous injection of human adipose tissue-derived mesenchymal stem cells in an oxazolone-induced atopic dermatitis model remarkably reduced trans-epidermal water loss by restoring normal epidermal barrier functions which are keratinocyte differentiation, epidermis development, and establishment of intact basement membrane.

In the present work, MSCs demonstrated efficacy in reduction of disease severity through regulating multiple pathways. Psoriatic symptoms, higher expression of inflammatory mediators, and the infiltration of immune cells to the skin were all alleviated after MSC administration. This shows that the MSC infusion had immunomodulatory and anti-inflammatory effects, thereby strongly inhibiting the severity and development of psoriasis as reported by other studies like Rokunohe et al. [35] who used adipose tissue-derived MSCs, Owczarczyk-Saczonek et al. [31] who used bone marrow-derived MSCs, Imai et al. [15] who used human amnion-derived MSCs and Chen et al. [6] who used hUCB-MSCs.

Immunohistochemical staining examination using (CD4 and CD8) antibodies in the MSCs-treated group in the current study revealed negative immune reaction. Similar findings were reported by Sah et al. [36]; Lee et al. [23] who added that MSCs can exert immunosuppressive effect by inducing apoptosis in CD8 T cells, inhibiting CD4 T cells proliferation and Th17 cell differentiation and induce regulatory T cells (Treg) differentiation.

Th17 cell homeostasis is the relationship with Tregs, whose imbalance may lead to the development of psoriasis as described by Rafei et al. [33] who confirmed that MSCs inhibit the activity of the Th17 cell, reducing the expression of IL-17 and decreasing inflammatory cell infiltration in the central nervous system.

Park et al. [32] found that human embryonic MSCs in experimental autoimmune arthritis suppressed T-cell proliferation, and down-regulated pro-inflammatory cytokine production. Moreover, these therapeutic effects were associated with an increase in CD4 Treg cells, inhibition of Th17 cell formation, and inhibited osteoclast differentiation.

In the current study, it was strongly believed that the beneficial effect of the MSCs on prevention the severity and progression of psoriasis may be due to the regulation of immune cell infiltration especially Th17 cells and by regulating epidermal functions and differentiations as reported by Kim et al. [20] who stated that the serum level of the Th1 cytokines (TNF-alpha, IFN-a, IFN-c, and IL-27) and Th17 cytokines (IL-17A and IL-23) were dramatically reduced by MSCs, which means that subcutaneous-injection of MSCs inhibit systemic IMQ-induced inflammation.

Kim et al. [20] added that there was correlation of the data from the skin lesions with the serum data. These results suggested that MSCs suppress the Th1- and Th17-associated cytokines and the psoriatic skin changes induced by IMQ.

The treatment and management of psoriasis is complex and depends on the patient's symptoms. The current clinical management of psoriasis generally involves topical corticosteroids and vitamin D3 analogues. However, the efficacy of topical agents has been reported to be limited for patients with moderate-to-severe psoriasis and is accompanied by side effects with long-term application. Moreover, systemic immunosuppressants including methotrexate and cyclosporine have been reported to carry the risk of teratogenicity and other side effects. More recently, new biological agents including anti-17 (secukinumab, ixekizumab, and brodalumab) and anti-23 (tildrakizumab, guselkumab, and risankizumab) antibodies have been approved for the treatment of psoriatic disease. However, they are expensive and several adverse reactions have been also reported [14]. Therefore, alternative treatment with more efficacy and safety is important in psoriasis.

A recent comprehensive review discussed by Park et al. (2021) [32] who reported that 6 patients affected by psoriasis were described in 4 clinical studies. Despite significant differences in their therapeutic protocols and clinical outcomes, the MSC-based regimens were efficacious in 100% of the cases. Chen et al. [5], reported 2 cases of patients affected by psoriasis vulgaris treated with umbilical cord derived MSCs (hUCB-MSCs). Both of them had no recurrence for 4 years. They assumed that MSCs might be involved in the following four aspects: migration to skin lesions, immunomodulation, limitation of autoimmunity. However, they caution that more cases are needed to determine the efficacy of hUCB-MSCs and their infusion dose, method, and delivery time.

CONCLUSIONS

The data presented here suggest that the application of hUCB-MSCs raises hope for developing a new, safe and effective therapy for psoriatic patients, although it still requires a lot of new research.

Conflict of interest: None declared

REFERENCES

1. Akeshita J, Grewal S, Langan S, et al. Psoriasis and comorbid diseases. J Am Acad Dermatol. 2017; 76(3): 393–403, doi: 10.1016/j.jaad.2016.07.065.

2. Bancroft JD, Gamble M. Theory and Practice of Histological Techniques. 6th ed. Churchill Livingstone, London 2008: London.

3. Bocheńska K, Smolińska E, Moskot M, et al. Models in the research process of psoriasis. Int J Mol Sci. 2017; 18(12), doi: 10.3390/ijms18122514, indexed in Pubmed: 29186769.

4. Chamcheu JC, Chaves-Rodriquez MI, Adhami VM, et al. Upregulation of PI3K/AKT/mTOR, FABP5 and PPARβ/δ in human psoriasis and imiquimod-induced murine psoriasiform dermatitis model. Acta Derm Venereol. 2016; 96(6): 854–856, doi: 10.2340/00015555-2359, indexed in Pubmed: 26833029.

5. Chen Hu, Niu JW, Ning HM, et al. Treatment of psoriasis with mesenchymal stem cells. Am J Med. 2016; 129(3): e13–e14, doi: 10.1016/j.amjmed.2015.11.001, indexed in Pubmed: 26582058.

6. Chen M, Peng J, Xie Qi, et al. Mesenchymal stem cells alleviate moderate-to-severe psoriasis by reducing the production of type i interferon (IFN-I) by plasmacytoid dendritic cells (pDCs). Stem Cells Int. 2019; 2019: 6961052, doi: 10.1155/2019/6961052, indexed in Pubmed: 31827531.

7. Chen W, Gong Yu, Zhang X, et al. Decreased expression of IL-27 in moderate-to-severe psoriasis and its anti-inflammation role in imiquimod-induced psoriasis-like mouse model. J Dermatol Sci. 2017; 85(2): 115–123, doi: 10.1016/j.jdermsci.2016.11.011, indexed in Pubmed: 27939414.

8. Connick P, Kolappan M, Crawley C, et al. Autologous mesenchymal stem cells for the treatment of secondary progressive multiple sclerosis: an open-label phase 2a proof-of-concept study. Lancet Neurology. 2012; 11(2): 150–156, doi: 10.1016/s1474-4422(11)70305-2.

9. Conrad C, Nestle FO. Animal models of psoriasis and psoriatic arthritis: an update. Curr Rheumatol Rep. 2006; 8(5): 342–347, doi: 10.1007/s11926-006-0063-x, indexed in Pubmed: 16973107.

10. de la Portilla F, Alba F, García-Olmo D, et al. Expanded allogeneic adipose-derived stem cells (eASCs) for the treatment of complex perianal fistula in Crohn's disease: results from a multicenter phase I/IIa clinical trial. Int J Colorectal Dis. 2013; 28(3): 313–323, doi: 10.1007/s00384-012-1581-9, indexed in Pubmed: 23053677.

11. Drury R, Wallington E. Carleton's Histologiacal Technique. 5th ed. London, New York, Tronto 1980: 520.

12. Ghoreschi K, Weigert C, Röcken M. Immunopathogenesis and role of T cells in psoriasis. Clin Dermatol. 2007; 25(6): 574–580, doi: 10.1016/j.clindermatol.2007.08.012, indexed in Pubmed: 18021895.

13. Gudjonsson JE, Johnston A, Dyson M, et al. Mouse models of psoriasis. J Invest Dermatol. 2007; 127(6): 1292–1308, doi: 10.1038/sj.jid.5700807, indexed in Pubmed: 17429444.

14. Hawkes JE, Chan TC, Krueger JG. Psoriasis pathogenesis and the development of novel targeted immune therapies. J Allergy Clin Immunol. 2017; 140(3): 645–653, doi: 10.1016/j.jaci.2017.07.004, indexed in Pubmed: 28887948.

15. Imai Y, Yamahara K, Hamada A, et al. Human amnion-derived mesenchymal stem cells ameliorate imiquimod-induced psoriasiform dermatitis in mice. J Dermatol. 2019; 46(3): 276–278, doi: 10.1111/1346-8138.14768, indexed in Pubmed: 30632187.

16. Irfan AR, Vivek KB, Jonghun H, et al. Imiquimod-induced psoriasis-like skin inflammation in mouse model. Bangladesh J Pharmacol. 2016; 11(4): 849–851, doi: 10.3329/bjp.v11i4.28662.

17. Jabeen M, Boisgard AS, Danoy A, et al. Advanced characterization of imiquimod-induced psoriasis-like mouse model. Pharmaceutics. 2020; 12(9), doi: 10.3390/pharmaceutics12090789, indexed in Pubmed: 32825447.

18. Jason EH, Johann G, Nicole WL, et al. The snowballing literature on imiquimod-induced skin inflammation in mice: a critical appraisal. J Invest Dermatol. 2017; 137(3): 546–549, doi: 10.1016/j.jid.2016.10.024, indexed in Pubmed: 27955901.

19. Kern S, Eichler H, Stoeve J, et al. Comparative analysis of mesenchymal stem cells from bone marrow, umbilical cord blood, or adipose tissue. Stem Cells. 2006; 24(5): 1294–1301, doi: 10.1634/stemcells.2005-0342, indexed in Pubmed: 16410387.

20. Kim CH, Lim CY, Lee JH, et al. Human embryonic stem cells-derived mesenchymal stem cells reduce the symptom of psoriasis in imiquimod-induced skin model. Tissue Eng Regen Med. 2019; 16(1): 93–102, doi: 10.1007/s13770-018-0165-3, indexed in Pubmed: 30815354.

21. Kim HS, Yun JW, Shin TH, et al. Human umbilical cord blood mesenchymal stem cell-derived PGE2 and TGF-β1 alleviate atopic dermatitis by reducing mast cell degranulation. Stem Cells. 2015; 33(4): 1254–1266, doi: 10.1002/stem.1913, indexed in Pubmed: 25522163.

22. Kim KH, Blasco-Morente G, Cuende N, et al. Mesenchymal stromal cells: properties and role in management of cutaneous diseases. J Eur Acad Dermatol Venereol. 2017; 31(3): 414–423, doi: 10.1111/jdv.13934, indexed in Pubmed: 27549663.

23. Lee YS, Sah SK, Lee JiH, et al. Human umbilical cord blood-derived mesenchymal stem cells ameliorate psoriasis-like skin inflammation in mice. Biochem Biophys Rep. 2017; 9: 281–288, doi: 10.1016/j.bbrep.2016.10.002, indexed in Pubmed: 28956015.

24. Lowe NJ, Breeding J, Kean C, et al. Psoriasiform dermatitis in a rhesus monkey. J Invest Dermatol. 1981; 76: 141–142.

25. Lowes M, Suárez-Fariñas M, Krueger J. Immunology of psoriasis. Ann Rev Immunol. 2014; 32(1): 227–255, doi: 10.1146/annurev-immunol-032713-120225.

26. Mori H, Arita K, Yamaguchi T, et al. Effects of topical application of betamethasone on imiquimod-induced psoriasis-like skin inflammation in mice. Kobe J Med Sci. 2016; 62(4): E79–E88, indexed in Pubmed: 28239073.

27. Murphy M, Kerr P, Grant-Kels JM. The histopathologic spectrum of psoriasis. Clin Dermatol. 2007; 25(6): 524–528, doi: 10.1016/j.clindermatol.2007.08.005, indexed in Pubmed: 18021888.

28. Natsumi A, Sugawara K, Yasumizu M, et al. Re-investigating the basement membrane zone of psoriatic epidermal lesions: is laminin-511 a new player in psoriasis patho-

genesis? J Histochem Cytochem. 2018; 66(12): 847–862, doi: 10.1369/0022155418782693, indexed in Pubmed: 29906214.

29. Nestle FO, Nickoloff BJ. Animal models of psoriasis: a brief update. J Eur Acad Dermatol Venereol. 2006; 20(s2): 24–27, doi: 10.1111/j.1468-3083.2006.01769.x.

30. Ogawa E, Sato Y, Minagawa A, et al. Pathogenesis of psoriasis and development of treatment. J Dermatol. 2018; 45(3): 264–272, doi: 10.1111/1346-8138.14139, indexed in Pubmed: 29226422.

31. Owczarczyk-Saczonek A, Krajewska-Włodarczyk M, Kruszewska A, et al. Stem cells as potential candidates for psoriasis cell-replacement therapy. Int J Mol Sci. 2017; 18(10), doi: 10.3390/ijms18102182, indexed in Pubmed: 29053579.

32. Park MJ, Park HS, Cho ML, et al. Transforming growth factor beta-transduced mesenchymal stem cells ameliorate experimental autoimmune arthritis through reciprocal regulation of Treg/Th17 cells and osteoclastogenesis. Arthritis Rheum. 2011; 63(6): 1668–1680, doi: 10.1002/art.30326, indexed in Pubmed: 21384335.

33. Rafei M, Campeau PM, Aguilar-Mahecha A, et al. Mesenchymal stromal cells ameliorate experimental autoimmune encephalomyelitis by inhibiting CD4 Th17 T cells in a CC chemokine ligand 2-dependent manner. J Immunol. 2009; 182(10): 5994–6002, doi: 10.4049/jimmunol.0803962, indexed in Pubmed: 19414750.

34. Raychaudhuri SK, Maverakis E, Raychaudhuri SP. Diagnosis and classification of psoriasis. Autoimmun Rev. 2014; 13(4-5): 490–495, doi: 10.1016/j.autrev.2014.01.008, indexed in Pubmed: 24434359.

35. Rokunohe A, Matsuzaki Y, Rokunohe D, et al. Immunosuppressive effect of adipose-derived stromal cells on imiquimod-induced psoriasis in mice. J Dermatol Sci. 2016; 82(1): 50–53, doi: 10.1016/j.jdermsci.2015.12.007, indexed in Pubmed: 26778737.

36. Sah SK, Park KHo, Yun CO, et al. Effects of human mesenchymal stem cells transduced with superoxide dismutase on imiquimod-induced psoriasis-like skin inflammation in mice. Antioxid Redox Signal. 2016; 24(5): 233–248, doi: 10.1089/ars.2015.6368, indexed in Pubmed: 26462411.

37. Sawilowsky S. Misconceptions leading to choosing the t test over the wilcoxon Mann-Whitney test for shift in location parameter. J Mod App Stat Methods. 2005; 4(2): 598–600, doi: 10.22237/jmasm/1130804700.

38. Shin KO, Ha DH, Kim JO, et al. Exosomes from human adipose tissue-derived mesenchymal stem cells promote epidermal barrier repair by inducing de novo synthesis of ceramides in atopic dermatitis. Cells. 2020; 9(3), doi: 10.3390/cells9030680, indexed in Pubmed: 32164386.

39. van der Fits L, Mourits S, Voerman JSA, et al. Imiquimod-induced psoriasis-like skin inflammation in mice is mediated via the IL-23/IL-17 axis. J Immunol. 2009; 182(9): 5836–5845, doi: 10.4049/jimmunol.0802999, indexed in Pubmed: 19380832.

40. Zanolli MD, Jayo MJ, Jayo JM. Evaluation of psoriatic plaques that spontaneously developed in a cynomolgus monkey (Macaca fascicularis). Acta Derm Venereol Suppl (Stockholm. 1989; 146: 58.

41. Zhou H, Guo M, Bian C, et al. Efficacy of bone marrow-derived mesenchymal stem cells in the treatment of sclerodermatous chronic graft-versus-host disease: clinical report. Biol Blood Marrow Transplant. 2010; 16(3): 403–412, doi: 10.1016/j.bbmt.2009.11.006, indexed in Pubmed: 19925878.

V M
VIA MEDICA

O R I G I N A L   A R T I C L E

Preventive effects of bone marrow-derived mesenchymal stem cell transplantation in a D-galactose-induced brain aging in rats

G. El-Akabawy[1, 2, 3], K. Aabed[4], L.A. Rashed[5], S.N. Amin[6, 7], I. AlSaati[2], M. Al-Fayez[8]

[1]Department of Basic Medical Sciences, College of Medicine, Ajman University, Ajman, United Arab Emirates
[2]Department of Basic Sciences, College of Medicine, Princess Nourah bint Abdulrahman University, Riyadh, Saudi Arabia
[3]Department of Anatomy and Embryology, Faculty of Medicine, Menoufia University, Menoufia, Egypt
[4]Department of Biology, College of Science, Princess Nourah bint Abdulrahman University, Riyadh, Saudi Arabia
[5]Department of Medical Biochemistry, Faculty of Medicine, Cairo University, Cairo, Egypt
[6]Department of Medical Physiology, Faculty of Medicine, Cairo University, Cairo, Egypt
[7]Department of Basic Medical Sciences, Faculty of Medicine, The Hashemite University, Zarqaa, Jordan
[8]Department of Anatomy, College of Medicine, King Saud University, Riyadh, Saudi Arabia

Background: Aging is a complex process accompanied by numerous morphological, functional, and metabolic impairments in the brain, and a critical risk factor involved in the increasing incidence of neurodegenerative diseases. Few studies have evaluated the efficacy of different sources of mesenchymal stem cells (MSCs) in ameliorating the early morphological and functional alterations in the aging brain. This study, for the first time, evaluated the potential efficacy of intravenous injection of bone marrow-derived mesenchymal stem cells (BMMSCs) in a D-galactose-induced rat model of brain aging.
Materials and methods: BMMSCs (1 × 10⁶) were intravenously injected into brain aging model rats once every 2 weeks for 8 weeks.
Results: The transplanted cells survived and migrated to the brain, and differentiated into astrocytes and neurons, including choline acetyltransferase neurons. BMMSC transplantation improved locomotor activity and cognitive functions, restored cholinergic system function, protected atrophic cholinergic neurons in the basal forebrain, induced antioxidative effects and restored neurotrophic factors, and modulated hippocampal synaptic plasticity by upregulating PSD95 and Egr1 expression.
Conclusions: Our findings demonstrated the efficacy of BMMSC injection in an aging rat model and suggest that these cells may be developed into an effective cell therapy for the aging brain. (Folia Morphol 2022; 81, 3: 632–649)

Key words: bone marrow-mesenchymal stem cells, D-galactose, rat, brain

INTRODUCTION

Aging is a progressive, complex process accompanied with morphological, functional, and metabolic alterations in the brain, and a critical risk factor involved in the escalating prevalence of neurodegenerative, age-related diseases, such as Alzheimer's disease (AD) and Parkinson's disease (PD) [19, 34, 63, 71, 94]. A distinction can be made between the gradual

decline in the structural and functional brain status in the non-diseased stage (primary or normal aging) and the progressive structural and functional loss resulting from age-related diseases (secondary aging) [43].

Cognitive functions controlled by the hippocampus and prefrontal cortex are greatly affected by normal aging. Both brain regions experience cellular and synaptic changes that are related to a deterioration in cognitive activities [8, 11, 35, 52, 53]. The brain cells the most vulnerable to the deleterious consequences of aging are cholinergic neurons. During normal aging, the cholinergic system of the basal forebrain undergoes moderate neurodegenerative alterations, while in AD, it shows severe deteriorations. Aging and AD are associated with a progressive degeneration of the cholinergic neurons, characterised by a decline in choline acetyltransferase (ChAT) activity, followed by a reduction in acetylcholine (ACh) release [28, 31, 33, 46, 48, 49, 72, 82]. The levels of neurotrophic factors, such as brain-derived neurotrophic factor (BDNF) and nerve growth factor (NGF), are also remarkably decreased in aging and AD, which can be linked to cognitive impairments [15, 50, 83]. In addition, it is well-established that aging is associated with declines in neurotransmitter and receptor levels, reduced synapse numbers, and increased oxidative stress, leading to the marked neurodegenerative status associated with age-related diseases [29, 38, 43, 47, 75, 94].

The structural and functional impairments associated with aging are accelerated in the presence of age-related diseases; hence, therapies that ameliorate primary and/or secondary aging are a principal target in aging research [42, 43]. Stem cell therapy has proven its efficacy in both AD and PD in pre-clinical and clinical studies. Among the different types of stem cells, mesenchymal stem cells (MSCs) are the most promising because they can differentiate toward the neuronal fate, release neurotrophic factors, and enhance endogenous brain repair. In addition, they have immunomodulatory, neuroprotective, angiogenic, and chemotactic properties [4, 10]. In rodent AD models, MSC transplantation has been demonstrated to down-regulate Aβ deposits, enhance neurogenesis and neuronal differentiation, and alleviate spatial learning and memory deficits. Further, MSCs have anti-inflammatory and immunomodulatory effects [25, 41, 54, 56, 58–60, 68, 85, 90, 92, 95]. Based on these and other studies, in 2015, the Food and Drug Administration (FDA) approved the first phase 2A clinical trial of MSCs for AD treatment, and sim-ilar trials were designed in Europe and Asia [36]. Recently, the FDA approved a phase 1/2 trial of autologous, adipose-derived MSCs for the treatment of AD (NCT04228666).

Most studies evaluating the efficacy of stem cells have been conducted in preclinical animal models or in patients with AD and PD, in which structural and functional brain capacities are extensively deteriorated. It could be postulated that early intervention to encounter the neuropathological alterations during primary aging would prevent or at least slow down the pathological processes leading to secondary aging, and hence reduce the incidence of age-related diseases [3, 42, 43, 64, 75, 94]. Notably, studies investigating the administration of human (h)MSCs derived from bone marrow or adipose tissue in mouse models of hind limb ischaemia have reported controversial outcomes regarding which type of MSCs is the most effective [13, 40]. Proof for the superiority of specific MSCs source for the treatment of neurodegenerative disorders is lacking. Since the potential differences between MSCs isolated from different sources may result in diverse clinical effects, studies to decide the most efficacious MSC types for each clinical condition are needed [84].

Few studies have evaluated the efficacy of MSC transplantation in animal models of aging [17, 39, 61, 74, 91]. Therefore, we sought to assess, for the first time, the potential beneficial effect of systemic transplantation of bone marrow (BM)-derived MSCs (BMMSCs) on the cortex, hippocampus, and forebrain in a D-galactose-induced rat model of brain aging in order to evaluate their potential as a preventive approach for age-related neurodegeneration.

MATERIALS AND METHODS
Animals
Thirty male Sprague Dawley rats (8 weeks old, 180–200 g) were purchased from the Theodor Bilharz Research Institute, Imbaba, Egypt and were kept in the animal house of the Faculty of Medicine, Menoufia University, Egypt. The rats were housed in standard polycarbonate cages with 2 rats in cage under standard laboratory conditions (22 ± 5°C, 60 ± 5% humidity, and a 12-h/12-h light/dark cycle). Standard laboratory chow and tap water were available *ad libitum*. All experimental procedures involving animals were approved by Institutional Review Board of Princess Nourah bint Abdulrahman University, KSA [IRB# 18-0165] and Institutional Review Board

of Menoufia University, Faculty of Medicine, Egypt [IRB# 191219ANAT] and were conducted in accordance with the guidelines on the ethical use of animals in the European Community Council Directive 2010/63/EU.

BMMSC isolation and culture

Bone marrow-derived MSCs were obtained from 6- to 8-week-old male Sprague Dawley rats as previously reported [65]. Briefly, BM plugs were collected from the femurs and tibias of the rats using a 23-gauge needle and centrifuged for 5 min at room temperature (RT) at 1,800 rpm. The pelleted cells were then resuspended in Dulbecco's modified Eagle's medium (DMEM, Gibco, Carlsbad, CA, USA) containing 10% foetal bovine serum (FBS) (Gibco) and 1% penicillin–streptomycin (Gibco) and seeded at a density of 1×10^6 cells/cm in 25 cm² cell culture flasks. The cells were incubated at 37°C in a humidified atmosphere with 5% CO_2. A complete medium change was performed every 3–4 days to remove non-adherent hematopoietic cells. When the confluence of the cells reached 70%, they were harvested for 2–5 min using 0.25% Trypsin–EDTA (Sigma-Aldrich, St. Louis, MO, USA), then neutralised with complete medium and centrifuged at $500 \times g$ for 5 min. Cell pellets were resuspended in complete medium. The viability of the cells was assessed by adding equal volumes of the cell suspension and 0.4% Trypan blue (Gibco), and loading 10 μL of the stained suspension into each chamber of a haemocytometer. Viable and dead cells were calculated within 5 min of sample preparation. Cells with greater than 90% viability were subcultured at a 1:3 (passage 1). Cells were used at passage 4.

Flow cytometry

Cells were resuspended in staining buffer (2% FBS/PBS) and surface-stained with FITC-conjugated mouse anti-rat CD44 (BioLegend, UK), FITCH-conjugated mouse anti-rat CD90 (BD Pharmingen, USA), or PE-conjugated rabbit anti-rat CD34 (Abcam, UK) at 4°C for 30 min. Isotype-matched antibodies served as controls. The cells were analysed using an EPICS XL flow cytometer (Beckman Coulter).

Experimental design

The rats were randomly assigned to three groups: control, D-galactose (D-gal)-treated, and D-gal + BMMSCs-treated (n = 10 in each group). The sample size was calculated using the G Power software. Rats in the D-gal- and D-gal + BMMSCs-treated groups received a subcutaneous injection of D-gal (300 mg/ /kg, Sigma-Aldrich, St. Louis, MO, USA) every day for 8 weeks. Rats in the D-gal + BMMSCs group were intravenously administered 1×10^6 BMMSCs labelled with the membrane-bound fluorescent marker PKH26 (Sigma-Aldrich) once every 2 weeks.

Behavioural tests

All animals were acclimatised 1 week following arrival to behavioural testing. Tests were conducted 1 week after the last transplantation. Test sessions were conducted between 2 PM and 5 PM. Two observers were present throughout each session and were blind to experimental condition.

Open-field test

The open-field test allows simultaneous evaluations of exploration, locomotion, and anxiety. A box of 1 m × 1 m and 50 cm in height was made of wood. The floor of the box was divided into equally areas. Each rat was positioned in the centre of the open field arena and the rearing frequency, number of crossing the lines (with both forepaws), and number and duration of central square entries (with both forepaws) were recorded using a video camera installed 2.5 m above the box for 5 min. The box was placed in a noiseless room with controlled illumination.

Y-maze test

The Y-maze task was used to evaluate spatial working memory. A Y-maze with three equal-sized wooden arms (60 cm, 12 cm, 25 cm) was designed. Each rat was placed in the centre of the maze and permitted to explore the three arms for 8 min. A correct choice was scored when any three successive choices of three different arms were entered. An alternation score was obtained as the total number of alternations divided by the total number of choices minus 2.

Measurement of body weight and the brain index

The general condition of the rats, including behavioural activity and glossiness and colour of the hair coat, was observed daily. Body weights were assessed weekly. At the end the experiment, the rats were anaesthetised through intraperitoneal injection of ketamine (90 mg/ /kg) and xylazine (15 mg/kg) and decapitated. Brains were immediately harvested from all rats and weighed. Brain indices were calculated in the following manner: brain tissue weight (mg)/final body weight (g).

Table I. List of primers used in quantitative reverse-transcription polymerase chain reaction

Gene name	Gene accession	Primer sequence forward/reverse 5'→3'
ChT1	NM_053521	CAAGACCAAGGAGGAAGCAG GCAAACATGGAACTTGCTGA
ChAT	XM_224626	TGAACGCCTGCCTCCATTCGGC CTGCTGA GTGCCATCTCGGCCCACCACG AACTGCA
VAChT	NM_031663	GCCACATCGTTCACTCTCTTG CGGTTCATCAAGCAACACATC
M1AChR	NM_080773	CCTACAGCTGGAAGGAAGAA GCCTGTGCTTCAGAATCTAC
nAChR α5	NM_017078	TGGAACACCTGAGCGACAAG CGTGACAGTGCCGTTGTACC
nAChR β2	NM_019297	CGGGAAGCAGTGGATGGCGTA GTCCTCCCTCACACTCTGGTCATCA
Egr1	NM_012551	AAGACACCCCCCCATGAAC CTCATCCGAGCGAGAAAAGC
BDNF	NM_012842	TGTCCGAGGTGGTAGTACTTCATC CATGCAACCGAAGTATGAAATAACC
VEGF	AF062644	GAGGAAAGGGAAAGGGTCAAAA CACAGTGAACGCTCCAGGATT
NGF	XM_227525	TGC ATA GCG TAA TGT CCA TGT TG CTG TGT CAA GGG AAT GCT GAA
BETA-ACTIN	NM_031144	ATTTGGCACCACACTTTCTACA TCACGCACGATTTCCCTCTCAG

Abbreviations — see text.

Assessment of oxidative stress and antioxidants indices

A spectrophotometer was used to determine the levels of malondialdehyde (MDA) and glutathione (GSH) in brain tissue. To assess the extent of lipid peroxidation, rats' cortices and hippocampi (100 mg) were homogenised in 1 mL of phosphate buffer solution (PBS; pH 7.0) and the MDA concentration was measured [87]. The homogenates were centrifuged after being mixed with trichloroacetic acid (TCA; 20%) at 5000 rpm for 15 min. The supernatants were treated with a 5% thiobarbituric acid (TBA) solution before being boiled in a water bath for 10 min. The absorbance at 532 nm was determined, and the MDA concentration was estimated using the standard curve. The results were given in nanomoles (nmol) per milligram (mg) of protein.

Ellman's method [22] was used to assess GSH levels. A solution of dithiobis nitrobenzoate (DTNB) was added to cortices and hippocampi tissue homogenate and incubated for 1 h. At 412 nm, the absorbance was measured. The standard curve was used to measure the GSH concentration. The findings were expressed in micromoles (mmol) per mg of protein.

Quantitative reverse-transcription polymerase chain reaction (RT-qPCR)

Total RNA was extracted from homogenised cortices and hippocampi of rats of each group using RNeasy Purification Reagent (Qiagen, Valencia, CA, USA) according to the manufacturer's protocol. RNA purity was assessed with a spectrophotometer; the wavelength absorption ratio (260/280 nm) was between 1.8 and 2.0 for all preparations. The RNA was reverse transcribed into cDNA using Superscript II (Gibco Life Technologies, Grand Island, NY, USA). qPCRs were run and analysed in a StepOneTM instrument with software version 3.1 (Applied Biosystems, Foster City, CA, USA). The reaction mixtures contained SYBR Green Master Mix (Applied Biosystems), a gene-specific primer pair (listed in Table 1), cDNA, and nuclease-free water. The cycling conditions were: 10 min at 95°C followed by 40 cycles of 15 s at 95°C and 60 s at 60°C. The ABI Prism sequence detection system software was used to analyse the data and quantification was achieved using the Sequence Detection Software v1.7 (PE Biosystems, Foster City, CA). Relative target gene expression was calculated using the comparative cycle threshold method [45]. All values were normalised to β-actin mRNA.

Immunohistochemical analysis

For immunohistochemical staining, brains were fixed in 10% formalin and embedded in paraffin wax. Five-micrometre sections were deparaffinised, rehydrated, rinsed with PBS, and blocked in 0.1% H_2O_2 for 30 min to block endogenous peroxidase activity. The sections were incubated in 10% normal goat serum (blocking solution) at RT for 1 h, then incubated with rabbit anti-polysynaptic density protein 95 (PSD95) primary antibody (1:500, Abcam, Cat. #ab18258) at RT for 1 h. After rinsing with PBS, the sections were incubated with a biotinylated goat anti-rabbit secondary antibody (1:200, Vector Labs, BA-1000, Peterborough, UK) at RT for 20 min. The sections were treated with the enzyme conjugate streptavidin–horseradish peroxidase solution for 10 min. Secondary antibody binding was detected using 3,3-diaminobenzoic acid dissolved in PBS with H_2O_2 (0.03%) added immediately before use. The sections were washed with PBS, counterstained with two drops (100 μL) of haematoxylin, and rinsed in distilled water until they turned blue. Finally, the slides were dehydrated in an ascending graded ethanol series (70%, 95%, and 100%) for 5 min per concentration, cleared in xylene, mounted with Histomount, and covered with a coverslip.

For immunofluorescence staining, brains were dissected and fixed at 4°C for 24 h, then cryoprotected in 30% sucrose at 4°C. Serial sections (40 μm) were cut by a cryostat and stored at –20°C until use. The sections were incubated in 10% blocking solution (10% normal goat serum in 0.3% Triton X-100 in PBS) at RT for 1 h, then incubated at 4°C overnight in the primary antibodies rabbit anti-Neun (1:1000, Abcam, Cat. #ab177487), rabbit anti-GFAP (1:1000, Abcam, Cat. #ab7260), or rabbit anti-ChAT (1:1000, Abcam, Cat. #ab1778850). The sections were then rinsed in PBS and a secondary antibody was applied (1:500, Alexa-488, Cat. #A-11034, Molecular Probes) at RT for 1 h. Finally, the sections were rinsed in PBS and mounted in Fluoroshield Mounting Medium with DAPI (Abcam, Cat. #ab104139).

Quantitative histological assessments

Five non-overlapping images per section were randomly captured from the cerebral cortex, whereas the entire basal forebrain and dentate gyral area were analysed for each brain section for each marker. Immunohistochemical images were captured using a Leica DML B2/11888111 microscope equipped

with a Leica DFC450 camera, using the Leica C PLAN 4×/0.10 or 10×/0.22 objectives. Immunofluorescence images were captured using a Leica DM5500 B/11888817/12 microscope equipped with a Leica DFC450C camera, using the Leica HI PLAN 10×/0.25 objective. For each image, the region of interest was the field of view at a magnification of 10×. From at least three sections/rat, immunopositive cells were counted using the ImageJ software (National Institutes of Health, Bethesda, Maryland, US) by a manual approach using the plugin/cell counter tool [70] and then averaged per field for each rat. Calculated numbers for 10 animals/experimental group were considered for comparison and statistical analyses.

Statistical analysis

The data are expressed as the mean ± standard error of mean (SEM). Normal distributions were evaluated using the D'Argostino and Pearson normality test, and data were analysed using one-way or two-way analysis of variance (ANOVA) followed by a post hoc Bonferroni test. $P < 0.05$ was considered statistically significant. Statistical analyses were performed using GraphPad Prism 5.03 (GraphPad Software, San Diego, California, USA).

RESULTS
Characterisation of BMMSCs

After 10 days of culture, MSCs derived from the BM of Sprague-Dawley rats were spindle-shaped fibroblast-like cells. Cells from passage 4 were evaluated by flow cytometry for the expression of the markers CD90, CD44 (mesenchymal cell marker), CD34 (hematopoietic lineage marker). More than 90% of the cells were CD90+ and CD44+, whereas less than 10% were CD34+ (Fig. 1). These results indicated that the cells were mostly non-hematopoietic MSCs.

BMMSC transplantation improves the physical characteristics, body weight, and brain indices

Rats in the D-gal group exhibited signs of general aging in terms of physical appearance, i.e., reduced activity and rough, dull, yellow hair coat with hair loss, while rats in the transplanted group exhibited normal activity and smooth, glossy, brightly coloured hair coat, suggesting that BMMSC treatment had beneficial effects on D-gal-induced aging. In the current study, the body weights of the rats in the control, D-gal, and transplanted groups were not
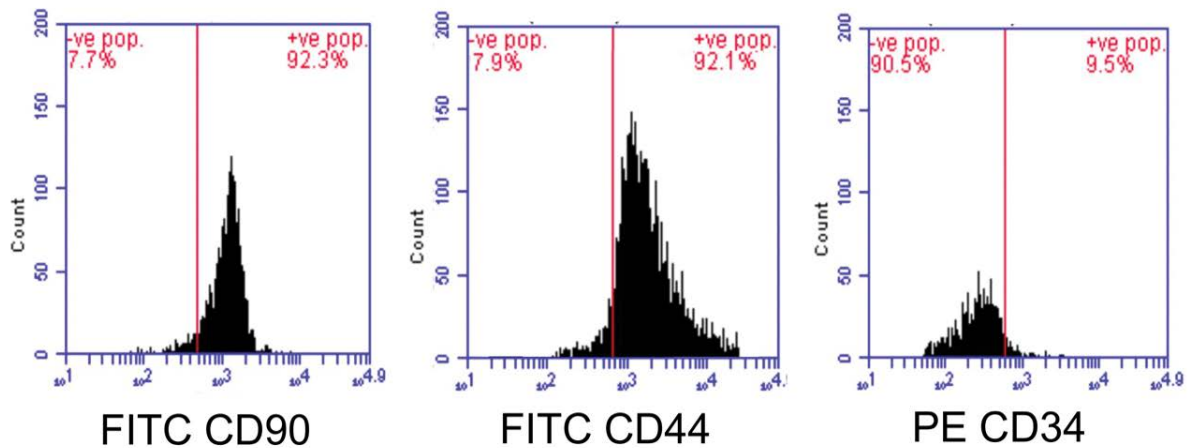
FITC CD90   FITC CD44   PE CD34

Figure 1. Characterisation of the bone marrow-derived mesenchymal stem cells (BMMSCs) population. The cell-surface phenotype of the BMMSCs was assessed by flow cytometry using antibodies against CD90, CD44, and CD34. In total, 92.3%, and 92.1% of the cells expressed CD90 and CD44, respectively, whereas only 9.5% expressed CD34.
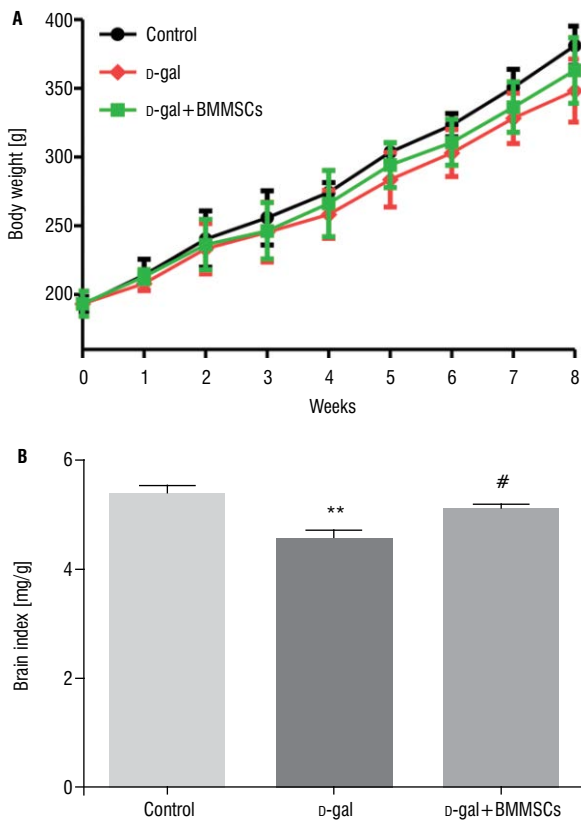

Figure 2. Body weight (**A**) and brain index (**B**) were evaluated in the control, aged (D-gal), and transplanted (D-gal + BMMSCs) rats; **P < 0.001 vs. control rats; #P < 0.01 vs. aged rats. Data are expressed as means ± standard error of mean; N = 10/group; BMMSCs — bone marrow-derived mesenchymal stem cells.

significantly different. However, the brain index was significantly decreased in D-gal-treated rats compared with that in the control rats, whereas BMMSC

treatment dramatically improved the brain index as compared with that in the aged rats (Fig. 2), indicating that transplanted cells prevented D-gal-induced brain atrophy.

BMMSCs improve spatial working memory, exploratory behaviour, and locomotion, and reduce anxiety in D-gal aging rats

Seven days after the last BMMSC injection, the reaction to a novel environment was evaluated using the open-field test. Aged rats showed significantly decreased exploratory behaviour and locomotion as indicated by significant declines in the rearing frequency and number of line crossings when compared to those in the control group (Fig. 3A, B). This was significantly improved by BMMSC injection as indicated by the significant increases in the rearing frequency and number of line crossings when compared to the values in the aging group (Fig. 3A, B). Parameters reflecting anxiety increased with aging. In the D-gal group, the frequency and duration of central square entries were significantly reduced as compared to those in the control group (Fig. 3C, D). BMMSC treatment ameliorated anxious behaviour and significantly increased the frequency and duration of central square entries as compared to those in the aged group (Fig. 3C, D).

The alternation score in the Y-maze task was dramatically decreased in the aged group when compared with the control group, which reflects impaired spatial working memory (Fig. 3E). BMMSC treatment significantly improved the spatial working memory
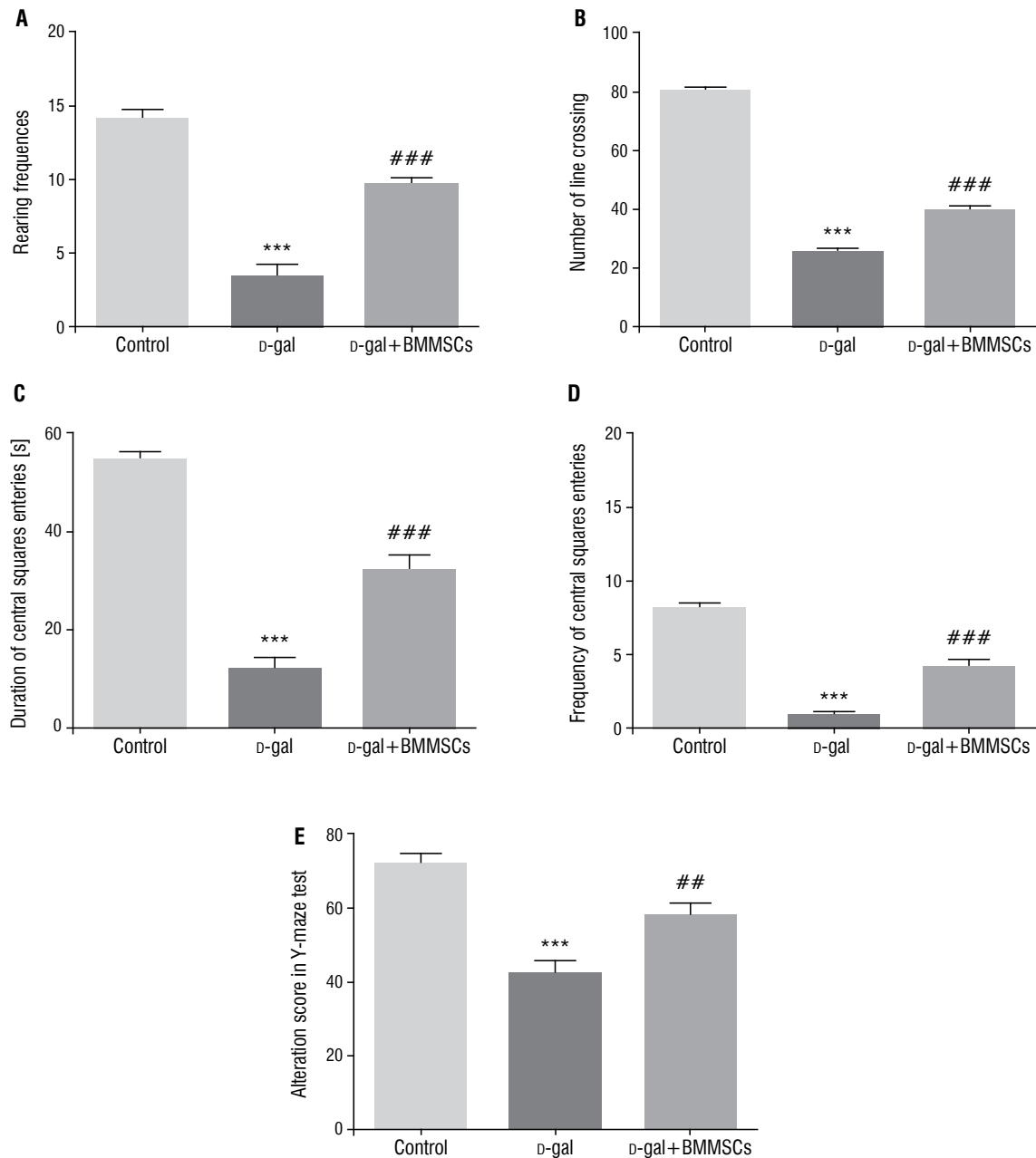
Figure 3. A–E. Locomotion, exploratory behaviour, spatial working memory, and anxiety were evaluated in control, aged (d-gal), and transplanted (d-gal + BMMSCs) rats. Locomotion and explanatory behaviour (horizontal locomotion and vertical rearing) and anxious behaviour (frequency and duration of central squares entries) were assessed for 5 min in an open field test, and spontaneous alternations between the arms of a Y-maze was assessed for 8 min; ***P < 0.001 vs. control rats; ##P < 0.01 and ###P < 0.001 vs. aged rats. Data are expressed as means ± standard error of mean; N = 10/group; BMMSCs — bone marrow-derived mesenchymal stem cells.

as indicated by an increased alternation score when compared to that of the aged group (Fig. 3E).

BMMSCs restore cholinergic system function

The functional integrity of the cholinergic system in the cerebral cortex and hippocampus is largely affected during aging [18, 20, 46]. The correlation between cholinergic system hypofunction and cog-

nitive deficits has led to the formulation of the cholinergic hypothesis of cognitive impairments in aging and AD [46]. Gene expression of the main functional elements of cholinergic neurons was assessed in the different groups. Gene expression of ChAT for acetylcholine synthesis; high-affinity choline transporter 1 (ChT1) and the vesicular ACh transporter (VAChT) for ACh transport into the vesicles; and the cholinergic
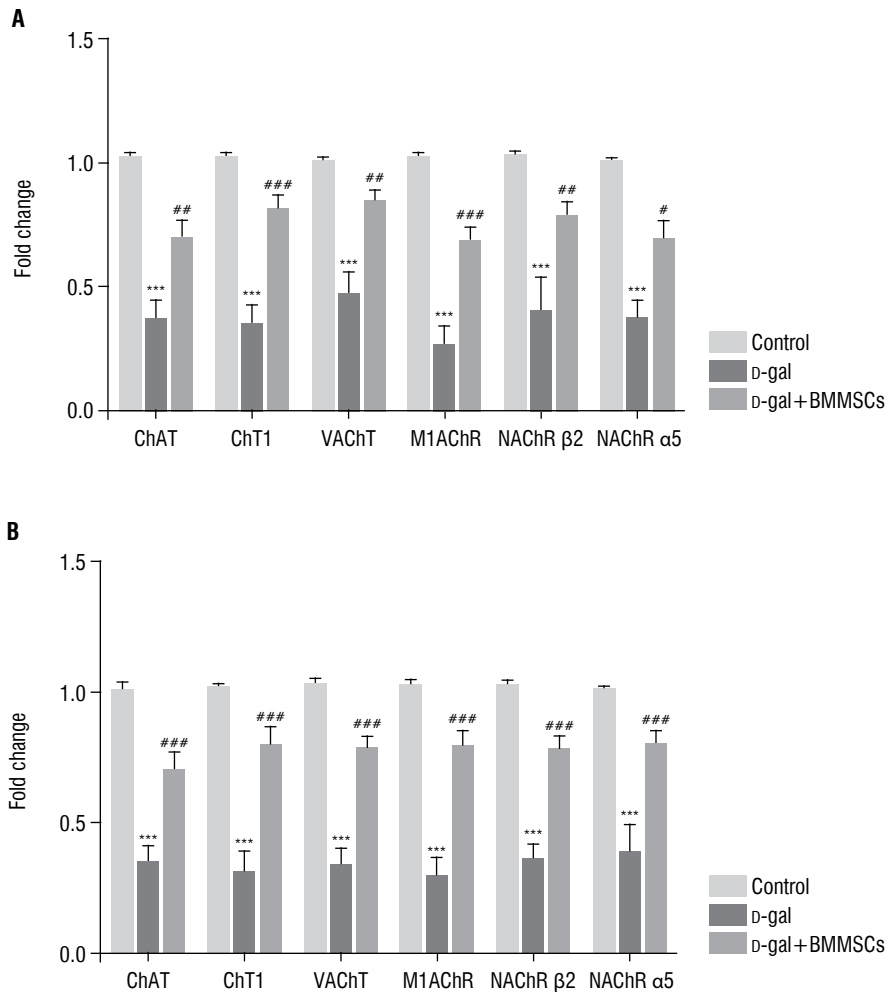
Figure 4. Gene expression of cholinergic nervous system markers in the cortex (**A**) and hippocampus (**B**) in control, aged (D-gal), and transplanted (D-gal + BMMSCs) rats as measured by quantitative reverse-transcription polymerase chain reaction; ***P < 0.001 vs. control rats; #P < 0.05, ##P < 0.01 and ###P < 0.001 vs. aged rats. Data are expressed as means ± standard error of mean; N = 10/group; BMMSCs — bone marrow-derived mesenchymal stem cells.

muscarinic (m1AChR) and nicotinic ACh receptors (nAChR α5 and nAChR β2) for synaptic signalling were decreased in both the cortex (Fig. 4A) and the hippocampus (Fig. 4B) of aged as compared with control rats. These changes in gene cholinergic nerve marker expression were markedly prevented in the D-gal + BMMSCs group in both the cortex and the hippocampus (Fig. 4A, B).

Transplanted BMMSCs survive and migrate to the brain, and differentiate into neurons and astrocytes

To assess the potential mechanisms by which BMMSCs improved motor and cognitive deficits and restored cholinergic system alterations, we first assessed whether the systemically administered BMMSCs homed to and survived in the brains of the transplanted

rats. PKH-labelled transplanted BMMSCs were found in brain sections of the transplanted group and were detected extensively in all examined brain regions. To characterise the fate of the migrated cells, the cells were recognised by PKH labelling, while their differentiation status was confirmed based on the expression of the neuronal marker Neun or the astrocyte marker glial fibrillary acidic protein (GFAP). In the cerebral cortices and hippocampi of transplanted rats, approximately 10% and 30% of the PKH-labelled cells co-expressed Neun (Fig. 5), and GFAP (Fig. 6), respectively, whereas a few transplanted cells expressed ChAT.

BMMSC transplantation protects cholinergic neurons in the basal forebrain

The cholinergic system involves neurons found mainly in the basal forebrain and their long axons
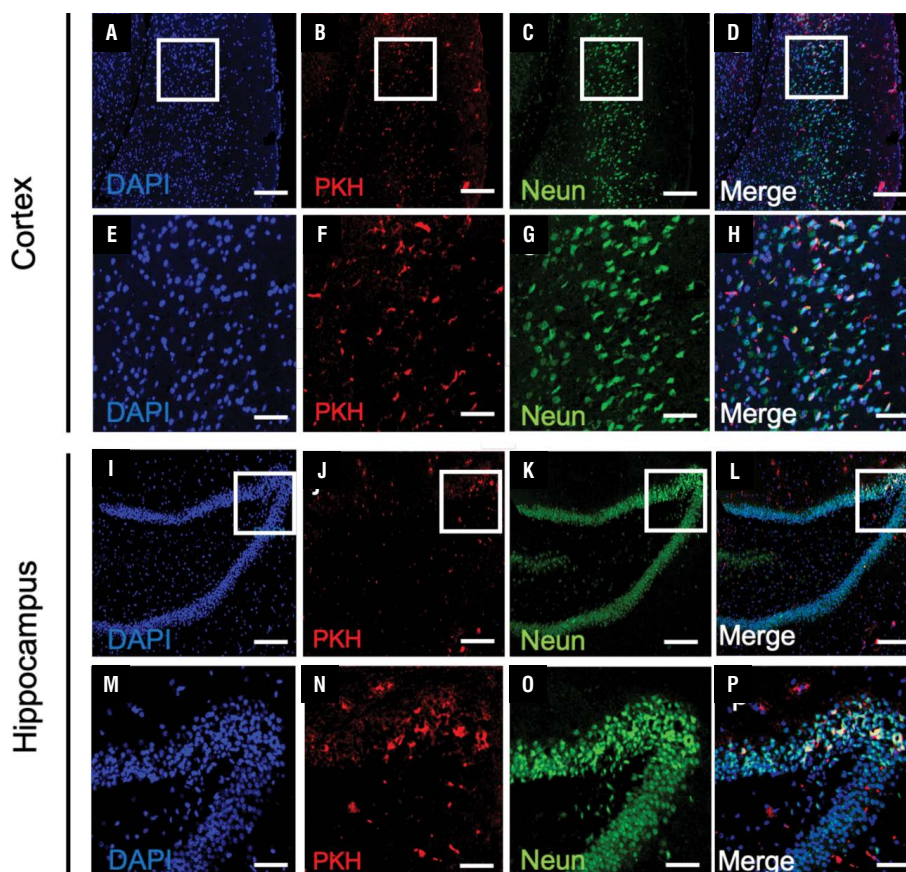
Figure 5. Survival and differentiation of transplanted bone marrow-derived mesenchymal stem cells (BMMSCs) into neurons in transplanted (D-gal + BMMSCs) rats. A number of PKH-labelled BMMSCs (red) (**B, J**) co-expressed Neun (green) in the cortex (**C, D**) and in the hippocampus (**K, L**). The boxed areas in **A–D** and **I–L** are magnified in **E–H** and **M–P**, respectively. PKH-labelled cells (red) (**B, F, J, N**), Neun-positive cells (green) (**C, G, K**, 0), DAPI-stained nuclei (blue) (**A, E, I, M**), and merged images (**D, H**, L, **P**). Scale bar = 500 μm (A–D, I–L) and 100 μm (E–H, M–P).

that projects diffusely to the cerebral cortex and the hippocampus. To determine whether BMMSC transplantation rescued atrophic cholinergic neurons in the basal forebrain in aged rats, ChAT-positive neurons were analysed. In D-gal-treated rats, ChAT-positive cells in the basal forebrain were markedly declined (Fig. 7A, B, D), whereas in the transplanted group, they were markedly increased (Fig. 7B–D). In the transplanted rats, some PKH-labelled cells in the basal forebrain co-expressed ChAT (Fig. 7C'–C''').

BMMSCs exert antioxidative effects and restore neurotrophic factors

One of the most well accepted theories for the mechanistic cause of brain ageing is the free-radical hypothesis of aging [26]. D-gal-treated rats had higher levels of MDA, an index of lipid peroxidation, in their cerebral cortex and hippocampus than control rats (Fig. 8A, C). In addition, the GSH levels in these brain regions were significantly (Fig. 8B, D) reduced in aged compared to control rats. In D-gal + BMMSCs-treated

rats, MDA levels in the cerebral cortices and hippocampi were significantly reduced (Fig. 8A, C), whereas the GSH levels were increased (Fig. 8B, D) when compared with the levels in D-gal-treated rats.

Neurotrophic factors, such as BDNF, NGF, and vascular endothelial growth factor (VEGF) play important role in cholinergic innervation and ChAT activity in the cortex and hippocampus, and their decline has been linked to impaired cognitive function in aged animals [23, 79]. The expression of *BDNF, NGF*, and *VEGF* in the cortex and hippocampus were remarkably decreased in aged rats (Fig. 9) when compared with the expression in control rats, and these declines were suppressed in both brain regions (Fig. 9) after BMMSC transplantation.

BMMSCs modulate hippocampal synaptic plasticity by upregulating the PSD95 expression and triggering Egr1 expression

The PSD95 protein is a component of the postsynaptic complex and plays a crucial role in synaptic plas-
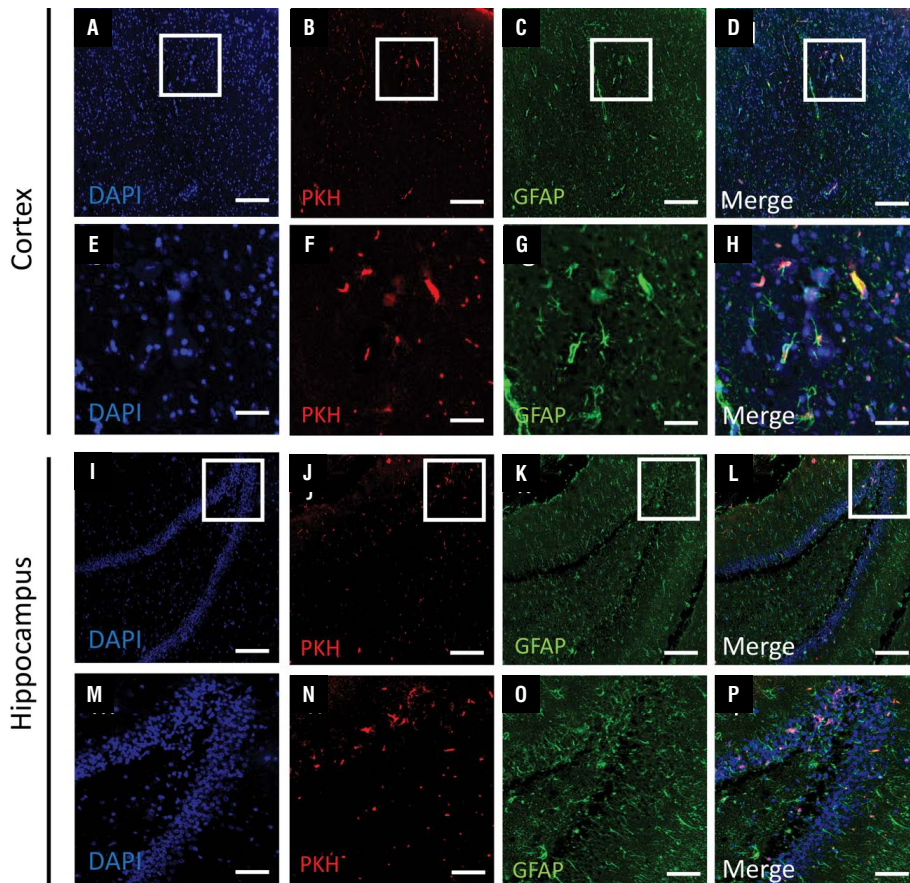
Figure 6. Survival and differentiation of transplanted bone marrow-derived mesenchymal stem cells (BMMSCs) into astrocytes in the transplanted (D-gal + BMMSCs) group. A number of PKH-labelled BMMSCs (red) (**B, J**) co-expressed GFAP (green) in the cortex (**C, D**) and in the hippocampus (**K, L**). The boxed areas in **A–D** and **I–L** are magnified in **E–H** and **M–P**, respectively. PKH-labelled cells (red) (**B, F, J, N**), GFAP-positive cells (green) (**C, G, K, O**), DAPI-stained nuclei (blue) (**A, E, I, M**) and merged images (**D, H, L, P**). Scale bar = 500 μm (A–D, I–L) and 100 μm (E–H, M–P).

ticity [16]. The numbers of PSD95-positive neurons in the hippocampus were markedly decreased in aged rats (Fig. 10A, B), whereas they were significantly increased in the transplanted group (Fig. 10A, B).

Reduced transcription of early growth response protein 1 (Egr1), an immediate early gene, in the hippocampus has been related to age-related memory deficits [21, 62, 93]. *Egr1* expression in the hippocampus was reduced in aged rats when compared with control rats (Fig. 10C), but was significantly restored in BMMSCs + D-gal rats (Fig. 10C).

DISCUSSION

In the central nervous system, aging is associated with altered structure and connectivity, which leads to a decline in normal function. The decreases in neuron numbers and brain function during aging may be a determinant factor in the morphological and functional changes observed in neurodegenerative diseases [19, 34, 63, 71, 94]. These changes are accompanied by the deterioration of motor coordination and cognition in normal aging, which is worsened in age-associated neurodegenerative disorders such as AD [8, 11, 35, 52, 53]. Thus, therapeutic strategies to ameliorate primary (normal) aging are a major goal in aging research [3, 42, 43, 64, 75, 94]. The replenishment of lost/malfunctioning cells by stem cell therapy has become the focus of recent research. Studies have demonstrated the therapeutic potential of different types of MSCs such as adipose-, umbilical cord (UC)-, and amniotic-derived MSCs in rodent aging models [17, 39, 61, 74, 91]. Given the lack of proof for the superiority of specific source of MSCs in alleviating structural and functional alterations in different parts of the aging brain as well as for the most effective injection route [84], this study aimed to evaluate, for the first time, the potential beneficial outcome of intravenous transplantation of BMMSCs on the brain in D-gal aging rats.
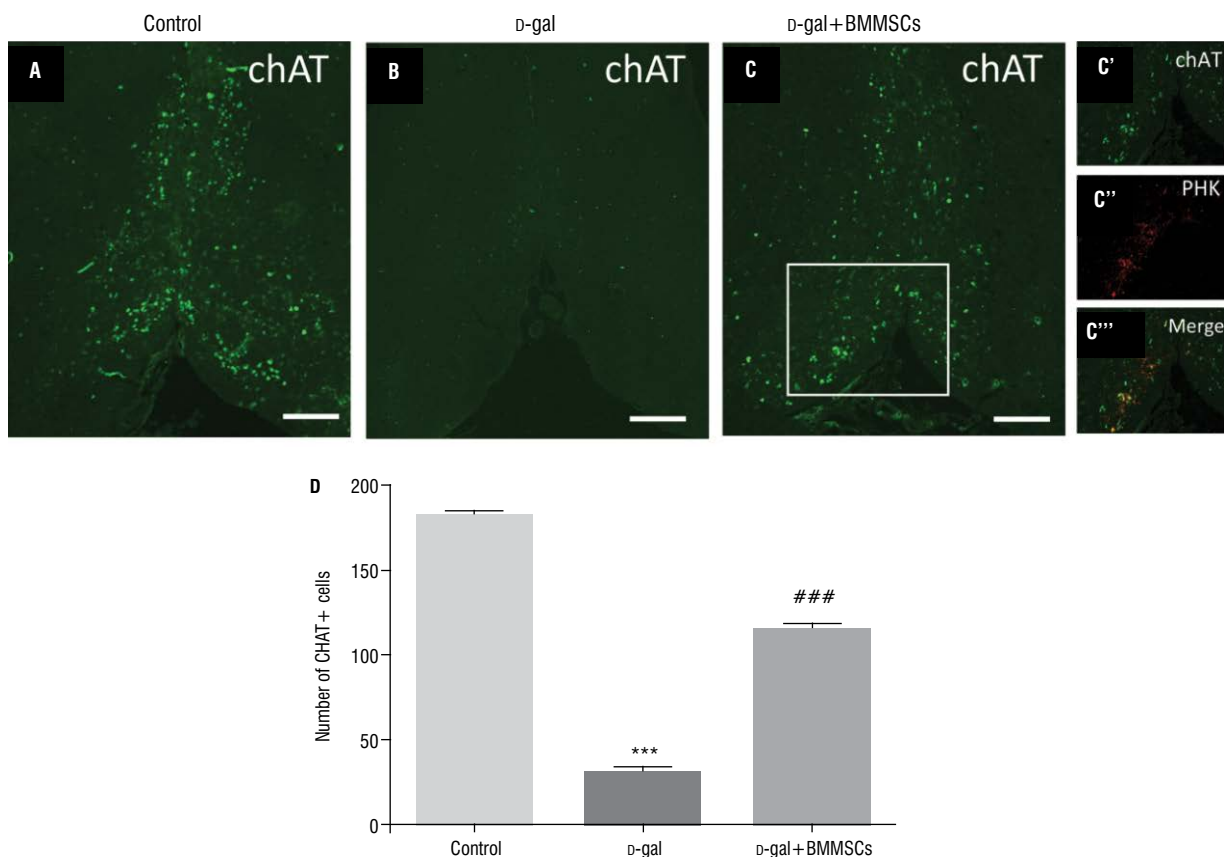
Figure 7. Number of cholinergic neurons in the basal forebrain in control, aged (ᴅ-gal), and transplanted (ᴅ-gal + BMMSCs) rats. A number of PKH-labelled BMMSCs (**C'''**, red) co-expressed ChAT (**C'''**, green). The boxed areas in panel **C** are magnified in panel **C'**. PKH-labelled cells (red) (**C''**), ChAT-positive cells (green) (**A–C** and **C'**), and merged images (**C'''**). Scale bar = 500 μm A–C; ***P < 0.001 vs. control rats; ###P < 0.001 vs. aged rats. Data are expressed as means ± standard error of mean; N = 10/group; BMMSCs — bone marrow-derived mesenchymal stem cells.

Aging is featured by a gradual decline in locomotion and cognition. With aging, various aspects of learning and memory progressively decline. In our study, BMMSCs improved exploratory behaviour, locomotion, and anxiety in ᴅ-gal + BMMSCs rats. Our results are consistent with previous findings. Intra-cerebroventricular human BMMSC transplantation in aged rats improved spatial memory accuracy capacity in locating goal sector in a Barnes maze [91]. Spatial learning and memory functions in ᴅ-gal aging mice enhanced after repeated intraperitoneal injections of hUCMSCs [17]. Repeated intravenous transplantations of human amniotic membrane (AM)-derived MSCs (AMMSCs) or adipose tissue (AD)-derived MSCs (ADMSCs) in 10-month-old male F344 rats improved motor coordination and cognitive function as indicated by improved rotarod, passive avoidance, and Morris water-maze performance [39]. Similarly, single or repeated intravenous or intra-cerebroventricular transplantation of ADMSCs increased physical activity and enhanced learning and memory performance in aged mice [61].

The strong involvement of the cholinergic circuits in age-related brain functional deterioration has led to the development of cholinergic hypothesis of geriatric cognitive impairments [9, 30, 72, 77, 81]. In normal aged brains, loss of cholinergic neurons, depletion of ACh, reduced ChAT activity, and declines in the densities of muscarinic and nicotinic ACh receptors have been reported [9, 18, 28, 49, 72, 77, 82]. Based on positron emission tomography, Albin et al. [2] reported region-specific declines in VAChT binding sites in the cortex and striatum in the aged brain. In our study, the gene expression of the cholinergic factors ChAT, ChT1, VAChT, m1AChR, and nAChRs α5 and β2 was increased in transplanted compared to aged rats. Therefore, it is plausible to conclude that the detected improvements in cognitive and motor activities might be due to improvements in the cholinergic system.
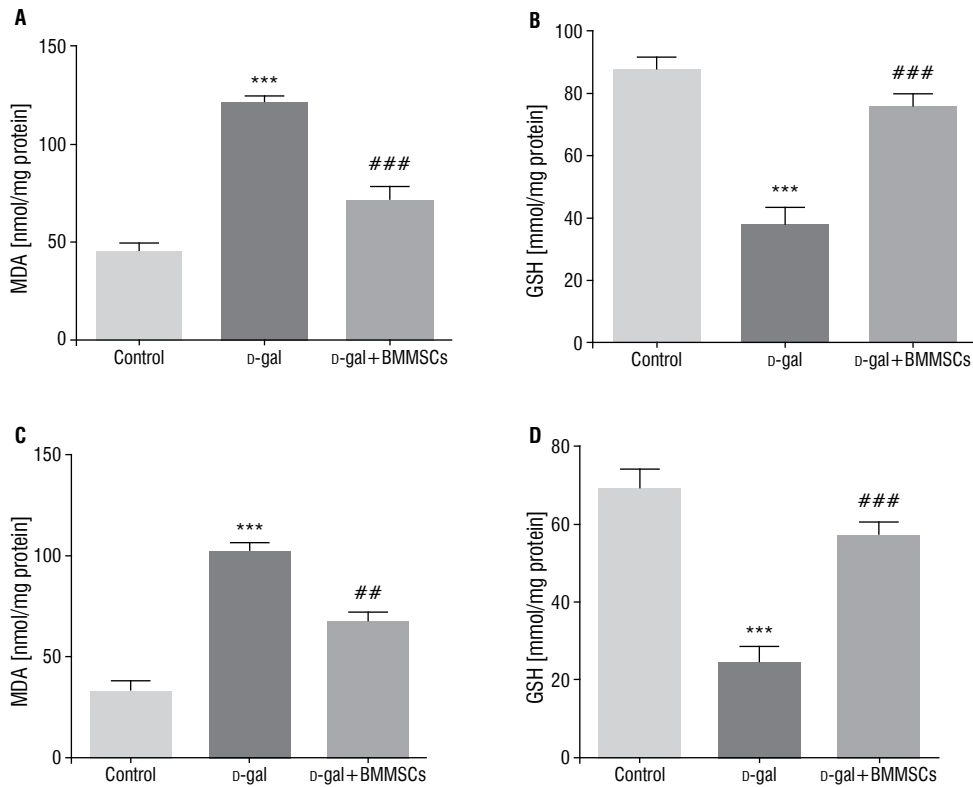
Figure 8. A–D. Status of malondialdehyde (MDA) and glutathione (GSH) in the cortex (**A**, **B**) and the hippocampus (**C**, **D**) of control, aged (D-gal), and transplanted (D-gal + BMMSCs) rats. ***P < 0.001 vs. control rats; ##P < 0.01 and ###P < 0.001 vs. aged rats. Data are expressed as means ± standard error of mean; N = 10/group; BMMSCs — bone marrow-derived mesenchymal stem cells.

Figure 9. Gene expression of *BDNF, NGF, and VEGF* in the cortex (**A**) and the hippocampus (**B**) of control, aged (D-gal), and transplanted (D-gal + BMMSCs) rats as measured by quantitative reverse-transcription polymerase chain reaction. ***P < 0.001 vs. control rats; ###P < 0.001 vs. aged rats. Data are expressed as means ± standard error of mean; N = 10/group; BMMSCs — bone marrow-derived mesenchymal stem cells.
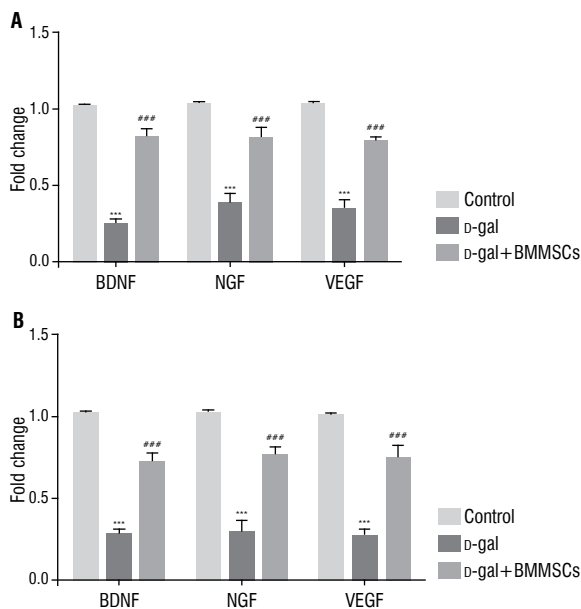
To reveal the mechanism underlying the behavioural and cholinergic functional improvements observed after BMMSC injection, we evaluated the survival, migration, and differentiation potential of the transplanted BMMSCs in D-gal aging rats. Repeated intravenous BMMSC transplantation was accompanied with a massive migration of the cells into all brain regions examined. These results were in line with previous findings. Interestingly, in both animals and humans, aging has been linked with increased blood-brain barrier permeability, which might be triggered by several aging-mediated events, such as increased oxidative stress and enhanced microglial activation [66, 76]. Demonstrating the therapeutic efficacy of a relatively non-invasive approach such as the intravenous route is of clinical relevance as invasive implantation techniques such as intracranial transplantation may damage intact brain tissues, increasing the burden of aging-related cell loss. Approximately 10% of the migrated cells differentiated into neurons and 30% differentiated into astrocytes. In addition, only few transplanted cells differentiated into ChAT+ cells. Substantial evidence suggests
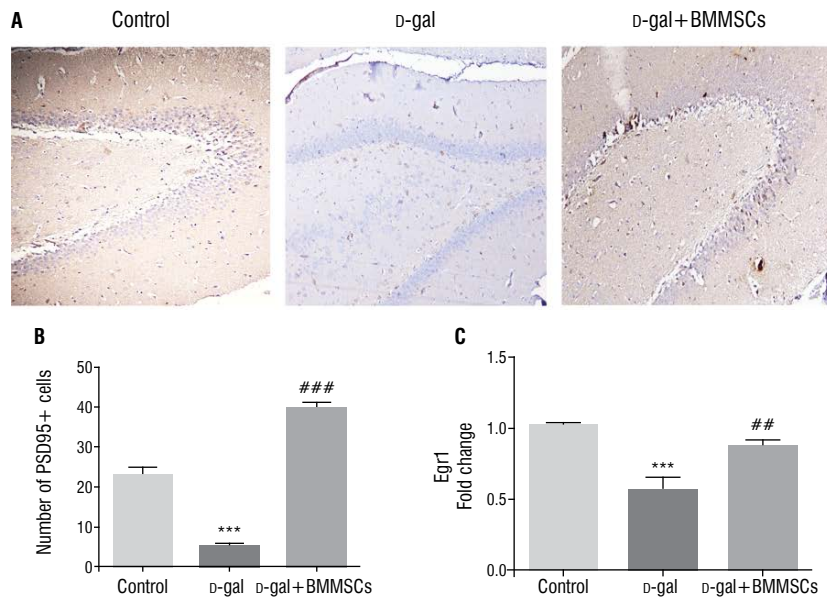
Figure 10. PSD95 expression as indicated by immunohistochemical staining (**A**, **B**) and *Egr1* gene expression as indicated by quantitative reverse-transcription polymerase chain reaction (**C**) in the hippocampus of control, aged (D-gal), and transplanted (D-gal + BMMSCs) rats. ***$P < 0.001$ vs. control rats; ##$P < 0.001$ and ###$P < 0.001$ vs. aged rats. Data are expressed as means ± standard error of mean; N = 10/group; BMMSCs — bone marrow-derived mesenchymal stem cells.

that BMMSCs can differentiate into neurons, and in particular, ChAT neurons [1, 5, 6, 12, 32, 55, 67, 78, 80, 88, 89]. The capabilities of intravenously injected MSCs from different sources to migrate and differentiate into the neuronal fate have been previously reported. In 10-month-old male F344 rats, repeated intravenously transplanted hAMMSC and hADMSCs homed to the cerebral cortex and hippocampus and differentiated into neurons, some of which co-expressed ChAT, and, in part, into astrocytes [39]. Similar results have been reported after repeated intravenous transplantation of hADMSCs [61]. However, these studies reported a higher potential of the transplanted cells to differentiate into neuronal phenotypes; in particular, ChAT-positive cells, than we observed. Differences in aging animal models, tissue source and species of the MSCs, and intravenous dose frequency may account for this discrepancy.

Previous studies have shown that the differentiation of transplanted cells into neurons and their subsequent projection to the target anatomical region is challenging, and that the beneficial effects observed in the transplanted brains could be mainly explained by transplanted stem cell-mediated protection rather than replacement. The cholinergic system involves neurons found mainly in the basal forebrain and their long axons that projects diffusely to the cerebral cortex and the hippocampus. We observed limited differentiation

of the transplanted cells into the neuronal fate in the cortex and hippocampus. Interestingly, we observed a significant increase in the number of endogenous ChAT-positive cells in the basal forebrain in transplanted rats when compared with aged rats, which cannot be explained by the limited number of transplanted cells that colocalised with ChAT immunostaining in the basal forebrains of these rats. These results indicated an endogenous regeneration of the host cholinergic system in the basal forebrain in transplanted rats. Therefore, we next sought to assess potential bystander-like mechanisms mediated by the transplanted BMMSCs that would contribute to the endogenous regeneration of the host cholinergic system and lead to the observed beneficial effects on functional and cognitive activities.

Cholinergic neurons in the basal forebrain depend for their survival and function on neurotrophic factors, such as BDNF and NGF, which are retrogradely transported from basal forebrain targets. Aging is accompanied by alterations in the neurotrophic signalling pathways, which have crucial roles in the cholinergic and cognitive deficits found in aging and AD [14, 15, 23, 50, 51, 79]. In cultured embryonic rat basal forebrain and cortical neurons in microfluidic chambers used as models of normal aging, significant declines in BDNF and proNGF transport have been observed, suggesting the susceptibility of aged forebrain cholinergic neurons to age-induced transport

malfunction [73]. BDNF-knockout mice possessed reduced numbers of cholinergic cells in the medial septum, which was associated with reduced ChAT activity and NGF expression in the hippocampus [27]. We observed decreased *BDNF* and *NGF* expressions in both the hippocampus and cortex in D-gal aging rats, which is in line with findings reported in several previous studies [24, 37, 44, 57]. These decreases were remarkably restored in BMMSC-transplanted rats. A substantial body of evidence suggests the neurotrophic and paracrine potential of stem cell transplantation, which is accomplished by increased concentrations of various neurotrophic factors such as BDNF, NGF, and glial cell-derived neurotrophic factor [7]. BDNF and NGF levels in F344 rat brains markedly increased after transplantation of hAMMSC and hADMSCs [56], and in aged mice after transplantation of ADMSCs [61]. In addition, hBMMSCs upregulate the BDNF level, rescuing cultured rodent cortical neurons from degeneration by trophic factor absence or oxidative stress [86] and ameliorating spinal cord injury *in vivo* by increasing both BDNF and NGF levels [69]. Hence, the observed restoration of cholinergic functions is most likely due to the secretion of neurotrophic factors by the migrated cells, which were then taken up by projected axonal terminals and retrogradely transported into cholinergic neuron bodies, preventing their loss.

To explore the pathways involved in the observed improvement of cognitive deficits in BMMSCs + D-gal-rats, we investigated factors involved in synaptic activity and plasticity. Reduced transcription of the immediate early gene *Egr1* in the hippocampus has been related to age-related memory deficits [21, 62, 93]. Our results showed that *Egr1* expression was reduced in the hippocampi of aged rats when compared with control rats. The restoration of competent spatial memory in the water maze test correlated with Egr1 expression in the hippocampi of aged mice [93]. In the present study, BMMSC transplantation triggered *Egr1* expression in the hippocampus in aging rats. Cao et al. [17] reported that hUCMSCs stimulated the intracellular MAPK-ERK signalling and subsequently enhanced several effectors, including Egr1 and PSD95. These effectors play important roles in neuron morphology, synaptic plasticity, and cognitive integrity in aged brain. Therefore, it is likely that the enhancement of Egr1 expression by BMMSCs in transplanted rats have contributed to the countering of the age-related cognitive decline.

Limitations of the study

Our study had some limitations. First, neuronal differentiation of the transplanted cells was limited. Enhancing the neuronal differentiation of the transplanted cells would further improve their therapeutic capacity; therefore, optimising strategies to further improve the neuronal differentiation potential of the transplanted cells are needed. Second, the effect of transplanted cells on neurogenesis was not assessed. Third, the transplanted BM population did not represent pure MSCs. According to phenotypic profiling, 9.5% of the BMMSCs utilised in this study expressed CD34. This cell population may have contributed to the beneficial effects observed in this study. Finally, the optimisation of the cell-delivery protocol, including the number of transplanted cells, frequency of injections, and route of delivery requires further investigation.

CONCLUSIONS

The current study demonstrated that intravenous transplantation of BMMSCs prevented cognitive and physical deficits in a D-gal aging rat model by restoring cholinergic system function, protecting atrophic cholinergic neurons in the basal forebrain, inducing antioxidative effects and restoring neurotrophic factors, and modulating hippocampal synaptic plasticity by triggering PSD95 and Egr1 expression. Our results provide evidence of the usability of systemic transplantation of BMMSCs as a potential therapeutic approach for the prevention of neurodegenerative changes associated with aging. However, prior to commencing clinical trials, further studies are needed to enhance the differentiation of these cells into the neuronal fate *in vivo* and to untangle the molecular mechanisms underlying the beneficial effects of BMMSC-secreted factors.

REFERENCES

1. Abdullah RH, Yaseen NY, Salih SM, et al. Induction of mice adult bone marrow mesenchymal stem cells into functional motor neuron-like cells. J Chem Neuroanat. 2016; 77: 129–142, doi: 10.1016/j.jchemneu.2016.07.003, indexed in Pubmed: 27417692.

2. Albin RL, Bohnen NI, Muller ML, et al. Regional vesicular acetylcholine transporter distribution in human brain: A [18 F]fluoroethoxybenzovesamicol positron emission tomography study. J Comp Neurol. 2018; 526(17): 2884–2897, doi: 10.1002/cne.24541, indexed in Pubmed: 30255936.

3. Artegiani B, Calegari F. Age-related cognitive decline: can neural stem cells help us? Aging (Albany NY). 2012; 4(3): 176–186, doi: 10.18632/aging.100446, indexed in Pubmed: 22466406.

4. Badyra B, Sułkowski M, Milczarek O, et al. Mesenchymal stem cells as a multimodal treatment for nervous system diseases. Stem Cells Transl Med. 2020; 9(10): 1174–1189, doi: 10.1002/sctm.19-0430, indexed in Pubmed: 32573961.

5. Bae KS, Park JB, Kim HS, et al. Neuron-like differentiation of bone marrow-derived mesenchymal stem cells. Yonsei Med J. 2011; 52(3): 401–412, doi: 10.3349/ymj.2011.52.3.401, indexed in Pubmed: 21488182.

6. Bai WF, Zhang Y, Xu W, et al. Isolation and characterization of neural progenitor cells from bone marrow in cell replacement therapy of brain injury. Front Cell Neurosci. 2020; 14: 49, doi: 10.3389/fncel.2020.00049, indexed in Pubmed: 32226361.

7. Bali P, Lahiri DK, Banik A, et al. Potential for stem cells therapy in Alzheimer's disease: do neurotrophic factors play critical role? Curr Alzheimer Res. 2017; 14(2): 208–220, doi: 10.2174/1567205013666160314145347, indexed in Pubmed: 26971940.

8. Barrientos RM, Kitt MM, Watkins LR, et al. Neuroinflammation in the normal aging hippocampus. Neuroscience. 2015; 309: 84–99, doi: 10.1016/j.neuroscience.2015.03.007, indexed in Pubmed: 25772789.

9. Bekdash RA. The cholinergic system, the adrenergic system and the neuropathology of Azheimer's disease. Int J Mol Sci. 2021; 22(3), doi: 10.3390/ijms22031273, indexed in Pubmed: 33525357.

10. Berebichez-Fridman R, Montero-Olvera PR. Sources and clinical applications of mesenchymal stem cells: state-of-the-art review. Sultan Qaboos Univ Med J. 2018; 18(3): e264–e277, doi: 10.18295/squmj.2018.18.03.002, indexed in Pubmed: 30607265.

11. Bishop NA, Lu T, Yankner BA. Neural mechanisms of ageing and cognitive decline. Nature. 2010; 464(7288): 529–535, doi: 10.1038/nature08983, indexed in Pubmed: 20336135.

12. Borkowska P, Fila-Danilow A, Paul-Samojedny M, et al. Differentiation of adult rat mesenchymal stem cells to GABAergic, dopaminergic and cholinergic neurons. Pharmacol Rep. 2015; 67(2): 179–186, doi: 10.1016/j.pharep.2014.08.022, indexed in Pubmed: 25712637.

13. Bortolotti F, Ukovich L, Razban V, et al. In vivo therapeutic potential of mesenchymal stromal cells depends on the source and the isolation procedure. Stem Cell Reports. 2015; 4(3): 332–339, doi: 10.1016/j.stemcr.2015.01.001, indexed in Pubmed: 25660405.

14. Boskovic Z, Meier S, Wang Y, et al. Regulation of cholinergic basal forebrain development, connectivity, and function by neurotrophin receptors. Neuronal Signal. 2019; 3(1): NS20180066, doi: 10.1042/NS20180066, indexed in Pubmed: 32269831.

15. Budni J, Bellettini-Santos T, Mina F, et al. The involvement of BDNF, NGF and GDNF in aging and Alzheimer's disease. Aging Dis. 2015; 6(5): 331–341, doi: 10.14336/AD.2015.0825, indexed in Pubmed: 26425388.

16. Bustos FJ, Ampuero E, Jury N, et al. Epigenetic editing of the Dlg4/PSD95 gene improves cognition in aged and Alzheimer's disease mice. Brain. 2017; 140(12): 3252–3268, doi: 10.1093/brain/awx272, indexed in Pubmed: 29155979.

17. Cao N, Liao T, Liu J, et al. Clinical-grade human umbilical cord-derived mesenchymal stem cells reverse cognitive aging via improving synaptic plasticity and endogenous neurogenesis. Cell Death Dis. 2017; 8(8): e2996, doi: 10.1038/cddis.2017.316, indexed in Pubmed: 28796260.

18. Casu MA, Wong TP, De Koninck Y, et al. Aging causes a preferential loss of cholinergic innervation of characterized neocortical pyramidal neurons. Cereb Cortex. 2002; 12(3): 329–337, doi: 10.1093/cercor/12.3.329, indexed in Pubmed: 11839606.

19. Daniele S, Giacomelli C, Martini C. Brain ageing and neurodegenerative disease: The role of cellular waste management. Biochem Pharmacol. 2018; 158: 207–216, doi: 10.1016/j.bcp.2018.10.030, indexed in Pubmed: 30393045.

20. Daulatzai MA. Early stages of pathogenesis in memory impairment during normal senescence and Alzheimer's disease. J Alzheimers Dis. 2010; 20(2): 355–367, doi: 10.3233/JAD-2010-1374, indexed in Pubmed: 20164576.

21. Duclot F, Kabbaj M. The role of early growth response 1 (EGR1) in brain plasticity and neuropsychiatric disorders. Front Behav Neurosci. 2017; 11: 35, doi: 10.3389/fnbeh.2017.00035, indexed in Pubmed: 28321184.

22. Ellman G. Tissue sulfhydryl groups. Arch Biochem Biophys. 1959; 82(1): 70–77, doi: 10.1016/0003-9861(59)90090-6.

23. Erickson KI, Prakash RS, Voss MW, et al. Brain-derived neurotrophic factor is associated with age-related decline in hippocampal volume. J Neurosci. 2010; 30(15): 5368–5375, doi: 10.1523/JNEUROSCI.6251-09.2010, indexed in Pubmed: 20392958.

24. Fatemi I, Khaluoi A, Kaeidi A, et al. Protective effect of metformin on D-galactose-induced aging model in mice. Iran J Basic Med Sci. 2018; 21(1): 19–25, doi: 10.22038/IJBMS.2017.24331.6071, indexed in Pubmed: 29372032.

25. Ge M, Zhang Y, Hao Q, et al. Effects of mesenchymal stem cells transplantation on cognitive deficits in animal models of Alzheimer's disease: a systematic review and meta-analysis. Brain Behav. 2018; 8(7): e00982, doi: 10.1002/brb3.982, indexed in Pubmed: 29877067.

26. Gemma C, Vila J, Bachstetter A, Bickford PC. Oxidative stress and the aging brain: from theory to prevention. In: riddle DR (ed.). Brain aging: models, methods, and mechanisms. Frontiers in neuroscience. Boca Raton, FL 2007.

27. Grosse G, Djalali S, Deng DR, et al. Area-specific effects of brain-derived neurotrophic factor (BDNF) genetic ablation on various neuronal subtypes of the mouse brain. Brain

Res Dev Brain Res. 2005; 156(2): 111–126, doi: 10.1016/j.devbrainres.2004.12.012, indexed in Pubmed: 16099299.

28. Grothe M, Heinsen H, Teipel SJ. Atrophy of the cholinergic Basal forebrain over the adult age range and in early stages of Alzheimer's disease. Biol Psychiatry. 2012; 71(9): 805–813, doi: 10.1016/j.biopsych.2011.06.019, indexed in Pubmed: 21816388.

29. Hajjar I, Hayek SS, Goldstein FC, et al. Oxidative stress predicts cognitive decline with aging in healthy adults: an observational study. J Neuroinflammation. 2018; 15(1): 17, doi: 10.1186/s12974-017-1026-z, indexed in Pubmed: 29338747.

30. Hampel H, Mesulam MM, Cuello AC, et al. The cholinergic system in the pathophysiology and treatment of Alzheimer's disease. Brain. 2018; 141(7): 1917–1933, doi: 10.1093/brain/awy132, indexed in Pubmed: 29850777.

31. Harada CN, Natelson Love MC, Triebel KL. Normal cognitive aging. Clin Geriatr Med. 2013; 29(4): 737–752, doi: 10.1016/j.cger.2013.07.002, indexed in Pubmed: 24094294.

32. Hernandez CM, Gearhart DA, Parikh V, et al. Comparison of galantamine and donepezil for effects on nerve growth factor, cholinergic markers, and memory performance in aged rats. J Pharmacol Exp Ther. 2006; 316(2): 679–694, doi: 10.1124/jpet.105.093047, indexed in Pubmed: 16214877.

33. Hernández R, Jiménez-Luna C, Perales-Adán J, et al. Differentiation of human mesenchymal stem cells towards neuronal lineage: clinical trials in nervous system disorders. Biomol Ther (Seoul). 2020; 28(1): 34–44, doi: 10.4062/biomolther.2019.065, indexed in Pubmed: 31649208.

34. Hou Y, Dan X, Babbar M, et al. Ageing as a risk factor for neurodegenerative disease. Nat Rev Neurol. 2019; 15(10): 565–581, doi: 10.1038/s41582-019-0244-7, indexed in Pubmed: 31501588.

35. Hu S, Li CSR. Age-Related structural and functional changes of the hippocampus and the relationship with inhibitory control. Brain Sci. 2020; 10(12), doi: 10.3390/brainsci10121013, indexed in Pubmed: 33352718.

36. Hunsberger J, Rao M, Kurtzberg J, et al. Accelerating stem cell trials for Alzheimer's disease. Lancet Neurol. 2016; 15(2): 219–230, doi: 10.1016/s1474-4422(15)00332-4.

37. Ibrahim WW, Abdelkader NF, Ismail HM, et al. Escitalopram ameliorates cognitive impairment in D-galactose-injected ovariectomized rats: modulation of JNK, GSK-3beta, and ERK signalling pathways. Sci Rep. 2019; 9(1): 10056, doi: 10.1038/s41598-019-46558-1, indexed in Pubmed: 31296935.

38. Isaev NK, Stelmashook EV, Genrikhs EE. Neurogenesis and brain aging. Rev Neurosci. 2019; 30(6): 573–580, doi: 10.1515/revneuro-2018-0084, indexed in Pubmed: 30763272.

39. Kim D, Kyung J, Park D, et al. Health span-extending activity of human amniotic membrane- and adipose tissue-derived stem cells in F344 rats. Stem Cells Transl Med. 2015; 4(10): 1144–1154, doi: 10.5966/sctm.2015-0011, indexed in Pubmed: 26315571.

40. Kim Y, Kim H, Cho H, et al. Direct comparison of human mesenchymal stem cells derived from adipose tissues and bone marrow in mediating neovascularization in response to vascular ischemia. Cell Physiol Biochem. 2007; 20(6): 867–876, doi: 10.1159/000110447, indexed in Pubmed: 17982269.

41. Lee HJu, Lee JK, Lee H, et al. Human umbilical cord blood-derived mesenchymal stem cells improve neuropathology and cognitive impairment in an Alzheimer's disease mouse model through modulation of neuroinflammation. Neurobiol Aging. 2012; 33(3): 588–602, doi: 10.1016/j.neurobiolaging.2010.03.024, indexed in Pubmed: 20471717.

42. Li Z, Zhang Z, Ren Y, et al. Aging and age-related diseases: from mechanisms to therapeutic strategies. Biogerontology. 2021; 22(2): 165–187, doi: 10.1007/s10522-021-09910-5, indexed in Pubmed: 33502634.

43. Limke TL, Rao MS. Neural stem cells in aging and disease. J Cell Mol Med. 2002; 6(4): 475–496, doi: 10.1111/j.1582-4934.2002.tb00451.x, indexed in Pubmed: 12611637.

44. Liu X, Wu C, Han D, et al. Partially hydrolyzed guar gum attenuates D-galactose-induced oxidative stress and restores gut microbiota in rats. Int J Mol Sci. 2019; 20(19), doi: 10.3390/ijms20194861, indexed in Pubmed: 31574948.

45. Livak KJ, Schmittgen TD. Analysis of relative gene expression data using real-time quantitative PCR and the 2(-Delta Delta C(T)) Method. Methods. 2001; 25(4): 402–408, doi: 10.1006/meth.2001.1262, indexed in Pubmed: 11846609.

46. Lopez-Leon M, Reggiani PC, Claudia B, et al. Regenerative medicine for the aging brain. Enliven J Stem Cell Res Regen Med. 2014; 01(01), doi: 10.18650/2379-5751.11001.

47. Lushchak VI. Interplay between bioenergetics and oxidative stress at normal brain aging. Aging as a result of increasing disbalance in the system oxidative stress-energy provision. Pflugers Arch. 2021; 473(5): 713–722, doi: 10.1007/s00424-021-02531-4, indexed in Pubmed: 33599804.

48. Ma S, Zang T, Liu ML, et al. Aging-relevant human basal forebrain cholinergic neurons as a cell model for Alzheimer's disease. Mol Neurodegener. 2020; 15(1): 61, doi: 10.1186/s13024-020-00411-6, indexed in Pubmed: 33087140.

49. Mesulam M. Cholinergic aspects of aging and Alzheimer's disease. Biol Psychiatry. 2012; 71(9): 760–761, doi: 10.1016/j.biopsych.2012.02.025, indexed in Pubmed: 22482884.

50. Miranda M, Morici JF, Zanoni MB, et al. Brain-derived neurotrophic factor: a key molecule for memory in the healthy and the pathological brain. Front Cell Neurosci. 2019; 13: 363, doi: 10.3389/fncel.2019.00363, indexed in Pubmed: 31440144.

51. Molinari C, Morsanuto V, Ruga S, et al. The role of BDNF on aging-modulation markers. Brain Sci. 2020; 10(5), doi: 10.3390/brainsci10050285, indexed in Pubmed: 32397504.

52. Morrison JH, Baxter MG. The ageing cortical synapse: hallmarks and implications for cognitive decline. Nat Rev Neurosci. 2012; 13(4): 240–250, doi: 10.1038/nrn3200, indexed in Pubmed: 22395804.

53. Mota C, Taipa R, das Neves SP, et al. Structural and molecular correlates of cognitive aging in the rat. Sci Rep. 2019; 9(1): 2005, doi: 10.1038/s41598-019-39645-w, indexed in Pubmed: 30765864.

54. Naaldijk Y, Jäger C, Fabian C, et al. Effect of systemic transplantation of bone marrow-derived mesenchymal stem cells on neuropathology markers in APP/PS1 Alzheimer

mice. Neuropathol Appl Neurobiol. 2017; 43(4): 299–314, doi: 10.1111/nan.12319, indexed in Pubmed: 26918424.

55. Naghdi M, Tiraihi T, Namin SA, et al. Transdifferentiation of bone marrow stromal cells into cholinergic neuronal phenotype: a potential source for cell therapy in spinal cord injury. Cytotherapy. 2009; 11(2): 137–152, doi: 10.1080/14653240802716582, indexed in Pubmed: 19253075.

56. Nakano M, Kubota K, Kobayashi E, et al. Bone marrow-derived mesenchymal stem cells improve cognitive impairment in an Alzheimer's disease model by increasing the expression of microRNA-146a in hippocampus. Sci Rep. 2020; 10(1): 10772, doi: 10.1038/s41598-020-67460-1, indexed in Pubmed: 32612165.

57. Nam SM, Seo M, Seo JS, et al. Ascorbic acid mitigates D-galactose-induced brain aging by increasing hippocampal neurogenesis and improving memory function. Nutrients. 2019; 11(1), doi: 10.3390/nu11010176, indexed in Pubmed: 30650605.

58. Nasiri E, Alizadeh A, Roushandeh AM, et al. Melatonin-pretreated adipose-derived mesenchymal stem cells efficeintly improved learning, memory, and cognition in an animal model of Alzheimer's disease. Metab Brain Dis. 2019; 34(4): 1131–1143, doi: 10.1007/s11011-019-00421-4, indexed in Pubmed: 31129766.

59. Neves AF, Camargo C, Premer C, et al. Intravenous administration of mesenchymal stem cells reduces Tau phosphorylation and inflammation in the 3xTg-AD mouse model of Alzheimer's disease. Exp Neurol. 2021; 341: 113706, doi: 10.1016/j.expneurol.2021.113706, indexed in Pubmed: 33757765.

60. Oh SeH, Kim HaNa, Park HJ, et al. Mesenchymal stem cells increase hippocampal neurogenesis and neuronal differentiation by enhancing the wnt signaling pathway in an Alzheimer's disease model. Cell Transplant. 2015; 24(6): 1097–1109, doi: 10.3727/096368914X679237, indexed in Pubmed: 24612635.

61. Park D, Yang G, Bae DK, et al. Human adipose tissue-derived mesenchymal stem cells improve cognitive function and physical activity in ageing mice. J Neurosci Res. 2013; 91(5): 660–670, doi: 10.1002/jnr.23182, indexed in Pubmed: 23404260.

62. Penner MR, Parrish RR, Hoang LT, et al. Age-related changes in Egr1 transcription and DNA methylation within the hippocampus. Hippocampus. 2016; 26(8): 1008–1020, doi: 10.1002/hipo.22583, indexed in Pubmed: 26972614.

63. Peters R. Ageing and the brain. Postgrad Med J. 2006; 82(964): 84–88, doi: 10.1136/pgmj.2005.036665, indexed in Pubmed: 16461469.

64. Piccardi L, Curcio G, Palermo L, et al. Ageing and neurodegenerative disorders. Behav Neurol. 2015; 2015: 149532, doi: 10.1155/2015/149532, indexed in Pubmed: 26185358.

65. Polisetti N, Chaitanya VG, Babu PP, et al. Isolation, characterization and differentiation potential of rat bone marrow stromal cells. Neurol India. 2010; 58(2): 201–208, doi: 10.4103/0028-3886.63789, indexed in Pubmed: 20508336.

66. Popescu BO, Toescu EC, Popescu LM, et al. Blood-brain barrier alterations in ageing and dementia. J Neurol Sci.

2009; 283(1-2): 99–106, doi: 10.1016/j.jns.2009.02.321, indexed in Pubmed: 19264328.

67. Qi Y, Zhang F, Song Ge, et al. Cholinergic neuronal differentiation of bone marrow mesenchymal stem cells in rhesus monkeys. Sci China Life Sci. 2010; 53(5): 573–580, doi: 10.1007/s11427-010-0009-4, indexed in Pubmed: 20596940.

68. Qin C, Lu Y, Wang K, et al. Transplantation of bone marrow mesenchymal stem cells improves cognitive deficits and alleviates neuropathology in animal models of Alzheimer's disease: a meta-analytic review on potential mechanisms. Transl Neurodegener. 2020; 9(1): 20, doi: 10.1186/s40035-020-00199-x, indexed in Pubmed: 32460886.

69. Ramalho BD, Almeida FM, Sales CM, et al. Injection of bone marrow mesenchymal stem cells by intravenous or intraperitoneal routes is a viable alternative to spinal cord injury treatment in mice. Neural Regen Res. 2018; 13(6): 1046–1053, doi: 10.4103/1673-5374.233448, indexed in Pubmed: 29926832.

70. Rangan GK, Tesch GH. Quantification of renal pathology by image analysis. Nephrology (Carlton). 2007; 12(6): 553–558, doi: 10.1111/j.1440-1797.2007.00855.x, indexed in Pubmed: 17995580.

71. Reeve A, Simcox E, Turnbull D. Ageing and Parkinson's disease: why is advancing age the biggest risk factor? Ageing Res Rev. 2014; 14: 19–30, doi: 10.1016/j.arr.2014.01.004, indexed in Pubmed: 24503004.

72. Schliebs R, Arendt T. The cholinergic system in aging and neuronal degeneration. Behav Brain Res. 2011; 221(2): 555–563, doi: 10.1016/j.bbr.2010.11.058, indexed in Pubmed: 21145918.

73. Shekari A, Fahnestock M. Retrograde axonal transport of BDNF and proNGF diminishes with age in basal forebrain cholinergic neurons. Neurobiol Aging. 2019; 84: 131–140, doi: 10.1016/j.neurobiolaging.2019.07.018, indexed in Pubmed: 31574357.

74. Shen J, Tsai YT, Dimarco NM, et al. Transplantation of mesenchymal stem cells from young donors delays aging in mice. Sci Rep. 2011; 1: 67, doi: 10.1038/srep00067, indexed in Pubmed: 22355586.

75. Sikora E, Bielak-Zmijewska A, Dudkowska M, et al. Cellular senescence in brain aging. Front Aging Neurosci. 2021; 13: 646924, doi: 10.3389/fnagi.2021.646924, indexed in Pubmed: 33732142.

76. Simpson JE, Wharton SB, Cooper J, et al. Alterations of the blood-brain barrier in cerebral white matter lesions in the ageing brain. Neurosci Lett. 2010; 486(3): 246–251, doi: 10.1016/j.neulet.2010.09.063, indexed in Pubmed: 20887772.

77. Stepanichev M, Nedogreeva O, Gulyaeva N. Cholinergic degeneration in early stages of Alzheimer's disease: loss of cholinergic phenotype or loss of cells? Alzheimers Dement Cogn Neurol. 2017; 1(2), doi: 10.15761/adcn.1000110.

78. Sun C, Shao J, Su Le, et al. Cholinergic neuron-like cells derived from bone marrow stromal cells induced by tricyclodecane-9-yl-xanthogenate promote functional recovery and neural protection after spinal cord injury. Cell Transplant. 2013; 22(6): 961–975, doi: 10.3727/096368912X657413, indexed in Pubmed: 23031841.

79. Tapia-Arancibia L, Aliaga E, Silhol M, et al. New insights into brain BDNF function in normal aging and Alzheimer dis-

ease. Brain Res Rev. 2008; 59(1): 201–220, doi: 10.1016/j.brainresrev.2008.07.007, indexed in Pubmed: 18708092.

80. Tropel P, Platet N, Platel JC, et al. Functional neuronal differentiation of bone marrow-derived mesenchymal stem cells. Stem Cells. 2006; 24(12): 2868–2876, doi: 10.1634/stemcells.2005-0636, indexed in Pubmed: 16902198.

81. Utkin YN. Aging affects nicotinic acetylcholine receptors in brain. Cent Nerv Syst Agents Med Chem. 2019; 19(2): 119–124, doi: 10.2174/1871524919666190320102834, indexed in Pubmed: 30894113.

82. Vallianatou T, Shariatgorji M, Nilsson A, et al. Molecular imaging identifies age-related attenuation of acetylcholine in retrosplenial cortex in response to acetylcholinesterase inhibition. Neuropsychopharmacology. 2019; 44(12): 2091–2098, doi: 10.1038/s41386-019-0397-5, indexed in Pubmed: 31009936.

83. Voigt RM, Raeisi S, Yang J, et al. Systemic brain derived neurotrophic factor but not intestinal barrier integrity is associated with cognitive decline and incident Alzheimer's disease. PLoS One. 2021; 16(3): e0240342, doi: 10.1371/journal.pone.0240342, indexed in Pubmed: 33661922.

84. Volkman R, Offen D. Concise review: mesenchymal stem cells in neurodegenerative diseases. Stem Cells. 2017; 35(8): 1867–1880, doi: 10.1002/stem.2651, indexed in Pubmed: 28589621.

85. Wang X, Ma S, Yang Bo, et al. Resveratrol promotes hUC-MSCs engraftment and neural repair in a mouse model of Alzheimer's disease. Behav Brain Res. 2018; 339: 297–304, doi: 10.1016/j.bbr.2017.10.032, indexed in Pubmed: 29102593.

86. Wilkins A, Kemp K, Ginty M, et al. Human bone marrow-derived mesenchymal stem cells secrete brain-derived neurotrophic factor which promotes neuronal survival in vitro. Stem Cell Res. 2009; 3(1): 63–70, doi: 10.1016/j.scr.2009.02.006, indexed in Pubmed: 19411199.

87. Wills ED. Evaluation of lipid peroxidation in lipids and biologicalmembranes. In: Snell K, Mullock B (eds.), Biochemical toxicology: a practicalapproach. Oxford, London 1987.

88. Wu QY, Li J, Feng ZT, et al. Bone marrow stromal cells of transgenic mice can improve the cognitive ability of an Alzheimer's disease rat model. Neurosci Lett. 2007; 417(3): 281–285, doi: 10.1016/j.neulet.2007.02.092, indexed in Pubmed: 17412501.

89. Yi TG, Cho YK, Lee HJ, et al. A novel immunomodulatory mechanism dependent on acetylcholine secreted by human bone marrow-derived mesenchymal stem cells. Int J Stem Cells. 2019; 12(2): 315–330, doi: 10.15283/ijsc18098, indexed in Pubmed: 31242717.

90. Yun HM, Kim HS, Park KR, et al. Placenta-derived mesenchymal stem cells improve memory dysfunction in an Aβ1-42-infused mouse model of Alzheimer's disease. Cell Death Dis. 2013; 4: e958, doi: 10.1038/cddis.2013.490, indexed in Pubmed: 24336078.

91. Zappa Villar MF, Lehmann M, García MG, et al. Mesenchymal stem cell therapy improves spatial memory and hippocampal structure in aging rats. Behav Brain Res. 2019; 374: 111887, doi: 10.1016/j.bbr.2019.04.001, indexed in Pubmed: 30951751.

92. Zhang XM, Ouyang YJ, Yu BQ, et al. Therapeutic potential of dental pulp stem cell transplantation in a rat model of Alzheimer's disease. Neural Regen Res. 2021; 16(5): 893–898, doi: 10.4103/1673-5374.297088, indexed in Pubmed: 33229725.

93. Zhou G, Xiong W, Zhang X, et al. Retrieval of consolidated spatial memory in the water maze is correlated with expression of pCREB and egr1 in the hippocampus of aged mice. Dement Geriatr Cogn Dis Extra. 2013; 3(1): 39–47, doi: 10.1159/000348349, indexed in Pubmed: 23569457.

94. Zia A, Pourbagher-Shahri AM, Farkhondeh T, et al. Molecular and cellular pathways contributing to brain aging. Behav Brain Funct. 2021; 17(1): 6, doi: 10.1186/s12993-021-00179-9, indexed in Pubmed: 34118939.

95. Zilka N, Zilkova M, Kazmerova Z, et al. Mesenchymal stem cells rescue the Alzheimer's disease cell model from cell death induced by misfolded truncated tau. Neuroscience. 2011; 193: 330–337, doi: 10.1016/j.neuroscience.2011.06.088, indexed in Pubmed: 21763758.

VIA MEDICA

ORIGINAL ARTICLE

Ultrastructural features on the oral cavity floor (tongue, sublingual caruncle) of the Egyptian water buffalo (*Bubalus bubalis*): gross, histology and scanning electron microscope

F.A. Farrag[1], S.F. Mahmoud[2], M.A. Kassab[3], A. Hassan[1], F. Abdelmohdy[3], M. Shukry[4], M.M.A. Abumandour[5], M. Fayed[1]

[1]Department of Anatomy and Embryology, Faculty of Veterinary Medicine, Kafrelsheikh University, Kafrelsheikh, Egypt
[2]Department of Biotechnology, College of Science, Taif University, Taif, Saudi Arabia
[3]Department of Cytology and Histology, Faculty of Veterinary Medicine, Kafrelsheikh University, Kafrelsheikh, Egypt
[4]Department of Physiology, Faculty of Veterinary Medicine, Kafrelsheikh University, Kafrelsheikh, Egypt
[5]Department of Anatomy and Embryology, Faculty of Veterinary Medicine, Alexandria University, Alexandria, Egypt

Background: The present work was focused on the evaluation of morphological characteristics of the lingual caruncles and tongue with its papillae of Egyptian water buffalo (Bubalus bubalis) using gross examination, light and scanning electron microscopy.

Materials and methods: The ventral surface of the sublingual caruncle carried a small opening of the duct of both monostomatic and mandibular salivary gland. The lingual mucosa of dorsal, lateral border and, to some extent, of ventral surface of apex had lingual papillae (filiform, fungiform), while the lingual mucosa of the lingual body especially at torus linguae had conical papillae, but circumvallate papillae observed at the caudal part of body and root. The dorsal surface of the apex and body carried numerous long, thread-like, with blunt apex, caudally directed filiform papillae that covered with keratinised scales without secondary papillae.

Results: The degree of keratinisation classified filiform papillae into rostral part of high keratinisation and caudal of less keratinisation. Conical papillary surface carried exfoliated epithelium with longitudinal groove on its rostral surface and carried secondary papillae. Fungiform papillae were scattered among filiform papillae on the dorsal and ventral surface of the apex and its convex surface had exfoliated keratinised epithelium. Circumvallate papillae were surrounded by circular deep groove bordered by vallum that carried small secondary papillae that ended into the primary groove. Taste buds of circumvallate papillae opened in the lateral lining epithelium facing the groove.

Conclusions: Von Ebner's glands were observed in computed tomography under papillae especially toward the groove and their ducts open into the base of the groove. (Folia Morphol 2022; 81, 3: 650–662)

Key words: lingual caruncles, tongue, lingual papillae, Egyptian water buffalo, histology, scanning electron microscope (SEM)

Address for correspondence: Prof. M. Abumandour, Department of Anatomy and Embryology, Faculty of Veterinary Medicine, Alexandria University, Alexandria, Egypt, Post Box: 22785, tel: +20 1000322937, fax: +20 452960450, e-mail: m.abumandour@yahoo.com or M.abumandour@alexu.edu.eg

INTRODUCTION

Egyptian water buffalo *Bubalus bubalis* (Linnaeus, 1758) subspecies was classified under *Bubalus bubalis* species, *Bubalus* genus, *Bovidae* family, *Artiodactyla* suborder, *Ruminantia* order. The Egyptian water buffalo is the most important domestic animal and their number reached 2.5 million [25] in Egypt. The Egyptian water buffalo feed mainly on the green grasses, plants, and other roughage materials with the help of large lips, and elongated protrusible tongue to collect the food materials [38, 39].

The tongue was the most important organ that was modified with characteristic feeding tendencies, behaviour, and various types of food particles that could be accessed; moreover, the lingual structure was modified to play different abilities, for example, feeding input, control, and ingestion of nutrition molecules [3]. The morphological appearance, prevalence, orientation, and structure of lingual papillae were modified in accordance with the nutritional requirements, the types of nutritional particles accessible, and the various environmental conditions [3]. Most previously published anatomical articles concerned on the tongue and its papillae of the domestic animal species [12, 15, 18, 20, 28, 32, 35, 37, 49] but there were rare data on the Egyptian water buffalo (*Bubalus bubalis*) from Egypt.

The available data about the sublingual caruncle and sublingual floor of the domestic animals including the Egyptian water buffalo (*Bubalus bubalis*) were scanty. The current work was conducted to give a full morphological characterisation of the tongue with its papillae, sublingual caruncle, and the sublingual floor of the Egyptian water buffalo (*Bubalus bubalis*) using the gross, scanning electron microscope (SEM), and histological techniques to describe the relation of our findings with the feeding mechanism of Egyptian water buffalo (*Bubalus bubalis*). Then, the obtained findings were compared with those reported in the formerly published articles on the ruminant and other domesticated animal species.

MATERIALS AND METHODS

Sample's collection

Twelve heads from the normal adult Egyptian water buffalo (*Bubalus bubalis*) of both sexes were collected from the local slaughterhouse in Kafrelsheikh Governate, Egypt. The samples were collected directly after slaughtering. The present investigation was prepared according to the guidelines for the using and caring of the laboratory animals and animal ethics and welfare in the Faculty of Veterinary Medicine, Alexandria University and according to the Egyptian laws.

Gross morphology observations

The tongue, sublingual caruncle, and sublingual floor were collected from four Egyptian water buffalo heads of both sexes, were prepared to demonstrate the gross morphology of the tongue, sublingual caruncle, and sublingual floor. Then, the collected samples were fixed in 10% formalin. The gross morphological images were examined and photographed by a digital camera (Cannon IXY 325, Japan). The anatomical terms followed the [46].

For histological and histochemistry studies

The tongue, sublingual caruncle, and sublingual floor from four heads of Egyptian water buffalo (*Bubalus bubalis*), were used in the histological techniques in the fresh state according to Suvarna et al. [52] to examine under a light microscope. The collected samples (tongue, sublingual caruncle, and sublingual floor) were fixed in 10% normal buffer formalin. After 24 h, the samples were gently transferred to 70% alcohol. Then, they were dehydrated in ascending graded series of ethanol. Then, the samples were cleared in xylene and impregnated and embedded in paraffin wax. Sections of 5–7 μm were cut using Leica rotatory microtome (RM 2035) and mounted on glass slides. Paraffin sections were used for conventional staining (haematoxylin and eosin) for general histological examinations [10].

For histochemistry processing, the sections were stained with Periodic Acid-Schiff (PAS) technique (ab150680) to demonstrate the neutral mucin [50], Alcian Blue (AB) at pH of 2.5 (ab150662) for acidic mucin [11, 51], Van Gieson (mixture of picric acid and acid fuchsin) for elastic fibres in connective tissue, trichrome for collage fibres in the connective tissue [42]. The histological techniques and stains were adopted according to Suvarna et al. [52].

For scanning electron microscopy

Four Egyptian water buffalo (*Bubalus bubalis*) heads were used to collect the samples (tongue, sublingual caruncle, and sublingual floor) used in the SEM technique [2, 5]. The collected samples (tongue, sublingual caruncle, and sublingual floor) were fixed at 4°C in a solution of fixation formed from: 2% formaldehyde, 1.25% glutaraldehyde in
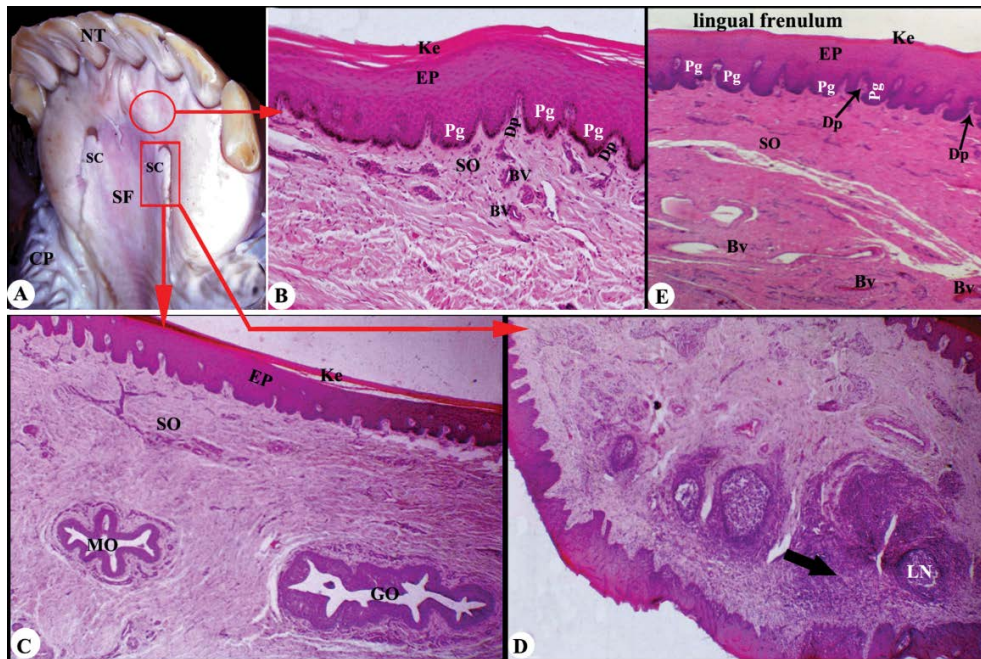
Figure 1. Macroscopic (**A**) and histological (**B–E**) images of the sublingual floor of the Egyptian water buffallo. Panel **A** to show: incisive teeth (NT), sublingual floor (SF), sublingual caruncles (SC), conical papillae of check (CP). Panels **B–D** of the sublingual caruncle to show: sligthly keratinised (Ke), stratified squamous epithelium (EP), epidermal peg (Pg), dermal papillae (Dp), submucosa (SO), blood vessls (BV), opening of minor sublingual salivary galnd (MO), opening of minor sublingual salivary galnd (GO), diffuse lymphatic tissue (black arrow), and lymph nodule (Ln). Panel **E** of lingual frenulum to show: keratinised (Ke), stratified squamous epithelium (EP), epidermal peg (Pg), dermal papillae (Dp), submucosa (SO), blood vessls (BV).

0.1 M sodium cacodylate buffer, pH 7.2. Once fixation occurs, the collected samples were washed in 0.1 M sodium cacodylate containing 5% sucrose, processed through tannic acid. Finally, the lingual samples were dehydrated by using an increasing concentration of ethanol (15 min each in 50, 70, 80, 90, 95, and 100% ethanol). The collected samples were then dried in carbon dioxide and attached to stubs with colloidal carbon and coated with gold palladium in a sputtering device. In the end, the collected samples were examined and photographed with a JEOL SEM operating at 15 kV, at the faculty of science, Alexandria University, Egypt.

RESULTS

Sublingual floor and sublingual caruncle
Gross morphological appearance of the sublingual floor and sublingual caruncles

The floor of the oral cavity had the tongue, the sublingual caruncles, and the musculocutaneous wall. The sublingual floor of the oral cavity was crescentic in shape and located under the tongue within the dental arch (Fig. 1A). It was subdivided into two parts:

the prefrenular part rostrally and the two sublingual recesses caudally. The prefrenular part was located caudal to the central incisors and extended caudally to the level of frenulum linguae. This part carried two sublingual caruncles (Fig. 1A; SC). The ventral surface of the sublingual caruncle carried a small opening at which opened the duct of both monostoamtic sublingual salivary gland and the mandibular salivary gland.

The frenulum lingua was a mucosal membrane fold connecting the ventral surface of the tongue with the floor of oral cavity. The frenulum lingua was wide, extensive, and single-fold, and it was located caudal to the level of the central incisors. The lateral sublingual recesses (Fig. 2A; SLR) were bounded laterally by the lower cheek teeth and medially by the lateral lingual surface. It was extended from the frenulum linguae rostrally till the level of the pterygomandibular fold caudally. This part had a conical papillae of pointed apex rostrally, while its caudal part was smooth. These conical papillae were arranged in two rows; the upper row had about 15 papillae and the lower one had about 10 papillae only (Fig. 1A; CP).
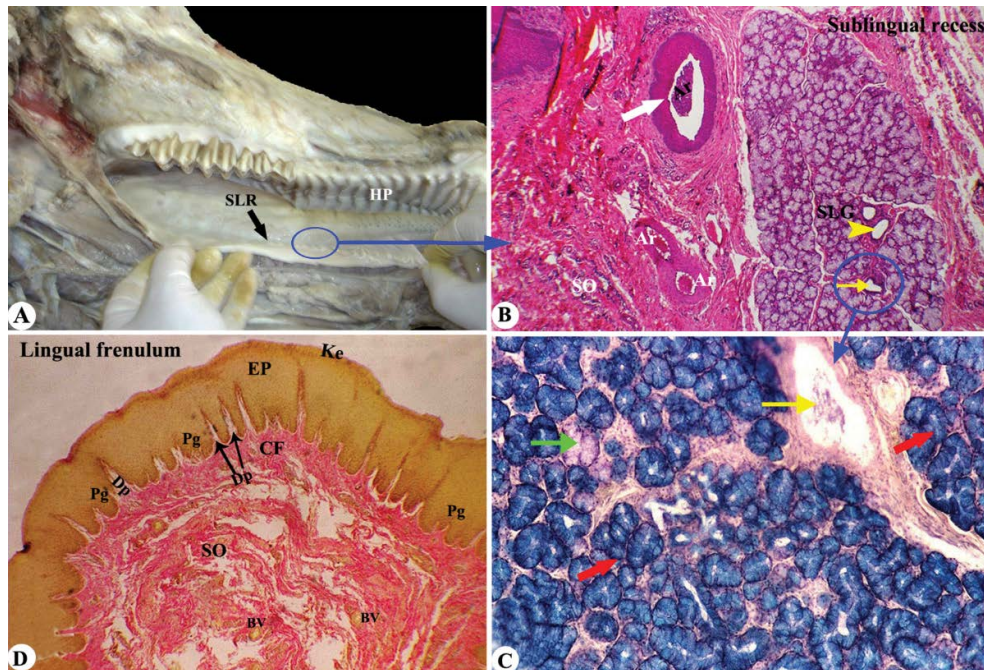
Figure 2. Macroscopic (**A**) and histological (**B–D**) images of the sublingual caruncles of the Egyptian water buffallo. Panel **A** to show: sublingual recess (SLR), hard palate (HP). Panels **B–C** to show: artery (Ar), sublingual gland (SLG), submucosa (SO), stained acini (red arrow), unstained acini (green arrows), interlobular duct (yellow arrow), striated duct (yeloow arrowheads). Panel **D** of lingual frenulum to show: sligthly keratinised (Ke), stratified squamous epithelium (EP), epidermal peg (Pg), dermal papillae (Dp), submucosa (SO), blood vessls (BV).

Histological observations of the sublingual floor and sublingual caruncles

The floor of oral cavity was lined by stratified squamous keratinised epithelium. Under the epithelium, there was a thick dense irregular connective tissue layer of propria-submucosa of the dermal layer. There were numerous epidermal pegs interdigitated with numerous dermal papillae (Fig. 1B). The sublingual caruncle was lined by stratified squamous keratinised epithelium. Under the epithelium, there was a thick dense irregular connective tissue layer that had two ducts, which opened to the ventral surface of the sublingual caruncle (Fig. 1C). The sublingual caruncle had two surfaces; the dorsal (like that of the floor) and the ventral surface that had aggregations of the lymphocytic nodule's (Fig. 1D). The two ducts in the submucosa of the ventral: one duct of the mandibular and other of monostoamtic sublingual salivary glands (Fig. 1D; MO, GO).

The sublingual recess consisted of stratified squamous keratinized epithelium. The submucosa was highly vascular, highly innervated dense irregular connective tissue contained the sublingual salivary glands. These glands were mucoserous in nature that had positive reaction of PAS and AB stain (Fig. 2C).

The frenulum lingua was lined with stratified squamous keratinised epithelium, and the submucosa consisted of dense irregular connective tissue that highly vascular and innervations. The submucosal layer sends dermal connective tissue papillae to invaginate the mucous membrane and interdigitated with the epidermal pegs. These connective tissue papillae carried secondary papillae (Fig. 1E, 2D).

Tongue

Gross morphological characters of the tongue

The tongue occupied the oral cavity proper in the sublingual floor when the upper and lower teeth were close to each other. It reached 36–38 cm in length (from the lingual root to the lingual apex) and 32 cm (from the palatoglossal fold to the apex). The free lingual part measured 9–10 cm in length that formed about 25% of the total lingual length. The lingual width was wider rostrally than caudally. The tongue is divided into three parts: the apex, the body and the root. The rostral lingual part (apex) was flattened dorsoventrally with two surfaces (dorsal and ventral) and two borders. While the caudal lingual part (body and root) had only the dorsal surface and two lateral borders (Fig. 3A). The dorsal lingual surface had a large, rounded prominence (torus linguae) that was located in front of its deep fossa (fossa linguae) (Fig. 3A, 4A; TL, FL).
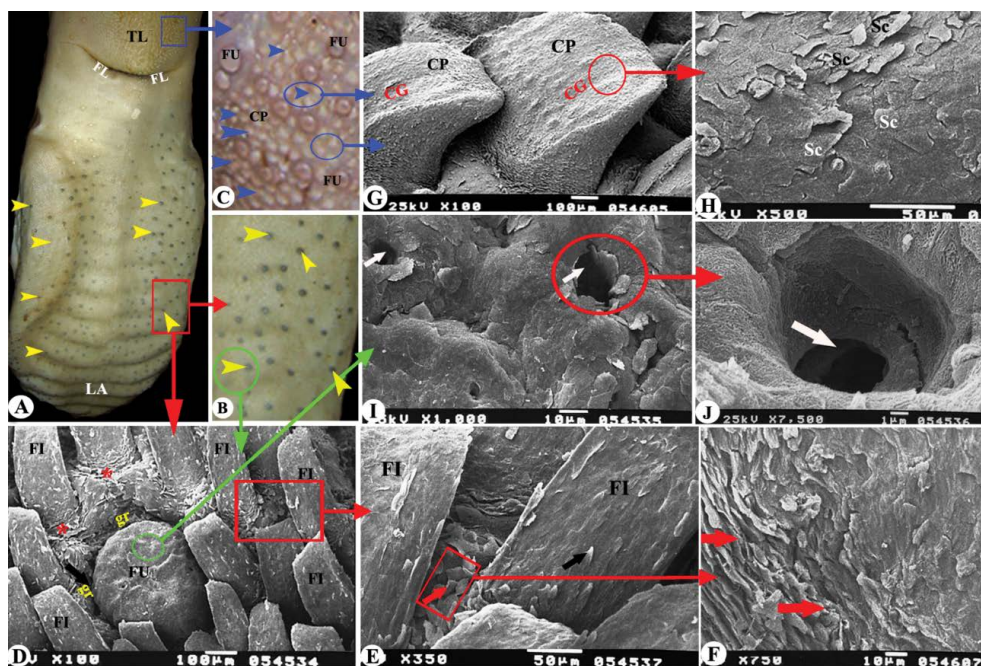
Figure 3. Macroscopic (**A–C**) and scanning electron microscope (**D–J**) images of the tongue of the Egyptian water buffallo. Panels **A–C** to show: lingual apex (LA), torus linguae (TL), fossa lingua (FL), pigmentated fungifrom papillae (yellow arrowheads), non-pigentated fungiform papillae (FU), conical papillae (CP), lentiform papillae (blue arrowheads). Panels **D–J** to show: filiform papillae (FI) with its depressed origin (red star) and keratinised scales (black arrow), interpapillary space had some exfoliated keratinised epithelia-like filiform papillae surface (red arrow), fungiform papillae (FU) surrounded by circular groove (gr) and carried taste pores on its dorsal surfae (white arrow), conical papillae (CP) with its central groove (CG) and keratinised scales (Sc) on its rostral surface.

The mechanical papillae represented by three papillary types: filiform, conical and lentiform papillae. The filiform papillae were the numerous papillae observed on the lingual mucosa that give the raspy appearance of the buffalo tongue. These papillae were distributed all over the dorsal lingual surface till the beginning of the torus linguae and extended to the lateral border and to some extent on the ventral surface (Fig. 3A). Also, these papillae were observed on the lateral border of the body. The caudally directed conical papillae were restricted only to the torus linguae, especially on its central part. These papillae were of different size; the large ones were observed at the centre of torus linguae and their size decreased at the peripheral of laterally directed areas (Fig. 3A–C; CP). The lentiform papillae of different sizes were observed on the dorsal lingual surface only at the torus linguae (Fig. 3A–C; blue arrowheads).

The gustatory papillae were represented by two papillary types: fungiform and circumvallate papillae. The fungiform papillae were widely distributed all over the dorsum surface and lateral border of the tongue. There were two subtypes of fungiform papillae: the first subtype was the pigmented pa-

pillae and concentrated only in the rostral part of the apex and the lateral border of the tongue (Fig. 3A, B; yellow arrowheads). The second subtype was non-pigmented and observed in the caudal part of the apex and torus linguae (Fig. 3C; FU). The circumvallate papillae were observed in the caudal lingual part in front of the palatoglossal fold (Fig. 4A, B; 7A, B). These papillae were arranged in 2–3 irregular rows with papillae of different sizes (Fig. 4B). They were rounded and surrounded by groove, which in turn was surrounded by an elevated part named vallum. There were two papillae with one groove and vallum (Fig. 4B; green ovoid). Their number ranged from 18–24 on each side of the tongue. There was some variation from right to left ranging from 1 to 2 papillae. The foliate papillae were absent and instead there were low mucosal folds in front of the glossopalatine fold.

The smooth lingual root was free from any papillary type but contained the openings of the posterior lingual gland that covered the root surface with their secretions (Fig. 4A). The ventral lingual surface was attached to the sublingual floor by the lingual frenulum; its mucous membrane was somewhat loosely attached to the underlying muscles.

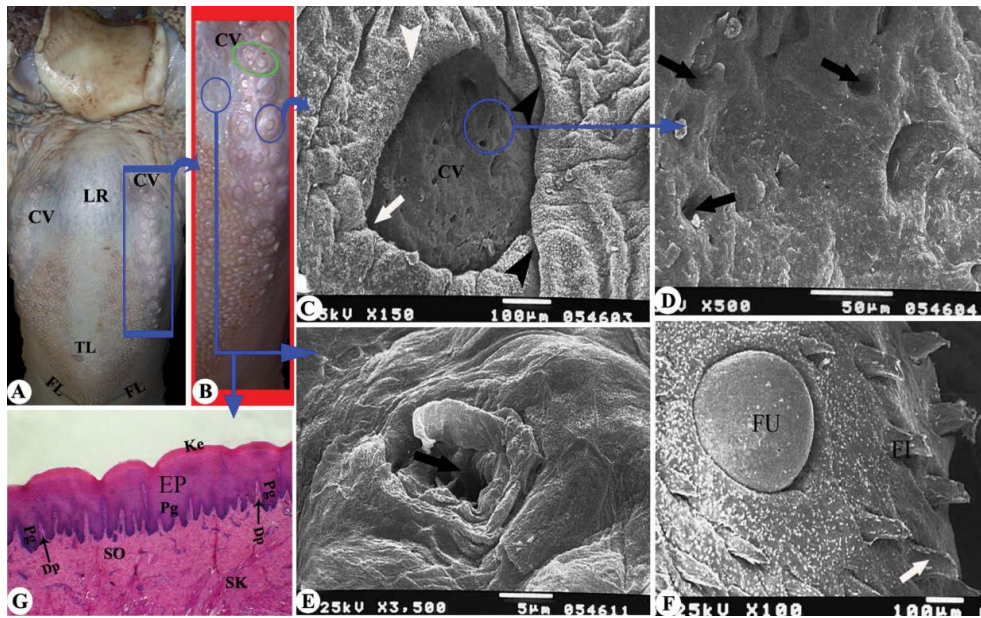**Figure 4.** Macroscopic (**A, B**), scanning electron microscope (**C–F**) and histological (**G**) images of the lingual root of the Egyptian water buffallo. Panels **A, B** to show: lingual root (LR), torus linguae (TL), fossa lingua (FL), circumvallate papillae (CV), two circumvallate papillae surrounded by one vallate (green circle). Panels **C–F** to show: circumvallate papillae (CV) with numerous small and rounded opening of taste pores (black arrow) and surrounded by circular deep (white arrow) groove that bordered by an elevated ridge named vallum (white arrowheads) that carried small secondary papillae that ended into the primary groove (black arrowheads); FU — fungiform papillae; Panel **G** to show: kertainised (Ke) stratified squamous (EP) with numerous epidermal peg (Pg) and dermal papillae (Dp), submucosa (SO), skeletal muscles (SK).

SEM characters of the tongue

The dorsal lingual surface of the apex and body carried numerous long, band thread-like, with blunt apex, caudally directed filiform papillae (Fig. 3D). The papillary surface was covered with keratinised scales without secondary papillae (Fig. 3E; black arrow). The origin of the filiform papillae appeared as a depressed area (Fig. 3D; red star). The interpapillary space had some exfoliated keratinised epithelia-like filiform papillae surface (Fig. 3E, F; red arrow). The filiform papillae on the ventral surface were less numerous, shorter than that observed on the dorsal surface. In addition, it carried pointed tips with longitudinal groove without secondary papillae.

The surface of the large, broad blunted, short conical papillae was rough and carried exfoliated epithelium (Fig. 3I; CP). The higher magnification showed the presence of longitudinal groove on its rostral surface (Fig. 3G; CG) and the interpapillary surface was exfoliated (Fig. 3G, H; Sc).

The circular or rounded or dome-shaped fungiform papillae were scattered among the filiform papillae on the dorsum of the tongue and the ventral surface of the apex (Figs. 3D, 4F; FU). The convex surface of the fungiform papillae had exfoliated keratinised epithelium and three circular openings of the taste pores (Fig. 3I, J; white arrows).

The rounded circumvallate papillae were surrounded by circular deep groove bordered by an elevated ridge (vallum), as appeared in (Fig. 4C; white arrow). The vallum carried small secondary papillae that ended into the primary groove (Fig. 4C; black arrowheads). The surface of the circumvallate papillae was flattened and raised above the lingual surface and carried numerous small and rounded opening of taste pores (Fig. 4D).

The lingual root had numerous folds and depression. By high magnification, the root revealed irregular shaped opening of posterior lingual glands (Fig. 4E; black arrow). The edges were elevated. The surface of the cells of root carried numerous microridges (Fig. 4E).

Histological characters of the tongue

The lingual epithelium was followed by a vascular highly innervated dense irregular connective tissue. The lingual core consisted of striated muscular fibres taking different orientations (Figs. 4G, 5–7). The lingual mucosa of the dorsal, lateral border and, to some extent, the ventral surface of the rostral part of the lingual apex had lingual papillae (filiform, and fungiform). While the lingual mucosa of body, especially at the torus linguae, had conical papillae, the circumvallate papillae observed at the caudal part of the lingual body and root.
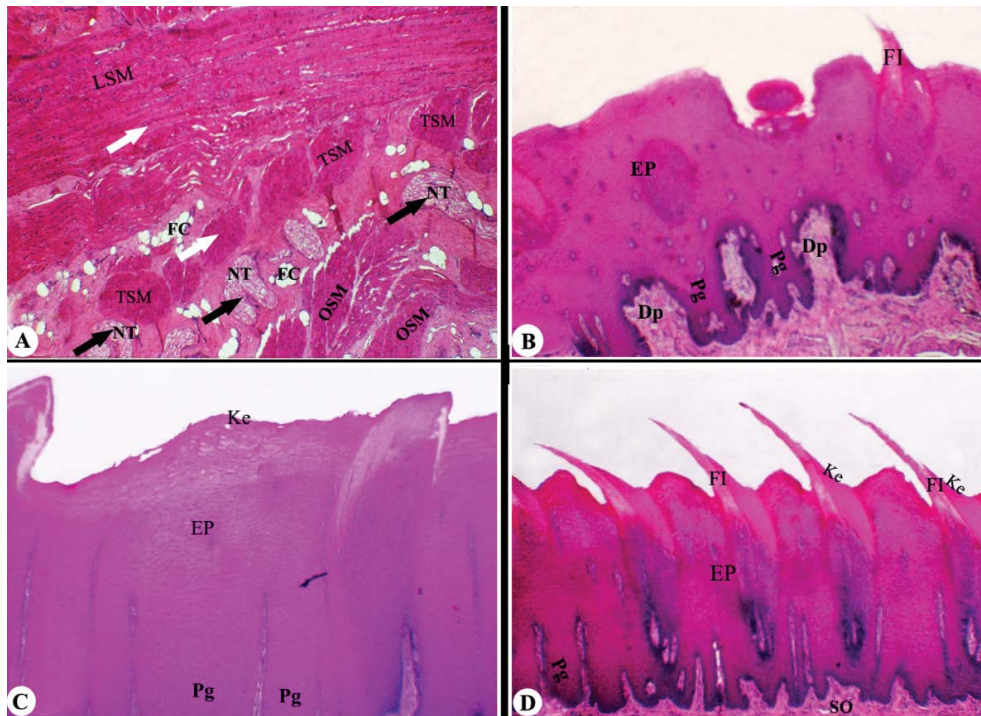
Figure 5. A–D. Histological images of the tongue of the Egyptian water buffalo to show: the longitidinal (LSM), transverse (TSM), and oblique (OSM) lingual muscles, nerve trunk (NT, black arrows), fat cells (FC), filiform papillae (FI), kertainised (Ke), stratified squamous (EP) with numerous epidermal peg (Pg) and dermal papillae (Dp), submucosa (SO).
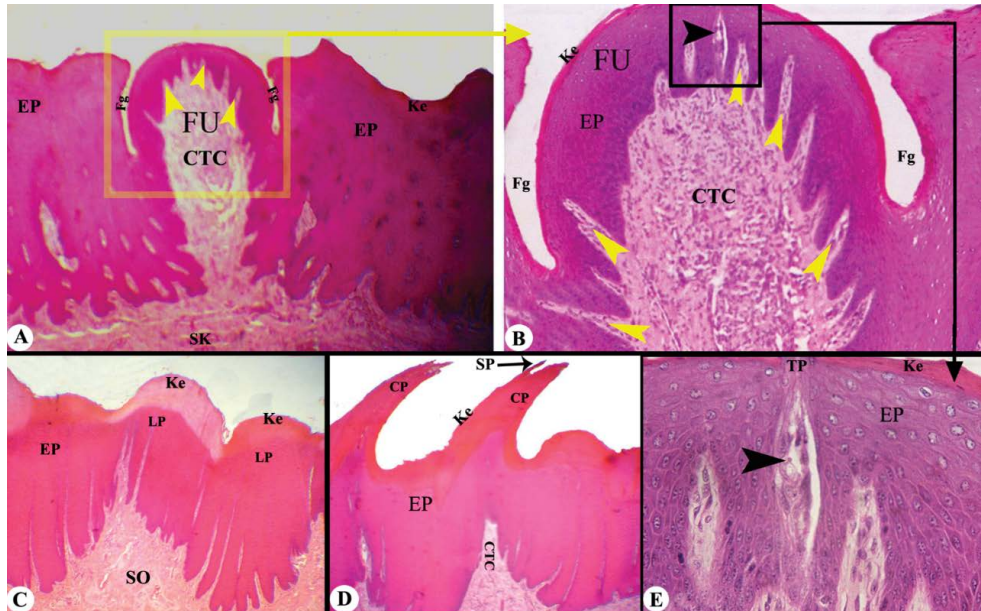
Figure 6. A–E. Histological images of the tongue of the Egyptian water buffalo to show: the fungiform papillae (FU) with taste buds (black arrowheads); taste pore (TP), and connective tisssue core (CTC) with secondary papillae (yellow arrowheads) and surrounded by circular groove (Fg), kertainised (Ke) stratified squamous epithelium (EP), skeletal muscles (SK) and dermal papillae (Dp), submucosa (SO), lentiform papillae (LP), conical papillae (CP), secondary papillae (SP).

The lingual papillae are divided into mechanical and gustatory papillae according to the presence of the taste buds. The mechanical papillae included the filiform, conical, and lentiform papillae, while the gustatory papillae included fungiform and circumvallate papillae (Figs. 5–7).
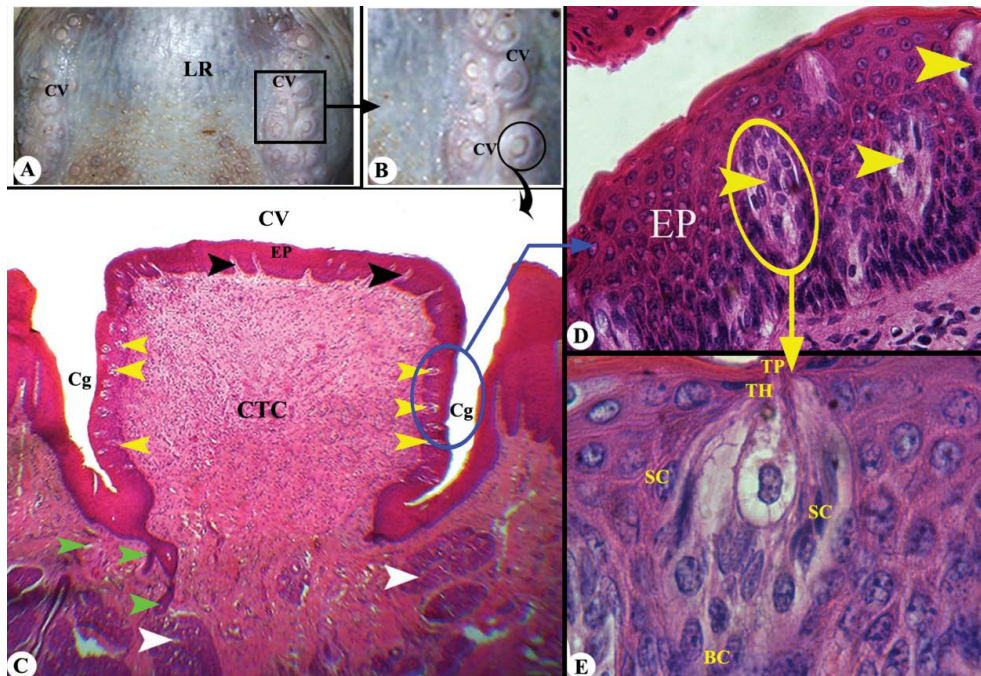
Figure 7. Gross (**A, B**) and histological (**C–E**) images of the lingual root of the Egyptian water buffalo to show: the lingual root (LR), circumvallate papillae (CV) with taste buds (yellow arrowheads), taste pore (TP) facing the groove (Cg) and surrounded by sustentacular cells (SC) and basal cells (BC), taste hair (TH), and connective tisssue core (CTC) with secondary papillae (black arrowheads), lobules of von Ebner's glands (white arrowheads) with their ducts (green arrowheads).

The filiform papillae were cornified and had a thread-like appearance with two surfaces: caudal concave and rostral convex surfaces. The keratinised layer differentiated into two parts according to the degree of keratinisation: the rostral part of highly keratinisation and the caudal part less keratinisation papillae (Fig. 5B–D). The conical papillae consisted of highly keratinised stratified squamous epithelium and connective tissue core which did not reach the level surface of epithelium and carried secondary papillae (Fig. 6D).

The fungiform papillae were surrounded by a shallow furrow (Fig. 6A, B, E). It was covered with stratified squamous keratinised epithelium, and its basal cell layers contained pigmented granules in some papillae. The fungiform papillae contained taste buds that opened by taste pore to the dorsal surface (Fig. 6B, E). The connective tissue core was highly vascular dense irregular connective from the secondary papillae originated from the underlying lamina propria (Fig. 6A, B).

The rounded circumvallate papillae were covered by stratified squamous epithelium that was keratinised at its dorsal surface and less keratinised at its lateral border. The taste buds were observed as a lightly stained small areas in the lateral lining epithelium facing the groove (Fig. 7C, D; yellow arrowheads, Cg) that opened by taste pore into the groove with taste hair on the taste duct (Fig. 7D–E; TP, TH). The papillary core consisted of highly vascular and innervated dense irregular connective tissue carrying secondary papillae that penetrated the epithelium lining of the papillae. The lobules of the serous glands (von Ebner's glands) were observed in the connective tissue under the papillae, especially toward the groove, and their ducts opened into the base of the groove (Fig. 7C; white arrowheads).

The lingual root had seromucoid and mucous glands were observed between the skeletal muscular bundles (Fig. 8). Their ducts opened in the dorsal lingual surface. The seromucoid glands were more numerous than mucous ones (Fig. 4G and 8).

DISCUSSION

The present study was performed to give a complete description of the gross, SEM, histological, and histochemistry characters of the sublingual floor, with their caruncles, and the tongue, with its papillary system, of the Egyptian water buffalo. Similar to some previously published articles [1, 4, 18, 32, 36, 54], the tongue of the mammalian species is subdivided into three parts: the apex, the body and the root. The cur-

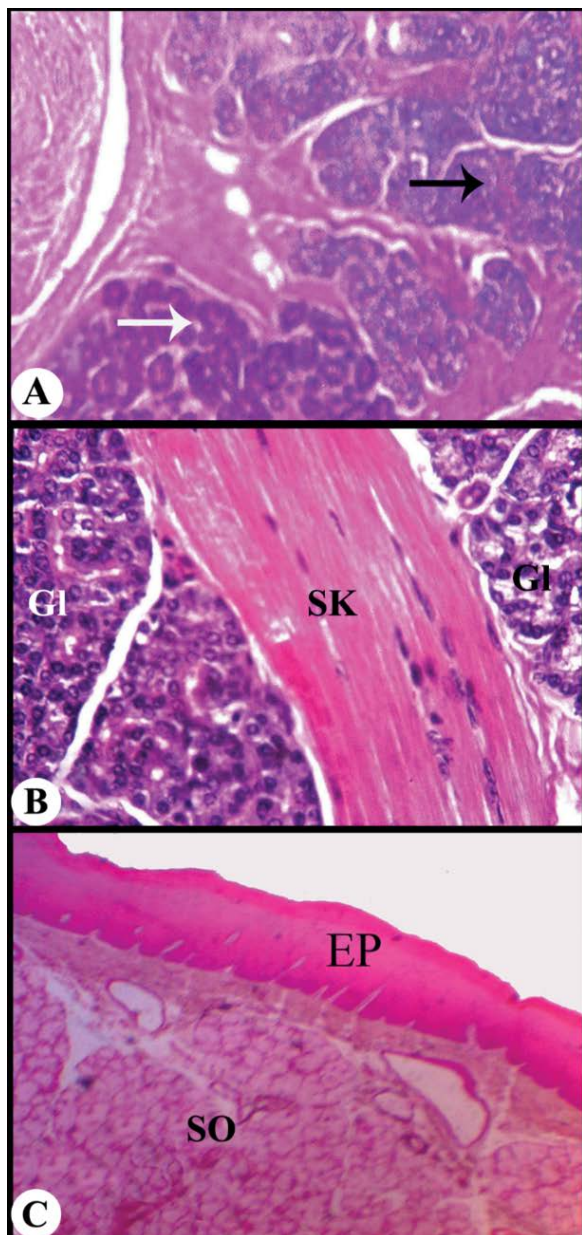**Figure 8. A–C.** Histological images of the lingual root of the Egyptian water buffalo to show: sublingual glands (Gl, black arrows), kertanised stratified squamous epithelium (EP), skeletal muscles (SK), submucosa (SO).

rent work described that the flattened dorsoventrally lingual apex had two surfaces (dorsal and ventral) and two borders, while the caudal lingual part (body and root) had only the dorsal surface and two lateral borders. Moreover, El-Bakary and Abumandour [18] classified the ventral lingual surface of the apex into the papillary and non-papillary region by the presence of the projected U-shaped line of fungiform papillae.

The current study observed that the sublingual caruncle was lined with stratified squamous kerati-

nised epithelium and the ventral surface of the sublingual caruncle had two ducts: one duct of mandibular and the other of monostoamtic sublingual salivary glands. These observations were similar to those reported by Dyce et al. [16].

The ruminant's species, similar to the herbivorous mammals, are characterised by the presence of the large, rounded prominence named the torus linguae that was bordered rostrally by the deep fossa (named the fossa linguae) on the dorsal lingual surface of the body, as described in the published textbooks about the ruminant's species [16], in addition to the some published articles about the ruminant's species as in Egyptian water buffalo [18, 20], cattle-yak (*Bos taurus*) [15], reeves' muntjac deer (*Muntiacus reevesi*) [55], Alpaca (*Vicugna pacos*) [27]. Also, the characteristic lingual prominence was described in other herbivorous mammalian species as in New Zealand white rabbits [4], Nile grass rat (*Arvicanthis niloticus*) [43]. Meanwhile, this lingual prominence was absent in the tongue of the carnivorous, omnivorous monkeys and pigs [22, 36]. Functionally, the presence of the lingual prominence on the dorsal surface of the body was correlated to the herbivorous habits of numerous mammalian species due to this prominence play an important role in the mastication process with the hard palate. The presence of the deep fossa lingua is a characteristic feature of the ruminant species [15, 18, 20].

The species-variations about the appearance, size, number, distribution, nomenclature, microstructure, and directions of the lingual papillae among different animal species, was related to the feeding habits and the available food particles [4, 15, 18–20, 22, 27, 36, 43, 55]. The current work confirmed the classifications of the lingual papillae into mechanical and gustatory papillae. The current study observed the presence of five types of lingual papillae, three types of mechanical papillae (filiform, conical, and lentiform) and two types of gustatory papillae (fungiform and circumvallate), similar to that described in other ruminant's species such as in Markhoz Goat (*Iranian Angora*) [26], cattle-yak (*Bos taurus*) [15] and chital deer (*Axis axis*) [23]. Meanwhile, the presence of four type — two mechanical (filiform and conical) and two gustatory (fungiform and circumvallate) papillae — was described in other ruminant's species such as Barking deer [6], and Bactrian camel [17], but the four papillae described as one mechanical (filiform) and three gustatory (fungiform, foliate and

circumvallate) were observed in other herbivorous species such as rabbit [4] and rat [43, 45]. Functionally, the description of the presence of the different five types of lingual papillae in the current examined Egyptian water buffalo had an important role in the identification and selection of the food particles in the Egyptian farms.

Functionally, the fungiform papillae are classified into three classifications according to function, distribution, and appearance. They are classified according to function into three types: the gustatory fungiform type was described in the currently examined Egyptian water buffalo, similar to that reported by some authors [4, 18, 24] in rabbit, Egyptian water buffalo, and pampas deer. At the same time, the mixed fungiform papillae (some papillae have taste buds and some do not have them) were described in the horse, buffalo, and cattle [13, 49]. While, the mechanical fungiform papillae (no taste buds) were described in small ruminants goat [37] and the donkey [41]. The other classification is based on the SEM appearance of the fungiform papillae. The current work observed the presence of the circular or rounded or dome-shaped fungiform papillae among the filiform papillae on the dorsum of the tongue and the ventral surface of the apex, while two shapes — rectangular on the dorsal surface of the apex, and round on the dorsal surface of the body — were described in Egyptian fruit bat [5]. Only one fungiform appearance was described in most mammalian species but with different shape: dome papillae were observed in the raccoon dog and fox [22], round papillae were observed in the tiger and in the pampas deer [21, 24], mushroom papillae were observed in the Saanen goat [37, 44], fungus papillae in mouse [29].

Circular or rounded or dome-shaped fungiform papillae observed in the present study were scattered among the filiform papillae on the dorsum of the lingual apex and body and, to some extent, on the lateral border and the ventral surface of the apex. Moreover, the presence of the round fungiform papillae was observed among the filiform papillae in the two lateral regions of the dorsal surface of the anterior and middle lingual part, in addition to the papillary region of the ventral surface of the lingual tip and the two lateral borders of the tongue [18] in Egyptian water buffalo (*Bubalus bubalis*). Generally, the fungiform papillae were scattered among the filiform papillae on the dorsal surface of the apex, as described in some herbivorous ruminants [6, 17,

35, 37, 54], but in the deer [23, 24] and Mazama species [34], the fungiform papillae distribution were extended to the torus linguae.

The current findings described the presence of the papillary circular groove surrounded the fungiform papillae, similar to that reported in some ruminant species [4, 6, 17, 18, 20, 37, 54], whereas this papillary groove was completely absent in some ruminant species, as described in pampas deer [24].

The lenticular papillae were observed only on the torus linguae. The same findings were described in other ruminants [17, 18], whereas the complete absence of the lenticular papillae on the torus linguae was reported in reeves, barking deer, or mazama species [6, 9, 34, 55]. Functionally, the presence of the mechanical conical and lenticular papillae had a great role in holding of the food particles during the mastication processes within the oral cavity and help in the movement of masticated food particles toward the pharyngeal cavity [18].

The SEM observations noted that the rough large-sized, broad blunted, short conical papillae were restricted only to the torus linguae, especially on its central part, and carried exfoliated epithelium with the presence of longitudinal groove on its rostral surface. The presence of these papillae on the torus linguae was reported in numerous ruminant species [6, 20, 24]. while some authors [18] observed the presence of the large conical papillae on the dorsal lingual surface of root just posteriorly to the torus linguae. However, the complete disappearance of the conical papillae was described in the Bactrian camel (*Camelus bactrianus*) [17]. Functionally, the presence of the conical papillae was joined with the fixation of the food particles during the mechanical mastication of the green grasses in all ruminant species.

The number of circumvallate papillae differ among mammalian species of the different feeding habits; one type of circumvallate papillae was described by Massoud and Abumandour [43] in Nile grass rat (*Arvicanthis niloticus*), while two circumvallate papillae were observed in New Zealand white rabbit [4], and horse [32], and three circumvallate papillae were described by Massoud and Abumandour [43] in Egyptian long-eared hedgehog (*Hemiechinus auritus*), in koala [31], and in Egyptian fruit bat [5]. Moreover, four circumvallate papillae were found in Japanese marten and tiger [21]. Furthermore, the current work agrees with the previous reports on other ruminants species that there were numerous cir-

cumvallate papillae such as in Egyptian water buffalo [18], cattle [8], reeves' muntjac deer (*Muntiacus reevesi*) [55], goat [37, 40], lambs [54], and deer [6, 7]. The observation of the prominent papillary groove surrounding the circumvallate papillae were described in the Egyptian water buffalo [18], gazelle [33], goat [35, 37], lamb [54], Alpaca [27] and cattle [14]. The current observation reported that the dorsal surface of the circumvallate papillae was rough and irregular, similar to that noticed by El-Bakary and Abumandour [18] and Emura et al. [22] in Egyptian water buffalo, dog, and fox; however, the smooth dorsal surface of the circumvallate papillae was observed in fox [30].

The degree of keratinisation of the tongue, especially its dorsal surface, is one of the most important lingual adaptations regarding the different feeding mechanisms with available food particles; moreover, this keratinisation extended to the lingual papillae [43]. The filiform papillae had keratinised layer differentiated into two parts according to the degree of keratinisation: the rostral part of high keratinisation and the caudal part less keratinisation papillae. Also the conical papillae had a highly keratinised stratified squamous epithelial layer. Moreover, the fungiform papillae had stratified squamous keratinised epithelium, but the circumvallate papillae had a stratified squamous keratinised layer at its dorsal surface and less keratinized at its lateral border.

The circumvallate taste bud's distribution had some variation among species. The current findings described the presence of numerous taste buds always along the entire length of the papillary wall faced the papillary groove; similar description were reported in camel [17, 47], cattle [48, 53] and deer [6].

CONCLUSIONS

The ventral surface of the sublingual caruncle carried a small opening of the duct of both monostoamtic and mandibular salivary gland. The lingual mucosa of the dorsal, lateral border and, to some extent, the ventral surface of apex had lingual papillae (filiform, fungiform). The dorsal surface of the apex and body carried numerous long, thread-like, with blunt apex, caudally directed filiform papillae that were covered with keratinised scales without secondary papillae. The degree of keratinisation classified filiform papillae into rostral part of highly keratinisation and caudal less keratinisation part. Fungiform papillae

were scattered among filiform papillae on the dorsal and ventral surface of apex. Taste buds of circumvallate papillae opened in the lateral lining epithelium facing the groove. Von Ebner's glands were observed in computed tomography under papillae, especially toward the groove, and their ducts opened into the base of the groove.

REFERENCES

1. Abd-Elnaeim MMM, Zayed AE, Leiser R. Morphological characteristics of the tongue and its papillae in the donkey (Equus asinus): a light and scanning electron microscopical study. Ann Anat. 2002; 184(5): 473–480, doi: 10.1016/S0940-9602(02)80081-4, indexed in Pubmed: 12392327.

2. Abumandour MMA. Surface ultrastructural (SEM) characteristics of oropharyngeal cavity of house sparrow (Passer domesticus). Anat Sci Int. 2018; 93(3): 384–393, doi: 10.1007/s12565-017-0426-6, indexed in Pubmed: 29270912.

3. Abumandour MMA. Morphological Comparison of the Filiform Papillae of New Zealand White Rabbits (Oryctolagus cuniculus) as Domestic Mammals and Egyptian Fruit Bat (Rousettus aegyptiacus) as Wild Mammals Using Scanning Electron Microscopic Specimens. Int J Morphol. 2014; 32(4): 1407–1417, doi: 10.4067/s0717-95022014000400045.

4. Abumandour MMA, El-Bakary RMA. Anatomic reference for morphological and scanning electron microscopic studies of the New Zealand white rabbits tongue (Orycotolagus cuniculus) and their lingual adaptation for feeding habits. J Morphol Sci. 2013; 30(4): 1–12.

5. Abumandour MMA, El-Bakary RMA. Morphological and scanning electron microscopic studies of the tongue of the Egyptian fruit bat (Rousettus aegyptiacus) and their lingual adaptation for its feeding habits. Vet Res Commun. 2013; 37(3): 229–238, doi: 10.1007/s11259-013-9567-9, indexed in Pubmed: 23709139.

6. Adnyane IKM, Zuki AB, Noordin MM, et al. Morphological study of the lingual papillae in the barking deer, Muntiacus muntjak. Anat Histol Embryol. 2011; 40(1): 73–77, doi: 10.1111/j.1439-0264.2010.01041.x, indexed in Pubmed: 21105898.

7. Agungpriyono S, Yamada J, Kitamura N, et al. Morphology of the dorsal lingual papillae in the lesser mouse deer,

Tragulus javanicus. J Anat. 1995; 187 (Pt 3): 635–640, indexed in Pubmed: 8586562.

8. Asami Y, Asami T, and Ko. Light microscopic and scanning electron microscopic studies on the lingual papillae and stereo structure of their connective tissue cores in cattle. Shigaku (Odontology). 1995; 82: 1223–1244.

9. Atoji Y, Yamamoto Y, Suzuki Y. Morphology of the tongue of a male Formosan serow (Capricornis crispus swinhoei). Anat Histol Embryol. 1998; 27(1): 17–19, doi: 10.1111/j.1439-0264.1998.tb00150.x, indexed in Pubmed: 9505441.

10. Bancroft JD, Gamble M. Theory and practice of histological techniques. Elsevier Health Sciences, China 2008.

11. Bancroft JD, Cook H, Turner D. Manual of Histological Techniques and Their Diagnostic Application, 2e. 1996.

12. Braekevelt CR. Fine structure of the choriocapillaris, Bruch's membrane and retinal epithelium of the cow. Anat Histol Embryol. 1986; 15(3): 205–214, doi: 10.1111/j.1439-0264.1986.tb00712.x, indexed in Pubmed: 2947517.

13. Chamorro CA, de Paz P, Sandoval J, et al. Comparative scanning electron-microscopic study of the lingual papillae in two species of domestic mammals (Equus caballus and Bos taurus). 1. Gustatory Papillae. Acta Anat (Basel). 1986; 125(2): 83–87, indexed in Pubmed: 3953255.

14. Chamorro CA, Sandoval J, Fernandez JG, et al. Estudio comparado de las Papilas linguales del Gato (Felis catus) y del Conejo (Oryctolagus cuniculus) mediante el Microscopio electrónico de barrido. Anat Histol Embryol. 2007; 16(1): 37–47, doi: 10.1111/j.1439-0264.1987.tb00722.x.

15. Ding Y, Yu S, Shao B. Anatomical and histological characteristic of the tongue and tongue mucosa linguae in the cattle-yak (Bos taurus × Bos grunniens). Front Biol. 2016; 11(2): 141–148, doi: 10.1007/s11515-016-1393-3.

16. Dyce KM, Sack WO, Wensing CJG. Text book of Veterinary anatomy. W.B. Saunders Company, Philadelphia, London and Toronto 2010.

17. Eerdunchaolu A, Takehana K, Yamamoto E, et al. Characteristics of dorsal lingual papillae of the Bactrian camel (Camelus bactrianus). Anat Histol Embryol. 2001; 30(3): 147–151, indexed in Pubmed: 11447938.

18. El-Bakary NER, Abumandour MMA. Morphological studies of the tongue of the egyptian water buffalo (bubalus bubalis) and their lingual papillae adaptation for its feeding habits. Anat Histol Embryol. 2017; 46(5): 474–486, doi: 10.1111/ahe.12292, indexed in Pubmed: 28833390.

19. El-Mansi A, Al-Kahtani MA, Abumandour M. Comparative phenotypic and structural adaptations of tongue and gastrointestinal tract in two bats having different feeding habits captured from Saudi Arabia: Egyptian fruit bat (Rousettus aegyptiacus) and Egyptian tomb bat (Taphozous perforatus). Zoologischer Anzeiger. 2019; 281: 24–38, doi: 10.1016/j.jcz.2019.05.005.

20. Emura S, El Bakary NER. Morphology of the lingual papillae of Egyptian buffalo (Bubalus bubalis). Okajimas Folia Anat Jpn. 2014; 91(1): 13–17, doi: 10.2535/ofaj.91.13, indexed in Pubmed: 25274404.

21. Emura S, Hayakawa D, Chen H, et al. Morphology of the lingual papillae in the tiger. Okajimas Folia Anat Jpn. 2004; 81(2-3): 39–43, doi: 10.2535/ofaj.81.39, indexed in Pubmed: 15455727.

22. Emura S, Okumura T, Chen H, et al. Morphology of the lingual papillae in the raccoon dog and fox. Okajimas Folia

Anat Jpn. 2006; 83(3): 73–76, doi: 10.2535/ofaj.83.73, indexed in Pubmed: 17154050.

23. Erdoğan S, Pérez W. Anatomical and scanning electron microscopic studies of the tongue and lingual papillae in the chital deer (Axis axis,Erxleben 1777). Acta Zoologica. 2013; 95(4): 484–492, doi: 10.1111/azo.12044.

24. Erdoğan S, Pérez W. Anatomical and scanning electron microscopic characteristics of the tongue in the pampas deer (Cervidae: Ozotoceros bezoarticus, Linnaeus 1758). Microsc Res Tech. 2013; 76(10): 1025–1034, doi: 10.1002/jemt.22263, indexed in Pubmed: 23857640.

25. FAO, Breeds reported by Pakistan: Buffalo. Domestic Animal Diversity Information System, Food and Agriculture Organisation of the United Nations, Rome. 2013.

26. Goodarzi N, Shah Hoseini T. Morphologic and osteometric analysis of the skull of markhoz goat (Iranian angora). Vet Med Int. 2014; 2014: 972682, doi: 10.1155/2014/972682, indexed in Pubmed: 24955281.

27. Goździewska-Harłajczuk K, Klećkowska-Nawrot J, Janeczek M, et al. Morphology of the Lingual and Buccal Papillae in Alpaca (Vicugna pacos) - Light and Scanning Electron Microscopy. Anat Histol Embryol. 2015; 44(5): 345–360, doi: 10.1111/ahe.12147, indexed in Pubmed: 25223623.

28. Igbokwe CO. and Okolie C. Morphological study of the lingual papillae at different stages of growth (Prepubertal, Pubertal, Post Pubertal and Adult) of the West African dwarf goat (Capra. Hircus). Int J Morphol. 2009; 27(1): 145–150.

29. Iwasaki Si, Miyata K, Kobayashi K. Comparative studies of the dorsal surface of the tongue in three mammalian species by scanning electron microscopy. Cells Tissues Organs. 2008; 128(2): 140–146, doi: 10.1159/000146330.

30. Jackowiak H, Godynicki S. The scanning electron microscopic study of lingual papillae in the silver fox (Vulpes vulpes fulva, Desmarest, 1820). Ann Anat. 2004; 186(2): 179–183, doi: 10.1016/S0940-9602(04)80037-2, indexed in Pubmed: 15125050.

31. Kobayashi K, Kumakura M, Yoshimura K, et al. Comparative morphological study of the lingual papillae and their connective tissue cores of the koala. Anat Embryol (Berl). 2003; 206(4): 247–254, doi: 10.1007/s00429-002-0296-z, indexed in Pubmed: 12649723.

32. Kobayashi K, Jackowiak H, Frackowiak H, et al. Comparative morphological study on the tongue and lingual papillae of horses (Perissodactyla) and selected ruminantia (Artiodactyla). Ital J Anat Embryol. 2005; 110(2 Suppl 1): 55.

33. Kocak-Harem M, Harem IS, Sari E, et al. Light and Scanning Electron Microscopic Study of the Dorsal Lingual Papillae of the Goitered Gazelle (Gazelle subgutturosa). J Animal Vet Advances. 2011; 10(15): 1906–1913, doi: 10.3923/javaa.2011.1906.1913.

34. Kokubun H, Esper G, Franciolli A, et al. Estudo histológico e comparativo das papilas linguais dos cervídeos Mazama americana e Mazama gouzoubira por microscopia de luz e eletrônica de varredura. Pesq Vet Bras. 2012; 32(10): 1061–1066, doi: 10.1590/s0100-736x2012001000021.

35. Kumar P, Kumar S, Singh Y. Tongue papillae in goat: a scanning electron-microscopic study. Anat Histol Embryol. 1998; 27(6): 355–357, doi: 10.1111/j.1439-0264.1998.tb00207.x, indexed in Pubmed: 9972641.

36. Kumar S, Bate LA. Scanning electron microscopy of the tongue papillae in the pig (Sus scrofa). Microsc Res Tech.

2004; 63(5): 253–258, doi: 10.1002/jemt.20036, indexed in Pubmed: 15170754.

37. Kurtul I, Atalgın SH. Scanning electron microscopic study on the structure of the lingual papillae of the Saanen goat. Small Ruminant Res. 2008; 80(1-3): 52–56, doi: 10.1016/j.smallrumres.2008.09.003.

38. Maala CP, Ducusin RJT, Rizori JA. The Gross Anatomy of the Hard Palate and Palatine Printing in Cattle. J Vet Med. 2007; 44(1): 1–7.

39. Maala CP, Ferriol G. Gross anatomy, histology and palatine prints of the hard palate of the Philippine carabao (Bubalus bubalis L. Philippine Agricultural Scientist, Philippines 2002.

40. Mahdy MAA, Abdalla KEH, Mohamed SA, et al. Morphological investigations on the lips and cheeks of the goat (Capra hircus): A scanning electron and light microscopic study. Microsc Res Tech. 2020; 83(9): 1095—1102, doi: 10.1002/jemt.23500, indexed in Pubmed: 32306484.

41. Mahmoud MMAE, Ahmed EZ, Rudolf L, et al. Morphological characteristics of the tongue and its papillae in the donkey (Equus asinus): a light and scanning electron microscopical study. Ann Anat Anat Anz. 2002; 184(5): 473–480, doi: 10.1016/s0940-9602(02)80081-4.

42. Masson P. Some histological methods: trichrome staining and their preliminary technique. J Tech Methods. 1929; 12: 75–90.

43. Massoud D, Abumandour MMA. Descriptive studies on the tongue of two micro-mammals inhabiting the Egyptian fauna; the Nile grass rat (Arvicanthis niloticus) and the Egyptian long-eared hedgehog (Hemiechinus auritus). Microsc Res Tech. 2019; 82(9): 1584–1592, doi: 10.1002/jemt.23324, indexed in Pubmed: 31225934.

44. Nasr E. Surface morphological structure of the tongue of the hedgehog, Hemiechinusauritus (Insectivora: Erinaceidae). J Am Sci. 2012; 8(4): 580–588.

45. Nasr E, Gamal A, and El. Light and scanning electron microscopic study of the dorsal lingual papillae of the rat Arvicanthis niloticus (Muridae, Rodentia). J Am Sci. 2012; 8(4): 619–627.

46. Nomina AnatomicaVeterinaria N. International Committee on Veterinary Gross Anatomical Nomenclature and authorized by the general assembly of the world Association of veterinary Anatomist. Knoxville, 3rd Ed. Ghent. Published by the Editorial Committee Hanover (Germany), Ghent (Belgium), Columbia, MO (U.S.A.), Rio de Janeiro (Brazil). 2017.

47. Qayyum MA, Fatani JA, Mohajir AM. Scanning electron microscopic study of the lingual papillae of the one humped camel, Camelus dromedarius. J Anat. 1988; 160: 21–26, indexed in Pubmed: 3253256.

48. Sari EK, Harem MK, Harem IS. Characteristics of dorsal lingual papillae of zavot cattle. J Animal Vet Advances. 2010; 9(1): 123–130, doi: 10.3923/javaa.2010.123.130.

49. Scala G, Mirabella N, Pelagalli GV. [Morphofunctional study of the lingual papillae in cattle (Bos taurus)]. Anat Histol Embryol. 1995; 24(2): 101–105, doi: 10.1111/j.1439-0264.1995.tb00019.x, indexed in Pubmed: 8588700.

50. Schumacher U, Duku M, Katoh M, et al. Histochemical similarities of mucins produced by Brunner's glands and pyloric glands: A comparative study. Anat Rec A Discov Mol Cell Evol Biol. 2004; 278(2): 540–550, doi: 10.1002/ar.a.20046, indexed in Pubmed: 15164342.

51. Suvarna KS, Layton C, Bancroft JD. Bancroft's theory and practice of histological techniques. E-Book. Elsevier Health Sciences 2018.

52. Suvarna SK, Layton C, Bancroft JD. Bancroft's Theory and Practice of Histological Techniques, Expert Consult: Online and Print,7: Bancroft's Theory and Practice of Histological Techniques. Elsevier, Churchill Livingstone 2013.

53. Tabata S, Wada A, Kobayashi T, et al. Bovine circumvallate taste buds: taste cell structure and immunoreactivity to alpha-gustducin. Anat Rec A Discov Mol Cell Evol Biol. 2003; 271(1): 217–224, doi: 10.1002/ar.a.10028, indexed in Pubmed: 12552638.

54. Tadjalli M, Pazhoomand R. Tongue papillae in lambs: a scanning electron microscopic study. Small Ruminant Research. 2004; 54(1-2): 157–164, doi: 10.1016/j.smallrumres.2003.11.005.

55. Zheng J, Kobayashi K. Comparative morphological study on the lingual papillae and their connective tissue cores (CTC) in reeves' muntjac deer (Muntiacus reevesi). Ann Anat. 2006; 188(6): 555–564, doi: 10.1016/j.aanat.2006.05.014, indexed in Pubmed: 17140149.

ORIGINAL ARTICLE

Keap1/Nrf2 pathway in sodium fluoride-induced cardiac toxicity and the prophylactic role of vitamin C versus platelet-rich plasma

H. Labib[1], A.M. Badr[2], M. Abdelgwad[2], T.I. Abd El-Galil[1]

[1]Department of Anatomy and Embryology, Cairo University, Cairo, Egypt
[2]Department of Medical Biochemistry and Molecular Biology, Faculty of Medicine,
Kasr Alainy, Cairo University, Cairo, Egypt

Background: The present study was conducted to investigate the role of vitamin C versus platelet-rich plasma (PRP) against sodium fluoride (NaF)-induced cardiotoxicity and cell death in rats' myocardium. Previous studies suggest that NaF decreased cellular viability and intracellular antioxidant power.

Materials and methods and Results: The present study revealed that NaF administration caused histological alterations in the cardiac muscle and increased the accumulation of intracellular reactive oxygen species, the expression of inducible nitric oxide synthases and proliferating cell nuclear antigen as well as collagen deposition in cardiac tissue. As supported by colorimetric analysis, an elevation in malondialdehyde level and a decrease in both superoxide dismutase (SOD) and thioredoxin-1 oxidoreductase (TrX) levels were seen, whereas molecular analysis revealed a decrease in Keap1 and an increase in Nrf2 and HO-1 gene expression. Pretreatment with vitamin C and PRP prior to NaF administration significantly improved the altered parameters and enhanced the cellular antioxidant capability of myocardium resulting in protection of cardiac muscle from NaF-induced cytotoxicity and apoptotic cell death.

Conclusions: The cyto-protective activity of PRP was found to be comparable to that of the known antioxidant, vitamin C. (Folia Morphol 2022; 81, 3: 663–678)

Key words: sodium fluoride, vitamin C, platelet-rich plasma, Keap1, Nrf2, TrX-1

INTRODUCTION

Fluoride is an inorganic, mono-atomic anion designated the chemical formula F−, the salts of which are colourless/white, bitter tasting and are neutral in terms of smell. It is used in the manufacture of fluorocarbons. Although classified as a weak base, concentrated fluoride causes skin erosion [27]. Fluoride is mandatory for bones and teeth development and for minimizing bone fractures. A fluoride concentration of 0.5–1.5 mg/L in drinking water is favourable, whereas exceeding intake of fluoride is toxic [45]. Fluoride is used in tooth decay prevention and oral hygiene products in the form of sodium fluoride (NaF) or sodium monofluorophosphate. Water fluoridation depends on the fluoride [29]. The United States Department of Agriculture has specified the

Dietary Reference Intakes of fluoride to be 10 mg/ /day, which is equal to 10 L of fluoridated water and 0.7 to 2.2 mg/day for the younger population [11]. A dose of 5–10 g (equivalent to 32–64 mg/kg) of NaF is considered to be lethal [4, 16].

Substantial histopathological and biochemical changes are seen in the myocardial tissue of rats exposed to chronic NaF ingestion. Myocardial cell necrosis, excessive cytoplasmic vacuolation, karyolysis in myositis and degenerative changes of the myocardial fibres are some of the encountered histopathological changes. In addition, an increase in oxidative stress markers is encountered biochemically. Such histopathological and biochemical changes lead to myocardial tissue damage [9].

Platelet-rich plasma (PRP) is a product of autologous fractionation of whole blood by means of centrifugation that aims to remove blood cells and acquire a concentrate of PRP protein [31]. The platelets in PRP are activated by the addition of thrombin and calcium chloride, enhancing the release of growth factors from their alpha granules [6]. PRP has the ability to modify the oxidative damage seen in skeletal muscle injury by enhancement of myocytes' mitochondrial function and increasing their antioxidant defence mechanisms [28]. PRP promotes angiogenesis in ischaemic heart disease through cell signalling. Although the role of PRP to restore a functional myocardium, either by resettling exogenous or by activating native stem cells, to induce endogenous repair has been recorded in ischaemic heart disease [44], its role in prevention of NaF-induced myocardial damage has not entered broad clinical practice yet.

Vitamin C (ascorbic acid) is a down regulator of oxidative stress and inflammation of the cardiac muscle [12]. Vitamin C causes enhancement of antioxidant capacity, induction of CRYAB and Hsp70 expression, reversal of elevated cardiac enzymes and modification of the histopathological findings in myocardium [50].

Nuclear factor erythroid 2-related factor 2 (Nrf2), also known as nuclear factor erythroid-derived 2-like 2, is a transcription factor encoded by the NFE2L2 gene in humans [30]. Nrf2 is a basic leucine zipper (bZIP) protein that balances the expression of antioxidant proteins, which in turn combat the oxidative stress caused by injury and inflammation [15].The vasculature has multiple protective means against oxidation and inflammation, many of them being regulated by the Nrf2 transcription factor. Haem oxygenase-1 (HO-1) is a Nrf2-regulated gene that protects against vascular inflammation; it is the inducible isoform of HO. Production of biliverdin, carbon monoxide, and release of ferrous iron occur as a result of an oxidative cleavage of the haem groups achieved by HO-1. It has an antioxidant, anti-inflammatory, anti-apoptotic, anti-proliferative, and immunomodulatory functions in vascular cells [3].

Nrf2 and thioredoxin-1 oxidoreductase (TrX-1) play a significant role in cardiovascular diseases prevention [22]. In cardiomyocytes, TrX-1 induces electron transport chain and the citric acid cycle via PGC-1 alpha and Nrf2 [1], whereas Nrf2 promotes expression of TrX-1 [22]. The Nrf2-induced HO-1 is another feed-forward loop to the TrX-1/Nrf2/TrX-1 axis that alleviates cardiomyocyte apoptosis [39]. Kelch-like ECH-associated protein 1 (Keap1) is the main intracellular regulator of Nrf2. Under basal conditions, Nrf2 is sequestered by cytoplasmic Keap1 and targeted to proteasomal de-gradation [47]. During oxidative stress, the Nrf2-Keap1 interaction is dose-dependent [21]. Free and newly synthesized Nrf2 translocated to the nucleus, influence the expression of many genes coding proteins that serve as antioxidizing agents, detoxifying enzymes, stress response proteins and metabolic enzymes [13].

Malondialdehyde (MDA) is a highly reactive compound that occurs as an enol. It is naturally occurring and is a marker for oxidative stress [33].

Nitric oxide synthases (NOS) are a group of enzymes responsible for catalysing the production of nitric oxide (NO) from L-arginine [10]. Through utilisation of NADPH and O2, NO is produced by three different enzymes belonging to the family of NOS: nNOS/NOS1 (neuronal), iNOS/NOS2 (inducible), and eNOS/NOS3 (endothelial). The activities of nNOS and eNOS demand Ca2+ for activation and produce NO at nanomolar levels for a short time. On the contrary, iNOS are induced by multiple stressors, without a need for Ca2+ for activation, and can generate NO at micromolar levels for much longer periods. iNOS, play a role in immune response by binding calmodulin and producing NO as an immune defence mechanism, since NO is a free radical with an unpaired electron [20]. We herein evaluate the oxidative stress seen in cardiac muscles of NaF-induced male rats and the role of vitamin C and PRP in its prevention.

Proliferating cell nuclear antigen (PCNA), also called 'cyclin', is a 36 KDa nuclear protein which functions as a secondary protein for DNA polymerase delta. PCNA is involved in DNA synthesis and cellular proliferation. PCNA expression lowers during mito-

sis and is difficult to detect immunohistochemically, but it peaks at the G1/S of interphase for which it is considered to be a histological marker. PCNA expression is also a marker for mitotic activity [46]. The involvement of PCNA in DNA synthesis and cellular proliferation is attributed to its nature as a cell cycle regulatory protein marker. Chromosome recombination, DNA methylation, nucleic acid metabolism and RNA transcription are other cellular processes with which PCNA is associated [52]. The present study investigates the PCNA expression in cardiac muscles of NaF-induced male rats.

In this study, we evaluate the impact of NaF oral consumption on oxidative stress markers, Keap1, Nrf2 and HO-1 gene expression and histological modifications in rats' myocardium. The prophylactic roles of oral vitamin C and parenteral PRP administration are compared when given as pretreatment prior to NaF administration.

MATERIALS AND METHODS

Animals

Thirty-six adult (2-months-old) male albino Wistar rats weighing approximately 250 g were purchased from and housed at the animal house at the Faculty of Medicine, Cairo University. The animals were accommodated 6 in a cage, at a constant room temperature of 22 ± 1°C under a 12 h light:12 h dark cycle. Food and water were supplied ad libitum. All procedures were in accordance with the principles of the Ethics Committee, Faculty of Medicine, Cairo University.

Ethical approval

All protocols for animal experiments were approved by the institutional animal Ethical Committee, Cairo University, Egypt.

Experimental design

The rats were equally divided (n = 6) into six groups where control group (I) received water ad libitum, vitamin C sham control group (II) received 100 mg/kg body weight (bw)/day of vitamin C, PRP sham control group (III) received 0.5 mL of PRP, Na fluoride group (IV) received NaF at a dose of 25 mg//kg bw/day (which was 1/10 of the oral LD50 values in rats) as recommended by Chinoy [8], Na fluoride ++ vitamin C group (V) pre administered with vitamin C daily (100 mg/kg bw/day) 90 min before the administration of Na fluoride at a dose similar to group IV and

Na fluoride + PRP group (VI) pre administered with 0.5 mL of PRP daily 90 min before the administration of Na fluoride at a dose similar to group IV and V. Na fluoride and vitamin C were administered orally via gastric intubation using an intravenous cannula, whereas PRP was injected intraperitoneally. For all groups, the duration of the experiment was 4 weeks.

On the 30th day, blood samples were collected from all rats by means of retro-orbital sampling under general anaesthesia by use of sodium pentobarbital (40 mg/kg, i.p.). Then the rats were sacrificed by decapitation. The hearts were removed and tissue samples were taken from the heart of each rat for biochemical and histological assessment. For biochemical analyses, the tissue samples were labelled in glass bottles and frozen at −80°C to be studied later.

Chemicals

Vitamin C tablets were purchased from Sigma Chemical Co. (St. Louis, MO). Each tablet (100 mg) of vitamin C was crushed and dissolved in 2 mL of distilled water to acquire a 50 mg/mL suspension and was prepared just prior to administration of Na fluoride was purchased from Sigma Chemical Co. (St. Louis, MO) in powder form and dissolved in normal saline.

Preparation of PRP was done by enrichment of whole blood platelets using a 2-step centrifugation technique. A 10 mL volume of whole blood was obtained from 6 randomly-picked rats into pre-chilled tubes containing anticoagulant citrate dextrose solution A (ACD-A) at a blood/ACD-A ratio of 9:1. Centrifugation of the blood samples followed, at 400 g for 10 min to obtain the three typical layers: red blood cells at the bottom, a 'buffy coat' layer in the middle and acellular plasma in the supernatant. Using a sterile pipette, the upper layer and buffy coat were transferred to another neutral tube and re-centrifuged at 800 g for 10 min. Approximately, 1 mL of PRP was collected from the bottom of the tube (for a total of 6 mL of PRP solution from 6 rats). The total platelet count in each sample of PRP was determined under a phase contrast microscope. Concentrations of the platelets in the two groups receiving PRPs were 692.458 ± 60.287/μL and 0.5 mL of PRP was then administered intraperitoneally.

Biochemical analysis

Homogenation of tissue samples was achieved by washing the heart samples with distilled water to wash out the remaining blood. A 10% homogenate (1000 U) from each sample was obtained at 5-min

Table 1. Details about the base sequences of the primers used

Gene	Name	Direction and primer sequence (5'–3')
Keap1	Kelch-like ECH-associated protein 1	Forward: 5'-TTCGCCTACACGGCCTC-3' Reverse: 5'-GAAGTTGGCGATGCCGATG-3'
Nrf2	Nuclear factor E2-related factor 2	Forward: 5'-TCTGACTCCGGCATTTCACT-3' Reverse: 5'-GGCACTGTCTAGCTCTTCCA-3'
HO-1	Haem oxygenase 1	Forward: 5'-CGTGCAGAGAATTCTGAGTTC-3' Reverse: 5'- AGACGCTTTACGTAGTGCTG-3'
GAPDH (internal control)	Glyceraldehyde 3-phosphate dehydrogenase	Forward: 5'-CACCCTGTTGCTGTAGCCATATTC-3' Reverse: 5'GACATCAAGAAGGTGGTGAAGCAG-3'

intervals in a homogenator (IKA Labor Technic Ul-tra-Turrax T 25 model) with 150 mM cold KCl. The homogenates were then centrifuged at 6000 xgat +4°C for 10 min for supernatants to be obtained. Protein concentrations of supernatant were determined by real time quantitative polymerase chain reaction (PCR).

Real time quantitative PCR of studied genes

Total RNA was extracted from heart tissue homogenate with RNA easy Min Kit (Thermoscientific, Lithuania). The quantity and quality were assessed by Beckman dual spectrophotometer (USA). SensiFAST™ SYBR® Hi-ROX One-Step Kit, catalogue no. PI-50217 V had been formulated for highly reproducible first--strand cDNA synthesis and subsequent real-time PCR in a single tube in a 48-well plate using the step one instrument (Applied Biosystem, USA). Normalisation for variation in the expression of each target gene was performed referring to the mean critical threshold values of glyceraldehyde 3-phosphate dehydrogenase (GAPDH) housekeeping gene expression by the $^{\Delta\Delta}$Ct method. Primers base sequences of the studied genes are listed in (Table 1).

Assessment of TrX-1 by ELISA

The amount of TrX-1 was measured using Rat (TrX) ELISA kit, catalogue #SRB-T-81639, Shanghai. The spectrophotometric absorbance was assessed at 450 nm in accordance with the manufacturer's instructions. The results were expressed as nmol per mg protein.

Assessment of MDA and SOD by colorimetry

The amount of MDA and activity of superoxide dismutase (SOD) were measured using colorimetry kit, Biodiagnostic, catalogue #MD 2529, SD 2521 respectively in accordance with the manufacturer's instructions. The results were expressed as nmol per g protein and U per mg protein.

Processing of specimens and stains for light microscopy

Tissue samples from left ventricle were fixed in buffered neutral formalin, processed through graded alcohols and xylene and embedded in paraffin blocks. Tissue sections of 4–6 μm were made at multiple levels. Sections were stained with haematoxylin and eosin (H&E).

For Masson's trichrome stain, the samples were first deparaffinised and rehydrated, washed in distilled water then fixed and rinsed. Staining in Weigert's iron haematoxylin and Biebrichscarlet-acid fuchsin solution was done for 10 min for each stain with intervening rinsing. Differentiation in phospho-molybdic-phosphotungstic acid solution, staining with aniline blue solution, washing and dehydration were done before finally mounting with resinous mounting medium.

Immunohistochemistry for iNOS was performed on biopsies of deparaffinised rat cardiac tissue. Heat-induced antigen retrieval was performed using 10 mM sodium citrate (pH 6.0) buffer and microwaved for 8–15 min for exposure of target proteins. Afterwards, tissues were blocked in 3% BSA-PBS for 30 min at room temperature. Tissues were then probed at a dilution of 1:200 with a rabbit polyclonal antibody recognizing iNOS (ab3523, ABCAM, USA) or without primary antibody (negative control) overnight at 4°C in a humidified chamber. Tissues were washed thoroughly with PBST and endogenous peroxidase activity was stopped by the addition of a peroxidase suppressor. Detection was performed using a biotin-conjugated secondary antibody and SA-HRP, followed by colorimetric detection using 3,30-diaminobenzidine (DAB). Tissues were counterstained with haematoxylin and prepped for mounting.

Immnunohistochemistry of PCNA entailed deparaffinisation and heating of paraffin-embedded heart sections in 0.01 M sodium citrate buffer (pH 6.0) for 15 min followed by overnight incubation with rabbit
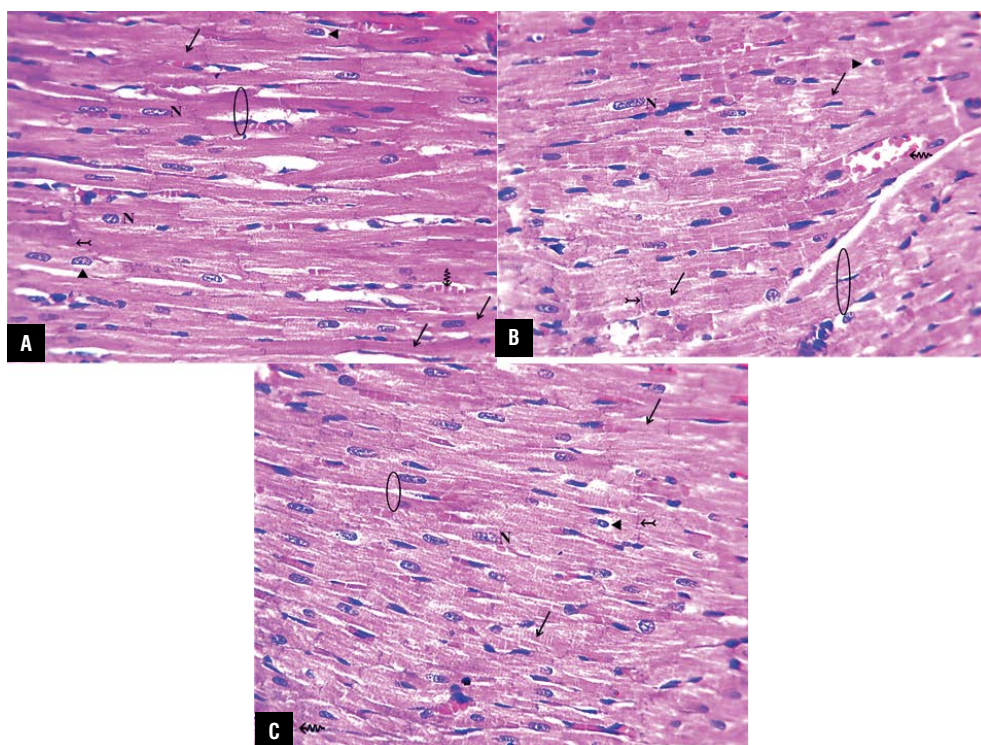
Figure 1. Haematoxylin and eosin (H&E)-stained sections of control (**A**), vitamin C sham control (**B**) and platelet-rich plasma (PRP) sham control (**C**) adult rat cardiac muscle exhibiting distinct cross-striations (arrows). Cardiac muscle fibres exhibit branching (circle) and one or two central vesicular nuclei (N) with perinuclear sarcoplasm (arrow heads). The terminal ends of adjacent cardiac muscle fibres reveal characteristic intercalated disks (tailed arrow). Narrow intercellular spaces with blood capillaries are seen (zigzag arrow). H&E ×400.

anti-PCNA antibodies (EPR382, ABCAM, USA) at 4°C. DAB was used as the chromogenic substrate and the sections were assessed by light microscopy. The characteristics and morphology of myocardial fibres for all previously mentioned stains were observed under a 400× magnification using a Leica DM 750 light field microscope and a Leica ICC50 HD camera.

Statistical analysis

Data were coded and entered using the Graph-Pad Prism version 7. Data was summarised using mean and standard deviation. Comparisons between groups were done using one way analysis of variance (ANOVA) with Tukey's multiple comparisons test when comparing more one variable in more than two groups.

RESULTS

Histological results

Haematoxylin and eosin-stained sections of the control and sham control groups showed normal histological architecture of heart cardiac muscle. The cardiac fibres exhibited cross-striations, branching and one or two central vesicular, open faced nuclei

with surrounding perinuclear sarcoplasm. The terminal ends of adjacent cardiac muscle fibres revealed characteristic and dense-staining, end-to-end junctional complexes called intercalated disks (Fig. 1).

In the heart tissues of the Na fluoride group (IV), vascular dilatation and congestion were detected along with Zenker's degeneration of the myocardium. Loss of cross striations, fragmentation and separation of the fibres were also seen (Fig. 2). In the heart tissues of groups V and VI, an apparent restoration of the normal architecture was featured in addition to mild hyperaemia at the myocardial interstitial intervals and in the capillaries (Fig. 3).

In Masson's trichrome-stained sections, the myocardial fibres were found to show a minimal positive reaction in groups I, II, III, V and VI, whereas a strong positive reaction was observed in group IV (Figs. 4, 5).

The immunohistochemical expressions of iNOS and PCNA in the cardiac tissue are shown in Figures 6 and 7, respectively. A weak expression was presented in the cardiac muscle of the control groups. However, iNOS and PCNA were significantly positively expressed in cardiac muscle, which presented as dark brown granules, in the NaF group. The apparent reduction
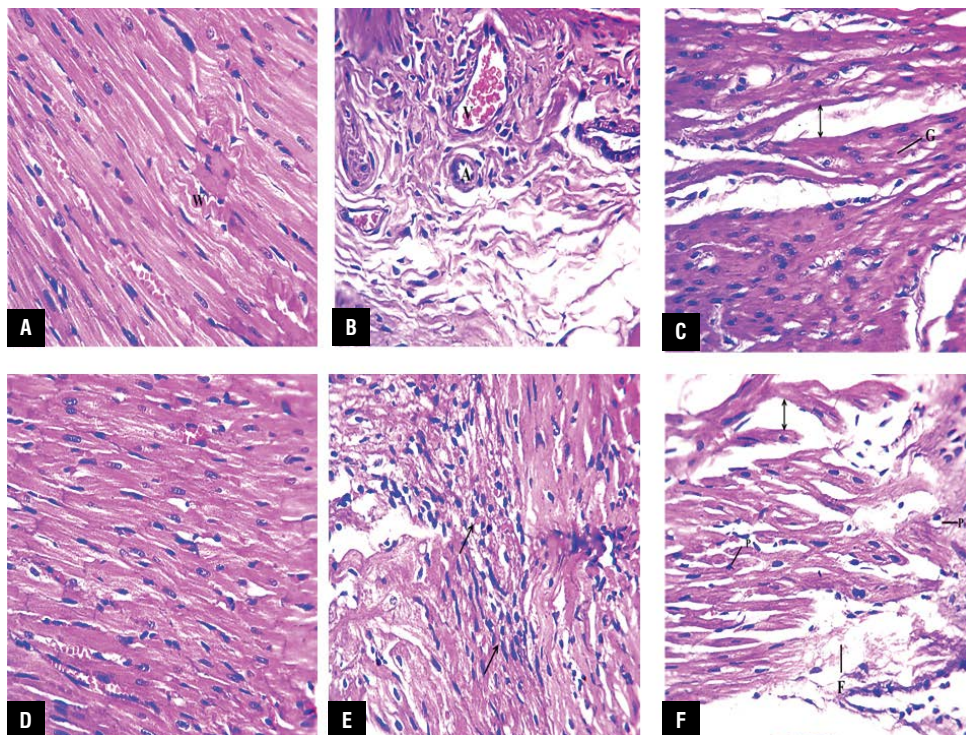
Figure 2. A–F. Haematoxylin and eosin (H&E)-stained sections of sodium fluoride (NaF)-treated adult rat cardiac muscle, showing Zenker's degeneration with widely separated myocardial fibres (double arrow), loss of cross-striations and fragmentation (F). Some myocardial fibres exhibit a wavy orientation (W). Areas of normal histological architecture in panel **D** alternate with areas of loss of architecture in panel **B**. Dilated and congested arteriole (A) and venule (V) are seen. Pyknotic nuclei (P) and ghost cells (G) are noticeable along with areas of inflammatory cellular infiltration (arrows). H&E ×400.
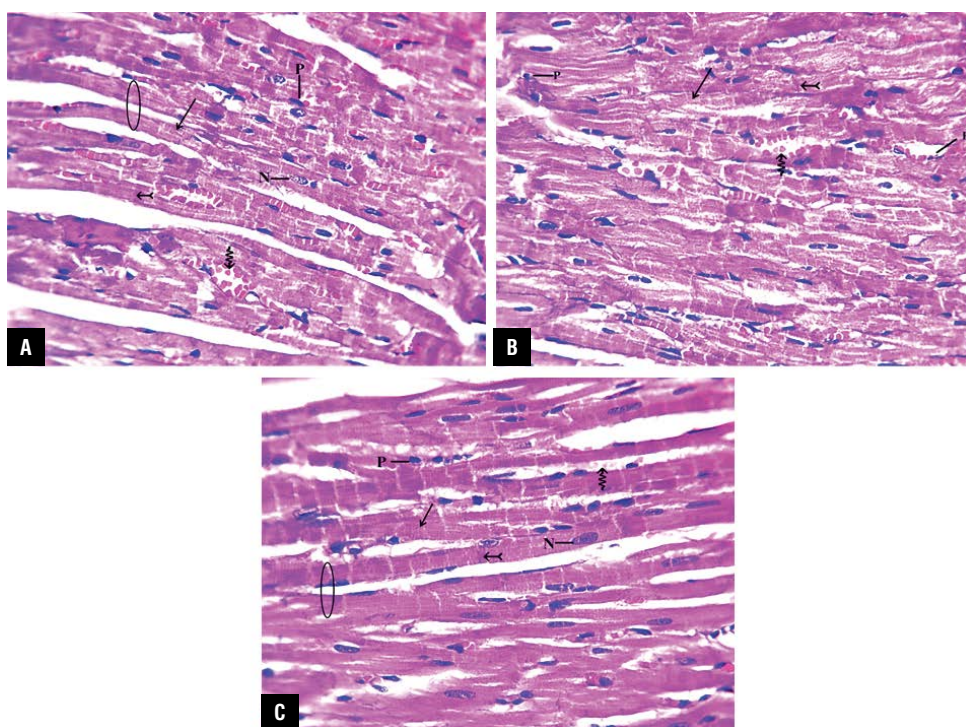

Figure 3. Haematoxylin and eosin (H&E)-stained sections of panel **A** and **B**. Sodium fluoride (NaF) + vitamin C-treated; **C.** NaF + platelet-rich plasma-treated adult rat cardiac muscle exhibiting normalisation of histological architecture. Distinct cross-striations (arrows) are seen. Cardiac muscle fibres show branching (circle) and central vesicular nuclei (N) with persistence of some nuclear pyknosis (P). The terminal ends of adjacent cardiac muscle fibres show intercalated disks (tailed arrow). Intercellular spaces with blood capillaries are also seen (zigzag arrow). H&E ×400.
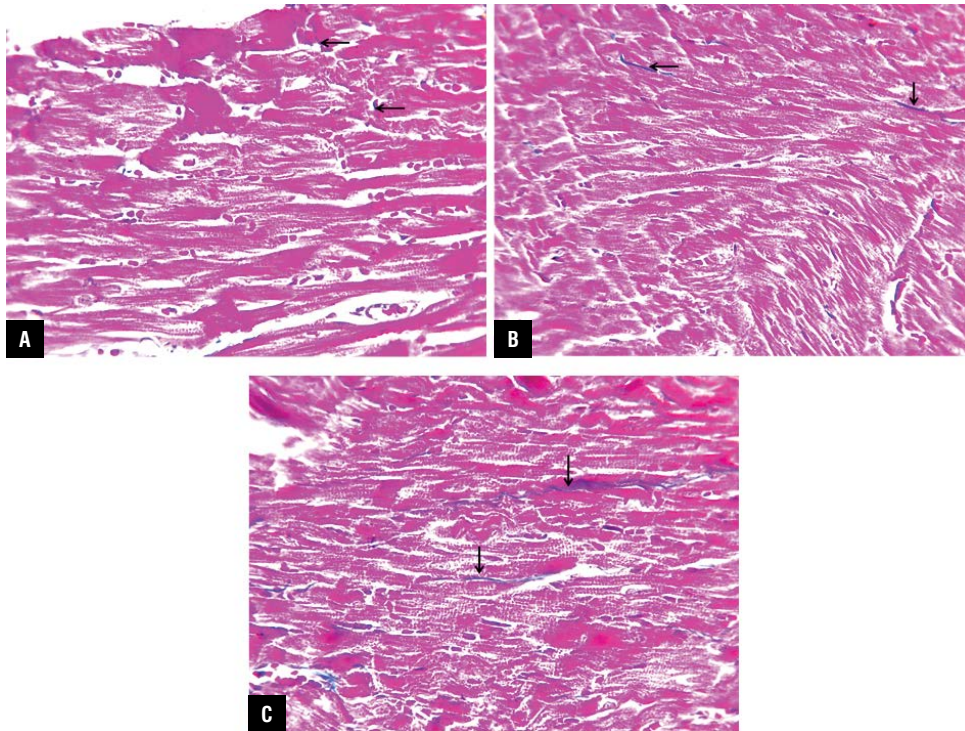
Figure 4. Masson's trichrome (MT)-stained panels of control (**A**), vitamin C sham control (**B**) and platelet-rich plasma sham control (**C**) adult rat cardiac muscle exhibiting positive reaction (arrows). Blue colour indicates positivity. MT ×400.

Figure 5. Masson's trichrome (MT)-stained sections of sodium fluoride (NaF)-treated adult rat cardiac muscle exhibiting a strong positive reaction (arrows) (**A**), NaF + vitamin C-treated (**B**) and NaF + platelet-rich plasma-treated adult rat cardiac muscle exhibiting positive reaction (arrows) (**C**). Blue colour indicates positivity. MT ×400.

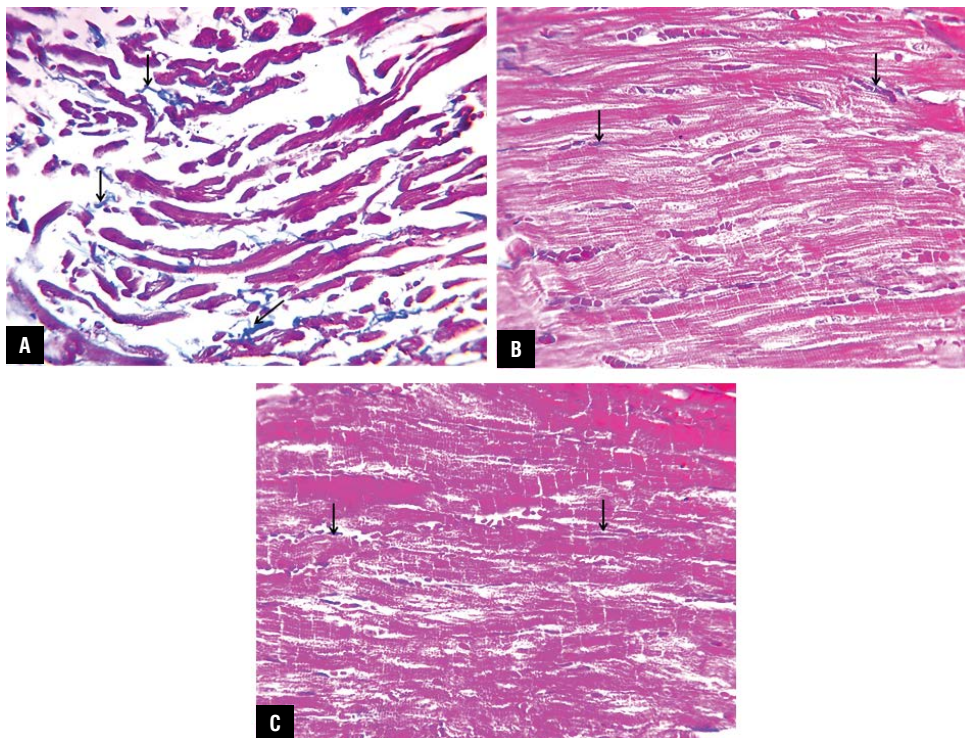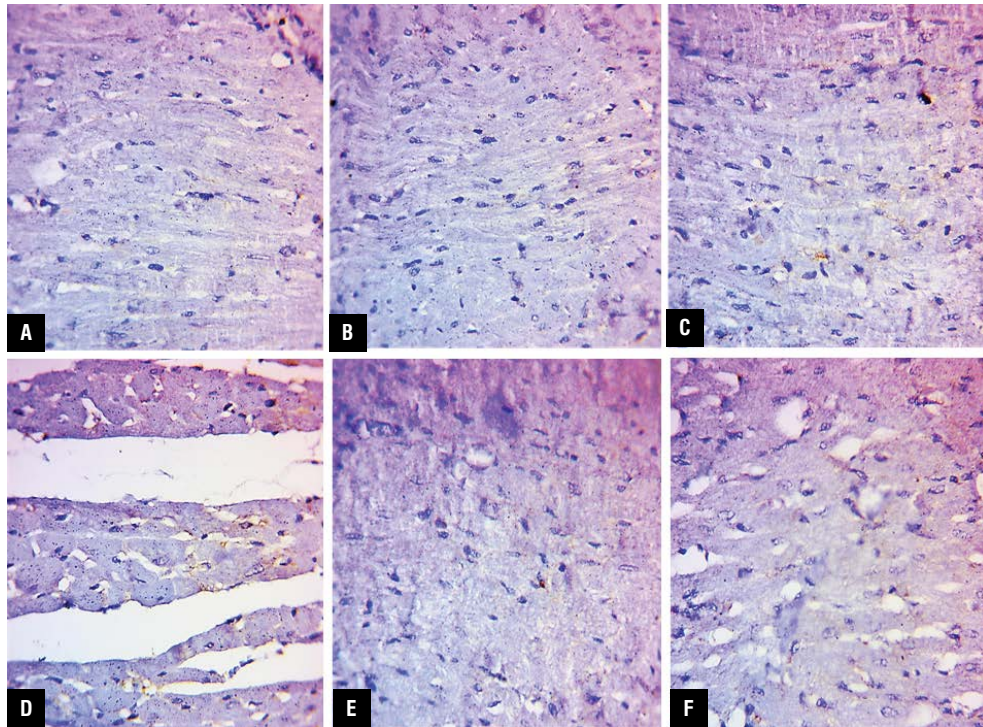**Figure 6.** Inducible nitric oxide synthases (iNOS) immunohistochemistry of adult rat cardiac muscle in control (**A**), vitamin C sham control (**B**) and platelet-rich plasma (PRP) sham control exhibiting minimal iNOS-immunopositivity (**C**). **D.** Apparent increase in iNOS-immunopositivity in sodium fluoride (NaF)-treated rat myocardium. Minimal iNOS expression in panel **E**. NaF + vitamin C-treated and NaF + PRP-treated rats (**F**). Brown colour indicates positivity. iNOS immunohistochemistry, haematoxylin counterstain ×400.
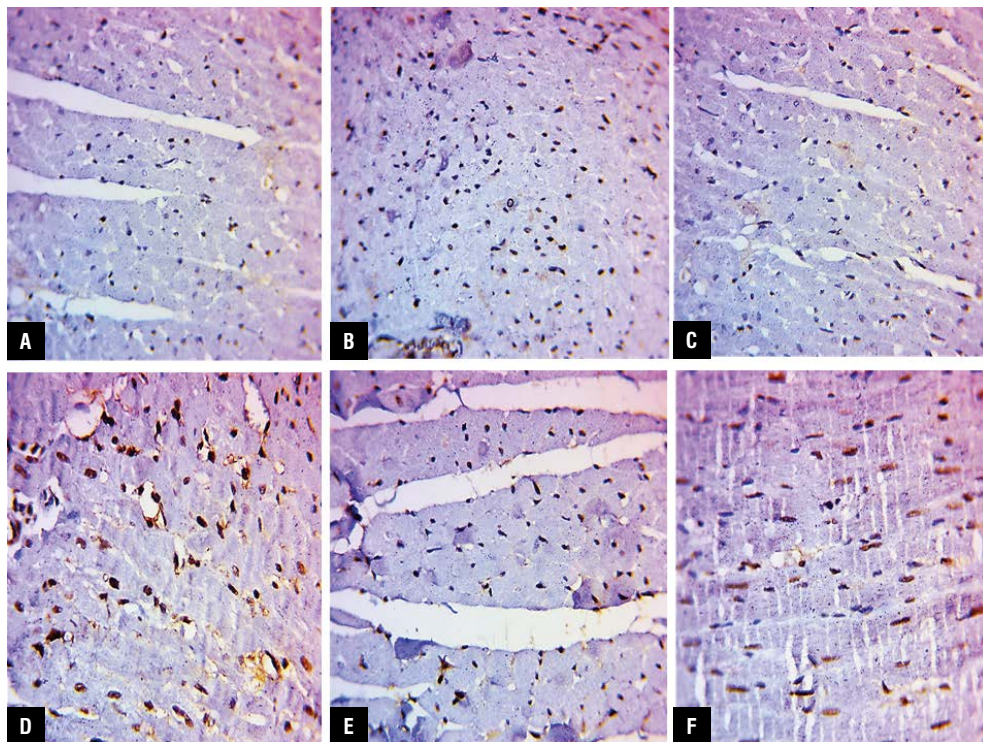
Figure 7. Proliferating cell nuclear antigen (PCNA) immunohistochemistry of adult rat cardiac muscle in control (**A**), vitamin C sham control (**B**) and platelet-rich plasma (PRP) sham control exhibiting minimal PCNA-immunopositivity (**C**). **D.** Apparent increase in PCNA-immunopositivity in sodium fluoride (NaF)-treated rat myocardium. Minimal PCNA expression in panel **E**. NaF + vitamin C-treated and moderate expression in panel **F**. NaF + PRP group. Brown colour indicates positivity. PCNA immunohistochemistry, ×400.

Table 2. Multiple comparisons of p values for Masson's trichrome, inducible nitric oxide synthases (iNOS) and proliferating cell nuclear antigen (PCNA) expression between the different experimental groups

Group	P
Masson's trichrome	
Control vs. sham control	1.000
NaF-treated	0.000
Vitamin C	0.002
PRP-treated	0.031
NaF vs. sham control	0.000
Vitamin C	0.000
PRP-treated	0.022
PRP vs. sham control	0.029
Vitamin C	1.000
Vitamin C vs. sham control	0.000
iNOS	
Control vs. sham control	1.000
NaF-treated	0.000
Vitamin C	0.000
PRP-treated	0.019
NaF vs. sham control	0.000
Vitamin C	0.000
PRP-treated	0.000
PRP vs. sham control	0.029
Vitamin C	1.000
Vitamin C vs. sham control	0.000
PCNA	
Control vs. sham control	1.000
NaF-treated	0.000
Vitamin C	0.000
PRP-treated	0.000
NaF vs. sham control	0.000
Vitamin C	0.000
PRP-treated	0.000
PRP vs. sham control	0.000
Vitamin C	1.000
Vitamin C vs. sham control	0.000

P < 0.05 is considered significant. NaF — sodium fluoride; PRP — platelet-rich plasma

in PCNA immunopositivity in group VI was not as marked as that of group V.

The relative densities of Masson's trichrome, iNOS and PCNA in the myocardium of the NaF group was also significantly higher (p < 0.05) than the control group and lower (p < 0.05) in the vitamin C and PRP groups than the NaF group (Tables 2, 3).

Biochemical and molecular results

Oxidative markers

MDA level in nmol/g tissue. A statistically significant difference was seen in MDA level between the different study groups (p < 0.0001). MDA level in the NaF-treated group (14 ± 0.46) was significantly increased compared to the control group (1.3 ± ± 0.13; p < 0.0001). In the vitamin C and PRP-treated groups, significant reductions in MDA level (4.1 ± ± 0.52 and 8.1 ± 0.28 with p < 0.0001 and p = 0.0003, respectively) were observed when compared to the NaF-treated group. In addition, there was a statistically significant decrease in MDA level in the vitamin C group compared to PRP group (p = 0.0017) (Fig. 8A).

SOD level in U/g tissue. A statistically significant difference was seen in SOD level between the different study groups (p = 0.03). SOD level in NaF-treated group (2.9 ± 0.05) was significantly decreased compared to the control group (4.0 ± 0.37; p = 0.033). In the vitamin C and PRP-treated groups, a non-significant increase in SOD level (3.8 ± 0.16 and 3.3 ± ± 0.27 with p = 0.067 and p = 0.37, respectively) were observed when compared with the NaF-treated group. In addition, there was no statistically significant difference in SOD level in the vitamin C group when compared with PRP group (p = 0.37) (Fig. 8B).

TrX-1 level in ng/g tissue. There was no statistically significant difference in TrX-1 level among the different study groups (p = 0.23). Its level in the control group was 21 ± 0.7 compared to 15 ± 0.56 in NaF-treated group. TrX-1 level in the vitamin C and PRP-treated groups was 23 ± 3.3 and 30 ± 11, respectively (Fig. 8C).

Table 3. Mean ± standard deviation for Masson's trichrome, inducible nitric oxide synthases (iNOS) and proliferating cell nuclear antigen (PCNA) expression between the different experimental groups

Groups	Masson's trichrome	iNOS	PCNA
Control	1.183 ± 0.123	1.851 ± 0.064	70 ± 0.44
Sham control	1.191 ± 0.91	1.924 ± 1.09	76 ± 0.53
NaF-treated	16.371 ± 1.171+	19.176 ± 3.327+	874 ± 1.09+
Vitamin C-treated	1.505 ± 0.423+*	8.924 ± 0.486+*	132 ± 0.411+*
PRP-treated	6.682 ± 1.401+*	12.326 ± 0.98+*	352 ± 0.82+*

Data are shown as mean ± standard deviation; +p < 0.05, significant difference compared to that of the control group; *p < 0.05, significant difference compared to that of the NaF-treated group; NaF — sodium fluoride; PRP — platelet-rich plasma
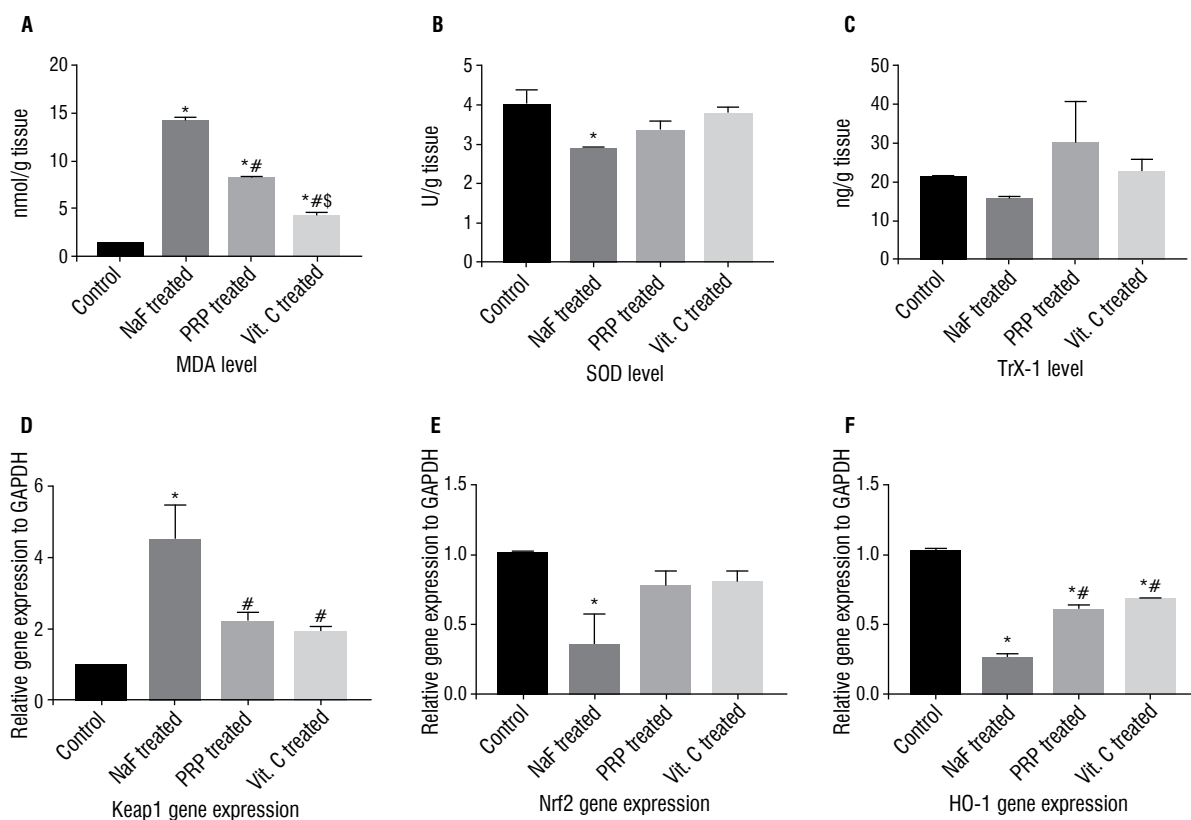
Figure 8. A–F. Different levels of biochemical and molecular markers. Data were expressed as mean ± standard deviation, p value < 0.05 was significant; *significant difference vs. control group; #significant difference vs. sodium fluoride (NaF)-treated group; $significant difference vs. platelet-rich plasma (PRP)-treated group; MDA — malondialdehyde; SOD — superoxide dismutase; TrX-1 — thioredoxin-1 oxidoreductase; Vit. — vitamin; GAPDH — glyceraldehyde 3-phosphate dehydrogenase.

Gene expression

Keap1

A statistically significant difference was seen in Keap1 gene expression among the different study groups (p = 0.01). Keap1 gene expression in NaF-treated group (4.5 ± 0.99) was significantly increased compared to control group (1 ± 0.007; p = 0.0008). In the vitamin C and PRP-treated groups, significant reductions in Keap1 gene expression (1.9 ± 0.16 and 2.2 ± 0.28 with p < 0.025 and 0.03, respectively) were observed when compared to the NaF-treated group. In addition, there was no a statistically significant difference in Keap1 gene expression in the vitamin C group compared to PRP group (p = 0.93) (Fig. 8D).

Nrf2

A statistically significant difference was seen in Nrf2 gene expression among the different study groups (p = 0.032). Nrf2 gene expression in NaF-treated group (0.35 ± 0.03) was significantly decreased compared to the control group (1 ± 0.014; p = 0.026). In the vitamin C and PRP-treated groups, there was

no a statistically significant difference between the PRP (7.7 ± 0.11) and vitamin C (0.8 ± 0.11) pre-treated groups compared with NaF-treated group (p = 0.1 and p = 0.08, respectively). In addition, there was non-significant difference in Keap1 gene expression in the vitamin C group compared to PRP group (p = 0.99) (Fig. 8E).

HO-1

A statistically significant difference was seen in HO-1 gene expression among the different study groups (p < 0.0001). HO-1 gene expression in NaF-treated group (0.26 ± 0.03) was significantly decreased compared to the control group (1 ± 0.02) (p < 0.0001). In the vitamin C and PRP-treated groups, significant difference in HO-1 gene expression (0.68 ± 0.02 and 0.61 ± 0.03 with p = 0.001 and p = 0.0005, respectively) were observed when compared to the control group. A statistically significant increase in HO-1 gene expression in PRP and vitamin C groups was seen when compared to NaF treated group (p = 0.0005 and p = 0.001, respectively) (Fig. 8F).

Statistical results

Statistical results for Masson's trichrome optical density and iNOS and PCNA immunohistochemical expression are shown in Table 2 and Table 3. Masson's trichrome's optical density of the NaF-intoxicated group (16.371 ± 1.171) significantly increased compared to the control (1.183 ± 0.123) and the sham control (1.191 ± 0.91) groups. The groups that were pretreated with vitamin C and PRP prior to NaF intoxication showed a significant reduction in optical density (1.505 ± 0.423 and 6.682 ± 1.401, respectively) when compared to the NaF group. Pretreatment with vitamin C (8.924 ± 0.486) and PRP (12.326 ± 0.98) significantly lowered the immunoexpression of iNOS when compared to the NaF group (19.176 ± 3.327), while the expression of the latter was significantly increased in comparison to the control (1.851 ± 0.064) and sham control (1.924 ± 1.09) groups. Intoxication with NaF caused a significant increase in PCNA immunoexpression (874 ± 1.09) when compared to the control (70 ± 0.44) and sham control (76 ± 0.53) groups. Vitamin C (132 ± 0.411) and PRP (352 ± 0.82) PCNA expression were decreased when compared to the NaF group. A statistically significant difference between the vitamin C and PRP-pretreated groups and the control groups was seen in all measured parameters.

DISCUSSION

Sodium fluoride toxicity continues to be a major health problem worldwide. In the current study, myocardial damage was induced in rats by oral ingestion of NaF. The purpose of our study was to evaluate the potential cardio protective role of vitamin C and PRP in NaF-induced cardiac toxicity in rat model. This was performed with reference to biochemical, molecular, immunohistochemical and histopathological changes.

Zhao et al. [52] suggested that DNA replication is an indicator of cellular proliferation. The authors also stated that DNA replication is lowered, because of the synthesis of PCNA, in inactive cells but varies according to the phase of the cell cycle, making PCNA expression a marker of cellular proliferation. In the present study, PCNA expression in the cardiac muscle was assayed by immunohistochemistry. In agreement with our results, Zhao et al. [52] observed a weak PCNA expression in the control group, and a significant positive PCNA expression in the fluoride-administered group of adult male rats' testes. They concluded

that spermatogenesis dysfunction and damage of tissue ultrastructure was caused by fluoride-induced apoptosis to which the positive PCNA expression was related, since according to the authors, apoptosis is associated with proliferation. Although previous studies have pointed out a reduction in cellular proliferation in response to fluoride exposure, the authors mentioned that cell proliferation could be maintained through the overexpression of PCNA as a response to fluoride-induced cellular apoptosis.

Shenoy et al. [42] assessed the effect of NaF administration at different concentrations on myoblast proliferation. In contrast our study where NaF was administered at a dose of 25 mg/kg, the author concluded that at a low concentration of 1.5 ppm (1 ppm being equivalent to 1 mg/kg), NaF administration resulted in myoblast proliferation and myotubular hypertrophy via an IGF-1/AKT pathway activation, whereas at a higher concentration of 5 ppm, NaF caused myotubular atrophy via an ubiquitin-proteosome pathway. Enhancement of skeletal muscle catabolism, production of reactive oxygen species (ROS) and inflammatory cytokines were also reported by the authors when higher concentrations of NaF were administered. As regards apoptosis, the authors recorded that via PI3K/Akt signalling, NaF was capable of induction of apoptosis and reduction in cell viability when administered in a dose higher than 40 ppm.

Luo et al. [26] investigated the underlying molecular mechanism of NaF-induced cytotoxicity and cell-cycle alterations in renal cells. In contrast to the present study, the authors reported that at more than 12 mg/kg body weight, a NaF-induced G2/M phase cell-cycle arrest was seen, leading to a significant increase in cell percentage present in the G2/M phase. According to the authors, the cycle arrest occurred by activating the ATM-Chk2-p53/Cdc25C signalling pathway which inhibited cellular proliferation and was associated with down regulation of PCNA mRNA expression.

In the present study, an increase in collagen fibres deposition was seen in the NaF group, as assayed by Masson's trichrome staining and image analysis. Chen et al. [7] investigated the role of tumour necrosis factor-like weak inducer of apoptosis (TWEAK)/fibroblast growth factor-inducible molecule 14 (Fn14) axis in myocardial fibrosis. The authors observed that stimulation of rat cardiac fibroblasts (CFs) with TWEAK increased CFs numbers and collagen synthesis via activation of the nuclear factor-kappaB (NF-κB) pathway

and a subsequent production of metalloproteinase-9 (MMP-9). The authors emphasized the importance of the TWEAK/Fn14 axis in control of myocardial fibrosis.

In contrast to the NaF-induced collagen deposition seen in the current study, Gupta et al. [17] detected that fluoride disturbs collagen synthesis causing the cells responsible for its synthesis to produce larger amounts of under-hydroxylated, inadequately cross-linked and rapidly catabolised collagen and/or non-collagenous proteins as a compensation. The net result is a decrease in the collagen content of tissues.

In the present study a statistically significant increase in NaF-induced iNOs expression was observed. In line with the observations of this study, Oyagbemi et al. [35] reported an increase in oxidative stress markers in cardiac tissue, in response to NaF administration. The latter authors recorded abnormalities in the histological architecture of the heart tissue and an increase in NF-κB expression as assayed by immunohistochemistry. The authors indicated that NaF-induced alterations were achieved through generation of reactive oxygen species and activation of cardiac NF-κB expression, oxidative stress being an activator of NF-κB. The authors mentioned that activation of NF-κB results in its release from cytosolic inhibitors and its translocation to the nucleus and consequently to the expression of NF-κB-target genes causing tissue inflammation and damage.

The mechanism of NaF-induced oxidative stress was explained by Gupta et al. [18]. The authors reported that fluoride causes a respiratory burst and oxygen free radicals production. The authors stated that hydroxyl radicals and superoxide radicals prevail at low and high concentrations of fluoride. The authors attributed the fluoride-induced oxidative stress to its ability to cause mitochondrial swelling and disruption and alteration of enzymes of cellular respiration. The net result is a decrease in adenosine triphosphate concentration, which in turn induces production of hydrogen peroxide and reactive oxygen species.

The current investigation revealed an increase in NaF-induced iNOs expression. He et al. [20] examined the possible effect of fluoride exposure on the expression of nitric oxide (NO) and iNOS on cultured chondrocytes. The authors stated that production of NO can be under control of iNOS and that both low and high levels of F– significantly increased the activity of iNOS and consequently the level of NO leading to oxidative tissue damage.

Ngoc et al. [34] investigated the manner of NaF-induced cell death and the mechanisms involved, where they found that it occurs mainly by apoptosis rather than necrosis. The authors reported that administration of more than 1 mMNaF leads to apoptosis through hydroxyl radical-dependent and caspase- and JNK mediated pathways. According to the authors, GADD45α plays a crucial role in the induction of apoptosis, in which its transcription and function are controlled either by JNK1 or JNK2. NaF administration stimulated the induction of GADD45α, whereas a JNK specific inhibitor inhibited such effect. The authors also reported that ROS are normally produced at low concentrations in a constant manner in living organisms, serving the function of immune cells. However, over-expression or decreased removal of intracellular ROS induces oxidative damage to cells and tissues. The authors mentioned that through an elevation of oxidative stress-mediated lipid peroxidation and subsequent mitochondrial stress, that fluoride induces apoptosis. They suggested that ROS are mediators of NaF-mediated apoptosis, where mitochondrial stress is at least in part involved. The authors concluded that the mitochondrial- and caspase-mediated signalling accompanied by intracellular ROS accumulation is involved in NaF-induced apoptosis. The authors also concluded that JNK-GADD45α- and p53-mediated signalling is critical for NaF-mediated apoptosis, where ROS act as the most crucial upstream mediator.

In agreement with the histological results of the current work, Oyagbemi et al. [35] reported an infiltration of the myocardial interstistium by inflammatory cells in response to NaF treatment. Yildirim et al. [49] investigated the effect of NaF on cardiac histopathology. The investigation revealed hyperaemia of interstitial vessels, hyaline degeneration and Zenker's necrosis in muscle fibres and mononuclear cell. A study done by Basha and Sujitha [5] recorded myocarditis with cloudy swelling, necrosis, haemorrhage, inflammation, and atherosclerosis in cardiac tissue with chronic fluorosis. Another experimental fluorosis study done by Al Shahat and Naggar [2] revealed capillary congestion, mononuclear cell infiltration and haemorrhage in the myofibrillar interval, severe muscle degeneration, and cytoplasmic vacuolisation. In our study, the NaF group revealed Zenker's degeneration with wide separation of myocardial fibres, loss of cross-striations and fragmentation. Dilatation and congestion of blood vessels, nuclear

pyknosis and inflammatory cellular infiltration were also noticeable.

The heart is vulnerable to oxidative stress due to the abundance of mitochondria; the site of basal ROS generation and due to its inherent low antioxidant defences [51]. Vitamin C is an electron donor, and this is the basis of all its known functions. It is a soluble antioxidant that prevents oxidative damage by eliminating free radicals [36]. In the present study, vitamin C significantly ameliorated the NaF-induced alterations seen in rats' myocardium.

The results of Ghosh et al. [14] suggest that vitamin C is capable of intracellular antioxidant enzymes restoration and maintenance of endogenous antioxidant molecules' levels, leading the authors to include it as a positive control to verify the experimental set up against NaF-induced oxidative stress and cell death.

Sirtuin 1 (Sirt1), which is a NAD-dependent class III histone deacetylase, plays a fundamental role in multiple cellular processes via deacetylation. It controls mitochondrial health by limiting the generation of mitochondrial-derived ROS (mROS). Sirt1 deacetylases manganese superoxide dismutase (SOD2); a key enzyme involved in regulating mROS production, consequently increasing SOD2 activity [48]. Low levels of Sirt1 are associated with increased mROS levels [38]. Liu et al. [25] mentioned that Sirt1 expression has antioxidant regulatory effects in cardiac tissue where it regulates antioxidant systems.

Peng et al. [37] investigated the beneficial effects of vitamin C against NaF-induced cytotoxicity and the underlying molecular mechanisms. The authors found that NaF caused cytotoxicity, stimulated mROS production, and prompted apoptosis in F9 embryonic carcinoma cells. NaF administration was also accompanied with decreased Sirt1 protein expression. They found that NaF-induced mitochondrial oxidative injuries were significantly attenuated by overexpression of Sirt1 or incubation with Mito-TEMPO (a SOD2 mimetic). The authors reported that pretreatment with vitamin C enhanced the expression of Sirt1 and decreased NaF-induced mitochondrial oxidative stress and apoptosis. The authors confirmed that vitamin C-induced reduction in mROS and apoptosis was blocked by a knockdown of Sirt1 by means of inhibiting Sirt1-SOD2 signalling. They also reported that sodium-dependent vitamin C transporter 2 (SVCT-2) siRNA was capable of hindering the capacity of vitamin C to stimulate Sirt1/SOD2 signalling.

Zaki et al. [51] revealed that the modulatory effect of mesenchymal stem cells (MSCs) pretreated with PRP on doxorubicin (DOX)-induced cardiotoxicity was superior to the modulatory effect of MSCs alone. The authors mentioned that oxidative stress underlies the DOX-induced cardiotoxicity and accordingly found the oxidant marker MDA to be elevated, while the antioxidant marker SOD decreased in DOX-treated groups. A significant improvement of both markers in the MSC- and PRP/MSC-treated groups was seen with a significant MDA difference in favour of PRP/MSC-treated group. A 100% higher Bcl2/Bax ratio was seen after MSCs were pretreated with PRP when apoptosis was assessed. In line with the present results, PRP showed a similar preventive role like vitamin C.

In the cardiovascular system, important antioxidative molecules are catalase, SOD, glutathione, glutathione S-transferases, glutathione peroxidases, haem oxygenases, thioredoxin reductases, and thioredoxins. The expression of those antioxidative molecules can be regulated by the transcription factor nuclear factor erythroid 2-related factor 2 [22].

The potential antioxidant properties of PRP and vitamin C to antagonise cardiac toxicity of NaF were studied in the current experiment. Their antioxidant potential was investigated through their effect on the Keap1/Nrf2/HO-1 as a redox signalling pathway. In the current study, the cardiac toxicity with NaF caused the depletion of SOD, TrX-1 and increase in MDA level and increase in Keap1 levels, and it decreased Nrf2 and HO-1 mRNA expressions levels, which are markers of oxidative stress. Many studies demonstrated that NaF administration reduces the activity of mitochondrial antioxidant enzymes leading to cardiotoxicity, finally resulting in myocardial necrosis [9]. Activation of Nrf2 is done to antagonise reactive oxidants, while decreased Nrf2 activity has the opposite action [43]. The treatment of tumour cells with vitamin C reduced the expression of Nrf2 at the mRNA and protein levels [32]. These are studies agreed with our study, PRP and vitamin C reduced Keap1 expression and increased the nuclear accumulation of Nrf2, which is associated with higher expression levels of HO-1, SOD, and mitochondrial antioxidant enzymes. These results are agreed with earlier studies suggesting PRP and vitamin C as an anti-oxidative stress agent [19, 23]. Lawal et al. [24] investigated the antioxidant efficacy of heated garlic juice (HGJ) in liver against ascorbic acid (AA) in rats exposed to cadmium. Their results

showed that AA was a more effective antioxidant than HGJ in avoiding cadmium-induced oxidative damage in liver and its action intervened through Nrf2-Keap1 pathway. Saif-Elnasr et al. [41] studied the treatment of hepatotoxicity induced by γ-radiation in albino rats by PRP and/or LMC. Their study revealed that treatment with PRP and/or LMC decrease hepatic MDA levels and increase Nrf2 levels. Another report proposed that vitamin C reduced the levels of the oxidants MDA in acute and regular exercise [40]. The present study proved that PRP and vitamin C can be used a cardio-protective agent in NaF toxicity, which is possibly associated with the modulation of the Keap1/ /Nrf2 pathway, stimulating the nuclear accumulation of Nrf2 and the upregulation of phase II antioxidant enzyme expression such as HO-1, SOD, and TrX-1.

CONCLUSIONS

The presented results suggest that pretreatment with vitamin C and PRP possess a potential cardio-protective effect against NaF intoxication in adult male albino rats. This study is the first to show that the cardio-protective effect of PRP, against NaF intoxication in the homogenates of rat heart tissues is comparable to that of vitamin C and might be considered for clinical trials. The results can be viewed as a starting point for further applications of this natural compound in the pharmaceutical industry after performing clinical researches. Our data illustrates a new molecular mechanism underlying the ability of vitamin C and PRP to be explored for future treatment of NaF-induced cytotoxicity.

Conflict of interest: None declared

REFERENCES

1. Ago T, Yeh I, Yamamoto M, et al. Thioredoxin1 upregulates mitochondrial proteins related to oxidative phosphorylation and TCA cycle in the heart. Antioxid Redox Signal. 2006; 8(9-10): 1635–1650, doi: 10.1089/ars.2006.8.1635, indexed in Pubmed: 16987018.
2. Al Shahat AA, Naggar A. Possible protective role of calcium against fluoride induced cardio toxicities in adult male albino rats. J Am Sci. 2013; 9(4): 1–5, doi: 10.7537/marsjas090413.01.
3. Araujo JA, Zhang M, Yin F. Heme oxygenase-1, oxidation, inflammation, and atherosclerosis. Front Pharmacol. 2012; 3: 119, doi: 10.3389/fphar.2012.00119, indexed in Pubmed: 22833723.
4. Hammett-Stabler CA. Disposition of toxic drugs and chemicals in man. RC Baselt. Foster City, CA: Chemical Toxicology Institute. 1999; 90, doi: 10.1093/clinchem/46.6.889a.
5. Basha MP, Sujitha NS. Chronic fluoride toxicity and myocardial damage: antioxidant offered protection in second generation rats. Toxicol Int. 2011; 18(2): 99–104, doi: 10.4103/0971-6580.84260, indexed in Pubmed: 21976813.
6. Bielecki T, Dohan Ehrenfest DM, Everts PA, et al. The role of leukocytes from L-PRP/L-PRF in wound healing and immune defense: new perspectives. Curr Pharm Biotechnol. 2012; 13(7): 1153–1162, doi: 10.2174/138920112800624373, indexed in Pubmed: 21740376.
7. Chen HN, Wang DJ, Ren MY, et al. TWEAK/Fn14 promotes the proliferation and collagen synthesis of rat cardiac fibroblasts via the NF-κB pathway. Mol Biol Rep. 2012; 39(8): 8231–8241, doi: 10.1007/s11033-012-1671-3, indexed in Pubmed: 22555979.
8. Chinoy NJ. Effects of fluoride on physiology of animals and human beings. Indian J Environ Toxicol. 1991; 1(1): 17–32.
9. Cicek E, Aydin G, Akdogan M, et al. Effects of chronic ingestion of sodium fluoride on myocardium in a second generation of rats. Hum Exp Toxicol. 2005; 24(2): 79–87, doi: 10.1191/0960327105ht505oa, indexed in Pubmed: 15850282.
10. Delker SL, Xue F, Li H, et al. Role of zinc in isoform-selective inhibitor binding to neuronal nitric oxide synthase . Biochemistry. 2010; 49(51): 10803–10810, doi: 10.1021/bi1013479, indexed in Pubmed: 21138269.
11. Erdal S, Buchanan SN. A quantitative look at fluorosis, fluoride exposure, and intake in children using a health risk assessment approach. Environ Health Perspect. 2005; 113(1): 111–117, doi: 10.1289/ehp.7077, indexed in Pubmed: 15626657.
12. Fabiyi-Edebor TD. Vitamin C ameliorated cardiac autonomic neuropathy in type 2 diabetic rats. World J Diabetes. 2020; 11(3): 52–65, doi: 10.4239/wjd.v11.i3.52, indexed in Pubmed: 32180894.
13. Fuse Y, Kobayashi M. Conservation of the Keap1-Nrf2 System: An Evolutionary Journey through Stressful Space and Time. Molecules. 2017; 22(3), doi: 10.3390/molecules22030436, indexed in Pubmed: 28282941.
14. Ghosh J, Das J, Manna P, et al. Cytoprotective effect of arjunolic acid in response to sodium fluoride mediated oxidative stress and cell death via necrotic pathway. Toxicol In Vitro. 2008; 22(8): 1918–1926, doi: 10.1016/j.tiv.2008.09.010, indexed in Pubmed: 18845235.
15. Gold R, Kappos L, Arnold DL, et al. Placebo-controlled phase 3 study of oral BG-12 for relapsing multiple sclerosis. N Engl J Med. 2012; 367(12): 1098–1107, doi: 10.1056/NEJMoa1114287, indexed in Pubmed: 22992073.
16. Goshman LM. Clinical toxicology of commercial products, By RE Gosselin, RP Smith, and HC Hodge. Williams and Wilkins, Baltimore 1984.
17. Gupta AR, Dey S, Saini M, et al. Protective effect of Tamarindus indica fruit pulp extract on collagen content and oxidative stress induced by sodium fluoride in the liver and kidney of rats. Toxicological & Environmental Chemistry. 2014; 95(9): 1611–1623, doi: 10.1080/02772248.2014.890724.
18. Gupta AR, Dey S, Swarup D, et al. Effects of excessive fluoride ingestion on collagen protein and expression of type I collagen gene in skeletal muscles of rats. Fluoride. 2013; 46(3): 149–55.

19. Hargrave BY. Autologous platelet rich plasma (platelet gel): an appropriate intervention for salvaging cardiac myocytes under oxidative stress after myocardial infarction. Anatomy & Physiology. 2013; 04(01), doi: 10.4172/2161-0940.1000134.

20. He WW, Wang WY, Deng J, et al. L-NMMA and1400W, inhibitor of iNOS, attenuate the induction of iNOS and NO in primary rabbit costal chondrocytes by fluoride. Fluoride. 2020; 53(2): 220–238.

21. Itoh K, Ishii T, Wakabayashi N, et al. Regulatory mechanisms of cellular response to oxidative stress. Free Radic Res. 1999; 31(4): 319–324, doi: 10.1080/10715769900300881, indexed in Pubmed: 10517536.

22. Jakobs P, Serbulea V, Leitinger N, et al. Nuclear factor (erythroid-derived 2)-like 2 and thioredoxin-1 in atherosclerosis and ischemia/reperfusion injury in the heart. Antioxid Redox Signal. 2017; 26(12): 630–644, doi: 10.1089/ars.2016.6795, indexed in Pubmed: 27923281.

23. Kojo S. Vitamin C: basic metabolism and its function as an index of oxidative stress. Curr Med Chem. 2004; 11(8): 1041–1064, doi: 10.2174/0929867043455567, indexed in Pubmed: 15078165.

24. Lawal AO, Lawal AF, Ologundudu A, et al. Antioxidant effects of heated garlic juice on cadmium-induced liver damage in rats as compared to ascorbic acid. J Toxicol Sci. 2011; 36(5): 549–557, doi: 10.2131/jts.36.549, indexed in Pubmed: 22008531.

25. Liu AJ, Li B, Yang M, et al. Sirtuin 1 mediates hydrogen sulfide-induced cytoprotection effects in neonatal mouse cardiomyocytes. Chinese Med J. 2017; 130(19): 2346, doi: 10.4103%2F0366-6999.215328.

26. Luo Q, Guo H, Kuang P, et al. Sodium Fluoride Arrests Renal G2/M Phase Cell-Cycle Progression by Activating ATM-Chk2-P53/Cdc25C Signaling Pathway in Mice. Cell Physiol Biochem. 2018; 51(5): 2421–2433, doi: 10.1159/000495899, indexed in Pubmed: 30537743.

27. Lusigi EM. Quality Assessment of Rain and Storm Water Runoff for Nairobi City Industrial and Sub-Urban Areas (Doctoral dissertation), University of Nairobi, 2017.

28. Martins RP, Hartmann DD, de Moraes JP, et al. Platelet-rich plasma reduces the oxidative damage determined by a skeletal muscle contusion in rats. Platelets. 2016; 27(8): 784–790, doi: 10.1080/09537104.2016.1184752, indexed in Pubmed: 27255146.

29. McDonagh MS, Whiting PF, Wilson PM, et al. Systematic review of water fluoridation. BMJ. 2000; 321(7265): 855–859, doi: 10.1136/bmj.321.7265.855, indexed in Pubmed: 11021861.

30. Moi P, Chan K, Asunis I, et al. Isolation of NF-E2-related factor 2 (Nrf2), a NF-E2-like basic leucine zipper transcriptional activator that binds to the tandem NF-E2/AP1 repeat of the beta-globin locus control region. Proc Natl Acad Sci U S A. 1994; 91(21): 9926–9930, doi: 10.1073/pnas.91.21.9926, indexed in Pubmed: 7937919.

31. Moraes VY, Lenza M, Tamaoki MJ, et al. Platelet-rich therapies for musculoskeletal soft tissue injuries. Cochrane Database Syst Rev. 2014(4): CD010071, doi: 10.1002/14651858.CD010071.pub3, indexed in Pubmed: 24782334.

32. Mostafavi-Pour Z, Ramezani F, Keshavarzi F, et al. The role of quercetin and vitamin C in Nrf2-dependent oxidative stress production in breast cancer cells. Oncol Lett. 2017;

33. 13(3): 1965–1973, doi: 10.3892/ol.2017.5619, indexed in Pubmed: 28454351.

33. Nair V, O'Neil C, Wang P. Malondialdehyde. Encyclopedia of Reagents for Organic Synthesis. 2008, doi: 10.1002/047084289x.rm013.pub2.

34. Ngoc TD, Son YO, Lim SS, et al. Sodium fluoride induces apoptosis in mouse embryonic stem cells through ROS-dependent and caspase- and JNK-mediated pathways. Toxicol Appl Pharmacol. 2012; 259(3): 329–337, doi: 10.1016/j.taap.2012.01.010, indexed in Pubmed: 22285274.

35. Oyagbemi AA, Omobowale TO, Asenuga ER, et al. Sodium fluoride induces hypertension and cardiac complications through generation of reactive oxygen species and activation of nuclear factor kappa beta. Environ Toxicol. 2017; 32(4): 1089–1101, doi: 10.1002/tox.22306, indexed in Pubmed: 27378751.

36. Padayatty SJ, Katz A, Wang Y, et al. Vitamin C as an antioxidant: evaluation of its role in disease prevention. J Am Coll Nutr. 2003; 22(1): 18–35, doi: 10.1080/07315724.2003.10719272, indexed in Pubmed: 12569111.

37. Peng W, Xu S, Zhang J, et al. Vitamin c attenuates sodium fluoride-induced mitochondrial oxidative stress and apoptosis via Sirt1-SOD2 pathway in F9 cells. Biol Trace Elem Res. 2019; 191(1): 189–198, doi: 10.1007/s12011-018-1599-0, indexed in Pubmed: 30565018.

38. Pi H, Xu S, Reiter RJ, et al. SIRT3-SOD2-mROS-dependent autophagy in cadmium-induced hepatotoxicity and salvage by melatonin. Autophagy. 2015; 11(7): 1037–1051, doi: 10.1080/15548627.2015.1052208, indexed in Pubmed: 26120888.

39. Piantadosi CA, Carraway MS, Babiker A, et al. Heme oxygenase-1 regulates cardiac mitochondrial biogenesis via Nrf2-mediated transcriptional control of nuclear respiratory factor-1. Circ Res. 2008; 103(11): 1232–1240, doi: 10.1161/01.RES.0000338597.71702.ad, indexed in Pubmed: 18845810.

40. Popovic LM, Mitic NR, Miric D, et al. Influence of vitamin C supplementation on oxidative stress and neutrophil inflammatory response in acute and regular exercise. Oxid Med Cell Longev. 2015; 2015: 295497, doi: 10.1155/2015/295497, indexed in Pubmed: 25802681.

41. Saif-Elnasr M, Abdel Fattah SM, Swailam HM. Treatment of hepatotoxicity induced by γ-radiation using platelet-rich plasma and/or low molecular weight chitosan in experimental rats. Int J Radiat Biol. 2019; 95(11): 1517–1528, doi: 10.1080/09553002.2019.1642538, indexed in Pubmed: 31290709.

42. Shenoy PS, Sen U, Kapoor S, et al. Sodium fluoride induced skeletal muscle changes: Degradation of proteins and signaling mechanism. Environ Pollut. 2019; 244: 534–548, doi: 10.1016/j.envpol.2018.10.034, indexed in Pubmed: 30384060.

43. Smith RE, Tran K, Smith CC, et al. The Role of the Nrf2/ARE antioxidant system in preventing cardiovascular diseases. Diseases. 2016; 4(4), doi: 10.3390/diseases4040034, indexed in Pubmed: 28933413.

44. Spartalis E, Tomos P, Moris D, et al. Role of platelet-rich plasma in ischemic heart disease: An update on the latest evidence. World J Cardiol. 2015; 7(10): 665–670, doi: 10.4330/wjc.v7.i10.665, indexed in Pubmed: 26516421.

45. Viswanathan G, Gopalakrishnan S, Siva Ilango S. Assessment of water contribution on total fluoride intake of various age groups of people in fluoride endemic and non-endemic areas of Dindigul District, Tamil Nadu, South India. Water Res. 2010; 44(20): 6186–6200, doi: 10.1016/j.watres.2010.07.041, indexed in Pubmed: 20728198.

46. Wang D, Shi JQ, Liu FX. Immunohistochemical detection of proliferating cell nuclear antigen in hepatocellular carcinoma. World J Gastroenterol. 1997; 3(2): 101–103, doi: 10.3748/wjg.v3.i2.101, indexed in Pubmed: 27041957.

47. Wakabayashi N, Itoh K, Wakabayashi J, et al. Keap1-null mutation leads to postnatal lethality due to constitutive Nrf2 activation. Nat Genet. 2003; 35(3): 238–245, doi: 10.1038/ng1248, indexed in Pubmed: 14517554.

48. Xu S, Gao Y, Zhang Q, et al. SIRT1/3 activation by resveratrol attenuates acute kidney injury in a septic rat model. Oxid Med Cell Longev. 2016; 2016: 7296092, doi: 10.1155/2016/7296092, indexed in Pubmed: 28003866.

49. Yildirim S, Ekin S, Huyut Z, et al. Effect of chronic exposure to sodium fluoride and 7, 12-dimethylbenz [a] anthracene on some blood parameters and hepatic, renal, and cardiac histopathology in rats. Fluoride. 2018; 51(3): 278–290.

50. Yin B, Di L, Tang S, et al. Vitamin CNa enhances the antioxidant ability of chicken myocardium cells and induces heat shock proteins to relieve heat stress injury. Res Vet Sci. 2020; 133: 124–130, doi: 10.1016/j.rvsc.2020.09.008, indexed in Pubmed: 32977120.

51. Zaki SM, Algaleel WaA, Imam RA, et al. Mesenchymal stem cells pretreated with platelet-rich plasma modulate doxorubicin-induced cardiotoxicity. Hum Exp Toxicol. 2019; 38(7): 857–874, doi: 10.1177/0960327119842613, indexed in Pubmed: 30991846.

52. Zhao WP, Wang HW, Liu J, et al. Positive PCNA and Ki-67 expression in the testis correlates with spermatogenesis dysfunction in fluoride-treated rats. Biol Trace Elem Res. 2018; 186(2): 489–497, doi: 10.1007/s12011-018-1338-6, indexed in Pubmed: 29748930.

ORIGINAL ARTICLE

Anatomy of parotid gland and its secretory ducts in sheep

G.B. Uzun[1] , B. Kamaşak[2] , T. Ulcay[2] , K. Aycan[2]

[1]Department of Medical Laboratory Services, Vocational School of Health Services,
Malatya Turgut Özal University, Malatya, Turkey
[2]Department of Anatomy, Faculty of Medicine, Kırşehir Ahi Evran University, Kırşehir, Turkey

Background: The parotid gland in sheep ends freely in front of the masseter muscle, and paracondylary section of occipital bone and extends deep until pterygoid extends of sphenoid bone and hyoid bone. The structure of salivary glands in mammals has been thoroughly studied using histological and sialographic method. This study aimed to reveal the detailed anatomic features and race-specific differences of the canal system of the parotid glands in Akkaraman sheep by using the corrosion cast technique.

Materials and methods: Thirteen sheep parotid glands from 7 Akkaraman sheep were used in this study. Parotid glands were removed from their places with ducts. Measurements were made with a calliper from back to front, top to bottom and inside to outside. After dissection of the parotid glands, their volumes were measured according to the 'Archimedes principle'. Also, 13 sheep parotid glands were examined using the polyester resin method.

Results: In the present study, our average metric results were: length of parotid duct was 10.92 ± 1.027 cm, length of parotid gland was 5.87 ± 1.04 cm, volume of parotid gland was 12.50 ± 2.48 cm³, thickness of parotid gland was 0.75 ± ± 0.36 cm and width of parotid gland was 4.07 ± 0.43 cm. The average weight of the parotid gland of Akkaraman sheep was identified as 25.3 g. Accessory parotid gland was not encountered in the current study.

Conclusions: It was observed that polyester entered into the parotid duct and filled up until the acinus and made both acinus and secretory ducts well-examined in this study. It was also observed that the parotid gland consisted of lobes and lobules. The average number of lobes was 12. The number of lobules in a lobe varied between 3 and 16, each lobe consisted of an average of 9 lobules. It was found that each lobe has its own lobar duct. (Folia Morphol 2022; 81, 3: 679–684)

Key words: parotid gland, corrosion, secretory duct

INTRODUCTION

The salivary glands play an important role in the ruminants and are classified as major and minor. In ruminants, the major salivary glands are parotid, submandibular, and sublingual, while minor salivary glands are buccal and labial [16, 21]. Their secretion, saliva, is serous and mucous in character, and is produced in large quantities, e.g. the amount of saliva

Address for correspondence: B. Kamaşak, R.A., Department of Anatomy, Faculty of Medicine, Kırşehir Ahi Evran University, Kırşehir, Turkey,
tel: +90 545 282 89 02, e-mail: brc1608@hotmail.com

secreted during a 24 hour period in sheep is 1–4 L [6] or 6–16 L [10, 22].

Histologically parotid salivary gland is usually a serous gland in all domestic animals, man and rodents; a few mucous cells or adenomeres may be present in carnivores [6, 10, 22].

The parotid gland, the largest salivary gland in sheep, is situated on the masseter muscle along the caudal border of the vertical ramus of the mandible from the zygomatic arch to the angle of the junction of the linguo-facial and maxillary veins and is located at the base of the ear between the back side of ramus mandibulae and transvers process of atlas.

The parotid duct leaves the gland at its ventral and rostral surface, coursing along the ventral and rostral border of the masseter muscle, as it is located between the muscle and the facial vein. It enters the oral cavity and opens into the papilla salivalis opposite to the upper second molar tooth [9, 15, 22].

Human parotid glands are the largest major glands (average weight: 25–30 g) located on each side of the head, behind the external auditory canal of the mandible and the skull base. The development of human parotid glands starts from the 5th and 6th week of the intrauterine stage. The main excretory duct of the parotid gland is Stensen's duct; it runs through the anterolateral edge of the gland over the masseter muscle, culminating at the buccal mucosa in the upper molar region. Parotid glands are exclusively formed by serous acini [2, 19].

Although the duct of the parotid gland is usually one, it can vary numerically. For example, a 46-year--old man has a double parotid canal on the right side of his face [1, 12, 13]. Sometimes an accessory parotid gland is found anterolaterally to the masseter muscle in humans [5].

The mass of the mandibular and parotid gland was reported to be 9.0 g and 11.0 g, respectively, in sheep [14, 22, 24]. In another study the mass of mandibular and parotid gland in sheep was reported to be 16.2 ± 4.6 g and 13.5 ± 2.6 g [7]. The mean length of the parotid gland was 6.04 ± 0.48 cm in sheep and 6.56 ± 0.361 cm in goat [18], and 3.96 ± ± 0.26 cm in dog [11]. Human parotid glands average weight is 25–30 g [19] and 14–28 g [25].

The mean diameters of mandibular and parotid ducts were 1.4 ± 0.3 mm and 3.1 ± 1.0 mm, respectively, in sheep [7]. The parotid duct measured about 20 ± 0.41 cm in length and 0.5 ± 0.2 cm in diameter in camel (Camelus dromedarius) [15]. Estecondo et

al. [11] showed that in Zaedyus pichiy, the submandibular gland consists of 2 lobes.

The parotid gland was irregular rectangular and had five processes. Both the parotid and the mandibular salivary glands could be divided into 4 segments [15].

The normal sheep mandibular and parotid salivary glands have a multilobular appearance in cadaver heads [7]. Sheep parotid gland was made up of 4 lobes (cranial, middle, caudal and accessory) and the main excretory duct was formed from union of 4 lobar ducts [20]. Human parotid gland is divided into superficial and deep lobes [25]. The duct system of the major salivary glands is starting from the acini, the intercalary duct, the intralobular duct (striated duct) (secretory tubule), the interlobular duct, the lobular duct, the intralobar duct and the (excretory duct) ductus parotideus, [2, 6, 8, 13, 23].

The structure of salivary glands in mammals has been thoroughly studied using histological, histochemical, and sialographic method [7, 10, 11, 18, 24].

However, there is no study on parotid ductal system in human and other animals with corrosion method. This study aimed to reveal the detailed anatomic features and race-specific differences of the canal system of the parotid glands in Akkaraman sheep by using the corrosion cast technique.

MATERIALS AND METHODS

Thirteen sheep parotid glands from 7 Akkaraman sheep (12–23 months old and 34–45 kg) were used in this study. We used 7 sheep in our study, but since the ducts of one of the parotid glands could not be removed to be examined under a microscope, we expressed it as 13 parotid glands.

Parotid glands were removed from their places with ducts (Fig. 1). Measurements were made with a calliper from back to front (length), top to bottom (length–height) and inside to outside (thickness). Course of parotid duct and length from the entrance of mouth to the gland were also measured. After dissection of the parotid glands, their volumes were measured according to the 'Archimedes principle'. For this reason, the parotid gland was placed into a measured container filled with physiological saline solution and the volume of the parotid gland was measured by determining the amount of water overflowed from the container. This process was repeated 6 times and the average was taken as the volume of the gland.
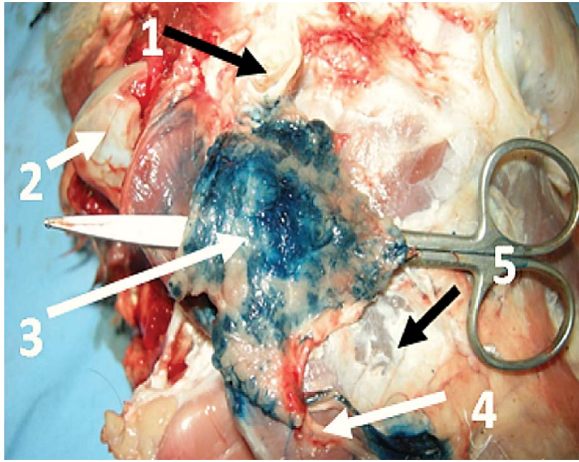
Figure 1. Head of sheep; 1 — external ear canal; 2 — occipital condyle; 3 — parotid gland; 4 — parotid duct; 5 — masseter muscle.
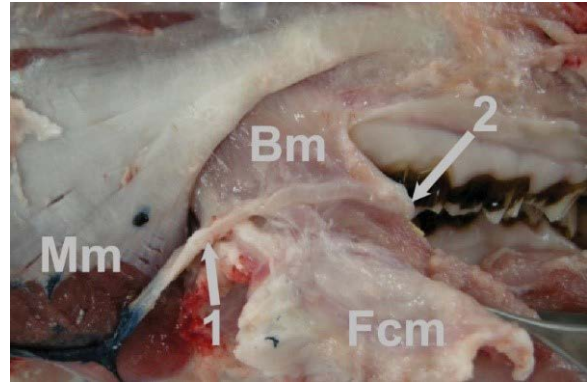

Figure 2. The course of parotid duct; 1 — ductus parotideus; 2 — papilla parotidea; Mm — masseter muscle; Bm — buccinator muscle; Fcm — facial muscle.

Table 1. Measurement values of parotid glands in Akkaraman sheep

Parameters	Right parotid gland	Left parotid gland	Min–Max	Total
Length of parotid gland [cm]	6.0 ± 0.2	5.7 ± 1.7	4.5–7.0	5.87 ± 1.04
Thickness of parotid gland [cm]	0.9 ± 0.4	0.5 ± 0.7	0.5–1.30	0.75 ± 0.36
Width of parotid gland [cm]	4.4 ± 0.1	3.7 ± 0.3	3.50–4.50	4.07 ± 0.43
Volume of parotid gland [cm³]	14.5 ± 0.7	10.5 ± 1.4	9.50–15	12.50 ± 2.48
Length of parotid duct [cm]	11.75 ± 0.35	10.1 ± 0.5	9.70–12	10.92 ± 1.027

Data are shown as mean ± standard deviation or minimum–maximum (Min–Max).

Ten millilitres physiological saline containing 2% heparin was injected into the parotid duct after cleaning the tissues surrounding the parotid gland. In order to show the duct system of parotid gland, 15 mL of the polyester resin solution was injected into parotid duct with a 120 mmHg pressure. Twenty-four hours passed for the solidification of the polyester solution. The parotid gland was put into a 37% HCL solution for 24 hours. Parotid gland tissues that were dissolved were washed under tap water and air-dried. With the use of a stereomicroscope, ducts of parotid gland were dissected with a forceps from the parotid gland [3, 4].

RESULTS

Present findings revealed that parotid gland of the sheep was located on the masseter muscle and settled outside the mandibula. Accessory parotid gland was not encountered in the present study. Parotid duct was separated from the gland at the level of angulus mandibulae. It was 2 cm above the inferior margin of mandibula and was extended parallel to this edge on the masseter muscle. After crossing the front edge of the masseter muscle, it run on the buccinator muscle. When it reached

the upper edge of buccinator muscle, it opened into the mouth through parotid papilla between the top 3rd premolar and the 1st molar maxillary teeth (Fig. 2).

In the present study, our metric results were shown in Table 1. The average weight of the parotid gland of Akkaraman sheep was identified as 25.3 g.

It was observed that polyester entered into the parotid duct and filled up until the acinus and made both acinus and secretion canals well-examined in this study.

Usually, parotid duct was initially formed by the combination of 2 interlobar duct, then the thickness or diameter of parotid duct increased with the number of canals participating in its formation. Parotid duct was formed by combining lobar ducts coming out of the lobes in the gland (Fig. 3). Every lobe of the parotid gland had a lobar duct, each lobar duct converged with each other to create the parotid duct.

It was also observed that the parotid gland consisted of lobes and lobules. The number of lobes of parotid glands varied from one gland to another. The average number of lobes was 12. The number of lobules in a lobe varied between 3 and 16, each lobe consisted of an average of 9 lobules. It was found
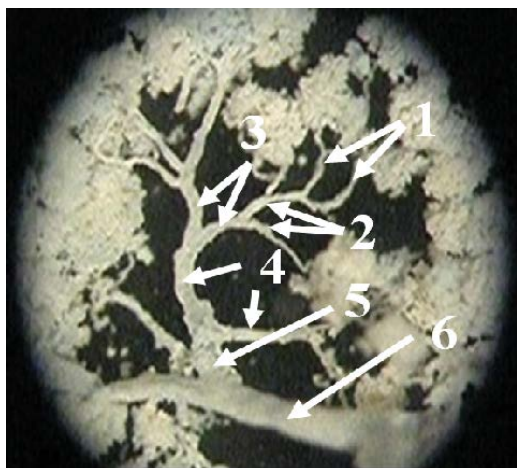
Figure 3. Ducts of a lobe and lobules in the parotid gland; 1 — intralobular duct; (striated duct); 2 — interlobular duct; 3 — lobular duct; 4 — intralobar duct; 5 — lobar duct; 6 — excretory duct (parotid duct).
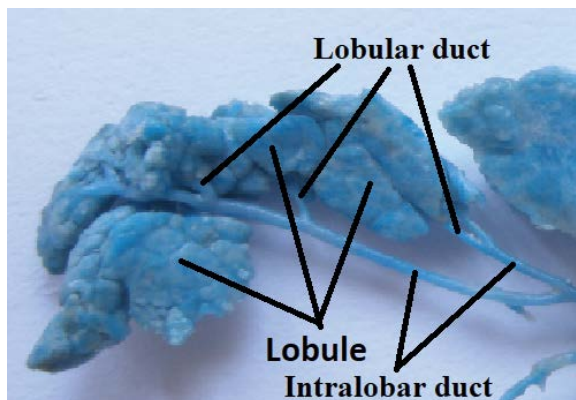

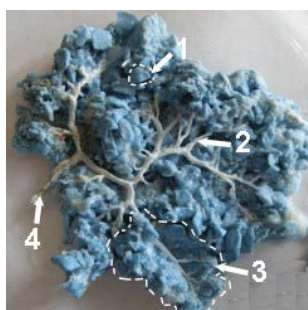**Figure 5.** Lobules of a lobe in parotid gland.

Figure 4. Structure of a parotid gland; 1 — lobule; 2 — interlobular duct; 3 — lobe; 4 — parotid duct.
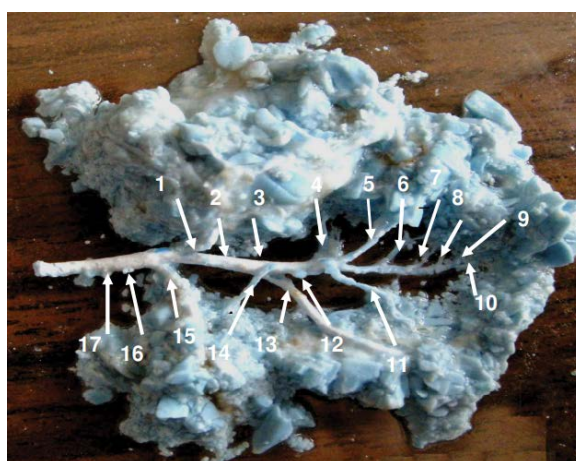

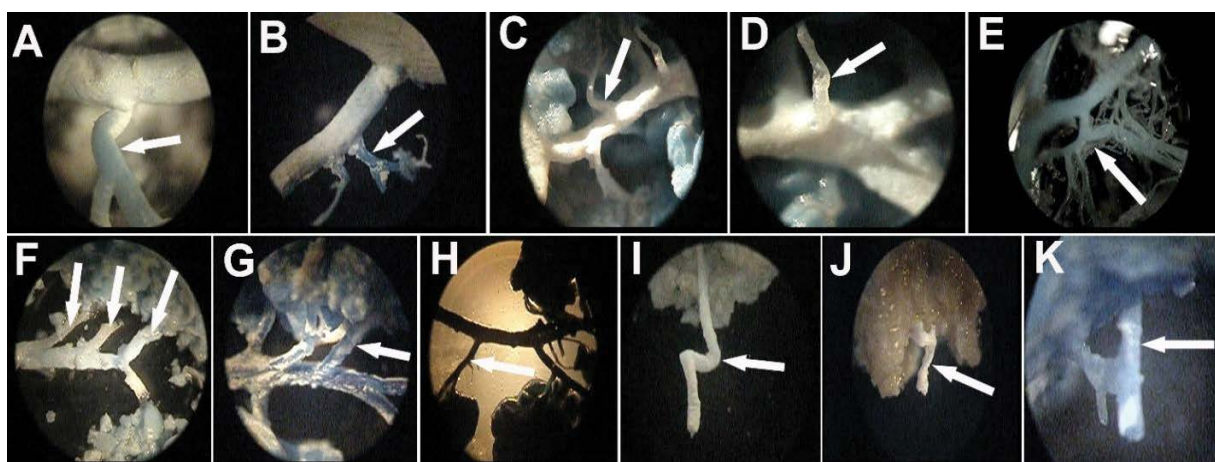**Figure 6.** Lobar duct (1–17), excretory duct (parotid duct) in parotid gland.

Figure 7. A–K. Connections (arrow) of ductus of parotid gland in sheep.

that each lobe had its own lobar duct (Figs. 3–6). Secretory pathways were clearly shown in parotid gland in our corrosion cast technique.

In this study, ductal connections of small-diameter ducts and large-diameter ducts were found in seven types (Fig. 7).

Accordingly:

— 23.08% of ducts formed slight curvatures at this connections (Fig. 7A, C, D);

— 7.69% of ducts connected other ducts at a right angle (Fig. 7B);

— 15.38% of ducts connected other duct at different angles (Fig. 7G, H);

— 7.69% of minor ducts connected initially with each other at the same direction, then connected with major ducts (Fig. 7E);

— 7.69% of minor and major ducts connections usually occurred after the combination of 2 ducts coming here at different angles (Fig. 7A);

— 7.69% of minor duct merged into the major ducts at the same angle, which paralleled to each other (Fig. 7F);

— 23.08% of the interlobar ducts exited the lobar duct without curvature, while the others came out with a curvature (Fig. 7I, J, K).

In our study, we did not statistically analyse the ductal connections of the parotid ducts. For this reason, we did not express it as a percentage.

DISCUSSION

We examined macroscopically parotid gland, parotid duct and microscopically ductal system of parotid gland in the current study.

The parotid gland is located on the lateral surface of the masseter muscle and surrounded back side of this muscle. It goes deep and is directly neighbouring ramus mandibulae. The upper part of the parotid gland is closed by the outer ear, and the paracondylar part by the caudal of the occipital bone. It extends deep until the pterygoid process of the sphenoid bone and the hyoid bone (Fig. 2).

Sometimes an accessory parotid gland is found anterolateral to the masseter muscle in humans [5], but accessory parotid gland was not encountered in the present study in sheep heads.

Some investigation indicated that parotid duct enters the oral cavity opposite to the upper second molar tooth in the sheep [9, 15, 22]. But our study shows parotid duct opens into the mouth through parotid papilla between the top 3rd premolar and the 1st molar maxillary teeth (Fig. 2).

Parotid gland has a parotid duct in animals, but double parotid duct was observed in a human patients, in the right aspect of the face of a 46-year-old man [1, 12, 13]. Double parotid duct was not found in our study.

In the literature, the mean length of the parotid gland of sheep was 6.04 ± 0.48 cm and 6.56 ± ± 0.361 cm in goat [18] and 3.96 ± 0.26 cm in dog [11]. In our study, the average length of the parotid gland in sheep was identified as 5.87 ± 1.04 cm (Table 1).

The length and diameter of the parotid duct in the camel were reported as 20 ± 0.41 cm and 0.5 ± ± 0.2 cm, respectively (*Camelus dromedarius*) [15]. The mean diameter of mandibular and parotid duct were 1.4 ± 0.3 mm and 3.1 ± 1.0 mm, respectively, in sheep [7]. Average length of parotid duct was 10.92 ± 1.027 cm in our study (Table 1).

The mass of the mandibular and parotid gland was reported to be 9.0 g and 11.0 g, respectively, in sheep [14, 22, 24]. In another study the mass of mandibular and parotid gland in sheep was reported to be 16.2 ± 4.6 g and 13.5 ± 2.6 g, respectively [7]. Human parotid glands' average weight was reported as 14–30 g [19, 25]. The average weight of the parotid gland of Akkaraman sheep was identified as 25.3 g in the current study (Table 1).

In our study, some parameters of the parotid gland, such as volume, thickness and width, which were not previously reported in the literature, were also measured. We found the average volume of the gland as 12.50 ± 2.48 cm^3, the average thickness as 0.75 ± 0.36 cm and the average width as 4.07 ± ± 0.43 cm (Table 1).

Parotid gland consists of lobes and lobules. The number of lobes of the parotid glands can vary from one gland to another. The number of lobes in the parotid gland is related to the number of ducts [17], and some studies have shown that the mandibular gland consists of 2 lobes [11]. Both parotid and mandibular salivary glands can be divided into 4 sections [15]. While sheep mandibular and parotid salivary glands have a multilobular appearance [7], the human parotid gland is divided into superficial and deep lobes [25]. The sheep parotid gland consists of 4 lobes: cranial, middle, caudal and accessory [20]. The present study showed that the parotid duct is divided into lobar ducts and each lobar duct represents one lobe, and in this context, the average number of lobes in the parotid gland is 12. Also, lobar duct is divided into lobular ducts, each lobe consists of an average of 9 lobules (Figs. 3–6). We believe that our research will be useful in studies on the ductal system of the parotid gland.

CONCLUSIONS

The structure of the salivary glands in mammals has been studied in depth by histological, histochemical, and sialographic method. Polyester injection and corrosion method shows the ductal anatomy of the salivary glands very well. However, there is no study about the corrosion method and parotid ductal system in mammals. Therefore, this study was conducted to define the histological and anatomical features of the adult sheep parotid acini and ductal system in this method. In this study, it was observed that the polyester entered the parotid duct and filled up to the acini and examined both the acinus and secretion channels well.

Conflict of interest: None declared

REFERENCES

1. Aktan ZA, Bilge O, Pinar YA, et al. Duplication of the parotid duct: a previously unreported anomaly. Surg Radiol Anat. 2001; 23(5): 353–354, doi: 10.1007/s00276-001-0353-y, indexed in Pubmed: 11824138.
2. Amano O, Mizobe K, Bando Y, et al. Anatomy and histology of rodent and human major salivary glands. Acta Histochem Cytochem. 2012; 45(5): 241–250, doi: 10.1267/ahc.12013.
3. Aycan K, Bilge A. Plastik enjeksiyon ve korozyon metodu ile vasküler sistem anatomisinin araştırılması. Erciyes Üniv Tıp Fak Dergisi. 1984; 6: 545–552.
4. Aycan K, Ulcay T, Kamaşak B. The morphology of the afferent and efferent domain of the sheep glomerulus. Folia Morphol. 2021; 80(4): 881–887, doi: 10.5603/FM.a2020.0124, indexed in Pubmed: 33084008.
5. Bahadir O, Bektas D, Caylan R, et al. Sialolithiasis of an accessory parotid gland. Ann Otol Rhinol Laryngol. 2004; 113(1): 52–54, doi: 10.1177/000348940411300112, indexed in Pubmed: 14763574.
6. Banks JW. Applied Veterinary Histology. 2nd ed. Williams and Wilkins, Baltimore 1986: 417–418.
7. Dehghani SN, Tadjalli M, Masoumzadeh MH. Sialography of sheep parotid and mandibular salivary glands. Res Vet Sci. 2000; 68(1): 3–7, doi: 10.1053/rvsc.1999.0318, indexed in Pubmed: 10684751.
8. Dellmann HD, Brown EM. Textbook of veterinary histology. 2nd ed. Lea Febiger, Philadelphia 1981.
9. Dursun N. Veteriner Anatomi. Medisan Yayınevi, Ankara 2006: 31–35.
10. Elewa YH, Bareedy MH, Abuel-Atta AA, et al. Structural characteristics of goat (Capra hircus) parotid salivary glands. Jpn J Vet Res. 2010; 58(2): 121–135, indexed in Pubmed: 20715422.
11. Estecondo S, Codón S, Casanave E. Histological study of the salivary glands in Zaedyus pichiy (Mammalia, Xenarthra, Dasypodidae). Int J Morphol. 2005; 23(1), doi: 10.4067/s0717-95022005000100004.
12. Fernandes A, Lima R, Rossi M, et al. Parotid Gland with Double Duct: An Anatomic Variation Description. Int J Morphol. 2009; 27(1), doi: 10.4067/s0717-95022009000100023.
13. Gartner PL. Essentials of Oral Histology and Embryology. 3nd ed. Jen House, publishing company, Baltimore 1999: 127–135.
14. Getty R. Sisson and Grossman's the anatomy of domestic animals. 5th ed. WB Saunders Co, Philadelphia 1975: 872–874.
15. Hamdy MR, Nora AS. Parotid and mandibular salivary glands segmentation of the one humped dromedary camel (Camelus dromedarius). Int J Adv Res Biol Sci. 2017; 4(11): 31–41, doi: 10.22192/ijarbs.
16. Kimura J, Habata I, Endo H, et al. Histochemistry of complex carbohydrate in the major salivary glands of hoary bamboo rats (Rhizomys purinosus). Anat Histol Embryol. 1998; 27(3): 147–153, doi: 10.1111/j.1439-0264.1998.tb00172.x, indexed in Pubmed: 9652141.
17. Mahdi S, Khojasteh B, Delashoub M. Microscopic anatomy of the parotid and submandibular salivary glands in European hamster (Cricetus cricetus L. Int Res J App Basic Sci. 2012; 3(7): 1544–1548.
18. Miyazaki T, Tatsukawa S, Kitamura H, et al. Morphological and functional changes of the rat parotid glandular cells by clipping and reopening the parotid duct, using HAM8 antibody. Anat Sci Int. 2008; 83(2): 89–95, doi: 10.1111/j.1447-073X.2007.00211.x, indexed in Pubmed: 18507618.
19. Paula F, Teshima TH, Hsieh R, et al. Overview of Human Salivary Glands: Highlights of Morphology and Developing Processes. Anat Rec (Hoboken). 2017; 300(7): 1180–1188, doi: 10.1002/ar.23569, indexed in Pubmed: 28192873.
20. Simawy MSH, Mahdi AA. Radiological comparative study of the mandibular salivary gland between adult male gazelle (subguttturosa) and sheep (awassi). Bas J Vet Res. 2019; 18(1): 122–133.
21. Singh AD, Jain RK, Pawan K. Topographic anatomy of buccal and labial glands in sheep. Haryana Vet. 2011; 50: 30–32.
22. Singh AD, Sasan S, ohn MA, et al. Gross and microscopic characterization of the parotid salivary gland of sheep. Indian Vet J. 2015; 92(1): 61–63.
23. Stevens A, Lowe SJ. Human Histology. 2nd ed. Mosby, Nottingham 1997: 188–189.
24. Tadjalli M, Dehghani SN, Basiri M. Sialography in dog: normal appearance. Veterinarski Arhiv. 2004; 74(3): 225–233.
25. Williams PL, Warwick R, Dyson M, Bannister LH. Gray's anatomy. 38th ed. Churchill Lvingtone, New York 1995: 1690–1691.

V M
VIA MEDICA

ORIGINAL ARTICLE

Primary synovial chondromatosis: an elemental investigation of a rare skeletal pathology

A.W. Beger[1], J.A. Millard[1], A. Bresnehan[1], B. Dudzik[1] , S. Kunigelis[2]

[1]Anatomy Department, DeBusk College of Osteopathic Medicine, Lincoln Memorial University, Harrogate, TN, United States of America
[2]Physiology Department, DeBusk College of Osteopathic Medicine, Lincoln Memorial University, Harrogate, TN, United States of America

Background: Primary synovial chondromatosis (PSC) is a rare idiopathic pathology characterised by the formation of osseocartilaginous nodules within synovial joints, tendons, or bursae. The mineralisation pattern of PSC nodules is poorly understood and has yet to be investigated using elemental analysis. Mapping this pattern could elucidate the progression of the disease.

Materials and methods: Primary synovial chondromatosis nodules discovered during dissection of a formalin fixed donor were analysed. Scanning electron microscopy paired with energy dispersive X-ray spectroscopy (SEM-EDS) was used to quantify calcium and phosphorus levels to distinguish mineralised components from cartilage, indicated by increased carbon and oxygen concentrations.

Results: Nine nodules with average dimensions 1.76 cm × 1.25 cm were identified in the semimembranosus bursa. SEM-EDS demonstrated increased calcium phosphate levels in nodular cores, while outer margins contained primarily carbon and oxygen. Quantification of these elements revealed nodular peripheries to contain 68.0% carbon, 30.2% oxygen, 0.8% calcium, and 1.0% phosphate, while cores were comprised of 38.1% carbon, 42.1% oxygen, 14.1% calcium, and 5.7% phosphate.

Conclusions: Nodules were found to have mineralised cores embedded within a cartilaginous matrix. This pattern suggests disease progression is facilitated by endochondral ossification, opening the potential for new therapeutic techniques. (Folia Morphol 2022; 81, 3: 685–693)

Key words: scanning electron microscopy, energy dispersive X-ray spectroscopy, nodules, loose bodies, semimembranosus bursa, popliteal cyst

INTRODUCTION

Primary synovial chondromatosis (PSC) is a rare, benign pathology characterised by the proliferation of osseocartilaginous nodules from the synovial lining of joints, bursae, or tendinous sheaths [29]. Disease onset is marked by chondroid metaplasia, where synoviocytes aberrantly modify their phenotype to secrete a cartilaginous matrix comprised of type II collagen, which can coalesce to form deposits of hyaline cartilage [1, 27]. These deposits can fuse, mineralize, and eventually ossify as intrasynovial loose bodies [28]. Secondary synovial chondromatosis has

been described, where intraarticular loose bodies instead appear as a result of degenerative arthropathy or trauma [10, 16]. PSC affects males up to 3 times more often than women [29] and is most often seen in the knee [25], although any synovial joint may be affected, including the hip [39], shoulder [38], and temporomandibular joint [4]. Patients often present with joint pain and swelling, limited range of motion, crepitus, or may be asymptomatic, depending on the stage, severity, and location of the condition [22, 33]. This ambiguous symptomatology makes the incidence rate difficult to estimate, but a rate of 1 per 100,000 has been reported [8]. In the presence of functional deficits, treatment will involve surgical extraction of loose bodies; synovectomy may also be recommended to prevent recurrence, although research has shown that it may have no influence on prognosis up to six years post-operation [36].

While researchers have done well to characterise various presentations of PSC, its label as an idiopathic condition persists. The limited understanding of disease progression is reflected in conflicting reports on the mineralisation patterning of osseocartilaginous nodules. Early investigators postulated that PSC nodules followed patterns of endochondral ossification, in which central mineralisation occurred within a cartilaginous matrix [26]. However, more recent reports describe ossification as first appearing peripherally, deviating from original claims [9]. Mapping the mineralisation pattern of PSC nodules through elemental analysis could clarify this discrepancy, while also providing evidence to assist with disease staging, medical imaging interpretation, and development of novel treatment options.

Scanning electron microscopy (SEM) coupled with energy-dispersive X-ray spectroscopy (EDS) conducts elemental analysis by first bombarding a sample with an electron beam. When a primary beam electron displaces a specimen inner shell electron, outer shell electrons move to replace it. Specific elements can be identified by their signature X-ray energy levels released as specimen electrons move to lower energy level orbitals. The utility of SEM-EDS is well-represented in various fields of biology, including forensic anthropology [30], dentistry [7], bioarcheology [6], and biomedical research [24]. Despite its widespread applications in biological research, to the knowledge of the authors, the utility of SEM-EDS has yet to be leveraged in the elemental investigation of intraarticular loose bodies, including those caused by PSC.

The aim of this research was to employ SEM-EDS to clarify the patterning of mineralisation in PSC nodules discovered during anatomical dissection. Dissection images and radiographs were included to support the clinician's understanding of this rare condition.

MATERIALS AND METHODS
Ethical approval
This research received ethical approval by the Institutional Review Board (Ref. #885V.1). Consent for the willfully donated tissue to be used for research purposes was provided by the donor premortem.

Cadaveric dissection
The right posterior knee of an 88-year-old formalin-fixed male donor was dissected by a group of first-year medical students. Investigation of the superomedial corner of the popliteal fossa revealed an enlarged semimembranosus bursa, situated between the semimembranosus tendon and medial head of gastrocnemius. Excision of the bursa revealed numerous hardened, semi-lobulated nodules bathed in synovial fluid (Fig. 1). Students followed similar protocols to dissect the left popliteal fossa, followed by bilateral intraarticular exploration of the tibiofemoral, patellofemoral, acetabulofemoral, and glenohumeral joints performed by an author (A.W.B.) to determine the extent of the pathology.

Medical imaging
Radiographs were taken to elucidate the patterning of mineralisation and *in situ* positioning of the nodules. Nodules were retained within the semimembranosus bursa as anterior-posterior and lateral radiographs were obtained (Del Medical Systems, model #RT100).

Sample preparation for SEM
Following medical imaging, nodules were extracted, counted, and measured using Neiko digital callipers. Eight nodules were randomly selected and processed for ultrastructure inspection via coring, freeze fracture, or bisection. Three were cored by manually driving a bone marrow biopsy "J" type needle (Argon Medical Devices, Frisco, TX) through its centre. Three were suspended in a polyurethane ice bucket containing liquid nitrogen for 60 s, and subsequently fragmented. Two were bisected by gently hammering a scalpel through their equator.

Figure 1. Posterior view of the right knee following dissection of the popliteal fossa. Skin and subcutaneous tissue have been removed. Nodules (N) were found within the semimembranosus bursa (incised), situated between the semimembranosus muscle (SM) and the medial head of gastrocnemius muscle (GM). Tendon of semitendinosus muscle (ST) is retracted laterally; GL — lateral head of gastrocnemius muscle; I — inferior; L — lateral; M — medial; S — superior.

Freeze fractured (n = 6), cored (n = 6), and bisected (n = 4) samples were fixed using phosphate buffer glutaraldehyde and osmium tetroxide, respectively. Following fixation, specimens were dehydrated using a graded series of ethanol (2 h each in 50%, 70%, 85%, 100% and replenished 100%) then further dried with hexamethyldisilazane (2 h each in 50%, 98%, and replenished 98%), with agitation throughout. Specimens were then mounted on 1 cm stubs and sputter coated using a gold-palladium target (Anatech USA Hummer 6.2 Sputtering System).

SEM-EDS

A Hitachi TM-3000 SEM was coupled with EDS (Bruker Quantax 70) to perform elemental analysis on the surface scans of samples. A targeted working distance of 8.3 mm was used to optimise X-ray detection. The concentrations of calcium, phosphorus, carbon, and oxygen in each sample were localised and quantified using the mapping, line scan, and spot mode EDS features. Mapping demonstrated patterning of elemental distribution across the entirety of the sample's surface, while line scan was used to depict fluctuations in the concentration of target elements along the length of a drawn vector. Spot mode quantified elemental composition within a target area, which was drawn with the smallest possible circumference so as to capture the narrowest window of X-ray counts required by the software to perform the analysis. Nodular cores and peripheries were targeted using this spot mode method to compare the elemental composition of these two regions. Results of line scan and mapping analyses were interpreted to describe the pattern and extent of mineralisation. Mineralised areas were indicated by increased concentrations of calcium and phosphorus, versus cartilaginous components as evidenced by the presence of primarily carbon and oxygen.

Statistical analysis

Nodule dimensions and results of elemental analysis were entered into Microsoft Excel (Microsoft Office 365, Version 16.44) for descriptive statistical analysis.

RESULTS

Cadaveric dissection

Nine total nodules were found within the right semimembranosus bursa (Fig. 1). Dissection of the left semimembranosus bursa revealed numerous cartilaginous deposits within the synovial membrane. No loose bodies were identified. Dissections of the patellofemoral, tibiofemoral, acetabulofemoral and glenohumeral joints were performed and were absent of cartilaginous deposits and loose bodies.

Medical imaging

Anterior-posterior and lateral plain radiographs of the right knee demonstrated the radiopaque nodules posterior to the knee joint (Fig. 2). Incidental findings included narrowing of tibiofemoral and patellofemoral joint spaces, osteophytic deposits on the distal femur and proximal tibia, and subchondral sclerosis denoted by increased radiopacity across the tibial plateau. Following extraction, nodules were found to have average dimensions of 1.76 cm × × 1.25 cm (Fig. 3), with bisected samples depicting a central core of mineralisation and cartilaginous shell (Fig. 4).

Figure 2. Lateral (**A**) and anteroposterior (**B**) radiographs of the right knee. Primary synovial chondromatosis nodules can be seen as collection of radiopacities posterior to the knee joint; A — anterior; I — inferior; L — lateral; M — medial; P — posterior; S — superior.

Figure 4. The inner face of a halved nodule depicts its internal morphology via light microscopy. Central swirl of mineralisation and outer cartilaginous shell can be seen. Intermediary lamellae of calcification support a gradient pattern of mineralization that is initiated centrally and proceeds towards the periphery.

Figure 3. Isolated nodules (n = 9) following extraction from the semimembranosus bursa, with average dimensions of 1.76 cm × 1.25 cm.

SEM-EDS

SEM-EDS was used to detect the presence of carbon (C), oxygen (O), calcium (Ca) and phosphorus (P) as an indicator of phosphate in all freeze fractured, cored, and bisected samples using mapping, line scan, and spot mode features. Mapping depicted a gradient pattern of calcium and phosphate levels, with greater deposition of these elements near the nodular centre, with only trace amounts of these elements detected in the outer shell. Carbon and oxygen levels were found throughout, with higher concentrations in the periphery (Fig. 5A–C). Line scan showed similar results, with concentrations of calcium and phosphate being higher near the nodular centre then gradually decreasing towards the periphery. Thin, lamellar depositions of calcium and phosphate radiating outwards were observed (Fig. 5D–F), supporting light microscopic observations under low magnification (Fig. 4).

Spot mode analysis was performed in the centre and periphery of all samples, and further indicated a pattern of increased mineralisation in nodular centres as evidenced by higher concentrations of calcium and phosphate (Fig. 5G–I). Collectively, outer margins were found to be composed of 68.0% C, 30.2% O, 0.7% Ca, and 1.0% P (Fig. 6A), with nodular cores containing 38.1% C, 42.1% O, 14.1% Ca, and 5.7% P (Fig. 6B).

DISCUSSION

Elemental analysis via SEM-EDS revealed PSC nodules to contain a mineralised core embedded in a shell of cartilage. This finding refutes recent claims that ossification is initiated peripherally [9], while supporting the original hypothesis put forth by Milgram [26] in 1971 that nodules contain outer margins of "lobular cartilage, with a central region of reactive
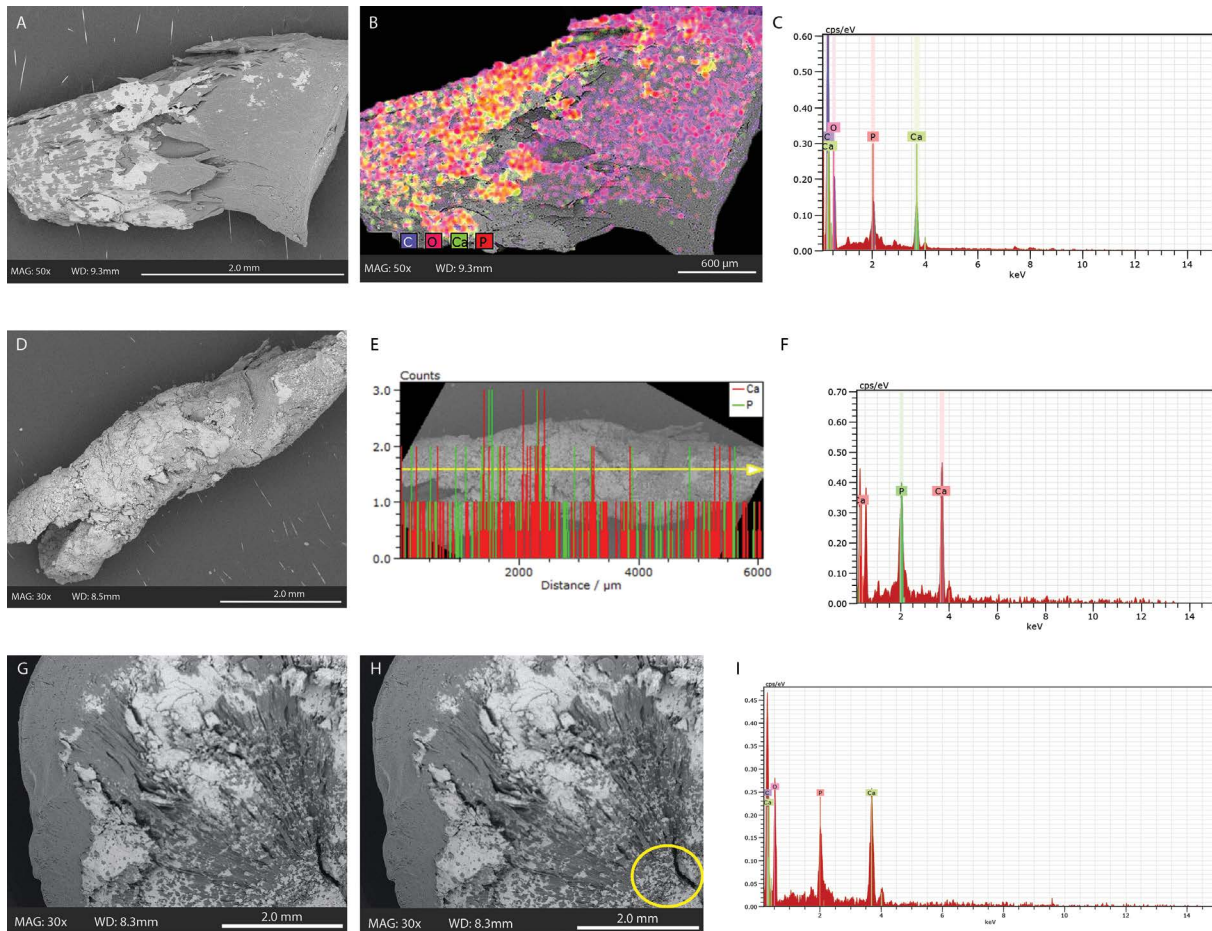
Figure 5. Scanning electron microscopy (SEM) paired with energy dispersive X-ray spectroscopy elemental analyses of primary synovial chondromatosis nodules; **A.** SEM image of freeze fractured sample, with centre of the nodule pointing the left; **B.** Sample from panel A analysed in mapping mode, indicating higher levels of calcium (Ca) and phosphorus (P) in the core; **C.** Spectrum plot from analysis in panel B, depicting elemental abundance in X-ray counts per second per electron volt (cps/eV), with elements identified via their kiloelectron volt (keV) signature; **D.** SEM image of cored sample, with centre of the nodule pointing to the bottom left; **E.** Sample from panel D analysed in line scan mode, indicating lamellar deposits of Ca and P; **F.** Spectrum plot from analysis in panel E, depicting elemental abundance in X-ray counts cps/eV, with elements identified via their keV signature; **G.** SEM image of halved nodule, with centre of the nodule located in the bottom right; **H.** The centre of bisected nodule (G) is analysed in spot mode; **I.** Spectrum plot from analysis in panel H, depicting elevated levels of Ca and P in X-ray counts cps/eV, with elements identified via their keV signature; C — carbon; O — oxygen; MAG — magnification; WD — working distance.

bone." Milgram [26] postulated that a remodelling process similar to endochondral ossification could be responsible for this pattern of central mineralisation. Endochondral ossification outlines the normal developmental processes involved the formation of the majority of the mammalian skeleton [20]. Briefly, this process begins with undifferentiated mesenchyme condensing to form precursors of skeletal structures. Mesenchymal stem cells in the centre of these precursors will differentiate into chondrocytes, which will form a model of the developing bone through secretion of a collagen matrix. Invasion of osteogenic cells promotes bone deposition in centrally located primary ossification centres. Meanwhile, chondro-

cytes continue to proliferate at the margins of the developing bone, facilitating growth, while bone deposition proceeds centrally. Modulating endochondral ossification processes are a host of transcription factors. Members of the fibroblast growth factor (FGF) family like FGF1 and FGF2 have been shown to provide essential signalling for cell survival within condensing mesenchyme [42], and regulation of osteocyte proliferation and differentiation in developing bone [43], while chondrocyte proliferation is promoted by FGF3 and FGF9 [13]. Interestingly, dysregulation of these transcription factors has been described in the synoviocytes and chondrocytes of PSC, implicating their role in the aberrant cellular differentiation that
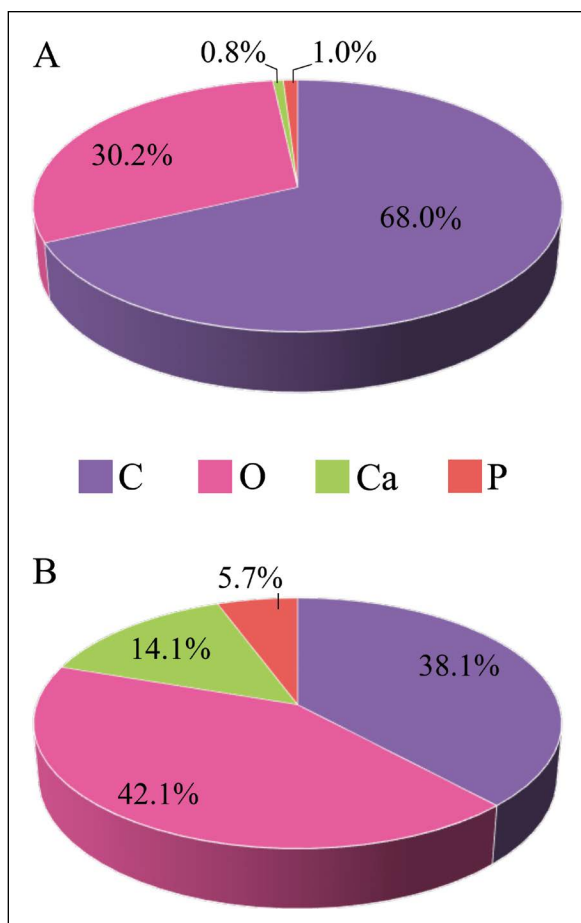
Figure 6. Pie charts depicting results of spot mode scanning electron microscopy paired with energy dispersive X-ray spectroscopy elemental analyses of cored, freeze fractured, and bisected specimens; **A.** Elemental composition of nodular periphery. High concentrations of organic elements (carbon and oxygen) suggest a predominantly cartilaginous composition; **B.** Elemental composition of the centre of nodules. Increased calcium and phosphate content suggest advanced mineralisation; C — carbon; O — oxygen; Ca — calcium; P — phosphorus.

is characteristic of the condition [31, 32]. Therapeutic interventions designed to target these molecular regulators could provide novel treatment options for PSC, not unlike those designed for ankylosing enthesitis, a chronic articular pathology that has been found to also manifest via endochondral ossification [21].

The progression of PSC has been outlined into three stages by Milgram [25]: stage I is marked by cartilaginous proliferations deposited within inflamed synovial tissue with no loose bodies present; stage II is distinguished by synovitis with well-formed nodules that may or may not have separated from the synovium to form loose bodies; stage III is characterised by the presence of intraarticular loose bodies with no active synovitis [25]. Applying Milgram's staging to

the results from the cadaveric dissection in this study, a diagnosis of bilateral, extraarticular PSC could be postulated: cartilaginous deposits found in the synovial membrane of the left semimembranosus bursa suggest a possible stage I disease state, with the loose bodies in the right indicating stage III. Bilateral, extraarticular presentations of PSC have been reported [2] but are exceedingly rare. More research is required to investigate potential underreporting of bilateral cases when staging is asymmetrical, with the more conspicuous side possibly overshadowing the other.

Differential diagnosis for PSC includes secondary synovial chondromatosis, and loose bodies formed from a chondrosarcoma malignancy [41], a critical demarcation as each requires unique interventions. Diagnosis typically relies on a combination of patient history and a series of radiographic and histopathological studies [28]. The differing pathophysiology of these conditions is reflected in the distinct mineralisation patterns observed in their respective nodular products [26]. PSC nodules are described as being primarily composed of cartilage, with characteristic "ring-and-arc" mineralisation patterns seen in advanced stages of the disease [28]. In contrast, osteochondrosarcomas have been described to be more heterogeneous with ill-defined, lobulated margins and punctate calcifications [17]. Secondary synovial chondromatosis nodules, meanwhile, would depict a hyperdense, ossified core with a thin margin of articular cartilage, reflecting their origin from fragments of developed bone [26]. These characteristics highlight the importance of elucidating the mineralisation pattern of intraarticular loose bodies so as to further facilitate this differential diagnosis process and aid in their identification on medical imaging studies.

Incidental findings of the lateral and anteroposterior radiographs suggested an additional diagnosis of osteoarthritis, evidenced by decreased joint space, osteophyte formation, and subchondral sclerosis [14]. The association between osteoarthritis and PSC is still poorly understood, however, a histopathological link is possible since both are associated with cellular alterations of the synovium [34]. Better understood is the relationship between osteoarthritis and secondary synovial chondromatosis, as the latter can be categorised by loose bodies formed from dislodged osteoarthritic osteophytes [16]. As the presence of osteoarthritis alone is not enough to distinguish between primary and secondary synovial chondromatosis, investigation of loose bodies could

aid in the differential diagnosis. In addition to their unique mineralisation patterns, PSC typically gives rise to numerous loose bodies that are homogenous in size, as seen in the subject in this study, while the secondary form of the disease most often presents with fewer loose bodies that are of varying size [9].

The location of the PSC nodules within the semimembranosus bursa is particularly noteworthy as this is the location of the more common synovial pathology known as a popliteal cyst [11]. This condition is characterised by the pathological accumulation of synovial fluid within the semimembranosus bursa, one of the six bursae around the knee that function to minimise mechanical friction forces [19, 37]. Inflammation of the intraarticular synovium, such as through osteoarthritis or PSC, leads to an effusion-caused increase in synovial fluid production within the knee joint capsule [40]. Excess fluid is able to escape into the semimembranosus bursa; however, a one-way valve prevents the fluid's return into the joint cavity [3, 15]. Accumulation of fluid within the semimembranosus bursa manifests as pain and swelling in the back of the knee with stiffness and a limited range of motion [11], potentially mimicking PSC. Our report adds to the thin body of literature describing extraarticular cases of PSC within a popliteal cyst [12, 35] and highlights the need for additional research into the relationship between the two.

Although our findings provide novel insight into the composition of PSC nodules, extrapolation of the results should be tempered due to the limited sample size. Broadening the scope to include multiple cases of PSC would offer greater insight into the epidemiology and pathophysiology of the condition. This research was further limited by a narrow medical history of the studied subject, which was either not included in the donor documentation or withheld for the purposes of protecting anonymity. Additionally, the original *in situ* presentation of the pathology may have been disturbed through the dissection process, thus limiting the interpretation of radiographs. Finally, it is not known how, or if, the elemental composition of PSC nodules was altered following the systemic formalin-fixation of this donor. Prior research has demonstrated the preservation of calcium in embalmed human bone using plasma mass spectrometry [5], while animal studies have implicated formalin-fixation in the fluctuations of heavy metal concentrations [23] and mechanical properties of bone, perhaps due to instability of mineral

content [18, 44]. Future studies could use SEM-EDS to demonstrate the stability of elements of interest throughout the formalin-fixation process by comparing pre- and post-fixed tissues, thereby validating the use embalmed donors as a sample source for future SEM-EDS investigations.

CONCLUSIONS

Primary synovial chondromatosis is a rare pathology characterised by the proliferation of osseocartilaginous loose bodies from metaplastic synovium of joints, tendon sheaths, or bursae. Elemental analysis revealed PSC loose bodies to consist of a mineralised core embedded in a cartilaginous matrix, supporting a progression that mirrors endochondral ossification.

REFERENCES

1. Apte SS, Athanasou NA. An immunohistological study of cartilage and synovium in primary synovial chondromatosis. J Pathol. 1992; 166(3): 277–281, doi: 10.1002/path.1711660310, indexed in Pubmed: 1381426.
2. Bassir RA, Ismael F, Elbardouni A, et al. Bilateral synovial chondromatosis in the knee joint with both intra and extra-articular diseases. Pan Afr Med J. 2014; 19: 57, doi: 10.11604/pamj.2014.19.57.4054, indexed in Pubmed: 25667719.
3. Boijsen E. Gastrocnemius-semimembranosus bursa and its relation to the knee joint. Acta Oncol (Madr.). 1983; 22(1): 1–2.
4. Brabyn PJ, Capote A, Muñoz-Guerra MF, et al. Arthroscopic management of synovial chondromatosis of the temporomandibular joint. Case series and systematic review. J Maxillofac Oral Surg. 2018; 17(4): 401–409, doi: 10.1007/s12663-018-1102-7, indexed in Pubmed: 30344377.
5. Bush VJ, Moyer TP, Batts KP, et al. Essential and toxic element concentrations in fresh and formalin-fixed human autopsy tissues. Clin Chem. 1995; 41(2): 284–294, indexed in Pubmed: 7874782.
6. Cadena EA. In situ SEM/EDS compositional characterization of osteocytes and blood vessels in fossil and extant turtles on untreated bone surfaces; different preserva-

tional pathways microns away. PeerJ. 2020; 8: e9833, doi: 10.7717/peerj.9833, indexed in Pubmed: 32913685.

7. Coceska E, Gjorgievska E, Coleman NJ, et al. Enamel alteration following tooth bleaching and remineralization. J Microsc. 2016; 262(3): 232–244, doi: 10.1111/jmi.12357, indexed in Pubmed: 27197087.

8. Felbel J, Gresser U, Lohmöller G, et al. Familial synovial chondromatosis combined with dwarfism. Hum Genet. 1992; 88(3): 351–354, doi: 10.1007/BF00197274, indexed in Pubmed: 1733839.

9. Habusta S, Tuck J. Synovial chondromatosis. StatPearls. 2021.

10. Hamada J, Tamai K, Koguchi Y, et al. Case report: A rare condition of secondary synovial osteochondromatosis of the shoulder joint in a young female patient. J Shoulder Elbow Surg. 2005; 14(6): 653–656, doi: 10.1016/j.jse.2004.12.004, indexed in Pubmed: 16337537.

11. Herman AM, Marzo JM. Popliteal cysts: a current review. Orthopedics. 2014; 37(8): e678–e684, doi: 10.3928/01477447-20140728-52, indexed in Pubmed: 25102502.

12. Ho SWl, Hoa LMh, Lee KT. A rare case of concomitant intra-articular and extra-articular synovial chondromatosis of the knee joint. Ann Acad Med Singap. 2019; 48(5): 161–164, indexed in Pubmed: 31210254.

13. Hung IH, Yu K, Lavine KJ, et al. FGF9 regulates early hypertrophic chondrocyte differentiation and skeletal vascularization in the developing stylopod. Dev Biol. 2007; 307(2): 300–313, doi: 10.1016/j.ydbio.2007.04.048, indexed in Pubmed: 17544391.

14. Hunter DJ, Guermazi A. Imaging techniques in osteoarthritis. PMR. 2012; 4(5 Suppl): S68–S74, doi: 10.1016/j.pmrj.2012.02.004, indexed in Pubmed: 22632705.

15. Jayson MI, Dixon AS. Valvular mechanisms in juxta-articular cysts. Ann Rheum Dis. 1970; 29(4): 415–420, doi: 10.1136/ard.29.4.415, indexed in Pubmed: 4916772.

16. Ji JH, Shafi M, Jeong DS. Secondary synovial chondromatosis of the shoulder. Knee Surg Sports Traumatol Arthrosc. 2015; 23(9): 2624–2627, doi: 10.1007/s00167-014-3024-3, indexed in Pubmed: 24803015.

17. Kang Y, Yuan W, Ding X, et al. Chondrosarcoma of the para-acetabulum: correlation of imaging features with histopathological grade. Radiol Med. 2016; 121(12): 897–904, doi: 10.1007/s11547-016-0673-y, indexed in Pubmed: 27553036.

18. Kikugawa H, Asaka T. Effect of long-term formalin preservation on the bending properties and fracture toughness of bovine compact bone. J Japan Institute Metals. 2005; 69(2): 267–271, doi: 10.2320/jinstmet.69.267.

19. LaPrade RF, Morgan PM, Wentorf FA, et al. The anatomy of the posterior aspect of the knee. An anatomic study. J Bone Joint Surg Am. 2007; 89(4): 758–764, doi: 10.2106/JBJS.F.00120, indexed in Pubmed: 17403797.

20. Long F, Ornitz DM. Development of the endochondral skeleton. Cold Spring Harb Perspect Biol. 2013; 5(1): a008334, doi: 10.1101/cshperspect.a008334, indexed in Pubmed: 23284041.

21. Lories RJU, Derese I, Luyten FP. Modulation of bone morphogenetic protein signaling inhibits the onset and progression of ankylosing enthesitis. J Clin Invest. 2005; 115(6): 1571–1579, doi: 10.1172/JCI23738, indexed in Pubmed: 15902307.

22. MacKenzie H, Gulati V, Tross S. A rare case of a swollen knee due to disseminated synovial chondromatosis: a case report. J Med Case Rep. 2010; 4: 113, doi: 10.1186/1752-1947-4-113, indexed in Pubmed: 20416049.

23. McCormack MA, Jackson BP, Dutton J. Effects of formalin fixation on trace element concentrations in bottlenose dolphin (Tursiops truncatus) tissues. Environ Toxicol Chem. 2020; 39(6): 1149–1164, doi: 10.1002/etc.4709, indexed in Pubmed: 32164038.

24. Mikroulis D, Mavrilas D, Kapolos J, et al. Physicochemical and microscopical study of calcific deposits from natural and bioprosthetic heart valves. Comparison and implications for mineralization mechanism. J Mater Sci Mater Med. 2002; 13(9): 885–889, doi: 10.1023/a:1016556514203, indexed in Pubmed: 15348554.

25. Milgram JW. Synovial osteochondromatosis: a histopathological study of thirty cases. J Bone Joint Surg Am. 1977; 59(6): 792–801, indexed in Pubmed: 908703.

26. Milgram JW. The classification of loose bodies in human joints. Clin Orthop Relat Res. 1977(124): 282–291, indexed in Pubmed: 598088.

27. Mohr W. Is synovial osteo-chondromatosis a proliferative disease? Pathol Res Pract. 2002; 198(9): 585–588, doi: 10.1078/0344-0338-00306, indexed in Pubmed: 12440780.

28. Murphey MD, Vidal JA, Fanburg-Smith JC, et al. Imaging of synovial chondromatosis with radiologic-pathologic correlation. Radiographics. 2007; 27(5): 1465–1488, doi: 10.1148/rg.275075116, indexed in Pubmed: 17848703.

29. Neumann J, Garrigues G, Brigman B, et al. Synovial chondromatosis. JBJS Reviews. 2016; 4(5), doi: 10.2106/jbjs.rvw.o.00054.

30. Palazzo E, Amadasi A, Boracchi M, et al. The detection of metallic residues in skin stab wounds by means of SEM-EDS: A pilot study. Sci Justice. 2018; 58(3): 232–236, doi: 10.1016/j.scijus.2017.12.007, indexed in Pubmed: 29685305.

31. Robinson D, Hasharoni A, Evron Z, et al. Synovial chondromatosis: the possible role of FGF 9 and FGF receptor 3 in its pathology. Int J Exp Pathol. 2000; 81(3): 183–189, doi: 10.1046/j.1365-2613.2000.00154.x, indexed in Pubmed: 10971739.

32. Sato J, Segami N, Suzuki T, et al. The expression of fibroblast growth factor-2 and fibroblast growth factor receptor-1 in chondrocytes in synovial chondromatosis of the temporomandibular joint. report of two cases. Int J Oral Maxillofac Surg. 2002; 31(5): 532–536, doi: 10.1054/ijom.2002.0248, indexed in Pubmed: 12418570.

33. Scholl DM, Taddie KL. Asymptomatic synovial chondromatosis of the ankle: an incidental finding. J Foot Ankle Surg. 2010; 49(6): 565.e13–565.e17, doi: 10.1053/j.jfas.2010.08.002, indexed in Pubmed: 20851002.

34. Sellam J, Berenbaum F. The role of synovitis in pathophysiology and clinical symptoms of osteoarthritis. Nat Rev Rheumatol. 2010; 6(11): 625–635, doi: 10.1038/nrrheum.2010.159, indexed in Pubmed: 20924410.

35. Shah DP, Diwakar M, Dargar N. Bakers cyst with synovial chondromatosis of knee: a rare case report. J Orthop Case Reports. 2016; 6(1): 17–179.

36. Shpitzer T, Ganel A, Engelberg S. Surgery for synovial chondromatosis. 26 cases followed up for 6 years. Acta Orthop Scand. 1990; 61(6): 567–569, doi: 10.3109/17453679008993585, indexed in Pubmed: 2281768.

37. Stein D, Cantlon M, Mackay B, et al. Cysts about the knee: evaluation and management. J Am Acad Orthop Surg. 2013; 21(8): 469–479, doi: 10.5435/JAAOS-21-08-469, indexed in Pubmed: 23908253.

38. Utashima D, Matsumura N, Suzuki T, et al. Clinical results of surgical resection and histopathological evaluation of synovial chondromatosis in the shoulder: a retrospective study and literature review. Clin Orthop Surg. 2020; 12(1): 68–75, doi: 10.4055/cios.2020.12.1.68, indexed in Pubmed: 32117541.

39. van der Valk MR, Veltman ES, Assink J, et al. Synovial chondromatosis of the hip, a case report and literature review. J Orthop. 2019; 16(3): 249–253, doi: 10.1016/j.jor.2019.02.010, indexed in Pubmed: 30923422.

40. Wang X, Blizzard L, Halliday A, et al. Association between MRI-detected knee joint regional effusion-synovitis and structural changes in older adults: a cohort study. Ann Rheum Dis. 2016; 75(3): 519–525, doi: 10.1136/annrheumdis-2014-206676, indexed in Pubmed: 25550336.

41. Wittkop B, Davies AM, Mangham DC. Primary synovial chondromatosis and synovial chondrosarcoma: a pictorial review. Eur Radiol. 2002; 12(8): 2112–2119, doi: 10.1007/s00330-002-1318-1, indexed in Pubmed: 12136332.

42. Yu K, Ornitz DM. FGF signaling regulates mesenchymal differentiation and skeletal patterning along the limb bud proximodistal axis. Development. 2008; 135(3): 483–491, doi: 10.1242/dev.013268, indexed in Pubmed: 18094024.

43. Yu K, Xu J, Liu Z, et al. Conditional inactivation of FGF receptor 2 reveals an essential role for FGF signaling in the regulation of osteoblast function and bone growth. Development. 2003; 130(13): 3063–3074, doi: 10.1242/dev.00491, indexed in Pubmed: 12756187.

44. Zhang G, Wang S, Xu S, et al. The effect of formalin preservation time and temperature on the material properties of bovine femoral cortical bone tissue. Ann Biomed Eng. 2019; 47(4): 937–952, doi: 10.1007/s10439-019-02197-1, indexed in Pubmed: 30671755.

VM VIA MEDICA

ORIGINAL ARTICLE

A computed tomography comprehensive evaluation of the ostium of the sphenoid sinus and its clinical significance

J. Jaworek-Troć[1, 2], J.A. Walocha[1], J. Skrzat[1], J. Iwanaga[3], R.S. Tubbs[3], M. Mazur[1], M. Lipski[1], A. Curlej-Wądrzyk[4], T. Gładysz[5], R. Chrzan[2], A. Urbanik[2], M.P. Zarzecki[1]

[1]Department of Anatomy, Jagiellonian University Medical College, Krakow, Poland
[2]Department of Radiology, Jagiellonian University Medical College, Krakow, Poland
[3]Department of Neurosurgery, Tulane University School of Medicine, New Orleans, United States
[4]Department of Integrated Dentistry, Institute of Dentistry, Jagiellonian University Medical College, Krakow, Poland
[5]Department of Oral Surgery, Institute of Dentistry, Jagiellonian University Medical College, Krakow, Poland

Background: The purpose of this research was to evaluate the size of the sphenoid sinuses' ostia, the distance between them and the distance between the medial margin of the ostia and the median line in the Polish adult population.

Materials and methods: The analysis was undertaken as a retrospective study of 296 computed tomography (CT) scans of patients (147 females, 149 males) with no comorbidities in their sphenoid sinuses. The paranasal sinuses were investigated by using Spiral CT Scanner (Siemens Somatom Sensation 16), in the option Siemens CARE Dose 4D, without administering any contrast medium. Having obtained transverse planes, multiplans reconstruction tool was used in order to glean sagittal and frontal planes.

Results: The average size of both sphenoid sinus ostia was 0.31 cm for both genders (for females ranging from 0.1 to 0.5 cm and from 0.1 to 0.6 cm for males). The mean distance between both sphenoid sinus ostia was 0.6 cm for both genders (the range for females was 0.1–1.4 cm, whereas 0.1–1.8 cm for males). The average distance between the medial margin of the ostium and the median line was 0.32 cm for both genders (0.31 cm for females in the range of 0–0.9 cm and 0.32 cm for males in the range of 0–1 cm).

Conclusions: Intraoperative identification of the sphenoid sinus ostia might prove difficult and their inadequate excision could lead to potential iatrogenic complications, hence detailed anatomical descriptions are still warranted in specific populations in order to perform safe and effective procedures. (Folia Morphol 2022; 81, 3: 694–700)

Key words: sphenoid sinus, sphenoid sinus ostium, anatomy

INTRODUCTION

The paranasal sinuses are pneumatic spaces that form a part of the upper respiratory tract and comprise of namely the sphenoid sinuses (typically two) that are of immense importance for trans-sphenoidal endoscopic or microscopic surgical approaches. Their

development is initiated by the intussusception of the nasal mucosa towards the sphenoid [7, 24], extending the sphenoethmoidal recess posteriorly towards the skull base [17] thus in exchange allowing for a communication between them. Migration of the connective tissue into the viscerocranium is the secondary stage of sphenoid sinus aeration [17].

Notwithstanding, the sphenoid sinuses are to date assessed from every possible angle due to their vastly complicated and varied anatomy. Some of the most recognizable variants include their dimensions, extensive pneumatisation and hence presence of recesses, as well as relation to the neighboring neurovascular entities, namely the internal carotid canal [10–16, 22].

When surgically approaching the sphenoid sinus, its ostium is typically found medially and inferiorly to the rim of the superior turbinate [1]. Having identified the ostium, the anterior wall of the sphenoid sinus is typically excised around the both ostia, allowing for a facilitated access into the sinus [3]. In order to perform a safe trans-sphenoidal endoscopic or microscopic procedure, it is also imperative for the surgeon to be spatially orientated about the maximum diameter of the sinus, location of the carotid canal, the optic canal and other major surrounding neurovascular entities [1, 11, 13].

This study aimed primarily to present the up--to-date morphometric assessment of the ostia of the sphenoid sinuses of Polish adult patients by the means of computed tomography (CT) imaging. The subgroup analysis was conducted in order to evaluate the possibility of existence of statistically significant differences between the particular dimensions of the ostia between males and females. To the best knowledge of the authors this is the first study that measures the distance between the medial margin of the sphenoid sinus ostia and the median line varying with laterality of the sinuses, as well as provides a comparison of the distances between the lateral margin of the sphenoid sinus ostia and the anterolateral wall of the sinuses for the right and left sides, respectively.

MATERIALS AND METHODS

A total of 359 medical images of patients referred to the Department of Medical Imaging of the University Hospital in Krakow to undergo a CT scan were accessed by the researchers. The inclusion criteria for participation in this analysis were: age of the patients over eighteen years and no pathologies pres-

ent in the sphenoid sinuses. Excluded patients (63) had suffered from a head trauma or had undergone nasal, orbital or cranial basis surgery prior to the research. The inclusion criteria were met by 296 patients (147 females, 149 males).

Spiral CT scanner Siemens Somatom Sensation 16 was used in the standard procedure in the option Siemens CARE Dose 4D. None of the patients had a contrast medium administered. Having obtained the images in the transverse planes, secondary reconstruction tool was applied — multiplans reconstruction — in order to glean images in the frontal and sagittal planes. Diagnostic station Siemens Volume Wizard was used in order to analyse the obtained data.

The analysis of the obtained images involved the location and size of the sphenoid sinus ostia — in reference to the median line (the size was measured from the medial margin of the ostia to the median line). Furthermore, the distance between the right sphenoid sinus ostium and the left sphenoid sinus ostium (between the medial margins of the ostia) as well as the distance between the lateral margin of the sphenoid sinus ostia and the anterolateral wall of the sinuses were also studied.

Ethical approval

All procedures performed in studies involving human participants were in accordance with the ethical standards of the institutional and/or national research committee and with the 1964 Helsinki declaration and its later amendments or comparable ethical standards. For this type of study formal consent is not required.

Statistical analysis

Statistical analysis in this study was conducted with the help of STATISTICA version 13.3 by TIBCO Software Inc®. Chi^2 test, Mann-Whitney test, Wilcoxon test and Fisher's exact test were utilised whilst probing for differences between the presence of the particular recesses and gender. A statistically significant value of $p < 0.05$ was chosen for all the results.

RESULTS

The average size of both sphenoid sinus ostia was 0.31 cm for both genders (0.29 cm for females and 0.33 cm for males). Statistically significant differences were found between the mean values for the sizes of sphenoid sinus ostia in females and males ($p < 0.001$, Mann-Whitney's test; Table 1, Fig. 1).

Table 1. The sizes of the sphenoid sinus ostia (SSO) in centimetre

The size of the SSO [cm]	Females	Males	Total
Mean ± standard deviation	0.29 ± 0.09	0.33 ± 0.09	0.31 ± 0.09
Median (Q$_1$–Q$_3$)	0.3 (0.2–0.35)	0.3 (0.25–0.4)	0.3 (0.2–0.4)
Minimum–maximum	0.1–0.5	0.1–0.6	0.1–0.6

Table 2. The distance between the sphenoid sinus ostia (SSO) in centimetre

The distance between the SSO [cm]	Females	Males	Total
Mean ± standard deviation	0.62 ± 0.24	0.65 ± 0.31	0.63 ± 0.28
Median (Q$_1$–Q$_3$)	0.6 (0.4–0.8)	0.6 (0.5–0.8)	0.6 (0.4–0.8)
Minimum–maximum	0.1–1.4	0.1–1.8	0.1–1.8

Figure 1. A computed tomography scan of female paranasal sinuses, transverse plane. The measurement method of the size of the sphenoid sinus ostium (on the right side).

Figure 2. A computed tomography scan of male paranasal sinuses, transverse plane. The measurement method of the distance between two sphenoid sinus ostia.

The average distance between the both sphenoid sinus ostia was 0.63 cm for both genders (0.62 cm for females, 0.65 cm for males). The mean value for the distance between the sphenoid sinus ostia did not differ significantly between the female and male groups (p = 0.480, Mann-Whitney's test; Table 2, Fig. 2).

The average distance between the medial margin of the ostia and the median line was 0.32 cm for both genders (0.31 cm for females and 0.32 cm for males). No statistically significant differences were found between the mean values of the distances between the medial margin of the sphenoid sinus ostium and the median line of males and females (p = 0.498, Mann-Whitney test). The average aforementioned distance for the right sphenoid sinus was 0.30 cm (0.29 cm for females and 0.31 cm for males), whereas 0.33 cm for the left sphenoid sinus (0.33 cm for females and 0.34 cm for males). Statistically significant results were found between the laterality of the results for both genders (p = 0.003, Wilcoxon test) and for females (p = 0.006, Wilcoxon test). However there were no statistically significant results amongst the distance between the medial margin of the ostium and the median line for right and left male sinuses (p = 0.125, Wilcoxon test; Table 3, Fig. 3).
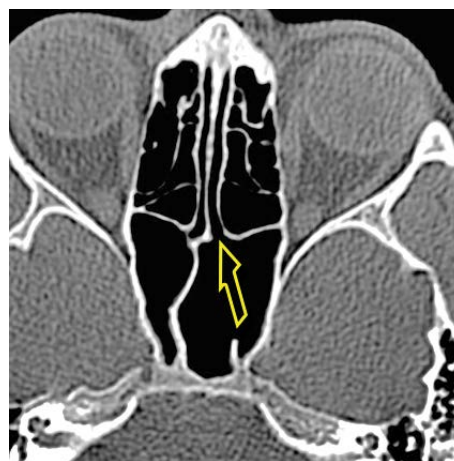
Equal distance between the medial margin of the sphenoid sinus ostia and the median line for both of the sinuses was found in 80 patients (41 females, 39 males), whereas different distances between the right and left sides were found in the majority of the patients — 216 (106 females, 110 males). Moreover, the ostium comprised the direct extension of the sphenoethmoidal recess in the straight line (the distance from the medial margin of the ostium to the median line was zero) in 18 patients (6 females,

Table 3. The distance between the medial margin of the sphenoid sinus ostia (SSO) and the median line in centimetre

The distance between the medial margin of the SSO and the median line [cm]	Females	Males	Total
Mean ± standard deviation	0.31 ± 0.12	0.32 ± 0.15	0.32 ± 0.14
Median (Q_1–Q_3)	0.3 (0.2–0.4)	0.3 (0.25–0.4)	0.3 (0.2–0.4)
Minimum–maximum	0–0.9	0–1	0–1

Table 4. The distance between the lateral margin of the sphenoid sinus ostia and the anterolateral wall of the sinuses in centimetre

The distance between the lateral margin of the sphenoid sinus ostium and the sinuses' anterolateral wall [cm]	Females	Males	Total
Mean ± standard deviation	0.90 ± 0.20	0.98 ± 0.24	0.93 ± 0.23
Median (Q_1–Q_3)	0.85 (0.75–1.00)	0.95 (0.8–1.1)	0.9 (0.8–1.05)
Minimum–maximum	0.35–1.55	0.35–1.7	0.35–1.7

Figure 3. A computed tomography scan of male paranasal sinuses, transverse plane. The measurement method of the distance between the medial margin of the sphenoid sinus ostium and the median line.

Figure 4. A computed tomography scan of female paranasal sinuses, transverse plane. The left sphenoid sinus ostium comprises the direct extension of the sphenoethmoidal recess in the straight line, as pointed by the arrow (the distance between the medial margin of the ostium and the median line is equal zero).

12 males): more frequently on the right side (12 patients: 4 females and 8 males) than on the left side (6 patients: 2 females and 4 males).

The frequency of the different/equal distances between the medial margin of the right and left sphenoid sinus ostia and the median line did not differ significantly between males and females (p = 0.740, χ^2 test). In both female and male groups, the different distances comprised approximately 73% of the cases.

Statistically significant differences were found between the distribution of the frequency of the distance between the medial margin of the sphenoid sinus ostia on the right or left sides and the median line equal zero (p = 0.046, Fisher's exact test; Fig. 4).

The average distance between the lateral margin of the sphenoid sinus ostia and the anterolateral wall of the sinuses was 0.9 cm for females, and 0.98 cm for males. The mean value for the distance between the lateral margin of the sphenoid sinus ostia and the anterolateral wall of the sinuses differed significantly between females and males (p = 0.001, Mann-Whitney's test; Table 4, Fig. 5).

Equal aforementioned distances for both of the sinuses were found in 64 patients (41 females, 23 males), but they were predominantly different between the right and left sides — in 232 patients (106 females, 126 males).

The frequency of the different or equal distances between the lateral margin of the right and left sphenoid sinus ostia and the anterolateral wall of the sinuses varied significantly between the female and male groups (p = 0.009, χ^2 test). The different

Figure 5. A computed tomography scan of male paranasal sinuses, transverse plane. The measurement method of the distance between the lateral margin of the ostium and the anterolateral wall of the sphenoid sinus.

distances were noted more often in males (126/232 cases, 54.3%), whereas the equal distances were more common in females (41/64 cases, 64.1%).

DISCUSSION

The average sizes of the sphenoid sinus ostia were equal in both genders. Moreover, they did not differ between the both sides of the main septum. They measured 0.35 cm on average in the range of 0.1–0.6 cm.

Elwany et al. [7] provided the following sizes of the sphenoid sinus ostia: the mean of 0.52 cm, the smallest 0.2 cm and the biggest 0.7 cm, but in another work they evaluated the mean size of the sinuses ostia as 0.28 cm [6]. This discrepancy may possibly be put down to the fact that in the second work the researchers stated the results only for the ostia defined by them as round in shape (that comprised 72% of all the ostia researched by them), but they did not measure the ostia that were defined as oval in shape.

The average distance between the ostia of both of the sinuses was 0.6 cm for both genders (for females in the range of 0.1–1.4 cm and 0.1–1.8 cm for males). Similar results were obtained by Mutlu et al. [18], who evaluated the mean distance between the right and left sphenoid sinus ostia as 0.8 cm (in the range of 0.13–1.5 cm).

The average distance between the medial margin of the ostium and the median line was 0.46 cm for both genders (0.45 cm for females ranging from 0 to 0.9 cm and 0.5 cm males in the range of 0–1 cm).

Similar results were obtained by Elwany et al. [6] (endoscopic study of 93 cadavers), who provided the following results for the distances between the medial margin of the ostium and the median line: the average 0.52 cm, the smallest 0.14 cm and the biggest 0.88 cm. On the contrary, different results were given by Sareen et al. [19] who noted the said distances as 0.2 cm on average (in the range of 0.1–0.4 cm). Nonetheless, the aforementioned scientists only stated the distance from the ostium (not mentioning the method of measurement of the point of the ostium — the medial margin, the lateral, or the central part of the ostium).

The same distance between the medial margin of the sphenoid sinus ostia and the medial margin for both of the sinuses was found in 27.03% of the patients (27.89% females, 26.17% males), whereas they were different in the majority of the patients — 72.97% (72.11% females, 73.83% males). Furthermore, the ostium comprised the direct extension of the sphenoethmoidal recess in the straight line (the distance from the medial margin of the ostium to the median line was equal zero) in 6.08% of the patients (4.08% females, 8.05% males): more often on the right side (4.05% patients: 2.72% females, 5.37% males) than on the left side (2.03% of the patients: 1.36% females, 2.68% males). To the best knowledge of the authors, there were no studies found in the available literature regarding the measurement of the distance between the medial margin of the sphenoid sinus ostia and the median line as varying with laterality of the sinuses.

The average distance between the lateral margin of the sphenoid sinus ostia and the anterolateral wall of the sinuses was 0.90 cm for females, and 0.98 cm for males. In the total research group, the mean distance was 0.93 cm (ranging from 0.35 to 1.7 cm). Similar results were obtained by Mutlu et al. [18], who evaluated the average distance between the lateral margin of the sphenoid sinus ostia and the anterolateral wall of the sinuses as 0.8 cm (in the range of 0.2–1.3 cm).

The same said distances for both of the sinuses were found in 21.62% of the patients (27.89% females, 15.44% males), whereas the distances differed between the right and left sides in the majority of the patients — in 78.38% (72.1% females, 84.56% males). To the best knowledge of the authors, there were no studies found in the available literature regarding the comparison of the distances between

the lateral margin of the sphenoid sinus ostia and the anterolateral wall of the sinuses for the right and left sides, respectively.

Identification of the sphenoid sinus ostium is one of the first steps undertaken during the trans-sphenoidal endoscopic or microscopic approach that can be achieved in two ways: by utilising anatomical landmarks close to the sinus (i.e. the sphenoethmoidal recess, upper turbinate, choanae and the sphenopalatine foramen) or by utilising landmarks located further from the sinus (namely the anterior nasal spine, the nasal floor and the nasal septum) [5]. The location of the ostium is usually close to the midline; however, it can be placed laterally to it by a few millimetres, and left and right ostia could possibly be placed on various horizontal levels [3], as shown by our analysis statistically significant for the overall and female results for the distance between the medial margin of the sphenoid sinus ostium and the median line. Henceforth, a surgeon has to be vigilant at all times and get acquainted with the possible anatomical variants, so as to avoid potential iatrogenic complications of the skull base. Excessive inferolateral excision upon the entrance to the sphenoid sinus could possibly result in damaging the sphenopalatine artery and its posterior septal branches (that lie inferiorly to the sphenoid sinus ostium) and hence iatrogenic bleeding hard to stop [8]. It is also worth noting that precise knowledge of parasympathetic innervation pathway of the sphenoid and ethmoid sinus is still poorly understood by both students and medical professionals [4].

Extensive pneumatisation of the sphenoid sinus, namely in the form of the septal recess and/or the vomeral recess, might obstruct the access towards the sphenoid sinus by constricting the sphenoethmoidal recess [2]. The aforementioned recesses were found in 8.78% and 25.34% of the patients of Polish origin, respectively [12]. Twigg et al. [23] report that they were not able to identify the ostia preoperatively on CT scans in 25% of their cases and they put it down to the fact that its dimensions might have been too small for the volume of the slices obtained by the CT. If a surgeon encounters difficulties in finding the sphenoid sinus ostium intraoperatively, they usually opt for accessing it approximately 15 mm superiorly to the choanae, or else at the crossing of the inferior 1/3 with the superior 2/3 of the superior turbinate [23].

The distance between the skull base and the ostium of the sphenoid sinus is of immense importance whilst widening the access to the sinus, especial-

ly with the cuts made superiorly. We would like to acknowledge Twigg et al. [23] in saying that the shorter the distance (the shortest distance measured by the said scientists was 2.7 mm), the higher the chance of iatrogenic injury and breaching the skull base that might lead to cerebrospinal fluid leakage and/or damage to the adjoining neurovascular and cerebral entities.

Henceforth, a detailed preoperative evaluation of the ostium of the sphenoid sinus is continuously warranted. Some of the most contemporary non-invasive methods of assessment of the sinuses might be utilizing three-dimensional CT imaging [9] or virtual dissection tables [21]. A surgeon might have a difficulty whilst attempting to find the ostium of the sphenoid sinus during a procedure and opt to use the C-arm fluoroscopy, but applying the aforementioned modern techniques might help diminish its intraoperative use [9]. CT scanning has superseded the use of lateral cephalometric radiographic evaluations, but the latter is still used in orthodontics [20].

Limitations of the study

This study has its limitations, as the only potentially confounding factor that could have influenced the results that was evaluated in this research was gender. Unfortunately, due to the scarce number of patients of a younger age (i.e. in the second, third and fourth decade of life), compared to the older participants, prevented us from reliably evaluating the potential effect of age upon the dimensions of the sphenoid sinus' ostia. Bearing in mind that the pneumatisation of the sphenoid sinuses is most commonly terminated in the third decade of life [25] it is plausible that the yet continued aeration process in patients in their 20s could lead to greater measurements if the CT scan was taken in the same person a few years later. Undoubtedly this aspect requires further research in a study that would recruit an objective proportion of patients across all ages.

CONCLUSIONS

The current study has found that the average size of both of the sphenoid sinus ostia was 0.31 cm, the average distance between them was 0.6 cm, and the average distance between the medial margin of the ostium and the median line was 0.32 cm for both genders. Intraoperative identification of the sphenoid sinus ostia might prove difficult due to the vast anatomical variety surrounding this anatomical entity

and their inadequate excision might lead to potential iatrogenic complications, hence detailed anatomical descriptions are still warranted for specific populations in order to perform safe and effective procedures.

Acknowledgements

Conflict of interest: None declared

REFERENCES

1. Ahmadipour Y, Lemonas E, Maslehaty H, et al. Critical analysis of anatomical landmarks within the sphenoid sinus for transsphenoidal surgery. Eur Arch Otorhinolaryngol. 2016; 273(11): 3929–3936, doi: 10.1007/s00405-016-4052-z, indexed in Pubmed: 27101471.

2. Beale TJ, Madani G, Morley SJ. Imaging of the paranasal sinuses and nasal cavity: normal anatomy and clinically relevant anatomical variants. Semin Ultrasound CT MR. 2009; 30(1): 2–16, doi: 10.1053/j.sult.2008.10.011, indexed in Pubmed: 19388234.

3. Campero A, Emmerich J, Socolovsky M, et al. Microsurgical anatomy of the sphenoid ostia. J Clin Neurosci. 2010; 17(10): 1298–1300, doi: 10.1016/j.jocn.2010.02.019, indexed in Pubmed: 20619658.

4. Carvey M, Baek W, Hage R. Bridging the divide: The widening gap between basic science and clinical research. Transl Res Anat. 2021; 24: 100117, doi: 10.1016/j.tria.2021.100117.

5. Ecevit MC, Zeybek G, Kiray A, et al. Sphenovomerine suture: a useful landmark for locating sphenoid sinus ostium. J Craniofac Surg. 2015; 26(1): 264–267, doi: 10.1097/SCS.0000000000001219, indexed in Pubmed: 25490575.

6. Elwany S, Elsaeid I, Thabet H. Endoscopic anatomy of the sphenoid sinus. J Laryngol Otol. 1999; 113(2): 122–126, doi: 10.1017/s0022215100143361, indexed in Pubmed: 10396560.

7. Elwany S, Yacout YM, Talaat M, et al. Surgical anatomy of the sphenoid sinus. J Laryngol Otol. 1983; 97(3): 227–241, doi: 10.1017/s0022215100094056, indexed in Pubmed: 6833847.

8. García-Garrigós E, Arenas-Jiménez JJ, Monjas-Cánovas I, et al. Transsphenoidal approach in endoscopic endonasal surgery for skull base lesions: what radiologists and surgeons need to know. Radiographics. 2015; 35(4): 1170–1185, doi: 10.1148/rg.2015140105, indexed in Pubmed: 26046941.

9. Göçmez C, Göya C, Hamidi C, et al. Evaluation of the surgical anatomy of sphenoid ostium with 3D computed tomography. Surg Radiol Anat. 2014; 36(8): 783–788, doi: 10.1007/s00276-013-1245-7, indexed in Pubmed: 24357354.

10. Jaworek-Troć J, Iwanaga J, Chrzan R, et al. Anatomical variations of the main septum of the sphenoidal sinus and its importance during transsphenoidal approaches to the sella turcica. Transl Res Anat. 2020; 21: 100079, doi: 10.1016/j.tria.2020.100079.

11. Jaworek-Troć J, Walocha JA, Chrzan R, et al. Protrusion of the carotid canal into the sphenoid sinuses: evaluation before endonasal endoscopic sinus surgery. Folia Morphol.

2021; 80(3): 642–649, doi: 10.5603/FM.a2020.0086, indexed in Pubmed: 32789847.

12. Jaworek-Troć J, Walocha JA, Loukas M, et al. Extensive pneumatisation of the sphenoid bone: anatomical investigation of the recesses of the sphenoid sinuses and their clinical importance. Folia Morphol. 2021; 80(4): 935–946, doi: 10.5603/FM.a2020.0120, indexed in Pubmed: 33084012.

13. Jaworek-Troć J, Zarzecki M, Bonczar A, et al. Sphenoid bone and its sinus - anatomo-clinical review of the literature including application to FESS. Folia Med Cracov. 2019; 59(2): 45–59, doi: 10.24425/fmc.2019.128453, indexed in Pubmed: 31659348.

14. Jaworek-Troć J, Zarzecki M, Mróz I, et al. The total number of septa and antra in the sphenoid sinuses - evaluation before the FESS. Folia Med Cracov. 2018; 58(3): 67–81, doi: 10.24425/fmc.2018.125073, indexed in Pubmed: 30521512.

15. Jaworek-Troć J, Zarzecki M, Zamojska I, et al. The height and type of the main septum in the sphenoid sinuses — evaluation before the fess. Folia Med Cracov. 2020; 60(3): 65–74, doi: 10.24425/fmc.2020.135796.

16. Jaworek-Troć J, Zarzecki M, Zamojska I, et al. The dimensions of the sphenoid sinuses: evaluation before the functional endoscopic sinus surgery. Folia Morphol. 2021; 80(2): 275–282, doi: 10.5603/FM.a2020.0059, indexed in Pubmed: 32488857.

17. Krzeski A, Osuch-Wójcikiewicz E, Szwedowicz P, et al. Chirurgia endoskopowa w leczeniu guzów jam nosa i zatok przynosowych. Mag ORL. 2004; 3(3): 79–84.

18. Mutlu C, Unlu HH, Goktan C, et al. Radiologic anatomy of the sphenoid sinus for intranasal surgery. Rhinology. 2001; 39(3): 128–132, indexed in Pubmed: 11721501.

19. Sareen D, Agarwal AK, Kaul JM, et al. Study of sphenoid sinus anatomy in relation to endoscopic surgery. Int J Morphol. 2005; 23(3): doi: 10.4067/s0717-95022005000300012.

20. Sinha S, Shetty A, Nayak K. The morphology of sella turcica in individuals with different skeletal malocclusions: a cephalometric study. Transl Res Anat. 2020; 18: 100054, doi: 10.1016/j.tria.2019.100054.

21. Stecco A, Boccafoschi F, Falaschi Z, et al. Virtual dissection table in diagnosis and classification of Le Fort fractures: A retrospective study of feasibility. Transl Res Anat. 2020; 18: 100060, doi: 10.1016/j.tria.2019.100060.

22. Tesfaye S, Hamba N, Gerbi A, et al. Radio-anatomic variability in sphenoid sinus pneumatization with its relationship to adjacent anatomical structures and their impact upon reduction of complications following endonasal transsphenoidal surgeries. Transl Res Anat. 2021; 24: 100126, doi: 10.1016/j.tria.2021.100126.

23. Twigg V, Carr SD, Balakumar R, et al. Radiological features for the approach in trans-sphenoidal pituitary surgery. Pituitary. 2017; 20(4): 395–402, doi: 10.1007/s11102-017-0787-9, indexed in Pubmed: 28154960.

24. Vidić B. The postnatal development of the sphenoidal sinus and its spread into the dorsum sellae and posterior clinoid processes. Am J Roentgenol Radium Ther Nucl Med. 1968; 104(1): 177–183, doi: 10.2214/ajr.104.1.177, indexed in Pubmed: 5672763.

25. Yonetsu K, Watanabe M, Nakamura T. Age-related expansion and reduction in aeration of the sphenoid sinus: volume assessment by helical CT scanning. Am J Neuroradiol. 2000; 21(1): 179–182, indexed in Pubmed: 10669247.

V M
VIA MEDICA

ORIGINAL ARTICLE

Elongation pattern of styloid process in Saudi population: a factor to remember in the prevention of Eagle syndrome

A. Alsweed[1], B.M. Almutairi[2]

[1]Saudi Board of Paediatric Dentistry, Saudi Commission for Health Specialties, Riyadh, Kingdom of Saudi Arabia
[2]Department of Oral and Maxillofacial Surgery and Diagnostic Sciences, College of Dentistry in Ar Rass, Qassim University, Saudi Arabia

Background: The aim of this study is to determine the prevalence of styloid process (SP) patterns in Saudi population.
Materials and methods: This retrospective, cross-sectional study included 2010 digital panoramic radiographs (PRs) selected randomly for adult patients who visited five major hospitals in the Qassim region, Saudi Arabia, PRs were examined to detect any SP elongation. Data were collected and analysed using SPSS v22.
Results: In this study, positive SP elongation was seen in 25.4% of the total cases, 14.2% and 11.2% male and female, respectively. The mean age was 34.3 ± ± 13.9 years. Type I was found in 19.1%, type II in 1.7%, and type III in 4.6% of the cases. Normal SP was seen in 74.7%. Patients between 30 and 50 years were significantly more affected with type I pattern. Normal SP was reported mostly in the youngest age group 18–24 years, in 31% of total cases.
Conclusions: Styloid process has many patterns and variations that could be detected on digital PRs taken daily in most of dental clinics. Dentists should be trained to detect patients with such variation so that signs associated with Eagle syndrome are not misinterpreted. (Folia Morphol 2022; 81, 3: 701–706)

Key words: elongated styloid process, eagle syndrome, panoramic radiograph

INTRODUCTION

X-ray considers the window that views all activities of the human body, either normal anatomy of the body or abnormal, physiological or pathological activities. One of the of X-ray divisions is orthopantomogram or panorama radiography which is a radiologic technique that provides an overview of the jaws and surrounding structures [23]. Panoramic radiographs (PRs) enable the dentist to see a wide area of the maxilla and mandible [24, 25]. It

is considered one of the best imaging modalities to view the styloid process (SP) bilaterally [26]. The SP is a cylindrical bone that emerges from the temporal bone in front of the stylomastoid foramen. It is usually around 25 mm in length, but it can vary from person to person, and even within the same person, from side to side [27]. Elongated SP has been examined in several populations by distinctive methods and techniques, either advanced or traditional. Wide variation prevalence of SP elongation was noted,

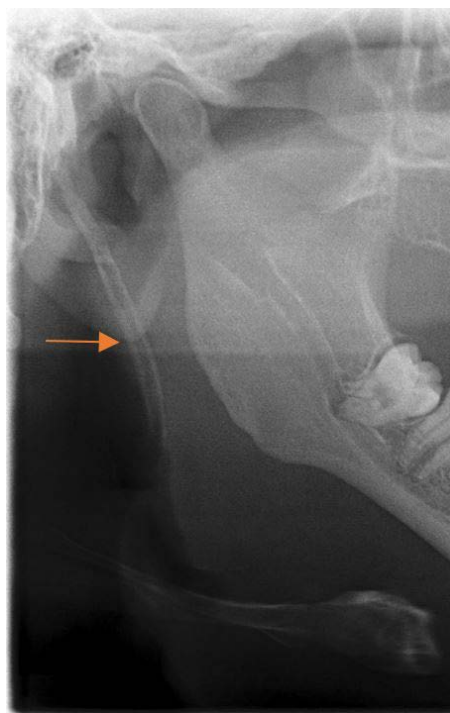**Figure 1.** Radiograph show type 0 elongated styloid process.

Figure 2. Radiograph show type 1 elongated styloid process.

extending from 4% to 30% [33]. Elongated SP comes usually with no symptoms. Eagle et al. [8] reported only 4% to 10.3% symptomatic cases characterising Eagle syndrome also known as styloid syndrome. Eagle syndrome symptoms may include throat pain or foreign body sensation, dysphagia, or facial pain. It may also cause neck or throat pain that radiate to the ipsilateral ear [9]. The cause is unknown, but several hypotheses have been proposed, including congenital elongation due to the persistence of an embryonic cartilaginous outgrowth, calcification of the stylohyoid ligament, and development of bone tissue at the ligament's insertion [10, 28]. SP can be assessed using an anatomical structure. An elongated SP and calcification of the stylohyoid ligament can be detected with proper clinical and radiographic examination [25]. This aim of this study is to determine the prevalence of SP patterns in Saudi population.

MATERIALS AND METHODS

This retrospective, cross-sectional study included 2010 digital PRs selected randomly for adult patients who visited five major hospitals in the Qassim region (Qassim University Dental Hospital, King Fahd Specialist Hospital, Buraydah Central Hospital, King Saud Hospital, and Alrass General Hospital) for den-

tal treatment between January 2017 and December 2017. From a diagnostic standpoint, the included digital radiographs had to be adequate, with optimum contrast and density and no distortion or obscuring structure. Poor-quality radiographs with insufficient exposure times or incorrect angulations were removed from this study. All digital radiographs for adult patients that met the study's criteria were examined extensively, and the patients' demographic details, such as gender and age, were registered. Patient information was kept private.

The radiographs were collected from the hospitals' digital archives and imported into the College of Dentistry at Qassim University, Radiology Department's computer system, where they were then displayed. Advanced digital radiograph imaging software (DIGORA® for Windows 2.7; SOREDEX) was used to examine them.

A single professional oral and maxillofacial radiologist reviewed and interpreted all of the radiographs. In a darkened room, all of the radiographs were investigated on the same 21-inch LCD monitor resolution (1920 × 1200 at 60 Hz); the same environmental conditions prevailed during the examination of all of the radiographs (Figs. 1–4). Each original digital image was magnified using the software's magnification feature, then manipulated by the examiner

Figure 3. Radiograph show type 2 elongated styloid process.

Figure 4. Radiograph show type 3 elongated styloid process.

Table 1. Types of elongated styloid process according to combined Langlais and modified MacDonald-Jankowski classifications [19]

Type	Characteristics
Type 0 (normal)	Non elongated styloid process; the tip of the process does not cross the mid portion of mandible body
Type 1 (elongated)	Uninterrupted styloid process; the tip of the process crosses the mid portion of mandibular body
Type 2 (pseudo-segmented)	The styloid process is apparently joined to the mineralised stylomandibular or stylohyoid ligament by a single pseudoarticulation, which is usually located superior to a level tangential to the inferior border of the mandible
Type 3 (segmented)	Two or more segments are seen, with interruptions either above or below the level of the inferior border of the mandible

to improve the image's contrast and brightness to provide the clearest image in the examined areas.

Sample divided into 1209 and 801 male and female, respectively. They were aged between 20 and 75 years. Data were collected regarding age, gender and SP morphology based on Langlais' classification [19] which classifies the pattern of SP to three types (Table 1).

Statistical analysis

Data was analysed using the statistical package SPSS 22.0 (SPSS Inc., Chicago, IL) and level of significance was set at $p < 0.05$. Inferential statistics was done using χ^2 test. The analysis using χ^2 test for proportion was done for two variables (age and gender) against the proportion of participants in various patterns of SP elongation.

RESULTS

Evaluating the SP for 2010 PRs divided into 1209 and 801 male and female, respectively. Sample age ranged between 20 and 75 years with a mean of 34.3 ± 13.9 years. The prevalence of type I elongation pattern (uninterrupted integrity of SP) was 382 (19.1%) cases, of them, 207 and 176 were male and female, respectively (Fig. 2). The mean age of positive type I is 38 ± 13.9 years.

Type II (pseudoarticulation pattern) showed in only 34 (1.7%) cases, of them, 18 and 16 were male and female, respectively, with mean age 35 ± 13.9 years (Fig. 3). Type III was present by 92 (4.6%) cases divided into 60 and 32 male and female, respectively, with mean age 37 ± 13.9 years (Fig. 4). Normal SP (non-elongated SP; the tip of the process does not

Table 2. Descriptive analysis of variables

Variables	Category	Number and percentage	Styloid process pattern				Chi-square value	P value	Chi-square value	P value
			Type I	Type II	Type III	Type 0				
Gender	Male	60.1% (1209)	17.2% (207)	1.6% (18)	5% (60)	76.2% (924)	0.915	0.82	60.56	0.001*
	Female	39.8% (801)	22% (176)	2 % (16)	4% (32)	72% (578)			57.76	0.001*
Age group	18–25	35.4% (712)	10.3% (73)	0.6% (4)	1.3% (9)	88% (626)	18.80	0.026*	83.26	0.001*
	26–40	31.0% (624)	29.1% (181)	2.4% (15)	7.4% (46)	61% (382)			42.11	0.001*
	41–54	23.5% (473)	18.7% (88)	2% (10)	6.2% (29)	73% (346)			54.04	0.001*
	≥ 55	10.1 (204)	20% (41)	2.3% (5)	4% (8)	74% (150)			59.60	0.001*

*P < 0.05 is statistically significant

cross the mid portion of mandible body) was showed in 1502 (74.8%), of them, 924 male and 578 female (Fig. 1). Although statistical analysis reported that there was no statistical significance in gender categories against the proportion of various patterns of SP elongation (p = 0.82, X^2 = 0.915).

Statistical analysis between categories of age against the proportion of various patterns of SP elongation was found to be statistically significant (p = 0.026*, X^2 = 18.80).

The analysis within all age/gender category against the proportion of various patterns of SP elongation reported to be statistically significant (p = 0.001*).

Patients between 26 and 40 years were more affected with type I pattern (p = 0.001*). The least pattern prevalence was type II pattern, it was only seen in 3.6%. Type III was most commonly seen in 26–40 age group with total percentage 7.4%. Normal SP was reported mostly in the youngest age group 18–24 years with 626 cases (p = 0.001*) (Table 2).

DISCUSSION

Styloid process term is derived from the Greek word "Stylos" which mean a pillar. It's a cylindrical bone originated from the temporal bone frontal to the stylomastoid foramen [27]. The anatomy of styloid complex includes SP of the temporal bone, stylohyoid ligament and lesser horn of the hyoid bone. SP can be described as slender, pointed, bony projection from the inferior aspect petrous temporal bone. Usually, its length ranges from a few millimetres to an average of 2.5 cm. Its proximal part is unsheathed by the tympanic plate, while muscles and ligaments are attached to its distal part [22, 29]. SP had been classified by Langlais according to the type of elongation. Langlais classified the SP elongation to three types of complexes. Type I, elongated; type II, pseudoarticulated; and type III, segmented [19].

The diagnosis of elongation of SP were done depending on PRs by many studies including Asutay et al. [1] on East Eagean, Gracco et al. [11] on Italian, Hettiarachchi et al. [12] on Sri Lanken population, Vieira et al. [34] on Brazilian and Sakhdari et al. [30] on Iranian. Other studies had evaluated the SP elongation based on dry skulls, including Vadgaonkar et al. [33] on Indian, Sakaew et al. [32] on Thai, Custodio et al. [5] on Brazilian, Natsis et al. [20] on Greek. In Poland, Iwańczyk et al. [13] published a study of 2 cases were having glomerulonephritis and diagnosed with Eagle syndrome by panoramic radiograph.

Cone beam computed tomography can be used as an advanced diagnostic tool to assess the SP pattern, Buyuk et al. [4], Donmez et al. [7], and Öztunç et al, [21] used it on Turkish population, Kailasam et al [14], and Ramadoss and Sha [31] on Indian population, Khairallah [15], used it on Lebanese population, Andrei et al. [2] used it on Romanian population, Czajka et al. [6] used it in Polish cases.

The normal length of SP ranges between 20 to 30 mm, below 20 mm is considered as short SP [16], while many studies suggest that SP should be considered elongated when it is longer than 30 mm [3, 17, 18, 30, 32]. Although, there is limited number of studies considering the SP elongated when it exceeds 45 mm [35].

This study found the prevalence of elongated SP in 36.8% of total samples, all 36.8% have SPs lengthening more than 30 mm and crossing the mid portion of mandibular body. While 56.6% of the samples had normal length SPs ranging 20–30 mm and the tip of the process did not cross the mid portion of mandible body.

In the present study, men were slightly more affected with different pattern of SPs, although no significant difference were proven considering male to female sample number (p = 0.82, X^2 = 0.915).

Investigation showed 293 out of 879 cases with unilateral elongated SPs while bilateral was reported in 586 cases. This is consisted with other studies including Sakhdari et al. [30] and Vieira et al. [34].

Further studies using computed tomography or cone-beam computed tomography for a three-dimensional evaluation of the SP are required to investigate in specific the prevalence of different pattern SP in Qassim population, Saudi Arabia.

CONCLUSIONS

Styloid process has many patterns and variations that could be detected on digital PRs taken daily in most of dental clinics. Elongated SP may often be asymptomatic, they can only be diagnosed coincidentally by routine PRs. Dentists should be trained to detect patients with such variation so that signs associated with Eagle syndrome are not misinterpreted.

Conflict of interest: None declared

REFERENCES

1. Asutay F, Erdem N, Atalay Y, et al. Prevalence of elongated styloid process and eagle syndrome in east eagean population. Bezmialem Science. 2019; 7(1): 28–32, doi: 10.14235/bas.galenos.2018.991.
2. Andrei F, Motoc AG, Didilescu AC, et al. A 3D cone beam computed tomography study of the styloid process of the temporal bone. Folia Morphol. 2013; 72(1): 29–35, doi: 10.5603/fm.2013.0005, indexed in Pubmed: 23749708.
3. Bagga MB, Kumar CA, Yeluri G. Clinicoradiologic evaluation of styloid process calcification. Imaging Sci Dent. 2012; 42(3): 155–161, doi: 10.5624/isd.2012.42.3.155, indexed in Pubmed: 23071965.
4. Buyuk C, Gunduz K, Avsever H. Morphological assessment of the stylohyoid complex variations with cone beam computed tomography in a Turkish population. Folia Morphol. 2018; 77(1): 79–89, doi: 10.5603/FM.a2017.0061, indexed in Pubmed: 28653301.
5. Custodio AL, Silva MR, Abreu MH, et al. Styloid process of the temporal bone: morphometric analysis and clinical implications. Biomed Res Int. 2016; 2016: 8792725, doi: 10.1155/2016/8792725, indexed in Pubmed: 27703982.
6. Czajka M, Szuta M, Zapała J, et al. Assessment of surgical treatment of Eagle's syndrome. Otolaryngol Pol. 2019; 73(3): 1–5, doi: 10.5604/01.3001.0013.1533.
7. Donmez M, Okumus O, Pekiner FN. Cone beam computed tomographic evaluation of styloid process: A retrospective study of 1000 patients. Eur J Dent. 2017; 11(2): 210–215, doi: 10.4103/ejd.ejd_56_17, indexed in Pubmed: 28729795.
8. Eagle WW. Elongated styloid process: Report of two cases. Arch Otolaryngol Head Neck Surg. 1937; 25(5): 584–587, doi: 10.1001/archotol.1937.00650010656008.
9. Ferreira PC, Mendanha M, Frada T, et al. Eagle syndrome. J Craniofac Surg. 2014; 25(1): e84–e86, doi:

10.1097/SCS.0000000000000392, indexed in Pubmed: 24406612.
10. Gokce C, Sisman Y, Ertas ET, et al. Prevalence of styloid process elongation on panoramic radiography in the Turkey population from cappadocia region. Eur J Dent. 2008; 2(1): 18–22, indexed in Pubmed: 19212504.
11. Gracco A, De Stefani A, Bruno G, et al. Elongated styloid process evaluation on digital panoramic radiograph in a North Italian population. J Clin Exp Dent. 2017; 9(3): e400–e404, doi: 10.4317/jced.53450, indexed in Pubmed: 28298982.
12. Hettiarachchi PV, Jayasinghe RM, Fonseka MC, et al. Evaluation of the styloid process in a Sri Lankan population using digital panoramic radiographs. J Oral Biol Craniofac Res. 2019; 9(1): 73–76, doi: 10.1016/j.jobcr.2018.10.001, indexed in Pubmed: 30302305.
13. Iwańczyk B, Nowak J, Szerszeń M, et al. Elongation of the styloid process – Eagle syndrome – case reports of patients on dialysis. Dental Medical Problems. 2015; 52: 366–370.
14. Kailasam S, Massillamani F, Potluri V, et al. Morphometric evaluation of styloid process using cone beam computed tomography: a retrospective study of chennai population. J Adv Med Med Res. 2018; 25(8): 1–12, doi: 10.9734/jammr/2018/39071.
15. Khairallah A. CBCT findings of complete calcification of the stylohyoide ligament: case reports. J Dent Health Oral Disord Ther. 2015; 2(2), doi: 10.15406/jdhodt.2015.02.00040.
16. Koshy JM, Narayan M, Narayanan S, et al. Elongated styloid process: A study. J Pharm Bioallied Sci. 2015; 7(Suppl 1): S131–S133, doi: 10.4103/0975-7406.155861, indexed in Pubmed: 26015690.
17. Kaufman SM, Elzay RP, Irish EF. Styloid process variation. Radiologic and clinical study. Arch Otolaryngol. 1970; 91(5): 460–463, doi: 10.1001/archotol.1970.00770040654013, indexed in Pubmed: 5442737.
18. Keur JJ, Campbell JP, McCarthy JF, et al. The clinical significance of the elongated styloid process. Oral Surg Oral Med Oral Pathol. 1986; 61(4): 399–404, doi: 10.1016/0030-4220(86)90426-3, indexed in Pubmed: 3458151.
19. Langlais R, Miles D, Dis MV. Elongated and mineralized stylohyoid ligament complex: A proposed classification and report of a case of Eagle's syndrome. Oral Surgery, Oral Medicine, Oral Pathology. 1986; 61(5): 527–532, doi: 10.1016/0030-4220(86)90400-7.
20. Natsis K, Repousi E, Noussios G, et al. The styloid process in a Greek population: an anatomical study with clinical implications. Anat Sci Int. 2015; 90(2): 67–74, doi: 10.1007/s12565-014-0232-3, indexed in Pubmed: 24664363.
21. Oztunç H, Evlice B, Tatli U, et al. Cone-beam computed tomographic evaluation of styloid process: a retrospective study of 208 patients with orofacial pain. Head Face Med. 2014; 10: 5, doi: 10.1186/1746-160X-10-5, indexed in Pubmed: 24528515.
22. Patil S, Ghosh S, Vasudeva N. Morphometric study of the styloid process of temporal bone. J Clin Diagn Res. 2014; 8(9): AC04–AC06, doi: 10.7860/JCDR/2014/9419.4867, indexed in Pubmed: 25386413.
23. Rodríguez-Vázquez JF, Mérida-Velasco JR, Verdugo-López S, et al. Morphogenesis of the second pharyngeal arch cartilage (Reichert's cartilage) in human embryos.

J Anat. 2006; 208(2): 179–189, doi: 10.1111/j.1469-7580.2006.00524.x, indexed in Pubmed: 16441562.

24. Radak D, Tanaskovic S, Kecmanovic V, et al. Bilateral Eagle syndrome with associated internal carotid artery kinking and significant stenosis. Ann Vasc Surg. 2016; 34: 271.e15–271.e18, doi: 10.1016/j.avsg.2016.01.015, indexed in Pubmed: 27174357.

25. Shah N, Bansal N, Logani A. Recent advances in imaging technologies in dentistry. World J Radiol. 2014; 6(10): 794–807, doi: 10.4329/wjr.v6.i10.794, indexed in Pubmed: 25349663.

26. Sridevi K, Mahesh N, Krishnaveni B, et al. Evaluation of styloid process and its anatomical variations: a digital panoramic study with systematic review. J Int Soc Prev Community Dent. 2019; 9(3): 256–262, doi: 10.4103/jispcd.JISPCD_8_19, indexed in Pubmed: 31198698.

27. Sudhakara RR, Sai Kiran Ch, Sai Madhavi N. Journal of the Spanish Society of Oral Surgery. Prevalence of elongation and calcification patterns of elongated styloid process in south India. 2013; 5(1): 30–35.

28. Saccomanno S, Greco F, DE Corso E, et al. Eagle's Syndrome, from clinical presentation to diagnosis and surgical treatment: a case report. Acta Otorhinolaryngol Ital. 2018; 38(2): 166–169, doi: 10.14639/0392-100X-1479, indexed in Pubmed: 29967562.

29. Standring S. Gray's Anatomy: The Anatomical Basis of Clinical Practice. 40th ed. Churchill Livingstone, New York 2008.

30. Sakhdari S, Saberi S, Shamshiri AR. Prevalence and pattern of styloid process elongation and calcification on digital panoramic radiographs in an iranian population. J Islam Dent Assoc Iran. 2018; 30(2): 44–51, doi: 10.30699/jisdreir.30.2.44.

31. Ramadoss T, Sha K. Assessment of the styloid process by cone beam computed tomography. Int J Radiol Radiat Ther. 2017; 2(5): 123–127, doi: 10.15406/ijrrt.2017.02.00038.

32. Sakaew W, Arnanteerakul T, Somintara S, et al. Sexual dimorphism using the interstyloid distances and clinical implication for elongated styloid process in northeastern thailand. Int J Morphol. 2016; 34(4): 1223–1227, doi: 10.4067/s0717-95022016000400008.

33. Vadgaonkar R, Murlimanju BV, Prabhu LV, et al. Morphological study of styloid process of the temporal bone and its clinical implications. Anat Cell Biol. 2015; 48(3): 195–200, doi: 10.5115/acb.2015.48.3.195, indexed in Pubmed: 26417479.

34. Vieira EM, Guedes OA, Morais SD, et al. Prevalence of Elongated Styloid Process in a Central Brazilian Population. J Clin Diagn Res. 2015; 9(9): ZC90–ZC92, doi: 10.7860/JCDR/2015/14599.6567, indexed in Pubmed: 26501021.

35. Jung T, Tschernitschek H, Hippen H, et al. Elongated styloid process: when is it really elongated? Dentomaxillofac Radiol. 2004; 33(2): 119–124, doi: 10.1259/dmfr/13491574, indexed in Pubmed: 15314005.

ORIGINAL ARTICLE

VM VIA MEDICA

Analysis of gender differences on pyriform aperture of human skulls using geometric morphometric method

A. Sarač-Hadžihalilović[1], Z. Ajanović[1], I. Hasanbegović[1], S. Šljuka[2], M. Rakanović-Todić[3], I. Aganović[4], I. Prazina[5], S. Maleškić Kapo[3], R. Hadžiselimović[6]

[1]Department of Anatomy, Faculty of Medicine, University of Sarajevo, Bosnia and Herzegovina
[2]Department of Biology, Faculty of Science, University of Sarajevo, Bosnia and Herzegovina
[3]Department of Pharmacology, Faculty of Medicine, University of Sarajevo, Bosnia and Herzegovina
[4]Department of Immunology, Faculty of Medicine, University of Sarajevo, Bosnia and Herzegovina
[5]University of Sarajevo, Bosnia and Herzegovina
[6]Academician, Prof. Emeritus, Institute for Genetic Engineering and Biotechnology Sarajevo (INGEB), University of Sarajevo, Bosnia and Herzegovina

Background: Piriform aperture is anterior opening of the nasal cavity formed by bones of the viscerocranium and knowledge about differences between genders is important for forensic scientists, anthropologists, orthopaedists, neurosurgeons and vascular surgeons. The aim of this study was to examine gender differences of piriform aperture on three-dimensional (3D) models of human skulls originating from Bosnian population using the geometric morphometric method.

Materials and methods: The study was conducted on 211 3D models of human skulls of known gender. 3D models were obtained by laser scanning. We analysed the gender differences of piriform aperture using geometric morphometrics method. On 3D models we marked four landmarks on piriform aperture in the Landmark Editor programme, after which we analysed its gender differences in MorphoJ programme.

Results: The first principal component analysis axis described 40.398% of total variability of piriform aperture. The greatest gender variability was present in the position of the landmark rhinion. Discriminant functional analysis of the shape and size of the piriform aperture allowed the gender determination with 64.03% accuracy for male and 70.83% accuracy for female gender. The size of the piriform aperture showed a statistically significant difference between genders. Discriminant functional analysis of the shape of the piriform aperture without affecting size enabled gender determination with 59.71% accuracy for male and 62.5% accuracy for female.

Conclusions: Analysis showed statistically significant differences in the shape and size of piriform aperture between genders. The accuracy for gender determination based on piriform aperture was higher in females. (Folia Morphol 2022; 81, 3: 707–714)

Key words: sex determination, human skull, nasal region, geometric morphometry

Address for correspondence: Dr. Z. Ajanović, Department of Anatomy, Faculty of Medicine, University of Sarajevo, Sarajevo, Bosnia and Herzegovina, tel: +387 61 914 412, e-mail: zurifa.ajanovic@mf.unsa.ba

INTRODUCTION

Differences between male and female human skull are expressed in size and shape. One of the parts where sexual dimorphism is expressed is the piriform aperture which is anterior opening of the nasal cavity [27].

Classical methods and geometric morphometrics method are used to examine sexual dimorphism in the human skull [17].

Even geometric morphometric analysis of the shape and size of skeletal remains for gender determination is a relatively young; it is very interesting method for determination of the gender. The idea of digitising skeletal remains, producing three-dimensional (3D) models of them, dates back to 1980 where large number of authors around the world used this methodology [17].

Bigoni et al. [6] studied geometric morphometry in the study of the sexual dimorphism of human skulls and found the largest differences between skulls of different genders in the upper part of the face and in the form of the midsagittal line.

Franklin et al. [11] conducted several studies of sexual dimorphism on skulls from the South African region using geometric morphometry. Thus, in 2006, they conducted a study on Bantu Negroid South African populations using special software to analyse the morphological characteristics of skulls of different genders. The authors concluded that maximal lateral projection of zygomatic arches (bizigomatic width) is the best diameter for gender determination with 87% accuracy [11]. In 2007, they used geometric morphometrics method for morphological differences on 298 skulls of Bantu-speaking individuals and Khoisan and concluded that Khoizan group skulls had a pentagonal vault, a more round forehead, a small face and less prognathion than the skulls of individuals from the Bantu speaking area. On the other side, the skulls of individuals from different Bantu-speaking populations had similarities (they are brachycephalic and the mandible prognathion is less pronounced) [12]. In the same year, the sexual dimorphism of subadult mandibles was investigated by geometric morphometry. The results of this study showed that there was no gender difference in the size and shape of the subadult mandibles [14]. In 2008, using geometric morphometry, they investigated sexual dimorphism on mandibles of 225 skulls of known gender and age from five local populations of South Africa [13].

Table 1. Anthropometric points (landmarks) of piriform aperture

Anthropometric points	Position
Apertion	Most lateral point on the piriform aperture
Akanthion	Point on the anterior nasal spine
Rhinion	Point on the top of piriform aperture

Kimmerle et al. [20] used geometric morphometry in their study of sexual dimorphism of the skulls and concluded that skull appearance was impacted by gender, regardless of race, while skulls of different size but of the same gender are not different in morphological characteristics.

Gonzalez et al. [16] studied sexual dimorphism on 125 images of skulls recorded with an Olympus SP-350 digital camera, which monitored 12 anthropometric points and 25 semilandmarks located in the glabella, mastoid, frontal, and zygomatic regions. They concluded that male skulls are larger and more robust than female skulls.

Chovalopoulou et al. [8] conducted several studies of the sexual dimorphism of the human skull using geometric morphometry, and in 2013 they investigated sexual dimorphism in the palate and at the base of the skull, in 2016 they analysed the sexual dimorphism of the craniofacial form [7]. In the same year, the same group of authors analysed the sexual dimorphism of the cranial vault and the mediosagittal line of the skull using geometric morphometrics method [9].

MATERIALS AND METHODS

The study included 211 human macerated and degreased skulls from Bosnian population, known gender (139 male skulls and 72 female skulls) and known age belonging to the Osteological Collection, Medical Faculty of Sarajevo.

All skulls of the tested simple were scanned using an HP 3D Structured Light Scanner Pro S2 after calibrating the scanner according to the manuscript for authors to obtain 3D skull models to perform geometric morphometric analysis of cranial sexual dimorphism. On the obtained 3D models of the tested skulls in the special programme Landmark Editor, we marked the clearly defined anthropometric points named also landmarks on the piriform aperture of each tested skull. For each examined skull, we marked four landmarks on the piriform aperture, two non-paired and one paired, whose names and their position on the skull are given in Table 1.

From the above programme we exported data for each individual skull in the form of NTSYS format, which had information about position of landmarks in the coordinate system, which were used for analyse the shape of the piriform aperture in a programme specially created for that called MorphoJ.

Statistical analysis

The analysis of the shape of the piriform aperture was performed in the MorphoJ programme (Klingenberg 2011) in which we conducted a series of statistical analyses that give us the results of our study. The overall variability in the shape of the piriform aperture over the entire sample was examined by principal component analysis (PCA). Using Prokrust's analysis, the variation that may arise from differences in piriform aperture size, orientation, or positioning during digitisation was eliminated, leaving only information related to differences in shape. To determine the differences in the form of piriform aperture between the genders, Mahalanobis and Prokrust distances were calculated and compared by permutation tests with 1000 permutations. PCA analyses the differences in mean of form of piriform aperture between the genders.

The next step was data processing using univariate analysis (ANOVA) and multivariate analysis — MANOVA. A discriminant analysis was also performed to compare the differences between male and female skulls and a validation test in MorphoJ comparing the piriform aperture forms of the two groups. In this way, even minimal gender differences can be visualised and observed. The STATISTICA for Windows 8 and MorphoJ (Klingenberg, 2011) were used in this study. The results of the study are presented using figures and tables.

RESULTS

Gender differences in the size and shape of the piriform aperture of the skull is shown by the principal components PC1 and PC2 where the largest variability was showed by the first component PC1 with 40.398% of variability, while the second component PC2 showed 36.871% of variability (Table 2) and patterns of charge in the shape of the piriform aperture described by the PC1 component is shown on Figure 1. Figure 2 shows the differentiation of the piriform aperture between genders by the first and second PC axes.

When we determine a statistically significant gender difference in the shape and size of the piriform

Table 2. Eigenvalues and percentage variability of shape and size of piriform aperture

PC	Eigenvalues	Percentage of variability	Cumulative percentage of variability
1	0.00325091	40.398%	40.398%
2	0.00296712	36.871%	77.269%
3	0.00182927	22.731%	100.000%

PC — principal component

Figure 1. Patterns of change in the shape of the piriform aperture described by the PC1 component (the blue circles represent the mean values of the specific points and the lines the direction and intensity of their changes).
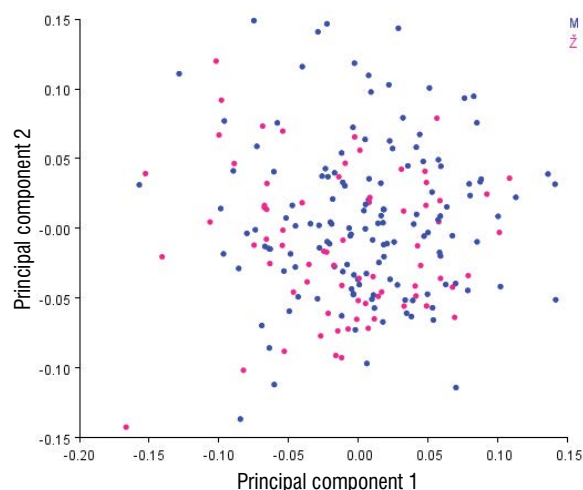

Figure 2. Position of the skulls of the test specimen based on differences in shape and size of the piriform aperture in the morphological space; M — men; Z — women.

aperture, we performed a test of correct classification, discriminant functional analysis. The calculated Procrust distance was 0.037 and the p value with permutation tests of 1000 repetitions was less than 0.0001, which shows a statistically significant gen-

709

der difference in the shape and size of the piriform aperture.

Of the 139 male skulls, 89 were classified correctly as male skulls by the classification test, while 50 were classified as female skulls, representing 64.03% accuracy (Table 3).

A test of correct classification of a total of 72 female skulls 51 were classified as female skulls, while 21 female skulls were classified as male skulls and predictability for female gender was 70.83% accuracy (Table 3).

The results of discriminant functional analysis of the influence of the shape and size of the piriform aperture on the sexual dimorphism of the skulls of the examined sample are shown in Figure 3.

After the test of correct classification, a regression analysis was performed in the MorphoJ programme, where we examined the influence of the size of piriform aperture on its shape. Mean values of the size of this region are presented as centroid size where the effect of size was 3.3712% which showed statistically significant effect (p < 0.0001, with 10,000 repetitions).

The influence of the size of the piriform aperture and the separation of the skulls in the morphological space conditioned by the size of the piriform aperture is shown on Figure 4.

After excluding the effect of size on the shape of the piriform aperture, we calculated the principal components again where the first two principal components describe 26.528% of the total variability in the shape of the piriform aperture (Table 4).

A gender difference analysis of the shape of piriform aperture was performed without affecting the size of this region, using a test of correct classification. The difference between the mean values expressed as Prokrust distance was 0.027. The p value with permutation test with 1000 repetitions was less than 0.004, showing a statistically significant sex difference in the shape of the piriform aperture without affecting its size on the shape (Fig. 5).

The test of correct classification was out of 139 male skulls, 83 correctly classified as male skulls, which was 59.71% accuracy (Table 5).

The test of correct classification of 72 female skulls classified 45 skulls as female skulls, which was 62.5% accuracy (Table 5).

The results of discriminant functional analysis of the influence of the shape of the piriform aperture on

Table 3. Gender predictability based on shape and size of piriform aperture

		Predictability of the gender		Total
		Shape and size	Shape and size	
Gender	Male	89	50	139
	Female	21	51	72
Total		110	101	211

The colours to indiate the difference between male and female sex, which is accurately determited.
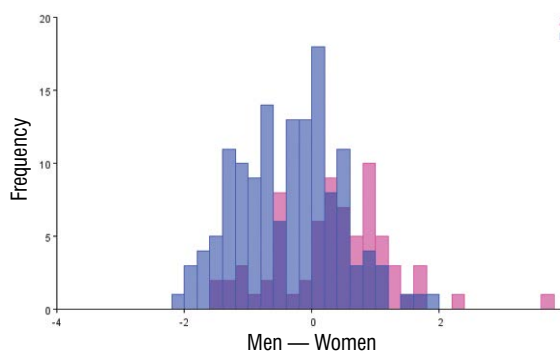

Figure 3. Discriminant functional analysis of gender differences of form of piriform aperture; M — men; Z — women.
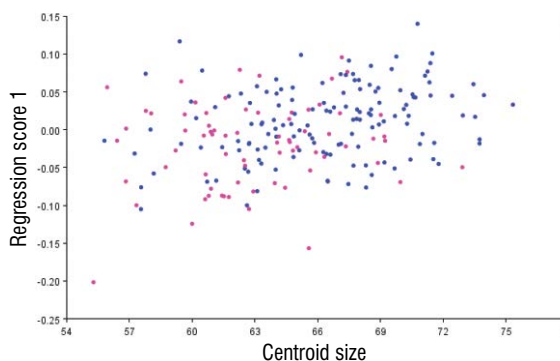

Figure 4. Influence of the size of piriform aperture on gender differences of the shape of piriform aperture; M — men; Z — women.

Table 4. Eigenvalues and percentage variability of the form of piriform aperture

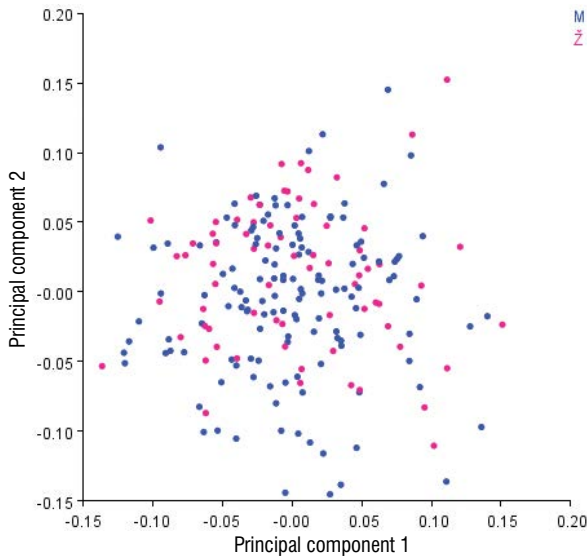| PC	Eigenvalues	Percentage of variability	Cumulative percentage of variability
1	0.00308146	39.628%	39.628%
2	0.00296485	38.128%	77.756%
3	0.00172970	22.244%	100.000%

PC — principal component

Figure 5. Position of the skulls based on differences in the shape of piriform aperture in the morphological space; M — men; Z — women.

Table 5. Predictability of gender based on the shape of piriform aperture

		Predictability of gender		Total
		Shape	**Shape**	
Gender	Male	83	56	139
	Female	27	45	72
Total		110	101	211

The colours to indiate the difference between male and female sex, which is accurately determited.
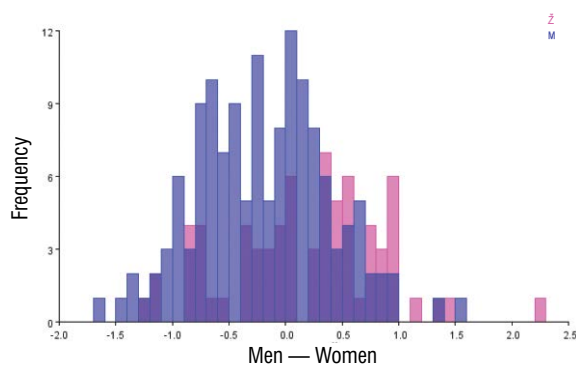
Figure 6. Discriminant functional of gender differences of shape of piriform aperture; M — men; Z — women.

the sexual dimorphism of the skulls of the examined sample are shown on Figure 6, while the interval of changes of the shape of the piriform aperture is shown on Figure 7.
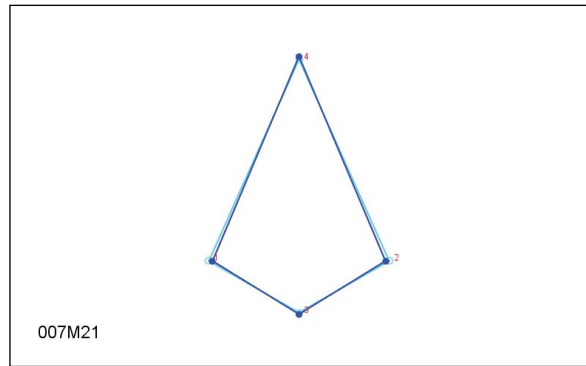
Figure 7. Interval of changes of shape of piriform aperture on examined skulls.

DISCUSSION

Gender differences of piriform aperture on 3D models of 211 human skulls (139 male skulls and 72 female skulls) was analysed using a geometric morphometric method. After the analyses, differences in the form of piriform aperture (size and shape) were observed where the first two components showed a total of 77.269% of the variability between the genders. By analysing the position of landmarks and its variability, the largest differences were observed in the position of landmark rhinion indicating the presence of differences in the height of the piriform aperture, and in the position of the right and left aperthion, indicating differences in the width of the piriform aperture.

We analysed results of other authors who studied gender differences of piriform aperture and nasal region and we noticed differences in the results that can be conditioned with different population.

In a study involving 118 human skulls (56 female skulls and 62 male skulls), nine landmarks were used for geometric morphometric analysis of the sexual dimorphism of nasal region. The results of the study showed significant differences between male and female skulls. In male skulls, the piriform aperture is higher and narrower, with a deep nasal base (position of landmark nasion and maxillonasofrontale). The piriform aperture in women is wider, the nasal bones are flattened, while the rhinion set lower, and the angle between the three landmarks, the aperthion-nasion-aperthion is sharper in the male skulls [6].

Chovalopoulou et al. [7] used geometric morphometry and eight landmarks to analyse the nasal region in her study. The results of the study did not show statistically significant significance for the sexual dimorphism of the nasal region in this study.

Araujo et al. [4], in their research conducted in 2018, used a classical morphometric method to analyse the sexual dimorphism of piriform aperture. The results of the study showed that the height of piriform aperture was higher in the skulls of the male gender than in the skulls of the female gender, but without statistically significant sex determination, while the width of the piriform aperture had the same mean values for both genders [4].

Megia et al. [23] analysed the sexual dimorphism of the nasal cavity using geometric morphometry, which concluded that the upper nasal meatus is larger in men than in women, and that there is a difference in size and shape of choanae between male and female.

Gardner [15] conducted a study analysing differences in the shape and size of piriform aperture between the skulls of Caucasians and the black population. Discriminant functional analysis showed the possibility of population differentiation with 77.4% accuracy based on piriform aperture. The step by step method extracted three linear diameters that have statistically significant effects on population proliferation with 79% accuracy [15].

Abdelaleem et al. [1] investigated the study of sexual dimorphism of piriform aperture on 250 patients of known gender. The authors measured the height and width of the piriform aperture and discriminant analysis of the obtained data showed that both diameters had a statistically significant effect in gender determination, where the width of the piriform aperture showing greater accuracy in determination [1].

Alves et al. [2] investigated the sexual dimorphism of the palate and piriform aperture on skulls from Brazilian population. Gender determination based on piriform aperture was possible with 61.9% accuracy in this study, while height of piriform aperture was best parameter for gender determination [2].

Asghar et al. [5], in their study of 40 unknown gender skulls from the Indian population, used the results of other studies to designate 12 skulls of male gender and 28 female skulls on the basis of morphological characteristics of the examined skull, after which they analysed the sexual dimorphism of piriform aperture. They measured the height and width of piriform aperture, where the mean values for the female skulls differed significantly from the mean values of the tested diameters in the male skulls [5].

Ammani et al. [3] conducted a study on 130 computed tomography (CT) images of individuals of known gender and age from Nigeria, analysing differ-

ences in the width of the nasal cavity. The results of the study showed that the lowest width of the piriform aperture was in the female group A (up to 10 years), while the largest width was in the group C (21–30 years). For men, the smallest width is in group B (11–20 years), while the largest width was in group F (51–60 years) [3].

Durga Devi et al. [10] investigated the sexual dimorphism of piriform aperture and nasal bones on 51 skulls of known gender from the Indian population. The results of the study showed that the height of the piriform aperture has a statistically significant effect in determination of gender, and that the shape of piriform aperture was between the oval and triangular in both genders [10].

Lopez et al. [22] analysed the gender differences of piriform aperture using classical morphometry. The study included 90 skulls of known gender, age and race from Brazil. They measured the height and upper and lower width of piriform aperture. They concluded that all measures were higher in male skulls, and that for sexual proliferation, only the height of piriform aperture showed a statistically significant effect [22].

Moreddu et al. [25] in his study analysed the gender differences of piriform aperture by classical and geometric morphometry on 170 CT images of patients of known gender and known age using size and shape of piriform aperture. They concluded that there are statistically significant differences between men and women, in shape and size of piriform aperture, using both methods [25].

Jaiyeoba-Ojigho et al. [18] analysed piriform aperture on 51 skulls of unknown gender and age from Nigeria where they analysed the type of piriform aperture. They concluded that shape of piriform aperture on skulls in this study is typical for African population [18].

In his study on 97 radiographs of individuals from the Brazilian population, Prado et al. [26] analysed the piriform aperture using classical morphometry, concluding that all measurements (height and width of piriform aperture) were higher on the men than on the women.

Meyvaci Sertel et al. [24] analysed the piriform aperture on CT scans of 83 patients of known gender and known age (42 women and 41 men), concluding that all parameters of piriform aperture (height and width) had a statistically significant effect in gender determination.

Kabakci et al. [19] published the results of a study where they analysed the piriform aperture on CT images of 200 healthy individuals from the Turkish population who did not have deformities in this area, measuring the height and width of the aperture and determining the golden ratio. The subjects were divided into groups by age. They concluded that the width of the piriform aperture increases with age [19].

In 2020, Lee et al. [21] published the results of his research in which he analyses a nasal profile on CT images of 389 Koreans of known gender and known age. In each obtained three-dimensional model, they indicated 16 specific landmarks, between which they measured 18 diameters and, based on regression analysis, created models for predicting gender.

Schlager and Rudell [28] conducted a study investigating population differences of piriform aperture on CT images of Germans (140 women and 127 men) and Chinese (135 women and 132 men) using 370 bilateral coordinates. They concluded that population differences are marked, and that gender differences within one population exist, and that they are similar to the gender differences observed within another population [28].

CONCLUSIONS

Principal component analysis showed that the first three PCA described 100% of variability between male and female. The first PCA axis describes 40.398% of the total variability of the analysed sample; the second PCA axis describes 36.871%, while the third PCA axis describes 22.731% variability between sexes.

The greatest variability between genders was present in the position of the anthropometric point (landmark) 8 (rhinion), which is located at the top of the piriform aperture. Variability was present in the position of the first and second anthropometric points, which are the most lateral points on the piriform aperture (aperthion — right and left).

Discriminant functional analysis of the shape and size of the piriform aperture allowed the gender determination with 64.03% accuracy for male gender and 70.83% accuracy for female gender.

The size of the piriform aperture showed a statistically significant effect for gender determination ($p < 0.0001$, the percentage influence of size was 3.3712%).

Discriminant functional analysis of piriform aperture shape without affecting size enabled gender determination with 59.71% accuracy for the male and 62.5% accuracy for the female gender.

Conflict of interest: None declared

REFERENCES

1. Abdelaleem S, Younis R, Kader M. Sex determination from the piriform aperture using multi slice computed tomography: Discriminant function analysis of Egyptian population in Minia Governorate. Egypt J Forensic Sci. 2016; 6(4): 429–434, doi: 10.1016/j.ejfs.2016.11.003.
2. Alves N, Deana NF, Ceballos F, et al. Sex prediction by metric and non-metric analysis of the hard palate and the pyriform aperture. Folia Morphol. 2019; 78(1): 137–144, doi: 10.5603/FM.a2018.0109, indexed in Pubmed: 30484270.
3. Ammani T, Zagga AD, Yunusa GH, et al. Cephalometric assessment of bony choanal aperture width (Bcaw) using computed tomographic (Ct) scan from usmanu danfodiyo university, Sokoto, Nigeria. IOSR-JDMS. 2019; 18(6): 36–42.
4. Araújo TM, da Silva C, de Medeiros L, et al. Morphometric analysis of piriform aperture in human skulls. Int J Morphol. 2018; 36(2): 483–487, doi: 10.4067/s0717-95022018000200483.
5. Asghar A, Dixit A, Rani M. Morphometric study of nasal bone and piriform aperture in human dry skull of indian origin. J Clin Diagn Res. 2016; 10(1): AC05–AC07, doi: 10.7860/JCDR/2016/15677.7148, indexed in Pubmed: 26894050.
6. Bigoni L, Velemínská J, Brůzek J. Three-dimensional geometric morphometric analysis of cranio-facial sexual dimorphism in a Central European sample of known sex. Homo. 2010; 61(1): 16–32, doi: 10.1016/j.jchb.2009.09.004, indexed in Pubmed: 20152969.
7. Chovalopoulou ME, Valakos ED, Manolis SK. Sex determination by three-dimensional geometric morphometrics of craniofacial form. Anthropol Anz. 2016; 73(3): 195–206, doi: 10.1127/anthranz/2016/0470, indexed in Pubmed: 27490899.
8. Chovalopoulou ME, Valakos ED, Manolis SK. Sex determination by three-dimensional geometric morphometrics of the palate and cranial base. Anthropol Anz. 2013; 70(4): 407–425, doi: 10.1127/0003-5548/2013/0363, indexed in Pubmed: 24620567.
9. Chovalopoulou ME, Valakos ED, Manolis SK. Sex determination by three-dimensional geometric morphometrics of the vault and midsagittal curve of the neurocranium in a modern Greek population sample. Homo. 2016; 67(3): 173–187, doi: 10.1016/j.jchb.2015.09.007, indexed in Pubmed: 27109917.
10. Durga Devi G, Archana R, Johnson WMS, et al. Morphometric study of nasal bone and piriform aperture in human dry skull of South Indian origin. Int J Anat Res. 2018; 6(4.3): 5970–5973, doi: 10.16965/ijar.2018.386.
11. Franklin D, Freedman L, Milne N, et al. A geometric morphometric study of sexual dimorphism in the crania of indigenous southern Africans. S Afr J Sci. 2006; 102: 229–238.
12. Franklin D, Freedman L, Milne N, et al. Geometric morphometric study of population variation in indigenous south-

ern African crania. Am J Hum Biol. 2007; 19(1): 20–33, doi: 10.1002/ajhb.20569, indexed in Pubmed: 17160981.

13. Franklin D, O´Higgins P, Oxnard CE. Sexual dimorphism in the mandible of indigenous South Africans: A geometric morphometric approach. S Afr J Sci. 2008; 104: 101–106.

14. Franklin D, Oxnard CE, O'Higgins P, et al. Sexual dimorphism in the subadult mandible: quantification using geometric morphometrics. J Forensic Sci. 2007; 52(1): 6–10, doi: 10.1111/j.1556-4029.2006.00311.x, indexed in Pubmed: 17209902.

15. Gardner S. A quantitative assessment of the morphology of the piriform aperture as an indicator of race. Forensic Med Anat Res. 2015; 03(01): 7–15, doi: 10.4236/fmar.2015.31002.

16. Gonzalez PN, Bernal V, Perez SI. Analysis of sexual dimorphism of craniofacial traits using geometric morphometric techniques. Int J Osteoarchaeol. 2011; 21(1): 82–91, doi: 10.1002/oa.1109.

17. Ivanović A, Kalezić M. Evoluciona morfologija: teorijske postavke i geometrijska morfometrija. Alta Nova Zemun. 2013.

18. Jaiyeoba-Ojigho EJ, Edilamode EI, Didia BC, et al. Morphometry of the nasal bones and piriform apertures of adult Nigerian skulls. Int J of Forensic Med Invest. 2019; 4(2): 22–28.

19. Kabakci A, Polat S, Öksüzler M, et al. The determination of the piriform aperture morphometry and golden ratio in healthy turkish subjects. A CT study. Int J Morphol. 2020; 38(2): 444–447, doi: 10.4067/s0717-95022020000200444.

20. Kimmerle EH, Ross A, Slice D. Sexual dimorphism in America: geometric morphometric analysis of the craniofacial region. J Forensic Sci. 2008; 53(1): 54–57, doi: 10.1111/j.1556-4029.2007.00627.x, indexed in Pubmed: 18279240.

21. Lee UY, Kim H, Song JK, et al. Assessment of nasal profiles for forensic facial approximation in a modern Korean population of known age and sex. Leg Med. 2020; 42: 101646, doi: 10.1016/j.legalmed.2019.101646, indexed in Pubmed: 31751793.

22. López MC, Galdames IS, Matamala DZ, et al. Sexual dimorphism determination by piriform aperture morphometric analysis in brazilian human skulls. Int J Morphol. 2009; 27(2), doi: 10.4067/s0717-95022009000200007.

23. Megia I, Torres-Tamayo N, Martinez DG et al. 3D analysis of sexual dimorphism in the nasal cavity of modern humans. Conference paper 2018.

24. Meyvaci Sertel S, Kosif R, Bamaç B, et al. Evaluation of apertura piriformis and related cranial anatomical structures through computed tomography: golden ratio. Folia Morphol. 2019; 78(4): 839–846, doi: 10.5603/fm.a2019.0021, indexed in Pubmed: 30835344.

25. Moreddu E, Puymerail L, Michel J, et al. Morphometric measurements and sexual dimorphism of the piriform aperture in adults. Surg Radiol Anat. 2013; 35(10): 917–924, doi: 10.1007/s00276-013-1116-2, indexed in Pubmed: 23625070.

26. Prado F, Caldas R, Rossi A, et al. Piriform aperture morphometry and nasal bones morphology in Brazilian population by postero-anterior caldwell radiographys. Int J Morphol. 2011; 29(2): 393–398, doi: 10.4067/s0717-95022011000200014.

27. Sarač-Hadžihalilović A. Anatomically-anthropological significance of the skull. . Medical Faculty, University of Sarajevo. 2017; 66, 69-71, 74, 76.

28. Schlager S, Rüdell A. Analysis of the human osseous nasal shape--population differences and sexual dimorphism. Am J Phys Anthropol. 2015; 157(4): 571–581, doi: 10.1002/ajpa.22749, indexed in Pubmed: 25845882.

V M
VIA MEDICA

O R I G I N A L   A R T I C L E

Ocular morphology of the fruit bat, *Eidolon helvum*, and the optical role of the choroidal papillae in the megachiropteran eye: a novel insight

I.K. Peter-Ajuzie[1], I.C. Nwaogu[1], L.O. Majesty-Alukagberie[2], A.C. Ajaebili[1], F.A. Farrag[3], M.A. Kassab[4], K. Morsy[5, 6], M. Abumandour[7]

[1]Department of Veterinary Anatomy, Faculty of Veterinary Medicine, University of Nigeria, Nsukka, Enugu State, Nigeria
[2]Department of Veterinary Public Health and Preventive Medicine, Faculty of Veterinary Medicine, University of Nigeria, Nsukka, Enugu State, Nigeria
[3]Department of Anatomy and Embryology, Faculty of Veterinary Medicine, Kafrelsheikh University, Kafrelsheikh, Egypt
[4]Department of Cytology and Histology, Faculty of Veterinary Medicine, Kafrelsheikh University, Kafrelsheikh, Egypt
[5]Biology Department, College of Science, King Khalid University, Abha, Saudi Arabia
[6]Zoology Department, Faculty of Science, Cairo University, Cairo, Egypt
[7]Department of Anatomy and Embryology, Faculty of Veterinary Medicine, Alexandria University, Alexandria, Egypt

Background: This work was designed to provide a morphologic, morphometric and histochemical description of the eye of the African straw-coloured fruit bat (Eidolon helvum). An explanation of the optical role of the choroidal papillae in the vision of megachiropteran bats was provided.

Materials and methods: Enucleated eyes of captured fruit bats were measured and processed for light microscopy.

Results: Typical gross features of the mammalian eye including an anterior transparent cornea, posterior whitish sclera and a golden-brown iris surrounding a round pupil were observed in the eye. Presence of undulating retina typically found in megachiropterans was also seen. The ratio of mean corneal diameter to mean axial eye diameter was 0.58 ± 0.08. The histochemical investigation of the eye indicated the presence of mucins, proteoglycans, hyaluronic acid, glycogen and/or glycoproteins in the corneal, scleral, choroidal and retinal tissues.

Conclusions: The presence of reflective materials of the tapetum lucidum on the undulating retina was shown to be a morphological adaptation for increased light sensitivity as each parabolic surface of the choroidal papillae served as a convex mirror, reflecting the light rays to the adjacent parabolic surface, thus sensitising photoreceptors in affected regions. This phenomenon thus empowers megachi-ropteran bats with improved scotopic visual capability and could explain why most of them are reliant on their vison without the need for echolocation. (Folia Morphol 2022; 81, 3: 715–722)

Key words: *Eidolon helvum*, eye, choroidal papillae, retina, megachiroptera

Address for correspondence: Dr. I.K. Peter-Ajuzie, Department of Veterinary Anatomy, Faculty of Veterinary Medicine, University of Nigeria, Nsukka, Enugu State, Nigeria, e-mail: iheanyi.peter-ajuzie@unn.edu.ng

INTRODUCTION

The eye of an organism enables it to perceive the myriad of emitted and reflected light rays in its environment. This perception is required for the survival of the organism especially during its periods of peak activity. The activity pattern of an animal is therefore related to its ocular morphological characteristics and has been reported by many ocular scientists [1, 10, 16–19, 22, 23, 32, 33].

The African straw-coloured fruit bat, *Eidolon helvum*, is a megabat that is widely distributed in sub-Saharan Africa [3]. The bats are nocturnal, live in large colonies, and can be found roosting on trees close to human habitation [27]. Some African communities use these bats for certain ritual purposes. Their frugivorous, arboreal and migratory nature enables them to function in plant pollination and plant geographical distribution [30]. The species has been identified as a natural reservoir of a number of zoonotic viral diseases such as those caused by the Ebola subtype Zaire and Lagos bat viruses [3]. Their close proximity and association with humans create a need for a comprehensive body of knowledge on their biology especially since they have been associated with some epidemics. This study therefore investigated the morphological features of the eyes of this species which were hitherto scarce in literature in order to expound its ocular biology and determine any relationship between its ocular characteristics and activity pattern. It also provided an explanation on the role of the choroidal papillae in the vision of megachiropterans which hitherto had been a subject of controversy among scientists. The results of this study might be helpful in the recognition of ocular pathology in this species and related species and in the determination of its corneal xenotransplantation potential in humans as well as the possible application of the eye morphology in technology.

MATERIALS AND METHODS

Sample collection

No animals were killed exclusively for this study. The 6 bats (3 males and 3 females) with mean body weight of 247.44 ± 45.77 g used for this study were part of the experimental animals approved by the Institutional Animal Care and Use Committee of the Faculty of Veterinary Medicine, University of Nigeria, Nsukka (Approval number: FVMUNN-IACUC-2019-0350) for the PhD studies of Dr. L.O. Obodoechi of the Department of Veterinary Public Health and Preventive Medicine, Faculty of Veterinary Medicine, University of Nigeria. Dr. Obodoechi needed only the brain sample of the captured animals for her PhD studies while the eye samples were obtained for this study. The animals were reportedly captured from the wild between January and February in Obiagu, Awgu L.G.A., Enugu State, Nigeria. Following euthanasia of the bats using 50 mg/kg ketamine hydrochloride, horizontal and vertical corneal diameters were obtained from each eye using Vernier calliper. Eyes were bilaterally enucleated [17], and the horizontal, vertical, and axial eye diameters were obtained as well as its gross anatomical and topographical characteristics.

Histology

Whole enucleated eyes were fixed in Davidson's fixative [2] for 18 hours and postfixed in 10% neutral buffered formalin. They were subsequently dehydrated in increasing concentrations of ethanol, cleared in xylene, infiltrated with paraffin and embedded in paraffin blocks. Five μm thick meridional sections were cut, mounted on glass slides, and routinely stained with haematoxylin and eosin (H&E) [7], Masson's trichrome [6] and Periodic Acid-Schiff-Alcian Blue (PAS-AB) (pH 2.5) [26] stains. Photomicrographs were captured using Moticam Images Plus 2.0 digital camera (Motic China Group Ltd., China). Corneal and retinal thicknesses were measured using the camera software.

Statistical analysis

Data were analysed using SPSS Statistics 17.0 software. Mean corneal diameter was taken as the mean of the horizontal and vertical corneal diameters while mean eye diameter was taken as the mean of the horizontal and vertical eye diameters. Data were presented as mean ± standard deviation. Data was tested for normality and paired samples t-test statistic (2-tailed) was used to determine any significant differences between the axial and horizontal eye diameters, vertical and horizontal eye diameters, vertical and axial eye diameters, and vertical and horizontal corneal diameters. Statistical significance was accepted at p < 0.05.

RESULTS

Gross anatomy

The eyes were located dorsolaterally in the orbital cavities of the skull and were separated by a flat frontal region (Fig. 1). They exhibited typical gross features of the mammalian eye including an anterior transparent cornea and a posterior whitish sclera as

Figure 1. A. The African straw-coloured fruit bat showing the dorsolaterally-located eyes separated by a flat frontal region; **B.** The golden-brown-coloured iris is visible through its transparent cornea as the bat hangs upside down in the cage.

well as a golden-brown iris surrounding a round pupil which were visible through the cornea.

The vertical and horizontal corneal diameters were 0.57 ± 0.10 cm and 0.56 ± 0.10 cm, respectively (n = 12). Both diameters were not significantly different (p < 0.05) from each other. The vertical, horizontal and axial eye diameters were 0.98 ± 0.10 cm, 0.99 ± 0.11 cm and 0.98 ± 0.06 cm, respectively (n = 12). They were also not significantly different (p < 0.05) from each other. The ratio of mean corneal diameter to mean eye diameter was 0.58 ± 0.09 (n = 12; range: 0.42–0.70) while the ratio of mean corneal diameter to mean axial eye diameter was 0.58 ± 0.08 (n = 12; range: 0.43–0.72).

Histology

Fibrous tunic. The cornea was lined anteriorly by non-keratinised stratified squamous corneal epithelium and posteriorly by simple squamous corneal endothelium, between which was dense regular fibrous connective tissue of the corneal stroma (Fig. 2). The basement membrane of the corneal endothelium known as the Descemet's membrane was thicker than that of the corneal epithelium. Both membranes were strongly PAS-positive while the corneal stroma which was bluish purple in colour was PAS-AB-positive. The sclera was a dense irregular fibrous connective tissue (Fig. 3). Its numerous collagen fibres were continuous with those of the corneal stroma.

Uvea. The iris was a heavily pigmented and vascularised tissue process that was attached to the ciliary body (Fig. 4B). The ciliary body which did not seem well-developed comprised a posterior pars plana and anterior ciliary processes (or pars plicata) both

of which were composed of ciliary epithelia overlying ciliary stroma (Fig. 4A, C). The ciliary epithelia comprised an outer pigmented epithelium and an inner non-pigmented simple cuboidal epithelium. The epithelia were continuous with the retina at the ora serrata. The vascularised pigmented choroid lay between the retina and the sclera. Its numerous projections, the choroidal papillae, projected markedly perpendicularly or obliquely towards the retina in the direction of the pupil (Figs. 3–5). These papillae caused undulations in the retinal tissues.

Retina. Undulating outer layers and non-undulating inner layers were observed in the retina (Fig. 3). The undulating layers comprised the retinal epithelium, photoreceptor layer, outer nuclear layer and outer plexiform layer while the non-undulating layers comprised the inner nuclear layer, inner plexiform layer, ganglion cells and nerve axons (Fig. 5). Some areas of the retina especially towards the ora serrata where choroidal papillae were absent lacked these retinal undulations (Fig. 5D). The photoreceptor layer was AB-positive and was composed of photoreceptor outer segment and photoreceptor inner segment. The outer segment was more deeply AB-positive than the inner segment while the outer and inner plexiform layers were weakly AB-positive (Fig. 5C). The retinal epithelium, inner nuclear layer and ganglion cell layers were weakly PAS-AB-positive. The retinal epithelium was simple cuboidal epithelium containing pigmented or non-pigmented mononuclear cells with basally-located nuclei and clear cytoplasm. It was tightly attached to the choroid, following all of its undulating contours. From the ora
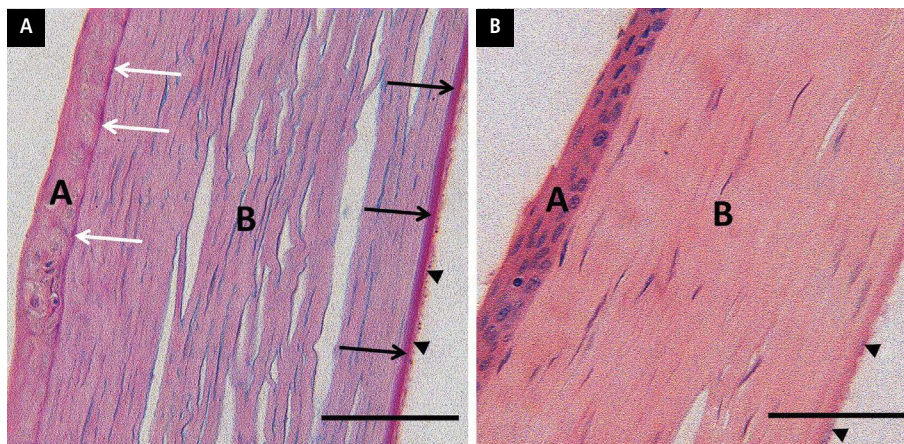
Figure 2. Photomicrographs of the cornea of the African straw-coloured fruit bat stained with Periodic Acid Schiff (PAS)-Alcian Blue stain at pH 2.5 (**A**) and haematoxylin and eosin (**B**). Corneal epithelium (A) with its thin PAS positive basement membrane (white arrows), corneal stroma (B), corneal endothelium (arrow heads) with its thick PAS-positive Descemet's membrane (black arrows); scale bars = 50 μm.
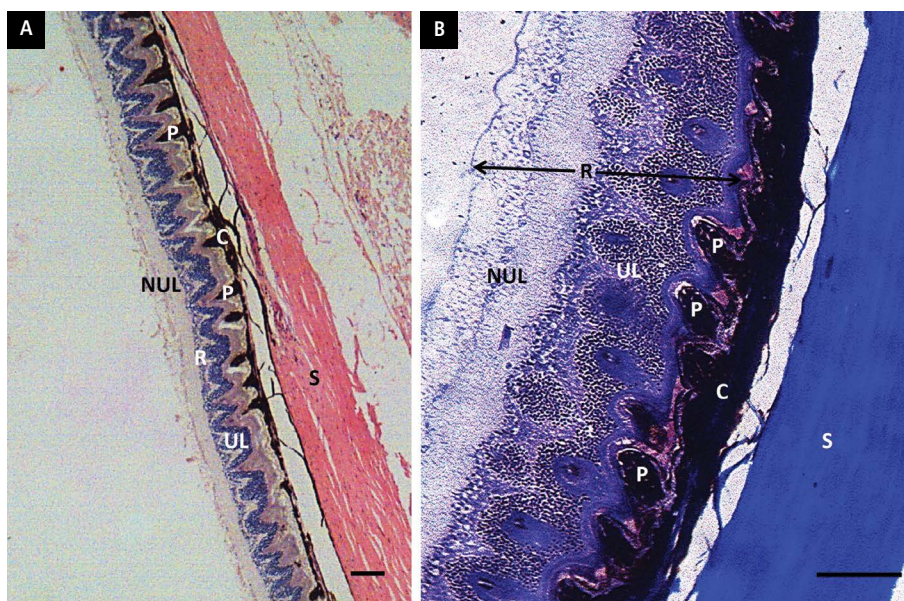

Figure 3. Photomicrographs of the eye of the African straw-coloured fruit bat stained with haematoxylin and eosin (**A**) and Masson's trichrome (**B**). Sclera (S), choroid (C) with its choroidal papillae (P), retina (R) with its undulating (UL) and non-undulating (NUL) layers; scale bars = 100 μm.

serrata to the posterior pole, the pigmented retinal epithelium gradually lost its apical melanin pigments such that towards the posterior pole, the epithelium lacked pigments. The nuclei of the photoreceptor cells in the outer nuclear layer were heterochromatic unlike the nuclei in the outer nuclear and ganglion cell layers which were euchromatic.

DISCUSSION AND CONCLUSIONS

Histochemistry

The PAS-AB histochemical stain which is used for the detection of some categories of carbohydrates and glycoconjugates was employed in this study to determine if the carbohydrate composition of the fruit bat eye was similar to those reported for other animals. The PAS-AB histochemical reactions indicated the presence of glycoproteins, proteoglycans, hyaluronic acid and/or glycogen in the corneal, scleral, choroidal and retinal tissues [26]. Different shades of blue colouration as seen in the inner and outer segments of the photoreceptor layer as well as in the outer and inner plexiform layers of the retina indicated a positive AB reaction which affirmed the presence of acid mucins, proteoglycans and/or hya-
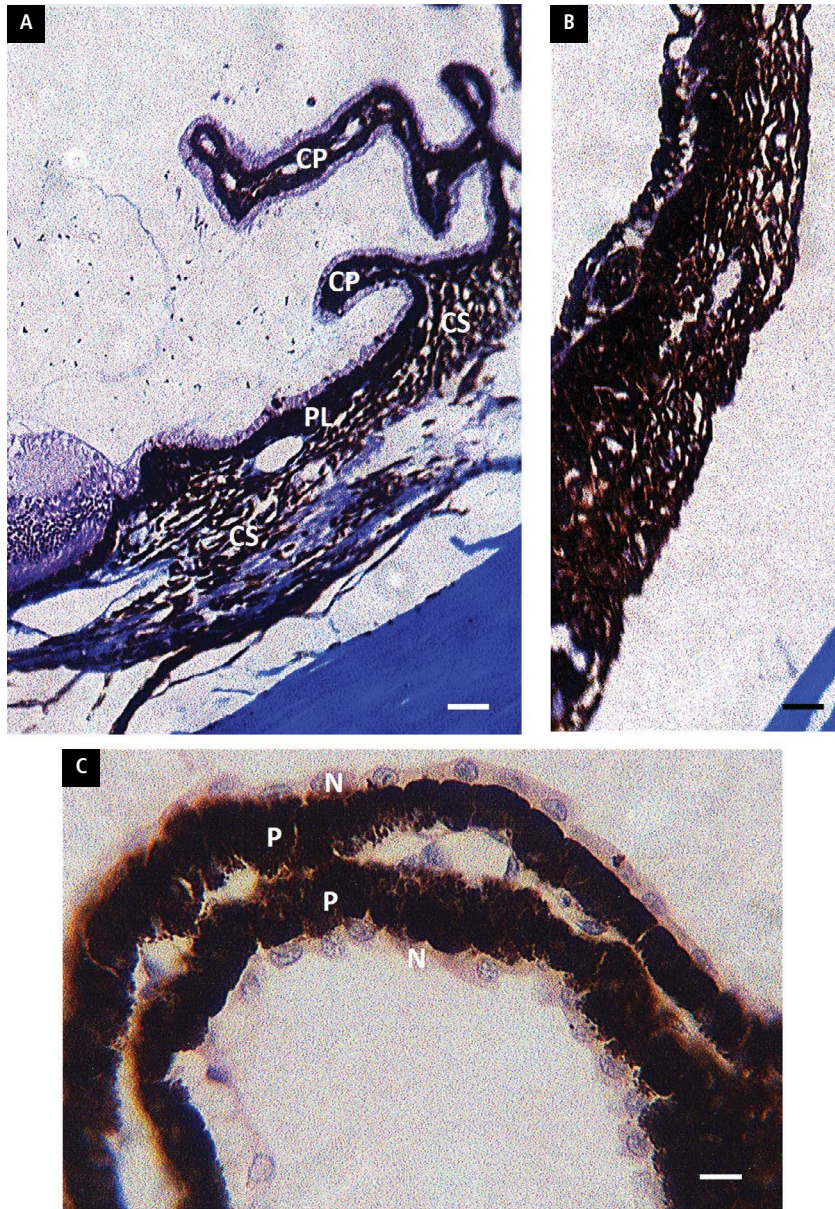
Figure 4. Photomicrographs of the ciliary body (**A**), iris (**B**) and ciliary process (**C**) of the African straw-coloured fruit bat; CP — ciliary process; PL — pars plana; CS — ciliary stroma; N — non-pigmented epithelium; P — pigmented epithelium. Scale bar and stain for panels A and B = 100 μm, Masson's trichrome. Scale bar and stain for panel C = 10 μm, haematoxylin and eosin.

luronic acid in those regions of the retina. Magenta colour as seen in the Descemet's membrane and basement membrane of the corneal epithelium indicated a positive PAS reaction which affirmed the presence of glycogen and/or glycoproteins in the corneal membranes. The different shades of bluish purple colouration observed in the corneal stroma, sclera, choroid, retinal epithelium, inner nuclear layer and ganglion cell layer indicated positive reactions to both AB and PAS. The blue colouration of the nuclei in the outer nuclear layer of the retina was a result of

the haematoxylin counterstain used for the PAS-AB staining procedure.

Online literature search on Google Scholar (www.scholar.google.com) using different keywords showed the absence of published work on the histochemical detection of glycoproteins, proteoglycans, hyaluronic acid or glycogen in the eye of bat as at the time of writing this paper. This study may thus be the first scientific attempt to describe the carbohydrate composition of the chiropteran eye. Though immunohistochemical staining would have been more specific in determining
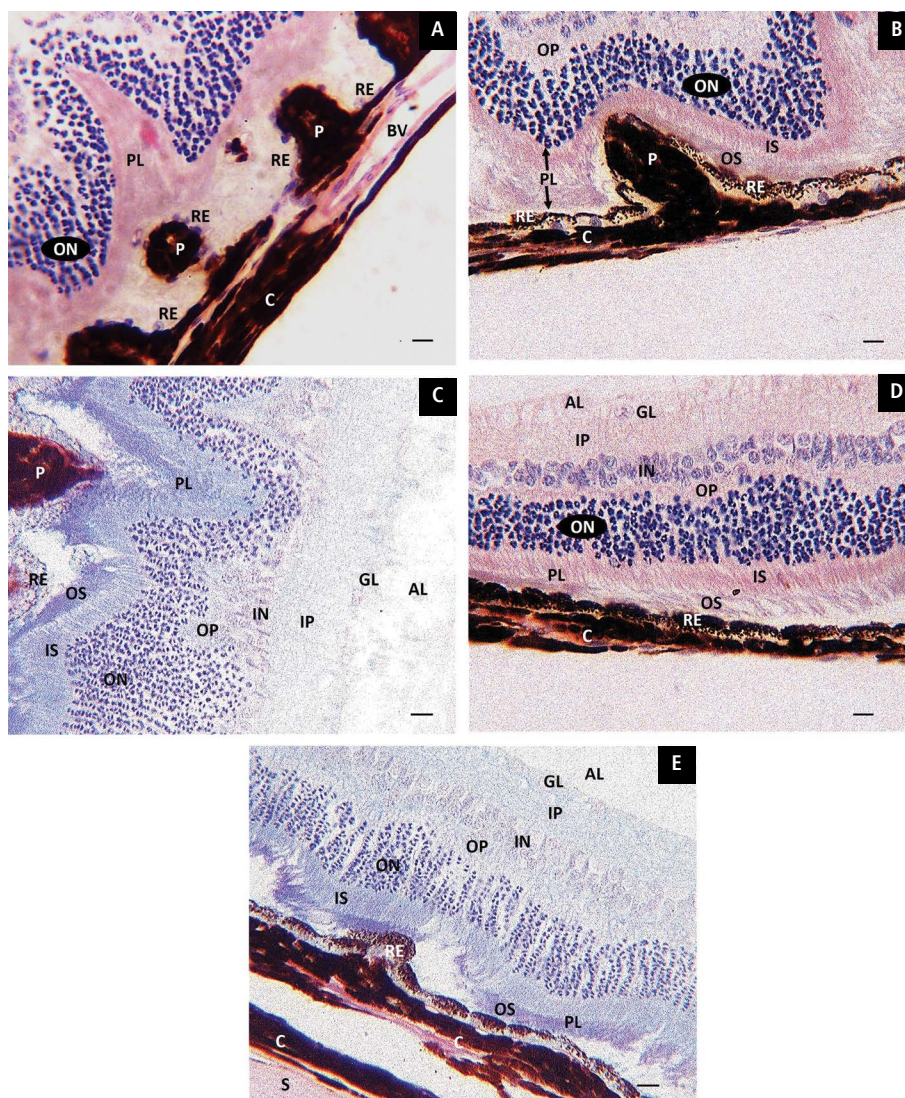
Figure 5. Photomicrographs of the retina, choroid and sclera of the African straw-coloured fruit bat. Choroidal papillae (P) with its consequent retinal undulations are present in panels **A**, **B** and **C**; absent in panel **D** and inconspicuous in panel **E**. Melanin pigments of the retinal epithelium (RE) were absent in panel A but gradually increased in quantity from panel C to panel B to panel E to panel D. Choroid (C), blood vessel (BV), photoreceptor layer (PL) comprising the inner segment (IS) and outer segment (OS), outer nuclear layer (ON), outer plexiform layer (OP), inner nuclear layer (IN), inner plexiform layer (IP), ganglion cell layer (GL), axon layer (AL), sclera (S). Haematoxylin and eosin stain (A, B and D). Periodic Acid Schiff-Alcian Blue stain, pH 2.5 (C and E). Scale bars = 10 μm.

carbohydrate composition, the PAS-AB staining, however, gives a relatively general idea of the carbohydrate composition. Proteoglycans have already been isolated from retinal tissues of other mammals where they were reported to play roles in retinal neuronal growth, repairs and synapse formation [5, 20, 21]. Hyaluronic acid has been detected in the sclera, choroid and retinal pigment epithelium of humans where it was said to maintain tissue fluidity, permeation and hydration [35] as well as function in the creation of retinal neural networks through its complexes with proteoglycans [20]. Glycoproteins, which also include mucins, have

been demonstrated in the cornea, sclera, ciliary body and retina of humans [15] and in the retina of cattle [4, 13] while glycogen which serves as cellular energy reserve has been reported in the corneal endothelium of man and rabbit [28]; retina, vitreous, lens, choroid, iris and cornea of cattle and rabbit [36]; retina of cat; corneal epithelium of rabbit [14]; and retina of guinea pig, rabbit, man, cat, cattle, hamster and fish [24].

Morphometry

The mean corneal diameter to mean axial eye diameter ratio observed in *Eidolon helvum* in this

study was at variance with those reported for most nocturnal mammals and birds which have higher ratios. The ratio was rather similar to those reported for most diurnal and cathemeral animals [16, 17, 23]. The authors had postulated that the scotopic environment of nocturnal animals necessitated a higher mean corneal diameter to mean axial eye diameter ratio to enable the animals capture as much light rays as is possible from the environment while the photopic environment of diurnal animals necessitated lower ratios so as to limit the amount of light rays entering the eyes from the light-rich environment. The possession of a relatively low ratio by the nocturnal fruit bat therefore suggests that its retina has higher sensitivity to light rays than those of most nocturnal animals. Such a situation therefore eliminates the need for a high mean corneal diameter to mean axial eye diameter ratio and might provide explanations for the unusual retinal morphology of the fruit bat. In addition, the relatively low ratio could also indicate an adaptation for vision in both scotopic and photopic environments as has been reported for cathemeral animals [16, 23].

Choroidoretinal undulations

The unusual choroidal and retinal morphology observed in this study for *Eidolon helvum* have since been reported for other megachiropteran, and in particular, pteropodid bats [1, 12, 25]. The role of the choroidal papillae in blood supply to retinal tissues has been well documented [9, 11] but their role in vision has been a matter of controversy among scientists with some scientists asserting that the presence of the choroidal papillae led to improved visual sensitivity through an increase in the photosensitive area and number of photoreceptors [11, 31]. This assertion has, however, been refuted by Suthers [34] who clarified that the choroidal papillae couldn't lead to an increase in the photosensitive area and number of photoreceptors without a decrease in photoreceptor diameter or decrease in the space between photoreceptors or a rearrangement of the long axis of all photoreceptors to be perpendicular to the plane of undulating choroidal surface. The author, however, didn't provide an explanation for the role of the papillae in vision.

Though we did not directly check for the presence of tapetum lucidum in the *Eidolon helvum*, the absence of melanin pigments in the retinal epithelium of the central retina strongly suggests the existence
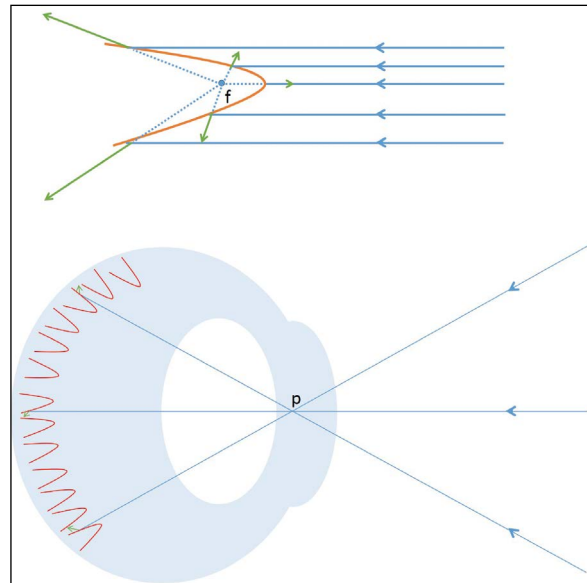
Figure 6. Schematic representation of the visual role of the choroidal papillae in the megachiropteran eye. The figure above shows a retinal tapetum lucidum-lined choroidal papilla with the incident rays (solid blue lines), reflected rays (green arrows) and the tracing of the reflected rays (dotted blue lines) from the focal point (f). The figure below shows the megachiropteran eye where incident light rays (solid blue lines) passes through the pupil (p) to become reflected (green arrows) on hitting the retinal tapetum lucidum-lined choroidal papillae. Refraction of light rays was not taken into consideration in this schematic representation.

of tapetum lucidum in the bat. This is because the presence of tapetum lucidum in mammals is generally characterised by the absence of melanin pigments in the retinal epithelium of the central retina [29, 33]. Available evidence in other megachiropterans and pteropodids nevertheless show that bats of these clades contain retinal tapetum lucidum in the cells of the retinal epithelium [8, 29, 31]. The presence of reflective materials of the tapetum lucidum on an undulating surface is therefore a major and unique morphological adaptation for increased light sensitivity as each parabolic surface serves as a convex mirror, reflecting the light rays to the adjacent parabolic surface (Fig. 6). Photoreceptors associated with both papillae therefore get sensitised. This implies that a higher number of photoreceptors get sensitised in a megachiropteran eye than in a non-megachiropteran eye if both are exposed to the same incident light rays. İt could also provide the much needed explanation why most megachiropterans are heavily reliant on their vison without the need for echolocation [1, 3, 8, 9, 25, 30] and why the relatively low mean corneal diameter to mean axial eye diameter ratio was observed in the fruit bat unlike the case in

most nocturnal animals. It is, however, worth noting that the plane of orientation of the reflective materials of the tapetum in the retinal epithelium will influence the angle of reflection of the light rays. Thus, further investigations on the plane of orientation of these materials may be required to determine the angle of reflection.

Acknowledgements

Conflict of interest: None declared

REFERENCES

1. Aboelnour A, Noreldin AE, Massoud D, et al. Retinal characterization in the eyes of two bats endemic in the Egyptian fauna, the Egyptian fruit bat (Rousettus aegyptiacus) and insectivorous bat (Pipistrellus kuhlii), using the light microscope and transmission electron microscope. Microsc Res Tech. 2020; 83(11): 1391–1400, doi: 10.1002/jemt.23530, indexed in Pubmed: 33405350.
2. Agrawal RN, He S, Spee C, et al. In vivo models of proliferative vitreoretinopathy. Nat Protoc. 2007; 2(1): 67–77, doi: 10.1038/nprot.2007.4, indexed in Pubmed: 17401340.
3. Cunhaalmeida F, Giannini N, Simmons N. The evolutionary history of the african fruit bats (Chiroptera: Pteropodidae). Acta Chiropterologica. 2016; 18(1): 73–90, doi: 10.3161/15081109acc2016.18.1.003.
4. Aon MA, Curtino JA. Evidence for the glycoprotein nature of retina glycogen. Eur J Biochem. 1984; 140(3): 557–566, doi: 10.1111/j.1432-1033.1984.tb08138.x, indexed in Pubmed: 6723649.
5. Aquino DA, Margolis RU, Margolis RK. Immunocytochemical localization of a chondroitin sulfate proteoglycan in nervous tissue. I. Adult brain, retina, and peripheral nerve. J Cell Biol. 1984; 99(3): 1117–1129, doi: 10.1083/jcb.99.3.1117, indexed in Pubmed: 6432802.
6. Bancroft JD, Layton C. Connective and mesenchymal tissues with their stains. In: Suvarna SK eds. 7th ed. Bancroft's Theory and Practice of Histological Techniques, Elsevier Ltd. 2013: 187–214.
7. Bancroft JD, Layton C. The hematoxylins and eosin. In: Suvarna SK eds. 7th ed. Bancroft's Theory and Practice of Histological Techniques, Elsevier Ltd. 2013: 172–186.
8. Bojarski C, Bernard R. Comparison of the morphology of the megachiropteran and microchiropteran eye. South African J Zool. 2015; 23(3): 155–160, doi: 10.1080/02541858.1988.11448095.
9. Brudenall DK, Schwab IR, Lloyd W, et al. Optimized architecture for nutrition in the avascular retina of Megachiroptera. Anat Histol Embryol. 2007; 36(5): 382–388, doi: 10.1111/j.1439-0264.2007.00779.x, indexed in Pubmed: 17845230.
10. Corfield JR, Gsell AC, Brunton D, et al. Anatomical specializations for nocturnality in a critically endangered parrot, the Kakapo (Strigops habroptilus). PLoS One. 2011; 6(8): e22945, doi: 10.1371/journal.pone.0022945, indexed in Pubmed: 21860663.
11. El-Mansi AA, Al-Kahtani MA, Al-Sayyad KM, et al. Visual adaptability and retinal characterization of the Egyptian fruit bat (Rousettus aegyptiacus, Pteropodidae): New insights into photoreceptors spatial distribution and melanosomal activity. Micron. 2020; 137: 102897, doi: 10.1016/j.micron.2020.102897, indexed in Pubmed: 32563026.
12. Farina LL, Lankton JS. Chiroptera. Elsevier Inc. 2014.
13. Fong SL, Liou GI, Landers RA, et al. Purification and characterization of a retinol-binding glycoprotein synthesized and secreted by bovine neural retina. J Biol Chem. 1984; 259(10): 6534–6542, doi: 10.1016/s0021-9258(20)82174-7.
14. Friend J, Kiorpes T, Kinoshita S. Glycogen and DNA content of corneal epithelium: comparison of preparation methods. Invest Ophthalmol Vis Sci. 1983; 24(2): 203–207, indexed in Pubmed: 6337970.
15. Gabriel LAR, Wang LW, Bader H, et al. ADAMTSL4, a secreted glycoprotein widely distributed in the eye, binds fibrillin-1 microfibrils and accelerates microfibril biogenesis. Invest Ophthalmol Vis Sci. 2012; 53(1): 461–469, doi: 10.1167/iovs.10-5955, indexed in Pubmed: 21989719.
16. Hall MI, Kamilar JM, Kirk EC. Eye shape and the nocturnal bottleneck of mammals. Proc Biol Sci. 2012; 279(1749): 4962–4968, doi: 10.1098/rspb.2012.2258, indexed in Pubmed: 23097513.
17. Hall MI. Comparative analysis of the size and shape of the lizard eye. Zoology (Jena). 2008; 111(1): 62–75, doi: 10.1016/j.zool.2007.04.003, indexed in Pubmed: 18054216.
18. Hall MI. The anatomical relationships between the avian eye, orbit and sclerotic ring: implications for inferring activity patterns in extinct birds. J Anat. 2008; 212(6): 781–794, doi: 10.1111/j.1469-7580.2008.00897.x, indexed in Pubmed: 18510506.
19. Hall MI, Ross CF. Eye shape and activity pattern in birds. J Zool. 2006; 271(4): 437–444, doi: 10.1111/j.1469-7998.2006.00227.x.
20. Inatani M, Tanihara H. Proteoglycans in retina. Prog Retin Eye Res. 2002; 21(5): 429–447, doi: 10.1016/s1350-9462(02)00009-5.
21. Inatani M, Tanihara H, Oohira A, et al. Upregulated expression of neurocan, a nervous tissue specific proteoglycan, in transient retinal ischemia. Invest Ophthalmol Vis Sci. 2000; 41(9): 2748–2754, indexed in Pubmed: 10937593.
22. Iwaniuk A, Heesy C, Hall M. Morphometrics of the eyes and orbits of the nocturnal Swallow-tailed Gull (Creagrus furcatus). Can J Zool. 2010; 88(9): 855–865, doi: 10.1139/z10-051.
23. Kirk EC. Comparative morphology of the eye in primates. Anat Rec A Discov Mol Cell Evol Biol. 2004; 281(1): 1095–1103, doi: 10.1002/ar.a.20115, indexed in Pubmed: 15470670.
24. Kuwabara T, Cogan DG. Retinal glycogen. Arch Ophthalmol. 1961; 59: 106–110, doi: 10.1001/archopht.1961.00960010682013, indexed in Pubmed: 14460992.
25. Kwiecinski G, Griffiths T. Rousettus egyptiacus. Mammalian Species. 1999(611): 1, doi: 10.2307/3504411.
26. Layton C, Bancroft JD. Carbohydrates. In: Suvarna SK eds. 7th ed. Bancroft's Theory and Practice of Histological Techniques., Elsevier Ltd. 2013: 215–238.
27. Magloire NCJ, Noel DD, Blaise K, et al. Spatiotemporal Activities of Eidolon helvum (Kerr, 1792) a Near-Threatened Species (Côte D'Ivoire, West Africa). Res Zool. 2018; 8(1): 6–11, doi: 10.5923/j.zoology.20180801.02.
28. Malinin GI, Bernstein H. Histochemical demonstration of glycogen in corneal endothelium. Exp Eye Res. 1979; 28(4): 381–385, doi: 10.1016/0014-4835(79)90113-1, indexed in Pubmed: 446566.
29. Ollivier FJ, Samuelson DA, Brooks DE, et al. Comparative morphology of the tapetum lucidum (among selected species). Vet Ophthalmol. 2004; 7(1): 11–22, doi: 10.1111/j.1463-5224.2004.00318.x, indexed in Pubmed: 14738502.
30. Ossa G, Kramer-Schadt S, Peel AJ, et al. The movement ecology of the straw-colored fruit bat, Eidolon helvum, in sub-Saharan Africa assessed by stable isotope ratios. PLoS One. 2012; 7(9): e45729, doi: 10.1371/journal.pone.0045729, indexed in Pubmed: 23029206.
31. Pedler C, Tilley R. The retina of a fruit bat (Pteropus giganteus Brünnich). Vision Res. 1969; 9(8): 909–922, doi: 10.1016/0042-6989(69)90097-2, indexed in Pubmed: 5802397.
32. Peter-Ajuzie IK, Nwaogu IC, Ajaebili AC. Preliminary anatomical assessment of the eye of the African giant rat (Cricetomys gambianus). Agric Sci Dig. 2020; 40(01), doi: 10.18805/ag.d-183.
33. Peter-Ajuzıe I, Nwaogu I, Igwebuike U. Anatomical assessment of the eye of the african grasscutter (Thryonomys swinderianus). J Appl Life Sci Int. 2019: 1–8, doi: 10.9734/jalsi/2019/v20i230077.
34. Suthers RA. A comment on the role of choroidal papillae in the fruit bat retina. Vision Res. 1970; 10(9): 921–923, doi: 10.1016/0042-6989(70)90174-4, indexed in Pubmed: 5492784.
35. Tate DJ, Oliver PD, Miceli MV, et al. Age-dependent change in the hyaluronic acid content of the human chorioretinal complex. Arch Ophthalmol. 1993; 111(7): 963–967, doi: 10.1001/archopht.1993.01090070083023, indexed in Pubmed: 8328939.
36. Wasilewa P, Hockwin O, Korte I. Glycogen concentration changes in retina, vitreous body and other eye tissues caused by disturbances of blood circulation. Albrecht Von Graefes Arch Klin Exp Ophthalmol. 1976; 199(2): 115–120, doi: 10.1007/BF02385207, indexed in Pubmed: 1083690.

V M
VIA MEDICA

O R I G I N A L   A R T I C L E

Does the horizontal condylar angle have a relationship to temporomandibular joint osteoarthritis and condylar position? A cone-beam computed tomography study

U. Pamukcu[1], H. Tetik[1], I. Peker[1], B. Altunkaynak[2], Z. Zafersoy Akarslan[1]

[1]Department of Dentomaxillofacial Radiology, Faculty of Dentistry, Gazi University, Ankara, Turkey
[2]Department of Statistics, Faculty of Sciences, Gazi University, Ankara, Turkey

Background: The aim of the study was to evaluate the relationship between the horizontal condylar angle (HCA), temporomandibular joint osteoarthritis (TMJ OA), and condylar position on cone-beam computed tomography (CBCT) images.
Materials and methods: Based on TMJ OA, joints were classified as affected and the unaffected. According to the OA condition of their joints, three groups of patients were formed: control group (n = 159, 41.1%), unilateral group (n = 121, 31.3%), and bilateral group (n = 107, 27.6%). In total, the HCAs of 774 TMJs of 387 patients were measured and their condylar positions were determined as concentric (n = 184, 23.8%), posterior (n = 338, 43.7%), and anterior (n = 252, 32.5%).
Results: The mean HCA of the bilateral group (22.7 ± 7.6°) was greater than those in both the control (19.5 ± 6.4°) and the unilateral (20.5 ± 6.5°) groups (p < 0.05). However, the difference was not statistically significant between the control and unilateral group (p > 0.05). In total patients, unlike the unilateral group, the affected joints had a greater mean HCA than the unaffected joints (p < 0.05). The mean HCAs of the joints according to the condylar position were as concentric: 20.6 ± 6.7°, posterior: 21.1 ± 7.8°, and anterior: 20.2 ± 7.9° (p > 0.05).
Conclusions: While the HCA increased in the presence of TMJ OA, no relationship was found between HCA and three different condylar positions. (Folia Morphol 2022; 81, 3: 723–731)

Key words: horizontal condylar angle, temporomandibular joint osteoarthritis, condylar position, cone-beam computed tomography

INTRODUCTION

Temporomandibular joint osteoarthritis (TMJ OA) is a degenerative joint disease that especially involves osseous structures and is accepted as an important subgroup of temporomandibular disorders (TMDs) [34]. TMJ OA is more sophisticated than the OA of other joints because of the architecture and composition of the TMJ tissues and the multiple forces the joint is subjected to as well [15]. The radiologically observed osseous changes associated with TMJ OA, in

both condyle and glenoid fossa are erosion and flattening of articular surfaces, subcortical sclerosis and cyst, osteophyte, generalised sclerosis, and loose joint bodies [1]. It has been claimed that because of the changes in the bone trabecular structure, biomechanical forces and muscle activities following the OA, the morphological structure of TMJ is transformed [15].

In the previous studies that examined the morphological changes of the TMJ related to OA, one of the less-focused parameters has been the horizontal condylar angle (HCA). The HCA is defined as the angle between the long axis of the mandibular condyle and the coronal plane perpendicular to the midsagittal plane on the axial sections [36]. Limited data in the literature suggested that a greater HCA was generally observed in TMJs that presented disc displacement, clinical TMD symptoms, the excessive pulling effect of the lateral pterygoid muscle, and also radiological OA findings [5, 6, 11, 14, 15, 35, 36]. Additionally, it was reported that a greater HCA could be the result of bone formation at the posterior medial pole and resorption at the anterior lateral pole of the condyle [10]. A greater HCA: is it a result of or a reason for TMJ OA? Whether the TMJ OA osseous changes increase the HCA or whether a large HCA contributes to the development of TMJ OA has not been proven yet.

The importance of condylar position on TMJ health is a controversial issue. The predominant opinion is that TMD patients generally have a posterior condylar position [4, 18, 22, 28]. However, some authors have suggested no significant association between condylar position and clinical or radiological findings of TMJ [19, 24].

The value of imaging modality cannot be ignored for establishing the accurate diagnosis of TMJ OA and determining the condylar position [1]. As it provides high resolution and precise three-dimensional images for evaluating the osseous changes and makes reliable linear and angular measurements of maxillofacial hard tissues, cone-beam computed tomography (CBCT) has been accepted as an adequate technique for the assessment of these parameters of TMJ [16, 26].

The first aim of this study was to evaluate the relationship between TMJ OA and HCA; the second aim was to evaluate the relationship between condylar position and HCA by scanning the CBCT images of patients retrospectively in a cross-sectional period.

MATERIALS AND METHODS

This study was approved by the Ethical Committee of Gazi University (date: 26/06/2019, number: 07). The CBCT images of patients who applied to Gazi University Faculty of Dentistry Oral and Maxillofacial Radiology Clinic between January 2015 and December 2019 for various dental reasons were analysed retrospectively. No additional CBCT scan was taken for the study. Informed consent was obtained from all participants included in the study.

The CBCT images were obtained by a Planmeca Promax 3D Mid (Planmeca, Helsinki, Finland) device, and the parameters were 140×92 mm^2 field of view (FOV), 90 kVp, 8 mA, 13.5 s, 0.4 mm^3 voxel or 140×52 mm^2 FOV, 90 kVp, 8 mA, 13.5 s, 0.4 mm^3 voxel. The original software programme Romexis 4.6.2.R (Planmeca, Helsinki, Finland) of the CBCT device was used to display the images. All images were analysed on the same 24-inch medical monitor (Philips, Luchu Hsiang, Taiwan) with an ideal screen display (resolution: 1920×1080 pixels) provided with an NVIDIA QUADRO FX 380 graphics card. All evaluations were made independently by two calibrated investigators who have competence in the CBCT interpretation for maxillofacial diagnosis, including the TMJ region, in a quiet room with subdued ambiance lighting, from about 50 cm. The obtained data were recorded in a form that was specially prepared for this study. In cases of disagreement regarding the presence or absence of osseous changes, the observers evaluated the images for the second time and a consensus was reached after a discussion [15].

All the exclusion and inclusion criteria and radiologic findings are based on CBCT reports and images, and health records. The primary inclusion criterion was that both the mandibular condyle and the glenoid fossa could be viewed simultaneously on the same CBCT image. Patients with a history of surgical operation (including orthognathic surgery), trauma, and pathology (including tumours and synovial chondromatosis) in the TMJ area, younger than 18 years (only patients who were aged ≥ 18 years were selected to ensure the TMJ development had been completed), images that had a failure in maximum occlusion position during the scan acquisition, and without sufficient diagnostic quality were excluded. A total of 387 patients' CBCT images were included in the study. Patients were between 18 and 71 years (mean 46.81 ± 13.82 years [standard devi-
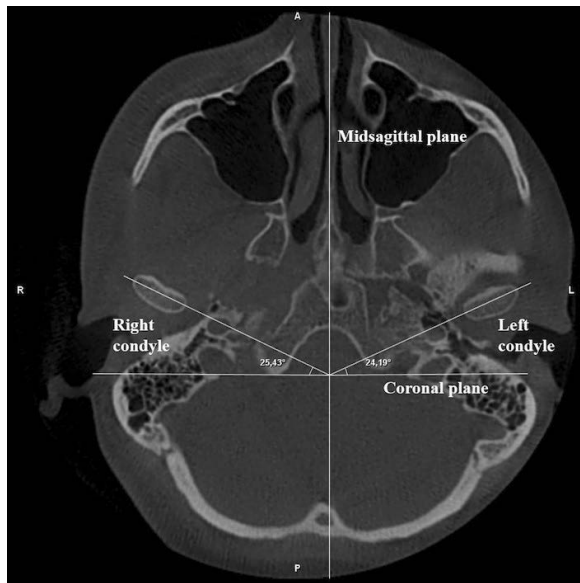
Figure 1. Measurement of horizontal condylar angle on the axial cone-beam computed tomography section.

ation, SD]) and comprised 225 (58.1%) females and 162 (41.9%) males.

Measurement of HCA

First, the maximum mediolateral length of both right and left condyles was determined as the long axis of the condyle on the appropriate axial CBCT section. The coronal plane was determined as a line drawn perpendicular to the midsagittal plane. Then the angle between the long axis and the coronal plane was defined as the HCA (Fig. 1) [36]. Because these images used to measure the HCA did not show indications of OA, all HCA measurements were performed blinded to the knowledge of the OA status of the joints.

Evaluation of TMJ OA

Each patient's right and left TMJ regions were evaluated separately on the reconstructed sagittal CBCT sections in one-millimetre intervals. The TMJ OA was diagnosed radiologically using the method defined by Ahmad et al. [1], in which osseous changes of the joint region were evaluated. The mandibular condyle head changes were gross hypoplasia or hyperplasia, flattening, erosion, subcortical sclerosis and cyst, osteophyte formation, generalised sclerosis, and loose joint bodies. Correspondingly, changes evaluated in the glenoid fossa were flattening of the articular eminence, sclerosis, and surface erosion (Fig. 2).

Joints were categorised as non-OA, indeterminate OA, or OA according to the findings obtained by evaluating the osseous structures on CBCT images. Afterward, the joints with non-OA or indeterminate OA changes were accepted as unaffected, and joints with OA changes were accepted as affected [14]. The patients were divided into three groups according to the presence of unaffected/affected joints as control group (bilaterally unaffected joints), unilateral group (one unaffected joint and one affected joint), and bilateral group (bilaterally affected joints). Furthermore, to evaluate the relationship between the TMJ OA and HCA from another window, only in the unilateral group the value obtained by subtracting the affected joint HCA from the unaffected joint HCA was recorded for each patient [29].

Determination of condylar position

The axial CBCT section where the mandibular condyle has the largest mediolateral diameter was chosen as the reference view for the secondary reconstruction. On this selected axial section, a reconstructed

Figure 2. Osseous changes of temporomandibular joint osteoarthritis observed in the temporomandibular joint region on the reconstructed sagittal cone-beam computed tomography sections; **A.** Flattening of articular eminence and erosion of condyle; **B.** Generalised sclerosis of articular eminence and condyle; **C.** Flattening and subcortical sclerosis of the condyle; **D.** Osteophyte formation; **E.** Subcortical cyst; **F.** Loose joint body and erosion of glenoid fossa.
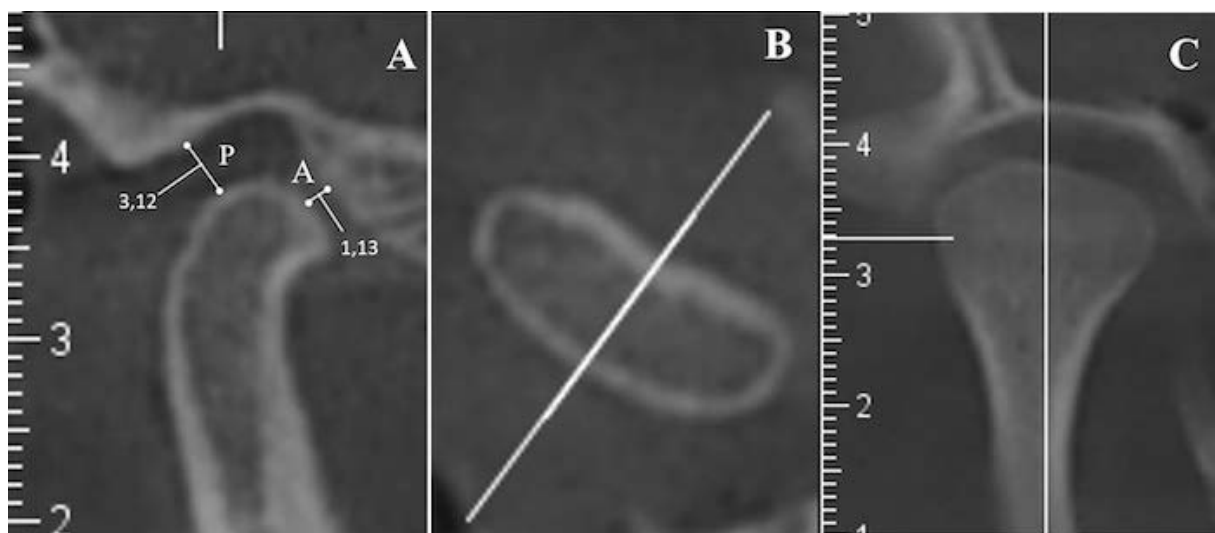
Figure 3. Measurements for determining the condylar position; **A.** Linear measurement of posterior (P), and anterior (A) joint spaces on the reconstructed sagittal cone-beam computed tomography sections with the axial (**B**) and coronal (**C**) cone-beam computed tomography sections as reference.

sagittal CBCT section was obtained by drawing a line parallel to the long axis of the condyle. The narrowest posterior (P) and anterior (A) joint spaces were measured linearly on this sagittal section (Fig. 3). The condylar position was determined according to the Pullinger and Hollender method: Condylar ratio $= (P - A) / (P + A) \times 100$ [21]. The condyle was accepted to be located in the concentric position if the calculated ratio was within ± 12%, in the posterior position if it was less than –12%, and in the anterior position, if it was greater than +12%.

Statistical analysis

The Kolmogorov-Smirnov test was used to examine whether the data were compatible with the normal distribution. Because the dimensions in the scale were from a population with a normal distribution, the independent sample t-test was used to compare two groups, and one-way analysis of variance (one-way ANOVA) was used to compare more than two groups. If the difference between the groups was statistically significant because of the variance analysis, the Tukey test (one of the multiple comparison tests) was applied to determine which groups were different from each other. The assumption of variance homogeneity in the tests related to the comparison of the groups was examined with Levene's test, and the results were used to decide which test statistics should be considered. The χ^2 test was used to examine categorical variables. The results obtained for the analysis were interpreted

at a significance level of 0.05, and IBM SPSS 20.0 programmes were used.

RESULTS

A total of 387 patients were divided into three groups according to the radiological OA findings of their 774 TMJs examined by CBCT:
— the control group consisted of 159 patients with two unaffected joints (n = 88, 55.3% females and n = 71, 44.7% males);
— the unilateral group consisted of 121 patients with one unaffected joint and one affected joint (n = 69, 57% females and n = 52, 43% males);
— the bilateral group consisted of 101 patients with two affected joints (n = 68, 63.6% females and n = 39, 36.4% males).

The mean ages of the patients for the three groups were similar (control group: 44.9 ± 13.7 years, unilateral group: 49.6 ± 13.1 years, bilateral group: 46.5 ± 14.5 years). When the mean HCAs of the TMJ OA groups were compared, the difference was statistically significant (p < 0.05). According to the results of the multiple comparison test, the bilateral group had a greater mean HCA than both the control and unilateral group, and the difference was statistically significant (p = 0.001 < 0.05) (Table 1). However, the difference was not statistically significant between the control and unilateral group (p = 0.199 > 0.05).

The mean HCA of the total 774 joints was 20.7 ± ± 7.7°. The difference between the mean HCAs of all joints in the control group (both unaffected) and

Table 1. Distribution of mean horizontal condylar angles (HCA) of temporomandibular joint osteoarthritis (TMH OA) groups, number (%) and the statistical analysis results

TMJ OA-HCA (patients)	N (%)	Mean HCA of right and left condyle ± SD (degree)	P	
Control group	159 (41.1)	19.5 ± 6.4[a]		
Unilateral group	121 (31.3)	20.5 ± 6.5[a]	} 0.199	
Bilateral group	107 (27.6)	22.7 ± 7.6[b]		} 0.001*
Total	387 (100)	20.7 ± 6.9		

[a, b]The letters next to the mean angles indicate groups that differ according to the Tukey HSD test; *p < 0.05, statistically significant; SD — standard deviation

Table 2. Distribution of mean horizontal condylar angles (HCA) of affected and unaffected joints in terms of temporomandibular joint osteoarthritis (TMJ OA), number (%) and the statistical analysis results

TMJ OA-HCA (joints)		N (%)	Mean HCA ± SD (degree)	P	
Unaffected joints	Control group	318 (41.1)	19.5 ± 6.4	} 0.852	
	Unilateral group's unaffected joint	121 (15.6)	19.7 ± 7.0		
	Total	439 (56.7)	19.6 ± 6.6		} 0.0001*
Affected joints	Bilateral group	214 (27.6)	22.7 ± 7.6	} 0.155	
	Unilateral group's affected joint	121 (15.6)	21.3 ± 7.5		
	Total	335 (43.3)	21.0 ± 7.6		
Total		774 (100)	20.7 ± 7.2		

*p < 0.05, statistically significant; SD — standard deviation

Table 3. Relationship between condylar position, temporomandibular joint osteoarthritis (TMH OA) groups, and mean horizontal condylar angle (HCA), number (%) and the statistical analysis results

Condylar position: TMJ OA groups and HCA (joints)		Control group, n (%)	Unilateral group, n (%)				Bilateral group, n (%)	Mean HCA ± SD (degree)
			Affected joints	Unaffected joints	Total	P		
Condylar position	Concentric	84 (26.4)	22 (18.2)	24 (19.8)	46 (19)	0.942[e]	54 (25.2)	20.6 ± 6.7
	Posterior	111 (34.9)	62 (51.2)	60 (49.6)	122 (50.4)		105 (49.1)	21.1 ± 7.8
	Anterior	123 (38.7)	37 (30.6)	37 (30.6)	74 (30.6)		55 (25.7)	20.2 ± 7.9
P		0.023[a]*	0.000[b]**	0.000[c]**	0.000[d]**		0.000[f]**	0.408[g]
				0.000[h]**				

*p < 0.05, **p < 0.01, statistically significant; SD — standard deviation; [a]comparison of condylar position frequencies in the control group; [b]comparison of condylar position frequencies of affected joints in the unilateral group; [c]comparison of condylar position frequencies of unaffected joints in the unilateral group; [d]comparison of condylar position frequencies in the unilateral group; [e]comparison of condylar position frequencies and OA status in the unilateral group; [f]comparison of condylar position frequencies in the bilateral group; [g]comparison of mean HCAs according to condylar positions; [h]comparison of condylar position frequencies according to TMJ OA groups

the unaffected joints in the unilateral group was not statistically significant (p = 0.852 > 0.05) (Table 2). Similarly, the difference between the mean HCAs of all joints in the bilateral group (both affected) and the affected joints in the unilateral group was not statistically significant (p = 0.155 > 0.05) (Table 2). However, while in total patients the difference between the mean HCAs of the unaffected joints and the affected joints was statistically significant (p = 0.0001 < 0.001) (Table 2), in the unilateral group, the difference between the mean HCAs of the unaffected joints and the affected joints was not statistically significant (p = 0.085 > 0.05).

The distribution of joints according to condylar positions and their mean HCAs were n = 184 (23.8%) in the concentric position with 20.6 ± 6.7° mean HCA, n = 338 (43.7%) in the posterior position with 21.1 ± 7.8° mean HCA, and n = 252 (32.5%) in the anterior position with 20.2 ± 7.9° mean HCA. The difference between the mean HCAs of the three condylar positions was not statistically significant (p = 0.408 > 0.05) (Table 3).

The relationship between the TMJ OA groups and the condylar position was statistically significant (p = 0.000 < 0.01) (Table 3). However, in the unilateral group, the relationship between the joints' OA

Table 4. Distribution of mean horizontal condylar angles (HCA) of temporomandibular joint osteoarthritis (TMJ OA) groups by sexes, number (%) and the statistical analysis results

Variables		Sexes				P
		Female		Male		
		N (%)	Mean HCA ± SD (degree)	N (%)	Mean HCA ± SD (degree)	
TMJ OA groups	Control	88 (39.1)	19.3 ± 6.4	71 (43.8)	19.8 ± 6.4	0.659
	Unilateral	69 (30.1)	21.5 ± 6.3	52 (32.1)	19.1 ± 6.5	0.039*
	Bilateral	68 (30.2)	22.9 ± 7.9	39 (24.1)	22.4 ± 7.2	0.711
Total		225 (100)	21.1 ± 6.9	162 (100)	20.2 ± 6.7	0.196

*p < 0.05, statistically significant; SD — standard deviation

status and the condylar positions was not statistically significant (p = 0.942 > 0.05) (Table 3). That is, the condylar positions distribution of the affected and unaffected joints in the unilateral group was similar. When we analysed each TMJ OA group independently according to the condylar position, mostly the posterior (except for the control group) and least the concentric condylar position was observed, and the differences were statistically significant (p < 0.05) (Table 3).

In the unilateral group, the mean value of the difference between the affected joints' HCAs and the unaffected joints' HCAs was positive, as 1.6 ± 6.5°. It was positive (5.7 ± 4.8°) in 70 (57.9%) patients, while negative (–3.9 ± 4.1°) in 51 (42.1%) patients, and the difference was statistically significant (p = 0.000 < 0.001).

According to TMJ OA groups, the mean HCAs of the sexes were close to each other in the control group, bilateral group, and in total patients, and the difference was not statistically significant (p > 0.05) (Table 4). Only in the unilateral group, the mean HCA of the females was greater than the males', and the difference was statistically significant (p = 0.039 < 0.05) (Table 4). Additionally, the correlation between the HCA and age was negatively and not statistically significantly (rs = –0.054, p = 0.436 > 0.05).

DISCUSSION

In the present study, the relationship between HCA, TMJ OA, and condylar position was evaluated by CBCT. The authors observed that HCA increased in the presence of TMJ OA, but no relationship between HCA and different condylar positions. In literature, various radiological imaging modalities such as submentovertex projection radiography (SPR) [3, 8, 25, 36, 38], magnetic resonance imaging (MRI) [6, 12, 13, 29, 32, 35], computed tomography (CT) [5, 9, 15, 23, 27, 33], and CBCT [2, 14] have been used alone or

combined in studies for measuring the HCA to date. In studies that used SPR, the HCA was found associated with disc position while not associated with osseous changes [8, 25, 36, 38]. In MRI studies, generally, a greater mean HCA was reported in TMJs with disc displacement and osseous changes [6, 13, 27, 29, 31, 35, 36]. Considering that TMJ OA was more common with initial and prolonged disc displacement [37], the findings of the present study overlapped these studies. Although the osseous structures of TMJ could be evaluated with MRI, it is superior in evaluating the soft tissues [17]. Additionally, in the context of HCA measurement, MRI has a low spatial resolution and few available axial sections and is not suitable for the secondary image reconstruction like CBCT [14]. In studies that used CT to evaluate the osseous structures or disc position in addition to HCA measurements, it was reported that the mean HCA increased in the case of osseous changes and disc displacement in TMJ [5, 15, 27]. In their prospective longitudinal study, Lee et al. [15] observed a mean 2.83° increase of the HCA in joints that developed OA over time and the increase did not regress even in rare cases where morphological osseous changes were reversed. They stated TMJ OA may cause a greater HCA, but an initially great HCA did not affect the development of TMJ OA [15]. Seo et al. [27] claimed the joints with greater HCAs could be explained by OA changes that were thought to be associated with disc displacement. The results authors reached in the present study showed similarity to the studies that examined the osseous changes of TMJ radiologically on CT.

Because it is an effective imaging modality for evaluating structural changes in the osseous morphology of TMJ, for both determination of the TMJ OA and the measurement of the HCA the CBCT was used in the current study [7]. In terms of TMJ OA groups, the mean HCA of the patients in the bilat-

eral group was greater than both the control and unilateral groups, and the difference was statistically significant. However, although the mean HCA of the patients in the unilateral group was greater than those in the control group, the difference was not statistically significant. When focused on the unilateral group, the mean HCA of the affected joints was greater than the unaffected joints, and the difference was statistically significant. In addition, the difference between the mean HCAs of total affected joints and total unaffected joints was also statistically significant. However, when the mean HCAs of similar joints in terms of OA in different groups were compared, the difference was not statistically significant. The results of the present study, which showed TMJ OA was associated with increased HCA, were consistent with each other and similar studies. In a CBCT study, Lee et al. [14] found the mean HCA was greater in OA-affected joints than the contralateral OA-unaffected joints, in the TMJ OA unilateral group, and the difference was statistically significant. However, the difference between the mean HCA of both joints of the control subjects and the mean HCA of the unaffected joints of the unilateral OA patients was not statistically significant [14]. These findings were exactly consistent with the present study. A clinical TMD study that used CBCT only to measure the HCA found a greater mean HCA in the control group [2], unlike the present study findings. That result may have arisen because there is no correlation between osseous changes in TMJ and clinical symptoms, including pain [20].

Another parameter examined was the relationship between condylar position and both TMJ OA and HCA. The authors did not find any studies in the literature investigating the relationship between condylar position and HCA. However, some studies found the posterior condylar position was associated with any TMD [18, 22, 28]. Cho et al. [4] concluded the posterior condylar position was more common in joints with osseous changes. The results obtained showed that the frequency of posterior condyle position was higher in the unilateral and bilateral TMJ OA groups compared to the control group. As the posterior condylar position was generally accepted as associated with disc displacement, OA, and clinical TMDs, these results were expected. In addition, although it was not addressed previously, the mean HCAs of three condylar positions were found close to each other.

Hüls et al. [11] reported a greater mean value for the difference between the right and left joints HCAs in TMD patients compared to the asymptomatic group. Taylor et al. [30] investigated the difference between the right and left joints HCAs only in asymptomatic adults. Sulun et al. [29] also indicated this difference was greater in patients with internal derangement than in the asymptomatic volunteers. From a different perspective, in the present study for each patient in the TMJ OA unilateral group the difference between the HCAs of the affected and unaffected joints, not the right and left joints, were examined. In the unilateral group, the mean value of this difference was found positive. Additionally, in the same group, the frequency of patients with positive value was higher than the patients with negative value, and the difference was statistically significant.

In many studies, like the present study, the relationship between the HCA and sexes and age was not found statistically significant [6, 15, 29, 35]. Contrary to these studies, Al-Rawi et al. [2] found a greater mean HCA for males both in TMD and control groups, but interestingly, the statistical difference was only in the control group. Christiansen et al. [5] found the HCA was positively significantly correlated with age.

Limitations of the study

This study had limitations. The dentition status of the patients and the presence or absence of mandibular asymmetry were not considered. Theoretically, the HCA could be affected by both parameters. In addition, due to the lack of clinical information, the HCA changes in the presence or absence of clinical signs of TMD could not evaluate.

CONCLUSIONS

The mean HCA of the bilateral group was statistically significantly greater than the control and unilateral groups. Unlike in the unilateral group, when all patients were considered, the mean HCA of the affected joints was greater than the unaffected joints. There was no statistically significant difference between the mean HCA values of the joints with the concentric, posterior, and anterior condylar positions. Posteriorly located condyles were observed more in the bilateral and unilateral TMJ OA groups, and anteriorly located condyles were observed more often in the control group. The mean HCAs of females and males were close. The results showed TMJ OA-related osseous changes positioned the condyle posteriorly in

the anteroposterior direction and rotated its position relative to the cranium resulting in an increase in HCA. While an undeniably strong relationship between the TMJ OA and the greater HCA was demonstrated, it is not easy to make a full judgment in the context of a cause-effect relationship. Although several studies investigated the HCA of patients with TMD and TMJ OA findings, the diagnostic value of this phenomenon has still been unclear because of various HCA values reported.

Conflict of interest: None declared

REFERENCES

1. Ahmad M, Hollender L, Anderson Q, et al. Research diagnostic criteria for temporomandibular disorders (RDC/TMD): development of image analysis criteria and examiner reliability for image analysis. Oral Surg Oral Med Oral Pathol Oral Radiol Endod. 2009; 107(6): 844–860, doi: 10.1016/j.tripleo.2009.02.023, indexed in Pubmed: 19464658.
2. Al-Rawi NH, Uthman AT, Sodeify SM. Spatial analysis of mandibular condyles in patients with temporomandibular disorders and normal controls using cone beam computed tomography. Eur J Dent. 2017; 11(1): 99–105, doi: 10.4103/ejd.ejd_202_16, indexed in Pubmed: 28435374.
3. Benson BW, Frederiksen NL. A reliability comparison of submentovertex and zonographic methods of horizontal condylar angle estimation. Oral Surg Oral Med Oral Pathol Oral Radiol Endod. 1998; 86(3): 370–375, doi: 10.1016/s1079-2104(98)90187-1, indexed in Pubmed: 9768430.
4. Cho BH, Jung YH. Osteoarthritic changes and condylar positioning of the temporomandibular joint in Korean children and adolescents. Imaging Sci Dent. 2012; 42(3): 169–174, doi: 10.5624/isd.2012.42.3.169, indexed in Pubmed: 23071967.
5. Christiansen EL, Thompson JR, Kopp SF, et al. Radiographic signs of temporomandibular joint diseases: an investigation utilizing X-ray computed tomography. Dentomaxillofac Radiol. 1985; 14(2): 83–91, doi: 10.1259/dmfr.1985.0011, indexed in Pubmed: 3869568.
6. Crusoé-Rebello IM, Campos PS, Rubira IR, et al. Evaluation of the relation between the horizontal condylar angle and the internal derangement of the TMJ — a magnetic resonance imaging study. Pesqui Odontol Bras. 2003; 17(2): 176–182, doi: 10.1590/s1517-74912003000200015, indexed in Pubmed: 14569363.
7. Derwich M, Mitus-Kenig M, Pawlowska E. Interdisciplinary approach to the temporomandibular joint osteoarthritis-review of the literature. Medicina (Kaunas). 2020; 56(5), doi: 10.3390/medicina56050225, indexed in Pubmed: 32397412.
8. Ebner KA, Otis LL, Zakhary R, et al. Axial temporomandibular joint morphology: a correlative study of radiographic and gross anatomic findings. Oral Surg Oral Med Oral Pathol. 1990; 69(2): 247–252, doi: 10.1016/0030-4220(90)90336-q, indexed in Pubmed: 2304751.
9. Eisenburger M, Haubitz B, Schmelzeisen R, et al. The human mandibular intercondylar angle measured by computed tomography. Arch Oral Biol. 1999; 44(11): 947–951, doi: 10.1016/s0003-9969(99)00085-0, indexed in Pubmed: 10580542.
10. Ha MH, Kim YI, Park SB, et al. Cone-beam computed tomographic evaluation of the condylar remodeling occurring after mandibular set-back by bilateral sagittal split ramus osteotomy and rigid fixation. Korean J Orthod. 2013; 43(6): 263–270, doi: 10.4041/kjod.2013.43.6.263, indexed in Pubmed: 24396735.
11. Hüls A, Schulte W, Voigt K. Neue Aspekte der Myoarthropathien durch die computertomographie. Dtsch Zahnarztl Z. 1981; 36(12): 776–786.
12. Junhasavasdikul T, Abadeh A, Tolend M, et al. Developing a reference MRI database for temporomandibular joints in healthy children and adolescents. Pediatr Radiol. 2018; 48(8): 1113–1122, doi: 10.1007/s00247-018-4142-8, indexed in Pubmed: 29789889.
13. Kurita H, Ohtsuka A, Kobayashi H, et al. Relationship between increased horizontal condylar angle and resorption of the posterosuperior region of the lateral pole of the mandibular condyle in temporomandibular joint internal derangement. Dentomaxillofac Radiol. 2003; 32(1): 26–29, doi: 10.1259/dmfr/23245517, indexed in Pubmed: 12820850.
14. Lee PP, Stanton AR, Hollender LG. Greater mandibular horizontal condylar angle is associated with temporomandibular joint osteoarthritis. Oral Surg Oral Med Oral Pathol Oral Radiol. 2017; 123(4): 502–507, doi: 10.1016/j.oooo.2016.12.008, indexed in Pubmed: 28189528.
15. Lee PP, Stanton AR, Schumacher AE, et al. Osteoarthritis of the temporomandibular joint and increase of the horizontal condylar angle: a longitudinal study. Oral Surg Oral Med Oral Pathol Oral Radiol. 2019; 127(4): 339–350, doi: 10.1016/j.oooo.2018.12.014, indexed in Pubmed: 30709753.
16. Mischkowski RA, Pulsfort R, Ritter L, et al. Geometric accuracy of a newly developed cone-beam device for maxillofacial imaging. Oral Surg Oral Med Oral Pathol Oral Radiol Endod. 2007; 104(4): 551–559, doi: 10.1016/j.tripleo.2007.02.021, indexed in Pubmed: 17613260.
17. Ohlmann B, Rammelsberg P, Henschel V, et al. Prediction of TMJ arthralgia according to clinical diagnosis and MRI findings. Int J Prosthodont. 2006; 19(4): 333–338, indexed in Pubmed: 16900815.
18. Paknahad M, Shahidi S. Association between mandibular condylar position and clinical dysfunction index. J Craniomaxillofac Surg. 2015; 43(4): 432–436, doi: 10.1016/j.jcms.2015.01.005, indexed in Pubmed: 25770652.
19. Paknahad M, Shahidi S, Iranpour S, et al. Cone-beam computed tomographic assessment of mandibular condylar position in patients with temporomandibular joint dysfunction and in healthy subjects. Int J Dent. 2015; 2015: 301796, doi: 10.1155/2015/301796, indexed in Pubmed: 26681944.
20. Palconet G, Ludlow JB, Tyndall DA, et al. Correlating cone beam CT results with temporomandibular joint pain of osteoarthritic origin. Dentomaxillofac Radiol. 2012; 41(2): 126–130, doi: 10.1259/dmfr/60489374, indexed in Pubmed: 22116122.

21. Pullinger A, Hollender L, Solberg W, et al. A tomographic study of mandibular condyle position in an asymptomatic population. J Prosthet Dent. 1985; 53(5): 706–713, doi: 10.1016/0022-3913(85)90029-0.

22. Pullinger AG, Solberg WK, Hollender L, et al. Tomographic analysis of mandibular condyle position in diagnostic subgroups of temporomandibular disorders. J Prosthet Dent. 1986; 55(6): 723–729, doi: 10.1016/0022-3913(86)90450-6, indexed in Pubmed: 3459874.

23. Raustia AM, Pyhtinen J. Morphology of the condyles and mandibular fossa as seen by computed tomography. J Prosthet Dent. 1990; 63(1): 77–82, doi: 10.1016/0022-3913(90)90271-d, indexed in Pubmed: 2295990.

24. Robinson de Senna B, Marques LS, França JP, et al. Condyle-disk-fossa position and relationship to clinical signs and symptoms of temporomandibular disorders in women. Oral Surg Oral Med Oral Pathol Oral Radiol Endod. 2009; 108(3): e117–e124, doi: 10.1016/j.tripleo.2009.04.034, indexed in Pubmed: 19716481.

25. Sato H, Fujii T, Kitamori H. The clinical significance of the horizontal condylar angle in patients with temporomandibular disorders. Cranio. 1997; 15(3): 229–235, doi: 10.1080/08869634.1997.11746016, indexed in Pubmed: 9586502.

26. Scarfe WC, Farman AG, Sukovic P. Clinical applications of cone-beam computed tomography in dental practice. J Can Dent Assoc. 2006; 72(1): 75–80, indexed in Pubmed: 16480609.

27. Seo BY, An JS, Chang MS, et al. Changes in condylar dimensions in temporomandibular joints with disk displacement. Oral Surg Oral Med Oral Pathol Oral Radiol. 2020; 129(1): 72–79, doi: 10.1016/j.oooo.2019.04.010, indexed in Pubmed: 31109845.

28. Shokri A, Zarch HH, Hafezmaleki F, et al. Comparative assessment of condylar position in patients with temporomandibular disorder (TMD) and asymptomatic patients using cone-beam computed tomography. Dent Med Probl. 2019; 56(1): 81–87, doi: 10.17219/dmp/102946, indexed in Pubmed: 30951623.

29. Sülün T, Akkayan B, Duc JM, et al. Axial condyle morphology and horizontal condylar angle in patients with internal derangement compared to asymptomatic volunteers. Cranio. 2001; 19(4): 237–245, doi: 10.1080/08869634.2001.11746174, indexed in Pubmed: 11725847.

30. Taylor R, Ware W, Fowler D, et al. A study of temporomandibular joint morphology and its relationship to the den-tition. Oral Surgery, Oral Medicine, Oral Pathology. 1972; 33(6): 1002–1013, doi: 10.1016/0030-4220(72)90192-2.

31. Teng HD, Shu JH, Sun TH, et al. [Three-dimensional morphological changes in the temporomandibular joints of patients with anterior disc displacement with reduction]. Hua Xi Kou Qiang Yi Xue Za Zhi. 2021; 39(2): 203–208, doi: 10.7518/hxkq.2021.02.012, indexed in Pubmed: 33834676.

32. Torres MG, Crusoé-Rebello IM, Rosário M, et al. Morphometric features of the mandibular condyle and association with disk abnormalities. Oral Surg Oral Med Oral Pathol Oral Radiol. 2016; 121(5): 566–572, doi: 10.1016/j.oooo.2016.01.020, indexed in Pubmed: 27068314.

33. Ueki K, Degerliyurt K, Hashiba Y, et al. Horizontal changes in the condylar head after sagittal split ramus osteotomy with bent plate fixation. Oral Surg Oral Med Oral Pathol Oral Radiol Endod. 2008; 106(5): 656–661, doi: 10.1016/j.tripleo.2008.03.016, indexed in Pubmed: 18602292.

34. Wang XD, Zhang JN, Gan YH, et al. Current understanding of pathogenesis and treatment of TMJ osteoarthritis. J Dent Res. 2015; 94(5): 666–673, doi: 10.1177/0022034515574770, indexed in Pubmed: 25744069.

35. Westesson PL, Bifano JA, Tallents RH, et al. Increased horizontal angle of the mandibular condyle in abnormal temporomandibular joints. A magnetic resonance imaging study. Oral Surg Oral Med Oral Pathol. 1991; 72(3): 359–363, doi: 10.1016/0030-4220(91)90233-3, indexed in Pubmed: 1923427.

36. Westesson PL, Liedberg J. Horizontal condylar angle in relation to internal derangement of the temporomandibular joint. Oral Surg Oral Med Oral Pathol. 1987; 64(4): 391–394, doi: 10.1016/0030-4220(87)90137-x, indexed in Pubmed: 3477757.

37. Westesson PL, Rohlin M. Internal derangement related to osteoarthrosis in temporomandibular joint autopsy specimens. Oral Surg Oral Med Oral Pathol. 1984; 57(1): 17–22, doi: 10.1016/0030-4220(84)90251-2, indexed in Pubmed: 6582426.

38. Williamson PC, Major PW, Nebbe B, et al. Landmark identification error in submentovertex cephalometrics. A computerized method for determining the condylar long axis. Oral Surg Oral Med Oral Pathol Oral Radiol Endod. 1998; 86(3): 360–369, doi: 10.1016/s1079-2104(98)90186-x, indexed in Pubmed: 9768429.

V M
VIA MEDICA

O R I G I N A L   A R T I C L E

Anatomic considerations for immediate implant placement in the mandibular molar region: a cross-sectional study using cone-beam computed tomography

J.Y. Ho[1, 2], W.C. Ngeow[3], D. Lim[3], C.S. Wong[3]

[1]Department of Restorative Dentistry, Faculty of Dentistry, University of Malaya, Kuala Lumpur, Malaysia
[2]Division of Restorative Dentistry, School of Dentistry, International Medical University, Kuala Lumpur, Malaysia
[3]Department of Oral and Maxillofacial Clinical Sciences, Faculty of Dentistry, University of Malaya, Kuala Lumpur, Malaysia

Background: There is concern regarding immediate implantation in the molar region because of discrepancy between socket size and inserted implant diameter. The purpose of this study was to assess the local anatomy of the posterior mandibular region in relation to immediate implant placement using cone-beam computed tomography (CBCT).

Materials and methods: Using CBCT imaging data, 204 mandibular first molars and 201 mandibular second molars were assessed for the interradicular and alveolar bone dimensions, tooth sizes and proximity to vital structures. The cross-sectional mandibular shape and root configuration of these molars were determined.

Results: Distances to the inferior alveolar canal (IAC) from the root apices of the first molar were significantly greater than the second molar. Up to 14.5% of second molars had less than 10 mm of vertical bone height between the IAC and furcation bone crest. Interradicular bone width of < 3 mm was found in 57% of second molars. All first molars in this study had two to three roots while 16% of second molars presented with a single root. The prevalent mandible shape at the first and second molars was the parallel and undercut ridges, respectively.

Conclusions: The mandibular second molars from samples of a Southeast Asian population presented with greater anatomical difficulties for immediate implant placement which include absent or inadequate interradicular bone thickness, higher incidence of unfavourable mandible shape and increased proximity to vital structures. (Folia Morphol 2022; 81, 3: 732–738)

Key words: cone-beam computed tomography, immediate dental implant loading, mandible, molar

INTRODUCTION

Dental implant is a popular treatment modality for replacing missing teeth. Immediate implant placement (IIP) protocol has risen in popularity because it shortens treatment time and reduces the number of surgeries required. However, there is concern regarding immediate implantation in the molar region as there is a discrepancy between the socket size and diameter of implant inserted. The primary stability in such cases is achieved by engaging the implant

fixture into the inter-radicular septal bone. Factors such as the proximity of the inferior alveolar canal (IAC), socket morphology, the availability of adequate inter-radicular septal bone and the presence of lingual concavities need to be considered prior to IIP at the mandibular molar region [15].

The advent of cone-beam computed tomography (CBCT) has revolutionised craniofacial imaging. CBCT presents clinicians with high resolution images of anatomical structures such as bone topography, periodontal ligament, and root morphology. In addition, the CBCT DICOM data generated can be used to design and fabricate a three-dimensional surgical guide to facilitate implant placement in a prosthetically driven position [11].

Previous studies on the morphology of posterior mandible in relation to IIP had been conducted primarily among Caucasoid populations [1, 2, 5–7, 9, 12]. Information pertaining to the Mongoloid (Southeast Asia) population remains scarce. In addition, not all studies looked into the interradicular bone, which is one of the primary areas of bone available for immediate implant anchorage.

This study aimed to evaluate the morphological features of mandibular first (M1) and second (M2) molars and their surrounding structures in a Mongoloid (Southeast Asian) population within the context of immediate implant placement, using CBCT images.

MATERIALS AND METHODS

A cross-sectional CBCT study was conducted at the Department of Oral and Maxillofacial Clinical Sciences, Faculty of Dentistry, University of Malaya between May 2020 and October 2020. Ethical approval was received from the Medical Ethics Committee, Faculty of Dentistry with reference number: DF OS2020/081(L). All patients whose CBCT data was used in this study had provided written consent agreeing to release their imaging data for research/academic purposes.

Cone-beam computed tomography imaging data of patients who visited the Oral Radiology Unit, Faculty of Dentistry, University of Malaya between 2010 and 2015 was screened. Included were Malaysian patients of different ethnicities, aged between 18 and 60 years old, without mandibular deformities, and presenting with M1 and M2 molars on either/both sides of the lower jaw. Excluded were subjects with history of dentoalveolar trauma or mandibular pathology, mixed dentition, poor quality CBCTs and evidence of surgical intervention to the mandible.

The sample size was calculated with the following formula [4]:

$$\text{Sample size} = \frac{Z_{1-\alpha/2}{}^2\, SD^2}{d^2}$$

where $Z_{1-\alpha}$ = standard normal variate; SD = standard deviation of variable measured; d = absolute error or precision.

Based on the standard deviation of 2.61 from a previous study by Chrcanovic et al. [5]:

$$\text{The sample size} = \frac{1.96^2 \times 2.61^2}{0.5^2} = 104.7$$

Primary outcomes were the morphometric measurements of the alveolar and interradicular bone of M1 and M2 and their cross-sectional mandible shapes. Secondary outcomes included proximity to the IAC, root configuration and tooth dimensions.

The CBCT scans were captured using the i-CAT Vision system developed by Imaging Sciences International (Pennsylvania, United States). All images were taken according to a standard protocol. The exposure parameter (120 KvP, 3–7 mA, 20 s) and the image acquisition at 0.3 mm voxel size were done by the same radiographer. The images were obtained from scans acquired with 16 cm (diameter) and 13 cm (height) dimensions, and the DICOM was reconstructed using proprietary i-CAT image reconstruction software. The following measurements were made: root length, distance between cementoenamel junction and the separation lines of the root cones, distance between separation lines of root cones to root apex (Fig. 1A), bucco-lingual and mesio-distal crown width (Fig. 1E), interradicular septal bone thickness (Fig. 2A), bucco-lingual width of cancellous portion of the alveolar bone (Fig. 2B), distance from the IAC to the crest of the interradicular septum and root apex (Fig. 2C, D). The mandible ridge form at M1 and M2 was classified into convex, parallel or undercut type, based on the description by Chan et al. [3] (Fig. 3A–C). The root configurations of M1 and M2 were visualised on cross-sectional slices to detect the presence of C-shaped root, single fused root, or additional roots (Fig. 3D). Data analysis was completed using IBM SPSS Statistics software version 20.

The radiographic measurements were performed by the principal examiner (H.J.Y.) with 3 years of post-graduation experience. For reliability testing, intraclass correlation coefficient (ICC) was determined according to the single measurement, absolute agreement, 2-way mixed effects model by repeating the
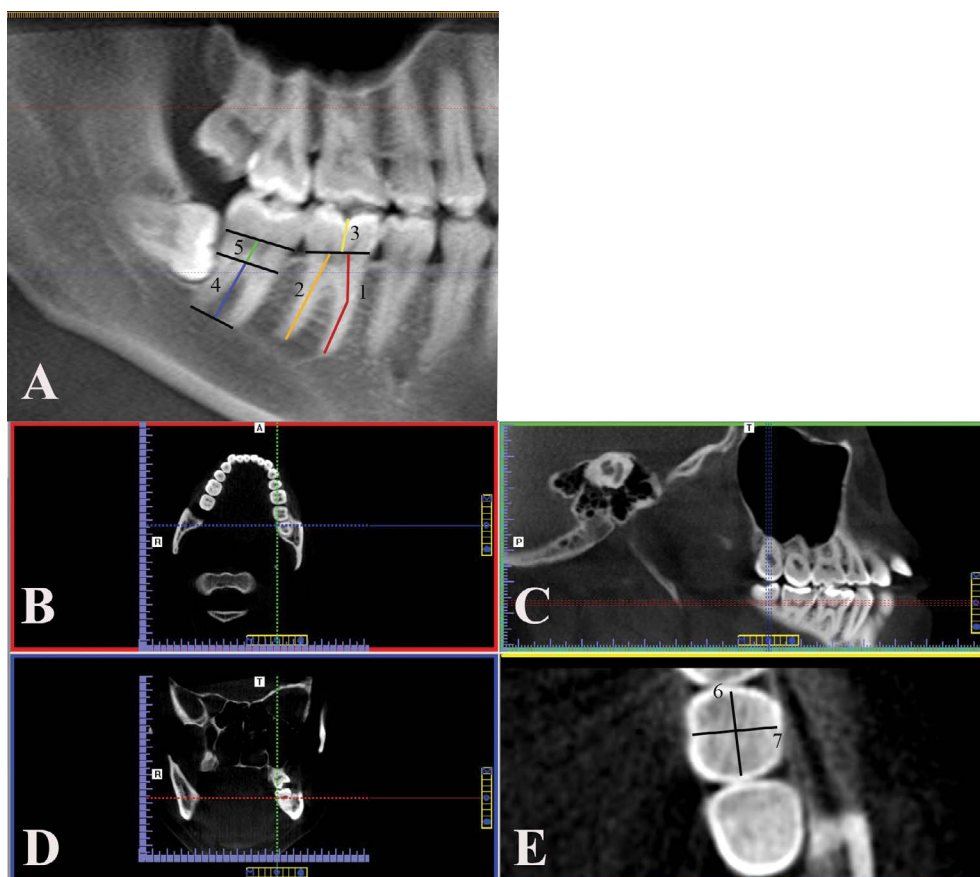
Figure 1. Quantitative measurement of crown and root dimensions; **A.** Panoramic view; **B.** Axial view; **C.** Sagittal view; **D.** Coronal view; **E.** Additional cut planes; 1 — mesial root length; 2 — distal root length; 3 — crown height; 4 — root cone; 5 — root trunk; 6 — mesio-distal crown width; 7 — bucco-lingual crown width.
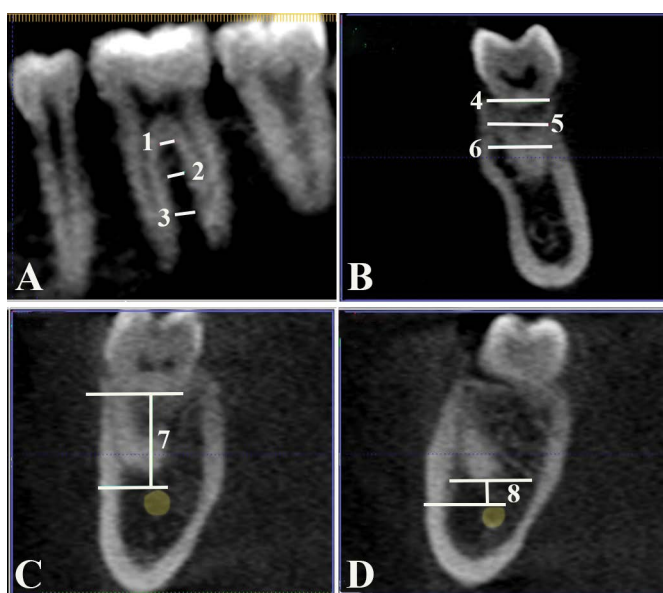

Figure 2. Sagittal and coronal section of the mandible; **A.** Mesio-distal width of interradicular bone at three different levels: crest of interradicular septum (1), 3 mm apical to interradicular septum crest (2), and 6 mm apical to interradicular septum crest (3); **B.** Bucco-lingual width of cancellous bone at three different levels: alveolar crest (4), 3 mm apical to alveolar crest (5) and 6 mm apical to alveolar crest (6); **C.** Distance between interradicular septum crest and inferior alveolar canal (7); **D.** Distance between root apex and inferior alveolar canal (8).

measurements for 30 datasets 2 weeks after the initial measurements. The ICC was 0.985 with a 95% confidence interval (CI) of 0.982–0.988. Therefore, the intra-rater reliability was excellent. An external examiner (W.C.S.) with 5 years of clinical experience was enlisted to determine the inter-rater reliability.
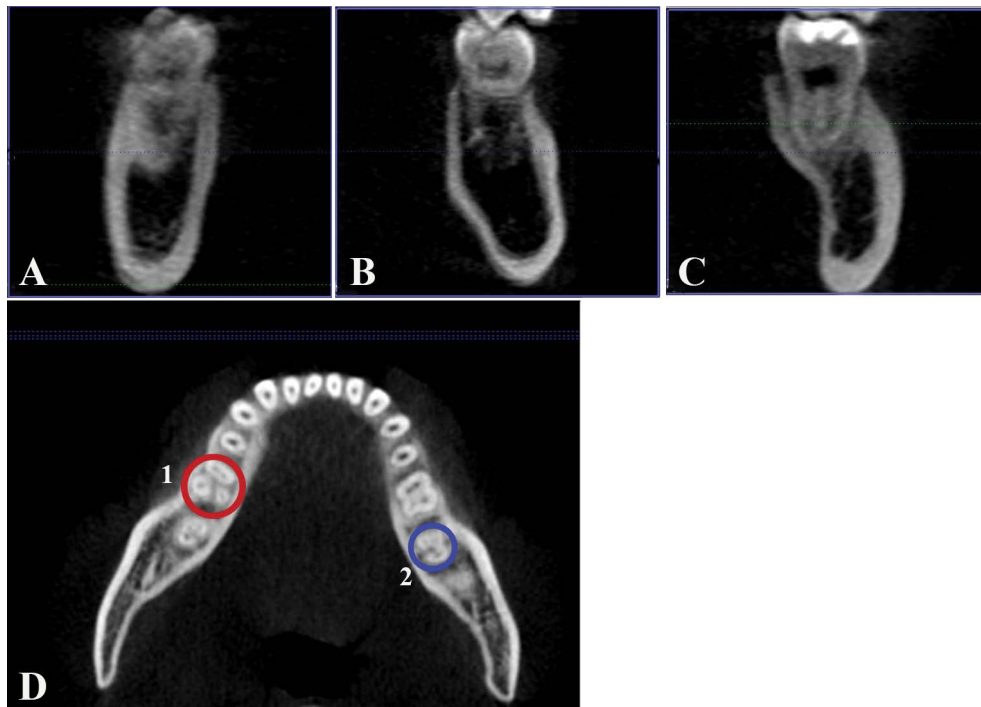
Figure 3. Alveolar ridge classification and anatomical variation of mandibular molar roots; **A.** Parallel type; **B.** Convergent type; **C.** Undercut type; **D.** 1— radix entomolaris; 2 — C-shaped root.

Table 1. Demographic data of study population

Age [year] (mean ± SD)		36 ± 11.92
Gender, n (%)	Male	70 (63.6%)
	Female	40 (36.4%)
Race, n (%)	Malay	46 (41.8%)
	Chinese	37 (33.6%)
	Indian	22 (20%)
	Others	5 (4.5%)

SD — standard deviation

Both of them had been calibrated with the senior supervisor in oral and maxillofacial surgery with 14 years of experience in using CBCT (W.C.N.) prior to the commencement of this study. The same ICC model was calculated, resulting in the ICC of 0.94 with a 95% CI of 0.88–0.97. Therefore, the level of reliability between different examiners was deemed as good to excellent.

Frequency distribution and descriptive statistics for each measurement were calculated. The normality of data was assessed using the Kolmogorov-Smirnov test. Independent samples t-test and Pearson χ^2 test were used to compare findings between groups. A p-value of less than 0.05 was considered as statistically significant.

RESULTS

The study population had a mean age of 35.9 ± ± 11.9 years. There were more males (64.5%) than females (35.5%) whose CBCT were included. The greatest proportion of the participants was Malay (41.8%), followed by the Chinese (33.6%) and Indian (20%) ethnicity (Table 1).

Two hundred four M1 and 201 M2 were analysed, with no significant difference found between contralateral sides (p > 0.05). The crown size of M1 was not significantly different than M2. All M1 had divergent roots while 16% of M2 were found to have fused roots (Table 2). M2 had significantly reduced interradicular bone thickness, greater alveolar bone width and closer proximity to the IAC compared to M1 (p < 0.001) (Fig. 4). Interradicular bone width < 3 mm was found in 76.8% of M2 and 44.6% of M1 (Table 3). Furcation to IAC distance of less than 10 mm was found in 3% of M1 and 13.4% of M2 (Table 3).

There was a significant association between tooth type and both ridge form and root configuration (p < 0.001). The most common ridge form at the M1 region was the parallel type (70.2%). The undercut ridge form was found in the majority (73.1%) of M2 (Table 2). The distance to the IAC of female subjects was shorter when measured from the crest of the

Table 2. Tooth dimensions, mandible shape and root configuration of the first and second mandibular molars

	M1 (mean ± SD)	M2 (mean ± SD)	P-value[a]
Crown size [mm]:			
Height	5.65 ± 0.90	5.74 ± 0.86	0.30
Mesio-distal	10.45 ± 0.76	10.22 ± 0.77	0.002*
Bucco-lingual	9.41 ± 0.86	9.44 ± 0.76	0.74
Root length [mm]:			
Mesial	12.83 ± 1.64	11.61 ± 1.76	< 0.001*
Distal	12.31 ± 1.54	11.04 ± 1.56	< 0.001*
Root complex [mm]:			
Root trunk	3.33 ± 0.55	3.36 ± 0.51	0.64
Root cone	9.83 ± 1.19	8.83 ± 1.17	< 0.001*

	M1 n (%)	M2 n (%)	P-value[b]
Mandible cross-sectional shape:			
Parallel	138 (70.8%)	48 (25.3%)	< 0.001*
Convergent	9 (4.6%)	2 (1.1%)	
Undercut	48 (24.6%)	140 (73.7%)	
Root configuration:			
Single conical root	0 (0%)	11 (5.7%)	< 0.001*
Double roots	174 (89.7%)	162 (83.5%)	
Three roots	20 (10.3%)	1 (0.5%)	
C-shaped root	0 (0%)	29 (10.3%)	

*Denote statistical significance (p < 0.05); [a]Independent samples t-test; [b]Pearson χ^2 test; M1 — mandibular 1st molar; M2 — mandibular 2nd molar; SD — standard deviation

Table 3. Proportion of teeth with compromised recipient site for immediate implants

Tooth	IRB < 3 mm	F-IAC < 10 mm	M-IAC < 2 mm	D-IAC < 2 mm
M1	86/193 (44.6%)	6/204 (3%)	14/204 (6.9%)	18/204 (8.8%)
M2	116/151 (76.8%)	27/201 (13.4%)	40/201 (20%)	67/191 (35%)

M1 — mandibular 1st molar; M2 — mandibular 2nd molar; IRB — interradicular bone width; F-IAC — bone height between furcation crest and inferior alveolar canal; M-IAC — bone height between mesial root apex and inferior alveolar canal; D-IAC — bone height between distal root apex and inferior alveolar canal

Figure 4. Bar graph demonstrating interradicular bone width (**A**), alveolar bone width (**B**) and proximity to inferior alveolar canal for mandibular first (M1) and mandibular second (M2) (**C**); IRB-0 — interradicular bone width at furcation crest; IRB-3 — interradicular bone width 3 mm apical to furcation crest; IRB-6 — interradicular bone width 6 mm apical to furcation crest; BLW-0 — bucco-lingual alveolar bone width at alveolar crest; BLW-3 — bucco-lingual alveolar bone width 3 mm apical to alveolar crest; BLW-6 — bucco-lingual alveolar bone width 6 mm apical to alveolar crest; F-IAC — bone height between furcation crest and inferior alveolar canal; M-IAC — bone height between mesial root apex and inferior alveolar canal; D-IAC — bone height between distal root apex and inferior alveolar canal; *indicates statistically significant difference between M1 and M2 (p < 0.05).

interradicular septum and mesial root apex (p < 0.05). On the other hand, males possessed greater root cone height of M1 and M2 than females (p < 0.05).

DISCUSSION

In immediate molar implantation, the socket size is large when compared to the diameter of standard implants. When inter-radicular septal bone is inadequate to provide primary stability, clinicians are advised to insert implant fixtures into the bone beyond the inter-dental base to achieve primary stability [15].

Dimensional changes of the external socket walls were reported to be more pronounced at the buccal aspect following IIP of molars [10]. Bucco-lingually, we observed a cancellous bone width of > 8.5 mm at M1 and > 9.5 mm at M2, so hypothetically, even when resorption is factored in, there shall be adequate bone to receive a wide diameter (≥ 4.5 mm) implant with little risk of thread exposure bucco-lin-

gually [13]. Mesiodistally, both M1 and M2 showed incremental width of the inter-radicular septal bone apically, due to the mesio-distal convergence of their roots. The average distance from the crest of the interradicular septum to the IAC was greater than 12 mm for both M1 and M2. A distance of less than 10 mm was found in 2.7% of M1 sites and 14.5% of M2 sites. Taken together these findings suggested that it is safe to insert a 10 mm-length implant into the inter-radicular septal bone of M1 without risking protrusion into the IAC. Combined with the finding that parallel mandible shape was predominant in about 70% of M1, the risk of immediate implant perforation into the sublingual fossa is lesser in M1 than M2.

As the prevalent mandible shape at M2 was the undercut type (73.1%), immediate implantation at this site is accompanied by a higher risk of lingual plate perforation. Moreover, 16% of M2 had a single root; therefore the immediate implant cannot engage the inter-radicular septal bone as it is non-existent. Instead, it shall be inserted into the apical bone. Vertically, most literatures recommended that implant should be placed at least > 3 mm apical to the extraction site [14]. Extra precaution is warranted, because even for two-rooted M2, the mesial and distal roots to IAC distances for M2 were on average, 3.78 ± 2.31 mm and 3.03 ± 2.24 mm, respectively. These reduced distances as compared to M1 may not permit immediate implant placement into the socket of M2 without risking damage to the inferior alveolar neurovascular bundle.

While the above information suggested that vertically it is safe to place a 10 mm long implant into the inter-radicular septal bone, its mesio-distal width is just sufficient to receive a standard diameter implant. Smith and Tarnow [15] proposed a classification system for molar extraction sites for immediate implant placement. Type A socket is the situation when an implant is completely fixed within the septal bone, without gaps between the implant and the socket walls. In type B socket, the implant has adequate but incomplete septal bone, resulting in gaps following implant insertion. Lastly, type C socket has insufficient septal bone, resulting in the need to engage the implant at the periphery of extraction sockets [15]. The current findings suggested that the majority of extraction sockets belonged to type B in M1 and M2, with type C observed in 16% of M2. In type C sockets, the primary stability will be provided by buccal, lingual and apical trabecular bone.

The geometry and anatomy of the mandible are crucial aspects that need to be considered carefully prior to immediate implantation. Previous studies observed that the undercut shaped ridge was the most common mandibular geometry at the posterior region [5, 9]. According to a virtual IIP simulation study, lingual bone plate perforation was more prevalent in U-shaped ridges, and more frequently affected the M2 sites [8, 16]. Similar findings regarding the anatomical limitations of M2 in relation to the IAC and sublingual fossa were observed in this study, which confirmed the findings of several studies [5–7, 9]. In contrast, the present study found that M2 demonstrated greater bucco-lingual width than M1. This broad alveolar crest observed easily allows for delayed implant treatment protocol. All facts considered, more M2 sockets observed in this study were not ideal for immediate implantation, as compared to M1.

Regarding gender differences in the parameters measured, our findings suggested that the distance of the IAC to the interradicular bony septum crest and mesial root apex was significantly lesser among female subjects. Therefore, female patients will face a higher risk of inferior alveolar neurovascular bundle injury when the apical bone was used to achieve primary stability.

Limitations of the study

The limitation of this study is that non-probability sampling method was used which might introduce selection bias. Therefore, inferences drawn from the data for the entire Malaysian population should be interpreted with caution. Moreover, the exact implications of these anatomical features during immediate implantation could be better appreciated with virtual implant simulation.

CONCLUSIONS

This study showed that the inter-radicular bone of two-rooted M1 and M2, and the periphery of M2 sockets with fused roots are possible sites for immediate implant placement. However, M2 sockets may be less ideal for immediate implantation on the account of their variable anatomy.

Conflict of interest: None declared

REFERENCES

1. Agostinelli C, Agostinelli A, Berardini M, et al. Radiological evaluation of the dimensions of lower molar alveoli. Implant Dent. 2018; 27(3): 271–275, doi: 10.1097/ID.0000000000000757, indexed in Pubmed: 29652756.

2. Braut V, Bornstein MM, Lauber R, et al. Bone dimensions in the posterior mandible: a retrospective radiographic study using cone beam computed tomography. Part 1 — analysis of dentate sites. Int J Periodontics Restorative Dent. 2012; 32(2): 175–184, indexed in Pubmed: 22292147.

3. Chan HL, Brooks SL, Fu JH, et al. Cross-sectional analysis of the mandibular lingual concavity using cone beam computed tomography. Clin Oral Implants Res. 2011; 22(2): 201–206, doi: 10.1111/j.1600-0501.2010.02018.x, indexed in Pubmed: 21044167.

4. Charan J, Biswas T. How to calculate sample size for different study designs in medical research? Indian J Psychol Med. 2013; 35(2): 121–126, doi: 10.4103/0253-7176.116232, indexed in Pubmed: 24049221.

5. Chrcanovic BR, de Carvalho Machado V, Gjelvold B. Immediate implant placement in the posterior mandible: A cone beam computed tomography study. Quintessence Int. 2016; 47(6): 505–514, doi: 10.3290/j.qi.a36008, indexed in Pubmed: 27092357.

6. Froum S, Casanova L, Byrne S, et al. Risk assessment before extraction for immediate implant placement in the posterior mandible: a computerized tomographic scan study. J Periodontol. 2011; 82(3): 395–402, doi: 10.1902/jop.2010.100360, indexed in Pubmed: 20809864.

7. Haj Yahya B, Chaushu G, Hamzani Y. Computed tomography for the assessment of the potential risk after implant placement in fresh extraction sites in the posterior mandible. J Oral Implantol. 2021; 47(1): 2–8, doi: 10.1563/aaid-joi-D-18-00227, indexed in Pubmed: 32662837.

8. Huang RY, Cochran DL, Cheng WC, et al. Risk of lingual plate perforation for virtual immediate implant placement in the posterior mandible: A computer simulation study. J Am Dent Assoc. 2015; 146(10): 735–742, doi: 10.1016/j.adaj.2015.04.027, indexed in Pubmed: 26409983.

9. Lin MH, Mau LP, Cochran DL, et al. Risk assessment of inferior alveolar nerve injury for immediate implant placement in the posterior mandible: a virtual implant placement study. J Dent. 2014; 42(3): 263–270, doi: 10.1016/j.jdent.2013.12.014, indexed in Pubmed: 24394585.

10. Matarasso S, Salvi GE, Iorio Siciliano V, et al. Dimensional ridge alterations following immediate implant placement in molar extraction sites: a six-month prospective cohort study with surgical re-entry. Clin Oral Implants Res. 2009; 20(10): 1092–1098, doi: 10.1111/j.1600-0501.2009.01803.x, indexed in Pubmed: 19719737.

11. Nagarajan A, Perumalsamy R, Thyagarajan R, et al. Diagnostic imaging for dental implant therapy. J Clin Imaging Sci. 2014; 4(Suppl 2): 4, doi: 10.4103/2156-7514.143440, indexed in Pubmed: 25379354.

12. Padhye NM, Shirsekar VU, Bhatavadekar NB. Three-dimensional alveolar bone assessment of mandibular first molars with implications for immediate implant placement. Int J Periodontics Restorative Dent. 2020; 40(4): e163–e167, doi: 10.11607/prd.4614, indexed in Pubmed: 32559042.

13. Renouard F, Nisand D. Impact of implant length and diameter on survival rates. Clin Oral Implants Res. 2006; 17(Suppl 2): 35–51, doi: 10.1111/j.1600-0501.2006.01349.x, indexed in Pubmed: 16968380.

14. Schwartz-Arad D, Chaushu G. The ways and wherefores of immediate placement of implants into fresh extraction sites: a literature review. J Periodontol. 1997; 68(10): 915–923, doi: 10.1902/jop.1997.68.10.915, indexed in Pubmed: 9358358.

15. Smith RB, Tarnow DP. Classification of molar extraction sites for immediate dental implant placement: technical note. Int J Oral Maxillofac Implants. 2013; 28(3): 911–916, doi: 10.11607/jomi.2627, indexed in Pubmed: 23748327.

16. Wang TY, Kuo PJ, Fu E, et al. Risks of angled implant placement on posterior mandible buccal/lingual plated perforation: A virtual immediate implant placement study using CBCT. J Dent Sci. 2019; 14(3): 234–240, doi: 10.1016/j.jds.2019.03.005, indexed in Pubmed: 31528250.

VIA MEDICA

ORIGINAL ARTICLE

Evaluation of the effects of Ankaferd haemostat application on bone regeneration in rats with calvarial defects: histochemical, immunohistochemical and scintigraphic study

M. Turgut[1, 2] , S. Karademir[2], H.K. Başaloğlu[2, 3] , C. Tomruk[4] , E.O. Cetin[5] ,
Y. Uyanikgil[4, 6, 7] , A. Cengiz[8]

[1]Department of Neurosurgery, Aydın Adnan Menderes University, Faculty of Medicine, Aydın, Turkey
[2]Department of Histology and Embryology, Aydın Adnan Menderes University, Health Sciences Institute, Aydın, Turkey
[3]Department of Histology and Embryology, Aydın Adnan Menderes University, Faculty of Medicine, Aydın, Turkey
[4]Department of Histology and Embryology, Ege University, Faculty of Medicine, Izmir, Turkey
[5]Department of Pharmaceutical Technology, Department of Biopharmaceutics and Pharmacokinetics,
Ege University Faculty of Pharmacy, Izmir, Turkey
[6]Department of Stem Cell, Ege University, Health Science Institue, Izmir, Turkey
[7]Cord Blood, Cell and Tissue Research and Application Centre, Ege University, Izmir, Turkey
[8]Department of Nuclear Medicine, Aydın Adnan Menderes University, Faculty of Medicine, Aydın, Turkey

Background: Bone wax, a haemostatic agent, is widely used in craniospinal surgical procedures for a long time, in spite of controversial results regarding its negative influence upon bone regeneration. In this experimental study, the effects of Ankaferd Blood Stopper (ABS), as an alternative haemostatic agent, were evaluated through histochemical, immunohistochemical and scintigraphic studies.

Materials and methods: The total of 30 adult female Wistar albino rats was randomly divided into three groups: intact control group (n = 10), bone wax group (n = 10), and ABS group (n = 10). Surgically, a 3.0 mm hole in diameter was drilled on the right side of calvarium of the rats using a Class Mini Grinder set in all three groups, as described previously. At the end of 8 weeks, bone healing and connective tissue alterations surrounding drilled calvarial defect areas of the rats were determined via haematoxylin and eosin and the Mallory's trichrome staining and anti-bone sialoprotein immunohistochemistry. Image Pro Express 4.5 programme was used for histomorphometric calculation of new bone and fibrotic tissue areas. All statistical analyses were made with SPSS 25.0 and analysis of variance (one-way ANOVA) followed by Bonferroni post hoc test was performed, p < 0.001 was considered as significance level.

Results: Histomorphometrically, it was found that he had the largest hole diameter and the least fibrotic scar area in the bone-wax group. In the bone wax group, it was observed that the material closed the hole and there was only a fibrotic scar tissue in the area between the bone tissue at the edge of the hole and bone wax, and a fibrotic tissue was formed in the bone wax area. During the histological procedure, this bone-wax material was poured and the sections were seen as a gap in this area. In the ABS haemostat group, the smallest hole diameter and the least fibrotic scar tissue were observed. Fibrotic scar tissue close to each other was found in the ABS haemostat and bone wax groups. Histological analysis of

Address for correspondence: E.O. Cetin, PhD, Department of Pharmaceutical Technology, Department of Biopharmaceutics
and Pharmacokinetics, Ege University Faculty of Pharmacy, Bornova, Izmir, Turkey, e-mail: emel.oyku.cetin@ege.edu.tr

samples also showed a statistical significance for fibrotic connective tissue area between groups (p < 0.05). Scintigraphically, osteoblastic activity related to blood flow in the animal taken from the group with application of ABS haemostat was more pronounced compared to the other two groups.

Conclusions: In our study, it has been concluded that the ABS yields affirmative effects on the bone healing, while bone wax leads to negative impact on the bone regeneration. Scintigraphic, histochemical and immunohistochemical data support the affirmative impact of the ABS haemostat application upon the bone regeneration apart from the quick stop of haemorrhage. (Folia Morphol 2022; 81, 3: 739–748)

Key words: Ankaferd Blood Stopper haemostat, bone wax, calvarium, osteogenesis, rat

INTRODUCTION

Today, cranial defect is one of the most frequently encountered problems in craniofacial reconstructive surgery, but there is still controversy about repair of cranial defects. Bone wax, which is frequently used as a haemostatic agent in the control of bone bleeding in surgical operations, is the oldest known and cheapest absorbable substance prepared by Horsley in 1892 [see 1, 14]. It is a mixture of bee wax and isopropyl palmitate and is used in small pieces. Bone wax, which does not have any coagulation mechanism, stops the osseous bleeding in a physical way and it must be removed from the cavity properly after application because it delays bone regeneration [21, 31]. Therefore, it has been suggested that this material should not be used in places exposed to pressure and expected to heal quickly. On the other hand, Ankaferd Blood Stopper (ABS), consisting of *Thymus vulgaris* (thyme), *Glycyrrhiza glabra* (liquorice), *Vitis vinifera* (grape vine), *Alpinia officinarum* (blue ginger), and *Urtica dioica* (nettle) plant extracts, has been used as an alternative haemostatic agent in folk medicine for many years [5, 6, 12]. Recently, it has been widely used in some clinical trials for various tissue injuries as a topical agent for control of minor or major haemorrhages that occur spontaneously, such as gastrointestinal bleeding, or during or following some surgical interventions, including adenoidectomy and thyroidectomy [5, 7]. Thus, it is well-known that it has a very rapid haemostatic effect in clinical practice, but few studies have assessed the influence of ABS haemostat on connective tissue and bone healing. In a previous experimental study by Bulut et al. (2014) [4], it has been reported that use of ABS as a haemostatic agent caused a negative effect on

proliferation, number, viability and morphology of fibroblast cells. In similar, Gul et al. (2020) [13] found that fibrosis was significantly higher in the ABS group in mucosal tissue, suggesting its positive effect on wound healing in rats.

Recent studies have revealed that bone sialoprotein (BSP) and osteocalcin (OC) are expressed with the initiation of mineralisation with type I, type II and type X collagens in the early period of bone formation [18, 29]. In past, some researchers have suggested that bone formation is reduced by impaired mineralisation in mice with BSP deficiency [18]. Furthermore, it has also been suggested that osteonectin (ON) and alkaline phosphatase (AP) in cells have important roles in bone healing process. Due to their effects on bone cell differentiation and mineral formation, therefore, ABS haemostat can be used for stimulation of bone regeneration and its effects upon bone cells such as osteoblasts and osteoclasts will be determined, if noncollagenous bone related proteins BSP, OC, ON and osteopontin (OP) are evaluated immunohistochemically as bone formation markers.

On the other hand, three-phase bone scintigraphy is a non-invasive technique that shows the vascularity and osteoblastic activity of the bone. In their study using different bone grafts, Aygit et al. (1999) [2] evaluated vascularity and osseous changes with bone scintigraphy. In this study, they noted that bone scintigraphy could be used as a non-invasive method to evaluate implant vascularity because of histological changes and scintigraphic findings.

Therefore, the objective of this study was to analyse the changes that occur in the bone tissue of rats subjected to bone wax and ABS haemostat applications, which are used as haemostatic agents in various
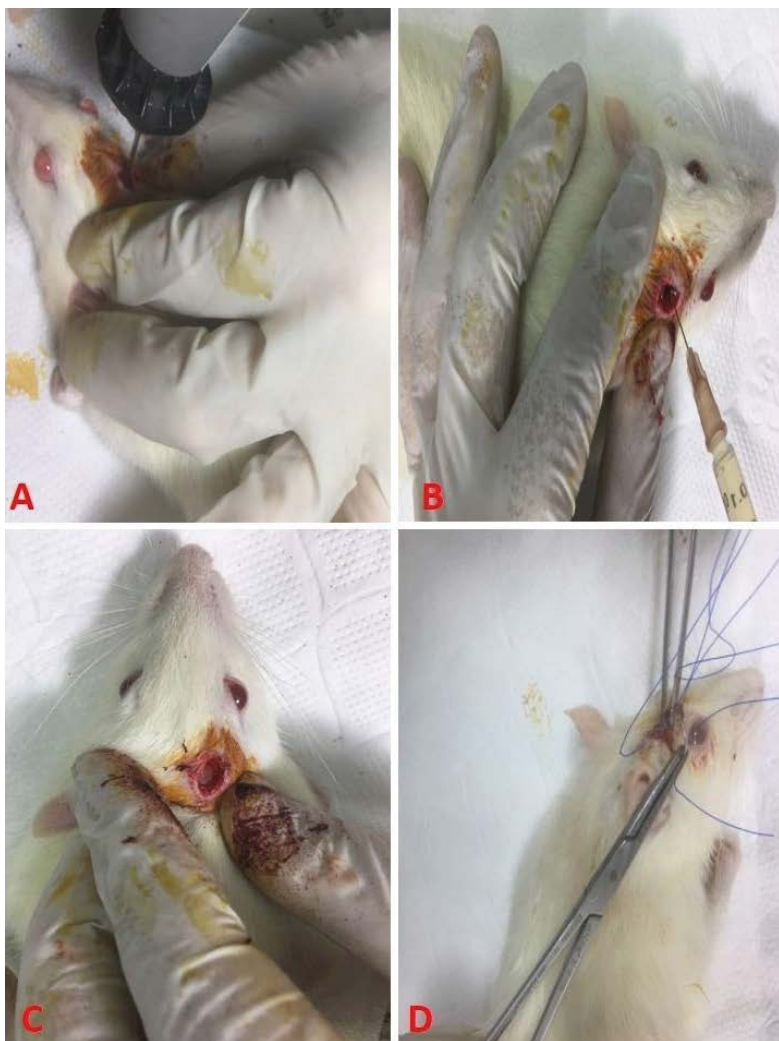
Figure 1. The process of establishing the animal model of bone defect as burr hole on the right side of the rat calvarium using a drill with 3 mm in diameter.

surgical procedures for a long time, comparatively through histochemical, immunohistochemical and scintigraphic studies.

MATERIALS AND METHODS

Animals and experimental groups

In this study, 30 adult 200 g female Wistar albino rats were used for the experiment. The experimental protocol was approved by the Ethical Committee of Aydın Adnan Menderes University (HADYEK 64583101/2016/78). Animals were housed in rat cages in standard conditions (24 ± 2°C and 50 ± 5% humidity), exposed to 12:12-h light/dark cycle, fed with standardised rodent chow and tap water ad libitum access. Rats were divided into three groups as intact control group (n = 10), bone wax group (n = 10), and ABS haemostat group (n = 10). Then, critical-sized burr-hole defects (diameter: 3.0 mm) were produced in the calvarium of all rats under general anaesthesia. At the end of the 8 weeks all animals were sacrificed following scintigraphic study and cranial tissue samples were taken from the defects for histological histochemical and immunohistochemical analyses.

Surgical procedure for burr hole production in rat calvarium

In the current study, all surgical procedures were performed under general anaesthesia provided with intraperitoneal combination of ketamine (50 mg/kg) and xylasine (5 mg/kg) anaesthesia. Following heads of rats were shaved in an area of about 2 cm in diameter and cleaned with baticon, a hole 3.0 mm in diameter was opened on the right sides of the rats' calvarium under sterile conditions, using an electric drill (CLASS Mini Grinder sets, PRC), and then the wound was closed, as described previously by Başaloğlu et al. (2021) [3] (Fig. 1).

Three-phase bone scintigraphy

Before sacrification of the animals for histological examination, one rat was randomly selected from each group for scintigraphic study of the calvarium defect. Dynamic images were obtained immediately after the injection of 37 MBq Tc-99m methylene diphosphonate (MDP) into the tail vein and static images were obtained after 2-h of injection with a double-headed Siemens syngo via gamma camera. Static images were acquired with a parallel hole collimator in a 256 × 256 matrix as 500 Kcount anterior and posterior views. Then, 10-min images were obtained from the rats' calvarial defect regions with a pin hole collimator and one of them was used as a representative figures of the groups. Tracer uptake was evaluated semiquantitatively in addition to visual evaluation. Region of interest was defined around the extracted side and the accumulation of Tc-99m-MDP in the regions was measured by software programme.

Histological examination of rat calvarium

After sacrification, the calvarial defects of the rats were taken into 10% formalin solution for 24 h before decalcification process using 20% formic acid for 2 months. When softening of the tissue was acceptable tissues were processed with routine histological protocols and embedded in paraffin. Five μm sections were obtained by Leica RM 2145 microtome and after deparaffinisation haematoxylin and eosin (H&E), Mallory's trichrome staining and anti-BSP (bs-4729R, Bioss, 1:100) immunohistochemical staining were applied for evaluation of the effects of bone wax on bone osteogenesis in comparison with ABS haemostat. All slides were examined at 10–20× magnification using an Olympus C5050 camera attached to Olympus BX51 light microscope.

Histomorphometry

For histomorphometric analysis, hole diameter measurements and fibrotic scar areas in the sections were evaluated. Measurement for new ossification areas and fibrotic scar areas was also calculated using Image Pro Express 4.5 (Media Cybernetics, Inc., Rockville, MD, USA) programme. Thus, the effects of bone wax upon bone healing were compared with those of ABS haemostat.

Statistical analyses

Data analysis was performed using IBM SPSS (Statistical Package for Social Sciences) Statistics for Windows, Version 25.0. (IBM Corp. Released 2017, Armonk, NY). Comparison between groups was made using the one-way analysis of variance method. Normality control was performed using the Shapiro-Wilk test, one of the obtained error estimates. Since there was no problem of adaptation to normal distribution, the study continued with one-way analysis of variance. Variance homogeneities were examined with Levene test, when there was no homogeneity problem, multi-group comparison was performed with F test; Bonferroni test was used as post hoc tests. In cases where variance homogeneity was not provided, Welch's test was used for multi-group comparison, Dunnett's T3 method was preferred as the post hoc test. All hypothesis checks were carried out at the 0.05 significance level, so $p < 0.05$ was considered significant.

RESULTS

Macroscopic examination

After the scalp of the rats was skinned, the holes opened in the calvarium were observed macroscopically. When the skull dissection was performed macroscopically, images belonging to all groups were taken. Accordingly, it was determined that the control group was in a normal physiological recovery process. In the bone wax group, it was determined that the material filled the hole and kept the hole closed without any changes during the elapsed time. In the ABS haemostat group, it was observed that the hole opened was closed in appearance and was better than the control group in terms of vascularisation (Fig. 2).

Microscopic examination

Orientation of the hole in the bone was adjusted in microscopic sections and serial sections were taken. H&E and Mallory's trichrome staining and anti-BSP immunohistochemical staining were performed to show the general structure in these sections. Importantly, these puncture structures were found to be filled with irregular dense connective tissue called fibrotic in both the control group and the ABS haemostat group (Fig. 2).

In the bone wax group, it was observed that there was fibrotic connective tissue in the area between the bone wax and the bone tissue at the edge of the hole where the material closed the hole, and there was no fibrotic tissue in the bone wax area. During histological follow-up, this bone wax material was seen as a gap in this area in the poured sections (Fig. 3).
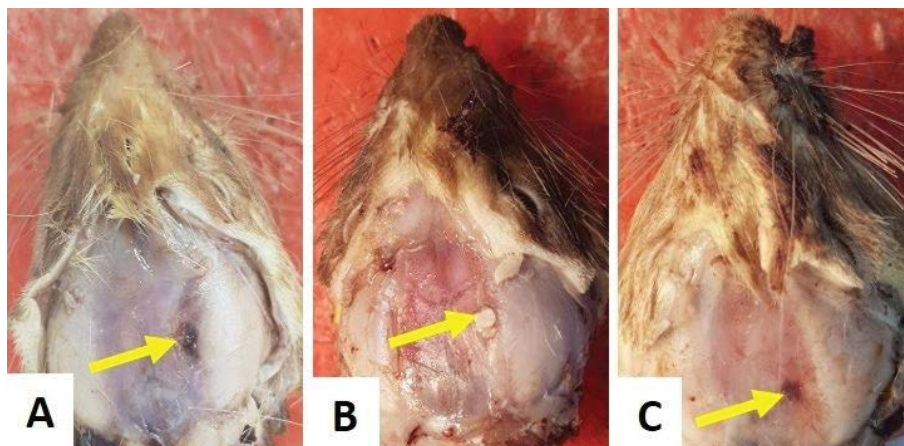
Figure 2. Demonstration of the experimentally produced bone lesions in all rat groups; **A.** Control group; **B.** Bone wax group; **C.** Ankaferd Blood Stopper haemostat group.
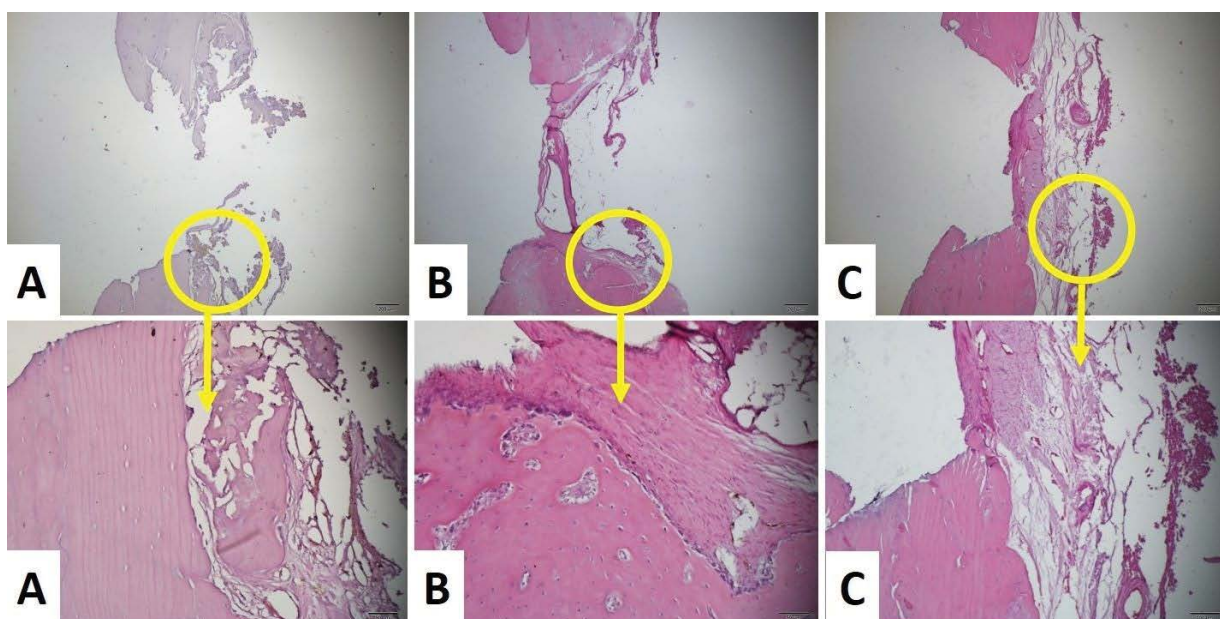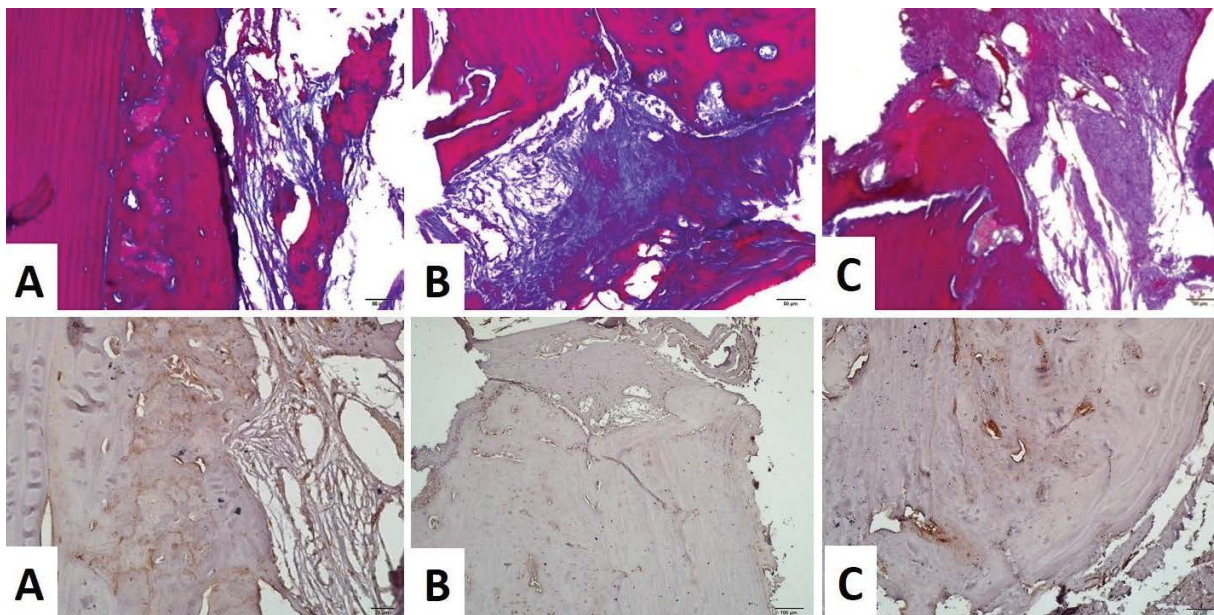

Figure 3. Microscopic evaluation of all groups; **A.** Control group; **B.** Bone wax group; **C.** Ankaferd Blood Stopper haemostat group. Haematoxylin and eosin staining.

When the fibrotic connective tissue structure was examined at higher magnification, it was found that they contained fibroblast-like cells and type I collagen bundles. In the control group, new bone spicules were found, probably formed by intramembranous ossification, where they settled in different regions within the connective tissue. More importantly, it was noted that this connective tissue area was small in the ABS haemostat group and ossification developed in most of the structure. With this appearance, it became the experimental group closest to the normal histological structure of the other groups. Mallory's trichrome staining showed that type I collagen bundles were stained blue, while the newly formed bone areas were red (Fig. 4). When the hole diameters were evaluated statistically, it was seen that the bone wax group had the largest hole diameter. It was found that the smallest hole diameter was in the ABS haemostat group. When the groups were compared with each other, a significant difference was found between control group and ABS haemostat group ($p < 0.001$) as well as bone wax group and ABS haemostat group ($p < 0.001$) (Fig. 5A).

When evaluated in terms of fibrotic scar area, it was found that the lowest scar area was in the bone

Figure 4. Microscopic evaluation of all groups showing; **A.** Control group; **B.** Bone wax group; **C.** Ankaferd Blood Stopper haemostat group. Top row: Mallory's trichrome staining; Bottom row: Anti-bone sialoprotein staining.
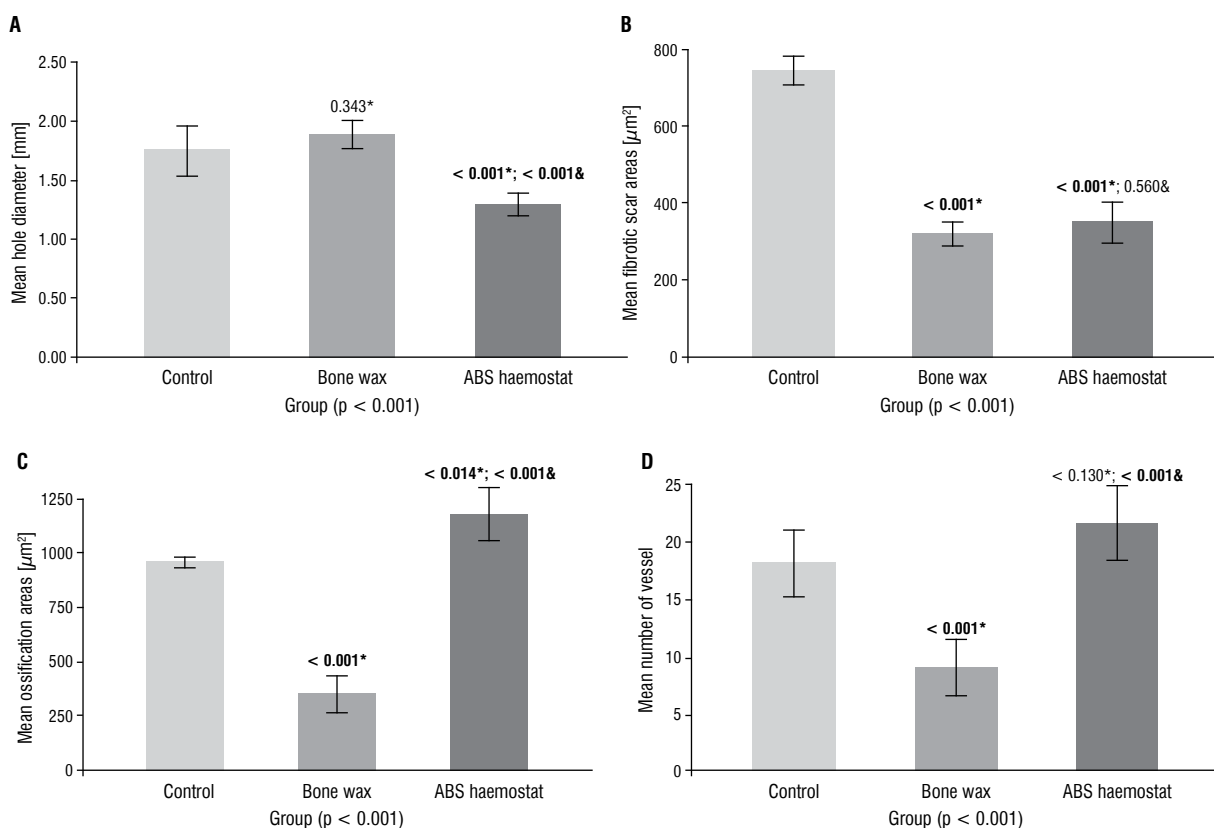
Figure 5. Statistical evaluation graph of histomorphometric analysis. Graphical representation of hole diameter (**A**), fibrotic scar area (**B**), ossification area (**C**) and number of vessels (**D**) in all groups; *Comparison with control group; & Comparison with bone wax group.

wax group. We think that the reason for this is that the bone wax material has not been lost yet, which delays wound healing. There is a statistical signifi-

cance between control group and bone wax group (p < 0.001) as well as bone wax group and ABS haemostat group (p < 0.001) (Fig. 5B). When eval-
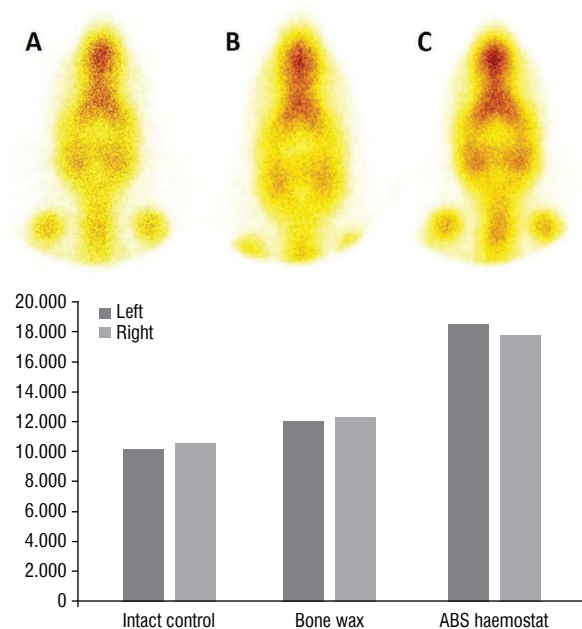
Figure 6. Scintigraphic imaging in rats; **A.** Control group; **B.** Bone wax group; **C.** Ankaferd Blood Stopper (ABS) haemostat group. Results of scintigraphic measurements show more pronounced osteoblastic activity depending on blood flow. In the lower part, the results obtained are also shown graphically.

uated in terms of ossification areas, it was seen that the most ossification area was in the ABS haemostat group, while the least ossified area was in the bone wax group. There is a statistical significance between control group and bone wax group ($p < 0.001$) as well as bone wax group and ABS haemostat group ($p < 0.001$) (Fig. 5C). In terms of vascularisation, among the scar areas and ossification areas, it was seen that the most vascular structure was in the ABS haemostat group and the least in the bone wax group. The difference between control group and bone wax group ($p < 0.001$) as well as bone wax group and ABS haemostat group ($p < 0.001$) was found to be significant (Fig. 5D).

Bone scintigraphy

As a result of quantitative examination of the right and left parietal regions of the calvarium of the rats: in the rat in the intact control group, left 10.158 count, right 10.541 count; in bone wax group, left 12.008 count, right 12.325 count; and in the rat in the group with application of ABS haemostat, 18.513 count on the left was found and 17.786 count on the right (Fig. 6). In the same rat, however, no significant result was obtained in terms of vascularity richness

in ossification in the right and left parietal regions. Furthermore, a significant amount of adhesion was detected in the rats in ABS haemostat group when compared to that of other two groups. The images were obtained with the pin-hole collimator in each group and they were evaluated visually for vascularity and osteoblastic activity of the region. Based on the results of scintigraphic measurements, osteoblastic activity related to blood flow in the subject taken from the group with application of ABS haemostat was more pronounced compared to that of the other two groups (Fig. 6).

DISCUSSION

The experimental design, in which the rat was used as a model, as in many other experimental studies due to its advantages in terms of ease of purchase and maintenance, followed the research line established by Başaloğlu et al. [3]. Our results clearly showed that osteoblastic activity related to blood flow was evident in the scintigraphy taken from animal with application of ABS haemostat and histological findings confirmed the positive effect of the ABS haemostat application upon the bone healing, while bone wax as a haemostatic agent had a negative impact on the bone regeneration. Also, a statistical difference was found between the groups for the area of fibrotic connective tissue ($p < 0.05$).

The cranium, mostly composed of symmetrical and paired bones, is the most important bone area of the body because it is the main defence system of the brain and brain stem [28]. We can say that it is biologically more inert because it has a different blood supply structure than bone marrow and other bones [22]. It protects the brain from the central nervous system elements that ensure regular and harmonious working coordination of vital functions. Therefore, there are many publications and experimental studies about the healing of cranial defects in the current literature.

When the literature was reviewed on how these substances used in the control of bleeding affect bone healing, it has been determined that significant differences can be detected in first 30 days [1, 9, 15]. In animal experiments, critical dimensional defect was defined as the smallest size bone wound that did not heal spontaneously throughout life without using any material [8, 25]. Such defects tend to fill with fibrous connective tissue and heal this way rather than by bone filling [10, 24]. In their study, Turnbull and

Freeman (1974) [30] examined the 2-mm-diameter experimental defects in the parietal bones of rats in terms of healing for 12 weeks and it was observed that there was no significant improvement at the end of this period. Mulliken and Glowacki (1980) [19] examined 2 mm parietal bone defects. While they could not find a bone filling at the end of the 6th month in control defects, they reported that they encountered bone formation in the experimental group where they applied demineralised bone powder [19].

Howard and Kelly (1969) [15] found that bone wax negatively affected healing in an experimental study they performed in rat tibia. They found that while there was almost complete recovery in the control group of rats that were sacrificed on day 31, the material was not resorbed and delayed osteoblastic activity in the group treated with bone wax [25]. Nooh et al. (2014) [21] used two haemostatic agents, surgicel and bone wax, in the bone defects formed in the lateral direction of the right and left metacarpal of goats. Sacrificed animals were subjected to computed tomography and histological examinations at 3 and 5 weeks. As a result, they stated that the surgicel group was superior to the bone wax group in terms of bone healing, and bone wax prevented osteogenesis and caused inflammation [21]. Raposo-Amaral et al. [23] performed histological and radiological examination of the use of bone wax in rats with cranial defects. After the surgery, computed tomography scan of the rats was performed at 12th week and as a result, they found that bone wax significantly reduced the bone rate, caused 18% in the healing of the cranial defect and caused fibrosis with infection in rats [23]. Similar results were obtained in animals treated with bone wax in our study, although the drill-opened defect area appeared to be closed macroscopically, this area melted after acid treatment and little fibrotic tissue remained. This situation suggests that bone wax prevents mineralisation. In this group, the intensity of osteoclastic activity along with osteoblastic activity is also noteworthy. Bone regeneration and bone resorption continue almost simultaneously. In intact control group, very few new bone spicules were encountered due to intramembranous ossification. The fact that intact control group has a higher ossification pattern compared to bone wax group suggests that it is significant in terms of revealing the negative effect of bone wax on ossification again. This situation is again consistent with similar studies in the literature [11].

On the other hand, however, there are quite a few studies in the literature regarding bone healing, both early and late, and similar to our study, there are also literature studies involving advanced bone healing. In previous histological studies investigating the effects of ABS on the bone tissue, it was found to have an acceleratory effect on the short-term bone healing process in samples taken on the 7th postoperative day [16, 27]. Recently, Kuruoğlu et al. (2017) [17] evaluated the late effects of the combination of ABS and β-tricalcium phosphate (TCP) using immunohistochemical methods and they found the bone healing effects of ABS haemostat in their study. Afterwards, Tanık et al. (2018) [29] also investigated the late period effects of the combination of ABS and β-TCP on the regeneration of bone tissue in rats. They found that both β-TCP and ABS had positive histological and radiological effects on wound healing and bone formation in samples taken on day 56 after surgery [29]. In the first macroscopic examination we observed in our study, it was determined that the group with the appearance of scar tissue most closely resembling normal structure was the group with application of ABS haemostat, suggesting a positive effect of ABS haemostat on wound healing.

Histologically, in the Mallory's trichrome staining, type I collagen bundles were stained in blue, and the newly formed bone areas were red in all groups in our study. In terms of hole diameters, it was determined that the bone wax group had the largest hole diameter and the ABS haemostat group had the smallest hole diameter. A statistically significant difference was found between control group and ABS haemostat group ($p < 0.001$) as well as bone wax group and ABS haemostat group ($p < 0.001$). When evaluated in terms of fibrotic scar area, it was found that the lowest scar area was in the bone wax group. We think that the reason for this is that the bone wax material has not been lost yet, which delays wound healing. There is a statistical significance between control group and bone wax group ($p < 0.001$) as well as bone wax group and ABS haemostat group ($p < 0.001$). In the literature review, however, immunohistochemically studies on bone repair of ABS haemostat are limited. In their experimental study in which they evaluated the use of platelet-rich plasma together with autogenous bone graft in the repair of bone defects by immunohistochemical analysis, Nagata et al. (2009) [20] found that the expression of OC and OP was significantly higher in the platelet-rich plasma

group. In our study, ossification is present in all three groups, although it seems that the mineralisation has not yet been completed. Therefore, absence of any analysis for inorganic material content of bone tissue mineralisation and difference of drilled defects from those in humans in terms of bone remodelling are limitations of our study. Moreover, lack of any imaging or mechanical study investigating the bone healing is another limitation of the study. Future studies including immunohistochemical determination of bone related proteins in the early stages of bone healing are needed for better understanding of impact of the ABS haemostat application upon bone remodelling apart from the quick stop of haemorrhage.

It is well-known that three-phase bone scintigraphy is a non-invasive technique showing the vascularity and osteoblastic activity of the bone. Based on their findings in a study, Aygit et al. (1999) [2] stated that bone scintigraphy could be used as a noninvasive method in evaluating implant vascularity because histological changes and scintigraphic findings were parallel. Tc-99m MDP is a radiopharmaceutical that can chemically adhere to all bones in the skeletal system after intravenous administration. It shows a significant accumulation especially at the points where bone metabolism increases. The common features of radiopharmaceuticals such as MDP, hydroxydiphosphonate (HDP) and hydroxymethylene diphosphonate (HMDP) marked with Tc-99m are that the diphosphonate core in their structure acts like hydroxyapatite, which is the basic building block of bone, and accumulates reversibly on bone surfaces and shows osteoblastic activity depending on blood flow. In this way, all bones belonging to the skeletal system get rid of the soft tissue effect and become visible in a plain state [26]. Diphosphonates attach to hydroxyapatite crystals, one of the main components of the bone matrix, by physicochemical absorption. This amount of adhesion varies according to the blood supply and osteoblastic activity in that area. Organization of haemostasis is of primary importance in fracture or defect repair. When scintigraphic imaging was performed there was no clear difference between the groups. Although MDP is a chemoabsorbable substance in all bones of the skeletal system, it shows a significant accumulation in places where bone metabolism is increased. Radiopharmaceuticals such as MDP, HDP, and HMDP act as hydroxyapatite, which is the main component of bone, and show

osteoblastic activity due to a reversible blood flow at the bone surfaces [28]. Although there are not many such studies in the literature, we think that performing bone scintigraphy in weekly periods starting from the defect opening will be more beneficial as it will provide comparable and observable data.

CONCLUSIONS

Bone fractures due to trauma or surgical operations are conditions that can be encountered in all stages of life. The primary functions of ABS haemostat and bone wax, which are used as haemostatic agents in neurosurgery, orthopaedic and traumatology surgery, oral and maxillofacial surgery, are to stop bleeding quickly. Taken as whole, our results showed that: (1) Histological, immunohistochemical and bone scintigraphic data support the positive effects of ABS, consisting of folkloric medicinal plant extracts, on bone healing as well as stopping bleeding rapidly. It was concluded that ABS haemostat also had a positive effect on bone regeneration, while bone wax had a negative effect on regeneration of the rats' calvarial defects; (2) We think it is important in various surgical procedures, to choose a blood stopping agent, such as ABS, that will both provide rapid control of bleeding and accelerate regeneration by helping bone repair. However, the effectiveness of this product as a therapeutic modality for possible future clinical applications should be evaluated for all types of bones, including extracranial, spongy and cortical, apart from cranial ones; (3) Furthermore, this study also suggests that the anti-inflammatory and antimicrobial properties of the plant ingredients of antihaemorrhagic ABS should be evaluated in terms of preventing various complications during the operation and postoperative period in future studies.

Conflict of interest: None declared

REFERENCES

1. Alberius P, Klinge B, Sjögren S. Effects of bone wax on rabbit cranial bone lesions. J Craniomaxillofac Surg. 1987;

15(2): 63–67, doi: 10.1016/s1010-5182(87)80020-3, indexed in Pubmed: 3294903.

2. Aygit AC, Sarikaya A, Candan L, et al. Comparison of alloplastic implants for facial bones by scintigraphy and histology: an experimental study. Eur J Plast Surg. 1999; 22(2-3): 102–106, doi: 10.1007/s002380050158.

3. Basaloglu HK, Turgut M, Şirin C, et al. The influence of functional pinealectomy and exogenous melatonin application on healing of burr hole in adult rat calvaria: a histological and immunohistochemical study. Folia Morphol. 2022 [Epub ahead of print]; 81(2): 271–279, doi: 10.5603/FM.a2021.0047, indexed in Pubmed: 33997947.

4. Bulut E, Baş B, Altunkaynak BZ, et al. Efficacy of Ankaferd Blood Stopper on bone healing in diabetic rats: a stereological and histopathological study. Biotech Histochem. 2014; 89(7): 535–543, doi: 10.3109/10520295.2014.906657, indexed in Pubmed: 24799094.

5. Ciftciler R, Ciftciler AE, Malkan UY, et al. Pharmacobiological management of hemostasis within clinical backgrounds via Ankaferd hemostat (Ankaferd blood stopper). SAGE Open Med. 2020; 8: 2050312120907811, doi: 10.1177/2050312120907811, indexed in Pubmed: 32110403.

6. Çiftçiler R, Haznedaroglu İC. Ankaferd hemostat: from molecules to medicine. Turk J Med Sci. 2020; 50(SI-2): 1739–1750, doi: 10.3906/sag-1908-161, indexed in Pubmed: 32283900.

7. Cipil HS, Kosar A, Kaya A, et al. In vivo hemostatic effect of the medicinal plant extract Ankaferd Blood Stopper in rats pretreated with warfarin. Clin Appl Thromb Hemost. 2009; 15(3): 270–276, doi: 10.1177/1076029608329578, indexed in Pubmed: 19117967.

8. Cook JL, Hung CT, Kuroki K, et al. Animal models of cartilage repair. Bone Joint Res. 2014; 3(4): 89–94, doi: 10.1302/2046-3758.34.2000238, indexed in Pubmed: 24695750.

9. Finn MD, Schow SR, Schneiderman ED. Osseous regeneration in the presence of four common hemostatic agents. J Oral Maxillofac Surg. 1992; 50(6): 608–612, doi: 10.1016/0278-2391(92)90443-4, indexed in Pubmed: 1593323.

10. Frame JW. A convenient animal model for testing bone substitute materials. J Oral Surg. 1980; 38(3): 176–180, indexed in Pubmed: 6928181.

11. Geary JR, Frantz VK. New absorbable hemastatik bonewax; experimental and clinical studies. Ann Surg. 1950; 132(6): 1128–1137, doi: 10.1097/00000658-195012000-00012, indexed in Pubmed: 14790584.

12. Goker H, Haznedaroglu IC, Ercetin S, et al. Haemostatic actions of the folkloric medicinal plant extract Ankaferd Blood Stopper. J Int Med Res. 2008; 36(1): 163–170, doi: 10.1177/147323000803600121, indexed in Pubmed: 18304416.

13. Gül M, Günay A, Tanik A. An evaluation of the effects of caffeic acid phenethyl ester and Ankaferd blood stopper on secondary wound healing of oral mucosal tissue. Turk J Med Sci. 2020; 50(1): 248–257, doi: 10.3906/sag-1908-114, indexed in Pubmed: 31769639.

14. Gupta G, Prestigiacomo CJ. From sealing wax to bone wax: predecessors to Horsley's development. Neurosurg Focus. 2007; 23(1): E16, doi: 10.3171/foc.2007.23.1.16, indexed in Pubmed: 17961057.

15. Howard TC, Kelley RR. The effect of bone wax on the healing of experimental rat tibial lesions. Clin Orthop Relat Res. 1969; 63: 226–232, indexed in Pubmed: 5781118.

16. Işler SC, Demircan S, Cakarer S, et al. Effects of folk medicinal plant extract Ankaferd Blood Stopper on early bone healing. J Appl Oral Sci. 2010; 18(4): 409–414, doi: 10.1590/s1678-77572010000400015, indexed in Pubmed: 20835578.

17. Kuruoglu E, Onger ME, Marangoz AH, et al. Postlaminectomy bone and scar formations in presence of Ankaferd Blood Stopper and Bitter Melon (Momordica Charantia): An experimental study. Turk Neurosurg. 2017; 27(3): 441–446, doi: 10.5137/1019-5149.JTN.16263-15.1, indexed in Pubmed: 27593811.

18. Malaval L, Wade-Guéye NM, Boudiffa M, et al. Bone sialoprotein plays a functional role in bone formation and osteoclastogenesis. J Exp Med. 2008; 205(5): 1145–1153, doi: 10.1084/jem.20071294, indexed in Pubmed: 18458111.

19. Mulliken JB, Glowacki J. Induced osteogenesis for repair and construction in the craniofacial region. Plast Reconstr Surg. 1980; 65(5): 553–560, doi: 10.1097/00006534-198005000-00001, indexed in Pubmed: 6988853.

20. Nagata M, Messora M, Okamoto R, et al. Influence of the proportion of particulate autogenous bone graft/platelet-rich plasma on bone healing in critical-size defects: an immunohistochemical analysis in rat calvaria. Bone. 2009; 45(2): 339–345, doi: 10.1016/j.bone.2009.04.246, indexed in Pubmed: 19410024.

21. Nooh N, Abdullah WA, Grawish MEA, et al. The effects of surgicel and bone wax hemostatic agents on bone healing: An experimental study. Indian J Orthop. 2014; 48(3): 319–325, doi: 10.4103/0019-5413.129451, indexed in Pubmed: 24932041.

22. Prolo DJ, Gutierrez RV, DeVine JS, et al. Clinical utility of allogeneic skull discs in human craniotomy. Neurosurgery. 1984; 14(2): 183–186, doi: 10.1227/00006123-198402000-00011, indexed in Pubmed: 6709140.

23. Raposo-Amaral CE, Almeida AB, Paschoal G, et al. Histological and radiological changes in cranial bone in the presence of bone wax. Acta Cir Bras. 2011; 26(4): 274–278, doi: 10.1590/s0102-86502011000400005, indexed in Pubmed: 21808839.

24. Rowe NL. Nonunion of the mandible and maxilla. J Oral Surg. 1969; 27(7): 520–529, indexed in Pubmed: 4893250.

25. Schmitz JP, Hollinger JO. The critical size defect as an experimental model for craniomandibulofacial nonunions. Clin Orthop Relat Res. 1986(205): 299–308, indexed in Pubmed: 3084153.

26. Sengöz T, Karaçalıoğlu AÖ, İnce S, et al. Cardiac Tc-99m metylene diphosphanate uptake in bone scintigraphy (in Turkish). Gülhane Tıp Dergisi. 2015; 57: 81–83.

27. Simşek HO, Tüzüm MŞ, Baykul T, et al. Experimental investigation of the effects of a blood stopper agent (ankaferd blood stopper) on bone surfaces. Turk J Haematol. 2013; 30(2): 177–183, doi: 10.4274/Tjh.2012.0092, indexed in Pubmed: 24385782.

28. Sirola K. Regeneration of defects in the calvaria. An experimental study. Ann Med Exp Biol Fenn. 1960; 38(Suppl 2): 1–87, indexed in Pubmed: 14447201.

29. Tanık A, Güler Doğru A, Akpolat V, et al. Investigation of the effect of combined use of alloplastic-based tricalcium phosphate bone graft and antihemorrhagic plant extract (ABS) on bone regeneration in surgically induced bone defects in nondiabetic rats: an experimental animal study. Turk J Med Sci. 2018; 48(6): 1302–1314, doi: 10.3906/sag-1803-201, indexed in Pubmed: 30543085.

30. Turnbull RS, Freeman E. Use of wounds in the parietal bone of the rat for evaluating bone marrow for grafting into periodontal defects. J Periodontal Res. 1974; 9(1): 39–43, doi: 10.1111/j.1600-0765.1974.tb00651.x, indexed in Pubmed: 4277754.

31. Zhou H, Ge J, Bai Y, et al. Translation of bone wax and its substitutes: History, clinical status and future directions. J Orthop Translat. 2019; 17: 64–72, doi: 10.1016/j.jot.2019.03.005, indexed in Pubmed: 31194062.

ORIGINAL ARTICLE

VIA MEDICA

New approach to morphometric analysis of Huschke's foramen

H. Çetin[1] , S. Akkaşoğlu[2] , S. Çalışkan[2]

[1]Department of Radiology, Faculty of Medicine, Ankara Yıldırım Beyazıt University, Ankara, Turkey
[2]Department of Anatomy, Faculty of Medicine, Ankara Yıldırım Beyazıt University, Ankara, Turkey

Background: The aim of the study is to analyse the demographic and anatomical details of the Huschke's foramen (HF) which have not been previously studied and to present a new clinical perspective.

Materials and methods: Multidetector computed tomography (MDCT) images of 495 patients were retrospectively evaluated. Presence of a HF, its' size, relations to side, age and gender were noted for every patient. Size of the foramen was measured in the axial plane, as well as on the reconstructed coronal and sagittal planes.

Results: Of the 495 patients 99 (20%) had HF. There was no significant difference between females and males according to the presence of the HF and the side of the HF. When the dimension of the left- and the right-sided HFs were compared, there were no significant differences on none of the axes for the patients with unilateral or bilateral HF. There was no significant linear correlation between age and the dimension in the axial axis, the dimension in the sagittal axis and the dimension in the coronal axis

Conclusions: The present work presenting morphologic and statistical variables of HF provides data for further studies which will indicate risk factors of herniation through HF. By the aid of MDCT, which is sensitive method for detection of the HF because of its thin sections, high spatial resolution, and multiplanar capabilities, lesions which were previously diagnosed as dehiscence were found to be defects. (Folia Morphol 2022; 81, 3: 749–755)

Key words: Huschke's foramen, multidetector computed tomography, herniation, coronal diameter

INTRODUCTION

Huschke's foramen (HF) is a developmental defect located on the antero-inferior wall of the external auditory canal (EAC) and communicates this canal to mandibular fossa. HF was first described by German anatomist and embryologist Emil Huschke in 1844 as 'Incisura meatus auditoria externi ossei' (Fig. 1) [15, 16, 20].

At birth, tympanic plate is a U-shaped, incompletely developed structure. At the first year of life, two ossification points, one anterior and one posterior to U shaped bone, grow towards each other and fuse. Tympanic plate ossifies and closes around the age of 5 years. Incomplete fusion leads to persistent HF [5, 6, 11].
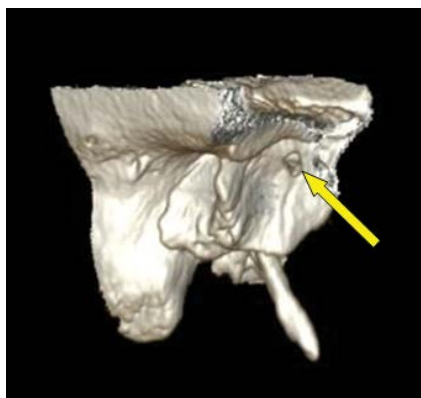
Figure 1. Three-dimensional image of right temporal bone. Defect on the anterior wall of the bony external auditory canal (yellow arrow). Image of mandible is removed.

Incidence of HF reported in the literature varies in a range from 3% to 25%. Patients with HF may be asymptomatic or may suffer from otalgia, otorrhoea, mastication-induced tinnitus, malocclusion and clicking sense during mastication. Moreover temporomandibular joint (TMJ) herniation from HF may lead to conductive hearing loss [2, 4, 13, 15, 17, 18, 21, 23].

Otorrhoea in patients with HF may develop due to salivary fistula between parotid gland and EAC [7, 18]. Clear discharge induced by mastication due to synovial fluid flow through a fistula interconnecting TMJ and EAC is another cause of otorrhoea. HF may present with the drainage of odontogenic abscesses and infectious or tumoural spread [11]. Medical conditions such as persistent otorrhoea, otitis externa, pain, hearing loss, tinnitus, and malocclusion are surgical indications and can be treated by grafts such as fascia, cartilage or miniplates. Conservative therapy options consisting of an anxiolytic, muscle relaxant, and soft diet are also defined in the literature [23, 30].

In the literature, there are radiologic, cadaveric and clinical studies examining HF. In this study, we aimed to define the prevalence and dimensions of the HF in living individuals based on objective data of multidetector computed tomography (MDCT) images and evaluate the differences related to side and gender. Preoperative detection of HF is an advantage for surgeons to avoid complications. The results of this study will be especially useful for surgeons dealing with otorhinolaryngology.

MATERIALS AND METHODS

This retrospectively planned radiologic study was carried out in Ankara Yıldırım Beyazıt University Med-ical Faculty. MDCT images of 495 patients obtained for head and neck pathologies from 2019 February to 2020 January were evaluated in the radiology department. A senior radiologist (H.Ç.) analysed the MDCT studies. Patients with history of head trauma, cholesteatoma, mandibular or temporal bone fracture, previous ear surgery and TMJ surgery and those younger than 5 years were not included in this study. The age-, gender- and side-related changes for each measure were statistically analysed.

All CT images were obtained using a 128-MDCT scanner (Revolution EVO, General Electrics Medical Systems USA) with 0.312-mm collimation and a 512 × 512 matrix. Transverse scans were acquired in a plane parallel to the orbitomeatal plane in the helical mode with 140 kV, 280 mAs, 1-second rotation time, 0.625-mm section thickness, beam pitch of 0.531, and field of view of 180 mm. The obtained image data were stored as a DICOM file and were transferred to a workstation, then the CT post processing workstation was used for multiplanar reconstruction, and the main rows of coronal and sagittal image reconstruction was performed. These images were displayed at a window centre of 500 HU and a window width of 3000 HU. For every patient, we noted the presence of a foramen and its size. We measured the size of the foramen in the axial plane, as well as on the reconstructed coronal and sagittal planes.

Ethics committee approval was received from Clinical Research Ethics Committee of the Ankara Yıldırım Beyazıt University Medical Faculty (Decision number: 26379996/128).

Statistical analysis

The distributions of age and the dimensions of the HF in axial, sagittal and coronal axes were examined by Shapiro-Wilk's test and normality plots. Age was summarised by median (min–max), while both mean ± standard deviation (mean ± SD) and median (min––max) were assessed for dimensions. Frequency and percentage (%) were reported for gender and side.

The males and females were compared with respect to the presence of HF and its side by χ^2 tests. The dimensions of left- and right-sided HFs in axial, sagittal and coronal axes were compared by the independent t test in the patients with unilateral HF and by paired t-test in the patients with bilateral HF. The correlations between the age and dimensions were analysed by Generalised Linear Mixed Model

Table 1. Distribution of Huschke's foramen (HF) and side based on gender

	Total	Female	Male	P
HF				0.684
Absent	396 (80.0%)	175 (79.2%)	221 (80.7%)	
Present	99 (20.0%)	46 (20.8%)	53 (19.3%)	
Side				0.124
Right	43 (35.4%)	25 (54.3%)	18 (34.0%)	
Left	35 (43.4%)	13 (28.3%)	22 (41.5%)	
Bilateral	21 (21.2%)	8 (17.4%)	13 (24.5%)	

Table 2. Dimension of Huschke's foramen in three axes

Size [mm]	Mean ± SD	Median (min–max)
Right (n = 64)		
Axial	3.36 ± 0.74	3.40 (1.6–4.8)
Sagittal	3.48 ± 0.79	3.60 (1.9–5.0)
Coronal	3.17 ± 0.73	3.30 (1.5–4.3)
Left (n = 56)		
Axial	3.33 ± 0.96	3.60 (1.3–5.2)
Sagittal	3.42 ± 0.95	3.75 (1.5–5.3)
Coronal	3.16 ± 0.95	3.45 (1.2–5.5)

SD — standard deviation; min — minimum; max — maximum

Table 3. Dimension comparison of left- and right-sided Huschke's foramen in unilateral and bilateral individuals

	Left		Right		P
	Mean ± SD	Median (min–max)	Mean ± SD	Median (min–max)	
Unilateral	N = 35		N = 43		
Axial	3.45 ± 0.88	3.8 (1.3–5.2)	3.43 ± 0.66	3.4 (1.6–4.5)	0.919
Sagittal	3.55 ± 0.92	3.8 (1.5–5.3)	3.54 ± 0.72	3.6 (1.9–4.8)	0.993
Coronal	3.23 ± 0.87	3.4 (1.2–5.0)	3.25 ± 0.70	3.4 (1.5–4.3)	0.945
Bilateral	N = 21		N = 21		
Axial	3.13 ± 1.06	3.1 (1.7–5.1)	3.22 ± 0.90	3.3 (1.8–4.8)	0.813
Sagittal	3.22 ± 0.99	3.3 (1.9–4.6)	3.36 ± 0.92	3.6 (2.0–5.0)	0.701
Coronal	3.04 ± 1.09	3.5 (1.5–5.5)	3.01 ± 0.77	3.2 (1.7–4.3)	0.925

SD — standard deviation; min — minimum; max — maximum

(GLMM) with random slope for sides to consider the inter-individual correlation between the dimension measurements. Spearman and Pearson correlation analysis were performed to evaluate the relationship between the age and dimensions of the left- and right-sided HFs, separately. A p value < 0.05 was considered as statistically significant.

All statistical analyses were performed via IBM SPSS Statistics 22.0 (IBM Corp. Released 2013 IBM SPSS Statistics for Windows, Version 22.0, Armonk, NY, IBM Corp.).

RESULTS

The median age of 495 individuals was 37 years (min–max: 14–76). Approximately 45% (n = 221) of the individuals were female. Twenty per cent (n = 99) had HF. Out of them, 43 (8.7%) had HF in the right ear, 35 (7.1%) had HF in the left ear and 21 (4.2%) had bilateral HF. Of the females, 20.8% (n = 46) and 19.3% (n = 53) of the males were shown to have HF (Table 1). There was no significant difference between females and males according to the presence of HF (p = 0.684) and the side of HF (p = 0.124).

The mean dimension of the right-sided HFs was 3.36 ± 0.74 mm in the axial axis, 3.48 ± 0.79 mm in the sagittal axis and 3.17 ± 0.73 mm in the coronal axis. The mean and median dimension of the left-sided HFs are given in Table 2.

When the dimension of the left- and the right-sided HFs were compared, there were no significant differences on none of the axes for the patients with unilateral or bilateral HFs (Table 3).

The GLMM analysis showed there was no significant linear correlation between age and the dimension in the axial axis (p = 0.983), the dimension in the sagittal axis (p = 0.923), and the dimension in the coronal axis (p = 0.982) of the HF. When the correlation between age and the dimension of the HF was evaluated for left- and right-sided HFs separately, the results were the same (p > 0.05).

DISCUSSION

We encountered many publications in the literature in which HF was analysed by different research techniques based on methodology. Wang et al. [29] found the prevalence of HF was 7.2% in their osteo-

logical study on 377 skulls. Bhanu et al. [1] presented 38% HF prevalence, but the materials included in the study consisted of skulls and single temporal bones of unknown sexes and age which did not provide accurate data to evaluate demographic statistics. Pękała et al. [19] compared radiologic and osteological studies and concluded that HF is more prevalent in cadavers (21.2%) than in radiologic studies (8.8%), but their results are not statistically significant. Osteological studies contribute valuable data to literature but to our opinion exact demographic data and dimensions of an anatomical feature are well defined on radiologic images. Besides, skull collections do not reflect single population and proper dimensions of an anatomical feature may not be claimed clearly due to possible trauma injuries. Age-, gender-, size- and side-related differences of bilateral structures are properly presented in radiologic studies (Table 1).

Tucunduva et al. [27] reported HF prevalence of 12.7% in their study including 150 patients' cone--bean computed tomography (CBCT) findings. Wang et al. [29] reported prevalence of 0.45% in osteological study performed on 377 dry skulls. Twelve per cent frequency was reported by Hashimato et al. [8] in their study including 997 dry skulls. In CBCT studies of Deniz et al. (200 cases) [3] and Tozoğlu et al. (207 cases) [26] prevalence of the feature was found 11.5% and 17.9%, respectively. Our data included MDCT findings of 495 patients and the prevalence detected was 20% (Table 1). Prevalence of HF in our data is not in consistent with the previously reported prevalence range in the literature. Because of the highly qualified technical details of MDCT device, smaller lesions which were previously misdiagnosed as dehiscence are proven to be defects. To our opinion high prevalence found in the present study is due to advanced technical details of imaging. Besides larger patient number is an additional value of the present study particularly showing the accuracy of descriptive statistics.

Present study provides scientific data to literature by presenting morphometry of HF and its' relations to side, age and gender. We measured dimensions of HF in three axes to reveal accurate sizes of this anatomical defect (Figs. 2–5). Of the three axes, coronal diameter, which was found to be the least one, was not measured in the previous publications. Lacout et al. [12] identified the foramina on axial images and confirmed their existence on coronal and sagittal reformatted MDCT images in their study consisting

Figure 2. Axial computed tomography image of temporal bone. Normal anteroinferior wall of external auditory canal (yellow arrows).
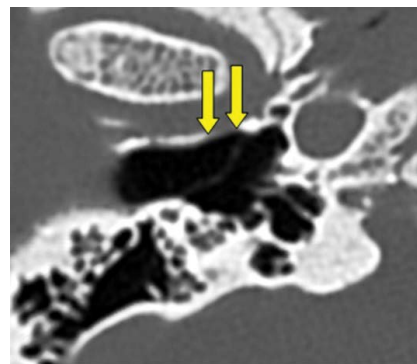
Figure 3. Axial computed tomography image of external auditory canal. Defect on the anterior wall of the bony external auditory canal (yellow arrows).
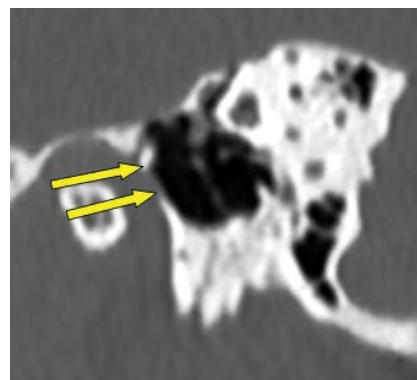
Figure 4. Sagittal computed tomography image of external auditory canal. Defect on the anterior wall of the bony external auditory canal (yellow arrows).

of 102 cases, but they only presented mean size of 4.2 mm in the axial plane and 3.6 mm in the sagittal plane. No attribute to coronal measurements was encountered.
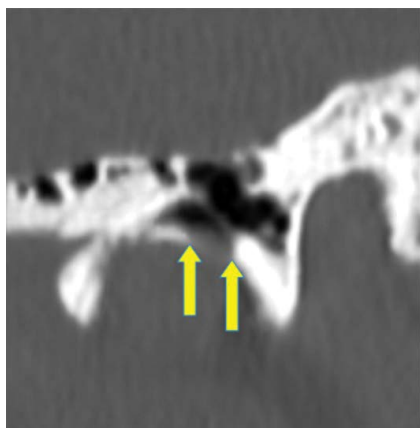
Figure 5. Coronal computed tomography image of external auditory canal. Defect on the anterior wall of the bony external auditory canal (yellow arrows).

Dimensions of an anatomical defect have critical importance to prevent potential complications and should not be measured in one plane. During TMJ arthroscopy, endoscopes with diameter smaller than 3 mm may cause tympanic membrane perforation, incus dislocation, salivary gland fistula and facial nerve damage by penetrating into the HF [6]. Van der Meer [28] concluded that spread of necrotizing external otitis from EAC to surrounding structures is associated with the increased size of HF. They performed their study on 39 cases with necrotizing external otitis and classified the HF as subtle, mild, moderate, or extensive dehiscence according to maximum width in the axial plane. Diameter of HF was measured only in axial plane in the mentioned study. In our study HF was analysed in three dimensions and coronal diameter was found to be the smallest one (Fig. 5, Tables 2, 3). Misleading point of mentioned study is that the coronal diameter not included in their study is the smallest one. Besides, HF was classified into four groups according to the axial diameter. To our opinion, measurements taken in a single plane are not scientifically appropriate when making a classification based on size.

Size of HF is reported to be an indicator of herniation but we did not come across a study in the literature indicating a cut off value for any diameter of HF which is more likely to allow herniation. Mittal et al. [15] reported that herniation is seen in one fourth of the cases with HF and is directly related to size of HF. Shapiro and Osborn [23] reported that 30

cases with herniated mandibular condyle into EAC were reported in the international literature. However, least size leading herniation is not presented in both publications. Prospective case series having the patient open and close the mouth while performing MDCT will show the displacement of tissue, which is critical for the diagnosis of the least HF diameter leading herniation. Studies with two stages of radiologic imaging with open and closed mouth will determine cut off value of diameter allowing herniation. Besides it will guide physicians to make the right decision between conservative or surgical treatment options. Although our study has a limitation from this point of view, it can inspire future studies.

Herniated tissue of TMJ through HF may mimic a mass and narrows EAC [28]. Acquired or congenital stenosis of EAC leads to conductive or mixed hearing loss. Differential diagnosis of mass in EAC leading to stenosis consists of exostosis, cholesteatoma or osteoma [14, 22]. Although herniation of TMJ through HF is a rare condition, radiologists may encounter this issue in daily practice [24]. Once this lesion is encountered, accurate differential diagnosis requires radiologist to be well experienced. They should take herniation into consideration when evaluating EAC pathologies. When opening the mouth, forward movement of herniated tissue of TMJ leads to a normal appearance of EAC [23]. It must be kept in mind of surgeons and radiologists to a correct preliminary diagnosis. The present study presenting morphologic and statistical variables of HF provides a data for further studies which will indicate risk factor of herniation through HF.

CONCLUSİONS

The present study contains complementary data on the missing points of publications in the literature. It was performed by an experienced radiologist on MDCT which is sensitive for detection of the HF because of its thin sections, high spatial resolution, and multiplanar capabilities. All demographic and morphometric details are revealed with the highest number of patients examined to date. To our opinion, the study that would be scientifically valuable to be done in the future is a prospective study that presents cut off value of coronal diameter of HF leading herniation. Present study gives an idea about risk factors of herniation for the suggested future study.

Acknowledgements

REFERENCES

1. Bhanu PS, Sankar KD. Incidence of Foramen of Huschke in South Andhra Population of India. J Clin Diagn Res. 2016; 10(6): AC01–AC03, doi: 10.7860/JCDR/2016/18735.8031, indexed in Pubmed: 27504269.

2. Burlak K, So TY, Maclaurin WA, et al. Foramen tympanicum with symptomatic temporomandibular joint herniation. Radiol Case Rep. 2018; 13(4): 822–824, doi: 10.1016/j.radcr.2018.05.009, indexed in Pubmed: 29988923.

3. Deniz Y, Geduk G, Zengin AZ. Examination of foramen tympanicum: an anatomical study using cone-beam computed tomography. Folia Morphol. 2018; 77(2): 335–339, doi: 10.5603/FM.a2017.0078, indexed in Pubmed: 28868610.

4. Ertugrul S. Rare cause of tinnitus: spontaneous temporomandibular joint herniation into the external auditory canal. J Craniofac Surg. 2018; 29(5): e521–e522, doi: 10.1097/SCS.0000000000004579, indexed in Pubmed: 29608483.

5. Ertugrul S, Keskin NK. Relationship between the degree of mastoid pneumatization and the presence of persistent foramen of Huschke. Int J Oral Maxillofac Surg. 2019; 48(8): 1072–1076, doi: 10.1016/j.ijom.2019.01.022, indexed in Pubmed: 30773335.

6. Ertugrul S, Keskin NK. Relationship of age to foramen of Huschke and investigation of the development of spontaneous temporomandibular joint herniation. Int J Oral Maxillofac Surg. 2019; 48(4): 534–539, doi: 10.1016/j.ijom.2018.08.011, indexed in Pubmed: 30205912.

7. Fusconi M, Benfari G, Franco M, et al. Foramen of Huschke: case report and experimental procedure for diagnosis of spontaneous salivary fistula. J Oral Maxillofac Surg. 2009; 67(8): 1747–1751, doi: 10.1016/j.joms.2008.12.065, indexed in Pubmed: 19615593.

8. Hashimoto T, Ojiri H, Kawai Y. The foramen of Huschke: age and gender specific features after childhood. Int J Oral Maxillofac Surg. 2011; 40(7): 743–746, doi: 10.1016/j.ijom.2011.03.017, indexed in Pubmed: 21549561.

9. Henry BM, Tomaszewski KA, Walocha JA. Methods of evidence-based anatomy: a guide to conducting systematic reviews and meta-analysis of anatomical studies. Ann Anat. 2016; 205: 16–21, doi: 10.1016/j.aanat.2015.12.002, indexed in Pubmed: 26844627.

10. Henry BM, Tomaszewski KA, Ramakrishnan PK, et al. Development of the anatomical quality assessment (AQUA) tool for the quality assessment of anatomical studies included in meta-analyses and systematic reviews. Clin Anat. 2017; 30(1): 6–13, doi: 10.1002/ca.22799, indexed in Pubmed: 27718281.

11. Jaju PP. Cone beam CT detection of foramen tympanicum or foramen of Huschke. Dentomaxillofac Radiol. 2012; 41(7): 619, doi: 10.1259/dmfr/50909630, indexed in Pubmed: 22933530.

12. Lacout A, Marsot-Dupuch K, Smoker WRK, et al. Foramen tympanicum, or foramen of Huschke: pathologic cases and anatomic CT study. Am J Neuroradiol. 2005; 26(6): 1317–1323, indexed in Pubmed: 15956489.

13. Lim KH, Jung JY, Rhee J, et al. Temporomandibular joint herniation through the foramen of Huschke with clicking tinnitus. Eur Ann Otorhinolaryngol Head Neck Dis. 2019; 136(6): 497–499, doi: 10.1016/j.anorl.2018.05.014, indexed in Pubmed: 31010735.

14. Magliulo G. Acquired atresia of the external auditory canal: recurrence and long-term results. Ann Otol Rhinol Laryngol. 2009; 118(5): 345–349, doi: 10.1177/000348940911800505, indexed in Pubmed: 19548383.

15. Mittal S, Singal S, Mittal A, et al. Identification of foramen of Huschke with reversible herniation of temporomandibular joint soft tissue into the external auditory canal on multidetector computed tomography. Proc (Bayl Univ Med Cent). 2017; 30(1): 92–93, doi: 10.1080/08998280.2017.11929544, indexed in Pubmed: 28127148.

16. Moreno R, Chilvarquer I, Hayek J, et al. Anatomic and radiograph study of the persistence of Foramen of Huschke. Braz J Otorhinolaryngol. 2005; 71(5): 676–679, doi: 10.1016/s1808-8694(15)31273-8.

17. Nakasato T, Nakayama T, Kikuchi K, et al. Spontaneous temporomandibular joint herniation into the external auditory canal through a persistent foramen tympanicum (Huschke): radiographic features. J Comput Assist Tomogr. 2013; 37(1): 111–113, doi: 10.1097/RCT.0b013e318272ef04, indexed in Pubmed: 23321842.

18. Park YHo, Kim HJ, Park MH. Temporomandibular joint herniation into the external auditory canal. Laryngoscope. 2010; 120(11): 2284–2288, doi: 10.1002/lary.21115, indexed in Pubmed: 20939076.

19. Pękala JR, Pękala PA, Satapathy B, et al. Incidence of Foramen Tympanicum (of Huschke): Comparing Cadaveric and Radiologic Studies. J Craniofac Surg. 2018; 29(8): 2348–2352, doi: 10.1097/SCS.0000000000004784, indexed in Pubmed: 30277949.

20. Pirsig W, Mudry A. Huschke's anterior external auditory canal foramen: art before medicine? Otol Neurotol. 2015; 36(3): 555–560, doi: 10.1097/MAO.0000000000000418, indexed in Pubmed: 24786542.

21. Prowse SJ, Kelly G, Agada F. Temporomandibular joint herniation and the foramen of Huschke: an unusual external auditory canal mass. J Laryngol Otol. 2011; 125(12): 1279–1281, doi: 10.1017/S0022215111002295, indexed in Pubmed: 21910955.

22. Sanna M, Russo A, Khrais T, et al. Canalplasty for severe external auditory meatus exostoses. J Laryngol Otol. 2004; 118(8): 607–611, doi: 10.1258/0022215041917808, indexed in Pubmed: 15453935.

23. Shapiro MC, Osborn T. Temporoparietal fascia flap and total temporomandibular joint replacement for the management of patent foramen of Huschke. Int J Oral Maxillofac Surg. 2016; 45(8): 1023–1026, doi: 10.1016/j.ijom.2016.03.006, indexed in Pubmed: 27066740.

24. Shin JE, Jeong KH, Ahn SH, et al. Temporomandibular joint herniation into the external auditory canal: two

cases involving a persistent foramen tympanicum. J Craniofac Surg. 2015; 26(4): e331–e333, doi: 10.1097/SCS.0000000000001630, indexed in Pubmed: 26080253.

25. Tomaszewski KA, Henry BM, Kumar Ramakrishnan P, et al. Development of the anatomical quality assurance (AQUA) checklist: guidelines for reporting original anatomical studies. Clin Anat. 2017; 30(1): 14–20, doi: 10.1002/ca.22800, indexed in Pubmed: 27801507.

26. Tozoglu U, Caglayan F, Harorli A. Foramen tympanicum or foramen of Huschke: anatomical cone beam CT study. Dentomaxillofac Radiol. 2012; 41(4): 294–297, doi: 10.1259/dmfr/62359484, indexed in Pubmed: 22517996.

27. Tucunduva RM, Lopes IA, Shinohara AL, et al. Usefulness of cone-bean computed tomography exams to detect foramen of huschke in diverse age group. J Craniofac Surg. 2019; 30(2): e138–e141, doi: 10.1097/SCS.0000000000005069, indexed in Pubmed: 30570591.

28. van der Meer WL, van Tilburg M, Mitea C, et al. A persistent foramen of huschke: a small road to misery in necrotizing external otitis. Am J Neuroradiol. 2019; 40(9): 1552–1556, doi: 10.3174/ajnr.A6161, indexed in Pubmed: 31395661.

29. Wang RG, Bingham B, Hawke M, et al. Persistence of the foramen of Huschke in the adult: an osteological study. J Otolaryngol. 1991; 20(4): 251–253, indexed in Pubmed: 1920577.

30. Yoo MH, Park JW, Lee HS, et al. Repair of the foramen of Huschke using an extended endaural approach. Laryngoscope. 2016; 126(9): 2137–2139, doi: 10.1002/lary.25718, indexed in Pubmed: 26466967.

VIA MEDICA

ORIGINAL ARTICLE

Determining anatomical localisations of cervical oesophagus, hiatal clamp and oesophagogastric junction with oesophagogastroduodenoscopy

E. Bozdag[1] , Z. Karaca Bozdag[2] , A. Kurkcuoglu[3] , A. Pamukcu Beyhan[4, 5] ,
H. Bozkurt[6] , A.S. Senger[6]

[1]Gastroenterology Surgery Clinic, Kanuni Sultan Süleyman TRH, Health Sciences University, Istanbul, Turkey
[2]Department of Anatomy, Faculty of Medicine, Istanbul Yeni Yüzyıl University, Istanbul, Turkey
[3]Department of Anatomy, Faculty of Medicine, Kırıkkale University, Kırıkkale, Turkey
[4]Department of Business Administration, Land NCO Vocational School, National Defence University, Balikesir, Turkey
[5]Department of Biostatistics and Medical Informatics, Faculty of Medicine, Ege University, Izmir, Turkey
[6]Gastroenterology Surgery Clinic, Kartal Koşuyolu High Specialisation TRH, Health Sciences University, Istanbul, Turkey

Background: In this study, the purpose was to determine the anatomical localisations of the cervical oesophagus length, hiatal clamp, and oesophagogastric junction depending on age and gender in patients who undergo oesophagogastroduodenoscopy (EGD).

Materials and methods: The images of the patients who underwent EGD between 2018 and 2020 were analysed retrospectively in this study. The distance of the anatomical localisations of the cervical oesophagus length, hiatal clamp, and oesophagogastric junction to the anterior incisors, and the relations of this distance with the demographic characteristics and clinical manifestations of the patients were investigated on the EGD data.

Results: A total of 298 patients (174 women, 124 men) were included in the study. The cervical oesophagus length and the distance of the oesophagogastric junction and hiatal clamp localisation of the patients were found to be 15.06 ± ± 0.57 cm, 37.51 ± 2.23 cm and 38.62 ± 2.23 cm, respectively. It was also found that the mean values of all lengths in males were higher at a statistically significant level than in females (p < 0.001; p < 0.01).

Conclusions: Knowing these anatomical localisations may be important in predicting complications that may occur in this region in EGD and planning the precautions to be taken. We also believe that it will guide clinicians in determining hiatal hernia and related deficiencies. (Folia Morphol 2022; 81, 3: 756–765)

Key words: oesophagogastroduodenoscopy, cervical oesophagus length, hiatal clamp, oesophagogastric junction

INTRODUCTION

Endoscopic examination of the gastrointestinal system (GIS) is accepted as the gold standard all over the world [17]. Oesophagogastroduodenoscopy (EGD) includes the imaging of the oropharynx, oesophagus, stomach, and proximal duodenum. The

oesophagus, after the oropharynx, is approximately 25 cm long and has the form of a collapsed tube unless inflated. It has three parts; the pars cervicalis extends from the lower edge of the cartilago cricoidea to the incisura jugularis at the level of the C6–T2 vertebra (5–8 cm). Pars thoracica is located at the level of T2–T10 vertebrae in mediastinum superius and posterius (15–18 cm). Pars abdominalis is the part (1–3 cm) passing through the hiatal clamp at the level of T10 vertebra and extending to the ostium cardiacum. Oesophagogastric junction is usually 40 cm after the anterior incisors [17]. Although the oesophagogastric junction is not an endoscopically visible part in patients without a hiatal hernia, it is considered to be the *Z* line where the lower oesophageal sphincter is also located. The hiatus oesophagus is the opening on the diaphragm where the oesophagus passes from the thorax to the abdomen, and is one of the three openings of the diaphragm localised in the crus dextrum. This opening is at the T10 level, elliptical, and is located in the muscular part of the diaphragm with a diameter of approximately 2.5 cm and 2–3 cm in length in the left posterior upper part of the hiatus aorticus slightly to the left at the middle part. This anatomical localisation, which is clinically called the hiatal clamp, is detected below the oesophagogastric junction on average 1 cm if viewed with EGD [7]. In the present study, hiatus oesophagus was used as the distance of the hiatal clamp to the anterior incisors, which is in line with the literature.

The stomach fundus, which begins after it passes through the oesophagogastric junction at the level of the thoracic eleventh vertebra, continues down and to the left with the corpus. The region that is called incisura angularis at the entrance of the antrum pyloricum in the stomach is an important point for EGD because it is the most common area of helicobacter pylori. Following the pars horizontalis (1st part), which is approximately 5 cm, of the duodenum that consists of four parts, the pars descendens (2nd part) begins as the part EGD process ends [10, 17].

Oesophagogastric junction is an important anatomical area with its basic functions. Where the oesophagus ends and the stomach begins is discussed among histologists, physiologists, gastroenterologists, radiologists, and surgeons for many years. It is important to understand that there are differences in the normality range which will be recognised and interpreted easily by an experienced gastroenterologist. Although monomeric evaluation is needed to evaluate

functional disorders, biopsy and EGD are essential to diagnose structural and histological abnormalities [30]. This diagnostic and therapeutic method might lead to some life-threatening complications. The most common cause of oesophageal perforations are particularly these iatrogenic damages. The incidence of this condition varies between 0.0009% and 0.01% [25]. Such iatrogenic injuries are most commonly detected in the part called "the cervical oesophagus". For this reason, preserving the tubular structure of the oesophagus when the oesophagus is entered is the most important aspect to be considered in this regard. However, since the oesophagogastric junction shows continuous peristalsis, the normal change in the mucosa can usually be distinguished with a little excess air insufflation [17]. Determining the length of these areas, which were mentioned in the present study, will guide the endoscopy specialist who performs the procedure to be more careful in the detected lengths when s/he passes through these and similar risky areas.

In the present study, the purpose was to determine the anatomic localisations of cervical oesophagus length, hiatal clamp, and oesophagogastric junction in patients who undergo EGD, depending on age and gender.

MATERIALS AND METHODS

In this study, the data of 695 patients who underwent EGD between 2018 and 2020 were retrospectively analysed. Among these patients, 56 patients who were under 18 years of age, 315 patients who had a history of upper gastrointestinal surgery, 9 patients who were diagnosed with upper gastrointestinal cancer, 1 with implanted PEG, and 16 patients with hiatal hernia were not included in the study. The present study was conducted with 298 patients.

After a full 6-hour oral intake restriction, verbal and written consent was obtained from the patient and necessary information was given. Before the procedure, pharyngeal anaesthesia was applied with 10% lidocaine spray. Afterwards, the patient was positioned to the left of the endoscopist, with the head slightly flexed and the chin closer to the chest. The Olympus GIF-Q scope was advanced by providing direct vision. The structures in the mouth were roughly evaluated, and the oesophagus was entered by observing the piriform sinuses. The distance from the anterior incisors to the first stricture after passing the epiglottis was considered as the cervical oesoph-
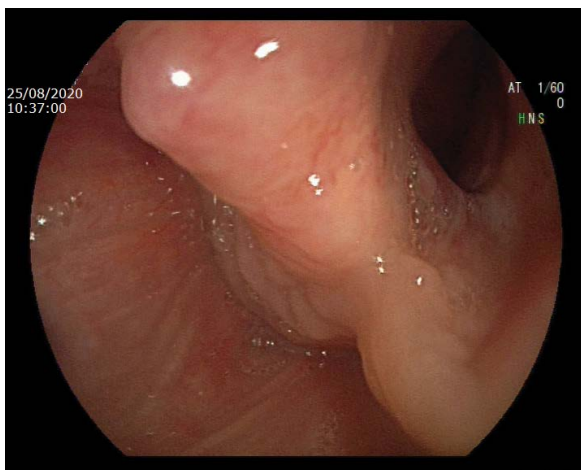
Figure 1. Entry to cervical oesophagus (oesophagogastroduodeno-scopy image).
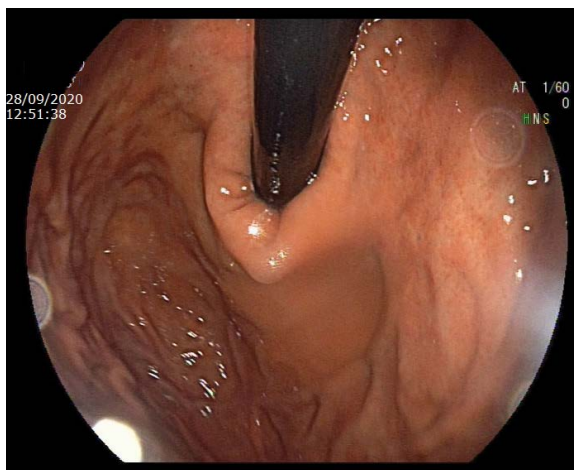

Figure 3. Hiatal clamp (oesophagogastroduodenoscopy image).

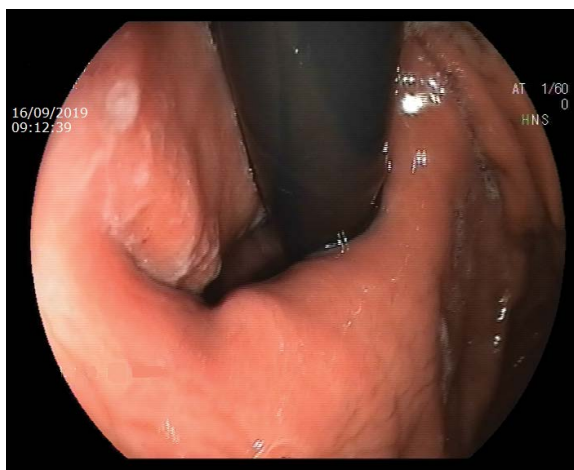**Figure 2.** Oesophagogastric junction, Z line (oesophagogastroduo-denoscopy image).

Figure 4. Hiatal hernia (loose hiatal clamp) (oesophagogastroduo-denoscopy image).

agus length (Fig. 1). The oesophagus was evaluated by providing adequate insufflation and the scope was pushed distally in a controlled manner. In the most distal part of the oesophagus, the squamocolumnar epithelial region (transition zone), Z line, where the squamous epithelium of the oesophagus ends and the columnar epithelium of the stomach begins, was observed. The distance between the anterior incisors and the Z line was measured as the distance to the anatomical localisation of the oesophagogastric junction (Fig. 2). The place where the diaphragm crus are seen approximately 1 cm after the oesophagogastric junction is considered as the hiatal clamp (hiatus oesophagus). The distance from the anterior incisors to this point was measured as the distance to the anatomical localisation of the hiatal clamp

(Figs. 3, 4). The stomach was entered by passing the hiatal clamps. After careful evaluation of the stomach structures, the duodenum was evaluated by passing the pylorus. The distal end portion of the duodenum, which was evaluated, was the second continent and was advanced until the scope reached this point. Afterwards, a detailed controlled examination was performed at the exit and the procedure was terminated by aspirating the air given during the procedure. All measurements were made by the same investigator. It was recommended that patients not take solid or liquid food for two hours after the procedure.

Previous studies have shown that these measurements can also be made with manometers and pH meters. If we look at the working principle of these methods, the pH meter is applied through the

nose and the lower oesophageal sphincter is directly reached without seeing the anatomical points we measured in the study. It is based on placing the catheter 5 cm above the sphincter and recording the pH changes on a digital recorder outside the catheter at 4–8 second intervals [29]. The manometer is suitable for use to detect oesophageal motor patterns and extreme motor abnormalities (e.g. achalasia and extreme hypomotility) [26]. In both methods, both the length cannot be determined objectively and the main indications differ. When these methods are considered and evaluated, the easiest, cheapest and most applicable method is endoscopy.

Statement of ethics

The approval of the Ethics Committee regarding the study was obtained from the Health Sciences University, Kartal Kosuyolu Training and Research Hospital, Non-Interventional Clinical Research Ethics Committee (IRB: 2019.4/26-203).

Statistical analysis

The population of the study consisted of approximately 1300 individuals who met the inclusion criteria in the evaluation between 2018 and 2019 based on EGD measurements. In this respect, in the calculation based on the following formula, the number of patients that would be included in the study was determined as a minimum of 297 patients, with n = 296.71 [28].

$$n = \frac{Nt^2 pq}{d^2(N-1) + t^2 pq}$$

(N — population; n — frequency of application to be included in the sampling; p — frequency of the occurrence of the investigated event; q — frequency of absence of the investigated event; t — the theoretical value found from the t table at a certain degree of freedom and the detected error level; d — the ± deviation desired to be done according to the incidence of the event)

When the findings obtained in the study were evaluated, the IBM® SPSS® (Statistical Package for the Social Sciences) software version 22 (IBM Corp. Armonk, NY, USA) was used for statistical analyses. The conformity of the variables to the normal distribution was evaluated with the Kolmogorov-Smirnov test, Q-Q graphs, and histograms. When the study data were evaluated, the Student-t test was used for the evaluation of the quantitative data between two groups along with descriptive statistical methods (i.e. mean, standard deviation, frequency, percentage). The Student-t test was used for the evaluation of the quantitative data between two groups. The One--Way Analysis of Variance (ANOVA) was used for the evaluation of quantitative data between more than two groups, and the Tukey Post-Hoc Test was used to determine the group which caused the difference. The Pearson Chi-Square Test, the Continuity (Yates) Corrected Chi-Square Test, and the Fisher's Full Chi--Square Test were used to evaluate qualitative data. Significance was taken as p < 0.05 level.

RESULTS

The present study was conducted with 298 patients who underwent EGD, 41.6% (n = 124) of whom were male, and 58.4% (n = 174) female. The ages of the patients ranged between 21 and 91 with a mean of 53.77 ± 13.47. A total of 6.7% (n = 20) of the patients were under 35 years old, 19.5% (n = 58) were 35–44 years of age, 24.2% (n = 72) were 45–54, 27.5% (n = 82) were 55–64, and 22.1% (n = 66) were at and above the age of 65.

The cervical oesophagus length of the patients varied between 14 and 16 cm with a mean of 15.06 ± ± 0.57 cm, and the oesophagogastric junction length varied between 30 and 44 cm with an average of 37.51 ± 2.23 cm, and the distance of the hiatal clamp localisation to the anterior incisors varied between 31 and 46 cm with a mean of 38.62 ± 2.23 cm.

It was found that there were statistically significant differences between the average length of the anatomical location of the hiatal clamp, the distance from the anterior incisors, and the age groups (p = 0.031, p < 0.05). As a result of the Tukey Post--Hoc Test that was applied to determine which age group the difference originated from, the mean hiatal clamp length of the patients who were under 35 years of age was significantly higher than the patients who were between the ages of 35–44 (p = 0.030; p < 0.05) (Table 1).

When the cervical oesophagus, oesophagogastric junction, and hiatus clamp lengths were compared according to gender, the mean values of all lengths were found to be higher in males at a statistically significant level than in females (p < 0.001; p < 0.01).

When the indications for EGD applied to the patients were evaluated, 48.7% (n = 145) had dyspepsia as the reason, 30.9% (n = 92) cancer screening, 6% (n = 18) follow-up, 5.4% (n = 16) gastroesophageal reflux disease (GERD), 5% (n = 12) GIS bleeding, and 4% (n = 15) other (dysphagia, intensive care patient nasogastric feeding).

759

Table 1. The evaluation of the oesophagogastroduodenoscopy (EGD) data according to the age groups

EGD data [cm]	Age group					F	P
	< 35 years	35–44 years	45–54 years	55–64 years	> 65 years		
Cervical oesophagus length [cm]	15.15 ± 0.67	15.07 ± 0.56	15.07 ± 0.54	15.04 ± 0.6	15.06 ± 0.58	0.161	0.958
Oesophagogastric junction length [cm]	38.35 ± 2.30	37.22 ± 2.24	37.86 ± 2.11	37.28 ± 2.41	37.42 ± 2.08	1.641	0.164
Hiatal clamp length [cm]	39.80 ± 2.71	38.14 ± 2.37	38.96 ± 2.04	38.51 ± 2.26	38.44 ± 2	**2.702**	**0.031***

Data are shown as mean ± standard deviation; F: One-Way Variance Analysis (ANOVA); *p < 0.05

Table 2. The evaluation of the patients' anatomical localizations according to the oesophagogastroduodenoscopy indications

Indications	Cervical oesophagus length [cm]	Oesophagogastric junction length [cm]	Hiatal clamp length [cm]
Dyspepsia	15.04 ± 0.54	37.36 ± 2.16	38.46 ± 2.18
Cancer screening	15.17 ± 0.72	38.75 ± 2.09	39.50 ± 2.39
Control	15.25 ± 0.58	37.56 ± 2.90	38.88 ± 2.60
GERD	15.07 ± 0.61	37.54 ± 2.30	38.66 ± 2.32
GIS bleeding	15.11 ± 0.58	37.83 ± 2.15	38.94 ± 2.13
Other	14.93 ± 0.59	37.40 ± 2.03	38.47 ± 1.92
F	0.634	0.959	0.653
P	0.674	0.443	0.660

Data are shown as mean ± standard deviation; F: One-Way Variance Analysis (ANOVA); GERD — gastroesophageal reflux disease; GIS — gastrointestinal system

Table 3. The evaluation of the indications of oesophagogastroduodenoscopy in patients according to the age groups

Indications	Age group					χ^2	P
	< 35 years	35–44 years	45–54 years	55–64 years	≥ 65 years		
Dyspepsia	10 (50%)	34 (58.6%)	34 (47.2%)	43 (52.4%)	24 (36.4%)	6.841	0.145
Cancer screen	5 (25%)	17 (29.3%)	25 (%34.7)	21 (%25.6)	24 (%36.4)	2.886	0.577
Control	1 5(%)	1 (1.7%)	6 (7.3%)	6 (7.3%)	4 (6.1%)	2.845	0.584
GERD	3 (15%)	2 (3.4%)	3 (4.2%)	3 (3.7%)	5 (7.6%)	5.382	0.250
GIS bleeding	1 (5%)	–	2 (2.8%)	6 (7.3%)	3 (4.5%)	–	–
Other	–	4 (6.9%)	2 (2.8%)	3 (3.7%)	6 (9.1%)	–	–

χ^2: Pearson Chi-Square Test; GERD — gastroesophageal reflux disease; GIS — gastrointestinal system

No statistically significant differences were detected between the indications EGD in the patients and the mean lengths of cervical oesophagus, hiatal clamp, and oesophagogastric junction localisations (p > 0.05) (Table 2).

No statistically significant differences were detected between the age groups and indications of performing EGD in patients (p > 0.05). The relations between the indications for EGD and gender were also investigated. In this respect, the rate of EGD because of dyspepsia was found to be higher in women (55.2%) at a statistically significant level than in men (39.5%) (p = 0.008; p < 0.01) (Table 3). Also, the rate of EGD because of GIS bleeding was found to be higher at a statistically significant level in males (7.3%) than in females (1.7%) (p = 0.032; p < 0.05).

A total of 27.2% (n = 81) of the patients who underwent EGD had antral gastritis diagnosis, 21.8% (n = 65) loose lower oesophageal sphincter (LES), 11.1% (n = 33) alkaline reflux, 10.4% (n = 31) pangastritis, 8.1% (n = 24) erosive gastritis, 3.4% (n = 10), ulcer (antrum), 5% (n = 15) other diagnoses (bulbitis, Barret's oesophagus, oesophagitis, pyloric strictures) and 4.7% (n = 14) normal.

No statistically significant differences were detected between the diagnoses of the patients after EGD and the mean lengths of cervical oesophagus, oesophagogastric junction, and hiatal pincer localizations (p > 0.05) (Table 4).

Table 4. The evaluation of the anatomical localisations according to the diagnosis of patients after oesophagogastroduodenoscopy

Diagnoses		Cervical oesophagus length [cm]	Oesophagogastric junction length [cm]	Hiatal clamp length [cm]
Antral gastritis	Yes	15.09 ± 0.57	37.59 ± 2.33	38.64 ± 2.30
	No	15.00 ± 0.57	37.32 ± 1.97	38.57 ± 2.06
	t	0.248	0.908	0.234
	p	0.242	0.365	0.815
Loose lower oesophagus sphincter	Yes	15.09 ± 0.49	37.43 ± 2.15	38.75 ± 2.05
	No	15.06 ± 0.60	37.54 ± 2.26	38.58 ± 2.28
	t	0.182	-0.337	0.556
	p	0.651	0.737	0.578
Alkalane reflux	Yes	14.97 ± 0.53	37.33 ± 2.07	38.82 ± 2.35
	No	15.08 ± 0.58	37.54 ± 2.26	38.59 ± 2.22
	t	−0.999	−0.490	0.547
	p	0.319	0.624	0.585
Pangastritis	Yes	15.00 ± 0.63	37.10 ± 2.48	38.39 ± 2.36
	No	15.07 ± 0.57	37.56 ± 2.21	38.64 ± 2.22
	t	−0.53	−1.097	−0.606
	p	0.514	0.274	0.545
Erosive gastritis	Yes	15.08 ± 0.50	37.25 ± 2.31	38.75 ± 1.87
	No	15.06 ± 0.58	37.54 ± 2.23	38.61 ± 2.26
	t	0.174	−0.601	0.303
	p	0.862	0.548	0.762
Polyp	Yes	15.07 ± 0.62	37.36 ± 2.21	38.43 ± 2.31
	No	15.06 ± 0.57	37.52 ± 2.24	38.63 ± 2.23
	t	0.051	−0.268	−0.324
	p	0.959	0.789	0.746
Ulcer	Yes	15.20 ± 0.63	38.30 ± 2.75	39.20 ± 2.53
	No	15.06 ± 0.57	37.49 ± 2.22	38.6 ± 2.22
	t	0.419	0.378	0.839
	p	0.446	0.258	0.402
Normal	Yes	15.07 ± 0.59	37.2 ± 2.27	38.27 ± 2.15
	No	15.06 ± 0.57	37.53 ± 2.24	38.64 ± 2.24
	t	0.981	0.903	0.677
	p	0.984	0.578	0.533

Data are shown as mean ± standard deviation; t: Student-t test

When the differences in the diagnosis were examined according to the age groups, no differences were detected except for the patients who were diagnosed with antral gastritis; however, statistically significant differences were detected in the incidence rates ($p < 0.001$; $p < 0.01$). It was also found that the rate of diagnosis of antral gastritis in those who were aged 65 and over was lower than in other age groups (Table 5).

When the diagnosis of the patients after EGD was evaluated according to gender, the rate of diagnosis of antral gastritis was found to be higher at a statistically significant level in women (77.6%) than in men (66.1%) ($p = 0.028$; $p < 0.05$) (Table 6).

The incidence of loose LES was found to be higher at a statistically significant level in men (28.2%) than in women (17.2%) ($p = 0.034$; $p < 0.05$) (Table 6).

DISCUSSION

The oesophagus is a muscular (smooth muscle) tube connecting the pharynx and the stomach, starting from the C6 vertebra level extending to the T11 level with an average length of 25–30 cm. In the literature, the oesophageal length is accepted as the distance between the upper oesophageal sphincter and the lower oesophageal sphincter [17]. Although Li et al. [21] found the oesophageal length as 22.9 cm on average in healthy individuals, Award et al. [5] found it to be 28.3 cm on average, and Yau et al. [33] as 23 cm, which is similar to the study of Li et al. [21]. In their study, Marshall et al. [22] found the oesophageal length to be significantly higher with a mean of 21.12 cm in men than in women (mean 20.15 cm). The length of the oesophagus is accepted as 25–30 cm on average in the literature, and was determined as 9–10 cm in newborns [23]. The cervical oesophagus, which starts

Table 5. The evaluation of the diagnoses of the patients after oesophagogastroduodenoscopy according to age groups

Diagnoses	Age group					χ²	P
	< 35 years	35–44 years	45–54 years	55–64 years	≥ 65 years		
Antral gastritis	15 (75%)	50 (86.2%)	54 (75%)	63 (76.8%)	35 (53%)	**19.197**	**< 0.001***
Loose lower oesophagus sphincter	5 (25%)	13 (22.4%)	9 (12.5%)	21 (25.6%)	17 (25.8%)	5.088	0.278
Alkalane reflux	5 (25%)	5 (8.6%)	6 (8.3%)	9 (11%)	8 (12.1%)	4.917	0.296
Pangastritis	2 (10%)	4 (6.9%)	8 (11.1%)	7 (8.5%)	10 (15.2%)	2.710	0.607
Erosive gastritis	–	4 (6.9%)	4 (5.6%)	7 (8.5%)	9 (13.9%)	–	–
Ulcer (in the antrum)	–	2 (3.4%)	2 (2.8%)	1 (1.2%)	5 (7.6%)	5.548	0.236
Other	2 (10%)	2 (3.4%)	5 (6.9%)	2 (2.4%)	4 (6.1%)	3.187	0.527
Normal	1 (5%)	3 (5.2%)	1 (1.4%)	3 (3.7%)	6 (9.1%)	4.837	0.307

χ²: Pearson Chi-Square Test; *p < 0.01

Table 6. The evaluation of the diagnoses of the patients after oesophagogastroduodenoscopy according to gender

Diagnoses	Gender		χ²	P
	Male	Female		
Antral gastritis	82 (66.1%)	135 (77.6%)	**4.802**[1]	**0.028***
Loose lower oesophagus sphincter	35 (28.2%)	30 (17.2%)	**5.122**[1]	**0.034***
Alkalane reflux	14 (11.3%)	19 (10.9%)	0.010[2]	0.920
Pangastritis	14 (11.3%)	17 (9.8%)	0.053[2]	0.817
Erosive gastritis	7 (5.6%)	17 (9.8%)	1.153[2]	0.283
Ulcer (in the antrum)	4 (3.2%)	6 (3.4%)	0.011[3]	1.000
Other	8 (6.5%)	7 (4%)	0.458[2]	0.499
Normal	6 (4.8%)	8 (4.6%)	0.001[2]	1.000

[1]χ²: Pearson Chi-Square Test; [2]χ²: Continuity (Yates) corrected Chi-Square Test; [3]χ²: Fisher Exact Chi-Square Test; *p < 0.05

from the lower edge of the cartilago cricoidea and ends at the lower edge of the first thoracic vertebra, is approximately 18 cm after the anterior incisors [3]. Because of the anatomical localisation of the cervical oesophagus in EGD procedure, it is a difficult area to measure as it activates the gag reflex when passing with the endoscope. Studies conducted on cervical oesophageal length are very limited in the literature. In the present study, in which the purpose was to investigate the cervical oesophagus length and the relations between age and gender, the average cervical oesophagus length was found to be 15.06 ± 0.57 cm. We believe that the fact that it is shorter that the value reported in the literature was because of the difference between races. Although no significant differences were detected in cervical oesophagus lengths between the age groups, cervical oesophagus length was found to be significantly higher in men (mean 15.31 cm) than in women (mean 14.85 cm) between genders.

In the clinical practice, the hiatal clamp is formed by the right and left crus of the diaphragm at the 10 vertebra level after the anterior incisors at an average of 38 cm [19]. Csendes et al. [8] investigated the localisation of the lower oesophageal sphincter in 778 patients comparing the results with 109 healthy control groups, and reported the lower oesophageal sphincter of the healthy group to be 38 cm on average [14]. Similarly, in the present study, the average length of the hiatal clamp distance from the anterior incisors was detected to be 38.6 cm. Also, the mean hiatal clamp length of patients under 35 years of age was found to be significantly higher than those of patients aged 35–44 in the study (p = 0.030; p < 0.05). It was also found that the mean hiatus oesophagus distance was statistically longer in men (39.77 cm) than women (37.8 cm) in the comparison between the genders.

Previous studies showed that the average distance from the anterior incisors to the oesophagogastric junction is 38–40 cm in men and 36–38 cm in women, which is 18 cm at birth, 22 cm at the age of 3, and 27 cm at the age of 10 [23, 27]. In the present study,

the average length of the oesophagogastric junction was found to be 37.5 cm, and no significant differences were detected between the age groups. This distance (mean 38.66 cm) was found to be longer in men than in women (mean 36.7 cm), which is consistent with the literature data.

Although the number of patients who were diagnosed with reflux oesophagitis was 43% in the study of Csendes et al. [8], it was reported that 15–25% of the patients who underwent EGB in western societies had oesophagitis. This frequency was much less common (0.8–16.3%) in other studies that were conducted in Asia [14, 31]. In the present study, the incidence of oesophagitis was found to be 6.5% under the heading of other diagnoses. We believe that the fact that this value was far below the literature data since it had a single-cantered design, and therefore the number of cases was low.

There are many accepted indications for EGD the main ones including evaluation of dysphagia, GIS bleeding, peptic ulcer disease, medically resistant GERD, oesophageal strictures, coeliac disease, and unexplained diarrhoea. The fact that the LES does not fully grasp the endoscope in endoscopic examinations performed with retroflexion from the fundus of the stomach despite deep inspiration and expiration and is considered as "LES laxity" [17]. In the present study, the incidence of LES laxity after endoscopy was found to be statistically significantly higher in men (28.2%) than in women (17.2%) (p = 0.034; p < 0.05). In a study that was conducted by Aksoy et al. [1] with geriatric patients, the rate of loose LES was reported as 34%. However, the rates were not given in this study for men and women.

Knowing the anatomical localisation of the hiatal clamp is important to diagnose hiatal hernia and identify hiatal insufficiency. Hiatal hernia is a common disease defined as the protrusion of the abdominal organs — often the stomach — from the enlarged hiatus oesophagus into the thoracic cavity [2]. Andujar et al. [3] argued that laparoscopic repair of large paraoesophageal hernia is associated with a low incidence of recurrence and reoperation. In their study conducted in 2006, Johnson et al. [16] reported that the incidence of hiatal hernia increases with age. The incidence of hiatal hernia in upper GIS endoscopies was found to be higher in men (15.5%) than in women (14%) in our country [12]. The patients who were diagnosed with hiatal hernia were not included in the present study as it would disrupt the standardisation of the normal

anatomical structure. A total of 16 of 335 retrospectively screened patients were excluded from the study since they were diagnosed with hiatal hernia.

Oesophagus strictures are among the most common problems in our present day. EGD must be performed to determine the underlying cause in oesophageal strictures. The overall rate of oesophageal strictures that require dilation among the patients who undergo upper gastrointestinal endoscopy was found to be 6%, and 3% of which were malignant, 2.7% benign, and 0.3% functional strictures [17]. In the study that was conducted by Chow et al. [6], it was argued that the presence of hiatal hernia doubles the risk of oesophageal carcinoma, and that the risk even increases cumulatively with the presence of reflux symptoms, dysphagia, and previously described symptoms of oesophagitis.

The definition of the oesophagogastric junction varies among specialty groups. One definition that was made by surgeons and endoscopy specialists where there is a sudden change of gastric mucosa in the mucosa passing through the oesophagus, and this jagged line was designated as the "Z line" [23]. This line is used as a baseline in distinguishing anatomical concepts associated with the oesophagus and measuring lengths. One of these is the measurement of the length of the LES. In the clinical practice, the LES length is used often for measuring the intraluminal pressure of the oesophagus and for pH monitoring. Knowing the length of this area will ensure correct placement of the catheter, which will result in the better recognition and easier diagnosis of diseases in this area such as GERD and achalasia. For this reason, proper placement of the probes in these localisations is necessary [32]. Knowing the normal anatomy will also guide us in the diagnosis of diseases in this area. For example, measuring these parts in the detection of hiatal hernias and detecting the short oesophagus in the surgeries in the clinical practice can guide the surgeon in terms of the problems which might be faced after the surgery. Knowing that there is a short oesophagus in patients who have hiatal hernia can guide the surgeon in dealing with related problems before the surgery about recurrences and complications which might occur in the postoperative period [20]. Another problem which might be faced in this area is the perforations as a result of endoscopic interventions. These iatrogenic perforations are most commonly detected in the hypopharynx and distal oesophagus. The clinical manifestation of this varies depending on the level of

the perforated area. For example, when patient present with symptoms such as neck pain, crepitation, etc. for perforation in the cervical parts, these symptoms cause other symptoms such as epigastric and shoulder pain as they progress towards the abdomen. The success in treatment also varies according to the localisation. For example, it is already known that stent migration is more and is more difficult to place in proximal perforations, which complicates the treatment increasing stent-related treatment failure [9].

As understood with the examples, the determination of anatomical localisations not only guides the problems that might appear, it also helps to determine the treatment methods that will be chosen. The present study is an anatomy study in which it was found that the length of the anatomical localisation of the hiatal clamp from the anterior incisors differed according to age and gender. It was also found that the hiatal clamp length is longer in young age than in older ages ($p = 0.035$, Table 3), and the hiatal clamp length is longer in male gender than female gender at statistically significant levels ($p < 0.001$, Table 4). In their study conducted on 50 cadavers, Shamiyeh et al. [24] reported that this length is important in repairing the crus in hiatal hernias and in the treatment of GERD. They measured this length by measuring the area defined as the hiatal surface area. As mentioned in this example, it was seen that the evaluation was made by measuring the hiatal surface area that can be measured during the operation. In another study that was conducted by Koch et al. [18], it was reported that this length measurement could not be made accurately with radiological and endoscopy methods, and only the size of hiatal hernias could be determined with these methods. It was reported in another study that the use of width measurement instead of length measurement would yield more accurate results because of the slippery nature of this area [11]. It was seen in the literature that the measurements of these lengths were made radiologically [15]. In the present study, the measurement was made only endoscopically and was not verified radiologically. Despite these limitations, we believe that the fact that the measurement was made and recorded by a single expert endoscopy specialist to provide a certain standard, and the number of patients included in the study was 298 increases the importance of the study.

In the data obtained here, it was determined in the evaluations of the indication of the procedure and gender in the patients who underwent EGD that the EGD procedure was more common in women because of dyspepsia, and that gastritis, duodenitis, and pep-

tic ulcer were more common in these patients than in men (Table 6). In the literature, in a study that included 12,213 people conducted by Freha et al. [13], it was reported that, unlike our study, gastritis was more common in male gender. Similarly, in the same study as well as in our study, upper GIS bleeding was found to be statistically higher in men than in women, which is consistent with the literature data ($p = 0.032$; $p < 0.05$). There are many factors, which can cause this situation such as smoking, drugs used, or accompanying comorbidities. This may be the subject of further studies.

Since no studies similar to our study were detected in the literature, it is not possible to verify and compare the relations of length measurements in these localisations with gender, age, and symptoms reported in other studies. At this point, we believe that the data found in this study will be important in terms of establishing a standardisation in Turkish society, and will also guide clinicians. We also believe that the relations between the anatomical localisations that were examined in the present study and the body mass index must be investigated in further studies.

CONCLUSIONS

Knowing the anatomical localisations of the cervical oesophagus length, hiatal clamp, and oesophagogastric junction may be important in planning the outcomes of the complications, which might occur in this region in EGD, and in planning the measures to be taken in this respect. It may also help clinicians to identify hiatal hernias and insufficiencies and to determine the treatment modalities to approach these diseases. In the future, if the present study is planned by including patients with certain symptoms and if the number of patients is increased, it will be more guiding for the interventions regarding treatment modalities. Also, these measurements should be supported with cadaver studies for the purpose of providing a standard and achieving measurements with more objective values.

Conflict of interest: None declared

REFERENCES

1. Aksoy EK, Akpınar M, Sapmaz FP, et al. Assessment of effectiveness and safety of upper gastrointestinal system endoscopy in geriatric patients. J Ankara Univ Fac Med. 2018; 71(3): 228–233, doi: 10.4274/atfm.20982.

2. Altorki NK, Yankelevitz D, Skinner DB. Massive hiatal hernias: the anatomic basis of repair. J Thorac Cardiovasc Surg. 1998; 115(4): 828–835, doi: 10.1016/S0022-5223(98)70363-0, indexed in Pubmed: 9576218.

3. Anatomy of the Esophagus | SEER Training. (n.d.). National Cancer Institute SEER Training Modules. https://training.seer.cancer.gov/ugi/anatomy/esophagus.html.

4. Andujar JJ, Papasavas PK, Birdas T, et al. Laparoscopic repair of large paraesophageal hernia is associated with a low incidence of recurrence and reoperation. Surg Endosc. 2004; 18(3): 444–447, doi: 10.1007/s00464-003-8823-4, indexed in Pubmed: 14752653.

5. Awad ZT, Watson P, Filipi CJ, et al. Correlations between esophageal diseases and manometric length: a study of 617 patients. J Gastrointest Surg. 1999; 3(5): 483–488, doi: 10.1016/s1091-255x(99)80101-2, indexed in Pubmed: 10482704.

6. Chow WH, Finkle WD, McLaughlin JK, et al. The relation of gastroesophageal reflux disease and its treatment to ade-nocarcinomas of the esophagus and gastric cardia. JAMA. 1995; 274(6): 474–477, indexed in Pubmed: 7629956.

7. Collis JL, Kelly TD, Wiley AM. Anatomy of the crura of the diaphragm and the surgery of hiatus hernia. Thorax. 1954; 9(3): 175–189, doi: 10.1136/thx.9.3.175, indexed in Pubmed: 13205524.

8. Csendes A, Maluenda F, Braghetto I, et al. Location of the lower oesophageal sphincter and the squamous columnar mucosal junction in 109 healthy controls and 778 patients with different degrees of endoscopic oesophagitis. Gut. 1993; 34(1): 21–27, doi: 10.1136/gut.34.1.21, indexed in Pubmed: 8432446.

9. Dormann AJ, Eisendrath P, Wigginghaus B, et al. Palliation of esophageal carcinoma with a new self-expanding plastic stent. Endoscopy. 2003; 35(3): 207–211, doi: 10.1055/s-2003-37252, indexed in Pubmed: 12584638.

10. El-Serag HB, Johanson JF. Risk factors for the severity of erosive esophagitis in Helicobacter pylori-nega-tive patients with gastroesophageal reflux disease. Scand J Gastroenterol. 2002; 37(8): 899–904, doi: 10.1080/003655202760230847, indexed in Pubmed: 12229963.

11. Evans RJ, Moore R. Hiatal width: a novel measure of hiatal hernia: 480. Official J Am Coll Gastroenterol ACG. 2018; 113: S276–S277.

12. Ferlengez E, Ferlengez AG, Çelik A, et al. Endoscopic and clinical characteristics of patients diagnosed at the gastrodu-odenoscopy unit of a secondary level state hospital our gas-troduodenoscopy results. Med Bull Haseki. 2012; 50: 131–135.

13. Freha NA, Gat R, Novack V, et al. Endoscopy and gender, similiarties and differences. ESGE Days. 2020; 52(1): 12, doi: 10.1055/s-0040-1704782.

14. Goh KL. Changing epidemiology of gastroesophageal reflux disease in the Asian-Pacific region: an overview. J Gastroenterol Hepatol. 2004; 19 (Suppl 3): S22–S25, doi: 10.1111/j.1440-1746.2004.03591.x, indexed in Pubmed: 15324378.

15. Han SH, Hong SuJ. [Transient lower esophageal sphincter relaxation and the related esophageal motor activities]. Ko-rean J Gastroenterol. 2012; 59(3): 205–210, doi: 10.4166/kjg.2012.59.3.205, indexed in Pubmed: 22460568.

16. Johnson DA, Ruffin WK. Hiatal hernia. Gastrointest Endosc Clin N Am. 1996; 6(3): 641–666, indexed in Pubmed: 8803572.

17. Kahraman Ö, Cingi A. Ed. Gastrointestinal Sistem En-doskopisi. Pelin Ofset Tipo Matbaacılık ve Tic. Ltd. Şti., Ankara 2016.

18. Koch OO, Kaindlstorfer A, Antoniou SA, et al. Influence of the esophageal hiatus size on the lower esophageal sphincter, on reflux activity and on symptomatology. Dis Esophagus. 2012; 25(3): 201–208, doi: 10.1111/j.1442-2050.2011.01238.x, indexed in Pubmed: 21895850.

19. Kumar D, Zifan A, Ghahremani G, et al. Morphology of the esophageal hiatus: is it different in 3 types of hiatus hernias? J Neurogastroenterol Motil. 2020; 26(1): 51–60, doi: 10.5056/jnm18208, indexed in Pubmed: 31677612.

20. Lal P, Tang A, Sarvepalli S, et al. Manometric esophageal length to height (MELH) ratio predicts hiatal hernia recurrence. J Clin Gastroenterol. 2020; 54(6): e56–e62, doi: 10.1097/MCG.0000000000001316, indexed in Pubmed: 31985712.

21. Li Q, Castell JA, Castell DO. Manometric determination of esophageal length. Am J Gastroenterol. 1994; 89(5): 722–725, indexed in Pubmed: 8172145.

22. Marshall RE, Anggiansah A, Anggiansah CL, et al. Es-ophageal body length, lower esophageal sphincter length, position and pressure in health and disease. Dis Esophagus. 1999; 12(4): 297–302, doi: 10.1046/j.1442-2050.1999.00060.x, indexed in Pubmed: 10770366.

23. Moore KL, Arthur F. Dalley. Clinically Oriented Anatomy. Lippincott Williams & Wilkins, A Wolters Kluwer Company 1999.

24. Shamiyeh A, Szabo K, Granderath FA, et al. The esophageal hiatus: what is the normal size? Surg Endosc. 2010; 24(5): 988–991, doi: 10.1007/s00464-009-0711-0, indexed in Pubmed: 19826867.

25. Sieg A, Hachmoeller-Eisenbach U, Eisenbach T. Pro-spective evaluation of complications in outpatient GI endoscopy: a survey among German gastroenterologists. Gastrointest Endosc. 2001; 53(6): 620–627, doi: 10.1067/mge.2001.114422, indexed in Pubmed: 11323588.

26. Staiano A, Clouse RE. Detection of incomplete lower esophageal sphincter relaxation with conventional point-pressure sensors. Am J Gastroenterol. 2001; 96(12): 3258–3267, doi: 10.1111/j.1572-0241.2001.05323.x, indexed in Pubmed: 11774934.

27. Themes U. Anatomy of the Esophagus. Thoracic Key. https://thoracickey.com/anatomy-of-the-esophagus/ . https://tho-racickey.com/anatomy-of-the-esophagus/ (2016, June 25).

28. Trost J. Statistically nonrepresentative stratified sampling: A sampling technique for qualitative studies. Qualitative Sociology. 1986; 9(1): 54–57, doi: 10.1007/bf00988249.

29. Wiener GJ, Richter JE, Copper JB, et al. The symptom index: a clinically important parameter of ambulatory 24-hour esophageal pH monitoring. Am J Gastroenterol. 1988; 83(4): 358–361, indexed in Pubmed: 3348191.

30. Wilson LJ, Ma W, Hirschowitz BI. Association of obesity with hiatal hernia and esophagitis. Am J Gastroen-terol. 1999; 94(10): 2840–2844, doi: 10.1111/j.1572-0241.1999.01426.x, indexed in Pubmed: 10520831.

31. Wong WM, Lim P, Wong BCY. Clinical practice pattern of gastroenterologists, primary care physicians, and otolaryngologists for the management of GERD in the Asia-Pacific region: the FAST survey. J Gastroenterol Hepa-tol. 2004; 19 (Suppl 3): S54–S60, doi: 10.1111/j.1440-1746.2004.03590.x, indexed in Pubmed: 15324383.

32. Yang GS, Bishop WP, Smith BJ, et al. Radiographic and endoscopic measurements of esophageal length in pedi-atric patients. Ann Otol Rhinol Laryngol. 2005; 114(8): 587–592, doi: 10.1177/000348940511400802, indexed in Pubmed: 16190090.

33. Yau P, Watson DI, Jamieson GG, et al. The influence of eso-phageal length on outcomes after laparoscopic fundoplica-tion. J Am Coll Surg. 2000; 191(4): 360–365, doi: 10.1016/s1072-7515(00)00363-x, indexed in Pubmed: 11030240.

Type and location of flexor hallucis longus musculotendinous junctions and its tendinous interconnections with flexor digitorum longus tendon: pertinent data for tendon harvesting and transfer

P. Wan-ae-loh[1], T. Huanmanop[2], S. Agthong[2], V. Chentanez[2]

[1]Medical Science Programme, Faculty of Medicine, King Chulalongkorn Memorial Hospital,
Chulalongkorn University, Bangkok, Thailand
[2]Department of Anatomy, Faculty of Medicine, King Chulalongkorn Memorial Hospital,
Chulalongkorn University, Bangkok, Thailand

Background: Anatomy of flexor hallucis longus (FHL) is essential for the achievement of tendon transfer and several procedures performed in the foot and ankle. The aim of this study was to evaluate the anatomical knowledge of FHL including the type and location of musculotendinous junction (MTJ), tendinous interconnections (TIC) morphology, its location related to Master Knot of Henry (MKH), and the pattern of TIC distribution.

Materials and methods: One hundred and sixty-six legs from 52 embalmed and 31 soft cadavers were assessed. The medial (MB) and lateral (LB) bellies of FHL were identified and traced until the end of the most distal muscle fibre to determine the medial and lateral MTJs. MTJ was classified into four types based on the existence and length of MB and LB: type 1, long LB and shorter MB; type 2, equal length of both bellies; type 3, only LB and no MB; type 4, long MB and shorter LB. Low lying muscle belly was defined as muscle extending beyond the zero point (the point of intersection between distal osseous part of tibia and FHL tendon). The distance between MTJ and zero point was measured. TIC was classified into seven types based on the direction and number of slip: type I, one slip from FHL to flexor digitorum longus (FDL); type II, crossed connection: type III, one slip from FDL to FHL; type IV, no connection; type V, two slip from FHL to FDL; type VI, two slip from FHL to FDL and one slip from FDL to FHL; type VII, two slips from FDL to FHL and one slip from FHL to FDL. The distance between the TIC and MKH was measured. TIC distribution was defined into four types based on slip distribution to lesser toes: type a, distributed to second toe; type b, distributed to second and third toes; type c, distributed to second to fourth toes, and type d, distributed to second to fifth toes.

Results: Type 1 and type 3 of MTJ morphology were found in 87.3% and 12.7%, respectively. Low lying LB was detected in 66.13% of cases with a mean distance of 13.10 ± 4.51 mm. All MBs ended proximal to the zero point with a mean

Address for correspondence: V. Chentanez, MD, PhD, Department of Anatomy, Faculty of Medicine, King Chulalongkorn Memorial Hospital, Chulalongkorn University, Bangkok 10330, Thailand, tel: 66-860701084, e-mail: fmedvct@gmail.com

distance of –21.99 ± 13.21 mm. Three types of TIC (I, II, V) were identified. The highest frequency was type I (82.93%). In addition, a new type of TIC was depicted in 8.53% of cases. Part of the FHL tendon in this type fused with FDL tendon and the rest extended directly to the first toe. TIC could be located either proximal, distal or at the MKH. The highest prevalence was distal to MKH in 51.67% of cases with a mean distance of 11.23 ± 5.13 mm and 8.73 ± 4.2 mm in low lying and non-low-lying groups, respectively. Four types of slip distribution to lesser toes were defined, mostly in type b. No statistically significant differences were detected among all parameters including genders, sides, and groups.
Conclusions: Knowledge of this investigation might enhance the clinical efficacy of tendon harvesting and transfer in foot and ankle surgery. (Folia Morphol 2022; 81, 3: 766–776)

Key words: flexor hallucis longus, flexor digitorum longus, musculotendinous junction, tendinous interconnection

INTRODUCTION

Flexor hallucis longus (FHL) transfer is a widely used technique for ankle and foot reconstruction, including posterior tibial insufficiency, Achilles tendinopathies, or peroneal tendon rupture [2, 4, 6, 13, 21, 22, 24]. The FHL is suitable for transfer because of its strength, axis and amplitude of contraction, and coincident action with gastrocnemius and soleus muscles [33]. The objectives of FHL transfer are to repair the length, strengthen the injured tendon, and corporate more muscle force [8]. Moreover, FHL transfer can decrease pain by normalising vascularity [1, 8]. Many techniques of FHL tendon graft harvesting are clinically utilised, including single incision, double incision, and minimally invasive techniques [16]. The indication, length of harvested tendon and location of incisions are different among techniques [16]. FHL tendons can be harvested behind the medial malleolus, proximal to superior border of the calcaneus, along medial edge of mid-foot at Master Knot of Henry (MKH), or over the medial plantar aspect of forefoot at the first metatarsophalangeal joint [2, 21, 28]. Despite the good to excellent clinical outcome following FHL transfer that was revealed previously, complications such as neurovascular injury, cock-up deformity, and functional loss of toes were also reported [1, 10, 16, 20].

Knowing the anatomical variation of the FHL muscle is helpful when planning an operation. If FHL muscle bellies are sufficient to cover the tendon defect, the other combining techniques are not necessary [17, 24]. Tendon transfer can improve blood supply in the injured region and covers possible existing soft tissue defects. To accomplish the clinical objective, knowledge of the anatomical variations of musculotendinous junction (MTJ) of FHL will provide important insights to decide upon the operation and administration of FHL transfer [17, 24].

Tendinous interconnections (TIC) between FHL and flexor digitorum longus (FDL) play an important role in tendon harvesting [25]. The benefit of these connections is to act as a natural tenodesis during harvesting tendon grafts proximal to MKH and to increase the length of tendon graft by cutting the connections [15, 23]. The connections between FHL and FDL, which have an important functional role in toe movements, might restrict harvesting of the FHL tendon proximal to MKH [10]. Previous research has suggested that, these interconnections must be cut when harvesting FHL tendon especially in minimal invasive technique [16, 25]. To reduce the risk of iatrogenic injury during surgical procedures and achieve medical procedures, essential knowledge of morphological type, location and distribution of TIC are necessary [26, 30]. The focus in this cadaveric study was to evaluate the anatomical knowledge of FHL including the type and location of MTJ, TIC morphology and its location related to MKH, and the pattern of TIC distribution.

MATERIALS AND METHODS

This study was performed in 166 legs from 52 embalmed (33 males, 19 females) and 31 soft cadavers (9 males and 22 females) supported by the Department of Anatomy and Chula Soft Cadaver Surgical Training Centre, Faculty of Medicine, Chulalongkorn
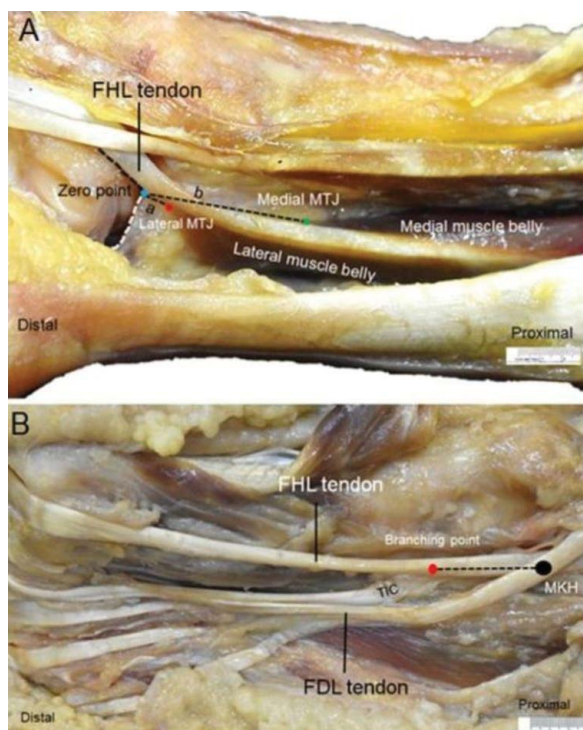
Figure 1. A. Photograph of left ankle showing; (a) distance from lateral musculotendinous junction (MTJ) (red dot) and (b) distance from medial MTJ (green dot) of flexor hallucis longus muscle (FHL) to zero point (blue dot) which is the intersection between distal osseous part of tibia (white dot line) and FHL tendon (black dot line); **B.** Photograph of right plantar surface of foot showing the distance from branching point of tendinous interconnection (TIC) (red dot) to master knot of Henry (MKH) (black dot); FDL — flexor digitorum longus muscle.

University. The mean age of the cadavers was 78.87 ± ± 13.69 years (range 32–100). None of the cadaveric legs, ankles and feet had damage, deformity, or scaring from previous surgery.

Cadaveric dissection

The skin, subcutaneous tissue, fascia of the leg, and plantar surface of the foot was detached to each side. At the medial side of the ankle, the flexor retinaculum was identified, and its posterior edge was cut to open the tarsal tunnel. The dissection was performed until adequate exposure of the FHL tendon was achieved. The medial and lateral bellies of FHL were identified and traced until the end of the most distal muscle fibre to determine the medial and lateral MTJs (Fig. 1A). Then, the plantar aponeurosis and medial plantar fascia of the foot were cut to expose the flexor digitorum brevis (FDB) and abductor hallucis muscle (AH). These two muscles were separated to disclose the tendon of FHL and FDL. MKH was indicated at the crossing point of FDL and FHL tendon

(Fig. 1B). The TIC was also explored. Finally, FHL and FDL together with TIC and quadratus plantae were harvested as one block from the cadaver to analyse the type of MTJ and TIC.

Observations and measurements
Type of MTJ, MTJ location and the presence of low lying FHL

The presence of medial (MB) and lateral (LB) bellies of FHL muscle was observed in both embalmed and soft cadavers. MTJ morphological types were classified according to the criteria established by Pichler et al. [24] and modified by Mao et al. [17] into four types: type 1, long LB and shorter MB; type 2, equal length of both bellies; type 3, only LB and no MB; type 4, long MB and shorter LB. The presence of other morphologies was also examined. However, the MTJ location and the presence of low lying FHL were examined only in soft cadavers since the foot and ankle joint should be set in a neutral position throughout these processes. The zero point was defined according to Pichler et al. [24] as the point of intersection between the distal osseous part of the tibia and FHL tendon (Fig. 1A) and the presence of low lying FHL was depicted if the muscle belly extended distal to the zero point. Distances from medial and lateral MTJs to the zero point were measured with a digital slide gauge (Mitutoyo® 0–150 mm; range 150 mm, resolution 0.01 mm) (Fig. 1A). This parameter was recorded as either a negative or positive value based on whether it located proximal or distal to the zero point, respectively.

Type of TIC, its distribution to the toes and its location regarding MKH

The presence and direction of TIC between FHL and FDL were examined in both embalmed and soft cadavers. Type of TIC was classified based on the criteria defined by Beger et al. [3] into seven types: type I, one slip from FHL to FDL; type II, crossed connection: type III, one slip from FDL to FHL; type IV, no connection; type V, two slip from FHL to FDL; type VI, two slip from FHL to FDL and one slip from FDL to FHL; type VII, two slips from FDL to FHL and one slip from FHL to FDL. The presence of other patterns was also examined. The distribution of TIC to the lesser toes was identified by pulling the FHL and observing the flexion of the toes. TIC distribution was defined into four types according to Plaass et al. [25] as the following: type a, distributed to second toe; type b,

distributed to second and third toes; type c, distributed to second to fourth toes and type d, distributed to second to fifth toes. Moreover, the distance from the branching point of TIC to MKH was measured to determine the location of TIC in 60 soft cadaver specimens (Fig. 1B). This parameter was recorded as negative or positive value based on whether it located proximal or distal to the MKH, respectively.

Each parameter was measured twice by the same investigator. The same digital Vernier calliper was used to ensure consistency.

Statistical analysis

Statistical analysis was performed by SPSS software version 22.0. Morphology of MTJ, TIC and the distribution of TIC were analysed as prevalence and percentage. All quantitative data was based on the criteria reported as range, mean and standard deviation. Unpaired t-test (for parametric test) and Mann-Whitney U test (for nonparametric test) were used to compare between genders and between low lying and non-low lying groups. The difference between left and right side was examined with paired t-test (for parametric test) or Wilcoxon signed-rank test (for nonparametric test). A p-value of less than 0.05 was defined as statistically significant.

Ethical consideration

The Institutional Review Board (IRB) of the Faculty of Medicine, Chulalongkorn University approved this anatomical study (IRB NO. 636/62).

RESULTS

Type of MTJ, MTJ location and the presence of low lying FHL

Musculotendinous junction morphology was examined in 166 specimens from both soft and embalmed cadavers. Two morphological types of MTJ were identified including type 1 (145 cases, 87.35%), in which the LB ended more distally than MB, and type 3 (21 cases, 12.65%), which showed only LB (Fig. 2, Table 1). Symmetrical type of MTJ morphology was found in 74 cadavers (89.16% of cases) and the highest frequency was type 1. However, FHL which had equal length of MB and LB or type 2 and those with MB ended more distally than LB or type 4 were not found in this study.

Musculotendinous junction location was determined in 62 legs of soft cadavers by measuring the distance from medial and lateral MTJs to the zero
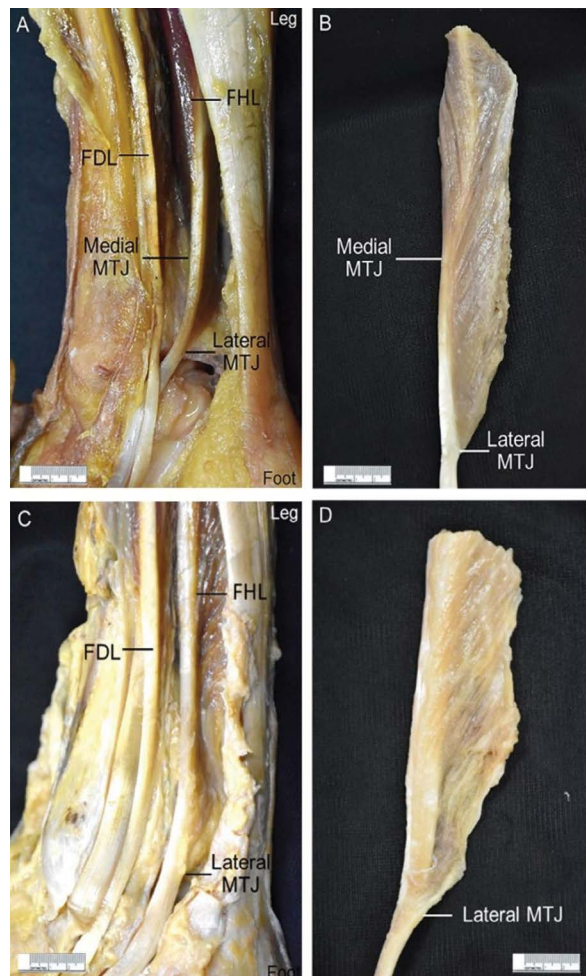
Figure 2. Photographs of medial side of right legs and resected flexor hallucis longus muscle (FHL) musculotendinous junction (MTJ) showing type 1 MTJ morphology with a longer lateral muscle belly than medial muscle belly (**A**, **B**), and type 3 MTJ morphology with only a lateral muscle belly (**C**, **D**); FDL — flexor digitorum longus.

point. Results are shown in Table 2. MTJ was found to reside either proximal (–) or distal (+) to zero point. LB extended beyond the zero point (low-lying) in 41 (66.13%) cases with a mean distance of 13.10 ± ± 4.51 mm. In the non-low-lying group of LB (21 cases, 33.87%), the mean distance from the zero point was –8.5 ± 7.30 mm. In contrast, all MB ended proximally to the zero point with a mean distance of –21.99 ± 13.21 mm. No statistically significant difference was found between genders, sides, and groups.

Type of TIC, its distribution to the toes and its location regarding MKH

Type of TIC was examined in 164 specimens (2 damaged specimens from dissection were excluded). According to Beger et al. [3], types I, II, V and

Table 1. Prevalence of musculotendinous junction (MTJ) morphology, low lying of flexor hallucis longus (FHL), tendinous interconnection (TIC) morphology and TIC distribution

	Male			Female			Total
	Left	Right	Total	Left	Right	Total	
Type of MTJ morphology (166 specimens)							
1	35 (21.08%)	32 (19.28%)	67 (40.36%)	39 (23.49%)	39 (23.49%)	78 (46.99%)	145 (87.35%)
3	7 (4.22%)	10 (6.02%)	17 (10.24%)	2 (1.20%)	2 (1.20%)	4 (2.41%)	21 (12.65%)
Low lying of FHL (62 soft cadaveric specimens)							
Lateral muscle belly	7 (11.29%)	7 (11.29%)	14 (22.58%)	13 (20.97%)	14 (22.58%)	27 (43.55%)	41 (66.13%)
Medial muscle belly	0 (0%)	0 (0%)	0 (0%)	0 (0%)	0 (0%)	0 (0%)	0 (0%)
Non low lying	2 (3.23%)	2 (3.23%)	4 (6.45%)	9 (14.52%)	8 (12.90%)	17 (27.42%)	21 (33.87%)
Type of TIC (164 specimens)							
I	34 (20.73%)	34 (20.73%)	68 (41.46%)	33 (20.12%)	35 (21.34%)	68 (41.46%)	136 (82.93%)
II	1 (0.61%)	0 (0%)	1 (0.61%)	0 (0%)	0 (0%)	0 (0%)	1 (0.61%)
V	4 (2.44%)	4 (2.44%)	8 (4.88%)	3 (1.83%)	2 (1.22%)	5 (3.05%)	13 (7.93%)
New type	2 (1.22%)	3 (1.83%)	5 (3.05%)	5 (3.05%)	4 (2.44%)	9 (5.49%)	14 (8.53%)
Type of TIC distribution (164 specimens)							
a	11 (6.71%)	7 (4.27%)	18 (10.98%)	6 (3.66%)	8 (4.88%)	14 (8.54%)	32 (19.51%)
b	25 (15.24%)	28 (17.07%)	53 (32.31%)	32 (19.51%)	26 (15.85%)	58 (35.36%)	111 (67.68%)
c	5 (3.05%)	6 (3.66%)	11 (6.71%)	1 (0.61%)	6 (3.66%)	7 (4.27%)	18 (10.98%)
d	0 (0%)	0 (0%)	0 (0%)	2 (1.22%)	1 (0.61%)	3 (1.83%)	3 (1.83%)

a new type were found (Table 1, Fig. 3). The highest frequency was type I (82.93%), which had a tendinous slip branching from FHL to FDL tendon followed numerically by type V (7.93%), which had double slip from FHL to FDL tendons and type II (0.61%), which showed the cross tendinous slips between FHL and FDL tendons, respectively. In addition, a new type of interconnection (14 cases or 8.54%) was found in which part of the FHL tendon fused with FDL tendon and the rest extended directly to the first toe (Fig. 3G, H). Symmetrical type of TIC was found in 61 cadavers (79.27% of cases) and the highest frequency was type 1.

Distribution of TIC to the lesser toes was determined by observing the movement of each toe when pulling the FHL. Prevalence of each type is shown in Table 1. The most common was type b (67.68%) and followed numerically by type a, type c and type d, respectively. Symmetrical type of slip distribution to lesser toes was found in 61 cadavers (74.39%) and the highest frequency was type b. The prevalence of TIC distribution in the new type of this study was type a (1 case), type b (10 cases) and type c (3 cases).

The location of TIC was investigated in 60 soft cadaver specimens of. It was located either proximal (–), distal (+) to MKH or at the MKH (Table 2). The

highest prevalence was located distally to MKH in 36.67% with a mean distance of 11.23 ± 5.13 mm in the low-lying group and 15% in the non-low-lying group with a mean distance of 8.73 ± 4.2 mm. In the new type of TIC, the fusion point in the soft cadaveric specimens was located either proximal (4 cases), distal (5 cases) or at the MKH (2 cases). No statistically significant difference was found between genders, sides, and groups.

DISCUSSION

Achilles tendon ruptures occur approximately at 2–6 cm above the calcaneal insertion and the blood supply in this region might be reduced [24]. FHL tendon transfer can cover the soft tissue defect and improve blood supply. The location of the MTJ is important in this instance. If MTJ is located proximally, the FHL muscle bellies are insufficient for the coverage of injured tendon and adequate vascular supply to the affected area. Therefore, knowledge of morphological variation of FHL muscle in this study will provide some benefits in tendon harvesting and transfer. In this study, only type 1 and 3 of MTJ morphology were found with the most frequent type as type 1 (LB longer than MB). Moreover, symmetrical type of MTJ morphology was found with high prevalence (89.16%

Table 2. Mean distances from medial and lateral musculotendinous junction (MTJ) to zero point and from tendinous interconnection (TIC) to Master Knot of Henry (MKH)

	Male			Female			Total
	Left	**Right**	**Total**	**Left**	**Right**	**Total**	
Mean distance from MTJ to zero point [mm] (62 soft cadaveric specimens)							
Lateral belly	9	9	18	22	22	44	62 (100%)
	8.59 ± 9.60	8.95 ± 10.24	8.77 ± 9.63	3.86 ± 11.77	5.40 ± 12.97	4.63 ± 12.26	5.83 ± 11.64
	(−6.54 − 20.88)	(−8.39 − 21.21)	(−8.39 − 21.21)	(−18.27 − 20.96)	(−30.62 − 5.54)	(−30.62 − 20.96)	(−30.62 − 21.21)
Low lying	7	7	14	13	14	27	41 (66.13%)
	12.73 ± 5.75	13.33 ± 6.15	13.03 ± 5.73	12.46 ± 4.03	13.76 ± 3.71	13.13 ± 3.85	13.10 ± 4.51
	(5.85 − 20.88)	(5.91 − 21.21)	(5.85 − 21.21)	(5.76 − 20.96)	(8.20 − 18.32)	(5.76 − 20.96)	(5.76 − 21.21)
Non low-lying	2	2	4	9	8	17	21 (33.87%)
	−5.88 ± 0.93	−6.37 ± 2.86	−6.13 ± 1.76	−8.56 ± 6.77	−9.23 ± 9.73	−8.87 ± 8.03	−8.35 ± 7.30
	(−6.54 − −5.22)	(−8.39 − −4.35)	(−8.39 − −4.35)	(-18.27 − 0.00)	(−30.62 − 0.00)	(−30.62 − 0.00)	(−30.62 − 0.00)
Medial belly	9	9	18	22	22	44	62
	−27.19 ± 11.32	−21.57 ± 6.46	−24.79 ± 9.66	−22.34 ± 13.84	−19.76 ± 14.70	−21.08 ± 14.16	−21.99 ± 13.21
	(−42.12 − −12.78)	(−28.13 − −12.08)	(−42.12 − −12.78)	(−51.02 − −4.93)	(−65.95 − −5.54)	(−65.95 − −4.93)	(−65.95 − −4.93)
Mean distance from TIC to MKH [mm] (60 soft cadaveric specimens)							
Low lying	6	6	12	13	14	27	39 (65%)
	3.68 ± 7.49	4.33 ± 13.95	4.01 ± 10.68	5.65 ± 11.62	0.98 ± 10.64	3.23 ± 11.16	3.47 ± 10.88
	(−9.04 − 12.34)	(−20.81− 17.56)	(−20.81− 17.56)	(−21.33− 18.06)	(−15.75 − 20.52)	(−21.33 − 20.52)	(−21.33 − 20.52)
Proximal	1	1	2	2	5	7	9 (15%)
	−9.04	−20.81	−14.93 ± 8.33	−15.94 ± 7.66	−10.00 ± 3.91	−11.70 ± 5.31	−12.42 ± 5.65
			(−20.81− −9.04)	(−21.33− −10.55)	(−15.75− −6.13)	(−21.33 − −6.13)	(−21.33 − −6.13)
At MKH	1	1	2	3	3	6	8 (13.33%)
	0.00	0.00	0.00	0.00	0.00	0.00	0.00
Distal	4	4	8	8	6	14	22 (36.67%)
	7.78 ± 3.58	11.70 ± 5.90	9.74 ± 4.98	13.16 ± 3.44	10.63 ± 7.01	12.08 ± 5.19	11.23 ± 5.13
	(4.58 − 12.34)	(4.14− 17.56)	(4.14− 17.56)	(7.96− 18.06)	(5.04− 20.52)	(5.04− 20.52)	(4.14 − 20.52)
Non-low-lying	2	2	4	9	8	17	21 (35%)
	9.69 ± 0.98	0.00	4.84 ± 5.62	0.08 ± 7.08	1.83 ± 9.10	0.90 ± 7.88	1.65 ± 7.55
	(9.00 − 10.38)	(0.00)	(0.00 − 10.38)	(−8.74 − 13.52)	(−10.41 − 15.14)	(−10.41 − 15.14)	(−10.41 − 15.14)
Proximal	0	0	0	4	2	6	6 (10%)
				−5.88 ± 2.77	−10.18 ± 0.32	−7.31 ± 3.10	−7.31 ± 3.10
				(−8.74 − −3.05)	(−10.41 − −9.96)	(−10.41 − −3.05)	(−10.41 − −3.05)
At MKH	0	2	2	2	2	4	6 (10%)
		0.00	0.00	0.00	0.00	0.00	0.00
Distal	2	0	2	3	4	7	9 (15%)
	9.69 ± 0.98		9.69 ± 0.98	8.07 ± 4.72	8.74 ± 5.56	8.46 ± 4.80	8.73 ± 4.20
	(9.00 − 10.38)		(9.00 − 10.38)	(5.22 − 13.52)	(3.62 − 15.14)	(3.62 − 15.14)	(3.62 − 15.14)
All	8	8	16	22	22	44	60 (100%)
	5.18 ± 6.93	3.25 ± 11.96	4.21 ± 9.49	3.37 ± 10.21	1.29 ± 9.89	2.33 ± 9.99	2.83 ± 9.81
	(−9.04 − 12.34)	(−20.81 − 17.56)	(−20.81 − 17.56)	(−21.33 − 18.06)	(−15.75 − 20.52)	(−21.33 − 20.52)	(−21.33 − 20.52)

Data are shown as mean ± standard deviation (min–max) or number (%); −: proximal to zero point

of cases). Therefore, awareness of symmetrical patterns should be emphasized. Location of LB could be found either proximal or distal to the zero point, similar to those found in previous studies [17, 24]. However, all MTJ of MB was located only proximally to the zero point at a mean distance of −21.99 ± ± 13.21 mm. Low lying lateral MTJ was detected in 66.13% of the cases and located at a mean distance of 13.10 ± 4.51 mm distal to the zero point (Table 2). The prevalence of MTJ type and its location as shown

in Table 3 differed from previous studies [17, 24]. The presence of low lying FHL is clinically relevant. It can provide a longer muscle belly for coverage of the injured region and provides adequate vascular supply. However, it can cause FHL tendon entrapment [5]. MTJ can get entrapped at the proximal end of the fibro-osseous tunnel, resulting in limitation of distal excursion of the tendon. This generally causes pain at the entrapment area or the first metatarsophalangeal joint [9, 19]. This injury is frequently seen in runners,
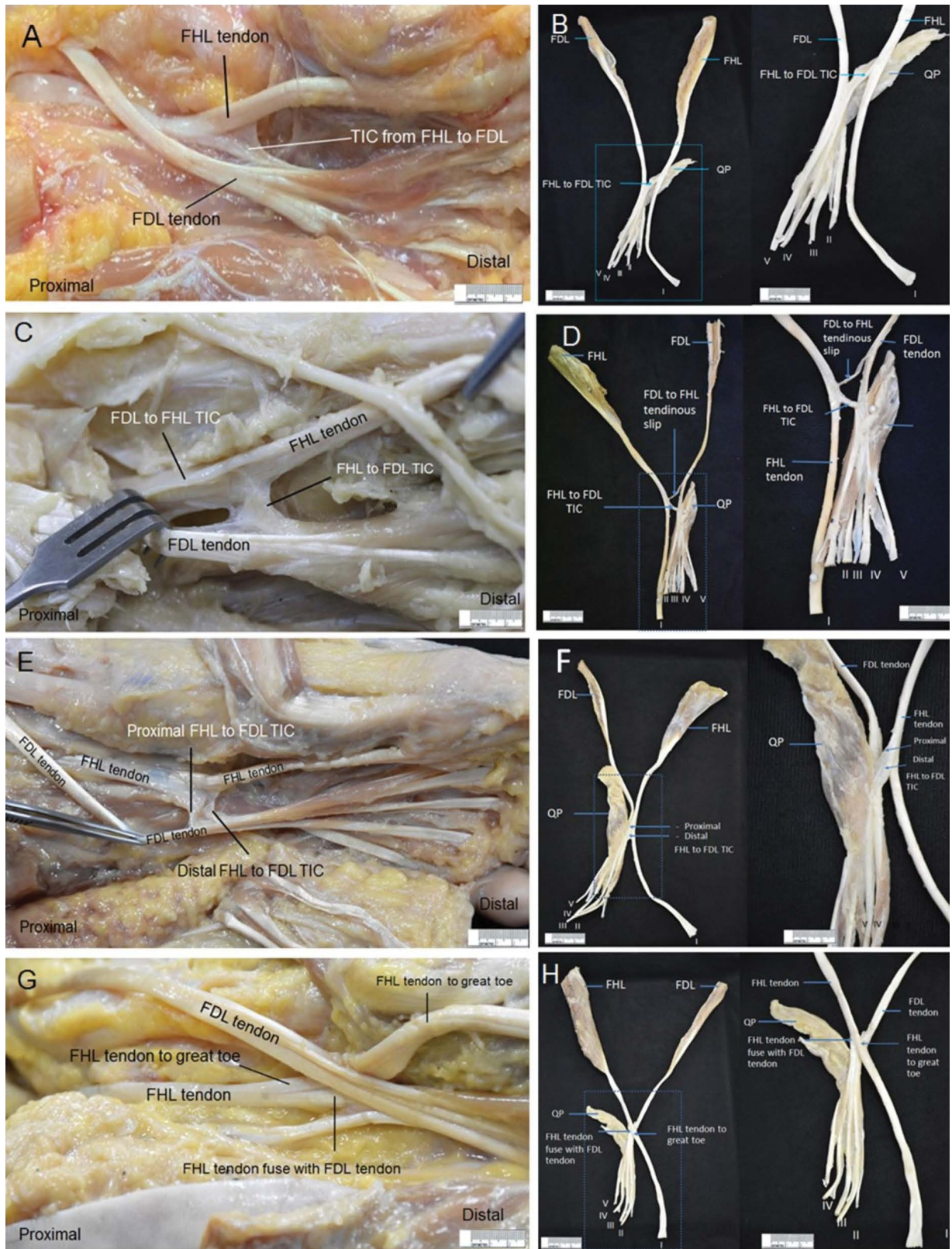
Figure 3. Photographs of left plantar surface of feet and resected flexor hallucis longus (FHL) and flexor digitorum longus (FDL) interconnection showing types of tendinous interconnection (TIC). Type I; FHL to FDL (**A**, **B**). Type II; FHL to FDL and FDL to FHL (**C**, **D**). Type V; double strands from FHL to FDL (**E**, **F**). New type; part of the FHL tendon fused with FDL tendon and the rest extended directly to the great toe (**G**, **H**); MTJ — musculotendinous junction; QP — quadratus plantae.

Table 3. Comparisons of musculotendinous junction (MTJ) type and distance from MTJ to measuring point

Author	Year	Race/ /Ethnicity	Cadaveric type	N	MTJ morphology			
					Type 1	Type 2	Type 3	Other
This study (2021)	2020	Thai						
Prevalence			Soft	62	145 (87.3%)	0 (0%)	21 (12.7%)	0 (0%)
			Embalmed	104				
Distance from MTJ to the crossing of distal osseous part of tibia and FHL tendon:			Soft	62				
Medial belly [mm]					–21.99 ± 13.21 (–65.95 – –4.93)			
Lateral belly [mm]					5.83 ± 11.64 (–30.62 – +21.21)			
Mao et al. (2018) [17]	2018	Asian						
Prevalence			Embalmed	70	63 (90%)	5 (7.1%)	2 (2.9%)	0 (0%)
Distance from MTJ to the crossing of distal osseous part of tibia and FHL tendon:				70				
Medial belly [mm]					–33.24 ± 1.5 (–115 – +8)			
Lateral belly [mm]					–3.14 ± 2.2 (–39 – +43)			
Pichler et al. (2005) [24]	2005	–						
Prevalence			Embalmed	80	70 (88%)	3 (4%)	5 (6%)	2 (3%)
Distance from MTJ to the bone cartilage transition of tibia:				80				
Medial belly [mm]					–34.64 ± 22.79 (–114 – +5.5)			
Lateral belly [mm]					–1.48 ± 12.92 (–57 – +25)			

+: proximal to measuring point; – : distal to measuring point; FHL — flexor hallucis longus

tennis players, and dancers, who require dynamic, repetitive, or push-off movement [19, 27].

The exact knowledge of TIC anatomy and variation is important for harvesting and estimation of functional loss after transposition [29]. In addition, awareness of the number of connections between FHL and FDL tendons while harvesting tendon grafts distal to MKH is essential [3]. Results have shown the existence of connection between FHL and FDL tendons in all specimens. The majority of cases in the present study were type I, which was similar to those in previous reports (Table 4) [7, 15, 16, 18, 20, 22, 25, 29, 32]. Types III, IV, VI and VII were not identified in the present study. In terms of overall proportions, this finding resembles the results of Edama et al. [7] and Mao et al. [17] in Asian cadavers (Table 4). In other ethnic studies, the prevalence of types III, IV, VI and VII varied from 0% to 30%. Vasudha et al. [29] reported 2.94% of cases with some unusual fibres from flexor digitorum accessories. Therefore, ethnic differences might exist.

In the results, a new type of TIC was depicted in 14 (8.5%) cases. The most common TIC distribution found in this type was type b. In the soft cadaveric specimens, the most prevalent location of the fusion point was distal to the MKH. In addition, all cases of the new type were categorised in type 1 MTJ morphology. Hence, the sample size of this study is greater than that of previous reports (Table 4). Therefore, more variations might be seen. The tendinous slips from FHL propose the stable base for toe-off movements [14]. Thus, types of interconnections play a crucial role in defining the level of functional gain of toe movement in the postoperative period [29]. TIC between FHL and FDL tendons might restrict the harvesting of the FHL tendon distal to MKH [10]. Therefore, it is important to investigate their locations. Moreover, the length of the graft can be increased by including the tendinous interconnection into the graft [29]. Anatomical landmarks including medial malleolus, navicular tuberosity, interphalangeal joint, MKH and FDL tendon division were used previously to locate the TIC between FHL and FDL tendons [3, 5, 25]. MKH was selected as the reference landmark in this study. The surface location of MKH has been reported in our recent study [31]. Results revealed that most of the TIC was located distal to MKH with a similarity to Beger et al. [3]. They also suggested that the interconnection from FHL to FDL could be cut at an average of 27.1 mm distal to the MKH. However, the average distance from MKH in our study was shorter (11.23 ± 5.13 mm in low-lying group and 8.73 ± ± 4.20 mm in non-low-lying group). The difference between studies may be due to the number of specimens, method of cadaveric preservation and ethnicity.

Table 4. Comparisons of the prevalence of types of tendinous interconnection between flexor halluces longus and flexor digitorum longus and type of the slip distribution to the lesser toes

	This study	Vasudha et al. [29]	Beger et al. [3]	Edama et al. [7]	Mao et al. [16]	Plaass et al. [25]	Hur et al. [14]	Mulier et al. [20]	LaRue et al. [15]	O'Sullivan et al. [22]	Wapner et al. [32]	Martin [18]
Year	2021	2019	2018	2016	2015	2013	2011	2007	2006	2005	1994	1964
Race	Thai	Indian	Turkish	Japanese	Chinese	Caucasian	Korean	Caucasian	Caucasian	British	US	Caucasian
Cadaveric type	Soft Embalmed	Embalmed	Embalmed	Embalmed	Embalmed	Embalmed	Embalmed	Embalmed Fresh	Embalmed Fresh	Embalmed	Embalmed	Embalmed
Number	164	36	20	100	64	60	100	24	24	16	85	33
Tendinous interconnections type (%)												
Type I	82.6	61.00	75	86	96.9	67		58	42	68	67	88
Type II	0.6	3.94	10	3	3.1	30		29	41	19	31	6
Type III	0.0	7.35	0	0	0	3		0	0	13	–	0
Type IV	0.0	14.70	0	0	0	0		13	17	0	2	6
Type V	7.9	8.82	5	11	–	–		–	–	–	–	–
Type VI	0.0	0.00	5	0	–	–		–	–	–	–	–
Type VII	0.0	1.47	5	0	–	–		–	–	–	–	–
Other	8.5	2.94	–	–	–	–		–	–	–	–	–
Tendinous interconnections distribution to lesser toes (%)												
Type a	19.5		33	31	31.3	33	8				41	
Type b	67.7		55	61	60.9	55	64				47	
Type c	11.0		7	8	7.8	7	28				9	
Type d	1.8		0	0	0	0	0				0	

In this study, type b was the most frequent finding of distribution of tendinous slip to lesser toes which was similar to previous reports as shown in Table 4 [3, 7, 14, 16, 25, 32]. Recently, Hirota et al. [12] introduced a FHL tendon branch test in 4 healthy men by electrical stimulation and electromyography recording of FHL and FDL. Considering the branching type, the FHL was presumed to not only act as the great toe flexor, but also play a significant role in the flexion of second and third toes [7, 16]. Toe flexor muscles are key muscles for foot stability and enhancement of sport performance. Therefore, this anatomical knowledge may lead to the benefit of toe muscle exercise for prevention of foot injuries and the improvement of sport performance [11, 12].

CONCLUSIONS

A revisit of FHL morphology including type and location of MTJ, TIC morphology, pattern of distribution and its location related to the MKH was performed in 31 soft and 52 embalmed cadavers. Two morphological types of MTJ were identified including type 1 (87.35%) and type 3 (12.65%). MTJ was found to reside either proximal (–) or distal (+) to the zero point. Lateral muscle belly extended beyond the zero point (low-lying) in 66.13% of cases with a mean distance of 13.10 ± 4.51 mm. All medial muscle bellies ended proximally to the zero point with a mean distance of –21.99 ± 13.21 mm. TIC type I, II, V and a new type were depicted. The most common was type I (82.93%). All types of TIC distribution were found and the most prevalent was type b (distributed to second and third toes) (67.68%). The most prevalent TIC location was distal to MKH with a mean distance of 11.23 ± ± 5.13 mm in the low-lying group and 8.73 ± 4.2 mm in the non-low-lying group. No statistically significant differences were found for all parameters including gender, side, and group.

REFERENCES

1. Alhaug OK, Berdal G, Husebye EE, et al. Flexor hallucis longus tendon transfer for chronic Achilles tendon rupture. A retrospective study. Foot Ankle Surg. 2019; 25(5): 630–635, doi: 10.1016/j.fas.2018.07.002, indexed in Pubmed: 30321934.
2. Amlang M, Rosenow MC, Friedrich A, et al. Direct plantar approach to Henry's knot for flexor hallucis longus transfer. Foot Ankle Int. 2012; 33(1): 7–13, doi: 10.3113/FAI.2012.0007, indexed in Pubmed: 22381230.
3. Beger O, Elvan Ö, Keskinbora M, et al. Anatomy of Master Knot of Henry: a morphometric study on cadavers. Acta Orthop Traumatol Turc. 2018; 52(2): 134–142, doi: 10.1016/j.aott.2018.01.001, indexed in Pubmed: 29366540.
4. Cerrato R, Campbell J. Tenodesis and transfer procedures for peroneal tears and tendinosis. Tech Foot Ankle Surg. 2009; 8(3): 119–125, doi: 10.1097/btf.0b013e3181b361e5.
5. Corte-Real NM, Moreira RM, Guerra-Pinto F. Arthroscopic treatment of tenosynovitis of the flexor hallucis longus tendon. Foot Ankle Int. 2012; 33(12): 1108–1112, doi: 10.3113/FAI.2012.1108, indexed in Pubmed: 23199862.
6. Coull R, Flavin R, Stephens MM. Flexor hallucis longus tendon transfer: evaluation of postoperative morbidity. Foot Ankle Int. 2003; 24(12): 931–934, doi: 10.1177/107110070302401211, indexed in Pubmed: 14733350.
7. Edama M, Kubo M, Onishi H, et al. Anatomical study of toe flexion by flexor hallucis longus. Ann Anat. 2016; 204: 80–85, doi: 10.1016/j.aanat.2015.11.008, indexed in Pubmed: 26704354.
8. Hahn F, Meyer P, Maiwald C, et al. Treatment of chronic achilles tendinopathy and ruptures with flexor hallucis tendon transfer: clinical outcome and MRI findings. Foot Ankle Int. 2008; 29(8): 794–802, doi: 10.3113/FAI.2008.0794, indexed in Pubmed: 18752777.
9. Hamilton WG. Stenosing tenosynovitis of the flexor hallucis longus tendon and posterior impingement upon the os trigonum in ballet dancers. Foot Ankle. 1982; 3(2): 74–80, doi: 10.1177/107110078200300204, indexed in Pubmed: 7141358.
10. Herbst SA, Miller SD. Transection of the medial plantar nerve and hallux cock-up deformity after flexor hallucis longus tendon transfer for Achilles tendinitis: case report. Foot Ankle Int. 2006; 27(8): 639–641, doi: 10.1177/107110070602700814, indexed in Pubmed: 16919220.
11. Hirota K, Watanabe K, Saito Y, et al. Flexor hallucis longus tendon branch test: Development and validation of a new method to assess anatomical variation of the tendinous slip. Foot Ankle Surg. 2020; 26(6): 607–613, doi: 10.1016/j.fas.2019.08.003, indexed in Pubmed: 31439503.
12. Hirota K, Watanabe K, Teramoto A, et al. Flexor hallucis longus tendinous slips and the relationship to toe flexor strength. Foot Ankle Surg. 2021; 27(8): 851–854, doi: 10.1016/j.fas.2020.11.002, indexed in Pubmed: 33229214.
13. Hockenbury R, Sammarco G. Medial sliding calcaneal osteotomy with flexor hallucis longus transfer for the treatment of posterior tibial tendon insufficiency. Foot

and Ankle Clinics. 2001; 6(3): 569–581, doi: 10.1016/s1083-7515(03)00114-1.

14. Hur MS, Kim JH, Woo JS, et al. An anatomic study of the quadratus plantae in relation to tendinous slips of the flexor hallucis longus for gait analysis. Clin Anat. 2011; 24(6): 768––773, doi: 10.1002/ca.21170, indexed in Pubmed: 21812033.

15. LaRue BG, Anctil EP. Distal anatomical relationship of the flexor hallucis longus and flexor digitorum longus tendons. Foot Ankle Int. 2006; 27(7): 528–532, doi: 10.1177/107110070602700708, indexed in Pubmed: 16842720.

16. Mao H, Shi Z, Wapner KL, et al. Anatomical study for flexor hallucis longus tendon transfer in treatment of Achilles tendinopathy. Surg Radiol Anat. 2015; 37(6): 639–647, doi: 10.1007/s00276-014-1399-y, indexed in Pubmed: 25542244.

17. Mao H, Wang L, Dong W, et al. Anatomical feasibility study of flexor hallucis longus transfer in treatment of Achilles tendon and posteromedial portal of ankle arthroscopy. Surg Radiol Anat. 2018; 40(9): 1031–1038, doi: 10.1007/s00276-018-2021-5, indexed in Pubmed: 29663091.

18. Martin BF. Observations on the muscles and tendons of the medial aspect of the sole of the foot. J Anat. 1964; 98: 437–453, indexed in Pubmed: 14193201.

19. Michelson J, Dunn L. Tenosynovitis of the flexor hallucis longus: a clinical study of the spectrum of presentation and treatment. Foot Ankle Int. 2005; 26(4): 291–303, doi: 10.1177/107110070502600405, indexed in Pubmed: 15829213.

20. Mulier T, Rummens E, Dereymaeker G. Risk of neurovascular injuries in flexor hallucis longus tendon transfers: an anatomic cadaver study. Foot Ankle Int. 2007; 28(8): 910–915, doi: 10.3113/FAI.2007.0910, indexed in Pubmed: 17697656.

21. Murphy RL, Womack JW, Anderson T. Technique tip: a new technique for harvest of the flexor hallucis longus tendon. Foot Ankle Int. 2010; 31(5): 457–459, doi: 10.3113/FAI.2010.0457, indexed in Pubmed: 20460076.

22. O'Sullivan E, Carare-Nnadi R, Greenslade J, et al. Clinical significance of variations in the interconnections between flexor digitorum longus and flexor hallucis longus in the region of the knot of Henry. Clin Anat. 2005; 18(2): 121–125, doi: 10.1002/ca.20029, indexed in Pubmed: 15696523.

23. Oddy MJ, Flowers MJ, Davies MB. Flexor digitorum longus tendon exposure for flatfoot reconstruction: a comparison of two methods in a cadaveric model. Foot Ankle Surg. 2010; 16(2): 87–90, doi: 10.1016/j.fas.2009.06.003, indexed in Pubmed: 20483141.

24. Pichler W, Tesch NP, Grechenig W, et al. Anatomical variations of the flexor hallucis longus muscle and the consequences for tendon transfer. A cadaver study. Surg Radiol Anat. 2005; 27(3): 227–231, doi: 10.1007/s00276-005-0314-y, indexed in Pubmed: 15789138.

25. Plaass C, Abuharbid G, Waizy H, et al. Anatomical variations of the flexor hallucis longus and flexor digitorum longus in the chiasma plantare. Foot Ankle Int. 2013; 34(11): 1580–1587, doi: 10.1177/1071100713494780, indexed in Pubmed: 23788233.

26. Rodriguez D, Devos Bevernage B, Maldague P, et al. Tarsal tunnel syndrome and flexor hallucis longus tendon hypertrophy. Orthop Traumatol Surg Res. 2010; 96(7): 829–831, doi: 10.1016/j.otsr.2010.03.026, indexed in Pubmed: 20851075.

27. Sharpe BD, Steginsky BD, Suhling M, et al. Posterior ankle impingement and flexor hallucis longus pathology. Clin Sports Med. 2020; 39(4): 911–930, doi: 10.1016/j.csm.2020.06.001, indexed in Pubmed: 32892975.

28. Sigvard T, Hansen J. Functional reconstruction of the foot and ankle. Lippincott Williams & Wilkins, a Wolters Kluwer Business, Philadelphia 2000: 422–429.

29. Vasudha TK, Vani PC, Sankaranarayanan G, et al. Communications between the tendons of flexor hallucis longus and flexor digitorum longus: a cadaveric study. Surg Radiol Anat. 2019; 41(12): 1411–1419, doi: 10.1007/s00276-019-02311-x, indexed in Pubmed: 31541272.

30. Vega J, Redó D, Savín G, et al. Anatomical variations of flexor hallucis longus tendon increase safety in hindfoot endoscopy. Knee Surg Sports Traumatol Arthrosc. 2017; 25(6): 1929–1935, doi: 10.1007/s00167-017-4465-2, indexed in Pubmed: 28220191.

31. Wan-Ae-Loh P, Danginthawat P, Huanmanop T, et al. Surface localisation of master knot of Henry, in situ and ex vivo length of flexor hallucis longus tendon: pertinent data for tendon harvesting and transfer. Folia Morphol. 2021; 80(2): 415–424, doi: 10.5603/FM.a2020.0045, indexed in Pubmed: 32301100.

32. Wapner KL, Hecht PJ, Shea JR, et al. Anatomy of second muscular layer of the foot: considerations for tendon selection in transfer for Achilles and posterior tibial tendon reconstruction. Foot Ankle Int. 1994; 15(8): 420–423, doi: 10.1177/107110079401500803, indexed in Pubmed: 7981812.

33. Wulker N, Stephens MM, Cracchiolo A. An atlas of foot and ankle surgery. 2nd ed. Talor & Francis, London 2005: 377–386.

VM
VIA MEDICA

C A S E   R E P O R T

Schwannoma in an accessory branch of the posterior cord of the brachial plexus: a rare case report

S. Banik[1], S. Sahoo[1], M.R. Gaikwad[1], S. Purkait[2], M. Patnaik[1]

[1]Department of Anatomy, All India Institute of Medical Sciences, Bhubaneswar, Odisha, India
[2]Department of Pathology, All India Institute of Medical Sciences, Bhubaneswar, Odisha, India

Background: Variation in the posterior cord of the brachial plexus is complicated and creates a risky relationship with the neighbouring structures. This is of importance to the surgeons and anaesthetists who must deal with the region in surgeries and procedures. Moreover, any benign tumour like schwannoma is rare in the plexus comprising 5% of total head and neck schwannomas.

Materials and methods: We present a case of schwannoma of the brachial plexus in a cadaver during routine anatomy dissection for the medical students. The origin and order of branching of the posterior cord were recorded and photographs were taken. The tumour was present in an accessory branch of the posterior cord and removal was made in-toto. An immunohistochemistry study was done for confirmation of diagnosis.

Results: The classical branching of the posterior cord was present. Additionally, a branch existed that was supplying the triceps muscle and emerged directly from the posterior cord. Tumour having the dimension of 2 × 1.8 × 0.5 cm was present.

Conclusions: Schwannomas are indolent but may cause compression of the nerve and resulting neurological symptoms. They might mimic nodules of supraclavicular fossa in breast carcinoma. Variations of the brachial plexus can also make the surgeons confused during surgery due to which anatomical knowledge of the possible variations is important. Pre- and post-operative complications can be easily predicted from it. Follow-up of the tumour is essential to track its progress and differentiation. (Folia Morphol 2022; 81, 3: 777–780)

Key words: brachial plexus, variation, schwannoma, breast carcinoma, posterior cord, triceps, nerve block

INTRODUCTION

One of the challenging structures a surgeon faces in neck and axillary region procedures is the brachial plexus. Formed by the anterior rami of the lower four cervical nerves and first thoracic nerve (C5, C6, C7, C8, and T1), the plexus often shows variations in distribution and arrangement of the root, trunk, division, or cord and even the branches, making this anatomical region extremely complicated. Variations are common at the junctions or sites of separation of individual parts, and collateral branches may arise from the trajectory of the entire plexus supplying scapular belt muscles [1].
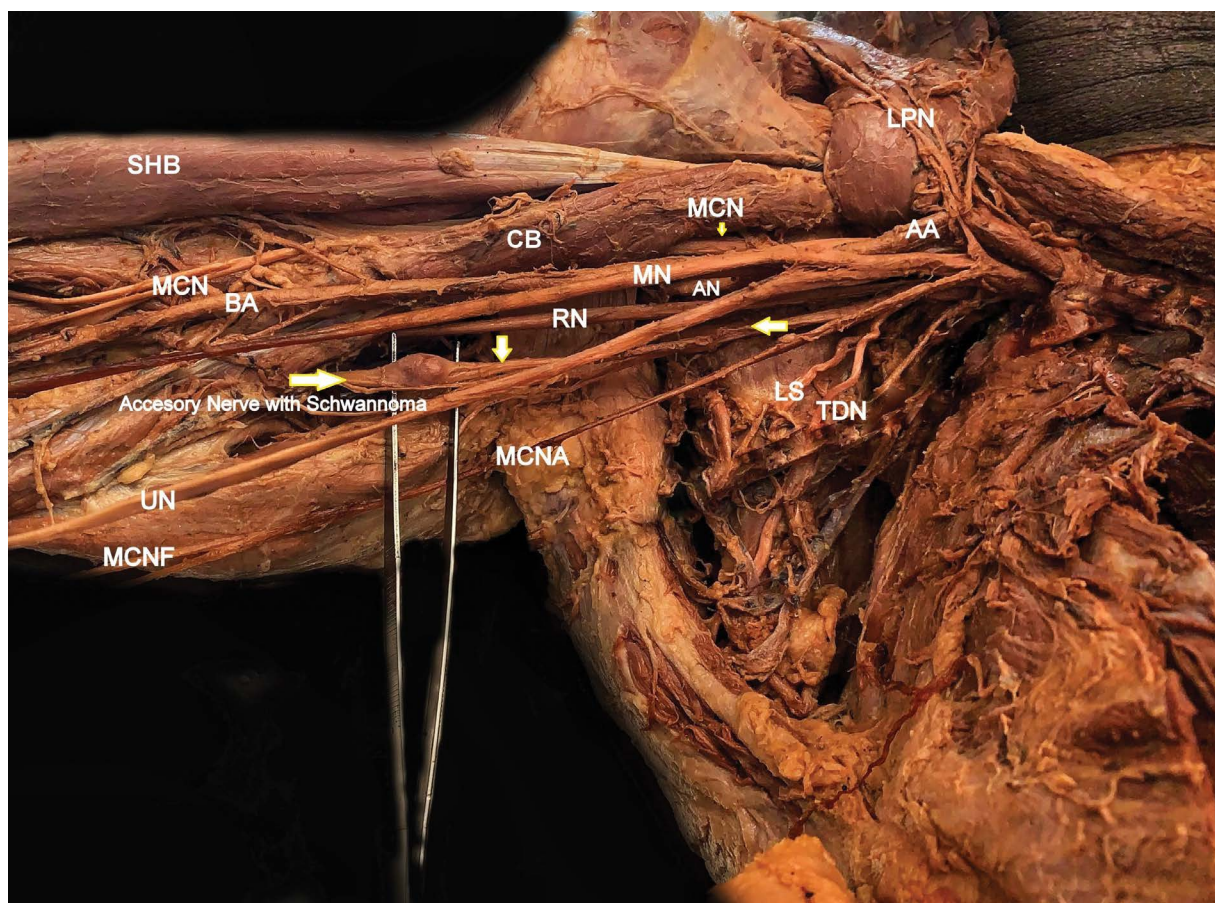
Figure 1. Dissected arm showing the brachial plexus with cords and branches. Notice the arrow that denotes the accessory branch arising out of the posterior cord of the plexus bearing the schwannoma; SHB — short head of biceps brachii; LPN — lateral pectoral nerve; AA — axillary artery; AN — axillary nerve; TDN — thoracodorsal nerve; MN — median nerve; LS — lower subscapular nerve; MCN — musculocutaneous nerve; CB — coracobrachialis; RN — radial nerve; MCNA — medial cutaneous nerve of arm; UN — ulnar nerve; BA — brachial artery; MCNF — medial cutaneous nerve of forearm.

Apart from variations in anatomy, the brachial plexus is a rare site for harbouring 5% of the total 25–45% of the head and neck schwannoma, which is a benign, encapsulated, well-demarcated tumour arising from the Schwann cells of cranial, peripheral, or autonomic nerve sheaths [4]. It is mostly sporadic in origin and shows slow, insidious growth, and is often solitary [3]. In the living, it may present as a painless, palpable neck mass [7], or it may sometimes present as a supraclavicular cystic mass [3]. Due to proximity to vital structures, rarity and anatomic complexity of the brachial plexus, a schwannoma in association with a branching variation, is of utmost caution to the surgeons, anaesthetists for surgical procedures and anaesthetic blocks as well as to physicians to locate compression symptoms like pain, sensory loss, wakefulness, and paresis [1].

We present a serendipitous case of schwannoma arising from an accessory branch of the posterior cord of the brachial plexus in a cadaver.

CASE REPORT

During the routine anatomic dissection of the brachial plexus, a variation was found in the posterior cord on the right side. The classical branching of the posterior cord into the upper subscapular, thoracodorsal, lower subscapular, axillary nerve and its distal continuation as radial nerve was observed. What additionally present was a nerve emerging from the posterior cord, medial to the radial nerve and branching distally with two branches supplying the triceps muscle. At the distal end of this additional nerve, almost 16.50 cm from the outer border of the clavicle and 18.5 cm from the olecranon process, a well-encapsulated 2 × 1.8 × 0.5 cm sized round tumour was noticed (Fig. 1). The tumour was resected in toto, and sections were subjected to histopathological examination. Tumour was well-circumscribed and encapsulated (Fig. 2A). The tumour cells were arranged in short fascicles. The cells were having an
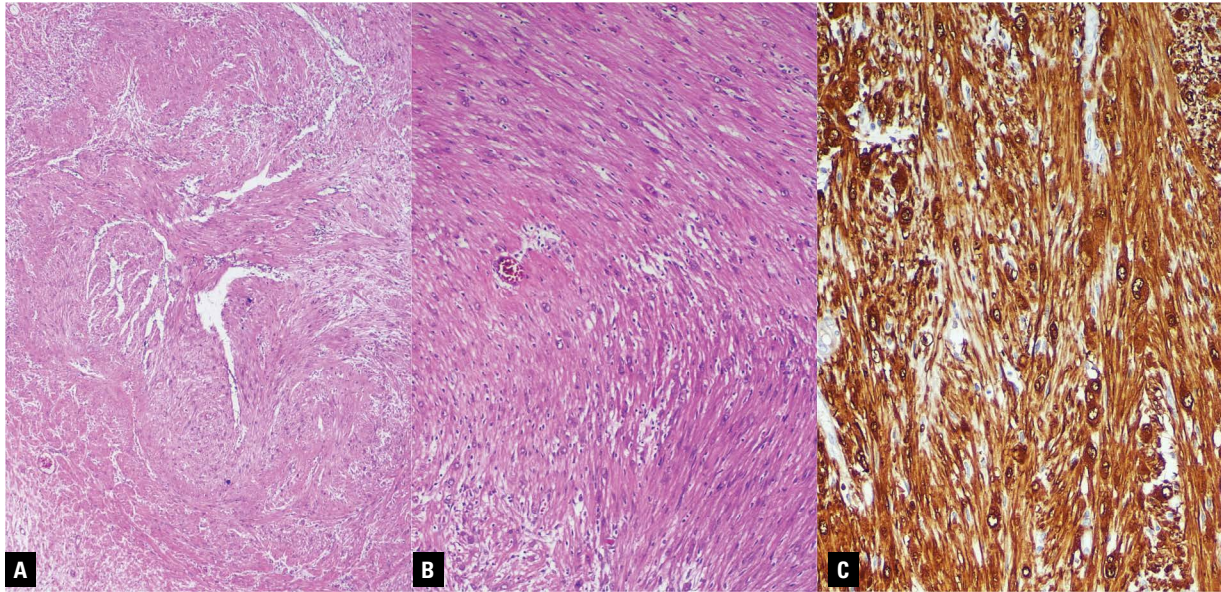
Figure 2. A. Representative photomicrograph showing a tumour which is well circumscribed and encapsulated; haematoxylin and eosin (H&E) ×40; **B.** The tumour cells are arranged in short fascicle. The cells have elongated vesicular nucleus and moderate fibrillary cytoplasm. No mitotic activity is seen; H&E ×40; **C.** The tumour cells showed strong immunopositivity for S-100; H&E ×200.

elongated vesicular nucleus and moderate fibrillary cytoplasm. No mitotic activity was seen (Fig. 2B). Immunohistochemical analysis of the tumour showed a strong, diffuse expression of S-100 positivity which confirmed it to be a schwannoma (Fig. 2C).

DISCUSSION AND CONCLUSIONS

Variation in the branching pattern of the posterior cord is common. Some existing studies have reported the classical branching pattern of brachial plexus in only 10.7% of cases [5]. The surgeons need to be aware of variant configurations of the cords of the brachial plexus while performing radical neck dissection and surgical exploration of the axilla and arm region to avoid damage to them. Moreover, the presence of communicating branches has to be kept in mind in the evaluation of unexplained sensory loss after trauma or surgical intervention in a particular area [8]. Neurotisation also needs proper identification of all the branches emerging from the posterior cord of the plexus. Entrapment neuropathy can be avoided if we know the plexus and its variations well enough [5]. The radial nerve can show variations in its origin, branching and communications. Abnormal communications of the radial nerve with the ulnar nerve have been reported in the plexus where the communicating branch was a separate filament given off from the radial nerve before entering the spiral groove where it did not mingle with the ulnar

nerve fibres but entered the sheath and finally ended supplying the triceps muscle [6]. In our study, the accessory branch that had schwannoma in it was supplying the triceps muscle. The calibre of the nerve was like independent branches of the cord, arising a possibility that it could be a very high branching of the radial nerve itself. As observed by Uysal et al. [see 1], 53.5% of the foetus has variations in brachial plexus. The variations were mostly on the right-hand side, as stated by Luis Ernesto Ballesteros and Ramirez, which is consistent with our report [1]. Multiple schwannomas can happen, but most of them arise sporadically as single benign tumours [9], and in our case too, the tumour was solitary with the opposite side showing no presence of a tumour. The gross appearance of the tumour is oval or plexiform, and its colour may range from pink, tan, yellow to grey [4], which matched our findings where the tumour was oval and fixed along the long axis of the nerve with a mild pinkish tinge. The clinical importance of the schwannoma lies in the fact that it can cause direct nerve invasion; it can infiltrate the surrounding tissues or exert a local mass effect [9]. The symptoms may range from mild paraesthesia and numbness to direct tenderness and radiating pain. Preoperative sensory and motor deficit can be present, with the former being more common, almost 54% vs. 41% [9]. They are mostly benign but may mimic malignancies such as breast carcinoma with supraclavicular mass and metastatic

lymph node [2]. Imaging studies like computed to-mography scan and gadolinium-enhanced magnetic resonance imaging are important diagnostic techniques for preoperative evaluation of schwannoma [4]. However, surgery for schwannoma is indicated only when it causes neurological dysfunction or pain, compression symptoms and suspicions of malignancy, but the real challenge lies in counselling patients about post-operative neurological deficits that are common. Despite easy enucleation of the tumour from the nerve, post-operative loss of sensation over the thumb or neurological phenomena due to C5–C6 severing has been reported [7]. Muscle transposition or primary nerve repair using nerve graft can prevent or reduce post-operative neurological symptoms. Brachial plexus schwannoma is a rare tumour entity, and coupled with an accessory branch of the posterior cord, it has immense importance in different branches of medicine as well as surgery and anaesthesia.

Conflict of interest: None declared

REFERENCES

1. Ballesteros LE, Ramirez LM. Variations of the origin of collateral branches emerging from the posterior aspect of the brachial plexus. J Brachial Plex Peripher Nerve Inj. 2007; 2: 14, doi: 10.1186/1749-7221-2-14, indexed in Pubmed: 17587464.

2. da Costa Vieira RA, de Araujo Silva I, de Souza Coelho RD, et al. Brachial plexus schwannoma mimicking advanced breast carcinoma. Breast Dis. 2020; 39(2): 109–113, doi: 10.3233/BD-190432, indexed in Pubmed: 32083563.

3. Kho JP, Prepageran N. Huge brachial plexus schwannoma, masking as a cystic neck mass. AME Case Rep. 2018; 2: 41, doi: 10.21037/acr.2018.08.01, indexed in Pubmed: 30363802.

4. Kumar A, Akhtar S. Schwannoma of brachial plexus. Indian J Surg. 2011; 73(1): 80–81, doi: 10.1007/s12262-010-0141-1, indexed in Pubmed: 22211049.

5. Muthoka JM, Sinkeet SR, Shahbal SH, et al. Variations in branching of the posterior cord of brachial plexus in a Kenyan population. J Brachial Plex Peripher Nerve Inj. 2011; 6: 1, doi: 10.1186/1749-7221-6-1, indexed in Pubmed: 21649927.

6. Natsis K, Giannakopoulou A, Piagkou M, et al. Connections between radial and ulnar nerve at high humeral level in cadavers: incidence, topography, and literature review. Surg Radiol Anat. 2018; 40(3): 313–322, doi: 10.1007/s00276-017-1939-3, indexed in Pubmed: 29124342.

7. Ranjan S, Arora N, Sethi D, et al. Schwannoma of the brachial plexus: a rare case report. Iran J Otorhinolaryngol. 2020; 32(111): 243–247, doi: 10.22038/ijorl.2020.40635.2330, indexed in Pubmed: 32850513.

8. Rastogi R, Budhiraja V, Bansal K. Posterior cord of brachial plexus and its branches: anatomical variations and clinical implication. ISRN Anat. 2013; 2013: 501813, doi: 10.5402/2013/501813, indexed in Pubmed: 25969826.

9. Vučemilo L, Lajtman Z, Mihalj J, et al. Brachial plexus schwannoma — case report and literature review. Acta Clin Croat. 2018; 57(2): 366–371, doi: 10.20471/acc.2018.57.02.19, indexed in Pubmed: 30431732.

CASE REPORT

VIA MEDICA

Bilateral absence of the transverse sinuses with fenestrated superior sagittal sinus draining through enlarged occipital and marginal sinuses

P.M. Rădoi[1, 2], D.I. Mincă[3], M.C. Rusu[3], C. Toader[1, 2]

[1]Faculty of General Medicine, "Carol Davila" University of Medicine and Pharmacy, Bucharest, Romania
[2]National Institute of Neurology and Neurovascular Diseases, Bucharest, Romania
[3]Division of Anatomy, Faculty of Dental Medicine, "Carol Davila" University of Medicine and Pharmacy, Bucharest, Romania

The endothelial-lined dural venous sinuses collect blood from the brain, menin-ges, and calvaria and drain it to the internal jugular veins. The adult drainage pathway of the venous sinuses confluent is commonly via the transverse and sigmoid sinuses to the jugular bulb. The occipital (OS) and marginal (MS) sinuses are well-represented before birth, in most cases. During a retrospective study of the computed tomography angiograms of a 64-year-old female was found a rare combination of variants of the posterior fossa sinuses. The confluence of the dural venous sinuses was rhomboidal and drained superiorly the superior sagittal sinus, and inferiorly a well-represented OS. The transverse sinuses were aplastic, on the right side, and hypoplastic on the opposite side. The OS further drained into the MS which, on each side, emptied into the respective jugular bulb. On each side a condylar vein left the junction of the sigmoid sinus and jugular bulb. Such posterior fossa drainage, exclusively on the OS-MS pathway, should be kept in mind when transections of the venous sinuses are intended during neurosurgical approaches of the foramen magnum. The OS-MS drainage is rather a persisting foetal pattern. The bilateral anatomical exclusion of the transverse sinuses is an added condition to spare the OS and MS. (Folia Morphol 2022; 81, 3: 781–784)

Key words: computed tomography, dura mater, venous sinus, foramen magnum, posterior cranial fossa

INTRODUCTION

The endothelial-lined dural venous sinuses collect blood from the brain, meninges, and calvaria and drain it to the internal jugular veins (IJVs) [2]. The superior group of the dural venous sinuses is the main one and consists of the sagittal sinuses, superior (SSS) and inferior, the straight sinus (StS), the occipital sinus (OS), the transverse sinus (TS) and the sigmoid sinus (SiS) [2]. The TS and the SiS represent the lateral sinus. The confluence of sinus-es (torcular Herophili) lies in front of the internal occipital protuberance.

The OS lies in the attached margin of the falx cerebelli and drains into the confluence of sinuses [2, 3]. Its presence was variably detected in 18–81.7% of cases, depending on the methods of study [6]. On computed tomography angiograms the OS was short, rudimentary, and untraceable to the foramen magnum in 33.3% of cases [6]. The OS functions as the main drainage pathway when the lateral sinus is rudimentary [15].
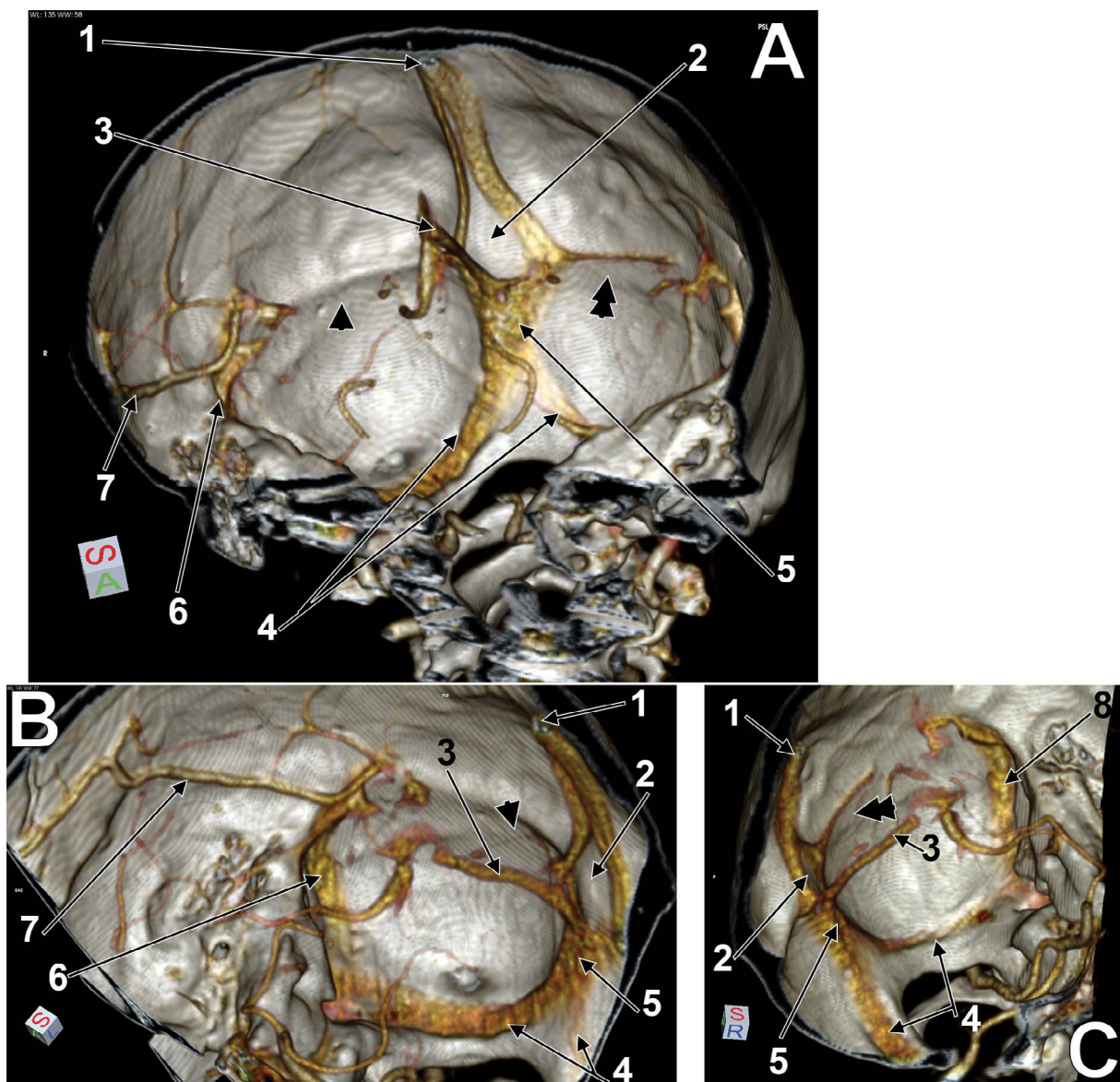
Figure 1. Three-dimensional volume renderings of the posterior fossa; **A.** Left antero-superior view; **B.** Left superior view; **C.** Right superior view; 1 — superior sagittal sinus; 2 — internal occipital protuberance; 3 — straight sinus; 4 — marginal sinuses; 5 — occipital sinus; 6 — right sigmoid sinus; 7 — vein of Labbé; 8 — left sigmoid sinus. On the right side the groove for transverse sinus lacks and there is aplasia of that sinus (arrowhead). On the left side the groove for transverse sinus lacks and that sinus is hypoplastic (double arrowhead).

CASE REPORT

A 64-year-old female was admitted to the neurosurgical department of the National Institute of Neurology and Neurovascular Diseases for further diagnosis and treatment. For evaluation of possible vascular malformations a brain computed tomography angiography was performed after injecting iodine radiocontrast agent into the cubital fossa veins, followed by saline medium. The scan was performed with a 32-slice machine (Siemens Multislice Perspective Scanner), using a 0.6 mm collimation and reconstruction of 0.75 mm thickness with 50% overlap for multiplanar, maximum intensity projection (MIP) and three-dimensional volume rendering (3D-VR) technique, as described previously [12, 13]. The case was documented using the Horos for iOS software (Horos Project). The research was conducted ethically in accordance with The Code of Ethics of the World Medical Association (Declaration of Helsinki).

On the inner side of the cranial vault, the SSS was identified and was further tracked posteriorly. At about 4 cm above the internal occipital protuberance the SSS was dividing into a left arm 0.50 cm thick and a right arm 0.23 cm thick. These two arms di-
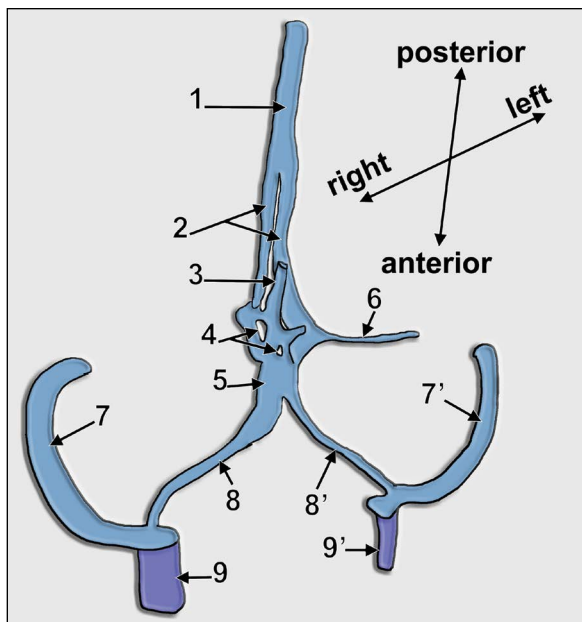
Figure 2. The confluent of the venous sinuses is drained via the occipito-marginal sinus. Right transverse sinus aplasia and left transverse sinus hypoplasia. Schema of the anatomic variant. Right anterior view; 1 — superior sagittal sinus; 2 — postero-inferior end of the superior sagittal sinus, divided into two divergent arms; 3 — straight sinus; 4 — venous network; 5 — occipital sinus; 6 — left hypoplastic transverse sinus, blind-ended; 7, 7' — sigmoid sinuses; 8, 8' — marginal sinuses; 9, 9' — internal jugular veins.
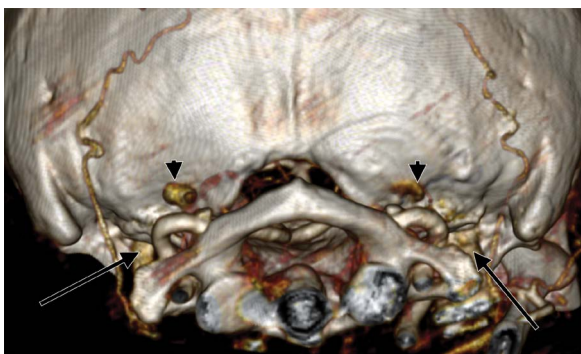
Figure 3. Three-dimensional volume rendering, postero-inferior view of the occipitovertebral junction. There are identified bilateral emissary condylar veins (arrowheads) and the internal jugular veins (arrows).

verged on the respective sides of the internal occipital protuberance, thus forming the superior borders of a venous rhomb (Figs. 1, 2). The right transverse sinus (TS) lacked (aplasia/agenesis), as also did the corresponding groove on the occipital squama. From the left angle of the venous rhomb left a hypoplastic TS, the length of which was 2.28 cm and the calibre 0.11 cm calibre; it was blind-ended. The inferior

borders of the venous rhomb joined inferior to the internal occipital protuberance to form the occipital sinus (OS) measuring 1.22 cm. The straight sinus was connected with the right angle of the venous rhomb and with the right infero-lateral border of the venous rhomb through a venous network. The OS further divided on the sides of the vermian fossa into the left and right marginal sinuses (MSs). These MS on each side ended into the respective sigmoid sinus (SS) proximally to the jugular bulb (JB). From the SS-JB junction left, on each side, condylar emissary veins coursing through posterior condylar canals (Fig. 3).

DISCUSSION AND CONCLUSIONS

A study of the evolution of venous sinuses drainage in hominids brought arguments suggesting that selection for bipedalism determined epigenetic adaptations, such as a large OS-MS path and available emissary veins, but after bipedalism became established these adaptations relaxed [5]. It is interesting to consider also the ontogenesis of the OS. It is not been developed yet in 3-month-old foetuses [6]. A couple of months later, the TS is enlarged and reaches the torcular but the SiS is underdeveloped; drainage is ensured by OS channels connected with the MS and the jugular sinus [6]. The OS regresses only after birth [6] when a shift from a fatal to a postnatal type of circulation occurs [11]. Therefore, an OS-to--IJV anatomical path of drainage could be regarded as a persistent foetal morphology. Interestingly, a dissection study in 33 neonatal cadavers found no hypoplastic or aplastic sinuses, all the specimens had OS, and no bilateral drainage of the OSs via MSs was found [9]. When the OS drains into the SiS, and not into the jugular bulb, is termed "oblique OS" [15]. Such previously reported rare morphologies [6, 14], including the present case, are presented in Figure 4.

Seemingly, the OS-MS pathway, as well as condylar emissary veins, are of use to compensate dysplastic TSs. Bergman's Encyclopedia of Human Anatomic Variation [1] quotes the report of Hamnett et al. [7] who found the bilateral absence of the TS (hypoplasia with contralateral aplasia), the OS providing the only drainage pathway for the SSS and the StS to the MSs and the jugular bulbs. That variant mostly corresponds to ours, the difference being that in the case reported here the SiSs also drained through condylar veins.

Dora and Zileli [4] documented different combined variants, such as bilateral hypoplastic lateral sinuses, but with OS absent, or hypoplastic lateral
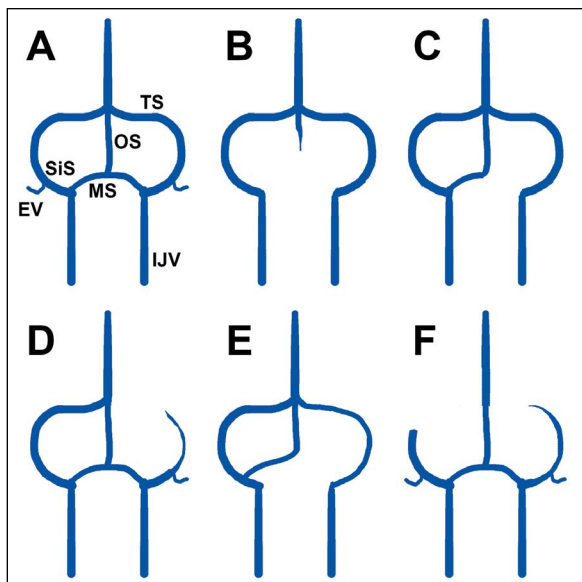
Figure 4. Different morphologies of the venous sinuses of the posterior fossa are compared to the complete prenatal one (**A**); **B.** Rudimentary OS, absent MSs; **C.** The OS drains unilaterally into the IJV bulb by a unilateral MS; **D.** The OS drains bilaterally through MSs into the IJVs but one of the SiSs is hypoplastic/aplastic and that drainage is compensated through an EV; **E.** The OS drains unilaterally through a MS into the SiS, and not the jugular bulb (oblique OS); **F** (present case). The OS drains bilaterally into the IJVs, aplastic and hypoplastic TSs are compensated with bilateral EVs; TS — transverse sinus; SiS — sigmoid sinus; OS — occipital sinus; MS — marginal sinus; EV — emissary vein; IJV — internal jugular vein.

sinus with OS present, but without MSs. None of the variants documented by these authors fits with the presently reported one.

A drainage pathway via the OS and MS with aplastic/hypoplastic TSs, such as in this case, stands as a unique possibility of emptying the confluent of sinuses. Therefore, surgical transection of the OS and/or MS would determine major perturbations in the venous drainage of the brain. The emissary veins could not compensate the resulted deficit because they are inserted into a variant of SiS unfilled from the confluent of sinuses.

Previously, in 1881, Knott [8] documented anatomical variants of the venous sinuses and discussed that both lateral sinuses, thus the TS continued as SiS, could be hypoplastic, the blood being drained via the OS and the MS. In the case reported here a TS was aplastic, and not hypoplastic.

The venous pattern of drainage is important in understanding the pathophysiology and risks associated with dural arteriovenous fistulas [10].

Conflict of interest: None declared

REFERENCES

1. Bergman RA, Tubbs RS, Shoja MM, Loukas M. Bergman's comprehensive encyclopedia of human anatomic variation. John Wiley & Sons, Hoboken, New Jersey 2016.
2. Curé J, Van Tassel P, Smith M. Normal and variant anatomy of the dural venous sinuses. Seminars in Ultrasound, CT and MRI. 1994; 15(6): 499–519, doi: 10.1016/s0887-2171(05)80019-8.
3. Das S, Abd Latiff A, Suhaimi FH, et al. An anatomico-radiological study of the grooves for occipital sinus in the posterior cranial fossa. Bratisl Lek Listy. 2008; 109: 520–524, indexed in Pubmed: 19205565.
4. Dora F, Zileli T. Common variations of the lateral and occipital sinuses at the confluens sinuum. Neuroradiology. 1980; 20(1): 23–27, doi: 10.1007/BF00346857, indexed in Pubmed: 7422118.
5. Falk D. Evolution of cranial blood drainage in hominids: enlarged occipital/marginal sinuses and emissary foramina. Am J Phys Anthropol. 1986; 70(3): 311–324, doi: 10.1002/ajpa.1330700306, indexed in Pubmed: 3092672.
6. Fukusumi A, Okudera T, Takahashi S, et al. Anatomical evaluation of the dural sinuses in the region of the torcular herophili using three dimensional CT venography. Acad Radiol. 2010; 17(9): 1103–1111, doi: 10.1016/j.acra.2010.04.020, indexed in Pubmed: 20619699.
7. Hamnett NTJ, Ogungbo B, Nahser H, et al. Anomalous cerebral venous sinus drainage. Br J Neurosurg. 2010; 24(4): 497–498, doi: 10.3109/02688697.2010.489657, indexed in Pubmed: 20726761.
8. Knott JF. On the cerebral sinuses and their variations. J Anat Physiol. 1881; 16: 27–42, indexed in Pubmed: 17231415.
9. Kopuz C, Aydin ME, Kale A, et al. The termination of superior sagittal sinus and drainage patterns of the lateral, occipital at confluens sinuum in newborns: clinical and embryological implications. Surg Radiol Anat. 2010; 32(9): 827–833, doi: 10.1007/s00276-010-0628-2, indexed in Pubmed: 20182724.
10. McDougall CG, Halbach VV, Dowd CF, et al. Dural arteriovenous fistulas of the marginal sinus. 1997; 18: 1565–1572, indexed in Pubmed: 9296201.
11. Okudera T, Huang YP, Ohta T, et al. Development of posterior fossa dural sinuses, emissary veins, and jugular bulb: Morphological and radiologic study. Am J Neuroradiol. 1994; 15: 1871–1883, indexed in Pubmed: 7863937.
12. Rădoi PM, Rusu MC, Dincă D, et al. Combined rare anatomic variants: persistent primitive olfactory artery and azygos pericallosal artery. Surg Radiol Anat. 2021; 43(8): 1305–1308, doi: 10.1007/s00276-021-02687-9, indexed in Pubmed: 33496800.
13. Rusu MC, Măru N, Rădoi PM, et al. Trifurcated external carotid artery and complete gamma-loop of its maxillary branch. Surg Radiol Anat. 2019; 41(2): 231–234, doi: 10.1007/s00276-018-2142-x, indexed in Pubmed: 30483866.
14. Tanoue S, Kiyosue H, Sagara Y, et al. Venous structures at the craniocervical junction: anatomical variations evaluated by multidetector row CT. Br J Radiol. 2010; 83(994): 831–840, doi: 10.1259/bjr/85248833, indexed in Pubmed: 20647517.
15. Tubbs RS, Bosmia AN, Shoja MM, et al. The oblique occipital sinus: a review of anatomy and imaging characteristics. Surg Radiol Anat. 2011; 33(9): 747–749, doi: 10.1007/s00276-011-0831-9, indexed in Pubmed: 21626273.

VIA MEDICA

CASE REPORT

Persistent trigeminal artery as a rare cause of vertebrobasilar insufficiency

K. Sulima[1], J. Chojdak-Łukasiewicz[1], B. Paradowski[1], M. Guziński[2]

[1]Department of Neurology, Wroclaw Medical University, Wroclaw, Poland
[2]Department of General Radiology, Interventional Radiology and Neuroradiology, Wroclaw Medical University, Wroclaw, Poland

The persistent trigeminal artery (PTA) is the most common foetal carotid-basilar anastomosis which may persist into adult life. In the literature there are numerous papers referring to the anatomical characteristics of this anomalous vessel. In the majority of cases PTA is an incidental finding and its clinical significance has been debated. Some authors describe the coincidence of PTA with various clinical syndromes. However, there are few reports linking PTA with the symptoms of vertebrobasilar insufficiency. We present a patient with a 3-year history of recurrent dizziness and impaired vision, precipitated by physical activity, in whom neuroimaging techniques revealed a left PTA. In our case the occurrence of PTA might have been related to the clinical manifestation and the potential mechanism will be discussed. (Folia Morphol 2022; 81, 3: 785–790)

Key words: persistent trigeminal artery, computed tomography angiogram, stroke, magnetic resonance imaging, vertebrobasilar insufficiency

INTRODUCTION

The persistent trigeminal artery (PTA) is the most common remnant of the primitive circulatory system that unites the internal carotid (anterior) and vertebrobasilar (posterior) systems. The PTA contributes to about 85% of known primitive persistent anastomoses [1, 25]. The reported incidence of the PTA ranges from 0.1% to 0.6% [7, 24]. Most cases are detected incidentally during brain imaging performed for unrelated reasons, so the real frequency can be higher, based on unrecognised cases. The PTA is usually asymptomatic; however, in some cases may be connected with III or VI nerves palsies, trigeminal neuralgia, vertigo, ataxia, stroke, migraine headache and other neurological symptoms [9, 14, 30, 35]. It may be also associated with other vascular abnormalities

such as basilar hypoplasia or anatomical variations of aortic arch and its branches [10, 29].

CASE REPORT

A 33-year-old man, with no prior comorbidities, presented to our clinic with a 3-year history of recurrent dizziness and impaired vision. The symptoms were transient, lasting usually over a few seconds, triggered by moderate physical activity, especially walking. Head rotation did not aggravate the symptoms. There was no prior history of arm claudication, as well as loss of consciousness or seizures. The patient was an underground copper miner, potentially exposed to dust and toxins. No neurological deficit was found on examination. Magnetic resonance imaging of the brain, with and without contrast enhancement, was

Figure 1. Computed tomography angiogram axial view show persistent trigeminal artery on the left (arrow). It is the most common variant of persistent carotid basilar anastomoses.
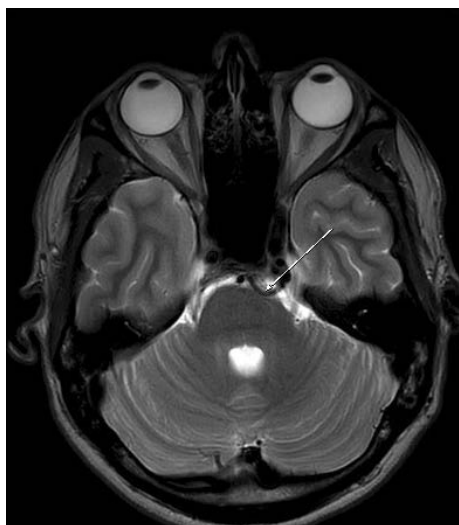
Figure 2. Magnetic resonance. Axial T2-weighted scan. Persistent trigeminal artery on the left (arrow).
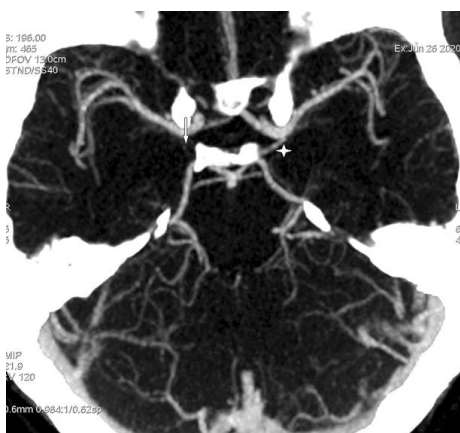
Figure 3. Computed tomography angiogram, maximum intensity projection reconstruction. Persistent trigeminal artery fills superior cerebellar arteries, posterior communicating arteries supplied via patent posterior communicating artery (PCoA) on the left (asterisk). The absence of right PCoA (arrow).
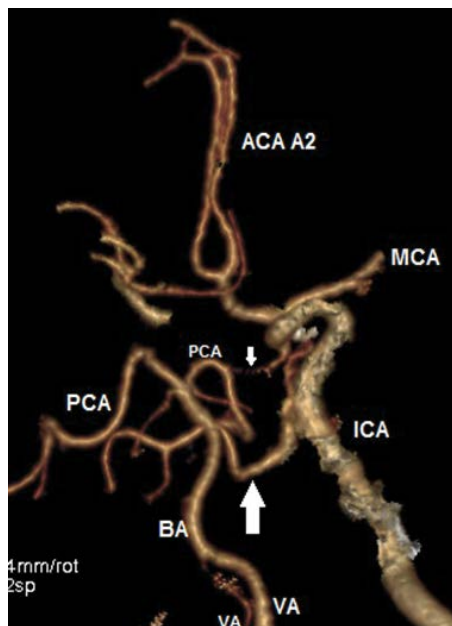
Figure 4. Volume rendering three-dimensional reconstruction, cerebral angiogram based on computed tomography angiogram examination. Bigger arrow persistent trigeminal artery (connection basilar artery [BA]-internal carotid artery [ICA]), smaller arrow posterior communicating artery (connection posterior communicating artery [PCA]-internal carotid artery [ICA]), both on left side; ACA — anterior cerebral artery; MCA — middle cerebral artery; VA — vertebral artery.

Figure 5. Posterior circulation computed tomography angiogram, maximum intensity projection oblique reconstruction; BA — basilar artery; PCA — posterior communicating artery; PTA — persistent trigeminal artery; SCA — superior cerebellar artery.

within the normal limits. A computed tomography angiogram was performed, revealing a left PTA, an anomalous vessel extending from the internal carotid artery (ICA) to the basilar artery (BA) (Fig. 1–5). The PTA arose from the junction between petrous and cavernous ICA, and ran posterolaterally along the trigeminal
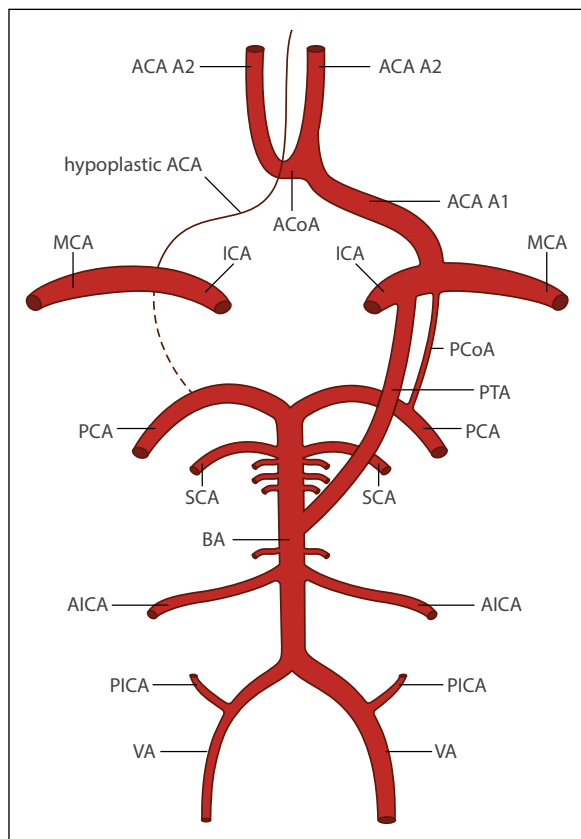
Figure 6. Schematic presentation of the cerebral vasculature anatomy in our patient; ACA A1 — A1 segment of anterior cerebral artery; ACA A2 — A2 segment of anterior cerebral artery; ACoA — anterior communicating artery; PCoA — posterior communicating artery; ICA — internal carotid artery; AICA — anterior inferior cerebellar artery; PICA — posterior inferior cerebellar artery; BA — basilar artery; MCA — middle cerebral artery; PCA — posterior communicating artery; PTA — persistent trigeminal artery; SCA — superior cerebellar artery; VA — vertebral artery

nerve, its diameter was about 2–3 mm. The PTA filled superior cerebellar arteries (SCAs), while the patent left posterior communicating artery (PCoA) supplied the posterior cerebral arteries (PCAs). According to its course and connections, the vessel was classified as Saltzman type II. The examination also showed the focal stenosis of the right vertebral artery (VA) at the C4 level, the absence of the right PCoA and hypoplasia of A1 segment of anterior cerebral artery (ACA) (Fig. 2). The Figure 6 is a pictorial presentation of the cerebral vasculature anatomy in our patient. No other variations were found in the vessels supplying the central nervous system. The patient was treated conservatively with acetylsalicylic acid (75 mg per day) and cinnarizine with dimenhydrinate (20 + 40 mg 3 times per day) as a short-term therapy for dizziness.

The potential benefits of surgical procedure would not justify the possible risk of such treatment.

DISCUSSION

There are many reports regarding intracranial vascular development, and one of the most significant was made by Padget in 1948 [2, 32]. During the evolution of the vertebrobasilar arterial system, the hindbrain is supplied predominantly by four foetal carotid-basilar anastomoses: the trigeminal, otic, hypoglossal, and proatlantal intersegmental arteries, arising at the 3 mm embryonic stage. The above-mentioned connections regress with the subsequent development of posterior communicating arteries and basilar artery and should disappear by the 14 mm stage [2]. Failure of this process results in persistence of these vessels into adult life. Within four persistent foetal carotid-basilar anastomoses, the trigeminal artery is the most common.

The PTA was firstly reported by Richard Quinn in 1844 during an autopsy [35]. In 1950 the PTA was recognised by Sutton, based on angiography [35].

The PTA typically arises from the posterior or lateral part of intracavernous (C4) segment of the ICA and terminates at the BA, between the first part of the SCA and anterior inferior cerebellar artery (AICA) [4, 12, 34]. In some cases pontine perforating branches of PTA are observed [3, 23, 33]. The incidence of PTA varies from 0.1% to 0.6% [11] and according to some studies is higher in women [5, 22]. In most cases the right or none-sided predominance of the PTA is detected.

The most common classification system, based on angiographic characteristics, was introduced by Georg-Frederik Saltzman in 1959 [4]. It divides the PTA into three groups according to its relationship to the basilar artery. In Salzmann type I, the PTA enters the basilar artery between the SCA and the AICA, supplying both PCA and SCA. The BA is typically hypoplastic and the ipsilateral posterior communicating artery is absent. In Saltzman type II, the PTA provides the anterior superior cerebellar artery, whereas the posterior cerebral arteries arise from the posterior communicating arteries. The first segment of BA is missing. Saltzman type III, the rarest type, is considered to be a combination of types I and II. In type III PCA is supplied by the ipsilateral PCoA, the other PCA and both SCA being supplied by the PTA. Saltzman type I is the most prevalent and accounts for about 24% of all cases [29, 35].

In 1998 Salas et al. [33] proposed a different classification, dividing the PTA into two types based on its relationship to the abducens nerve: the lateral (petrosal) and medial (sphenoidal). The lateral type is recognised when the artery courses laterally to the abducens nerve and pierces the dura mater just medially to the sensory root of the trigeminal nerve. The second, medial type, is recognised when the artery courses medially to the abducens nerve, penetrates the dorsum sellae and joins the distal third of the basilar artery [33]. The study indicated that the latter type is more common [31, 36].

Most cases of PTA are recognised incidentally in imaging diagnostic tests performed for other reasons. Typically PTA is associated with BA hypoplasia, the observation being confirmed in the large neuroimaging series [10, 31]. There are some reports in the literature regarding the correlation of the PTA with other abnormalities in the circle of Willis, such as the absence of the ipsilateral PCoA, VA or BA. Due to embryonic error in vasculogenesis, the PTA is frequently observed in PHACE syndrome [19]. The connection with the increased risk of aneurysm is controversial. The high incidence of aneurysm is explained by haemodynamic changes in blood flow, which promote aneurysm formation [31]. In an older study [1, 18], the prevalence of associated intracranial aneurysms in patients with PTA was reported to be up to 14–32%. In the newest reports based on magnetic resonance imaging examination, the prevalence is estimated to be approximately 16% [12]. However, Meckel et al. [29] suggested that the real frequency of aneurysm coexisting with the PTA does not differ from that in the general population (4.2% vs. 3.7%) [25, 29]. Aneurysm connected with the PTA has a lot of potential sites. Behari described an aneurysm on the posterior communicating artery, Maeshima et al. [28] showed a case of PTA connected with multiple aneurysms on ACA and middle cerebral artery [8, 28]. Bechri et al. [7] in 2020 reported a case of a posterior meningeal artery aneurysm coexisting with PTA. In a great number of cases the persistent trigeminal artery is an incidental discovery and its clinical significance has been debated. The symptoms may depend on associated vascular abnormalities or their localisation. The PTA has been identified as a rare cause of cranial nerves dysfunction, including incomplete oculomotor and abducens nerve palsies, trigeminal neuralgia and hemifacial spasm. The ischaemic events related to the PTA are rare and can occur through the steal phenomenon or thrombosis in anterior circulation [16, 21]. Typically, persistent trigeminal artery aneurysms (PTAA) are discovered incidentally in patients with subarachnoid haemorrhage (SAH) due to the rupture of a simultaneous aneurysm in another localisation. Ruptured PTAA can be presented with symptoms of headache and posterior cranial fossa symptoms, according to the SAH [29]. In the case of large and giant cavernous PTAAs, cranial neuropathy or facial pain can be observed [13]. Furthermore, PTA was postulated as a potential cause of vertebrobasilar insufficiency (VBI), which could be defined as inadequate blood flow through the posterior circulation system, without actual infarction, with a temporary inability to meet cerebral metabolic needs as a consequence [20]. Posterior circulation supplies the brainstem, cerebellum, thalamus, occipital lobe, some portions of temporooccipital and parietooccipital junctions and even the inner ear through the labyrinthine artery [6]. Dizziness is the most common symptom of VBI, but the diversity of brain regions being supplied by vertebrobasilar vasculature explains the variety of complaints, such as diplopia, blindness, visual field deficits, imbalance, and ataxia [20]. Patients with VBI usually present more than one symptom at the same time. The most frequent pathology underlying VBI is atherosclerosis; however, other causes such as embolism, arterial dissection, migraine and fibromuscular dysplasia may occur [27]. As during embryonic development PTA originates from ICA, the physiological direction of blood flow through PTA is mostly from the ICA to the BA [6, 15]. Nevertheless, the reverse of this direction may occur in certain clinical situations. In case of severe stenosis or occlusion of the ipsilateral ICA, the reversal of flow through PTA may play a protective role and be sufficient to perfuse ICA and its branches, keeping the patient free of hypoperfusion symptoms [26]. Conversely, if PTA coexists with other anomalies of the intracranial vessels, such as hypoplastic vertebral artery, ICA may be the sole supply to the posterior circulation system. In that case if carotid stenosis occurs, the patient may develop symptoms of VBI [6]. However, our patient did not have any risk factors for cardiovascular disease, and there were also no radiologic signs of atherosclerosis. The review of the literature revealed only one previously reported case linking PTA with VBI symptoms, without the simultaneous presence of carotid pathology, in which dilatation of PTA and BA was the speculated mechanism [17]. In our patient

the lack of the right PCoA, together with the stenosis of the right VA, might have resulted in the left ICA being the main supply to the posterior circulation system. In the case of the exercise-induced increase of metabolism in the anterior portion of the brain, PTA might have been insufficient to perfuse the posterior fossa region of the brain, leading to VBI symptoms. We could not exclude the potential reverse of blood flow direction in this case, from the vertebrobasilar system to the carotid artery.

CONCLUSIONS

Due to the high prevalence of dizziness in the general population, awareness of its rare causes seems to be crucial. The PTA may play a role in the production of VBI symptoms. In patients with VBI of unknown origin, a computed tomography angiogram should be considered as a diagnostic procedure.

Conflict of interest: None declared

REFERENCES

1. Agnoli AL. Vascular anomalies and subarachnoid haemorrhage associated with persisting embryonic vessels. Acta Neurochir (Wien). 1982; 60(3-4): 183–199, doi: 10.1007/BF01406306, indexed in Pubmed: 7072535.
2. Ali S, Radaideh MM, Shaibani A, et al. Persistent trigeminal artery terminating in the posterior inferior cerebellar artery: case report. Neurosurgery. 2008; 62(3): E746–8; discussion E746, doi: 10.1227/01.neu.0000317327.17225.f8, indexed in Pubmed: 18425001.
3. Alcalá-Cerra G, Tubbs RS, Niño-Hernández LM. Anatomical features and clinical relevance of a persistent trigeminal artery. Surg Neurol Int. 2012; 3: 111, doi: 10.4103/2152-7806.101798, indexed in Pubmed: 23087827.
4. Arráez-Aybar LA, Fuentes-Redondo T, Millán JM. Persistent trigeminal artery: a cross-sectional study based on over 3 years conventional angiography, CT angiography and MR angiography images. Surg Radiol Anat. 2016; 38(4): 445–453, doi: 10.1007/s00276-015-1578-5, indexed in Pubmed: 26499125.
5. Bai M, Guo Q, Li S. Persistent trigeminal artery/persistent trigeminal artery variant and coexisting variants of the head and neck vessels diagnosed using 3 T MRA. Clin Radiol. 2013; 68(11): e578–e585, doi: 10.1016/j.crad.2013.05.099, indexed in Pubmed: 23845929.
6. Battista RA, Kwartler JA, Martinez DM. Persistent trigeminal artery as a cause of dizziness. Ear Nose Throat J. 1997; 76(1): 43–45, indexed in Pubmed: 9018936.
7. Bechri H, Louraoui SM, Fikri M, et al. Persistence of a trigeminal artery associated with a posterior meningeal artery aneurysm: case report and literature review. J Surg Case Rep. 2020; 2020(2): rjz389, doi: 10.1093/jscr/rjz389, indexed in Pubmed: 32047593.
8. Behari S, Krishna H, Kumar MV, et al. Association between an aplastic basilar artery, unaccompanied by a primitive carotid-vertebrobasilar anastomosis, and multiple aneurysms on the dominant posterior communicating artery. J Neurosurg. 2004; 100(5): 946–949, doi: 10.3171/jns.2004.100.5.0946, indexed in Pubmed: 15137614.
9. Bosco D, Consoli D, Lanza PL, et al. Complete oculomotor palsy caused by persistent trigeminal artery. Neurol Sci. 2010; 31(5): 657–659, doi: 10.1007/s10072-010-0342-1, indexed in Pubmed: 20552240.
10. Boyko OB, Curnes JT, Blatter DD, et al. MRI of basilar artery hypoplasia associated with persistent primitive trigeminal artery. Neuroradiology. 1996; 38(1): 11–14, doi: 10.1007/BF00593207, indexed in Pubmed: 8773267.
11. Brzegowy K, Pękala PA, Zarzecki MP, et al. Prevalence and clinical implications of the primitive trigeminal artery and its variants: a meta-analysis. World Neurosurg. 2020; 133: e401–e411, doi: 10.1016/j.wneu.2019.09.042, indexed in Pubmed: 31536812.
12. Chen YC, Li MH, Chen SW, et al. Incidental findings of persistent primitive trigeminal artery on 3-dimensional time-of-flight magnetic resonance angiography at 3.0 T: an analysis of 25 cases. J Neuroimaging. 2011; 21(2): 152–158, doi: 10.1111/j.1552-6569.2010.00472.x, indexed in Pubmed: 20331497.
13. Cloft HJ, Razack N, Kallmes DF. Prevalence of cerebral aneurysms in patients with persistent primitive trigeminal artery. J Neurosurg. 1999; 90(5): 865–867, doi: 10.3171/jns.1999.90.5.0865, indexed in Pubmed: 10223452.
14. Engelhardt J, El Hage G, Bojanowski MW. Persistent trigeminal artery as collateral circulation in ischemic stroke. World Neurosurg. 2021; 148: 67–69, doi: 10.1016/j.wneu.2021.01.034, indexed in Pubmed: 33476776.
15. Enomoto T, Sato A, Maki Y. Carotid-cavernous sinus fistula caused by rupture of a primitive trigeminal artery aneurysm. Case report. J Neurosurg. 1977; 46(3): 373–376, doi: 10.3171/jns.1977.46.3.0373, indexed in Pubmed: 839263.
16. Ferreira A, Coelho PS, Cruz VT. Persistent trigeminal artery in a patient with posterior circulation stroke treated with rt-PA: case report. BMC Neurol. 2019; 19(1): 257, doi: 10.1186/s12883-019-1492-2, indexed in Pubmed: 31656167.
17. Fields WS. The significance of persistent trigeminal artery. Carotid-Basilar anastomosis. Radiology. 1968; 91(6): 1095–1101, indexed in Pubmed: 5699609.
18. George AE, Lin JP, Morantz RA. Intracranial aneurysm on a persistent primitive trigeminal artery. Case report. J Neurosurg. 1971; 35(5): 601–604, doi: 10.3171/jns.1971.35.5.0601, indexed in Pubmed: 5120008.
19. Heyer GL, Dowling MM, Licht DJ, et al. The cerebral vasculopathy of PHACES syndrome. Stroke. 2008; 39(2): 308–316, doi: 10.1161/STROKEAHA.107.485185, indexed in Pubmed: 18174492.
20. Hirschberg M, Hofferberth B. Calcium antagonists in an animal model of vertebrobasilar insufficiency. Acta Otolaryngol Suppl. 1988; 460: 61–65, doi: 10.3109/00016488809125136, indexed in Pubmed: 3074620.
21. Iancu D, Anxionnat R, Bracard S. Brainstem infarction in a patient with internal carotid dissection and persistent trigeminal artery: a case report. BMC Med Imaging. 2010; 10: 14, doi: 10.1186/1471-2342-10-14, indexed in Pubmed: 20598138.

22. Kim MJ, Kim MS. Persistent primitive trigeminal artery: analysis of anatomical characteristics and clinical significances. Surg Radiol Anat. 2015; 37(1): 69–74, doi: 10.1007/s00276-014-1318-2, indexed in Pubmed: 24899147.

23. Khodadad G. Trigeminal artery and occlusive cerebrovascular disease. Stroke. 1977; 8(2): 177–181, doi: 10.1161/01.str.8.2.177, indexed in Pubmed: 847781.

24. Komiyama M. Persistent trigeminal artery and its variants. Interv Neuroradiol. 2019; 25(6): 635–637, doi: 10.1177/1591019919863110, indexed in Pubmed: 31296065.

25. Lam JJ, Shah MT, Chung SLi, et al. Persistent primitive trigeminal artery associated with a cavernous carotid aneurysm. Case report and literature review. J Radiol Case Rep. 2018; 12(11): 1–11, doi: 10.3941/jrcr.v12i11.3500, indexed in Pubmed: 30647831.

26. Lewis VL, Cail WS. Persistent trigeminal artery with internal carotid artery occlusion. Neurosurgery. 1983; 13(3): 314–315, doi: 10.1227/00006123-198309000-00018, indexed in Pubmed: 6621844.

27. Lima Neto AC, Bittar R, Gattas GS, et al. Pathophysiology and diagnosis of vertebrobasilar insufficiency: a review of the literature. Int Arch Otorhinolaryngol. 2017; 21(3): 302–307, doi: 10.1055/s-0036-1593448, indexed in Pubmed: 28680502.

28. Maeshima S, Tereda T, Masuo O, et al. Multiple cerebral aneurysms with persistent primitive trigeminal artery. J Clin Neurosci. 1999; 6(1): 52–54, doi: 10.1016/s0967-5868(99)90606-9.

29. Meckel S, Spittau B, McAuliffe W. The persistent trigeminal artery: development, imaging anatomy, variants, and associated vascular pathologies. Neuroradiology. 2013; 55(1): 5–16, doi: 10.1007/s00234-011-0995-3, indexed in Pubmed: 22170080.

30. Momma F, Ohara S, Ohyama T. Persistent trigeminal artery associated with brainstem infarct--case report. Neurol Med Chir (Tokyo). 1992; 32(5): 289–291, doi: 10.2176/nmc.32.289, indexed in Pubmed: 1378946.

31. O'uchi E, O'uchi T. Persistent primitive trigeminal arteries (PTA) and its variant (PTAV): analysis of 103 cases detected in 16,415 cases of MRA over 3 years. Neuroradiology. 2010; 52(12): 1111–1119, doi: 10.1007/s00234-010-0669-6, indexed in Pubmed: 20309534.

32. Padget DH. The development of the cranial arteries in the human embryo. Contribution to embryology. Carnegie Institution. 1948; 205–261.

33. Salas E, Ziyal IM, Sekhar LN, et al. Persistent trigeminal artery: an anatomic study. Neurosurgery. 1998; 43(3): 557––561; discussion 561, doi: 10.1097/00006123-199809000-00082, indexed in Pubmed: 9733310.

34. Tubbs RS, Verma K, Riech S, et al. Persistent fetal intracranial arteries: a comprehensive review of anatomical and clinical significance. J Neurosurg. 2011; 114(4): 1127–1134, doi: 10.3171/2010.11.JNS101527, indexed in Pubmed: 21235309.

35. Tyagi G, Sadashiva N, Konar S, et al. Persistent Trigeminal Artery: Neuroanatomic and Clinical Relevance. World Neurosurg. 2020; 134: e214–e223, doi: 10.1016/j.wneu.2019.10.025, indexed in Pubmed: 31627002.

36. Uchino A, Saito N, Okada Y, et al. Persistent trigeminal artery and its variants on MR angiography. Surg Radiol Anat. 2012; 34(3): 271–276, doi: 10.1007/s00276-011-0848-0, indexed in Pubmed: 21739246.

VM
VIA MEDICA

CASE REPORT

A case of distal limb arterial tortuosity and dilation: observations and potential clinical significance

Y. Carter[1], D.J. Bennett[2], V. Molla[2], A.E. Wink[1], A.J. Collins[1], E.L. Giannaris[1]

[1]Division of Translational Anatomy, Department of Radiology, University of Massachusetts Medical School, Worcester, MA, United States of America
[2]Undergraduate Medical Education, University of Massachusetts Medical School, Worcester, MA, United States of America

Arterial tortuosity describes variation via bending of the arterial wall and has been noted in several arteries throughout the body. Tortuous blood vessels can cause nerve compression, as well as present difficulties to surgeons and radiologists. Here we present an unusual case of multi-vessel arterial tortuosity discovered in 78-year-old Hispanic male cadaver, independent of systemic pathology. The left ulnar and right tibial arteries were dissected, and using calibrated digital callipers, their external and internal diameters were measured both at the origin site and at the site of greatest dilation. Both wall thickness and the number of inflection points were also measured. Six bends were noticed in the ulnar artery and its diameter measured 8.11 mm at its widest, with a wall thickness of 0.88 mm. On the lower extremity, the right tibial artery had three bends and its diameter measured 4.86 mm at its widest, with a wall thickness of 1.32 mm. This uncommon tortuosity is not only more prone to laceration during surgery, but the bending and thickening can be mistaken for tumours. Finally, fluid dynamics can be altered, resulting in an impact on blood pressure in the extremities. Thus, raising awareness is crucial to prevent both symptoms and iatrogenic complications. (Folia Morphol 2022; 81, 3: 791–797)

Key words: arterial, tortuosity, ulnar, tibial, cadaveric

INTRODUCTION

Arterial tortuosity involves varying degrees of abnormal twists and bends [7]. There are a few arteries known for their tortuous course, including the classic descriptions of the splenic and facial arteries [40]; however, there have been numerous reports of incidental findings of anatomical variation in arteries throughout all regions of the body including the head and neck [6, 14], thorax [42], abdomen and pelvis [27], upper limb and lower limb [45, 46]. These incidental cases report findings generally with involvement of a single vessel are distinct from arterial tortuosity syndrome, which is characterized by "severe and widespread arterial tortuosity of the aorta and middle-sized arteries" plus craniofacial involvement and skin or connective tissue disorder [5]. While the exact causal mechanisms of arterial tortuosity are unknown, it has been associated with senescence, high blood pressure as well as other cardiovascular risks, and is more common in females [7].

Clinically, both arterial and venous abnormal tortuosity has been associated with compression of nerves [11, 15, 26, 49]. A tortuous ulnar artery may also present difficulties to neuroradiologists, radiologists and surgeons during relevant procedures [36, 44]. Regarding the lower limb, previous reports had no comment on clinical implications of posterior tibial arterial tortuosity; though tortuosity of the accompanying posterior tibial veins has been linked to entrapment of the tibial nerve within the tarsal tunnel [31].

Here we report and discuss a unique case of distal limb arterial tortuosity discovered during a routine cadaveric dissection. While there have been reports in distal limb vessels, to our knowledge, these have not been reported in the same individual outside of arterial tortuosity syndrome.

CASE REPORT

The presence of an enlarged and tortuous ulnar artery was observed during a routine dissection of a left upper limb in a 78-year-old Hispanic male cadaver. The left ulnar artery had a typical appearance at its origin from the brachial artery; however, ~66 mm proximal to the flexor retinaculum, a significant winding pattern was observed with sinusoidal bends and a widened appearance (Fig. 1). Further dissection revealed a mildly enlarged but not tortuous artery on the right side (Fig. 2). Dissection of the lower extremities revealed a similar pattern in the tibial artery with enlargement and tortuosity noted on the right side (Fig. 3), while the left appeared relatively normal. Further inspection and dissection of the arteries in all other regions were unremarkable.

In a questionnaire filled out prior to the donor's death, they self-reported a brief smoking history over 50 years prior during young adulthood as well as a cancer history but did not specify which type. No enlarged lymph nodes or abnormal masses were seen. The University of Massachusetts Medical School (UMMS) Institutional Review Board determined this case report (#H00020805) is not human subject research.

METHODS

Terminology for describing vessel appearance and classification of the anatomical variation is based on Ciurica et al. [7]. While there is currently no standard-

Figure 1. Ulnar artery on left side. Arrows signify abnormal sinusoidal bends.

Figure 2. Ulnar artery on right side. There was mild external enlargement and a slight winding nature.
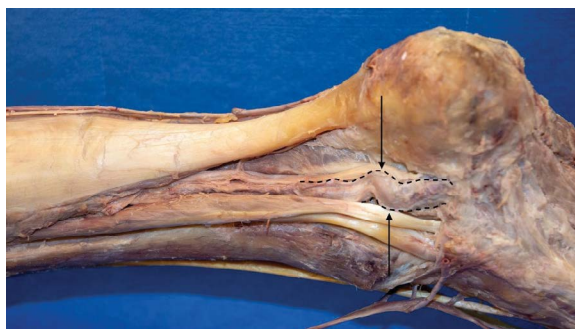
Figure 3. Tibial artery on right side. Arrows signify abnormal sinusoidal bends. Dotted lines highlight the area of external enlargement and a slight winding nature.

Table 1. Results of measurements of arteries in millimetres

Measure	Left ulnar artery	Right ulnar artery	Right tibial artery
SLM	132.06 ± 2.14	75.45 ± 3.14	115.73 ± 1.27
Path	151.86 ± 3.94	93.98 ± 0.91	130.22 ± 1.97
Number of inflections	6 ± 0	3 ± 0	4 ± 0
External MD origin	4.66 ± 0.11	5.70 ± 0.26	3.47 ± 0.04
External MD — widest point	8.11 ± 0.49	8.16 ± 0.42	4.86 ± 0.11
Internal MD — origin	4.58 ± 0.06	–	3.66 ± 0.11
Internal MD — widest point	4.07 ± 0.11	–	2.77 ± 0.07
Wall thickness — origin	0.57 ± 0.05	–	0.81 ± 0.01
Wall thickness — widest point	0.88 ± 0.01	–	1.32 ± 0.03

Data are shown as average ± standard deviation; MD — maximal diameter; SLM — straight-line measure

ised measure for determining the amount of arterial tortuosity in two-dimensions, three main methods are used consistently in the literature. The first method is based on a sum-of-angles metric, typically defined as the deviation from the anatomical normal straight path of the vessel. This metric is usually provided as a total number of degrees or as a ratio of straight-line length [12, 35, 48]. The second method calculates the degree of angulation from a centre line of flow, often as a mathematical measure of curvature, or amplitude [4]. This measure can be thought of as representing 'wave-height'. Lastly is the 'distance metric' which provides a ratio of the vessel path to the straight-line measure and can be used to describe the actual length of the vessel versus the anatomical normal length. In cadaveric studies this usually involves excision and straightening of the vessel before measuring [10, 41]. Distance metric was chosen as the optimal assessment of vessel tortuosity for this study as it would more accurately represent the normally straight arteries involved. To achieve this, measures were collected for straight-line length and path. The two vessels with greatest variation (left ulnar artery and right tibial artery) were subsequently removed for further analysis. For these, vessel external and internal (lumen) diameter was measured at both the origin and at the site of greatest dilation, wall thickness was also determined at the same sites. Additionally, the number of inflection points (bends) was noted for all vessels. All of the measures were taken by two observers with calibrated digital callipers.

RESULTS

The diameter of the tortuous segment of the ulnar artery measured 8.11 mm at its widest, whereas it was only 4.66 mm at its origin (Table 1). The arterial walls of the tortuous segment appeared thickened, and the lumen of the artery measured 4.2 mm (Fig. 2). Six bends were noted in the left ulnar artery prior to diving under the palmar carpal ligament and continuing into the ulnar tunnel (Guyon's canal). Upon continued dissection of the hand, the ulnar artery terminated into the superficial palmar arch and common palmar digital arteries. The tortuosity seen in the ulnar artery continued into the distal palmar arteries. In the area of tortuosity, the wall thickness was greater (0.88 mm) than at the origin (0.47), resulting in a reduced internal diameter of the lumen (4.07 mm vs. 4.58 mm). The left ulnar artery was then traced proximally and was noted to be typical in size and shape proximal to the bends, with no aneurysms apparent. No abnormalities were seen at the origin of the vessel from the brachial artery. The brachial artery was also traced proximally and had a typical appearance. Dissection of the right arm revealed a slightly enlarged ulnar artery which had a diameter of 5.70 mm at the origin (Fig. 2). The right ulnar artery also exhibited a slight bend, 30 mm proximal of Guyon's canal, but a torturous pattern did not exist.

Dissection of the lower extremities revealed a tortuous tibial artery on the right side (Fig. 3) with the left appearing normal. The diameter of the tortuous segment of the right tibial artery measured 4.86 mm at its widest and 3.47 mm at its origin. Again, in the area of tortuosity, the wall thickness was much larger (1.32 mm) than at the origin (0.81), resulting in a reduced internal diameter of the lumen (2.77 mm vs. 3.66 mm). No other vascular variants were observed.

DISCUSSION

Numerous distal limb arterial variations have been reported in the literature [17, 21, 32, 38, 44, 49]. The present case reports a cadaveric dissection revealing distally tortuous ulnar and posterior tibial arteries, without any other vascular abnormalities. This is a particular import given that multi-site tortuosity is associated with systemic pathologies such as arterial tortuosity syndrome. While the exact cause of arterial tortuosity is unknown, several mechanisms have been suggested including calcification of the arterial wall as well as inconsistent arterial repair mechanisms [13]. Additionally, it can be related to age, loss of arterial elasticity, and position relative to the joint axis [45]. Both genetics and vascular pathologies, including hypertension and atherosclerosis, may play a role [13]. The presence of tortuous tibial arteries as well could suggest a systemic pathology, or genetic cause, as the reason for the tortuosity in this donor.

The ulnar artery is one of two terminal branches of the brachial artery. It arises from the brachial artery in the medial aspect of the forearm, typically distal to the antecubital fossa, and is the primary source of blood supply of the medial forearm. Typically, it is accompanied by the median nerve in the proximal forearm and by the ulnar nerve medially in the distal forearm and wrist. The ulnar artery terminates at the superficial palmar arch, where the arch anastomoses with a branch of the radial artery, the other terminal branch of the brachial artery [39]. The posterior tibial artery is the more posterior branch of the popliteal artery and supplies the posterior compartment of the leg. It gives rise to the fibular artery and terminally bifurcates into the medial and lateral plantar arteries. The posterior tibial artery courses with the tibial nerve and accompanying veins in the tarsal tunnel.

Variations in the upper limb vasculature have been well documented in the literature. Previous studies have described and classified upper limb arterial variations such as a superficial brachial artery, an accessory brachial artery, a superficial radial artery, and arteries with higher origins from the brachial artery, among others [22, 30, 38]. For the ulnar artery, thrombosis and aneurysmal dilatations are the most common [2]; other variations include proximal origins and superficial courses. There have been well-documented cases of variations such as a superficial ulnar artery, which poses a significant issue during forearm free flap harvesting [2, 3, 28] yet there are only a limited number of cases reporting a tortuous ulnar artery. It has been reported that a looped and tortuous ulnar artery is the rarest anatomical variation seen in the ulnar artery [44].

Arterial tortuosity has also been described in the lower limb. Tortuosity has also been reported in the popliteal artery and tibial-peroneal trunk [34]. Reported variation of the posterior tibial artery is primarily related to the level of its origin or terminal bifurcation, as well as aplasia or hypoplasia [20]. Studies examining tortuosity in the posterior tibial artery reported a prevalence of 26–35% [16, 18]; these studies focused on the region surrounding the tarsal tunnel.

Using ultrasound and Doppler, Ashraf et al. [1] determined that the mean average internal diameter of the ulnar and radial arteries were 2.4 ± 0.4 mm and 2.3 ± 0.4 mm on the right and 2.3 ± 0.3 mm and 2.2 ± 0.4 mm on the left. A cadaveric study also reports the mean internal diameter of the ulnar and radial arteries to be 2.5 and 3.2 mm on the right and 2.4 and 3.0 mm on the left [37]. We report an internal diameter of 4.2 mm of the left ulnar artery with an 8 mm external diameter suggesting that the tortuosity increases artery lumen and overall size. Early computational fluid dynamics studies in tortuous coronary arteries suggest that such changes may impede the ability of the artery to self-regulate blood flow during increased demand [47]. Nevertheless, tortuous distal limb arteries carry significant clinical implications.

Clinical implications

Vascular lesions in the ulnar artery, including a tortuous artery, can result in nerve compression. Reports have linked a tortuous ulnar artery to Guyon's canal syndrome, a condition that causes hand numbness, pain, and tingling, resulting in a significant decline in quality of life [9]. The canal of Guyon, also called the distal ulnar tunnel, is a fibro-osseous space containing the ulnar nerve and its branches, the ulnar artery, as well as veins and lymphatic vessels [8]. Symptoms may be caused by ulnar nerve entrapment in Guyon's canal, due to the proximity of the nerve to the malshaped ulnar artery [11, 15, 49]. This is also true of the tarsal tunnel in the lower extremity. Machiels et al. [25] reported that dilated or tortuous veins in the tarsal tunnel can cause compression of the posterior tibial nerve resulting in tarsal tunnel syndrome. The variation seen here in the posterior tibial artery may also have implications for tibial nerve blocks and calcaneal pin insertions. A tortuous posterior tibial

artery is exceedingly rare in the literature, but it is reasonable to conclude that such an artery can compress the posterior tibial nerve and cause symptoms.

Tortuous vessels are problematic during surgery, imaging, and interventional procedures. On imaging, tortuous arteries can appear as solid masses, which can be mistaken for tumours [26]. A winding and tortuous artery is also more prone to laceration during surgery [26]. Further, the multiple bends seen in these vessels are at risk of perforation in various procedures [44]. The ulnar artery is also becoming more frequently used for percutaneous coronary intervention if the radial artery is deemed unusable [43]. In this circumstance, understanding the exact shape of the ulnar artery is necessary. In addition, the ulnar artery can be used for cerebral angiography under certain circumstances [23]. Finally, in patients undergoing dialysis, the ulnar artery can be used for creating arterio-venous fistulas [24].

In the aforementioned cases, knowledge of the ulnar artery's actual shape and positioning is crucial. Ultrasound and magnetic resonance imaging can be used to determine this information when necessary, in attempts to reduce both the symptoms of disorders as well as iatrogenic mishaps.

The abnormal variation in the arterial pattern noted here would have an impact on blood pressure to the extremities. Blood is an incompressible viscous fluid, and basic fluid flow mechanics principles can be used to extrapolate the impact of the variation on velocity and pressure [29]. The Hagen–Poiseuille equation is used to calculate the flow of viscous fluid in a cylindrical pipe [29].

As per Poiseuille's law, the viscosity of blood will cause a pressure drop, proportional to the length travelled [29], therefore the longer path created by the tortuosity seen here would result in lowered blood pressure travelling through the artery. While the vessels appear externally to be enlarged at the site of tortuosity this is an impact of increased wall thickness which actually results in a decrease in diameter of the lumen. When blood flows out of a larger circular pipe, into a narrower diameter its velocity will be increased; however, its pressure will decrease [33]. The narrowing of the vessel and the elongated path of the tortuosity could then be described cumulatively acting to result in decreased pressure. Additionally a decrease in pressure would be created by the inflection points (bends) [19].

Limitations of the study

The analyses presented here had a number of limitations, importantly the vessel's external and internal diameter was measured in two dimensions, essentially a representation of flattened width versus true diameter but this was internally controlled as all were measured in the same manner. Additionally, the dryness of vessels as part of the embalming and dissection process may have led to some shrinkage of the tissues. While vessels from both sides of the body were able to be measured for the upper limb it was not possible to take measurements from the contralateral lower limb as the donor was cremated and returned due to the family's urgent request.

CONCLUSIONS

The current report suggests that arterial tortuosity can occur in multiple sites distinct from the systemic, arterial tortuosity syndrome. A proper understanding of a patient's specific regional anatomy is vital for radiologists, surgeons, and clinicians in general, as unknown variations can lead to unexplained pain and iatrogenic injuries. Raising awareness regarding ulnar artery tortuosity should help to reduce such events.

Conflict of interest: None declared

REFERENCES

1. Ashraf T, Panhwar Z, Habib S, et al. Size of radial and ulnar artery in local population. J Pak Med Assoc. 2010; 60(10): 817–819, indexed in Pubmed: 21381609.
2. Bell RA, Schneider DS, Wax MK. Superficial ulnar artery: a contraindication to radial forearm free tissue transfer. Laryngoscope. 2011; 121(5): 933–936, doi: 10.1002/lary.21465, indexed in Pubmed: 21520105.
3. Bondaz M, Lepivert JC, Majoufre-Lefebvre C, et al. À propos d'un cas d'artère ulnaire superficielle. Rev Stomatol Chir Maxillofac Chir Orale. 2016; 117(3): 173–175, doi: 10.1016/j.revsto.2016.04.001.
4. Bullitt E, Gerig G, Pizer SM, et al. Measuring tortuosity of the intracerebral vasculature from MRA images. IEEE Trans

Med Imaging. 2003; 22(9): 1163–1171, doi: 10.1109/TMI.2003.816964, indexed in Pubmed: 12956271.

5. Callewaert B, De Paepe A, Coucke P. Arterial Tortuosity Syndrome. University of Washington, Seattle; 1993. http://www.ncbi.nlm.nih.gov/pubmed/25392904 (Accessed October 16, 2020).

6. Choi G, Han SH, Choi JO. Tortuous common carotid artery encountered during neck dissection. Eur Arch Otorhinolaryngol. 1998; 255(5): 269–270, doi: 10.1007/s004050050056, indexed in Pubmed: 9638471.

7. Ciurică S, Lopez-Sublet M, Loeys BL, et al. Arterial Tortuosity. Hypertension. 2019; 73(5): 951–960, doi: 10.1161/HYPERTENSIONAHA.118.11647, indexed in Pubmed: 30852920.

8. Depukat P, Mizia E, Klosinski M, et al. Anatomy of Guyon's canal: a systematic review. Folia Med Cracov. 2014; 54(2): 81–86, indexed in Pubmed: 25648313.

9. Depukat P, Mizia E, Kuniewicz M, et al. Syndrome of canal of Guyon: definition, diagnosis, treatment and complication. Folia Med Cracov. 2015; 55(1): 17–23, indexed in Pubmed: 26774628.

10. Dowson N, Boult M, Cowled P, et al. Development of an automated measure of iliac artery tortuosity that successfully predicts early graft-related complications associated with endovascular aneurysm repair. Eur J Vasc Endovasc Surg. 2014; 48(2): 153–160, doi: 10.1016/j.ejvs.2014.04.033, indexed in Pubmed: 24939664.

11. Emel E, Guzey KF, Alatas I. Guyon's canal syndrome due to tortuous ulnar artery: a case report. Turk Neurosurg. 2003; 13: 107–110.

12. Faggioli G, Ferri M, Gargiulo M, et al. Measurement and impact of proximal and distal tortuosity in carotid stenting procedures. J Vasc Surg. 2007; 46(6): 1119–1124, doi: 10.1016/j.jvs.2007.08.027, indexed in Pubmed: 18154988.

13. Han HC. Twisted blood vessels: symptoms, etiology and biomechanical mechanisms. J Vasc Res. 2012; 49(3): 185–197, doi: 10.1159/000335123, indexed in Pubmed: 22433458.

14. Iwanaga J, Watanabe K, Tsuyoshi S, et al. Tortuous common carotid artery: a report of four cases observed in cadaveric dissections. Case Rep Otolaryngol. 2016; 2016: 2028402, doi: 10.1155/2016/2028402, indexed in Pubmed: 27818819.

15. Jose RM, Bragg T, Srivastava S. Ulnar nerve compression in Guyon's canal in the presence of a tortuous ulnar artery. J Hand Surg Br. 2006; 31(2): 200–202, doi: 10.1016/j.jhsb.2005.10.003, indexed in Pubmed: 16290914.

16. Joshi SS, Joshu SD, Athavale S. Anatomy of tarsal tunnel and its applied significance. J Anat Soc India. 2006; 55(1): 52–56.

17. Kalisman M, Laborde K, Wolff TW. Ulnar nerve compression secondary to ulnar artery false aneurysm at the Guyon's canal. J Hand Surg Am. 1982; 7(2): 137–139, doi: 10.1016/s0363-5023(82)80077-4, indexed in Pubmed: 7069168.

18. Kalpana R. Neurovascular branching pattern in the tarsal tunnel with reference to medio malleolar calcaneal axis: a cadaveric study. PhD diss. Published online. 2014.

19. Keulegan GH, Hilding Beij K. Pressure losses for fluid flow in curved pipes. US Government Printing Office. 1937.

20. Kil SW, Jung GS. Anatomical variations of the popliteal artery and its tibial branches: analysis in 1242 extremities. Cardiovasc Intervent Radiol. 2009; 32(2): 233–240, doi: 10.1007/s00270-008-9460-z, indexed in Pubmed: 18982387.

21. Kim SS, Kim JH, Kang HIn, et al. Ulnar nerve compression at Guyon's canal by an arteriovenous malformation. J Korean Neurosurg Soc. 2009; 45(1): 57–59, doi: 10.3340/jkns.2009.45.1.57, indexed in Pubmed: 19242575.

22. Kusztal M, Weyde W, Letachowicz K, et al. Anatomical vascular variations and practical implications for access creation on the upper limb. J Vasc Access. 2014; 15 (Suppl 7): S70–S75, doi: 10.5301/jva.5000257, indexed in Pubmed: 24817459.

23. Layton KF, Kallmes DF, Kaufmann TJ. Use of the ulnar artery as an alternative access site for cerebral angiography. Am J Neuroradiol. 2006; 27(10): 2073–2074, indexed in Pubmed: 17110669.

24. Liu W, Lagaac R, Pettigrew GJ, et al. Outcomes after ulnar-basilic arteriovenous fistula formation. Ann Vasc Surg. 2013; 27(2): 232–237, doi: 10.1016/j.avsg.2012.04.014, indexed in Pubmed: 22981015.

25. Machiels F, Shahabpour M, De Maeseneer M, et al. Tarsal tunnel syndrome: ultrasonographic and MRI features. JBR-BTR. 1999; 82(2): 49–50, indexed in Pubmed: 10874388.

26. Mahajan R, Raheja S, Agarwal S, et al. Tortuous ulnar artery and Gantzer's muscle: a rare presentation with clinical implications. IAIM. 2015; 2(7): 141–146.

27. Moul JW, Wind GG, Wright CR. Tortuous and aberrant external iliac artery precluding radical retropubic prostatectomy for prostate cancer. Urology. 1993; 42(4): 450–452, doi: 10.1016/0090-4295(93)90384-m, indexed in Pubmed: 8212448.

28. Moullot P, Gay AM, Guidicelli T, et al. [Superficial ulnar artery while harvesting a radial forearm flap]. Ann Chir Plast Esthet. 2015; 60(1): 74–77, doi: 10.1016/j.anplas.2013.08.009, indexed in Pubmed: 24095106.

29. Nakayama Y. Introduction to fluid mechanics. Butterworth-Heinemann. 2018.

30. Natsis K, Papadopoulou A, Paraskevas G, et al. High origin of a superficial ulnar artery arising from the axillary artery: anatomy, embryology, clinical significance and a review of the literature. Folia Morphol. 2006; 65(4): 400–405, indexed in Pubmed: 17171623.

31. Oh SJ, Meyer RD. Entrapment neuropathies of the tibial (posterior tibial) nerve. Neurol Clin. 1999; 17(3): 593–615, vii, doi: 10.1016/s0733-8619(05)70154-7, indexed in Pubmed: 10393755.

32. Ortiz-Pomales Y, Smith J, Weiss J, et al. Tortuous axillary artery aneurysm causing median nerve compression. Ann Vasc Surg. 2014; 28(1): 122.e1–122.e3, doi: 10.1016/j.avsg.2013.07.004, indexed in Pubmed: 24189011.

33. Ostadfar A. Biofluid Mechanics: Principles and Applications. Elsevier 2016.

34. Ozgur Z, Ucerler H, Aktan Ikiz ZA. Branching patterns of the popliteal artery and its clinical importance. Surg Radiol Anat. 2009; 31(5): 357–362, doi: 10.1007/s00276-008-0454-y, indexed in Pubmed: 19142562.

35. Pappu S, Dardik A, Tagare H, et al. Beyond fusiform and saccular: a novel quantitative tortuosity index may help

classify aneurysm shape and predict aneurysm rupture potential. Ann Vasc Surg. 2008; 22(1): 88–97, doi: 10.1016/j.avsg.2007.09.004, indexed in Pubmed: 18023556.

36. Ramakrishnan G, Fontem RF, Sheth SU. Tortuous ulnar artery presenting as left distal forearm mass. J Vasc Surg Cases Innov Tech. 2020; 6(3): 430–432, doi: 10.1016/j.jvscit.2020.06.010, indexed in Pubmed: 32775848.

37. Riekkinen H, Karkola K, Kankainen A. The radial artery is larger than the ulnar. Ann Thorac Surg. 2003; 75(3): 882–884, doi: 10.1016/s0003-4975(02)04557-5.

38. Rodríguez-Niedenführ M, Vázquez T, Nearn L, et al. Variations of the arterial pattern in the upper limb revisited: a morphological and statistical study, with a review of the literature. J Anat. 2001; 199(Pt 5): 547–566, doi: 10.1046/j.1469-7580.2001.19950547.x, indexed in Pubmed: 11760886.

39. Sgueglia GA, Di Giorgio A, Gaspardone A, et al. Anatomic basis and physiological rationale of distal radial artery access for percutaneous coronary and endovascular procedures. JACC Cardiovasc Interv. 2018; 11(20): 2113–2119, doi: 10.1016/j.jcin.2018.04.045, indexed in Pubmed: 30336816.

40. Soikkonen K, Wolf J, Hietanen J, et al. Three main arteries of the face and their tortuosity. Br J Oral Maxillofac Surg. 1991; 29(6): 395–398, doi: 10.1016/0266-4356(91)90009-t, indexed in Pubmed: 1772861.

41. Sylvester PA, Stewart R, Ellis H. Tortuosity of the human splenic artery. Clin Anat. 1995; 8(3): 214–218, doi: 10.1002/ca.980080306, indexed in Pubmed: 7606595.

42. Tsutsumi K, Shimizu H. A case of a highly tortuous descending thoracic aortic aneurysm treated by surgical exclusion. SAGE Open Med Case Rep. 2020; 8: 2050313X20926440, doi: 10.1177/2050313X20926440, indexed in Pubmed: 32537162.

43. Valsecchi O, Vassileva A, Musumeci G, et al. Failure of transradial approach during coronary interventions: anatomic considerations. Catheter Cardiovasc Interv. 2006; 67(6): 870–878, doi: 10.1002/ccd.20732, indexed in Pubmed: 16649233.

44. Vincent R, Mohandas Kg R, Shivananda N, et al. Looped and tortuous ulnar artery: an erratic unilateral vascular presentation in the proximal forearm. J Clin Diagn Res. 2016; 10(6): AD03–AD04, doi: 10.7860/JCDR/2016/20771.7948, indexed in Pubmed: 27504273.

45. Wensing PJW, Scholten FG, Buijs PC, et al. Arterior tortuosity in the femoropopliteal region during knee flexion: a magnetic resonance angiographic study. J Anat. 1995; 186: 133–139, indexed in Pubmed: 7591974.

46. Wood NB, Zhao SZ, Zambanini A, et al. Curvature and tortuosity of the superficial femoral artery: a possible risk factor for peripheral arterial disease. J Appl Physiol. 2006; 101(5): 1412–1418, doi: 10.1152/japplphysiol.00051.2006, indexed in Pubmed: 16825527.

47. Xie X, Wang Y, Zhu H, et al. Impact of coronary tortuosity on coronary blood supply: a patient-specific study. PLoS One. 2013; 8(5): e64564, doi: 10.1371/journal.pone.0064564, indexed in Pubmed: 23691249.

48. Yoo BS, Yoon J, Ko JY, et al. Anatomical consideration of the radial artery for transradial coronary procedures: arterial diameter, branching anomaly and vessel tortuosity. Int J Cardiol. 2005; 101(3): 421–427, doi: 10.1016/j.ijcard.2004.03.061, indexed in Pubmed: 15907410.

49. Zeeshan M, Ahmed F, Kanwal D, et al. Guyon's canal syndrome due to tortuous ulnar artery with DeQuervain stenosing tenosynovitis, ligamentous injuries and dorsal intercalated segmental instability syndrome, a rare presentation: a case report. Cases J. 2009; 2: 9390, doi: 10.1186/1757-1626-2-9390, indexed in Pubmed: 20076781.

VIA MEDICA

C A S E   R E P O R T

Accessory right hepatic artery and aberrant bile duct in the hepatocystic triangle: a rare case with clinical implications

N. Eid[1], M. Allouh[1], Y. Ito[2], K. Taniguchi[2], E. Adeghate[1]

[1]Department of Anatomy, College of Medicine and Health Sciences, United Arab Emirates University, Al Ain, United Arab Emirates
[2]Department of General and Gastroenterological Surgery, Osaka Medical and Pharmaceutical University, Takatsuki, Osaka, Japan

Awareness of variations in the hepatic vasculature and biliary system is extremely important for avoiding iatrogenic injury in upper-abdominal surgery. The objective of this study is to describe a rare case of abnormal vascular and biliary structures in the hepatocystic triangle (HCT) (the modern Calot's triangle). During anatomical dissection of the coeliac trunk (CT) in an old man, the authors observed the presence of a hepatosplenic trunk arising from the CT and bifurcating into common hepatic and splenic arteries. The common hepatic artery divided into hepatic artery proper and gastroduodenal artery. The presence of accessory right hepatic artery (ARHA) arising from the superior mesenteric artery was also notable. The aberrant artery ascended retropancreatically ventral to the splenic vein, then posterolaterally to the portal vein before termination into the right hepatic lobe in the HCT. Within this triangle, there was an aberrant bile duct originating in the right hepatic lobe and ending in the common hepatic duct. This accessory duct crossed the ARHA and an associated branch (the cystic artery). There is no known previous report on the co-existence of an ARHA and an aberrant bile duct within the HCT, in addition to the hepatosplenic trunk. The clinical implications of the current case are addressed in discussion. (Folia Morphol 2022; 81, 3: 798–803)

Key words: hepatocystic triangle, triangle of Calot, accessory right hepatic artery, aberrant bile duct, hepatosplenic trunk, variations, coeliac trunk

INTRODUCTION

Variations in blood supply to the hepatic arteries are not rare. According to anatomy text books, the common hepatic branch of the coeliac trunk (CT) supplies the liver in 55–88% of cases. Variations of liver blood supply are frequent. Thus, the liver may be supplied by aberrant branches of the left gastric artery, the superior mesenteric artery (SMA), the aorta or other gut arteries. These aberrant arteries may be accessory or replaced [4, 5, 6, 9, 22].

Recognition of variations in hepatic arterial anatomy is of major importance in the planning and conducting of surgical and radiological procedures on the upper-abdomen area, such as transplantation, cholecystectomy and pancreaticoduodenectomy [6, 8, 9, 22]. Based on records of 1000 patients who
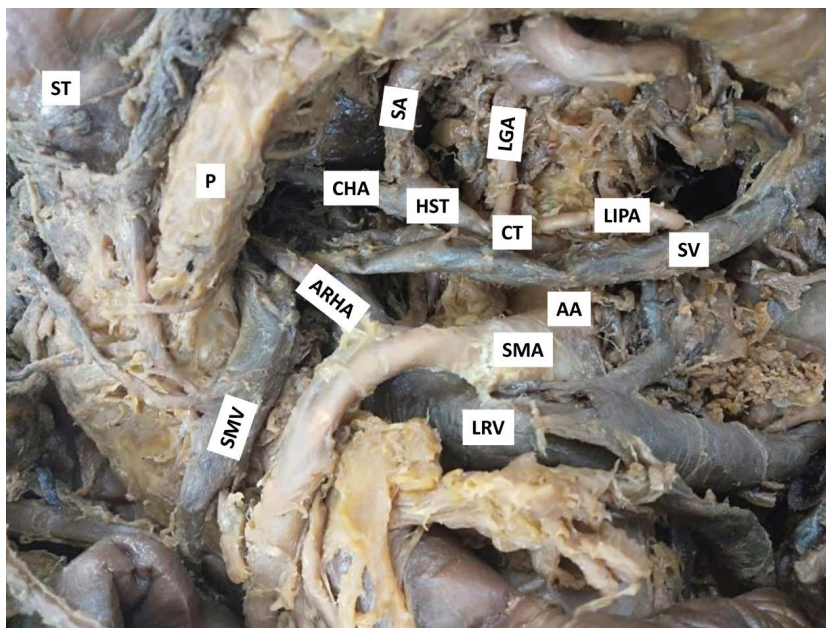
Figure 1. Accessory right hepatic artery (ARHA) arising from the superior mesenteric artery (SMA) in the pancreatic bed. The stomach (ST) and pancreas (P) are retracted to show the variation; AA — abdominal aorta; CHA — common hepatic artery; CT — coeliac trunk; HST — hepatosplenic trunk; LGA — left gastric artery; LIPA — left inferior phrenic artery; LRV — left renal vein; SA — splenic artery; SMA — superior mesenteric artery; SMV — superior mesenteric vein; SV — splenic vein.

underwent liver harvesting for orthotopic transplantation, Hiatt et al. [9] investigated the surgical anatomy of hepatic arteries. They found six types of hepatic artery variations. Type 1 — normal (the common hepatic artery [CHA] branched from CT) (75.7%); type 2 — replaced (accessory) left hepatic artery branched from left gastric (9.7%); type 3 — replaced (accessory) right hepatic artery branched from SMA (10.6%); type 4 — replaced or accessory right hepatic artery + replaced or accessory left hepatic artery (2.3%); type 5 — the CHA branched from SMA (1.5%), and type 6 — the CHA originated from abdominal aorta (0.2%). The presence of an aberrant right hepatic artery is the most frequently encountered variation, and this may be either a replacement or an accessory (Hiatt type III, 10.6% incidence) [5, 9]. This aberrant artery may be accidentally injured during upper-abdomen operations resulting in fatal complications such as severe haemorrhage and hepatic necrosis [5, 6, 9, 22]. Importantly, biliary tract variations — specifically, the presence of aberrant or accessory bile ducts — may complicate laparoscopic cholecystectomy. During this procedure, only two structures (the cystic duct and the cystic artery) should usually be seen entering the gallbladder within the hepatocystic triangle (HCT) (the modern Calot's triangle), which is bounded by the cystic duct, the common hepatic duct (CHD) and

the liver. This is different from the earlier description of Calot: the Calot's triangle is demarcated by the cystic duct on right side, the CHD on left side, and the cystic artery above [1, 16, 17]. In a previous study, the authors reported a rare case of a right hepatic artery forming a caterpillar hump perforating Calot's triangle into the cystic plate in association with a variant branching pattern of the CT [7]. In the current study, the authors referenced cadaveric dissection results to examine another rare case involving the coexistence of three variations with clinically important implications in hepatobiliary and pancreatic surgery. These variations include two structures (an accessory right hepatic artery [ARHA] and an aberrant bile duct) within the HCT, in addition to the hepatosplenic trunk.

CASE REPORT

During anatomical dissection of the CT in a male cadaver (among 8 dissections) at the Department of Anatomy in the College of Medicine and Health Sciences at the United Arab Emirates University, multiple variations in hepatic vasculature and the biliary system were observed. The CT was exposed after severing the greater omentum and upward reflection of stomach. The CT bifurcated into the left gastric artery and hepatosplenic trunk (Fig. 1). The hepatosplenic trunk divided into CHA and splenic artery.
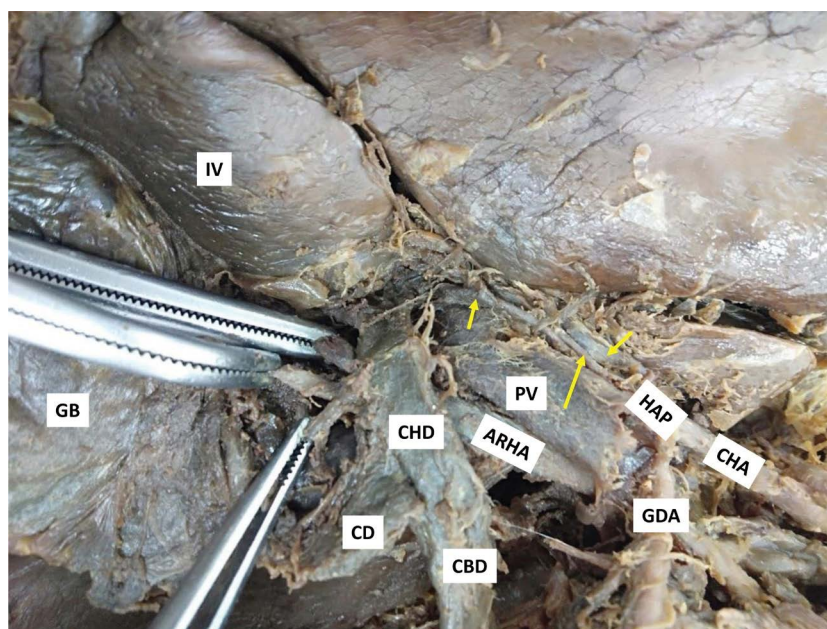
Figure 2. Accessory right hepatic artery (ARHA) passing into the hepatocystic triangle in association with the accessory bile duct and cystic artery. The upper, middle and lower haemostats within the triangle hold the ARHA, cystic artery and anomalous bile duct, respectively. The yellow arrows mark the right, left and middle hepatic branches of the hepatic artery proper (HAP); CBD — common bile duct; CD — cystic duct; CHA — common hepatic artery; CHD — common hepatic duct; GB — gallbladder; GDA — gastroduodenal artery; IV — hepatic segment 4; PV — portal vein.

The CHA then branched into gastroduodenal artery and hepatic artery proper (HAP), which trifurcated into right, left and middle hepatic branches (Fig. 2). This trifurcation of HAP was observed after dissection of the hepatoduodenal ligament. Further dissection of the pancreatic bed demonstrated the presence of an ARHA arising from the SMA. The ARHA ascended retropancreatically ventral to the splenic vein at its junction with the superior mesenteric vein parallel to the CHA (Fig. 1). Notably, it passed posterolaterally to the portal vein and the CHD, entering the HCT and terminating into the right hepatic lobe close to the cystic plate. In this triangle, the ARHA gave rise to the cystic artery, and both arteries were crossed ventrally by an aberrant bile duct arising from the right hepatic lobe and joining the right side of the CHD (Fig. 2). The gallbladder was dissected from the cystic plate via upward retraction and severing of its peritoneal attachment, thereby clearly revealing the contents of HCT — the ARHA, the aberrant bile duct and the cystic artery based on the criteria of Critical View of Safety (CVS) for laparoscopic cholecystectomy by Strasberg (Fig. 3) [16, 17]. The CVS has three requirements. First, the HCT must be cleared of fat and fibrous tissue. The second requirement is that the inferior part of the gallbladder be separated from

the cystic plate (hepatic bed of gallbladder), the flat fibrous surface to which the non-peritonealised side of the gallbladder is attached. The third requirement is that only two structures (cystic duct and cystic artery), must be seen getting into the gallbladder. Once these three criteria have been fulfilled, CVS has been attained. The normal and variant anatomy of HCT is shown in Figure 4 with digital art based on schema of Figure 2.

DISCUSSION

In the case reported here, the ARHA and the anomalous bile duct were observed simultaneously as variant structures in the HCT, along with a variant branching pattern of the CT with formation of the hepatosplenic trunk. Up to our knowledge, there are no known previous reports on the coexistence of these variations.

The detection of an ARHA arising from the SMA in the current case is consistent with Hiatt type III (10.6% incidence) [5, 9]. This artery ascended superficial to the splenic vein and deep to the pancreatic neck. Accordingly, there may have been compression of the splenic vein by the enlarged ARHA and the pancreas, resulting in splenic vein thrombosis and left-sided portal hypertension [19]. In addition, the entry of the
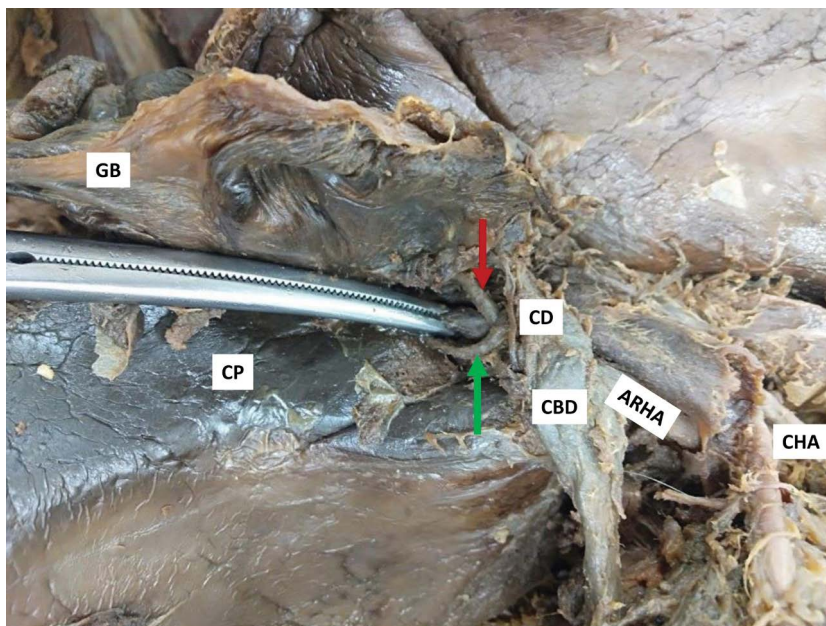
Figure 3. Dissection and upward retraction of gall bladder (GB) for exposure of cystic plate and detection of anomalous structures in the hepatocystic triangle based on criteria of Critical View of Safety. Note that the accessory right hepatic artery (ARHA) is grasped by the haemostat, whereas the cystic artery and aberrant bile duct are marked by the red and green arrows, respectively; CBD — common bile duct; CD — cystic duct; CHA — common hepatic artery; CP — cystic plate.
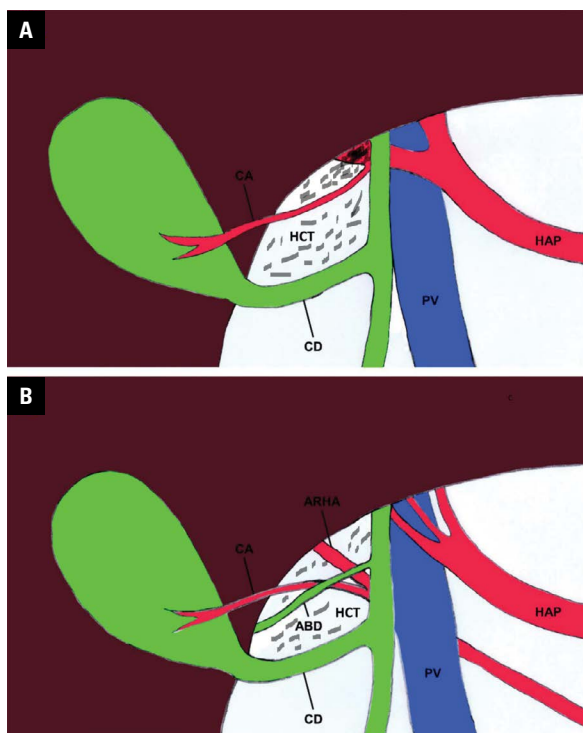
Figure 4. A schema and digital art (**A, B**) showing the normal (**A**) and variant anatomy of the hepatocystic triangle (HCT; highlighted with black lines) of Calot (**B**). The digital art of B is based on Figure 2; ABD — aberrant bile duct; ARHA — accessory right hepatic artery; CA — cystic artery; CD — cystic duct; HAP — hepatic artery proper; PV — portal vein.

ARHA into the HCT has great surgical relevance, as injury may occur during laparoscopic cholecystectomy with catastrophic complications such as bleeding and liver ischaemia [6, 16, 17, 22]. The ARHA may also be damaged in various procedures associated with tumour-related pancreaticoduodenectomy [8]. Developmentally, the presence of ARHA may result from persistence and/or abnormal regression of the embryonic hepatic arteries [5].

The presence of an ARHA within the HCT has been reported in a couple of studies [6, 12, 15], but was here associated with the aberrant bile duct, which may complicate CVS during laparoscopic cholecystectomy [16, 17]. On the other side, some studies have shown that the replaced right hepatic artery is a beneficial variant in the right hepatic lobe living-donor transplant. This could be explained by the fact that the shorter hepatic artery graft could lead to a postoperative complication (hepatic artery thrombosis). However, the replaced right liver artery in such cases provides a longer and bigger graft, thereby reducing the chances of hepatic thrombosis. This could be applicable to our case as ARHA seems to be longer than the HAP [22]. Recent studies investigated the presence of ARHA using computed tomography, multidetector computed tomography

angiography and magnetic resonance imaging (MRI). An enhanced computed tomography scan revealed variations in hepatic arteries in a 67-year-old woman diagnosed with intrahepatic cholangiocarcinoma [11]. These variations included ARHA branching from SMA and an accessory left hepatic artery arising from the left gastric artery. Using computed tomography angiography or/and MRI angiography findings in 532 patients, Yamaguchi et al. [21] observed a case of aberrant right hepatic artery arising from the gastroduodenal artery. They recommended the use of preoperative computed tomography and/or MRI and intraoperative liver Doppler ultrasound for the prevention of injury during pancreaticoduodenectomy in patients with this type of hepatic artery variation. Some researchers believe that ultrasound is always the method of choice for the diagnosis of various hepatobiliary diseases. They recommend a perfect study and a good understanding of the sonographic appearance of the normal hepatic vascular tree and its anatomical variations [3].

Importantly, the laparoscopic cholecystectomy CVS requirements [16, 17] applied during HCT dissection in the current study can also be used for practical anatomy teaching in medical schools. This may encourage undergraduate and postgraduate students to perform research on anatomical variations with clinical relevance.

Accidental injury or ligation of an aberrant bile duct as observed in the present case during cholecystectomy may result in severe complications such as biliary leakage and biliary cirrhosis [10, 13, 16–18]. However, some researchers consider any bile duct activity from the right lobe of the liver and interaction with the CHD as aberrant. Therefore, the lack of interductal communication in the liver may indicate that this duct may be the sole drainage of this particular part of the liver. When such an aberrant duct enters the main duct near the cystic duct, it may be easily injured, resulting in partial or total segmental duct occlusion. These ducts have a relatively high prevalence (8.4%) and should be investigated using intraoperative cholangiography [10]. As shown in Figure 4, the cystic artery in our case is bridged by the aberrant bile duct, therefore, there is great possibility of injury of the duct during cholecystectomy. A recent study for the first time reported that fluorescence cholangiography concomitant with angiography was useful for identifying an aberrant bile duct and the cystic artery during laparoscopic cholecystectomy in

old patient. The authors concluded that abnormal bile ducts are clinically important due to higher sensitivity to lesions during cholecystectomy. About 27% of clinically significant bile duct leakage was reported to be due to an aberrant bile duct lesion [18].

A recent report highlighted the coexistence of an ARHA and a left hepatic artery originating directly from the CT in a patient who had undergone an elective pancreaticoduodenectomy via the Whipple procedure [2]. In the current case, in addition to the ARHA, the authors observed the presence of a hepatosplenic trunk arising from the CT. The presence of this trunk was reported as a type-II CT based on Adachi classification (4.3%) [5]. Recent studies also found that a hepatosplenic trunk is observed in 10% of cases based on cadaveric dissection [14] and in 3.88% of subjects based on multidetector computed tomography [20]. The authors concluded that this CT variation was relevant to the planning of radiological and surgical procedures on the abdominal part of the oesophagus, the stomach, the duodenum, the liver, the pancreas, the gallbladder and the spleen, and in operations such as liver transplantation.

CONCLUSIONS

This unique study on the simultaneous presence of an ARHA, aberrant bile duct and a hepatosplenic trunk has important surgical implications; specifically, in hepatobiliary surgery. Further research on large number of cases using cadaveric dissection and imaging tools such as ultrasound, MRI and computed tomography are required to explore the abnormal contents of HCT.

Conflict of interest: None declared

REFERENCES

1. Abdalla S, Pierre S, Ellis H. Calot's triangle. Clin Anat. 2013; 26(4): 493–501, doi: 10.1002/ca.22170, indexed in Pubmed: 23519829.
2. Asif M, Anewenah LS, Reddy N, et al. Replaced right and left hepatic arteries: a variation in origin and course. BMJ Case Rep. 2017; 2017, doi: 10.1136/bcr-2016-218345, indexed in Pubmed: 28143859.
3. Battaglia S, Fachinetti C, Draghi F, et al. Ultrasound examination of the liver: Variations in the vascular anatomy. J Ultrasound. 2010; 13(2): 49–56, doi: 10.1016/j.jus.2010.07.003, indexed in Pubmed: 23396863.

4. Bergamaschi R, Ignjatovic D. More than two structures in Calot's triangle. A postmortem study. Surg Endosc. 2000; 14(4): 354–357, doi: 10.1007/s004640000154, indexed in Pubmed: 10790554.

5. Chen H, Yano R, Emura S, et al. Anatomic variation of the celiac trunk with special reference to hepatic artery patterns. Ann Anat. 2009; 191(4): 399–407, doi: 10.1016/j.aanat.2009.05.002, indexed in Pubmed: 19540742.

6. Dolenšek J. Triple arterial blood supply to the liver and double cystic arteries. Folia Morphol. 2017; 76(3): 523––526, doi: 10.5603/FM.a2017.0008, indexed in Pubmed: 28150275.

7. Eid N, Ito Y, Otsuki Y. Right hepatic artery forming caterpillar hump, perforating Calot's triangle into the cystic plate and associated with a variant branching pattern of the parent vessel. J Hepatobiliary Pancreat Sci. 2015; 22(5): 402–403, doi: 10.1002/jhbp.231, indexed in Pubmed: 25755109.

8. El Amrani M, Pruvot FR, Truant S. Management of the right hepatic artery in pancreaticoduodenectomy: a systematic review. J Gastrointest Oncol. 2016; 7(2): 298–305, doi: 10.3978/j.issn.2078-6891.2015.093, indexed in Pubmed: 27034799.

9. Hiatt JR, Gabbay J, Busuttil RW. Surgical anatomy of the hepatic arteries in 1000 cases. Ann Surg. 1994; 220(1): 50–52, doi: 10.1097/00000658-199407000-00008, indexed in Pubmed: 8024358.

10. Kullman E, Borch K, Lindström E, et al. Value of routine intraoperative cholangiography in detecting aberrant bile ducts and bile duct injuries during laparoscopic cholecystectomy. Br J Surg. 1996; 83(2): 171–175, indexed in Pubmed: 8689155.

11. Li X, Zhang X, Lu Q, et al. An accessory right hepatic artery derived from the superior mesenteric artery for anterior right liver lobe supply: a case report. Surg Radiol Anat. 2019; 41(8): 969–971, doi: 10.1007/s00276-018-2173-3, indexed in Pubmed: 30580394.

12. Mugunthan N, Kannan R, Jebakani CF, et al. Variations in the origin and course of right hepatic artery and its surgical significance. J Clin Diagn Res. 2016; 10(9): AC01–AC04, doi: 10.7860/JCDR/2016/22126.8428, indexed in Pubmed: 27790413.

13. Nagral S. Anatomy relevant to cholecystectomy. J Minim Access Surg. 2005; 1(2): 53–58, doi: 10.4103/0972-9941.16527, indexed in Pubmed: 21206646.

14. Olewnik Ł, Wysiadecki G, Polguj M, et al. Types of coeliac trunk branching including accessory hepatic arteries: a new point of view based on cadaveric study. Folia Morphol. 2017; 76(4): 660–667, doi: 10.5603/FM.a2017.0053, indexed in Pubmed: 28612916.

15. Polguj M, Podgórski M, Hogendorf P, et al. Variations of the hepatobiliary vasculature including coexistence of accessory right hepatic artery with unusually arising double cystic arteries: case report and literature review. Anat Sci Int. 2014; 89(3): 195–198, doi: 10.1007/s12565-013-0219-5, indexed in Pubmed: 24310410.

16. Strasberg SM. A three-step conceptual roadmap for avoiding bile duct injury in laparoscopic cholecystectomy: an invited perspective review. J Hepatobiliary Pancreat Sci. 2019; 26(4): 123–127, doi: 10.1002/jhbp.616, indexed in Pubmed: 30828991.

17. Strasberg S, Brunt M. Rationale and use of the critical view of safety in laparoscopic cholecystectomy. J Am Coll Surg. 2010; 211(1): 132–138, doi: 10.1016/j.jamcollsurg.2010.02.053.

18. Tsuruda Y, Okumura H, Setoyama T, et al. Laparoscopic cholecystectomy with aberrant bile duct detected by intraoperative fluorescent cholangiography concomitant with angiography: A case report. Int J Surg Case Rep. 2018; 51: 14–16, doi: 10.1016/j.ijscr.2018.08.009, indexed in Pubmed: 30130667.

19. Uy PP, Francisco DM, Trivedi A, et al. Vascular diseases of the spleen: a review. J Clin Transl Hepatol. 2017; 5(2): 152–164, doi: 10.14218/JCTH.2016.00062, indexed in Pubmed: 28660153.

20. Whitley A, Oliverius M, Kocián P, et al. Variations of the celiac trunk investigated by multidetector computed tomography: Systematic review and meta-analysis with clinical correlations. Clin Anat. 2020; 33(8): 1249–1262, doi: 10.1002/ca.23576, indexed in Pubmed: 32012339.

21. Yamaguchi T, Hasegawa K, Sauvain MO, et al. An aberrant right hepatic artery arising from the gastroduodenal artery: a pitfall encountered during pancreaticoduodenectomy. Surg Today. 2021; 51(10): 1577–1582, doi: 10.1007/s00595-021-02242-4, indexed in Pubmed: 33575949.

22. Zaki SM, Abdelmaksoud AHK, Khaled BEA, et al. Anatomical variations of hepatic artery using the multidetector computed tomography angiography. Folia Morphol. 2020; 79(2): 247–254, doi: 10.5603/FM.a2019.0090, indexed in Pubmed: 31436302.

VM VIA MEDICA

C A S E   R E P O R T

A case of atlanto-occipital fusion with other multiple anatomic variations

H. Yang#, J. Li#, L. Liao, Y. Li

School of Traditional Chinese Medicine, Southern Medical University, Guangzhou, China

In the routine anatomic measurement study on Asian dry skulls, a skull of atlanto-occipital fusion with other multiple anatomic variations was observed. The entire right half of the atlas vertebra, including the anterior arch, anterior tubercle, posterior arch, and lateral masses, was fused entirely with the occipital bone, while the left fused partly. Besides the atlanto-occipital fusion, the target skull specimen also includes posterior arch defects of the atlas, metopic suture, and wormian bones. So many anatomical variations rarely exist in one specimen. This paper aims to present detailed anatomic case reports and discuss related diseases in an anatomic and clinical study. (Folia Morphol 2022; 81, 3: 804–808)

Key words: atlanto-occipital fusion, metopic suture, anatomic variations, skull

INTRODUCTION

The atlanto-occipital fusion (AOF) is also known as atlas occipital ossification, atlas assimilation, or atlas occipital fusion. It is a congenital osseous or fibrous anomaly caused by the partial or complete fusion of the atlas to the occipital bone [22]. The range of AOF involves any part of the atlanto-occipital joint, and most of the fusion is asymmetrical. According to the degree of atlas and occipital fusion, it can be divided into two types: complete atlanto-occipital segment insufficiency, that is, complete atlas fusion with the edge of the occipital foramen magnum; and partial atlanto-occipital segment insufficiency, which is often separated by atlas anterior arch fusion and posterior arch separation, one occipital condyle fuses with the superior articular surface of the atlas, but the other side is not fused [25].

The AOF was first described by Rokitansky in 1844 and demonstrated roentgenographically by Schuller in 1911 [see 3]. According to the report, the inci-

dence of AOF ranges from 0.14% to 0.75% of the population [19]. As more profound research goes, it was found that the prevalence ranges from 0.08% to 2.79% of the general population; males and females were equally affected but may differ in races [31]. Individuals with AOF may have a low hairline, torticollis, restricted neck movements with or without abnormal short neck [20].

Vault consists of several curved plates separated by sutures rather than a single bone. The metopic suture (MS) is one of the primary sutures of the skull, which is located on the left and right sides of the frontal bone [28]. As people age, the cranial sutures fuse gradually, transforming the skull into a single, rigid element. The MS unites and disappears early in life, but there is no conclusion about the fusion time. Rice [24] thinks that the MS fusion starts at the age of one and completes before seven; according to other opinions it occurs at three years old; however, most authors believe it ends before 9 months [29, 30]. The

---

Address for correspondence: Dr. Y. Li, School of Traditional Chinese Medicine, Southern Medical University, No. 1838, North of Guangzhou Great Road, BaiYun District, Guangzhou, Guangdong Province, 510515, China, tel: +86 13114466285, e-mail: 1065485398@qq.com; ortho@fimmu.com
#These authors contributed equally to this work. Han Yang is the first author, and Junhua Li is the co-first.
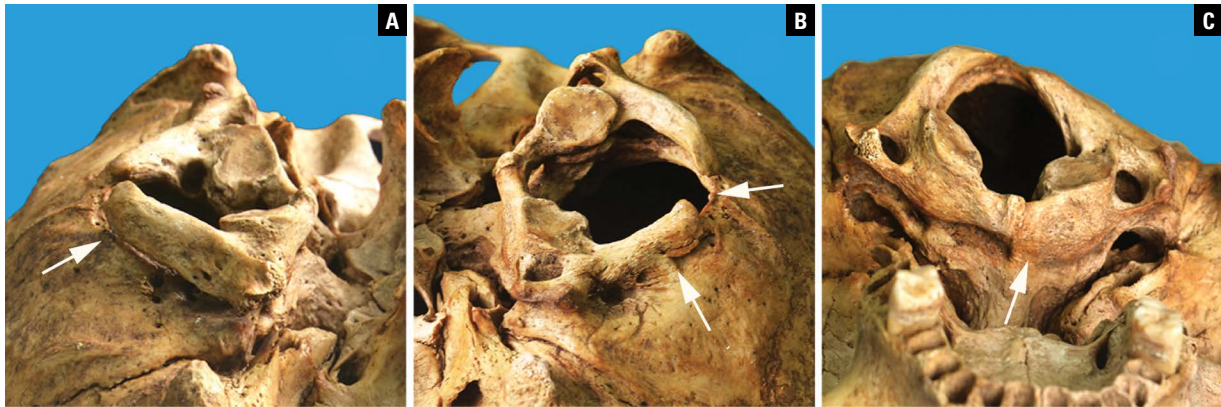
Figure 1. A. The left posterior arch was incompletely fused with the occipital bone (arrow); **B.** The posterior arch defects of the atlas, and the posterior tubercle was absent (arrow). The right posterior arch was fused entirely with the occipital bone (arrow); **C.** Partial fusion of the left anterior arch and anterior tubercle of the atlas with the occipital bone, and complete fusion of the right anterior arch and anterior tubercle with the occipital bone (arrow).

premature closure of MS will cause trigonocephaly and affect brain development in turn. It is still unclear why the closure of MS continues into adulthood. The existence of the MS in an adult cranium is described as a *median frontal suture* or a *persistent metopic suture* [11]. It is generally recognized as a normal variation. Studies have reported that the incidence of MS is 2.20–8.1%. Meanwhile, racial and gender factors vary in MS [7, 11].

This report presents a rare case of AOF, posterior arch defects of the atlas (PADA), MS, wormian bones (WBs). The specimen was an adult male and belonged to the Southern Medical University, China.

CASE REPORT

In this specimen, the left anterior arch of the atlas and the anterior tuberosity were partially fused with the occipital bone, and the right anterior arch and the anterior tuberosity were completely fused with the occipital bone (Fig. 1).

The posterior arch of the atlas was deficient, and the posterior tubercle was absent. The right posterior arch was shorter (29.9 mm) and completely fused with the occipital bone (Fig. 1B). In comparison, the left posterior arch was longer (36.2 mm) and incompletely fused with the occipital bone (Fig. 1A). Findings indicate that the shape of the posterior cranial fossa is significantly associated with occipitalisation with and without cleft of the posterior arch of the atlas [8]. The fusion typically involves the anterior arch and foramen magnum; the posterior fusion involving lateral masses or the posterior arch is comparatively uncommon.

The distribution of the left and right mass of the atlas was asymmetrically fused with the occipital bone, the articular surface of the left mass was oval and small (transverse diameter: 17.9 mm, vertical diameter: 15.8 mm), and the articular surface of the right mass was irregular and large (transverse diameter: 20.1 mm, vertical diameter: 17.4 mm), which led to the irregularity of occipital foramen shape (sagittal diameter: 36.4 mm, transverse diameter: 32.1 mm) (Fig. 2B). The studies suggest a fusion between AOF and the dimensions of the foramen magnum that the sagittal dimensions and area of the foramen magnum were significantly smaller in skulls with occipitalisation [8]. Foramen magnum is an important landmark, which is closely associated with the brainstem and spinal cord [27]. AOF, reduced foramen magnum and basilar invagination may compress the medulla-spinal cord transition and the spinal cord or brain stem [15].

In addition, we found the disclosure of the MS in the skull of this case (Fig. 2A). The MS was complete, and the length from the bregma to the nasion was about 132 mm (Fig. 2C). In this case, there are multiple WBs in the lambdoid suture (Fig. 2D).

DISCUSSION

So many anatomical variations rarely exist in one specimen. An early defect in embryogenesis is postulated for such a combination, which may exemplify specific associations in which multiple embryological abnormalities were present.

The bony cranial base develops in the process of endochondral ossification, and a combination of
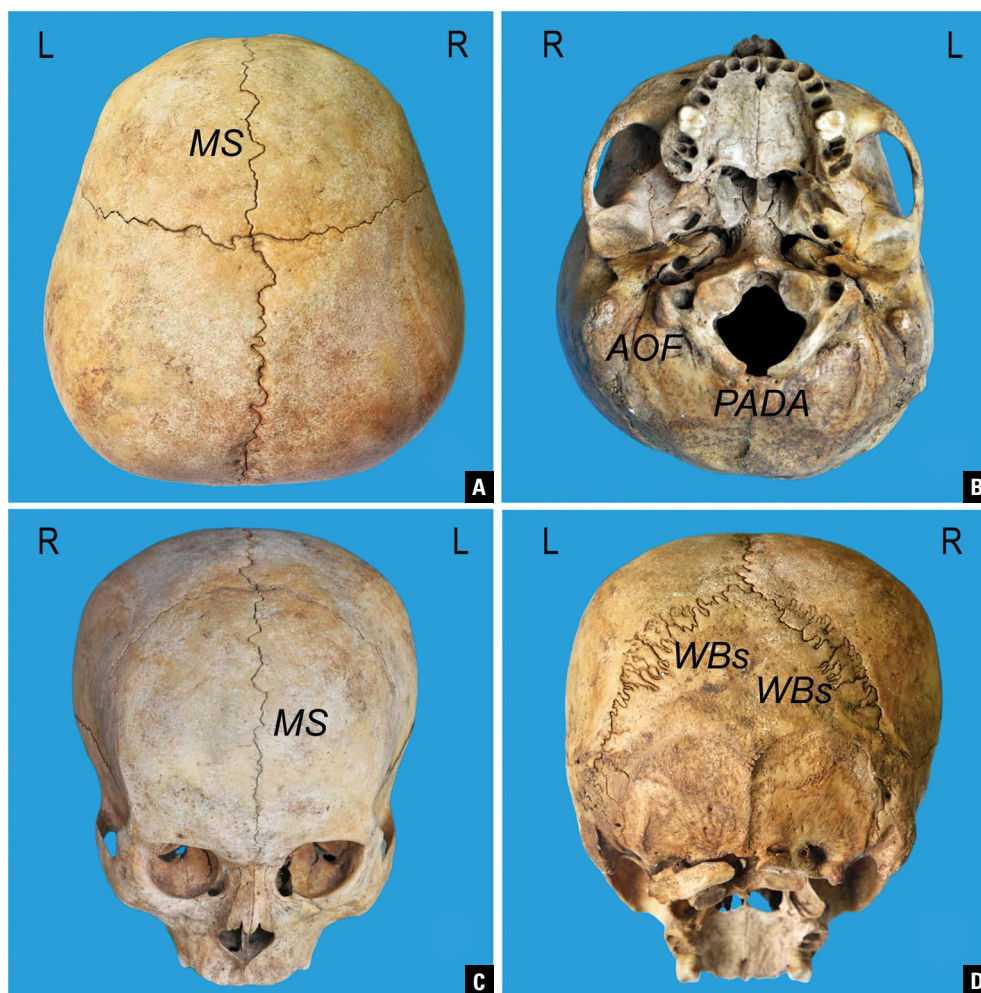
Figure 1. A. Metopic suture (MS); **B.** Atlanto-occipital fusion (AOF); posterior arch defects of the atlas (PADA); **C.** Metopic suture (MS); **D.** Wormian bones (WBs).

bony accretion and sutural growth is necessary for its development. The absence of both cartilaginous and bony components of the posterior elements implies a very early defect in embryogenesis [17, 23]. AOF usually refers to the anatomic form of atlas and occipital bone not separated as scheduled during embryonic development. The congenital fusion of AOF includes a bony or fibrous fusion of part and all of the atlas anterior arch, posterior arch, and lateral mass with the occipital bone. And it is often accompanied by cervical 1–2 (C1–2) instability, cervical 2–3 (C2–3) fusion, basilar invagination, occipital dysplasia, Kleipper-Feil syndrome, and other diseases. It is a common congenital craniocervical junction malformation [13, 16, 18, 21].

As early as the 5th–6th week of the embryonic stage, the earliest vertebral body embryo is formed in the upper half of the next vertebral segment and the lower half of the upper vertebral segment. The atlas formation occurs primarily by the first spinal sclerotome, with a minor contribution from the proatlas [3]. In the vertebral chain of the human, the spine undergoes chondrification and ossification, and the 1st–4th occipital segments fuse with each other to form the base of the occipital bone. The head end of the 4th occipital segment fuses with the 1st cervical segment to form the atlas, and the acquired AOF is caused by incomplete segments [26]. AOF is usually congenital, but it may result from a disease such as osteomyelitis, arthritis, syphilis, or tuberculosis in rare cases.

The skeletal dysplasias are often associated with structural weakness and collapse of the skeleton [17]. Children affected by spondyloepiphyseal dysplasia, achondroplasia, and other forms of dwarfism have an increased incidence of craniovertebral

abnormalities. There are various congenital, hereditary, developmental, and acquired abnormalities at the craniovertebral junction, either single or in combination. A significant number of children had both neural and osseous abnormalities [26]. Still, the studies indicate that occipitalisation is associated with the surrounding bony structures and not with the craniofacial morphology in general [8, 10]. So we can't make a diagnosis just by the surface; detailed radiologic studies, possibly with volumetric reconstructions, are necessary in cases of AOF before surgical interventions in the region of craniovertebral junction [10].

The MS may reside as a partial pattern or a complete pattern. The partial patterns expand upward from the nasion or downward from the bregma, different from the completes spanning from the bregma to the nasion [1, 4, 32]. The suture forms from the bregma and develops toward the nasion. Inversely, the suture closes from the nasion toward the bregma [9]. Studies have shown that 91.66% of skulls with MS are associated with WBs [11].

The MS plays an important role in the shaping of the skull during the delivery of the baby. Because the baby has to be squeezed through the pelvis during delivery and due to many changes in bipedalism, the shape of the maternal pelvis is short and wide. In terms of modern women, the average sagittal plane of the entrance to the pelvis is 113 mm, which is lower than 124 mm of the newborn's head. Therefore, cranial sutures such as MS can deal with strain by dissipating tension and shear force to help babies squeeze through the birth canal. The high incidence of up to 30% of parturition complications associated with MS has been confirmed [12]. Another study model the effect of brain growth on cranial bones by means of finite-element analysis and geometric morphometric techniques, further elucidated the relationship between cranial sutures and brain development [5].

Metopic suture may be confused with midline fractures of the frontal bone in radiology which is of clinical significance. In addition, studies have shown that MS is associated with other clinically significant findings, such as frontal sinus abnormality, cleft lip, visceral inversion, cleft palate, cretinism, and intelligence deficits [2, 6, 14, 32].

In addition, this paper also discusses the causes of this congenital malformation from the perspective of embryology. The knowledge of this uncommon

anatomic variation is imperative for radiologists, neurologists, and neurosurgeons [3].

CONCLUSIONS

We reported a case of AOF with other multiple anatomic variations. So many anatomy variations rarely exist in one specimen. This paper presents detailed anatomic case reports and discusses related diseases in an anatomic and clinical study.

Acknowledgements

Conflict of interest: None declared

REFERENCES

1. Aksu F, Cirpan S, Mas NG, et al. Anatomic features of metopic suture in adult dry skulls. J Craniofac Surg. 2014; 25(3): 1044–1046, doi: 10.1097/SCS.0000000000000564, indexed in Pubmed: 24699103.
2. Allanson JE, Cunniff C, Hoyme HE, et al. Elements of morphology: standard terminology for the head and face. Am J Med Genet A. 2009; 149A(1): 6–28, doi: 10.1002/ajmg.a.32612, indexed in Pubmed: 19125436.
3. Al-Motabagani M, Surendra M. Total occipitalization of the atlas. Anat Sci Int. 2006; 81(3): 173–180, doi: 10.1111/j.1447-073x.2006.00129.x.
4. Bademci G, Kendi T, Agalar F. Persistent metopic suture can mimic the skull fractures in the emergency setting? Neurocirugia (Astur). 2007; 18(3): 238–240, indexed in Pubmed: 17622463.
5. Barbeito-Andrés J, Bonfili N, Nogué JM, et al. Modeling the effect of brain growth on cranial bones using finite-element analysis and geometric morphometrics. Surg Radiol Anat. 2020; 42(7): 741–748, doi: 10.1007/s00276-020-02466-y, indexed in Pubmed: 32266441.
6. Bilgin S, Kantarcı UH, Duymus M, et al. Association between frontal sinus development and persistent metopic suture. Folia Morphol. 2013; 72(4): 306–310, doi: 10.5603/fm.2013.0051, indexed in Pubmed: 24402751.
7. Çalışkan S, Oğuz KK, Tunalı S, et al. Morphology of cranial sutures and radiologic evaluation of the variations of intersutural bones. Folia Morphol. 2018; 77(4): 730–735, doi: 10.5603/FM.a2018.0030, indexed in Pubmed: 29569704.
8. Caspersen LM, Kjaer I, Sonnesen L. How does occipitalization influence the dimensions of the cranium? Orthod Craniofac Res. 2010; 13(3): 162–168, doi: 10.1111/j.1601-6343.2010.01492.x, indexed in Pubmed: 20618718.

9. Chaoui R, Levaillant JM, Benoit B, et al. Three-dimensional sonographic description of abnormal metopic suture in second- and third-trimester fetuses. Ultrasound Obstet Gynecol. 2005; 26(7): 761–764, doi: 10.1002/uog.2650, indexed in Pubmed: 16308900.

10. Ciołkowski M, Krajewski P, Ciszek B. A case of atlas assimilation: description of bony and soft structures. Surg Radiol Anat. 2013; 36(8): 833–836, doi: 10.1007/s00276-013-1235-9.

11. Cirpan S, Aksu F, Mas N, et al. Coexistence of wormian bones with metopism, and vice versa, in adult skulls. J Craniofac Surg. 2016; 27(2): 493–495, doi: 10.1097/SCS.0000000000002370, indexed in Pubmed: 26845093.

12. Cornelissen MJ, Söfteland M, Apon I, et al. Perinatal complications in patients with unisutural craniosynostosis: An international multicentre retrospective cohort study. J Craniomaxillofac Surg. 2017; 45(11): 1809–1814, doi: 10.1016/j.jcms.2017.08.012, indexed in Pubmed: 28935489.

13. Dolenšek J, Cvetko E, Snoj Ž, et al. Complete occipitalization of the atlas with bilateral external auditory canal atresia. Surg Radiol Anat. 2017; 39(9): 1053–1059, doi: 10.1007/s00276-017-1826-y, indexed in Pubmed: 28214971.

14. Guerram A, Le Minor JM, Renger S, et al. Brief communication: The size of the human frontal sinuses in adults presenting complete persistence of the metopic suture. Am J Phys Anthropol. 2014; 154(4): 621–627, doi: 10.1002/ajpa.22532, indexed in Pubmed: 24888448.

15. Honjo RS, Castro MA, Ferraciolli SF, et al. Cerebellofaciodental syndrome in an adult patient: Expanding the phenotypic and natural history characteristics. Am J Med Genet A. 2021; 185(5): 1561–1568, doi: 10.1002/ajmg.a.62140, indexed in Pubmed: 33645901.

16. Kalla AK, Khanna S, Singh IP, et al. A genetic and anthropological study of atlanto-occipital fusion. Hum Genet. 1989; 81(2): 105–112, doi: 10.1007/BF00293884, indexed in Pubmed: 2912881.

17. Kumar R, Kalra SK, Vaid VK, et al. Craniovertebral junction anomaly with atlas assimilation and reducible atlantoaxial dislocation: a rare constellation of bony abnormalities. Pediatr Neurosurg. 2008; 44(5): 402–405, doi: 10.1159/000149909, indexed in Pubmed: 18703888.

18. Ma L, Song Y. A rare case of Klippel-Feil syndrome associated with atlantoaxial rotatory subluxation, atlanto-occipital fusion, and spina bifida. Spine J. 2015; 15(12): e57–e58, doi: 10.1016/j.spinee.2015.07.459, indexed in Pubmed: 26259886.

19. Macalister A. Notes on the development and variations of the atlas. J Anat Physiol. 1893; 27(Pt 4): 519–542, indexed in Pubmed: 17232056.

20. Mcrae DL, Barnum AS. Occipitalization of the atlas. Am J Roentgenol Radium Ther Nucl Med. 1953; 70(1): 23–46, indexed in Pubmed: 13058024.

21. Menezes AH. Craniocervical developmental anatomy and its implications. Childs Nerv Syst. 2008; 24(10): 1109–1122, doi: 10.1007/s00381-008-0600-1, indexed in Pubmed: 18401563.

22. Natsis K, Lyrtzis C, Totlis T, et al. A morphometric study of the atlas occipitalization and coexisted congenital anomalies of the vertebrae and posterior cranial fossa with neurological importance. Surg Radiol Anat. 2017; 39(1): 39–49, doi: 10.1007/s00276-016-1687-9, indexed in Pubmed: 27192980.

23. O'Rahilly R, Müller F, Meyer DB. The human vertebral column at the end of the embryonic period proper. 2. The occipitocervical region. J Anat. 1983; 136(Pt 1): 181–195, indexed in Pubmed: 6833119.

24. Rice DP. Developmental anatomy of craniofacial sutures. Front Oral Biol. 2008; 12: 1–21, doi: 10.1159/000115028, indexed in Pubmed: 18391492.

25. Sharma DK, Sharma D, Sharma V. Atlantooccipital fusion: prevalence and its developmental and clinical correlation. J Clin Diagn Res. 2017; 11(6): AC01–AC03, doi: 10.7860/JCDR/2017/26183.9999, indexed in Pubmed: 28764139.

26. Stratemeier PH, Jensen SR. Partial regressive occipital vertebra. Neuroradiology. 1980; 19(1): 47–49, doi: 10.1007/BF00369089, indexed in Pubmed: 7354918.

27. Ulcay T, Kamaşak B, Görgülü Ö, et al. A golden ratio for foramen magnum: an anatomical pilot study. Folia Morphol. 2022; 81(1): 220–226, doi: 10.5603/FM.a2021.0018, indexed in Pubmed: 33634836.

28. Vinchon M. The metopic suture: Natural history. Neurochirurgie. 2019; 65(5): 239–245, doi: 10.1016/j.neuchi.2019.09.006, indexed in Pubmed: 31562880.

29. Vu HL, Panchal J, Parker EE, et al. The timing of physiologic closure of the metopic suture: a review of 159 patients using reconstructed 3D CT scans of the craniofacial region. J Craniofac Surg. 2001; 12(6): 527–532, doi: 10.1097/00001665-200111000-00005, indexed in Pubmed: 11711818.

30. Weinzweig J, Kirschner RE, Farley A, et al. Metopic synostosis: Defining the temporal sequence of normal suture fusion and differentiating it from synostosis on the basis of computed tomography images. Plast Reconstr Surg. 2003; 112(5): 1211–1218, doi: 10.1097/01.PRS.0000080729.28749.A3, indexed in Pubmed: 14504503.

31. Yin Yh, Yu Xg, Zhou Db, et al. Three-dimensional configuration and morphometric analysis of the lateral atlantoaxial articulation in congenital anomaly with occipitalization of the atlas. Spine (Phila Pa 1976). 2012; 37(3): E170–E173, doi: 10.1097/BRS.0b013e318227efe7, indexed in Pubmed: 21681136.

32. Zdilla M, Russell M, Koons A, et al. Metopism: a Study of the Persistent Metopic Suture. J Craniofac Surg. 2018; 29(1): 204–208, doi: 10.1097/scs.0000000000004030.

V M

VIA MEDICA

C A S E   R E P O R T

Six-headed coracobrachialis muscle

N. Zielinska[1], Ł. Olewnik[1]

Department of Anatomical Dissection and Donation, Medical University of Lodz, Poland

The coracobrachialis muscle is the smallest muscle of the anterior compartment of the arm. It is responsible for flexion and abduction in the glenohumeral joint. The coracobrachialis muscle is morphologically variable both in its insertion and origin. Moreover, some additional heads or structures may also occur. The present report describes a six-headed coracobrachialis muscle originated as a common junction with the short head of the biceps brachii muscle from the coracoid process. All of these heads insert into the medial surface of the humeral shaft. It is important to note that the musculocutaneous nerve was piercing the fourth belly. Other heads were innervated by branches from the musculocutaneous nerve. Knowledge of the morphological variability of this muscle is essential not only for anatomists but for clinicians as well. (Folia Morphol 2022; 81, 3: 809–813)

Key words: coracobrachialis muscle, morphological variations, compression, additional head, quadriceps femoris, biceps brachii, embryology, clinical implications

INTRODUCTION

Coracobrachialis muscle (CBM) belongs to the anterior group of the arm region. Its origin is located on the coracoid process but is represented by a common junction with the short head of the biceps brachii muscle (SHBB). Its distal attachment is located on the medial surface and border of the body of the humerus. Three parts of the CBM can be distinguished: the proximal, middle and distal part. The last one is the largest and the most superficial [6, 25]. The CBM is innervated by the musculocutaneous nerve (MCN), piercing this muscle in most cases [23]. Oxygenated blood is delivered to the CBM by muscular branches of the brachial artery [25].

The CBM is responsible for flexion and abduction in the glenohumeral joint. Additionally, it is involved in providing stabilisation of the humeral head [15]. However, apart from its anatomical function, progress in science allows surgeons to use the CBM during reconstruction of the breast (after mastectomy) or axillary malformations. The CBM may be also used in the treatment of long-standing facial palsy [10, 12].

There are numerous morphological variations of the CBM. For example, in some cases, an additional head occurs. Olewnik et al. [20] found a four-headed CBM. Another case was described by Catli et al. [7], in which the CBM was represented by three heads. Szewczyk et al. [23] created a classification system basing on the number of heads and its site of proximal attachment. In the available literature, we can also find descriptions of accessory structures connected with the CBM, like the coracobrachialis longus muscle (CBL) [18], coracocapsularis muscle [25], coracobrachialis brevis muscle [18], or the minor coracobrachial muscle of Cruveilhier [9].

The occurrence of an additional structure usually is connected with some kind of compression of neural or vascular elements [11]. One of the examples is the

compression of the MCN, when it courses between two CBM heads [18, 23]. It is responsible for motor innervation of muscles from the anterior compartment of the arm. It may lead to weakness of these muscles and some problems in flexion and abduction in the glenohumeral joint. On the other hand, the MCN provides sensory innervation to the elbow joint, lateral part of the forearm, and lateral part of the hand. In the case of MCN compression, tingling or numbness may occur in these regions [18].

The present report describes a six headed CBM originated as a common junction with the SHBB from the coracoid process. All heads insert into the medial surface of the humeral shaft. It is important to note that the MCN was piercing the fourth head. Knowledge of the morphological variability of this muscle is essential for all clinicians. To our knowledge, this is the first description of such a case.

Ethical approval and consent to participate

The cadaver belonged to the Department of Anatomical Dissection and Donation, Medical University of Lodz, Poland.

CASE REPORT

An 81-year-old body donor (height 183 cm) was subjected to routine anatomical dissection for research and teaching purposes at the Department of Anatomical Dissection and Donation. The donor did not have any surgeries in the upper limb area. The right upper limb was subjected to traditional anatomical dissection [17, 26–28], and a morphological variation of a number of CBM heads was found (Fig. 1).

In the present case, the CBM was represented by six distinct heads which created a proximal attachment with the SHBB as a common junction. Such an origin was located on the coracoid process. In this place, the common junction was 12.25 mm wide and 2.61 mm thick.

All distinct heads had a distal attachment on the medial surface of the humeral shaft. The first head was arising from the common junction, and its length was 32.27 mm. In its proximal part, it was 8.08 mm wide and 2.08 thick. The width of its insertion was 6.85 mm and thickness was 2.55 mm.

The second head was 5.03 mm wide and 2.00 mm thick in the place of division. Its distal attachment was 5.38 mm wide and 2.60 mm thick. The length of this head was 32.29 mm.
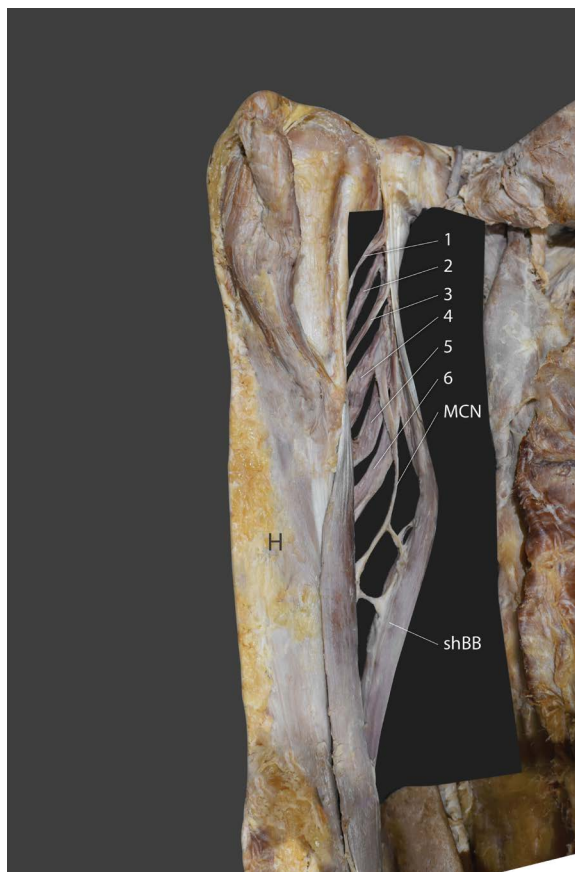
Figure 1. Six-headed coracobrachialis muscle. Right upper limb; H — humerus; shBB — short head of the biceps brachii; MCN — musculocutaneous nerve; 1 — the first head of the coracobrachialis muscle; 2 — the second head of the coracobrachialis muscle; 3 — the third head of the coracobrachialis muscle; 4 — the fourth head of the coracobrachialis muscle; 5 — the fifth head of the coracobrachialis muscle; 6 — the sixth head of the coracobrachialis muscle.

The width of the third head in its proximal part was 5.30 mm. The thickness of this head in the same place was 2.60 mm. The length from this place to the insertion was really similar to the previous one — 33.19 mm. The distal attachment was the widest of all and equalled 15.34 mm. The thickness in this place was 3.67 mm.

The fourth head was 32.84 mm long. In the point of the division, the width was 10.14 mm and the thickness was 4.88 mm. Next, its distal attachment was 10.04 mm wide and 5.67 mm thick (it was the thickest insertion).

The length of the fifth head was 36.18 mm. It was 6.57 mm wide and 1.67 mm thick in its proximal part arising from the common junction with the SHBB. In its attachment to the bone, it was 7.88 mm wide and 3.62 mm thick.

Table 1. Morphometric measurements of individual heads of the coracobrachialis muscle

	1st head	2nd head	3rd head	4th head	5th head	6th head
Length	32.27 mm	32.29 mm	33.19 mm	32.84 mm	36.18 mm	47.92 mm
Origin	Common junction with the SHBB					
Width	12.25 mm					
Thickness	2.61 mm					
Division*						
Width	8.08 mm	5.03 mm	5.30 mm	10.14 mm	6.57 mm	7.13 mm
Thickness	2.08 mm	2.00 mm	2.60 mm	4.88 mm	1.67 mm	2.22 mm
Insertion	Medial surface of the shaft of the humerus					
Width	6.85 mm	5.38 mm	15.34 mm	10.04 mm	7.88 mm	11.36 mm
Thickness	2.55 mm	2.60 mm	3.67 mm	5.67 mm	3.62 mm	3.93 mm

*Division of the common junction for distinct heads of the coracobrachialis muscle; SHBB — short head of the biceps brachii muscle

The last head appeared to be the longest and equalled 47.92 mm. Its width in the proximal part was 7.13 mm, while the thickness in the same place was 2.22 mm. The insertion of this head was 11.36 mm wide and 3.93 mm thick.

It is important to point out that the MCN was piercing the fourth head. In this place, a diameter of the MCN nerve was 6.66 mm. Some small branches from the MCN innervated distinct heads of the CBM.

An electronic calliper (Mitutoyo Corporation, Kawasaki-shi, Kanagawa, Japan) was used to complete all necessary measurements. Each measurement was repeated twice with an accuracy of up to 0.1 mm.

No other morphological variabilities were found. Table 1 shows the morphometric measurements of the presented case.

DISCUSSION

The presence of one additional head has been described in literature many times. Moreover, there are some muscles which may be represented by few accessory bellies, and such case reports usually describe very rare structures. For example, the fifth head of the quadriceps femoris (QF) is nothing special. Willan et al. [24], in 1990, carried out a study in which one additional head of the QF was present in about one third of the limbs. On the other hand, Ruzik et al. [22] found the QF with seven heads. Two additional muscle bellies were composed of tendons, and another one was a tensor of the vastus intermedius [22]. Olewnik et al. [19] created the first classification system of additional heads of the QF, in which the most common (75%) was five-headed QF. Moreover, they found six-headed (21%), seven-headed (2.9%), and eight-headed (1.9%) QF [19].

Another muscle with high morphological variability is the biceps brachii (BB). In the literature, we can find some descriptions of one additional head. For example, Mujahid Ansari et al. [16] found a case of three-headed BB. However, Ballesteros et al. [1] carried out a study in which the results showed that one additional head of the BB is not a rare variant because it occurred in 21% of specimens. Moreover, there are some cases of four-headed BB. Catli et al. [7] detected the BB with two supernumerary heads, originated in various places. A very interesting case was a five-headed BB, described by Je et al. [13]. One supernumerary head originated from the anterior surface of the distal tendinous part of the pectoralis major muscle. The other two originated from the body of the humerus [13].

Coming back to the CBM, the situation is similar. There are some descriptions of one extra head of the CBM, like this found by Gabrelotti et al. [11]. To confirm the statement that one additional head is usually nothing special, we should look at the results of the study carried out by Szewczyk et al. [23]. It turned out that the CBM was represented by a double muscle belly in 42.6% of specimen. Catli et al. [7] described a rare variant of the CBM, which was characterized by two additional heads. In the study carried out by Szewczyk et al. [23], we can also find a description of such a structure, and its prevalence was around 8% (8/101 upper limbs). Two of these supernumerary heads originated from the coracoid process and the last one originated from the SHBB [23]. There is also a description of four-headed CBM, and such a structure has not been found by Szewczyk et al. [23]. The CBM with additional three heads was described

by Olewnik et al. [21]. All heads were innervated by the MCN [21].

Our present case is something like the eight-headed QF or five-headed BB. It originated as a common junction with the SHBB from the coracoid process. All six heads had their distal attachment on the medial surface of the humeral shaft. The reason for the occurrence of such a complex structure is astonishing and most likely is associated with changes occurring during the embryological growth. In the first stage, brachialis muscle, BB, and CBM muscles are tightly connected in a common pre-muscle mass. When embryos achieve the length of 14 to 16 mm, these three muscles can be recognized as distinct structures [2–4]. Probably, additional heads of the CBM are formed at this stage of embryonic development (14–16 mm) or maybe this embryological process lasts longer and the single mass of the CBM divides into smaller parts recognized as distinct supernumerary heads.

Looking for embryological development of QF and its additional heads, our hypothesis seems to make sense. QF is represented by a single mass overlying the anterolateral region when embryo is 11 mm long. Then the differentiation occurs and in the 20-mm embryo four distinct structures of the QF may be distinguished [2–4]. Similarly, additional heads may be created from 11 to 19 mm of embryonal length. However, there is also a possibility that this process occurs later, because the muscle mass is smaller than that observed in standard parts of the QF. However, our statement is only a hypothesis, so a further embryological research should be performed to confirm it.

The presence of an additional head is usually connected with some clinical implications. A supernumerary head of the CBM may compress the MCN, especially when this nerve courses between two bellies [18, 23]. The MCN is responsible for motor innervation of muscles from the anterior compartment of the arm, so its entrapment may cause some problems with flexion and abduction in the glenohumeral joint. Structures like the elbow joint, lateral parts of the forearm and hand receive sensory innervation from the MCN, so the compression of the MCN may manifest in tingling or numbness [18]. However, in our case, the MCN was piercing the fourth head of the CBM, and in our opinion, the possibility of entrapment is lower.

The occurrence of an extra head of the CBM may be important not only for anatomists but also for clinicians. Upper limb injuries are very common, which

is connected with various (sometimes really invasive) surgical operations. For that reason, some results of computed tomography or magnetic resonance showing such variations may confuse a surgeon. It is even worse if the change is detected during an operation. This may cause some complications or prolong the surgery [14]. Moreover, if additional heads occur only unilaterally, it can result in asymmetry between right and left side, and sometimes it may be wrongly recognized as some kind of tumour [8].

As mentioned above, not only variations connected with the number of heads take place. For example, Szewczyk et al. [23] classified the CBM, basing on its different place and representation of insertion, and distinguished two types. The first one was represented by a single insertion onto the distal 1/3 of the humerus. In turn, the second one was characterized by a double insertion: one to the distal 1/3 of the humerus (as the previous one), and one which created fusion with the medial head of the triceps brachii [23]. Moreover, they also divided the CBM basing on the course of the MCN. Type I was represented by the nerve piercing the muscle belly. Type II was represented by the MCN passing between heads of the CBM [23]. In the present case, only the fourth head was pierced by this nerve and some small branches innervated other heads.

There are also some interesting muscles connected with the CBM. For example, the CBM brevis, whose origin is located on the anterior surface of the coracoid process. It may insert onto the lesser tuberosity or surgical neck of the humerus [5]. A special kind of the CBM brevis is the coracocapsularis muscle, whose proximal attachment is fused with the capsule of the shoulder joint [25]. Another example of high variability of the CBM is coracobrachialis minor secundus which is characterized by a connection with the pectoralis major tendon [6], or coracobrachial muscle of Cruveilhier, also represented by fusion, but with the latissimus dorsi muscle [9]. A really rare structure is a CBM longus whose point of insertion may be variable [18].

Summing up this section, due to high morphological variability of the CBM, there is a possibility to find some interesting structures which have not been described in the literature yet.

CONCLUSIONS

The CBM is associated with high morphological variability. All of these variations seem to be impor-

tant not only for anatomists but also for clinicians. The most possible reason for the occurrence of the six-headed coracobrachialis muscle presented in this case report is an improper embryological development; however, further embryological investigations should be performed to confirm this phenomenon.

Conflict of interest: None declared

REFERENCES

1. Ballesteros LE, Forero PL, Buitrago ER. Evaluation of additional head of biceps brachii: a study with autopsy material. Folia Morphol. 2014; 73(2): 193–198, doi: 10.5603/FM.2014.0028, indexed in Pubmed: 24902098.
2. Bardeen C. Studies of the development of the human skeleton. Am J Anat. 1905: 265–302.
3. Bardeen C. Development and variation of the nerves and the musculature of the inferior extremity and of the neighboring regions of the trunk in man. Am J Anat. 2005; 6(1): 259–390, doi: 10.1002/aja.1000060108.
4. Bardeen C. Development and variation of the nerves and the musculature of the inferior extremity and of the neighboring regions of the trunk in man. Am J Anat. 2005; 6(1): 259–390, doi: 10.1002/aja.1000060108.
5. Bauones S, Moraux A. The accessory coracobrachialis muscle: ultrasound and MR features. Skeletal Radiol. 2015; 44(9): 1273–1278, doi: 10.1007/s00256-015-2153-1, indexed in Pubmed: 25924580.
6. Bergman R, Afifi A, Miyauchi R. Illustrated encyclopedia of human anatomic variations. Anatomy Atlas 2017.
7. Catli MM, Ozsoy U, Kaya Y, et al. Four-headed biceps brachii, three-headed coracobrachialis muscles associated with arterial and nervous anomalies in the upper limb. Anat Cell Biol. 2012; 45(2): 136–139, doi: 10.5115/acb.2012.45.2.136, indexed in Pubmed: 22822469.
8. Cheema P, Singla R. Low incidence of the third head of the biceps brachii in the north indian population. J Clin Diagnostic Res. 2012; 5: 1323–1326.
9. Cruveilhier J. Traité d'anatomie descriptive I. Asselin, Paris 1862.
10. El-Naggar MM, Al-Saggaf S. Variant of the coracobrachialis muscle with a tunnel for the median nerve and brachial artery. Clin Anat. 2004; 17(2): 139–143, doi: 10.1002/ca.10213, indexed in Pubmed: 14974102.
11. Garbelotti SA, Marques SR, Rocha PR, et al. An unusual case of accessory head of coracobrachialis muscle involving lateral cord of brachial plexus and its clinical significance. Folia Morphol. 2017; 76(4): 762–765, doi: 10.5603/FM.a2017.0033, indexed in Pubmed: 28353299.
12. Georgiev GP, Tubbs RS, Landzhov B. Coracobrachialis longus muscle: humeroepitrochlearis. Cureus. 2018; 10(5): e2615, doi: 10.7759/cureus.2615, indexed in Pubmed: 30027007.
13. Je SS, Park B, Kim J, et al. Five-headed biceps brachii muscle with a rare origin from the tendon of pectoralis major muscle. Anat Sci Int. 2016; 91(1): 110–113, doi: 10.1007/s12565-015-0288-8, indexed in Pubmed: 26012790.
14. Kopuz C, Içten N, Yildirim M. A rare accessory coracobrachialis muscle: a review of the literature. Surg Radiol Anat. 2003; 24(6): 406–410, doi: 10.1007/s00276-002-0079-5, indexed in Pubmed: 12652369.
15. Moore KL, Agur A, Dalley A. Clinically Oriented Anatomy. Lippincott Williams&Wilkins, 2013.
16. Mujahid Ansari M, Gupta UK, Laique Ahmed M, et al. Third head of biceps brachii with anatomical consideration and clinical implication: a case report. J Evol Med Dent Sci. 2013; 2(6): 630–634, doi: 10.14260/jemds/314.
17. Olewnik Ł, Karauda P, Gonera B, et al. Impact of plantaris ligamentous tendon. Sci Rep. 2021; 11(1): 4550, doi: 10.1038/s41598-021-84186-w, indexed in Pubmed: 33633305.
18. Olewnik Ł, Paulsen F, Tubbs RS, et al. Potential compression of the musculocutaneous, median and ulnar nerves by a very rare variant of the coracobrachialis longus muscle. Folia Morphol. 2021; 80(3): 707–713, doi: 10.5603/FM.a2020.0085, indexed in Pubmed: 32844391.
19. Olewnik Ł, Tubbs RS, Ruzik K, et al. Quadriceps or multiceps femoris?-Cadaveric study. Clin Anat. 2021; 34(1): 71–81, doi: 10.1002/ca.23646, indexed in Pubmed: 32644202.
20. Olewnik Ł, Zielinska N, Karauda P, et al. The co-occurrence of a four-headed coracobrachialis muscle, split coracoid process and tunnel for the median and musculocutaneous nerves: the potential clinical relevance of a very rare variation. Surg Radiol Anat. 2021; 43(5): 661–669, doi: 10.1007/s00276-020-02580-x, indexed in Pubmed: 32979058.
21. Olewnik Ł, Zielinska N, Karauda P, et al. The co-occurrence of a four-headed coracobrachialis muscle, split coracoid process and tunnel for the median and musculocutaneous nerves: the potential clinical relevance of a very rare variation. Surg Radiol Anat. 2021; 43(5): 661–669, doi: 10.1007/s00276-020-02580-x, indexed in Pubmed: 32979058.
22. Ruzik K, Waśniewska A, Olewnik Ł, et al. Unusual case report of seven-headed quadriceps femoris muscle. Surg Radiol Anat. 2020; 42(10): 1225–1229, doi: 10.1007/s00276-020-02472-0, indexed in Pubmed: 32318799.
23. Szewczyk B, Polguj M, Paulsen F, et al. A proposal for a new classification of coracobrachialis muscle morphology. Surg Radiol Anat. 2021; 43(5): 679–688, doi: 10.1007/s00276-021-02700-1, indexed in Pubmed: 33564931.
24. Willan PL, Mahon M, Golland JA. Morphological variations of the human vastus lateralis muscle. J Anat. 1990; 168: 235–239, indexed in Pubmed: 2323995.
25. Wood J. On human muscular variations and their relation to comperative anatomy. J Anat Physiol. 1867: 44–59.
26. Zielinska N, Olewnik Ł, Karauda P, et al. A very rare case of an accessory subscapularis muscle and its potential clinical significance. Surg Radiol Anat. 2021; 43(1): 19–25, doi: 10.1007/s00276-020-02531-6, indexed in Pubmed: 32656573.
27. Zielinska N, Szewczyk B, Tubbs RS, et al. Coexistence of two accessory flexor pollicis longus heads or coexistence of two-headed flexor pollicis longus with an unrecognized anatomical structure? Surg Radiol Anat. 2021; 43(5): 763–769, doi: 10.1007/s00276-021-02721-w, indexed in Pubmed: 33656594.
28. Zielinska N, Tubbs RS, Podgórski M, et al. The subscapularis tendon: A proposed classification system. Ann Anat. 2021; 233: 151615, doi: 10.1016/j.aanat.2020.151615, indexed in Pubmed: 33068734.

CONTENTS

←

*Cover picture: Anterior view of cerebellum. Bilateral origin of posterior inferior cerebellar artery from the vertebral artery's extraspinal segment.
The lower loop of the tonsilomedullary segment is related with the tonsils' inferior surface; BA — basilar artery; OM — medulla oblongata;
RCH — right cerebellar hemisphere; RVA — right vertebral artery; RPICA — right posterior inferior cerebellar artery; LPICA — left posterior inferior
cerebellar artery; double arrow — double left anterior inferior cerebellar artery; triangular asterisk — anterior inferior cerebellar artery. For details see:
L.E. Ballesteros-Acuña et al., Folia Morphol 2022; 81, 3: 559–566.*